UCRL 17299

cy 2
(c.2 mcg)

NUCLEAR CHEMISTRY
Annual Report 1966

TWO-WEEK LOAN COPY

This is a Library Circulating Copy which may be borrowed for two weeks. For a personal retention copy, call Tech. Info. Division, Ext. 5545

Lawrence Radiation Laboratory
University of California Berkeley

UCRL-17299
cy 2
(c.2 mcg)

DISCLAIMER

This document was prepared as an account of work sponsored by the United States Government. While this document is believed to contain correct information, neither the United States Government nor any agency thereof, nor the Regents of the University of California, nor any of their employees, makes any warranty, express or implied, or assumes any legal responsibility for the accuracy, completeness, or usefulness of any information, apparatus, product, or process disclosed, or represents that its use would not infringe privately owned rights. Reference herein to any specific commercial product, process, or service by its trade name, trademark, manufacturer, or otherwise, does not necessarily constitute or imply its endorsement, recommendation, or favoring by the United States Government or any agency thereof, or the Regents of the University of California. The views and opinions of authors expressed herein do not necessarily state or reflect those of the United States Government or any agency thereof or the Regents of the University of California.

UCRL-17299
UC-4 Chemistry
TID-4500 (49th Ed.)

UNIVERSITY OF CALIFORNIA
Lawrence Radiation Laboratory
Berkeley, California

AEC Contract No. W-7405-eng-48

NUCLEAR CHEMISTRY DIVISION ANNUAL REPORT, 1966

January 1967

I. Perlman, Director, Nuclear Chemistry Division
Editors: B. B. Cunningham, F. L. Reynolds, and F. S. Stephens

Work done under the auspices of the U. S. Atomic Energy Commission

Printed in the United States of America
Available from
Clearinghouse for Federal Scientific and Technical Information
National Bureau of Standards, U.S. Department of Commerce
Springfield, Virginia 22151
Price: Printed Copy $3.00; Microfiche $0.65

NUCLEAR CHEMISTRY DIVISION ANNUAL REPORT, 1966

Contents

A. NUCLEAR SPECTROSCOPY

1. Table of Isotopes (C. M. Lederer, J. M. Hollander, and I. Perlman) 1

2. Energy Levels of ^{237}Np. I. The α Decay of ^{241}Am (C. M. Lederer, J. K. Poggenburg, F. Asaro, J. O. Rasmussen, and I. Perlman) 4

3. New Transitions and Precise Energy and Intensity Determinations in the Decay of ^{177m}Lu (A. J. Haverfield, F. M. Bernthal, and J. M. Hollander) 9

4. g Factor of the 243-keV Level in ^{86}Y (William J. Treytl and E. Matthias . . . 17

5. Decay of ^{139}Nd (J. Gilat and William J. Treytl) 20

6. Neutron-Deficient Actinium Isotopes (William J. Treytl, E. K. Hyde, and Kalevi Valli) 23

7. Alpha Decay of Neutron-Deficient Radium Isotopes (Kalevi Valli, William T. Treytl, and Earl K. Hyde) 24

8. Alpha Decay of Neutron-Deficient Francium Isotopes (Kalevi Valli, Earl K. Hyde, and William J. Treytl) 28

9. Alpha-Decay Properties of Neutron-Deficient Isotopes of Emanation (Kalevi Valli, Matti J. Nurmia, and Earl K. Hyde) 30

10. Alpha Decay of Neutron-Deficient Astatine Isotopes (William J. Treytl and Kalevi Valli) 32

11. New Isotopes: ^{11}Li, ^{14}B, and ^{15}B (A. M. Poskanzer, S. W. Cosper, Earl K. Hyde, and Joseph Cerny) 37

12. A New Californium Isotope, ^{242}Cf (Torbjorn Sikkeland and Albert Ghiorso) . . . 41

13. Decay Properties of ^{243}Cf and ^{244}Cf (Torbjorn Sikkeland, Albert Ghiorso, Jaromir Maly, and Matti Nurmia). 42

14. Isotopes of Element-102 with Mass 251 to 257 (Albert Ghiorso, Torbjorn Sikkeland, and Matti J. Nurmia) 43

15. The Application of Semiconductor x-Ray Detectors to the Study of Heavy-Ion Reactions (H. R. Bowman, J. B. Wilhelmy, R. L. Watson, R. C. Jared, and S. G. Thompson) 46

16. Ground-State (Quasi-) Rotational Levels in Light Os, Pt, and Hg Nuclei (J. Burde, R. M. Diamond, and F. S. Stephens). 48

17. Collective Excitations in Neutron-Deficient Barium, Xenon, and Cerium Isotopes (Jack E. Clarkson, R. M. Diamond, F. S. Stephens, and I. Perlman) 53

18. The Rotational States of ^{184}Os, ^{186}Os, and ^{188}Os (J. O. Newton, F. S. Stephens, and R. M. Diamond) 60

19. Nuclear Alignment in Heavy-Ion Reactions (R. M. Diamond, E. Matthias, J. O. Newton, and F. S. Stephens) 64

20. Angular Distributions of Gamma Rays Emitted in ^{197}Au(p, 2n)^{196}Hg and ^{197}Au(p, 4n)^{194}Hg Reactions (T. Yamazaki and D. L. Hendrie) 67

21. Tables of Coefficients for Angular Distribution of γ Rays From Aligned Nuclei (T. Yamazaki) 69

22. Gamma-Vibrational Bands in ^{182}Os and ^{184}Os (T. Yamazaki and D. L. Hendrie) . 71

23. Levels of ^{188}Os Populated by ^{188}Re and ^{188}Ir (T. Yamazaki, J. Sato, Y. Yokoyama, S. Baba, H. Ikegami, and M. Sakai) 74

24. The Pulsed Beam Method for the Systematic Observation of Isomeric States in the 3 ~ 500 nsec Range Populated by (Particle, xn) Reactions (T. Yamazaki and G. T. Ewan) 76

25. Isomeric States in Po and Sn Isotopes (T. Yamazaki, G. T. Ewan, and S. G. Prussin) 78

B. NUCLEAR REACTIONS AND SCATTERING

1. Polarization in p-^{3}He Scattering Between 10 and 20 MeV (W. F. Tivol, D. J. Clark, H. E. Conzett, J. S. C. McKee, E. Shield, and R. J. Slobodrian) . . 83

2. Scattering of Polarized Protons by Deuterium in the Energy Region 10 to 20 MeV (J. S. C. McKee, D. J. Clark, R. J. Slobodrian, and W. F. Tivol) 84

3. The 2p Final-State Interaction in the ^{3}He(^{3}He, α)2p Reaction (R. J. Slobodrian, D. J. Clark, J. S. C. McKee, W. F. Tivol, and T. A. Tombrello) 86

4. Proton-Proton Scattering Between 4.2 and 10 MeV and the $^{1}S_{0}$ Shape-Dependent Scattering Parameters (R. J. Slobodrian, H. E. Conzett, E. Shield, and W. F. Tivol) 88

5. Determination of the Neutron-Neutron Scattering Length from the Reaction T(d, ^{3}He)2n (E. Baumgartner, H. E. Conzett, E. Shield, and R. J. Slobodrian 91

6. Proton-Neutron Two-Particle Excited States of $(d_{5/2})^{2}_{5+}$ Configurations in Light Nuclides (C. C. Lu and B. G. Harvey) 95

7. The ^{12}C(^{3}He, p)^{14}N Reaction at E(^{3}He) = 20 MeV (Nolan F. Mangelson and Bernard G. Harvey) 97

8. Excited States in ^{6}Be and ^{10}C (Nolan F. Mangelson, Fay Ajzenberg-Selove, Mary F. Reed, and Chi Chang Lu) 106

9. The Masses and Excited States of ^{24}Al and ^{28}P (Nolan F. Mangelson, Mary F. Reed, Chi Chang Lu, and Fay Ajzenberg-Selove) 109

10. A Study of Mass 5 and 7 Nuclei by (p, t) and (p, ^{3}He) Reactions on ^{7}Li and ^{9}Be (J. Cerny, C. Détraz, and R. H. Pehl) 112

11. Mass of ^{8}He from the Four-Neutron Transfer Reaction ^{26}Mg(α, ^{8}He)^{22}Mg (J. Cerny, S. W. Cosper, G. W. Butler, R. H. Pehl, F. S. Goulding, D. A. Landis, and C. Détraz) 114

12. A J Dependence in the (^{3}He, α) Reaction Confirming New Spectroscopic Assignments in ^{14}N and ^{13}C (Gordon C. Ball and Joseph Cerny) 118

13. The ^{14}N(^{3}He, t)^{14}O Reaction and Excited Isospin Triads in Mass 14 (Gordon C. Ball and Joseph Cerny) 121

14. Nuclear Reaction Q Values (C. Maples, G. W. Goth, and J. Cerny) 123

15. The ^{24}Mg(α, α') Reaction at 50 MeV (D. L. Hendrie, B. G. Harvey, J. Mahoney, and J. R. Meriwether) 124

16. Production of the 3+ Unnatural-Parity State in ^{24}Mg by Inelastic α Scattering (Mary F. Reed, Bernard G. Harvey, and David L. Hendrie) . . . 127

17. Excitation of Rotational Levels in ^{152}Sm and ^{154}Sm (B. G. Harvey, D. L. Hendrie, O. N. Jarvis, J. Mahoney, and J. Valentin) 130

18. Elastic Scattering of 55-MeV Protons from ^{3}He (D. L. Hendrie, B. G. Harvey, O. N. Jarvis, J. Mahoney, and W. Tivol) 133

*

C. NUCLEAR STRUCTURE THEORY

1. The $^{1}S_{0}$ p-p Scattering Parameters Obtained from a Reanalysis of Experimental Data (R. J. Slobodrian) 135

2. Small-Angle High-Energy Scattering by Deuterons (Victor Franco) 139

3. High-Energy Deuteron-Deuteron Cross Sections (Victor Franco) 141

4. High-Energy Deuteron Cross Sections: Charge-Exchange Effects (Victor Franco and Roy J. Glauber) 142

5. Double Scattering in High-Energy Elastic Collisions with Deuterons (Victor Franco and Ernest Coleman) 144

6. Inelastic Scattering (Norman K. Glendenning) 146

7. Test of a Microscopic Description of Nickel Isotopes by Inelastic Proton Scattering (Norman K. Glendenning, B. G. Harvey, D. L. Hendrie, O. N. Jarvis, and J. Mahoney) 147

8. Analysis of the $^{208}Pb(p, t)$ Reaction (Norman K. Glendenning) 149

9. Calculations of the Flattening of Idealized Nuclei During Head-On Collisions (Jaromir Maly and James Rayford Nix) 154

10. Predictions of New Magic Regions and Masses for Superheavy Nuclei from Calculations with Realistic Shell-Model Single-Particle Hamiltonians (Heiner Meldner) 157

11. Shell Structure and Nuclear Level Densities (Arnold Gilbert) 160

D. FISSION

1. Calculations in the Liquid-Drop Theory of Nuclear Fission (James Rayford Nix) . 165

2. The Normal Modes of Oscillation of a Uniformly Charged Drop About its Saddle-Point Shape (James Rayford Nix) 167

3. Long-Range Particles of Z = 1 to 4 Emitted During the Spontaneous Fission of ^{252}Cf (S. W. Cosper, J. Cerny, and R. C. Gatti) 170

4. Experimental Determination of First-Chance-Fission Probability in ^{4}He-Induced Fission of Some Tungsten Isotopes (Luciano G. Moretto, Raymond C. Gatti, and Stanley G. Thompson) 173

5. Possible Evidence of Large Pairing Effects at the Saddle Point of Some Po and At Isotopes (Luciano G. Moretto, Raymond C. Gatti, John R. Huizenga, John O. Rasmussen, and Stanley G. Thompson) 175

6. Studies of Fragment Angular Distributions in the Fission of ^{209}Bi and ^{238}U Induced by α Particles of Energies up to 115 MeV (S. S. Kapoor, H. Baba, and S. G. Thompson) 178

* Excitation of Dipole States by Inelastic α Scattering (J. M. Moss and B. G. Harvey) Misplaced in Sec. I. 8 - see page 336.

7. Kinetic Energy and Mass Distributions from the Fission of Nuclei Lighter Than Radium (F. Plasil, D. S. Burnett, H. C. Britt, and S. G. Thompson) . 181

8. Electron Binding Energies for Highly Ionized Fission Fragment Atoms (R. L. Watson and J. O. Rasmussen) 184

9. x-Ray, γ-Ray Coincidence Measurements on Fission Products (J. B. Wilhelmy, S. G. Thompson, and J. O. Rasmussen) 189

10. An Empirical Formula for the Number of ^{252}Cf Spontaneous-Fission Neutrons as a Function of the Fission Mass Pair and the Total Kinetic Energy (Eiko Takekoshi and Stanley G. Thompson) 194

E. HYPERFINE INTERACTIONS

1. Nuclear Magnetic Resonance in Polarized Nuclei (E. Matthias and R. J. Holliday) 197

2. Nuclear Magnetic Resonance Detected by Perturbed Angular Correlations (E. Matthias and B. A. Olsen) 199

3. Temperature Dependence of Hyperfine Fields of ^{111}Cd and ^{99}Ru in Nickel (S. S. Rosenblum, E. Matthias, and D. A. Shirley) 201

4. Digital Analysis of Perturbed Angular Correlations (E. Matthias and D. A. Shirley) 206

5. Nuclear Magnetic Resonance in the 75-keV State of ^{100}Rh Detected by Angular Correlations (E. Matthias, N. Edelstein, H. J. Körner, and D. A. Shirley) 209

6. Detection of Nuclear Magnetic Resonance in a 235-nsec Nuclear State by Perturbed Angular Correlations (E. Matthias, D. A. Shirley, M. P. Klein, and N. Edelstein) 212

7. An Investigation of the Hyperfine Structure of Trivalent ^{158}Tb by Nuclear Alignment and Paramagnetic Resonance: Determination of the Spin, Dipole Moment, and Quadrupole Moment of ^{158}Tb (J. A. Barclay, W. C. Easley, and D. A. Shirley) 215

8. The Nuclear Spin of ^{249}Bk from the Hyperfine Structure in its Emission Spectrum (Earl F. Worden, E. K. Hulet, Ronald Lougheed, and John G. Conway) 218

F. MASS SPECTROSCOPY

1. Excitation by Electron Impact of Long-Lived States in Molecules (R. Clampitt and Amos S. Newton) 221

2. A Search for Auto-Ionizing States of Highly Excited Ions of the Noble Gases (Amos S. Newton, A. F. Sciamanna, and R. Clampitt) 222

3. Surface-Induced Transitions in Highly Excited Noble Gas Ions and Quasi-Metastable Peaks in the Mass Spectra of the Noble Gases (Amos S. Newton, A. F. Sciamanna, and R. Clampitt) 224

G. CHEMISTRY

1. Some Chemical Properties of Element 97 (J. R. Peterson and B. B. Cunningham) 231

2. Chemical Effects on Core Electron Binding Energies in Iodine and Europium (C. S. Fadley, S. B. M. Hagstrom, J. M. Hollander, D. A. Shirley, and M. P. Klein) 233

3. Extraction of Metal Pyridine Azides. Spectrophotometric Determination of Copper, Nickel, and Palladium (Ray G. Clem and E. H. Huffman) . . . 238

4. Isotopic Oxygen Analysis by ^{3}He Activation: Excitation Function for the Reaction $^{18}O(^{3}He, p)^{20}F$ (J. F. Lamb, D. M. Lee, and S. S. Markowitz) 240

5. Preparation of Oxygen Standards for Charged-Particle Activation Analysis (J. F. Lamb, D. M. Lee, and S. S. Markowitz) 242

6. An Improved Correlation for the Heats of Formation of Inorganic Compounds (Waseem Brelvi and L. A. Bromley) 245

7. The Absorption Spectra of Bk in Solution (R. G. Gutmacher, E. K. Hulet, Ronald Lougheed, John G. Conway, W. T. Carnall, Donald Cohen, T. K. Keenan, and R. D. Baybarz) 245

8. The Solution Absorption Spectrum of Cf^{3+} (John G. Conway, S. Fried, R. M. Latimer, R. McLaughlin, R. G. Gutmacher, W. T. Carnall, and P. Fields) 246

9. Energy Levels of Single-Crystal Erbium Oxide (K. Rajnak and John G. Conway) . 247

10. Optical Spectra of Tripositive Curium-244 in Lanthanum Trichloride (J. B. Gruber, W. R. Cochran, John G. Conway, and A. T. Nicol) 247

11. Optical and Electron Paramagnetic Resonance Spectroscopy of Cm in CaF_2 (N. Edelstein, W. Easley, and R. McLaughlin) 248

12. Optical Spectra of Pu in CaF_2 (R. McLaughlin, R. White, and N. Edelstein) . . 250

13. Atomic Beam Study of the Stark Effect in the Cesium and Rubidium D Lines (Douglas McColm, Richard Marrus, and Joseph Yellin) 253

14. Molecular Beam Electric Resonance Experiments on LiF, KCl, RbF, and CsF (Alvin J. Hebert, Craig D. Hollowell, Frank J. Lovas, and Kenneth Street, Jr.) 254

15. Dependence of Laser Axial Beat-Note Amplitude on Zeeman Separation (Lloyd Armstrong, Jr., Dolores Ali, and Tetsuo Hadeishi) 256

16. The Crystal and Molecular Structure of Tetraphenylarsonium cis-Diaquotetrachlororuthenate Monohydrate (Ted E. Hopkins, Allan Zalkin, David H. Templeton, and Martyn G. Adamson) 258

17. The Crystal Structure of Cesium Aquopentachlororuthenate (Ted E. Hopkins, Allan Zalkin, David H. Templeton, and Martyn G. Adamson) 261

18. The Crystal Structure of $(B_9C_2H_{11})Re(CO)_3Cs$ (Allan Zalkin, Ted E. Hopkins, and David H. Templeton) 263

19. The Crystal Structure of Chlorothiodiazyl Chloride, $S_3N_2Cl_2$ (Allan Zalkin, Ted E. Hopkins, and David H. Templeton) 267

20. The Atomic Parameters in the Lanthanum Trifluoride Structure (Allan Zalkin, David H. Templeton, and Ted E. Hopkins) 270

21. Studies of Oxygen-Initiated Pyrolysis of Hydrocarbons (Edwin D. Hausmann and C. Judson King) 274

22. Chemical Evidence for Main-Chain Scission as a Major Decomposition Mode in the Radiolysis of Solid Peptides (Warren M. Garrison, Michael E. Jayko, Boyd M. Weeks, Harvey A. Sokol, and Winifred Bennett-Corniea) 275

23. Identification of a Specific Mode of Oxidation in the Radiolysis of the Purine Bases in Oxygenated Aqueous Solution (John Holian and Warren M. Garrison) 278

24. Radiation-Induced Oxidation of Cytosine and Uracil in Aqueous Solutions of Cu^{2+} (John Holian and Warren M. Garrison) 279

25. The Radiation-Induced Oxidation of Peptides in Aqueous Solution (Harriette L. Atkins, Winifred Bennett-Corniea, and Warren M. Garrison) . 281

H. SEPARATION AND PURIFICATION PROCESSES

1. Statistical Thermodynamics of Particulate Fluidization (James A. Saxton and Theodore Vermeulen) 285

2. Heat and Mass Transfer Between Fluid Phases (Charles H. Byers, Michael W. Clark, and C. Judson King) 287

3. Fluid-Phase Mass Transfer in Dialysis (Richard D. Newman and C. R. Wilke) . 289

4. Liquid Diffusivities in the Glycol Water System (Charles H. Byers and C. Judson King) 292

5. Axial Dispersion in Liquid Flow Through Packed Beds (Steven F. Miller, C. Judson King, and Theodore Vermeulen) 293

6. Filtration Studies with Ultrafine Particles (Ashok Bhagat and C. R. Wilke) . . 295

7. The Dispersion of Bacteria (Francis G. Rust and Charles R. Wilke). 297

8. An Economic Study of Sulfate Removal from Brines with Bacteria Based on a Hypothetical Design (Ronald H. Charron and Charles R. Wilke) 302

I. INSTRUMENTATION

1. Cyclotron Beam Diagnostics and Instrumentation (D. J. Clark) 305

2. Machine Development at the Berkeley 88-Inch Cyclotron (R. Burger, D. J. Clark, E. Close, and H. Kim) 309

3. Regenerative Beam Extraction for the Berkeley 88-Inch Cyclotron (D. J. Clark, E. Close, H. A. Grunder, Hogil Kim, P. Pellissier, and B. H. Smith) 317

4. Regenerative Beam Extraction (Hogil Kim) 321

5. Influence of Cyclotron Beam Properties on Experiments (H. E. Conzett) . . . 325

6. Mechanical Design of a Regenerative Deflector for the Berkeley 88-Inch Cyclotron (Don Elo, A. R. Carneiro, Fred Bierlein, and J. L. Wong) . . 329

7. Heavy-Ion Identification Using the Power Law Technique (J. Cerny, S. W. Cosper, G. W. Butler, H. Brunnader, R. L. McGrath, and F. S. Goulding) . . . 335

8. Excitation of Dipole States by Inelastic α Scattering (J. M. Moss and B. G. Harvey) 336

9. Automatic Control of the Trim-Coil Power Supplies at the Berkeley 88-Inch Cyclotron (David R. Struthers) 339

10. A New Microcalorimeter for Thermodynamic Measurements on Actinide Elements (Lester R. Morss and Dennis K. Fujita) 342

11. A Magnetic Steering Device for Electron Coincidence Experiments (R. L. Watson, H. R. Bowman, S. G. Thompson, and J. O. Rasmussen) 343

12. Detection of High Energy Protons by Thin-Window Lithium-Drifted Germanium Counters (R. H. Pehl, D. A. Landis, and F. S. Goulding) . . 347

13. Germanium Radiation Detector and High Resolution System Development (R. H. Pehl, R. C. Cordi, F. S. Goulding, D. A. Landis, W. A. Maertens, D. F. Malone, and G. I. Saucedo) 348

14. High-Voltage Lithium-Drifted Silicon Detectors (Robert P. Lothrop and F. S. Goulding) 349

15. Liquid Nitrogen Cooled Cryosorption Vacuum Pump (R. Hintz and R. Parsons) 353

16. A Semiconductor Detector Cryostat (C. Eugene Miner) 355

17. High Resolution β- and γ-Ray Spectrometer (Emanuel Elad and Michiyuki Nakamura) 357

18. A Low-Noise Distributed Amplifier Using Field-Effect Transistors (Michiyuki Nakamura, Frederick E. Vogelsberg, and W. Larry Crowder) 358

19. An Inexpensive Special-Purpose Computer for Linking Pulse-Height Analyzers with a Digital Incremental Plotter (Richard LaPierre and Michiyuki Nakamura) 359

20. A 35-GHz Superheterodyne Electron Spin Resonance Spectrometer System (Warren Easley and Richard LaPierre) 359

21. An Investigation into the Characteristics of a Helium-Neon cw Laser for Telemetry Applications (Richard LaPierre and Ron Zane) 360

22. PUZZLE: A Program for Computer-Aided Design of Printed-Circuit Layout (D. A. Wilber and Ron Zane) 362

23. Four General-Purpose Modular Instruments (Ron Zane) 364

24. Mössbauer-Effect Instrumentation (Ron Zane) 366

25. The Electronic Sizing and Counting of Bacteria (Victor H. Edwards and Charles R. Wilke) 367

J. THESIS ABSTRACTS

1. Nuclear Spectroscopic Studies of Some Very Heavy Odd-Mass Nuclides (Ph. D. - Ahmad) 371

2. Some of the Physical Properties of Curium and Protactinium Metals and Protactinium Tetrafluoride (Ph. D. - Bansal) 372

3. Filtration Studies with Ultrafine Particles (M. S. - Bhagat) 372

4. An Improved Correlation for the Heats of Formation of Inorganic Compounds (M. S. - Brelvi) 373

5. Convective Transfer Processes in Laminar Gas-Liquid Channel Flow (Ph. D. - Byers) 373

6. An Economic Study of Sulfate Removal from Brines with Bacteria Based on a Hypothetical Design
(M. S. - Charron) 374

7. Environmental Effects on the Decay Constant of $^{90m_1}Nb$
(Ph. D. - Cooper) 374

8. The Absorption Spectrum of Cf^{3+} and Crystallography of Californium Sesquioxide and Californium Trichloride
(Ph. D. - Green) 375

9. I. The Measurement of Internal Conversion Coefficients Utilizing Semiconductor Detectors
II. Decay Scheme Studies of the Odd-Mass Gold Isotopes
(Ph. D. - Haverfield) 376

10. The Molecular-Beam Electric-Resonance Spectra of LiF, NaF, and KCl
(Ph. D. - Hollowell) 376

11. Fission Properties of Some Elements Below Radium
(Ph. D. - Khodai-Joopari) 377

12. Fluid Phase Mass Transfer in Dialysis
(M. S. - Newman) 377

13. The X-Ray Crystallographic Structure Determination of Various Compounds
(Ph. D. - Pettersen) 378

14. The Dispersion of Bacteria
(M. S. - Rust) 378

15. A Study of the Internal Conversion Electrons Emitted Within 3 nsec After the Spontaneous Fission of ^{252}Cf
(Ph. D. - Watson) 379

K. AUTHOR INDEX

1. Papers Published and UCRL Reports Issued, 1966 381

2. Contributions to this Report 406

NUCLEAR CHEMISTRY DIVISION ANNUAL REPORT, 1966

Lawrence Radiation Laboratory
University of California
Berkeley, California

December 1966

A. NUCLEAR SPECTROSCOPY

1. TABLE OF ISOTOPES

C. M. Lederer, J. M. Hollander, and I. Perlman

The sixth edition of the Table of Isotopes, over 3 years in preparation, was completed at the end of 1966. The present revision is marked by more extensive changes than any previous edition. One of these, the division into two major tables, is illustrated in the accompanying examples of pages from the two sections, Figs. A. 1-1 and A. 1-2. This division was decided upon in order to make the Table more useful to "nonspecialists"--applied users of radioactive substances--and to make better use of space. Table I contains the more general data arranged by atomic number; in addition to items found in the 1958 edition, it contains masses, neutron cross sections, means of production, and a condensed table of the most prominent radiations. Table II, arranged by mass number, contains the spectroscopic data and decay schemes. The Table is rounded out with an appendix of useful tables and graphs, and a list of more than 11 000 references.

The authors had considerable help in preparing the sixth edition. Among those who contributed were Virginia Shirley (literature search), Liwana Blau (typing), Judy Yee, Richard Blumenthal, Henry Chang, and Robert Stevens (Illustrating), Eileen Leon (proofreading), William Louie, Joan Delmonte, and Sedong Kim (compiling, data checking, and preparation of the final copy), and members of the Graphic Arts Photography group (preparation of negatives).

The sixth edition of the Table is being published by John Wiley & Sons, Inc., by the photo-offset method, from negatives supplied by LRL. It will appear in the early months of 1967 both in soft cover and hard cover editions.

Isotope Z A	Half-life	Type of decay (☢); % abundance; Mass excess ($\Delta \equiv M-A$), MeV ($C^{12}=0$); Thermal neutron cross section (σ), barns	Class; Identification; Genetic relationships	Major radiations: approximate energies (MeV) and intensities	Principal means of production
$_{94}Pu^{240}$	6580 y genet (IngM51) others (DokY59, ButlJP56a, WestE51, FarwG56) $t_{1/2}$ (SF): 1.34×10^{11} y (WatD62b) 1.45×10^{11} y (MalkL63) others (BarcF54, ChambO54)	☢ α (JameR49) β stable (cons energy) (ForB58) Δ 50.14 (MTW) σ_c 286 (GoldmDT64) σ_f <0.08 (GoldmDT64)	A chem, n-capt, mass spect (ChambO44, FarwG46, BartlA44) daughter Cm^{244} (FrieA54)	α 5.17 (76%), 5.12 (24%) γ U L X-rays, 0.65 (complex, 2×10^{-5}%) e^- 0.026, 0.040	multiple n-capt from U^{238}, Pu^{239} (HydE64)
Pu^{241}	13.2 y (BrowF60) others (HallG56, MKenD53, RosB56, SmiH61, ThomS50d)	☢ β^- 99+%, α 2.3×10^{-3}% (BrowF60, SmiH61) others (AsaF57a, SeaG49a, GhiA50, IvaR63) Δ 52.98 (MTW) σ_c 425 (GoldmDT64) σ_f 950 (GoldmDT64)	A chem, n-capt, mass spect, excit, genet (SeaG49a, SeaG49, GhiA50) parent Am^{241} (SeaG49a, CunB49a) parent U^{237} (SeaG49a) daughter Cm^{245} (FrieA54)	β^- 0.021 max α 4.90 (0.0019%), 4.85 (0.0003%) γ U X-rays, 0.145 (1.6×10^{-4}%) daughter radiations from Am^{241}	multiple n-capt from U^{238}, Pu^{239}, etc. (HydE64)
Pu^{242}	3.79×10^5 y sp act (ButlJP56a) 3.73×10^5 y sp act (ButlJP56) others (MecJ56, ThomS50d) $t_{1/2}$ (SF): 7.1×10^{10} y (MecJ56) 7.4×10^{10} y (MalkL63) 6.6×10^{10} y (ButlJP56) others (DruV61a)	☢ α (ThomS50d) β stable (cons energy) (ForB58) Δ 54.74 (MTW) σ_c 19 (GoldmDT64) σ_f <0.2 (GoldmDT64)	A chem, mass spect, n-capt, genet (ThomS50d) daughter Am^{242} (AsaF60, OKelG50) daughter Cm^{246} (FrieA54)	α 4.90 (76%), 4.86 (24%) γ [U L X-rays]	multiple n-capt from U^{238}, Pu^{239}, etc. (HydE64) daughter Am^{242} (ButlJP56, HydE64)
Pu^{243}	4.98 h (EngeD53) others (SulJ51, ThomS51)	☢ β^- (SulJ51) Δ 57.77 (MTW) σ_c 170 (GoldmDT64)	A chem, n-capt, cross bomb (SulJ51) genet (ThomS51) parent Am^{243} (ThomS51)	β^- 0.58 max e^- 0.019, 0.036 γ Am L X-rays, 0.084 (21%), 0.381 (0.7%)	Pu^{242}(n, γ) (HydE64, SulJ51, ThomS51)
Pu^{244}	≈7.6×10^7 y genet (DiaH56) ≈7.5×10^7 y genet (ButlJP56a) $t_{1/2}$ (SF) 2.5×10^{10} y (FieP55a)	☢ [α] (StuM54a) β stable (cons energy) (ForB58) Δ 59.83 (MTW) σ_c 1.8 (GoldmDT64)	A chem, n-capt, mass spect, genet (StuM54a, ButlJP56a, DiaH56) ancestor Np^{240m}, parent U^{240} (ButlJP56a, DiaH56) daughter Am^{244m} (FieP55a)	α [4.58] daughter radiations from U^{240}, Np^{240m}	multiple n-capture from U^{238}, Pu^{239}, etc. (HydE64, EngeD55, StuM54a)
Pu^{245}	10.1 h (FieP55) 10.6 h genet (ButlJP56a) others (BrowCI55)	☢ β^- (FieP55) Δ 63 (MTW) σ_c ≈260 (GoldmDT64)	B chem, n-capt (FieP55, BrowCI55) parent Am^{245} (ButlJP56a, FieP55)	daughter radiations from Am^{245}	Pu^{244}(n, γ); multiple n-capt from U^{238}, Pu^{239}, etc. (HydE64, ButlJP56a)
Pu^{246}	10.85 d (HoffD56) others (EngeD55)	☢ β^- (EngeD55) Δ 65.3 (MTW)	A chem, n-capt, mass spect (EngeD55) parent Am^{246} (EngeD55)	β^- 0.33 max (10%), 0.15 max e^- 0.020, 0.038, 0.055, 0.156 γ Am X-rays, 0.044 (30%), 0.180 (10%), 0.224 (25%) daughter radiations from Am^{246}	multiple n-capt from U^{238} (EngeD55, HydE64)
$_{95}Am^{237}$	≈1.3 h (HigG52a)	☢ EC 99+%, α 0.005% (HigG52a) Δ 47 (MTW)	B chem, excit (HigG52a)	α 6.02	Pu^{239}(p, 3n), Pu^{239}(d, 4n) (HigG52a)
Am^{238}	1.9 h (GlasR60) others (HigG52a)	☢ EC (StreK50a) no α, lim 3×10^{-4}% (HigG52a) Δ 48 (MTW)	B chem, excit (StreK50a)	γ Pu X-rays, 0.36 (12%), 0.58 (29%), 0.98 (80%, doublet), 1.35 (76%)	Pu^{239}(p, 2n) (GlasR60) Pu^{239}(d, 3n) (StreK50a, HydE64) Np^{237}(α, 3n) (HydE64)
Am^{239}	12.1 h (GlasR60) 12 h (SeaG49a)	☢ EC 99+%, α 0.005% (GlasR60) EC 99+%, α 0.003% (HigG52a) Δ 49.41 (MTW)	A chem, excit (SeaG49a) genet energy levels (SmiW57) daughter Bk^{243} (ThomS50b)	γ Pu X-rays, 0.209 (5%), 0.228 (18%, doublet), 0.278 (17%) e^- 0.02-0.04, 0.048, 0.088, 0.106, 0.156 α 5.78	Pu^{239}(p, n) (StreK50a) Pu^{239}(d, 2n) (GlasR60, HigG52a, SeaG49a) Np^{237}(α, 2n) (SeaG49a)

Fig. A. 1-1. A page from Table I of the Table of Isotopes.

Am^{245} (2.1 h):

β^-: **0.91** mag spect (BrowCI55)
others (ButlJP56a, FieP55)

γ: γ_1 **0.036**, γ_2 **0.06** (?), γ_3 **0.078** (?), γ_4 **0.140**, γ_5 **0.153**, γ_6 **0.230**, γ_7 **0.255** (e_K/γ 0.19, K/L 5), (γ_7 coinc γ_1, γ_2, γ_3, γ_5), (γ_6 coinc γ_1, γ_2, γ_3, γ_4), scint spect, mag spect conv, γγ coinc (BrowCI55)
others (FieP55, ButlJP56a)

Cm^{245} (9.3 x 10^3 y):

α: α_0 **5.532** (≤2%), α_{72} **5.461** (≤8%), α_{125} **5.409** ? (≤1.2%), α_{172} **5.362** (80%), α_{230} **5.306** (7%), α_{291} **5.246** (2%) mag spect (DzhB63b)
others (AsaF61, BeloL63, HulE54, PerlmI56, HulE51)

γ: **0.13** (γ 5%), **0.173** (γ 14%) scint spect (AsaF57a)

Bk^{245} (4.98 d):

α: α_0 **6.358** (↑ 16), α_{42} **6.317** (↑ 15), α_{95} **6.265** (↑ 1.4), α_{161} **6.200** (↑ 1.4), α_{207} **6.153** (↑ 19), α_{237} **6.124** (↑ 15), α_{275} **6.087** (↑ 5.6), α_{324} **6.038** (↑ 0.6), α_{378} **5.985** (↑ 0.2), α_{474} **5.889** (↑ 22), α_{505} **5.858** (↑ 4.0)
semicond spect (AhmI66)
others (MagL56, HulE51)

γ with EC: γ_1 **0.2527** ($\uparrow_\gamma$100), γ_2 **0.3805** ($\uparrow_\gamma$8), γ_3 **0.3846** ($\uparrow_\gamma$1.8) semicond spect (AhmI66)
γ_1 (γ 31%, e_K/γ 1.8, K/L+M+... 4), $\gamma_2 + \gamma_3$ (γ 5%, e_K/γ 0.2, coinc γ_1) mag spect conv, γγ coinc, scint spect (MagL56, MagL57a)

γ with α: **0.1655** (γ/α 0.07), **0.2074** (γ/α 0.33), **0.474** (γ/α 0.20) γα coinc (AhmI66)
others (ChetA56b)

EC to **0.253** level of Cm^{245}: EC(K)/EC(L+M+...) 3.0 (MagL56)
2.4 (ChetA56b)

EC to **0.633** level of Cm^{245}: EC(K)/EC(L+M+...) ≈0.2 (ChetA56b)

Cf^{245} (44 m):

α: **7.12** ion ch (ChetA56)
others (ThomS50c, GuseL56)

Es^{245} (1.3 m)

α: **7.70** semicond spect (MikV66)
7.65 semicond spect (GhiA61a)

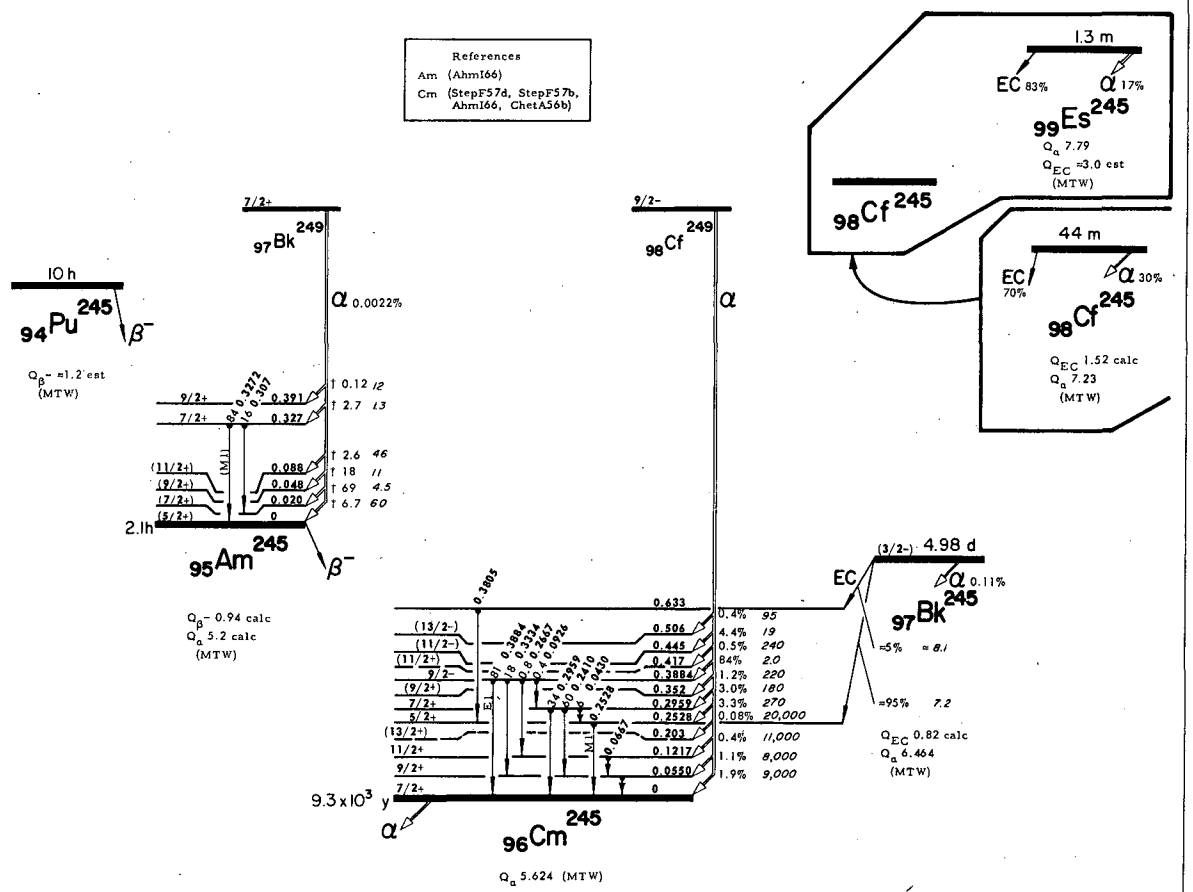

Pu^{246} (10.9 d):

β^-: **0.33** (27%), **0.15** (73%) βγ coinc, scint spect (HoffD56)

γ: γ_2 **0.044** (γ ≈30%), γ_5 **0.180** (γ 10%), γ_6 **0.224** (γ 25%) semicond spect, γγ coinc (StepF65a)
γ_1 **0.027** ($\uparrow_\gamma$13, e/γ ≤1.9), γ_2 **0.047** ($\uparrow_\gamma$30, e/γ ≤0.23), γ_3 **0.08** ($\uparrow_\gamma$3), γ_4 **0.10** (?), γ_5 **0.18** ($\uparrow_\gamma$3), γ_6 **0.22** scint spect, βγ, γγ coinc (HoffD56)
γ_2 **0.041**, γ_4 **0.100** (?), γ_5 **0.175** (K/L 5), γ_6 **0.225** mag spect conv, scint spect (SmiH56)
others (EngeD55)

Am^{246} (25.0 m):

β^-: **2.10** (7%), **1.60** (14%), **1.31** (79%) mag spect, scint spect (SmiH56, EngeD55)

γ: **0.171**, **0.228**, **0.238** (γ 0.3%), **0.245** (γ 1.5%), **0.256** (γ 0.2%), **0.262** (γ 0.14%), **0.270** (γ 1.0%), **0.288** (γ 0.1%), **0.402** (γ 0.3%), **0.734** (γ 1.2%), **0.752** (γ 1%), **0.759** (γ 0.8%), **0.799** (γ 29%), **0.834** (γ 2.2%), **0.987** (γ 1.1%), **1.037** (γ 14%), **1.063** (γ 19%), **1.079** (γ 32%), **1.086** (γ 1.7%) semicond spect, γγ coinc (StepF65a)
others (SmiH56, EngeD55)

0.044 level of Am^{246}: $t_{1/2}$ 4.3 x 10^{-9} s delay coinc (StepF65a)

Fig. A. 1-2. A page from Table II of the Table of Isotopes.

2. ENERGY LEVELS OF ^{237}Np. I. THE α DECAY OF ^{241}Am†

C. M. Lederer, J. K. Poggenburg,* F. Asaro, J. O. Rasmussen, and I. Perlman

Advances in the theory of α-decay rates[1-4] and the availability of Ge(Li) γ-ray spectrometers have prompted a complete restudy of the levels of ^{237}Np populated in the α decay of ^{241}Am. The α spectrum is already well known from the work of Baranov, Kulakov, and Shatinsky;[5] we have studied the γ-ray spectrum from 80 to 850 keV (at 3.2 keV resolution) and measured coincidences of α particles with γ rays and conversion electrons. We have also done a microscopic calculation of α intensities, based on Nilsson wave functions, which played a significant role in unraveling the complicated band structure of ^{237}Np.

Table A. 2-I gives the results of our γ-ray measurements, together with complementary data (referenced) from other works. More than 30 of the transitions in this complex spectra had not previously been seen in the decay of ^{241}Am.

Figure A. 2-1 shows the resulting decay scheme. The rotational bands are labeled on the left side of the figure, and the γ-ray transitions have been correspondingly labeled in column 1 of Table A. 2-I. Bands labeled A, B, and D have previously been given Nilsson assignments 5/2+[642], 5/2-[523], and 1/2+[400].[6] The band labeled C was particularly difficult to locate because (a) its 1/2- member is not populated to any appreciable extent by α decay; (b) its 7/2- member lies close to the $D_{1/2^+}$ state, and in fact Baranov et al.[5] misassigned the α group to that state; and (c) only the well-known 3/2- (lowest) member at 267.54 keV decays by high-energy interband transitions; higher-band members apparently decay by low-energy, highly converted intraband transitions which are too weak to observe.

Clues leading to the identification of the states assigned to band C as members of the 1/2-[530] band include the intensity balance between the α and γ spectra, which revealed the presence of a state at 327 keV distinct from the 332-keV member of band D, and the theoretical α-intensity calculations, which show the spin 1/2 member of the 1/2-[530] band should indeed be populated too weakly to be observed (see Fig. A. 2-2). The resulting prediction that this state should lie near 280 keV and decay almost entirely by a ≈ 13 keV M1+E2 transition to the 3/2- member at 267 keV is strikingly confirmed by a new study of ^{237}U β^- decay.[7]

Comparison of experimental and theoretical α intensities for states assigned to single-particle configurations is given in Fig. A. 2-2. The intensity pattern within a rotational band is rather well matched by the calculations, and forms a "signature" by which the bands can be identified. The absolute intensities are also rather well predicted, except for the 1/2+[400] band (D), for which the predictions are about an order of magnitude low. Since α intensities for different bands can differ by factors of 10^3 to 10^4 even after corrections for energy dependence, the calculated absolute intensities also provide a useful tool for identifying single-particle states.

Levels at 721.9 keV and 755.8 keV (band B') are assigned as a β vibration based on the 5/2-[523] band, both from the low hindrance factors and from the E0 component of the 662.3-keV transition, as demonstrated in the coincidence measurements. The level at 770 keV is probably a 7/2+ level, and probably also of vibrational character. More detailed properties of all the levels are discussed in the full paper.

Footnotes and References

†C. M. Lederer, J. K. Poggenburg, F. Asaro, J. O. Rasmussen, and I. Perlman, Nucl. Phys. 84, 481 (1966).

*Present address: Oak Ridge National Laboratory, Oak Ridge, Tennessee.

1. H.-J. Mang, Ann. Rev. Nucl. Sci., 14, 1, (1964).
2. H.-J. Mang and J. O. Rasmussen, Kgl. Danske Videnskab. Selskab Mat.-Fys. Skr. 2, No. 3 (1962).
3. H.-J. Mang, J. K. Poggenburg, and J. O. Rasmussen, Nucl. Phys. 64, 353 (1965).
4. J. K. Poggenburg, Theoretical Alpha Decay Rates of Deformed Nuclei (Ph. D. Thesis), UCRL-16187, Aug. 1965.
5. S. A. Baranov, V. M. Kulakov, and V. M. Shatinsky, Nucl. Phys. 56, 252 (1964).
6. J. O. Rasmussen, F. L. Canavan, and J. M. Hollander, Phys. Rev. 107, 141 (1957).
7. T. Yamazaki and J. M. Hollander, Nucl. Phys. 84, 505 (1966); Nuclear Chemistry Division Annual Report, UCRL-16580, Jan. 1966, p. 91.

8. L. B. Magnusson, Phys. Rev. 107, 161 (1957).
9. J. L. Wolfson and J. J. H. Park, Can. J. Phys. 42, 1387 (1964).
10. P. P. Day, Phys. Rev. 97, 689 (1955).
11. J. O. Newton, Physica 22, 1129 (1956); Nucl. Phys. 5, 218 (1958).
12. F. Asaro, F. S. Stephens, J. M. Hollander, and I. Perlman, Phys. Rev. 117, 492 (1960).
13. B. Bleany, P. M. Llewellyn, M. H. L. Pryce, and G. R. Hall, Phil. Mag. 45, 992 (1954).
14. L. A. Sliv and I. M. Band, Coefficients of Internal Conversion of γ Radiation, [Academy of Sciences of the USSR, Moscow-Leningrad, Part I (1956), Part II (1958)].

Table A. 2-I. ^{241}Am γ-ray spectrum.

1 Transition initial state → final state	2 Transition energy (keV)	3 Photons per 100 ^{241}Am α decays	4 Multipolarity (mixing ratios refer to photon intensities)	5 Transitions per 100 ^{241}Am α decays
C 1/2- → C 3/2-[a]	13.81[b]		M1 + 0.15% E2	
B 5/2- → A 7/2+	26.35[b]	2.5 ± 0.2[c]	E1[b, d]	
A 7/2+ → A 5/2+	33.20[b]	0.014[c, e]	M1 + 1.4% E2[b]	21 ± 4[f]
D 3/2+ → D 1/2+[a]	38.54[b]		E2/M1 > 0.3[b]	< 1.2 × 10^{-4} [f]
A 9/2+ → A 7/2+[g, h]	42.6[i]		[M1 + E2][j]	
B 7/2- → B 5/2-	43.42[b]	0.07[c]	M1 + 14% E2[b, d]	15 ± 3[k]
D 1/2+ → C 1/2-[a]	51.01[b]		E1[b]	(7±2) × 10^{-5} [f]
B 9/2- → B 7/2-	55.56[d]		M1 + 17% E2[d]	1.4 ± 0.3[k]
B 5/2- → A 5/2+	59.54[b]	35.9 ± 0.7[c]	E1[l, b]	76 ± 7[f]
D 1/2+ → C 3/2-[a]	64.83[b]		E1[b]	(2.5 ± 0.8) × 10^{-4} [f]
B 11/2- → B 9/2-	67.5[d]		M1 + 10% E2[m]	(9±4) × 10^{-4} [k]
A 9/2+ → A 5/2+[h]	76[n]		[E2][j]	
B 9/2- → B 5/2-	98.7 ± 1.0 99.00[d]	0.024±0.003[o] 0.023[c]	E2[d]	0.35 ± 0.07[k]
B 7/2- → A 5/2+	102.7 ± 1.0	0.019±0.003[p] 0.019[c]	[E1][j]	0.021 ± 0.003
not assigned	106.3 ± 2.0 ?	< 0.001		
Np K_β x-rays	113.8 ± 1.5	(7±4) × 10^{-4}		
B 11/2- → B 7/2-	122.1 ± 2.0 ?	≤ 0.002	[E2][j]	≤ 0.013
B 9/2- → A 7/2+	125.1 ± 2.0	(5±2) × 10^{-3}	[E1][j]	(6±2) × 10^{-3}
B 13/2- → B 9/2-	146.3 ± 1.0	(1.6±0.6) × 10^{-4}	[E2][j]	(5.9±2.3) × 10^{-4}
B 11/2- → A 9/2+	150 ± 2 ?	≤ 2.4 × 10^{-5}	[E1][j]	≤ 2.9 × 10^{-5}
C 3/2- → B 7/2-	164.4 ± 1.0 164.61[b]	(4.1±2.1) × 10^{-5}	E2[b]	(1.1±0.6) × 10^{-4}
B 15/2- → B 11/2-	169.2 ± 1.0	(1.0±0.4) × 10^{-4}	[E2][j]	(2.5±1.0) × 10^{-4}
C 3/2- → B 5/2-	208.2 ± 0.5 208.00[b]	(5.6±1.0) × 10^{-4}	M1 + 2.1% E2	(2.2±0.4) × 10^{-3}
not assigned[q]	221.5 ± 1.0	(3.5±0.8) × 10^{-5}		
C 1/2- → B 5/2-[a]	221.80[b]		E2[b]	
C 3/2- → A 7/2+[a]	234.40[b]		M2[b]	(5±1) × 10^{-6} [f]
C 3/2- → A 5/2+	267.2 ± 1.0 267.54[b]	(2.7±0.7) × 10^{-5}	E1 + M2[b]	(5±2) × 10^{-5} [f]
D 5/2+ → A 9/2+	292.0 ± 1.5 292.7[b]	(2.1±0.7) × 10^{-5}	[E2][j]	(2.5±0.8) × 10^{-5}
not assigned	311.9 ± 1.0	(2.7±0.8) × 10^{-5}		
D 9/2+ → A 11/2+	322.6 ± 0.5	(1.6±0.3) × 10^{-4}	[M1]	(3.0±0.6) × 10^{-4}
D 1/2+ → A 5/2+	332.4 ± 0.7 332.36[b]	(1.8±0.4) × 10^{-4}	E2[b]	(2.1±0.5) × 10^{-4}
D 5/2+ → A 7/2+	335.3 ± 0.5 335.38[b]	(5.7±1.0) × 10^{-4}	M1, < 15% E2[b]	(1.0±0.2) × 10^{-3}
D 3/2+ → A 7/2+[a]	337.7 ± 0.5[b]		[E2][j]	< 4 × 10^{-6}

Table A. 2-I. (Continued)

1 Transition initial state → final state	2 Transition energy (keV)	3 Photons per 100 ^{241}Am α decays	4 Multipolarity (mixing ratios refer to photon intensities)	5 Transitions per 100 ^{241}Am α decays
D 5/2+ → A 5/2+	368.5± 1.0 368.59[b]	$(2.8\pm0.6)\times10^{-4}$ [r]	M1, < 15% E2[b]	$(4.5\pm1.0)\times10^{-4}$
D 3/2+ → A 5/2+	370.94[b]	$<5\times10^{-5}$ [r]	M1, < 15% E2[b]	$<8\times10^{-5}$
D 9/2+ → A 9/2+	376.8± 0.5	$(1.6\pm0.3)\times10^{-4}$	[M1]	$(2.5\pm0.5)\times10^{-4}$
D 7/2+ → A 9/2+	383.9± 1.0	$(2.9\pm0.8)\times10^{-5}$	[M1]	$(4.4\pm1.2)\times10^{-5}$
D 9/2+ → A 7/2+	419.6± 1.0	$(3.6\pm1.0)\times10^{-5}$	[M1]	$(5.2\pm1.4)\times10^{-5}$
D 7/2+ → A 7/2+	426.7± 1.0	$(3.3\pm0.9)\times10^{-5}$	[M1]	$(4.7\pm1.3)\times10^{-5}$
D 9/2+ → A 5/2+	454 ± 2 ? ?	$<1.7\times10^{-5}$	[E2][j]	$<1.9\times10^{-5}$
D 7/2+ → A 5/2+	(460) not observed	$<1.0\times10^{-5}$	[M1]	$<1.3\times10^{-5}$
B' 7/2- → B 11/2-	(530) not observed	$<7\times10^{-6}$	[E2][j]	$<7\times10^{-6}$
B' 5/2- → B 9/2-	(563) not observed	$<5\times10^{-6}$	[E2][j]	$<5\times10^{-6}$
not assigned	570.2± 2.0	$(1.0\pm0.5)\times10^{-5}$		
B' 7/2- → B 9/2-	597.4± 1.5	$(1.0\pm0.5)\times10^{-5}$	M1[s]	$(1.2\pm0.6)\times10^{-5}$
B' 5/2- → B 7/2-	618.9± 0.5	$(8.5\pm0.5)\times10^{-5}$	M1[s]	$(9.9\pm0.6)\times10^{-5}$
E(7/2+) → A 11/2+	641.5± 1.5	$(1.0\pm0.3)\times10^{-5}$		$(1.0\pm0.3)\times10^{-5}$
B' 7/2- → B 7/2-	652.7± 0.5	$(5.5\pm0.3)\times10^{-5}$	M1 [+E0][s]	$(7\pm1)\times10^{-5}$
B' 5/2- → B 5/2-	662.3± 0.3	$(5.3\pm0.3)\times10^{-4}$	M1 + 8% E0[t]	$(6.4\pm0.5)\times10^{-4}$
not assigned	676 ± 2 ? ?	$\leq 2.2\times10^{-6}$		
B' 7/2- → A 9/2+	680.0± 1.5	$(5.3\pm1.7)\times10^{-6}$	[E1][j]	$(5.3\pm1.7)\times10^{-6}$
B' 5/2- → A 7/2+	688.7± 0.5	$(4.3\pm0.5)\times10^{-5}$	[E1][j]	$(4.3\pm0.5)\times10^{-5}$
B' 7/2- → B 5/2-	695.4± 1.0	$(1.0\pm0.2)\times10^{-5}$	M1[s]	$(1.2\pm0.2)\times10^{-5}$
E(7/2+) → B 5/2-	709.8± 1.0	$(9\pm2)\times10^{-6}$		$(9\pm2)\times10^{-6}$
B' 5/2- → A 5/2+	722.1± 0.5	$(2.8\pm0.2)\times10^{-4}$	E1[j, u]	$(2.8\pm0.2)\times10^{-4}$
E(7/2+) → A 7/2+	737.0± 1.0	$(1.2\pm0.2)\times10^{-5}$		$(1.3\pm0.2)\times10^{-5}$
B' 7/2- → A 5/2+	756.8± 1.0	$(1.3\pm0.2)\times10^{-5}$	[E1][j]	$(1.3\pm0.2)\times10^{-5}$
not assigned	767.0± 2.0	$(8\pm3)\times10^{-6}$		
E(7/2+) → A 5/2+	770.7± 2.0	$(1.0\pm0.3)\times10^{-5}$		$(1.1\pm0.3)\times10^{-5}$

a. Observed only in ^{237}U β^- decay
b. See Ref. 7
c. See Ref. 8
d. See Ref. 9
e. See Ref. 10
f. Calculated with the use of ^{237}U intensity data[7]
g. Observed in ^{237}Pu EC decay
h. Observed in Coulomb excitation of ^{237}Np
i. See Ref. 11
j. Required by the decay scheme
k. Calculated with the use of relative electron intensities[9] normalized to the conversion coefficient of the 59.54-keV transition
l. See Ref. 12
m. Recalculated from the L_I/L_{II} ratio[9] with use of theoretical conversion coefficients of Sliv and Band[14]
n. See Ref. 13
o. A small contribution from Np $K_{\alpha II}$ x rays has been subtracted
p. A small contribution from Np $K_{\alpha I}$ x rays has been subtracted
q. This γ ray is two orders of magnitude too intense to be the C 1/2- → B 5/2- transition
r. The intensities of the unresolved 368.59- and 370.94-keV γ rays are apportioned by use of the intensity ratio $W_\gamma(368.59)/W_\gamma(335.38)$ known from ^{237}U decay[7]
s. From the branching ratios
t. From the measured K-conversion coefficient. The E0 component is expressed as the fraction of total transitions.
u. The measured limit on the K-conversion coefficient (< 0.02) is consistent only with an E1 or E2 assignment

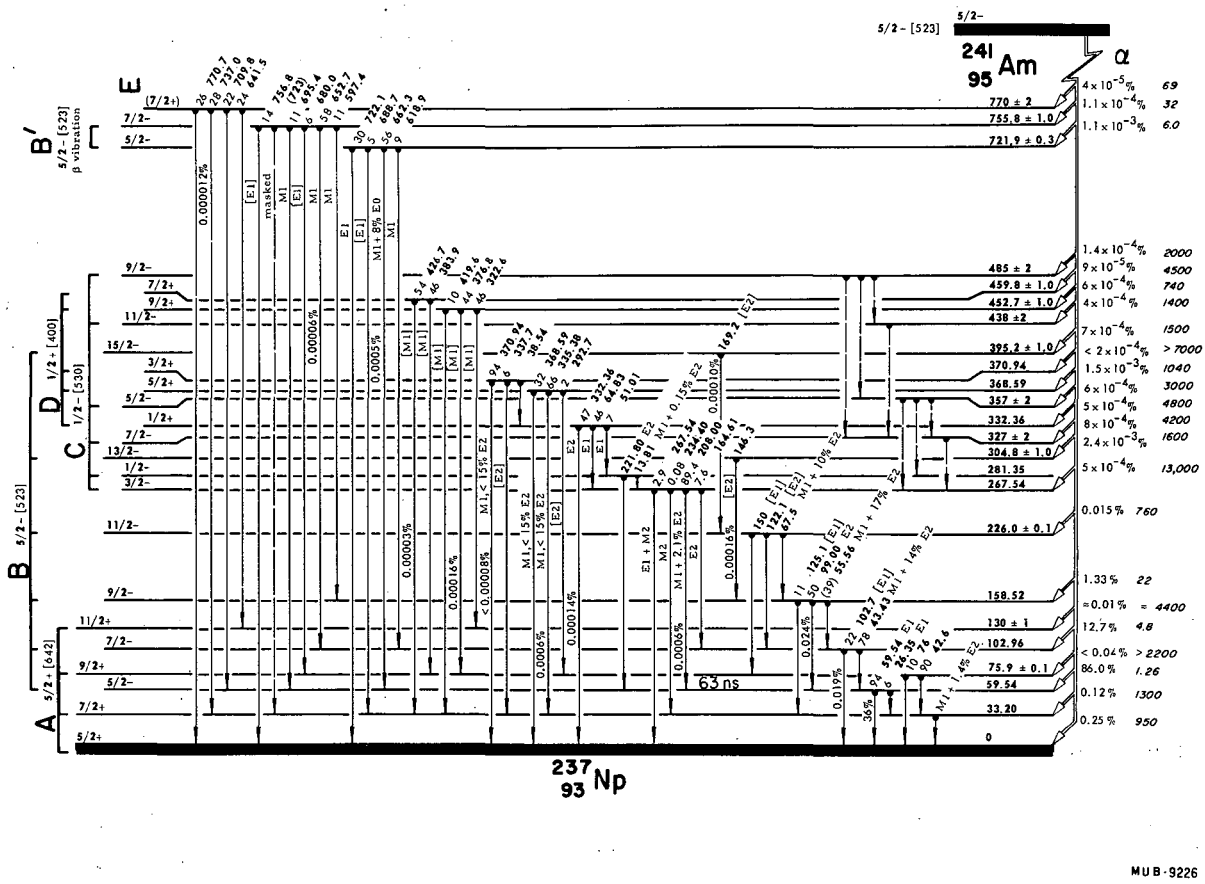

Fig. A. 2-1. Decay scheme for ^{241}Am. Energies (in keV) and spins are given in boldface type. Absolute photon intensities are given on the γ rays, and relative photon intensities (normalized to 100 for each level) above the γ rays, all intensities being in lighter type. Slant numbers to the right of the α intensities are hindrance factors.

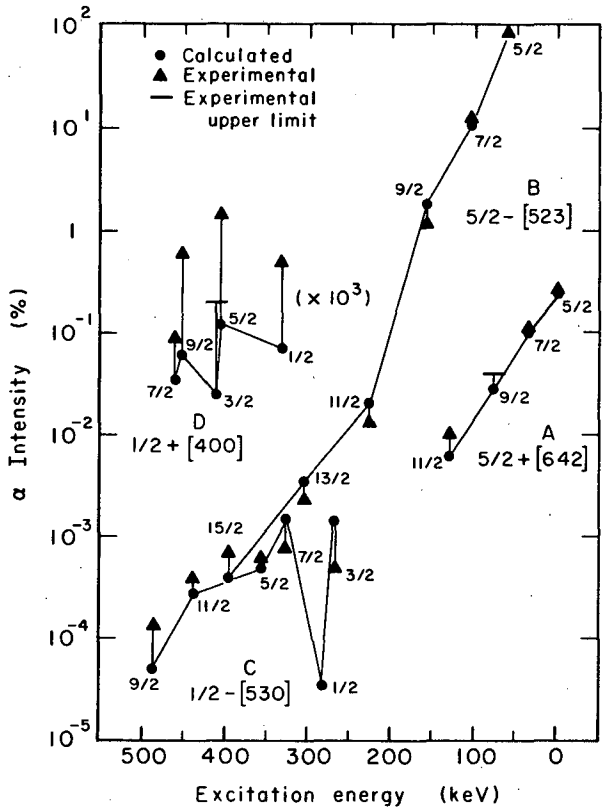

Fig. A. 2-2. Comparison of calculated with experimental α intensities. Calculated intensities for members of a rotational band are connected with lines. The 1/2+[400] band is displaced upwards three decades for clarity.

3. NEW TRANSITIONS AND PRECISE ENERGY AND INTENSITY DETERMINATIONS IN THE DECAY OF ^{177m}Lu †

A. J. Haverfield,‡ F. M. Bernthal, and J. M. Hollander

Decay of the 155-day spin-23/2 three-particle isomer of ^{177}Lu allows population of high-spin members of low-lying rotational bands in both ^{177}Lu and ^{177}Hf. A sensitive test of the rotational model is provided by the numerous intraband transitions. Information on the large number of $\Delta K = 1$ E1 transitions in ^{177}Hf is particularly important in view of the present interest in hindered E1 transition rates.

A number of studies[1-4] have contributed to the now well-established decay scheme of ^{177m}Lu. Primary among these was the high-resolution study of the γ-ray spectrum by Alexander et al.,[2] with the use of a bent-crystal spectrometer. Significant new data have now been obtained by use of a Ge(Li) detector system with resolution of 1.3 keV at 122 keV.

Samples of 7-day ^{177}Lu and 155-day ^{177m}Lu were prepared by irradiating Lu metal for periods ranging from 6 to 41 days with a neutron flux greater than 2.2×10^{14}. The lutetium was separated by ion-exchange methods from all other activities present.

The energies and relative intensities of the lines found in our γ-ray spectrum of 7-day ^{177}Lu are listed in Table A. 3-I. The intensity data and known internal conversion coefficients have been used to derive β-decay branching ratios from the ground state of ^{177}Lu to the 113.0-, 249.6-, and 321.3-keV levels of ^{177}Hf. Table A. 3-II compares our values with those obtained by Alexander et. al.

Figures A. 3-1 through A. 3-5 show the γ-ray spectrum of ^{177m}Lu. Analysis of this spectrum has allowed the identification of the 283.4-keV ^{177}Hf interband transition from the 21/2+ (K = 9/2) to the 19/2- (K = 7/2) level, the 291.4-keV interband 17/2+ to 15/2- transition, and the 292.5-keV interband 19/2+ to 15/2- transition. In addition, the 182.0-keV cascade transition leading from the 15/2- to the 13/2- level within the K = 7/2- band of ^{177}Hf has been identified. Tentative assignment as the ^{177}Hf interband 19/2+ to 19/2- transition has been made for a very weak γ at 69.2 keV. We do not observe the 41.0-keV transition reported by Bodenstedt.[4] If this interband transition were present with the reported intensity, it should have been easily observed in our spectrum.

Table A. 3-III contains a summary of our energy and relative intensity values for the γ rays emitted in the decay of ^{177m}Lu. Not included in the table are additional weak lines at 168.4, 262.9, 264.1, 337.1, 432.4, 433.7, 436.4, 439.9, 441.9, and 473.7 keV. These lines have been interpreted as arising from "solid-angle summing" of the K x rays with prominent γ rays. Figure A. 3-6 shows the decay scheme of ^{177m}Lu with additions from the present work.

The intensity data on ^{177m}Lu provide an excellent opportunity to test the rotational model. The model predicts a constant value for the quantity $|g_K - g_R|$ within an unperturbed rotational band. Improved intensity data obtained in this work have allowed a recalculation of the quantity $[(g_K - g_R)/Q_0]^2$. Our results are compared in Table A. 3-IV with those obtained earlier by Alexander et al.[2]

One of the unusual aspects of the decay of ^{177m}Lu is the large number of interband electric dipole transitions that are observed to take place between levels of the K = 9/2+ [624] band and the 7/2- [514] band in ^{177}Hf. We have identified and obtained much-improved intensity measurements for at least 12 of these E1 transitions.

The transition rates of electric dipole transitions in deformed nuclei have not yet been satisfactorily described by any quantitative theory. Two groups of authors[6,7] have considered the question of the contributions to the E1-transition probabilities from Coriolis admixed components, and have shown that the simple assumption of a K = 7/2+ component admixed into the predominant K = 9/2+ [624] band of ^{177}Hf yields branching ratios in fairly good agreement with the values observed by Alexander et al.

We have now used our data for a calculation of the absolute E1-transition probabilities with a method similar to that used by Vergnes and Rasmussen.[6] In Table A. 3-V are given the calculated theoretical E1 transition rates and the experimental rates found in this work. Table A. 3-VI shows the branching ratios, in comparison with the simple geometric ratios of Alaga and with the theoretical ratios. Although the calculated absolute transition probabilities (Table A. 3-V) exhibit increasing positive disagreement with experiment for spins greater than 13/2, nevertheless the predicted branching ratios shown in Table A. 3-VI still agree quite well with experiment, at least through $I_i = 15/2$. On the basis of the weak line observed at 69.2 keV, we have made a tentative intensity assignment to this E1. The corresponding branching ratio would seem to agree quite well with the simple theoretical prediction.

These results lend further support to the apparent necessity to consider Coriolis admixing in any comprehensive treatment of ΔK = ± 1 E1 transitions in deformed odd-mass nuclei.

Footnotes and References

†Condensation of a paper to be published in Nucl. Phys.

‡Present address: Batelle Memorial Institute, Pacific Northwest Laboratory, Richland, Wash.

1. M. Jorgensen, O. B. Nielsen, and G. Sidenius, Phys. Letters 1, 321 (1962).
2. P. Alexander, F. Boehm, and E. Kankeleit, Phys. Rev. 133, B284 (1964).
3. J. Blok and D. A. Shirley, Phys. Letters 13, 232 (1964).
4. E. Bodenstedt, J. Radeloff, N. Buttler, P. Meyer, L. Shanzler, M. Forker, H. F. Wagner, K. Krein, and K. G. Plingen, Z. Physik 190, 60 (1966).
5. P. Marmier and F. Boehm, Phys. Rev. 97, 103 (1955).
6. M. N. Vergnes and J. O. Rasmussen, Nucl. Phys. 62, 233 (1965).
7. Yu. T. Grin and I. M. Pavlichenkov, Nucl. Phys. 65, 686 (1965).

Table A. 3-I. Relative intensities of γ rays from 7-day ^{177}Lu.

Gamma-ray energy (keV)	Relative intensity: This work	Alexander et al. (Ref. 2)	Marmier and Boehm (Ref. 5)
71.66	2.4 (1)	2.4 (1)	2.0 (4)
112.95	100	100	100
136.72	0.92 (6)	0.74 (4)	---
208.34	164 (10)	171 (9)	220 (44)
249.65	3.0 (2)	3.3 (2)	3.0 (6)
321.32	3.6 (2)	3.4 (2)	3.2 (6)

Table A. 3-II. Beta-decay branchings from decay of 7-day ^{177}Lu into states of spin I in ^{177}Hf.

K	I	Percent branching: Present work	Alexander et al. (Ref. 2)
7/2	7/2-	87.2 ± 1.1	86.3 ± 1.3
	9/2-	6.0 ± 0.8	7 ± 1
	11/2-	0.07 ± 0.02	0.03 ± 0.03
9/2	9/2+	6.7 ± 0.3	6.7 ± 0.3

Table A. 3-III. Energies and relative intensities of γ rays from the decay of 155-day ^{177m}Lu.

Present work: Gamma-ray energy (keV)		Relative intensity		Present work: Gamma-ray energy (keV)		Relative intensity	
69.19		(0.08)		233.83	(6)	45	(4)
71.66	(6)	6.8	(4)	249.65	(6)	47	(4)
105.31	(5)	100[a]		268.79	(6)	25	(3)
112.95	(5)	179	(13)	281.78	(7)	108	(9)
115.96	(10)	5.0	(4)	283.42	(13)	4.7	(1.2)
117.17	(13)	1.8	(2)	291.42	(10)	7.7	(9)
121.63	(5)	52	(4)	292.51	(10)	7.8	(9)
128.50	(5)	127	(8)	296.45	(8)	38	(4)
136.72	(5)	11.7	(8)	299.03	(10)	12	(2)
145.78	(10)	6.6	(9)	305.52	(8)	14	(1)
147.15	(8)	29	(2)	313.69	(8)	9.4	(7)
153.29	(6)	133	(8)	318.98	(8)	78	(8)
159.75	(8)	5.4	(5)	321.32	(12)	9	(1)
171.85	(10)	37	(4)	327.66	(8)	136	(8)
174.42	(6)	96	(8)	341.64	(8)	13	(1)
177.03	(8)	26	(3)	367.41	(8)	23	(2)
181.98	(10)	0.75	(13)	378.51	(8)	222	(17)
195.52	(6)	7.0	(6)	385.02	(8)	24	(2)
204.08	(6)	114	(8)	413.64	(12)	131	(10)
208.34	(6)	485	(40)	418.51	(10)	161	(12)
214.45	(6)	48	(4)	426.29	(10)	3.4	(4)
218.06	(6)	27	(3)	465.96	(12)	19	(2)
228.44	(6)	287	(26)				

a. Normalized to 100 units

Table A. 3-IV. Branching ratios and g factors for the K = 7/2+ [404] rotational band in ^{177}Lu and the K = 7/2- [514] and K = 9/2+ [624] bands in ^{177}Hf. Lambda is the experimental crossover-to-cascade ratio, where I is the initial spin state, Q_0 is the intrinsic quadrupole moment for the nucleus in spin state I, g_K-g_R is associated with transitions I → I-1, and $1/\delta^2$ is the M1/E2 branching ratio for I → I-1 cascade transitions.

	I	λ		$[(g_K-g_R)/Q_0]^2 \times 10^3$		$1/\delta^2$	
		This work	Alexander et al.[2]	This work	Alexander et al.[2]	This work	Alexander et al.[2]
^{177}Lu K = 7/2+	11/2	0.86±0.12	1.19±0.21	2.6 ±0.4	1.7±0.5	4.0	2.6
	13/2	2.1 ±0.3	2.10±0.25	2.4 ±0.3	2.4±0.35	4.0	3.8
	15/2	3.3 ±0.4	2.8 ±0.8	2.6 ±0.3	3.2±1.0	4.3	5.6
	17/2	4.9 ±0.7	4.7 ±0.8	2.5 ±0.4	2.8±0.6	4.4	4.8
^{177}Hf K = 7/2-	11/2	4.0 ±0.4	4.5 ±0.3	$0.043^{+.068}_{-.043}$	< 0.002	0.077	< 0.035
	13/2	7.0 ±1.0	13±3	$0.26^{+.14}_{-.10}$	< 0.001	0.48	< 0.02
	15/2	17.3 ±3.3	> 7	$0.24^{+.16}_{-.11}$	< 0.007	0.45	< 1.3
^{177}Hf K = 9/2+	13/2	0.35±0.04	0.34±0.04	2.7 ±0.3	2.8±0.4	7.8	8.0
	15/2	0.81±0.08	0.90±0.07	2.8 ±0.3	2.5±0.2	7.6	6.8
	17/2	1.42±0.14	1.35±0.16	2.9 ±0.3	3.0±0.4	7.8	8.1
	19/2	1.95±0.20	1.72±0.23	3.0 ±0.3	3.5±0.5	7.5	8.6
	21/2	3.35±0.42	2.33±0.35	2.7 ±0.3	4.1±0.6	7.4	11.0

Table A. 3-V. E1-transition rates between the K = 9/2+ and K = 7/2- bands in ^{177}Hf (Weisskopf units).

I_i	I_f	E_γ	$\frac{T(E1)}{T_w(E1)^a} \times 10^5$ Experiment: This work	Experiment: Alexander et al.[2]	Theory (after Ref. 6)
9/2	7/2	321.3	0.012[b]	0.013	---
9/2	9/2	208.3	2.4[b]	3	---
9/2	11/2	71.7	0.81[b]	1.2	1.1
11/2	9/2	313.7	0.15[c]	0.5	0.28
11/2	11/2	177.0	2.2[c]	7	3.6
11/2	13/2	(17.2)	--	--	2.9
13/2	11/2	305.5	0.52[d]	0.9	1.2
13/2	13/2	145.8	2.3[d]	7	4.4
15/2	13/2	299.0	1.0[e]	0.6	2.7
15/2	15/2	117.2	2.5[e]	12	4.9
17/2	15/2	291.4	1.7[f]	--	4.4
17/2	17/2	(88.4)	--	--	5.2
19/2	17/2	292.5	2.5[g]	3	6.8
19/2	19/2	(69.2)	(2)[g]	--	5.5
21/2	19/2	283.4	4.5[h]	--	9.3
21/2	21/2	(41.0)	--	--	5.7

a. $T_w(E1)$ is the "Weisskopf estimate" $T(E1) = 1.5\times10^5\ A^{2/3}\ E_\gamma^{\ 3}$ in keV and sec.

b. Based on $\tau_{1/2} = 6.3\times10^{-10}$ sec of the 321-keV state.

c. Based on the rotational transition rate for the 105.3-keV transition, with $[g_K - g_R/Q_0]^2 = 2.8\times10^{-3}$, and $Q_0(K = 9/2) = 6.85$ barns.

d. Based on the rotational electric quadrupole transition rate T(E2) of the 233.8-keV transition from the 13/2 state ($Q_0 = 6.85$ barns).

e. Based on T(E2) of the 281.8-keV transition.

f. Based on T(E2) of the 327.7-keV transition.

g. Based on T(E2) of the 378.5-keV transition.

h. Based on T(E2) of the 418.5-keV transition.

Table A. 3-VI. Relative reduced strengths for E1 transitions from the K = 9/2+ to K = 7/2- bands in ^{177}Hf.

I_i	I_f	I'_f	$\frac{Int_\gamma}{Int_{\gamma'}}$	$\frac{B(E1)\ I_i \to I_f}{B(E1)\ I_i \to I'_f}$ Experiment: This work	Experiment: Alexander et al.[a]	Theory: Alaga[b]	Theory: After Ref. 6
9/2	9/2	7/2	54	200	175	0.23	200[c]
9/2	11/2	9/2	0.014	0.35	0.37	0.10	0.48
11/2	11/2	9/2	2.8	15.4	15.4	0.41	13
11/2	13/2	11/2	0.0008[d]			0.14	0.79
13/2	13/2	11/2	0.47	4.4	7.7	0.56	3.7
15/2	15/2	13/2	0.15	2.5	20	0.70	1.9
17/2	17/2	15/2	0.033[d]			0.79	1.2
19/2	19/2	17/2	(0.01)	(1.)		0.88	0.81
21/2	21/2	19/2	0.002[d]			0.96	0.61

a. See Ref. 2

b. Alaga's rule for branching between members of two rotational bands is the squared ratio of Clebsch-Gordan coefficients $[(I_i\ 1\ K_i - 1\ |I_f\ K_f)/(I_i 1\ K_i - 1|I'_f\ K_f)]^2$.

c. Assumed value for fixing parameters.

d. Indicates theoretical ratios, in cases where one of the γ rays is unobserved.

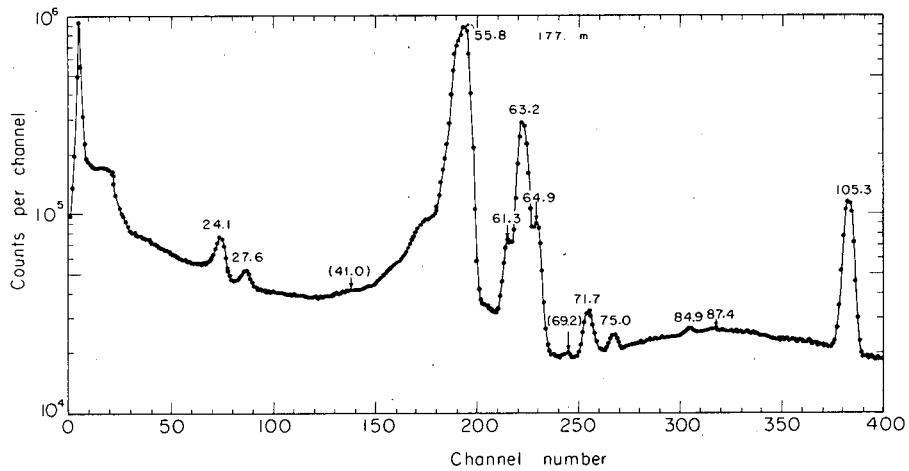

Fig. A. 3-1. Gamma-ray spectrum of ^{177m}Lu in the energy region 0 to 108 keV as observed on a Ge(Li) detector 1 cm^2 by 5 mm deep with FET preamp.

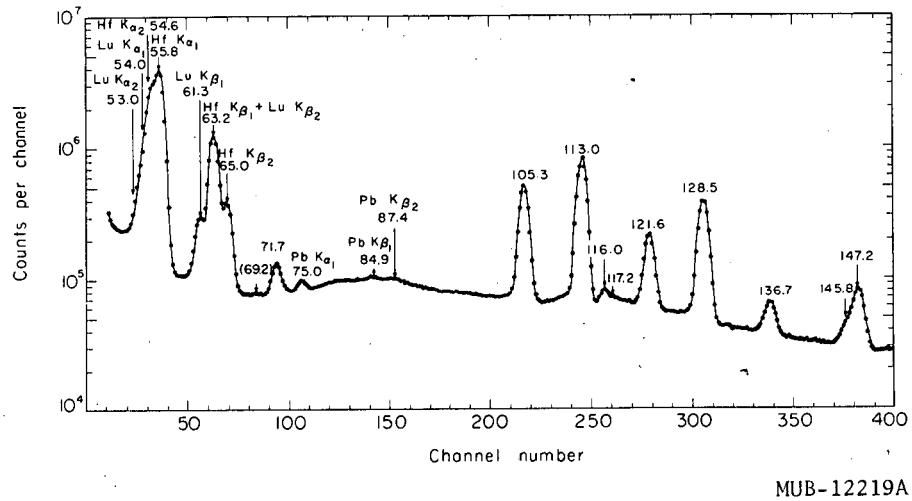

Fig. A. 3-2. Gamma-ray spectrum of ^{177m}Lu in the energy region 40 to 150 keV. Same detector conditions as Fig. A. 3-1. The γ rays are identified by their energies in keV.

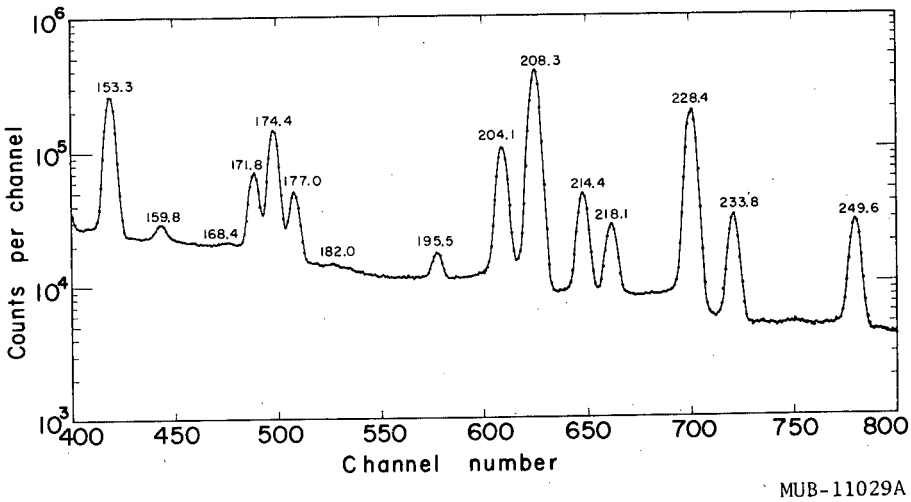

Fig. A. 3-3. Gamma-ray spectrum of ^{177m}Lu in the energy region 150 to 225 keV. Same detector conditions as Fig. A. 3-1.

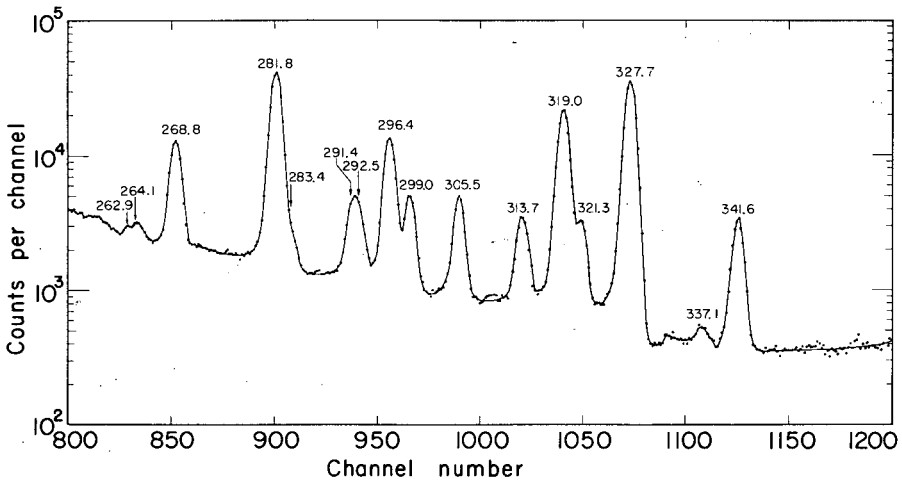

MUB-11027A

Fig. A. 3-4. Gamma-ray spectrum of ^{177m}Lu in the energy region 255 to 360 keV. Same detector conditions as Fig. A. 3-1.

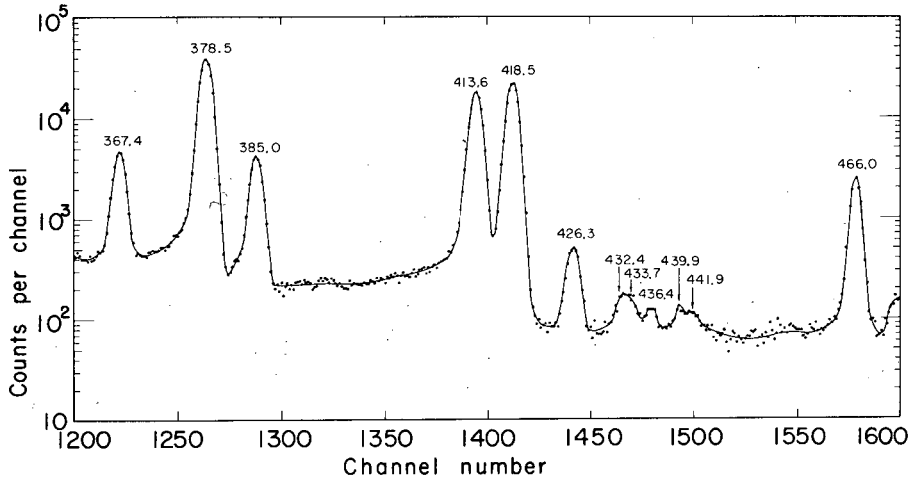

MUB-11026A

Fig. A. 3-5. Gamma-ray spectrum of ^{177m}Lu in the energy region 360 to 470 keV. Same detector conditions as Fig. A. 3-1.

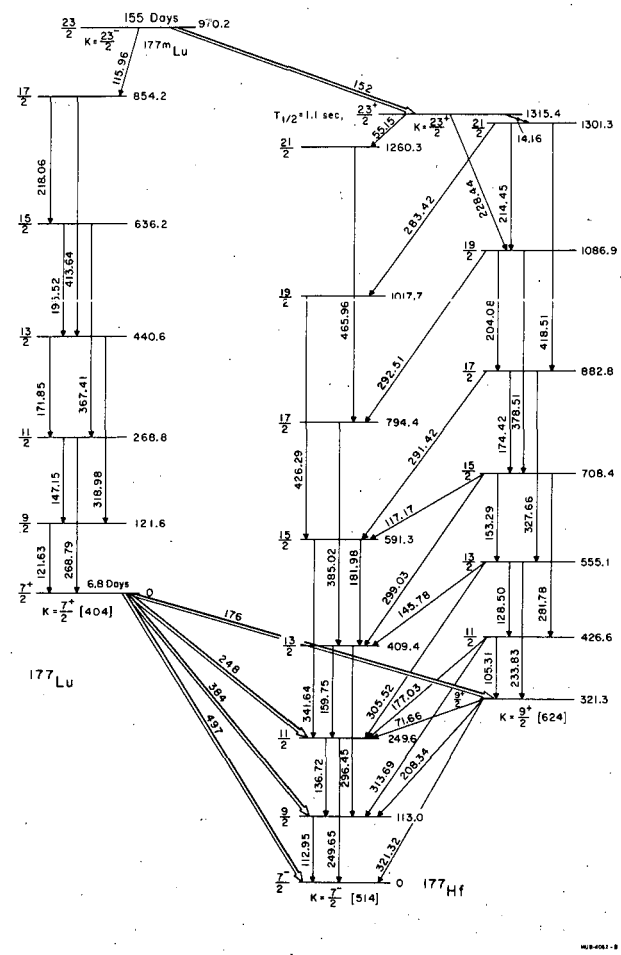

Fig. A. 3-6. Decay scheme of ^{177m}Lu taken from Ref. 2 with additions from Refs. 3 and 4 and the present work.

4. g FACTOR OF THE 243-keV LEVEL IN ^{86}Y

William J. Treytl and E. Matthias

The decay properties of ^{86}Zr have been reported in recent studies.[1,2] In the most recent investigation,[2] a relatively complete decay scheme was proposed which, in addition to assigning energies, spins, and parities for the ^{86}Y levels populated, also postulated probable nucleon configurations for the levels. The decay scheme is given in Fig. A. 4-1. One difficulty was encountered with the 2- level at 243 keV, which is the lowest excited ^{86}Y level populated by ^{86}Zr decay. Log ft values, conversion coefficients, and transition rates all argue strongly for straightforward single-particle transitions in this cascade. These considerations would argue for a $(\pi p_{1/2}\, \nu d_{5/2})_{-2}$ configuration for the 243-keV level, but according to the shell model, the closest available $d_{5/2}$ orbital should lie considerably higher than 243 keV. Other configurations are possible, but in such cases, one would not expect such good agreement with single-particle transition theory as was observed. For these reasons, no nucleon configuration was assigned to that level.

In favorable cases, g factors of excited nuclear levels can be determined by measuring the perturbed angular correlations.[3] The requirements are a sufficiently large anisotropy in the cascade, and half-life and g-factor values such that with the magnetic fields applied, the Larmor precession frequency is short relative to the life time. The 243-keV level in ^{86}Y is a borderline case, having a half-life of 29 nsec, an anisotropy of -8%, and an expected g factor (for the favored configuration) of about -0.5. A successful measurement, however, would greatly clarify

the configuration of this level.

Measurements were performed in liquid solution with a field of 41.5 kG. Two γ detectors were placed at 135 deg, with the centrally located source in the magnetic field. Coincidence measurements of the time spectra were taken with the field up ($C\uparrow$) and down ($C\downarrow$). The ratio $R_i = 2(C_i\downarrow - C\uparrow)/(C_i\downarrow + C_i\uparrow)$ was calculated for each channel number. It can be shown[4] that $R_i = a\cos 2(\omega_L - \phi) + c$, where ω_L is the Larmor precession frequency. The details of this type of experiment have been described earlier.[5,6]

Considerable difficulty was encountered because of the small anisotropy of the 28 to 243 keV cascade, as well as the high absorption and large conversion coefficient of the 28-keV γ. To date, one successful measurement has been performed (Fig. A. 4-2). The g factor calculated from this curve is $g = -0.536 \pm 0.021$.

The most likely oxidation state of Y is Y(III). In this state, the 4d shell is vacant and the outer s electrons are paired. We expect, then, that the paramagnetic correction should be very small.

With the use of proton and neutron values from neighboring nuclei,[7] the expected g factor for a $(\pi p_{1/2}\ \nu d_{5/2})_{-2}$ configuration is -0.56. This figure agrees well with the measured value. Other possible configurations do not agree as well, but more data are required for more definite conclusions to be drawn.

References

1. Y. Awaya and Y. Tendow, J. Phys. Soc. Japan 19, 606 (1964).
2. E. K. Hyde, W. J. Treytl, A. Siivola, D. H. Sisson, and D. J. Horen, Phys. Rev. 142, 657 (1966).
3. R. M. Steffen and H. Frauenfelder, Perturbed Angular Correlations, Eds. E. Karlsson, E. Matthias, and K. Siegbahn (North Holland Pub. Co., Amsterdam, 1964), p. 1.
4. E. Matthias, L. Boström, A. Maciel, M. Salomon, and T. Lindquist, Nucl. Phys. 40, 656 (1963).
5. E. Matthias, D. A. Shirley, J. S. Evans, and R. A. Naumann, Phys. Rev. 140, B264 (1965).
6. E. Matthias, S. S. Rosenblum, and D. A. Shirley, Phys. Rev. 139, B532 (1965).
7. I. Lindgren, in Alpha, Beta, and Gamma-Ray Spectroscopy, Ed. K. Siegbahn (North-Holland Publishing Co., Amsterdam, 1965) Appendix 4, p. 1621.

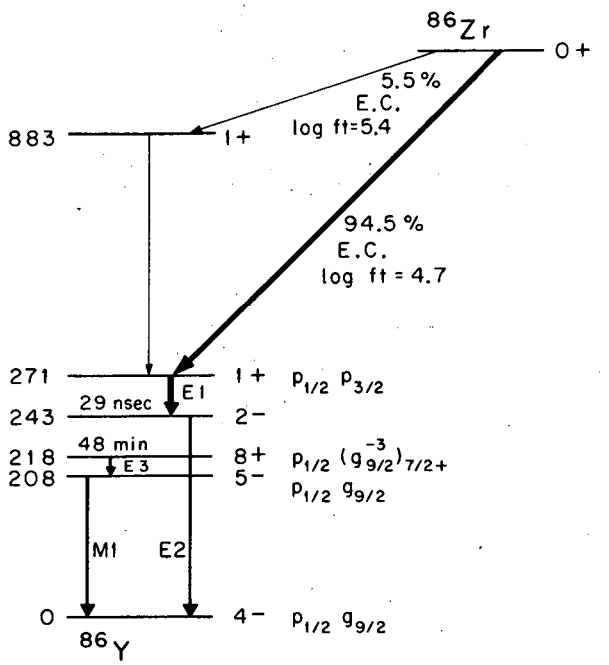

Fig. A. 4-1. Decay scheme of ^{86}Zr.

MUB-7880A

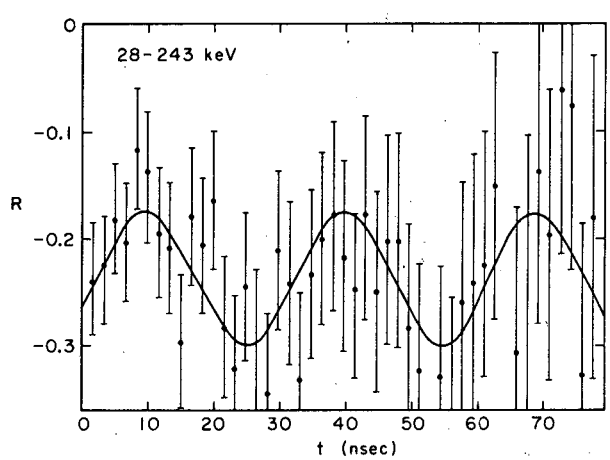

Fig. A. 4-2. Measurement of the time pattern of the angular correlation precessing in an external field of 41.5 kG, using a liquid source. The γ rays were detected with NaI(Tl) crystals, 1.5 by 1 in., at a distance of 5 cm.

XBL671-182

5. DECAY OF ^{139}Nd

J. Gilat* and William J. Treytl

In 1951 5.5-h ^{139}Nd was first produced.[1] It has been subsequently investigated by several workers.[2-5] The most recent report used electron spectroscopy and γ-γ coincidence measurements and proposed a partial decay scheme for the system. All work to date has made use of magnetic electron spectrometers and NaI(Tl) scintillation gamma detectors. Since the gamma spectrum in the ^{139}Nd decay is complex and the reported decay scheme incomplete, we felt that it would be profitable to reinvestigate the decay of ^{139}Nd with high-resolution Ge(Li) gamma detectors and Si(Li) electron detectors.

We have performed extensive measurements on the $^{139}\text{Nd} \xrightarrow{\beta} {}^{139}\text{Pr}$ system, with particular emphasis on γ-γ coincidence, both detectors being semiconductors. We have developed a technique by which unwanted effects of Compton distributions lying within the gating channels are corrected. Because of the much higher resolution of the detectors, we were able to observe a number of details in the gamma spectra that previously were either unnoticed or incorrectly interpreted. A typical γ singles spectrum is shown in Fig. A. 5-1. Numerous γ-γ coincidence spectra, sum coincidence spectra, and pair coincidence spectra were taken in order to establish the order and cascade relationships in the ^{139}Pr levels populated.

Our electron data are not superior to the magnetic spectrometer data; the resolution is no better and there is considerable interference from the positron continuum. However, some valuable coincidence and relative intensity information could be obtained. In particular, we were able to substantiate the assignment of ^{139m}Nd as the 5.5-h activity. A typical electron spectrum is given in Fig. A. 5-2.

A partial decay scheme for ^{139}Nd is shown in Fig. A. 5-3. Not all the transitions have been assigned, but the general features can be well supported on the basis of our data. There are considerable differences between this decay scheme and the previously reported one.[6] This can probably be traced to the complexity of the scheme and to the improvement in detector technology.

Footnote and References

*Present address, Soreq Nuclear Research Centre, Yavne, Israel.

1. B. J. Stover, Phys. Rev. 81, 8 (1951).
2. N. A. Bonch-Osmolovskaya, B. S. Dzhelepov, O. T. Kraft, and Yüeh-wa Chou, Izvest. Akad. Nauk. S.S.S.R. Ser. Fiz., 25, 826 (1961); Columbia Tech.Transl. p. 837.
3. B. S. Dzhelepov, L. K. Peker, and A. G. Sergeev, Skhemy Raspada-Radioaktivnykh Yader [Aka. Nauk. S.S.S.R. (1963)].
4. G. M. Kolesov, T. V. Malysheva and L. N. Nikityuk, Isvest. Akad. Nauk. S.S.S.R., Ser. Fiz., 27, 1267 (1963); Columbia Tech. Transl. p. 1245.
5. A. A. Sorokin, Dissertation, Scientific Research Institute of Nuclear Physics, Moscow State University, 1962.
6. K. Ya. Gromov, S. S. Danagalyan, L. N. Nikityuk, V. V. Murav'eva, A. A. Sorokin, M. Z. Shtal', and V. S. Shpinel'. Soviet Phys. JETP 20, [5], 1104 (1965).

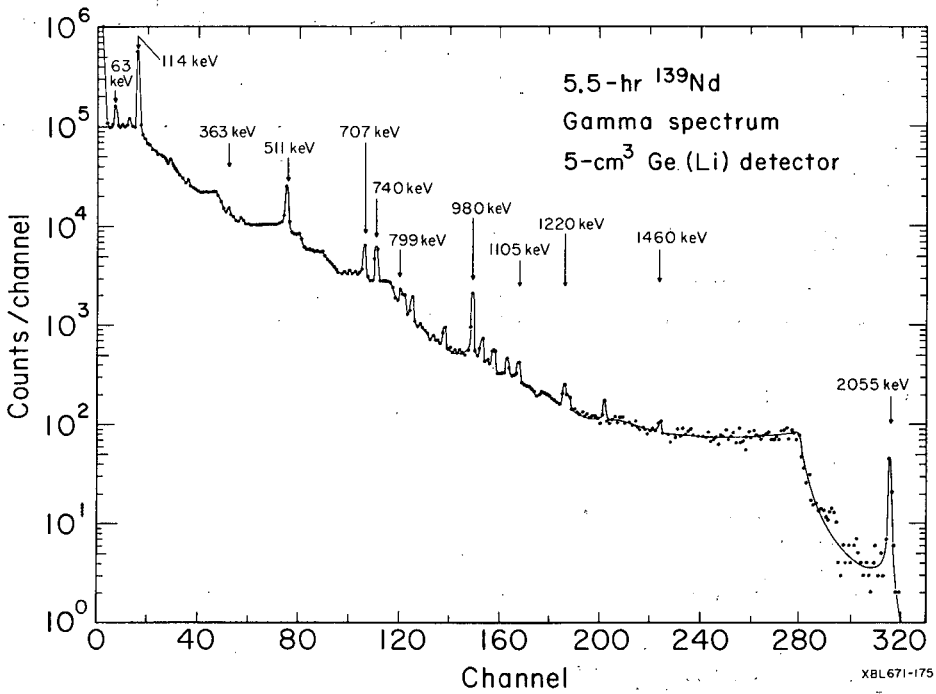

Fig. A. 5-1. A typical singles gamma spectrum, determined with a 5-cm^3 Ge(Li) detector.

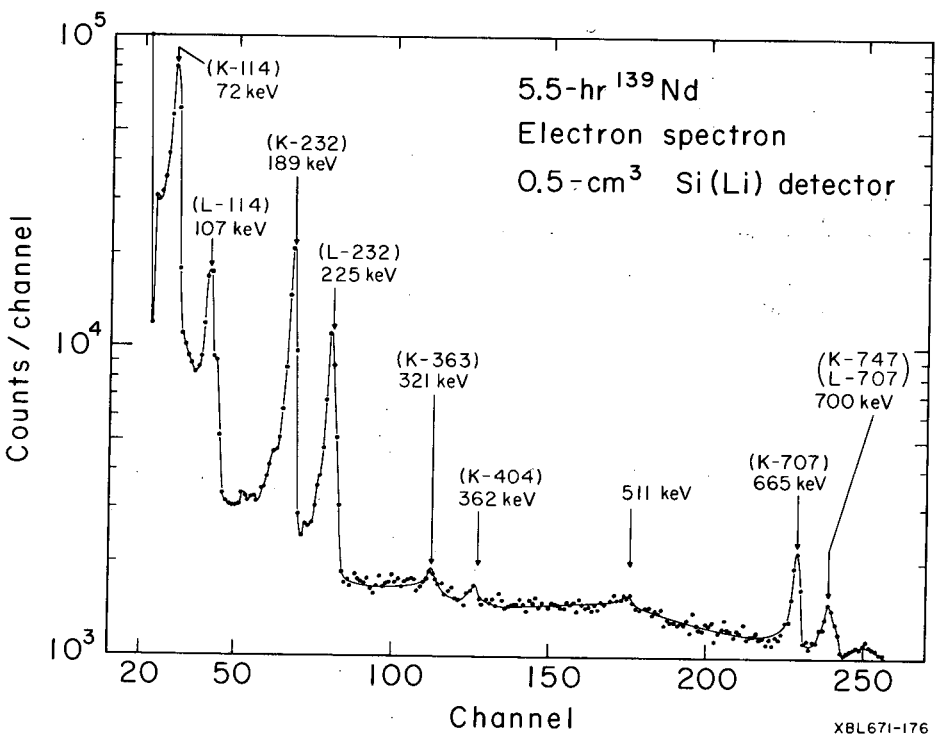

Fig. A. 5-2. A typical singles electron spectrum, determined with a 0.5-cm^3 Si(Li) detector.

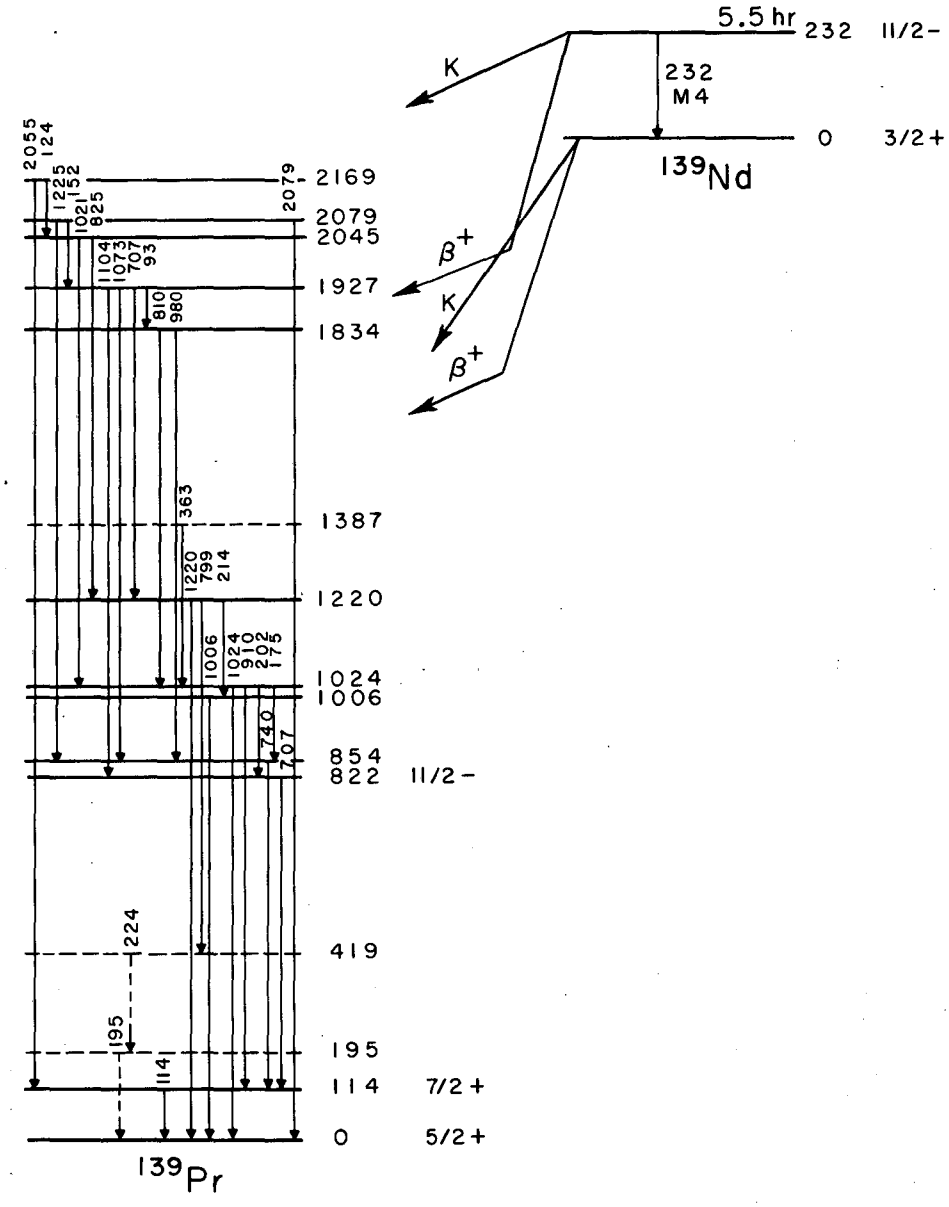

Fig. A. 5-3. Proposed partial decay scheme of ^{139}Nd.

6. NEUTRON-DEFICIENT ACTINIUM ISOTOPES

William J. Treytl, E. K, Hyde, and Kalevi Valli

Alpha energies and half-lives have been previously reported[1] for ^{214}Ac and ^{213}Ac. As part of our systematic study of neutron-deficient nuclides in this mass region, we are investigating the light actinium isotopes. As before, experiments are conducted at the Hilac, and the gaseous collection techniques described earlier[2] are being used.

This study has not been completed, but those results of which we are confident are presented in Table A.6-I. We have identified α energies and half-lives of ^{214}Ac through ^{210}Ac. There are disparities between our ^{214}Ac results and earlier reported values.[1] Most notably, we find that the 7.18-MeV peak previously ascribed to ^{214}Ac belongs to the electron-capture daughter, ^{214}Ra.

These α energies and mass assignments fit well with the mass-energy systematics extrapolated from the behavior of isotopes of radium, francium, emanation, and astatine.

References

1. E. K. Hyde, I. Perlman, and G. T. Seaborg, The Nuclear Properties of the Heavy Elements (Prentice-Hall, Inc., Englewood Cliffs, New Jersey, 1964, Vol. II, p. 1104.
2. W. J. Treytl and K. Valli, Alpha Decay of Neutron-Deficient Astatine Isotopes, UCRL-17194, 1966.

Table A.6-I. Summary of results on actinium isotopes.

Isotope	This work			Griffioen and Macfarlane[a]		
	Alpha energy (MeV)	Half-life (sec)	%	Alpha energy (MeV)	Half-life (sec)	%
^{214}Ac	7.213±0.008	8.0±0.3	52±3	7.24	12	33
				7.18		33
	7.080±0.008	8.0±0.3	44±3	7.12		33
	7.010±0.008	8.0±0.5	4±1			
^{213}Ac	7.355±0.008	0.80±0.05			≈ 1	
^{212}Ac	7.363±0.008	0.93±0.05				
^{211}Ac	7.475±0.008	0.2				
^{210}Ac	7.475±0.008	0.3				

a. Unpublished results.

7. ALPHA DECAY OF NEUTRON-DEFICIENT RADIUM ISOTOPES

Kalevi Valli, William T. Treytl, and Earl K. Hyde

Alpha-decay properties of light radium isotopes ^{214}Ra, ^{213}Ra, and ^{212}Ra have been studied previously.[1] In the present investigation, radium isotopes ^{206}Ra through ^{214}Ra were studied at the Heavy Ion Linear Accelerator by bombardment of ^{206}Pb with ^{12}C, and ^{197}Au with ^{19}F. The products recoiling from a thin target were slowed down in a helium atmosphere, swept through a small nozzle onto a catcher foil in an adjacent vacuum chamber, and detected with a Si(Au) surface-barrier detector. Details of the method are described in a previous article.[2]

Half-lives and accurate α energies were measured for the radium isotopes. Excitation functions were determined for both the radium isotopes and their α-active daughters. The assignments of the radium isotopes are based principally on these curves, on systematic trends in α-decay properties, and on half-life data. In most cases the radium isotope was identified through its β-decay francium daughter and through its α-decay emanation daughter; in several cases even the astatine granddaughter was observed.

Some typical α spectra are shown in Figs. A.7-1 and A.7-2. Excitation functions for the two target-projectile combinations are shown in Figs. A.7-3 and A.7-4. A summary of the results is given in Table A.7-I. The β branches of ^{213}Ra and ^{214}Ra were determined to be 20±5 and 0.09±0.03 percent, respectively. As a byproduct, the α energy of ^{214}Fr was remeasured to be 8.430±0.008 MeV.

A detailed report on the work will appear as UCRL-17322.

References

1. R. D. Griffioen and R. D. Macfarlane, unpublished results; E. K. Hyde, I. Perlman, and G. T. Seaborg, The Nuclear Properties of Heavy Elements (Prentice-Hall, Inc., Englewood Cliffs, New Jersey, 1964), Vol. II, p. 1104.
2. W. Treytl and K. Valli, Alpha Decay of Neutron-Deficient Astatine Isotopes, UCRL-17194, 1966.

Table A.7-I. Summary of results on radium isotopes.

Isotope	This work			Griffioen and Macfarlane[1]		
	Alpha energy (MeV)	Half-life	%	Alpha energy (MeV)	Half-life	%
^{214}Ra	7.136±0.005	2.6±0.2 sec	100	7.17	2.6 sec	
^{213}Ra	6.730±0.005	2.75±0.15 min	45±2	6.74	2.7 min	≈ 50
	6.623±0.005	2.75±0.15 min	49±2	6.61	2.7 min	≈ 50
	6.520±0.005	2.8 ±0.2 min	6±1			
^{212}Ra	6.896±0.005	13±2 sec		6.90	18 sec	
^{211}Ra	6.910±0.005	15±2 sec				
^{210}Ra	7.018±0.005	3.8±0.2 sec				
^{209}Ra	7.008±0.005	4.7±0.2 sec				
^{208}Ra	7.131±0.005	1.2±0.2 sec				
^{207}Ra	7.131±0.005	1.3±0.2 sec				
^{206}Ra	7.270±0.005	0.4±0.2 sec				
^{214}Fr	8.430±0.008			8.55	3.9 msec	

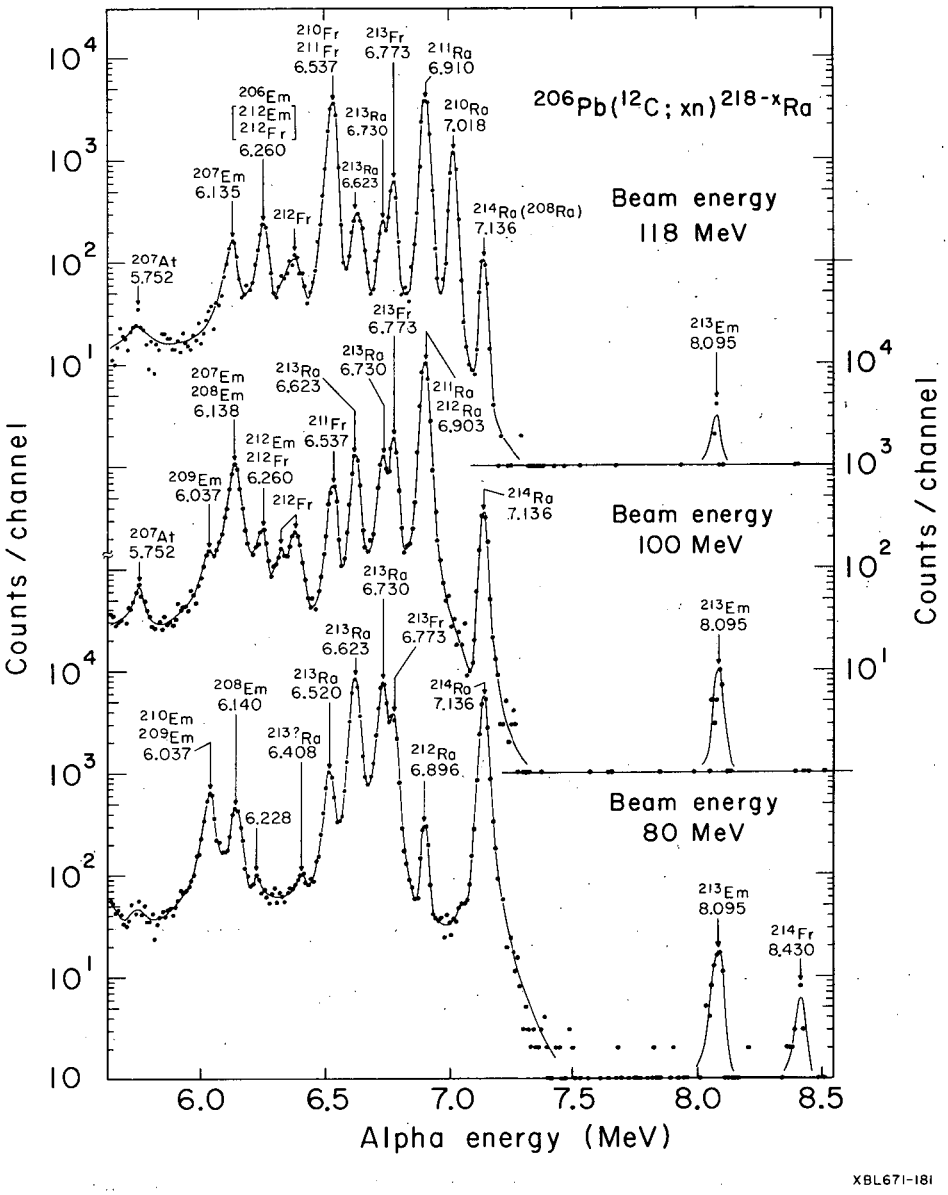

Fig. A.7-1. Alpha spectra of recoil products collected from the reactions $^{206}Pb(^{12}C, xn)^{218-x}Ra$ at three different beam energies. The top and bottom curves refer to the scale on the left, the middle curve to the scale on the right.

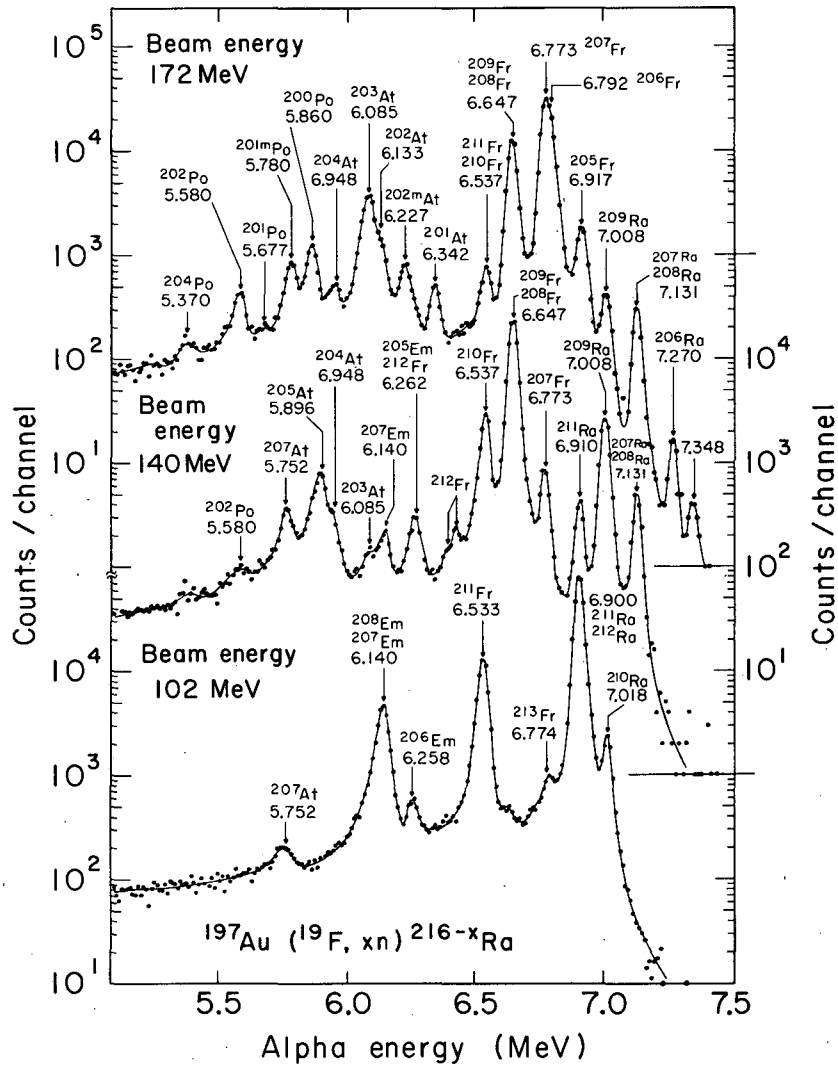

Fig. A.7-2. Alpha spectra of recoil products collected from the reactions $^{197}Au(^{19}F, xn)^{216-x}Ra$ at three different beam energies.

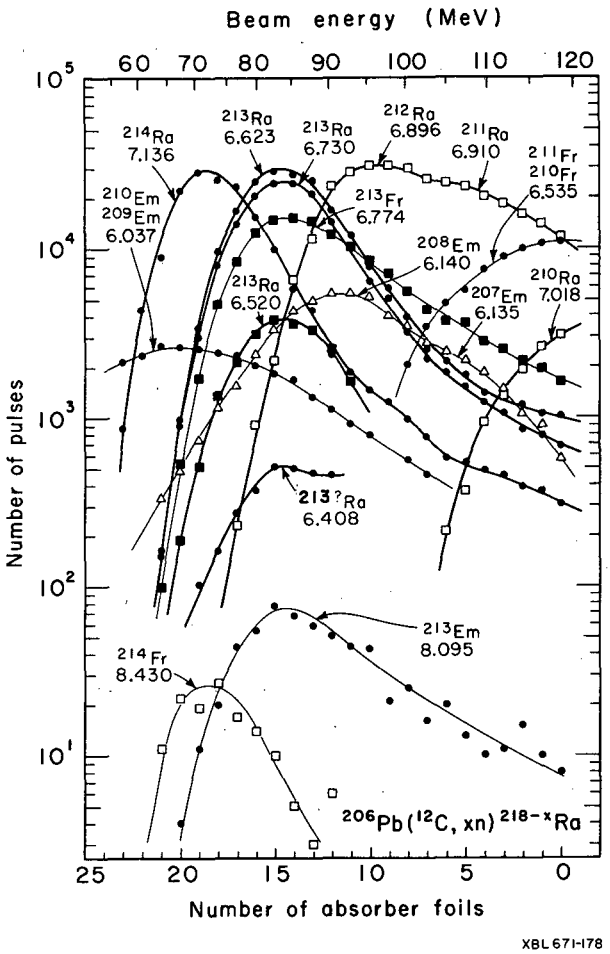

Fig. A. 7-3. Excitation functions for α activities observed in the reactions $^{206}Pb(^{12}C, xn)^{218-x}Ra$.

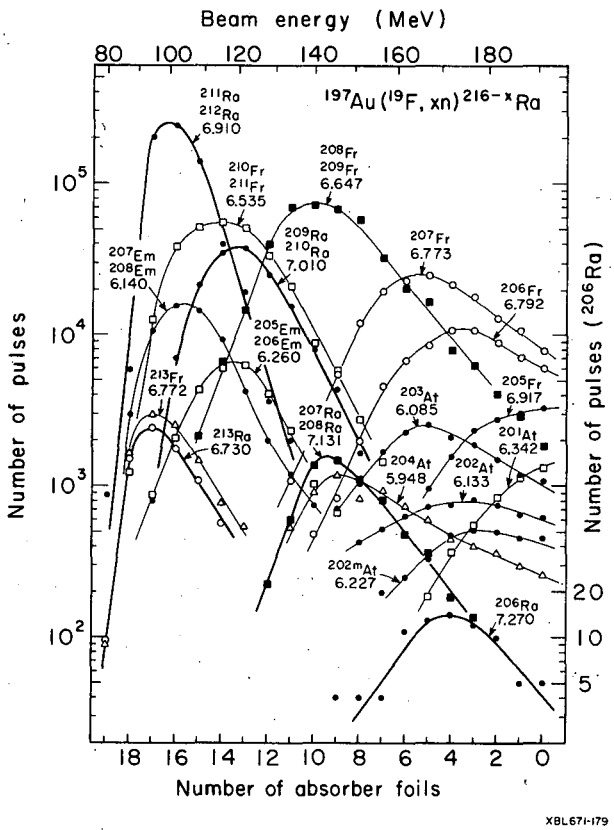

Fig. A. 7-4. Excitation functions for α activities observed in the reactions $^{197}Au(^{19}F, xn)^{216-x}Ra$.

8. ALPHA DECAY OF NEUTRON-DEFICIENT FRANCIUM ISOTOPES

Kalevi Valli, Earl K. Hyde, and William J. Treytl

Isotopes of francium lighter than mass 214 were studied at the Heavy Ion Linear Accelerator by bombardment of ^{197}Au with ^{16}O and of ^{205}Tl with ^{12}C. The recoil products were stopped in helium gas and collected on a metal foil which could be positioned before a Si(Au) surface barrier detector. The experimental techniques were similar to those described in Ref. 1. The previous work of Griffioen and Macfarlane[2] on francium isotopes was checked and extended.

Some typical α spectra are shown in Fig. A. 8-1 and one of the sets of excitation functions is shown in Fig. A. 8-2. A summary of data on the neutron-deficient francium isotopes below mass 210 is given in Table A. 8-I. The α decay energies are also plotted in Fig. A. 10-4. A complete description of this work will appear in UCRL-17272.

References

1. W. Treytl and K. Valli, Alpha Decay of Neutron-Deficient Astatine Isotopes, UCRL-17194, 1966.
2. R. D. Griffioen and R. D. Macfarlane, Phys. Rev. 133, B1373 (1964).

Table A. 8-I. Data on neutron-deficient francium isotopes.

Isotope	This work		Griffioen and Macfarlane[2]	
	Alpha energy (MeV)	Half-life (sec)	Alpha energy (MeV)	Half-life (sec)
^{203}Fr	7.130±0.005	0.7±0.2		
^{204m}Fr	7.028±0.005	2.2±0.2	7.02±0.03	2.0±0.5
^{204}Fr	6.973±0.005	3.3±0.2		
^{205}Fr	6.917±0.005	3.7±0.2	6.91±0.02	3.7±0.4
^{206}Fr	6.792±0.005	15.7±0.5	6.79±0.02	15.8±0.4
^{207}Fr	6.773±0.005	14.7±0.5	6.77±0.02	18.7±0.8
^{208}Fr	6.647±0.005	60 ± 2.0	6.65±0.02	37.5±2.0
^{209}Fr	6.647±0.005	52 ± 2.0	6.65±0.02	54.7±1.0
^{210}Fr	6.537±0.005	190 ± 5.0	6.55±0.02	159 ± 5.0
^{211}Fr	6.533±0.005	184 ± 5.0	6.55±0.02	186± 4.0
^{213}Fr	6.773±0.005	37 ± 2.0	6.77±0.01	33.7±1.5
^{213}Em	8.095±0.008			

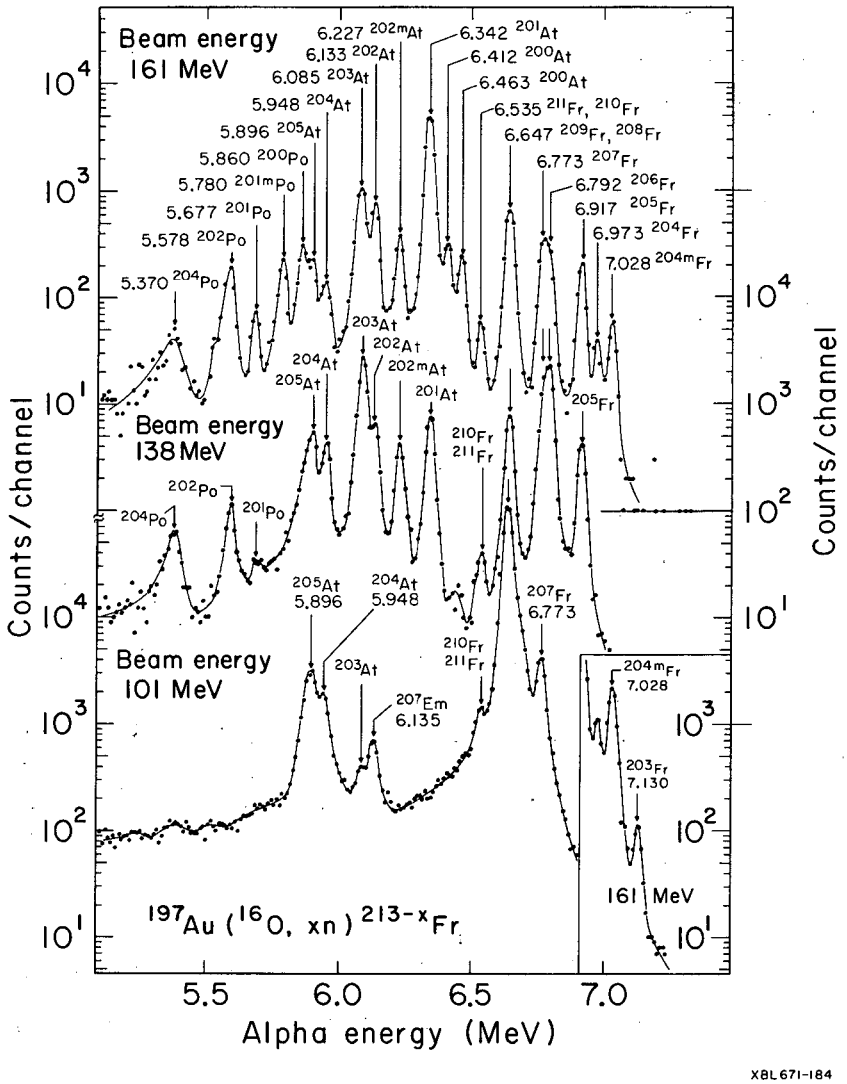

Fig. A. 8-1. Alpha spectra of recoil products collected from the reaction $^{197}Au + ^{16}O$ at three bombarding energies.

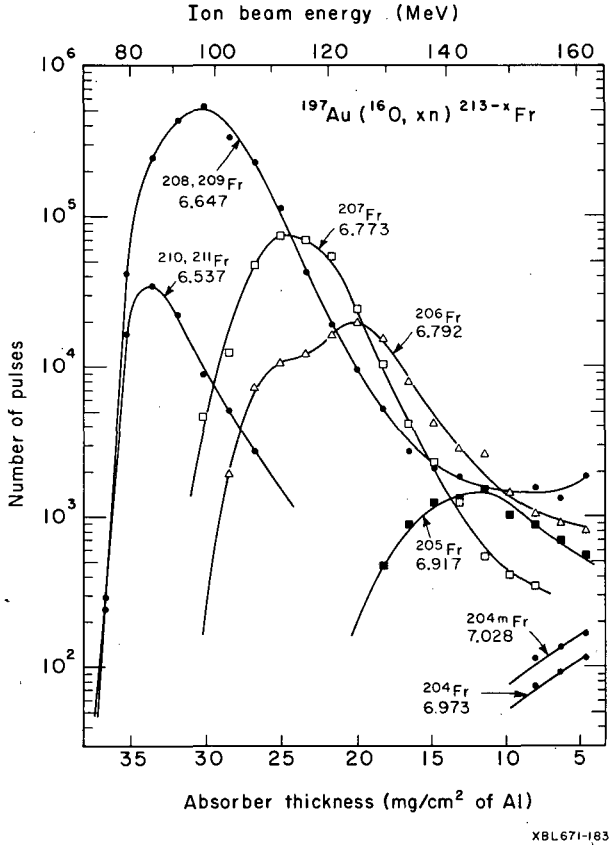

Fig. A. 8-2. Excitation functions for francium isotopes produced in the reaction, ^{197}Au + ^{16}O. The α-particle energies for the $^{210-211}$Fr pair and the $^{209-208}$Fr pair are too nearly identical to permit their separation with the semiconductor detector technique. Hence composite excitation curves are plotted. In the case of ^{207}Fr and ^{206}Fr, a partial resolution was possible.

9. ALPHA-DECAY PROPERTIES OF NEUTRON-DEFICIENT ISOTOPES OF EMANATION

Kalevi Valli, Matti J. Nurmia, and Earl K. Hyde

Isotopes of emanation (element 86) with 126 or fewer neutrons were prepared at the Heavy Ion Linear Accelerator by bombardment of platinum, gold, mercury, and thallium targets with nuclei of ^{16}O, ^{14}N, and ^{12}C. Several techniques were developed for isolation of the gaseous products. Surface-barrier detectors of Si(Au) were used to measure α particles emitted by emanation isotopes and by their polonium and astatine daughters. Mass-number assignments of new isotopes of mass 201 through 205 were based on genetic relationships and on excitation functions.

Figure A. 9-1 shows some typical α spectra in the case of thin gold targets bombarded with ^{14}N ions of different energies. Excitation functions for the emanation isotopes are shown in Fig. A. 9-2. A summary of new results is given in Table A. 9-I.

A complete description of this work is given in UCRL-16735, which has been submitted for publication in the Physical Review.

Table A. 9-I. New results on emanation isotopes with mass 207 or less.

Isotope	Half-life	α-particle energy (MeV)
^{207}Em		6.135±0.003
^{206}Em	6.5±1 min	6.258±0.003
^{205}Em	1.8±0.5 min	6.262±0.003
^{204}Em	75±2 sec	6.416±0.003
^{203}Em	45±5 sec	6.497±0.005
^{203m}Em	28±2 sec	6.547±0.003
^{202}Em	13±2 sec	6.636±0.003
^{201m}Em(?)	3±1.5 sec	6.768±0.005

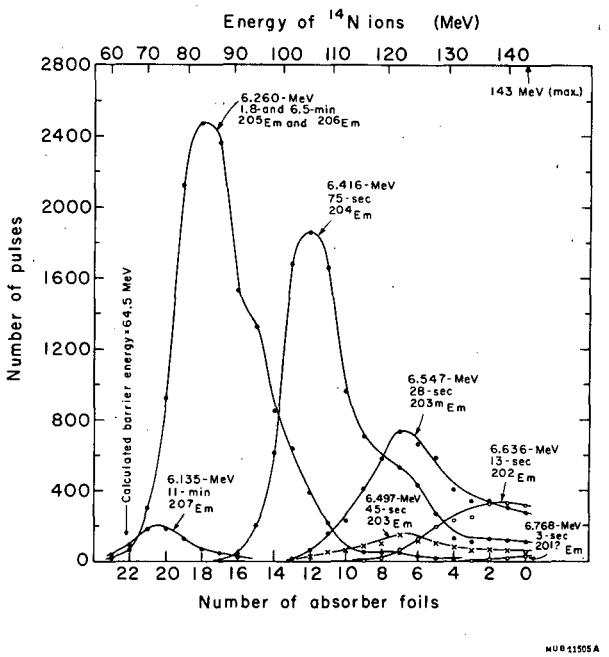

Fig. A. 9-2. Excitation functions for light emanation isotopes produced by bombardment of a thin gold target (2.5 mg/cm^2) with ^{14}N ions. Lower scale shows number of 0.00025-in. aluminum absorber foils placed in front of the target. Upper scale shows corresponding beam energy. Same integrated beam was used in each experiment. The indicated Coulombic barrier is a rough estimate from tangent spheres calculation.

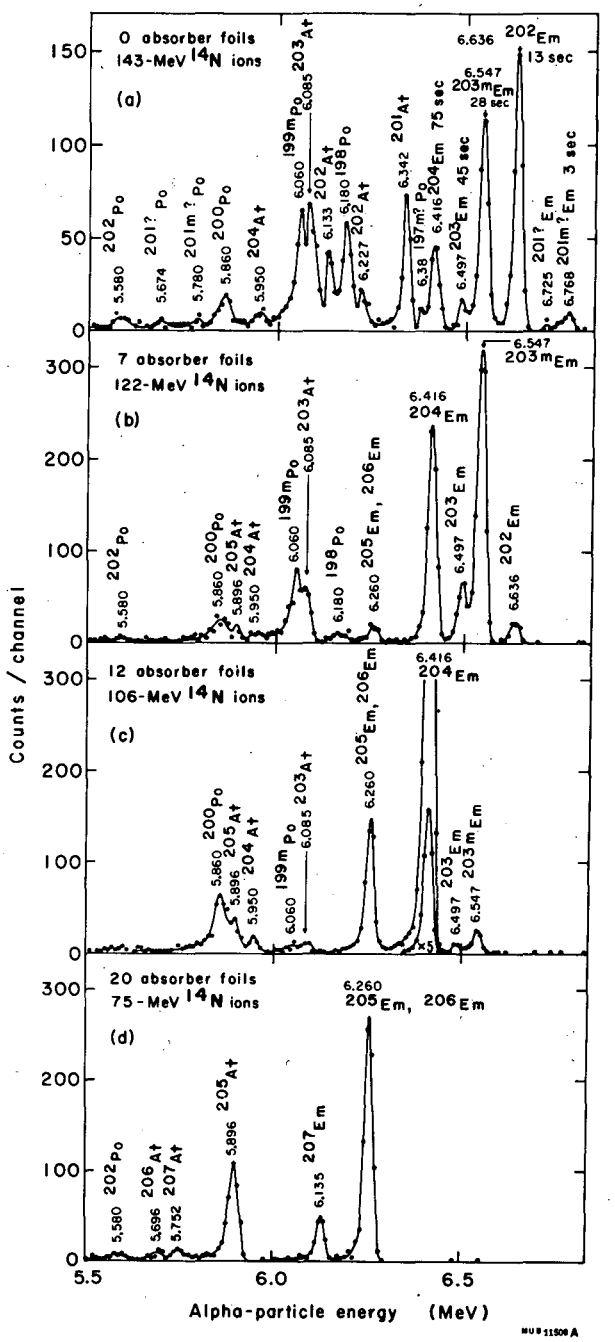

Fig. A. 9-1. Four examples of "thin target" alpha spectra obtained by bombarding a 2.5 mg/cm^2 (0.00005 in.) gold target with ^{14}N ions of different energies. The energy of the beam was regulated by placing different numbers of 0.00025-in. aluminum absorbers in front of the target. Beam intensity was about 1 μA and measuring times were 20 to 25 minutes. These and other spectra were used to prepare the excitation functions shown in Fig. A. 9-2.

10. ALPHA DECAY OF NEUTRON-DEFICIENT ASTATINE ISOTOPES†

William J. Treytl and Kalevi Valli

Alpha decay of neutron-deficient astatine isotopes has been studied previously by several groups;[1] the lightest isotope positively identified is ^{201}At (Ref. 2). In the present investigation, astatine isotopes ^{196}At through ^{204}At were studied at the Heavy Ion Linear Accelerator using separated ^{185}Re and ^{187}Re targets and ^{20}Ne ion beam.

Half lives and accurate alpha energies were measured for the astatine isotopes and for their α active daughters. Excitation functions were determined for both the astatine isotopes and the daughters. As the α decay properties of light polonium isotopes are known from several investigations,[2-5] positive mass assignments of the astatine isotopes could be made by comparing their excitation functions with those of the polonium daughters. Systematic trends in the α decay properties and the half-lives were also considered.

An alpha spectrum obtained by bombarding a thin ^{185}Re target with 160-MeV ^{20}Ne ions is shown in Fig. A. 10-1. Figures A. 10-2 and A. 10-3 show excitation functions of the astatine isotopes produced in the reactions ^{185}Re (^{20}Ne, xn)$^{205-x}$At, together with the excitation functions of their daughters. A summary of the present astatine results is given in Table A. 10-I; in Table A. 10-II, present energy values of light polonium isotopes are compared with those given in earlier reports.

When alpha energies of different isotopes are plotted as a function of neutron number for different elements, a set of step-like curves is obtained, as shown in Fig. A. 10-4. This figure includes all alpha energies observed in our recent studies of polonium, astatine, emanation, francium, radium, and actinium isotopes. It is interesting to note the systematic occurrence of isomerism in odd-neutron isotopes below 118 neutrons; this occurrence is probably related to the $i_{13/2}$ neutron level.

Footnote and References

†A more complete report of the present work is given in UCRL-17194 (submitted to Nucl. Phys.).

1. E. K. Hyde, I. Perlman, and G. T. Seaborg, The Nuclear Properties of Heavy Elements (Prentice Hall, Inc., Englewood Cliffs, New Jersey, 1964), Vol. II, p. 1077.
2. R. W. Hoff, F. Asaro, and I. Perlman, J. Inorg. Nucl. Chem. 25, 1303 (1963).
3. A. Siivola, in Nuclear Chemistry Division Annual Report UCRL-11828, Jan. 1965, p. 26.
4. E. Tielsch, Phys. Letters 17, 273 (1965).
5. C. Brun, Y. LeBeyec, and M. Lefort, Phys. Letters 16, 286 (1965).

Table A. 10-I. Astatine results obtained in this work compared with those of Hoff et al.[2]

Isotope	This work		Hoff et al.	
	α Energy (MeV)	Half-life	α Energy (MeV)	Half-life (min)
^{196}At	7.055±0.007	0.3±0.1 sec		
^{197}At	6.957±0.005	0.4±0.1 sec		
^{198m}At	6.847±0.005	1.5±0.3 sec		
^{198}At	6.747±0.005	4.9±0.5 sec		
^{199}At	6.638±0.005	7.2±0.5 sec		
^{200m}At	6.536±0.005	4.3±0.3 sec		
^{200}At	6.463±0.005	42 ±2 sec	6.465±0.011	0.9±0.2
^{200}At	6.412±0.005	42 ±2 sec	6.412±0.009	0.9±0.2
^{201}At	6.342±0.003	90 ±44 sec	6.342±0.006	1.5±0.1
^{202m}At	6.226±0.003	2.6±0.3 min	6.227±0.003[a]	3.0±0.2[a]
^{202}At	6.133±0.003	3.0±0.3 min	6.133±0.002[a]	3.0±0.2[a]
^{203}At	6.086±0.003		6.085±0.001	7.4±0.3
^{204}At	5.947±0.003		5.948±0.003	9.3±0.2

a. Both groups attributed to ^{202}At ground state.

Table A. 10-II. Polonium α energies obtained in this work compared with those reported previously.

Isotope	Alpha energy (MeV)				
	This work	Siivola[3]	Tielsch[4]	Brun et al.[5]	Hoff et al.[2]
^{193}Po		7.00			
^{194}Po	6.845±0.007	6.85			
^{195m}Po	6.698±0.005	6.72			
^{195}Po	6.608±0.005	6.63			
^{196}Po	6.517±0.005	6.53			
^{197m}Po	6.378±0.005	6.39		6.37±0.03	
^{197}Po	6.280±0.005	6.30		6.27±0.03	
^{198}Po	6.178±0.005	6.18		6.16±0.02	
^{199m}Po	6.053±0.005		6.05	6.04±0.01	
^{199}Po	5.950±0.008	6.06	5.95	5.93±0.02	
^{200}Po	5.860±0.003	5.86	5.85	5.85±0.01	5.860±0.006
^{201m}Po	5.780±0.005		5.77	5.77±0.01	5.780±0.007
^{201}Po	5.677±0.005		5.67	5.67±0.01	5.674±0.009
^{202}Po	5.578±0.005		5.57	5.57	5.580±0.010

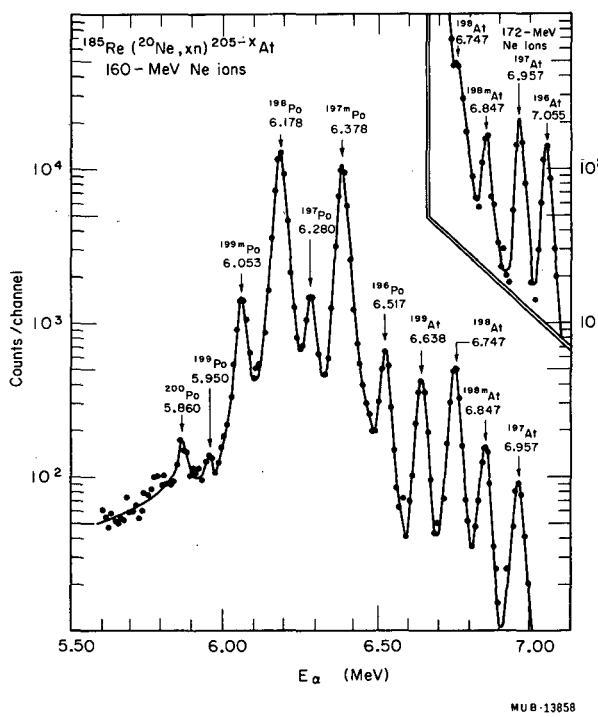

Fig. A. 10-1. Alpha spectrum showing the lightest astatine isotopes and their polonium daughters.

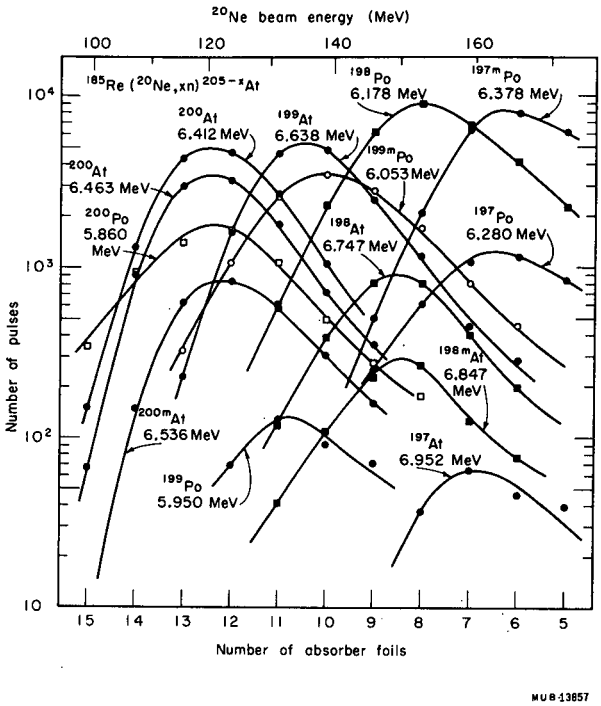

Fig. A. 10-2. Excitation functions of ^{197}At through ^{200}At and their polonium daughters.

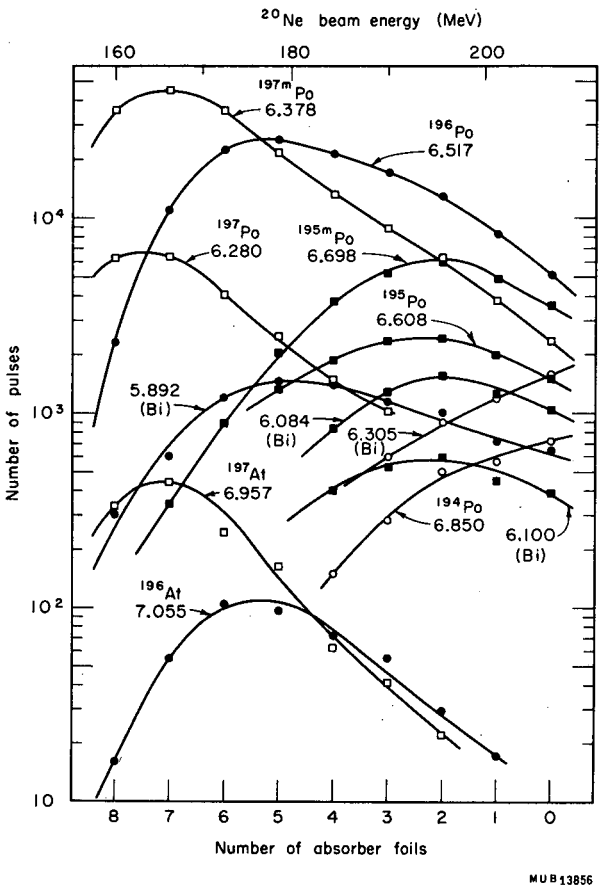

Fig. A. 10-3. Excitation functions of the lightest astatine and polonium isotopes.

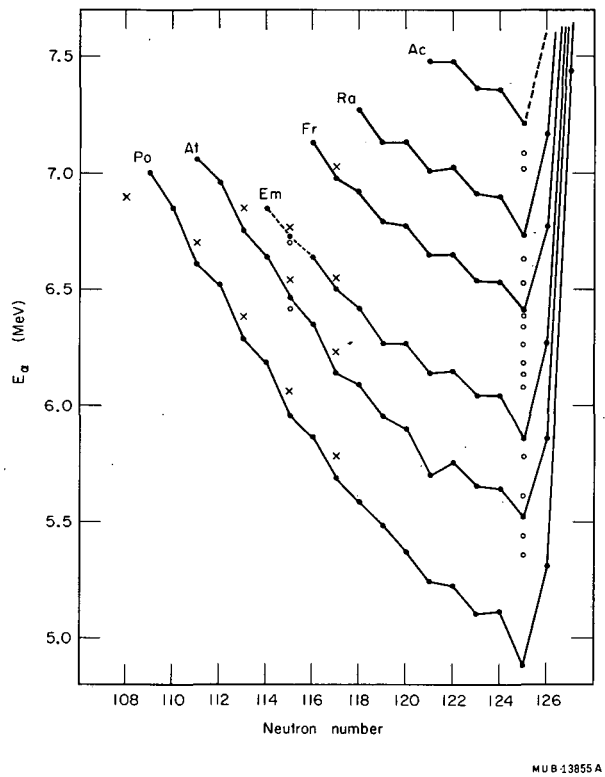

Fig. A. 10-4. Alpha energy versus neutron number for different elements in the area below the 126-neutron shell and above the 82-proton shell. Solid circles indicate energies assigned to ground-state α decay. The crosses represent α energies assigned to isomeric states. The open circles are alpha transitions to excited levels in the daughter nuclei (α fine structure).

11. NEW ISOTOPES: ^{11}Li, ^{14}B, AND ^{15}B †

A. M. Poskanzer, S. W. Cosper, Earl K. Hyde, and Joseph Cerny

The feasibility of using semiconductor detectors in conjunction with a power-law type particle identifier[1, 2] as a tool for the study of light fragments produced in reactions of GeV protons with heavy target nuclei has been successfully demonstrated. All the known particle-stable isotopes with $Z \leq 6$ (with the exception of ^{9}C and ^{16}C) were readily observed. As a preliminary experiment, prior to conducting the study outlined above, a search for new particle-stable isotopes with $Z \leq 5$ was undertaken. The initial measurements centered on the possibly bound nuclei ^{14}B (Ref. 3) and ^{15}B (Refs. 3 and 4), since no unknown isotopes of $Z \leq 4$ were expected.[3, 4] As a result of these investigations, we wish to report the identification of three new isotopes: ^{11}Li, ^{14}B, and ^{15}B.

This experiment was performed in the Bevatron's 5.3-GeV external proton beam which impinged on a 26 mg/cm^2 uranium foil mounted in the center of an evacuated scattering chamber 36-in. diam. Beam pulses 0.8 second long and containing an average of 5×10^{11} protons occurred every 6 seconds. A counter telescope consisting of two ΔE detectors (82- and 61-μ thick), an E detector (300 μ) and a rejection detector (100 μ) was placed at an angle of 40 degrees. All the counters were phosphorous-diffused silicon transmission detectors. A magnet and an 8.5-mg/cm^2 aluminum foil were placed in front of the telescope and all detectors except the rejection detector were separately collimated. (Also see Ref. 5).

The signals from these detectors fed a power-law type particle identifier system which has been completely described elsewhere.[1, 2, 5, 6] Basically, two identifications of each particle traversing the counter telescope were made, and stringent requirements were set on their agreement in order to improve the resolution of the identifier spectra and aid the search for small peaks in the presence of much larger ones. Consequently, only 50 percent of the events were accepted. Fast coincidence and pile-up rejection techniques were employed to reduce background (see Refs. 1 and 6). Total energy and particle-identifier signals were stored in a two-parameter, 4096-channel pulse-height analyzer, and the particle-identifier signal was also stored simultaneously in a 400-channel pulse-height analyzer.

Figure A.11-1 presents two particle-identifier spectra, covering isotopes of Li, Be, B, and C, obtained under identical conditions except that the data for the lower curve were taken at one-half the counting rate of those for the upper curve. The predicted locations of the observed ^{14}B and ^{15}B peaks are indicated on the figure by arrows, as are also the expected positions of the neighboring isotopes ^{9}C and ^{10}C. An additional peak at the predicted location for ^{11}Li was also observed.[7] A third experiment under somewhat different conditions yielded results exactly comparable to those in the lower curve.

It is necessary to eliminate the possibility that these small peaks corresponding to ^{11}Li, ^{14}B, and ^{15}B were caused by pile-up effects (see Refs. 5 and 6) arising from the high counting rates encountered in these experiments. This was accomplished in two ways. First, observation of chance coincidence spectra arising from pulser-simulated particles in coincidence with real events showed no indication of peaks in the positions of these proposed new isotopes. Second, since effects due to pile-up should be proportional to counting rate, the two sets of data presented in Fig. A.11-1 were taken. If any one of these new peaks arose from pile-up phenomena, that peak should be a factor of two smaller in the lower curve. All peak heights are the same in both curves, although the reduction of pile-up can be observed in the deeper valleys around the smaller peaks of the lower curve.[8]

Figure A.11-2 presents two-parameter data from an additional experiment centered on the ^{11}Li region. The contour plot and its projection again show a peak for ^{11}Li, and the fact that the ^{11}Li events appear in the expected energy range supports the assignment. The two-parameter data for the ^{14}B and ^{15}B isotopes also appeared in their appropriate energy intervals. Furthermore, the areas of the ^{11}Li, ^{14}B, and ^{15}B peaks seem reasonable, especially when one notes that the ratios of the ^{14}B and ^{15}B peaks relative to ^{13}B are quite similar to those of ^{11}Be and ^{12}Be relative to ^{10}Be. These peak areas do not accurately represent relative yields because of the narrow and different ranges of total energy accepted for each particle.[9]

Isotopes Not Observed

The particle instability of ^{10}Li is clearly shown by the absence of a peak in the expected position, especially since ^{11}Li is observed. If ^{13}Be were particle stable, we would have expected a much larger yield at its predicted position; this indicates that ^{13}Be is probably unbound. Investigations of the helium isotopes showed the presence of ^{3}He, ^{4}He, ^{6}He, and ^{8}He nuclei.[10] The possible isotope ^{10}He was not observed, and an upper limit for its intensity of 1/100 the ^{8}He peak can be set; however, this limit is not as low as that previously established from ^{252}Cf fission data.[5] The instability of ^{10}He, ^{10}Li, and ^{13}Be is in accordance with prediction.[3,4]

Observed Isotopes

Since ^{15}B was predicted to be bound[3,4] and ^{14}B was expected to be marginally bound,[3] the present observations of their existence were not unexpected. On the other hand, the generally reliable calculations of Garvey and Kelson[3] predicted ^{11}Li to be unbound by 2.5 MeV. Our observation of this isotope was, therefore, very surprising. However, only for this isotope and[6] for ^{8}He have their binding energies been significantly outside their expected errors.

For lack of a successful theory in this mass region, we may examine the systematics of two-neutron binding energies as a function of charge for a given neutron number.[11] The curve for N=6 has a kink, which reflects the fact that ^{9}Li and ^{8}He are appreciably better bound than one would expect by extrapolation from masses nearer stability. Thus a similar kink in the N=8 curve would be reasonable and would be consistent with the particle stability of ^{11}Li. A continued extrapolation, however, would still be consistent with the instability of ^{10}He.

These three new isotopes should have β-decay Q values of about 20 MeV and should all be delayed neutron emitters – ^{15}B in almost 100% of its decays. In fact, the assignment[12] of an 11.4±0.5 msec delayed neutron activity to ^{12}Be on the assumption that ^{11}Li was particle unstable must be re-examined. The log ft values for the β decay of ^{11}Li have been calculated for us by Kurath[13] and are consistent with an 11.4-msec half-life if ^{11}Li is bound by 3.5±2 MeV, which appears somewhat large. As was reported earlier,[12] this half-life is consistent with the log ft values calculated for ^{12}Be if its Q_β is 11.7±1 MeV. This Q_β is in very good agreement with the Q_β of 11.5±0.2 MeV calculated from a ^{12}Be mass based[14] on the T=2 states of ^{12}C and ^{12}B. Thus the 11.4-msec half-life is slightly more consistent with estimates of the decay properties of ^{12}Be than of ^{11}Li, but is certainly open to question at present. The assignment cannot be clarified on the basis of cross-section systematics.[15] In any event, the particle stability of both ^{11}Li and ^{12}Be is established by the present data.

We wish to acknowledge the important contributions of F. S. Goulding and D. A. Landis. We are also indebted to R. P. Lothrop and M. D. Roach for making the detectors and to R. F. Burton and Thomas Chan for designing the scattering chamber. We acknowledge the cooperation and assistance of the Bevatron staff. Finally, we wish to thank Dr. D. Kurath of the Argonne National Laboratory for the log ft calculations.

Footnote and References

†Phys. Rev. Letters 17, 1271 (1966).

1. F. S. Goulding, D. A. Landis, J. Cerny, and R. H. Pehl, IEEE Trans. Nucl. Sci. NS-13, 514 (1966).
2. J. Cerny, S. W. Cosper, G. W. Butler, H. Brunnader, R. L. McGrath, and F. S. Goulding, Nucl. Instr. Methods (in press).
3. G. T. Garvey and I. Kelson, Phys. Rev. Letters 16, 197 (1966).
4. A. E. Baz', V. I. Gol'danskii and Ya. B. Zel'dovich, Usp. Fiz. Nauk 72, 211 (1960) [English transl.: Soviet Phys. - Usp. 3, 729 (1961)].
5. S. W. Cosper, J. Cerny, and R. C. Gatti, Phys. Rev. (in press).
6. J. Cerny, S. W. Cosper, G. W. Butler, R. H. Pehl, F. S. Goulding, D. A. Landis, and C. Détraz, Phys. Rev. Letters 16, 469 (1966).
7. This peak falls exactly half-way between the positions that would be occupied by the unbound nuclei ^{6}Be and ^{5}Be.
8. It was also considered that a peak could arise from the disintegration of a nucleus in the Al foil or the front surface of the first ΔE detector [see R. W. Ollerhead, C. Chasman, and D. A. Bromley, Phys. Rev. 134, B74 (1964)]. However, calculation shows that this process is orders of magnitude too small to account for the observed peaks. The peaks

could not be due to hyperfragments because their expected short lifetimes would make the yields at the two distances from the target very different.
9. The energies observed in these experiments are considerably above the Coulomb barriers for the emission of these fragments from uranium and, therefore, are in a region where fragment intensity is decreasing with increasing energy.
10. No peaks were observed in the positions expected for ^{7}He and ^{9}He, in agreement with previous results (see Ref. 5).
11. A. Schwarzschild, A. M. Poskanzer, G. T. Emery, and M. Goldhaber, Phys. Rev. 133, B1 (1964).
12. A. M. Poskanzer, P. L. Reeder, and I. Dostrovsky, Phys. Rev. 138, B18 (1965).
13. D. Kurath (private communication), 1966; see also S. Cohen and D. Kurath, Nucl. Phys. 73, 1 (1965).
14. J. Cerny and G. T. Garvey, Isobaric Spin in Nuclear Physics, J. D. Fox and D. Robson, Eds., (Academic Press, New York, 1966), pp. 514 and 517.
15. I. Dostrovsky, R. Davis, A. M. Poskanzer, and P. L. Reeder, Phys. Rev. 139, B1513 (1965); A. M. Poskanzer, R. A. Esterlund, and R. McPherson, Phys. Rev. Letters 15, 1030 (1965).

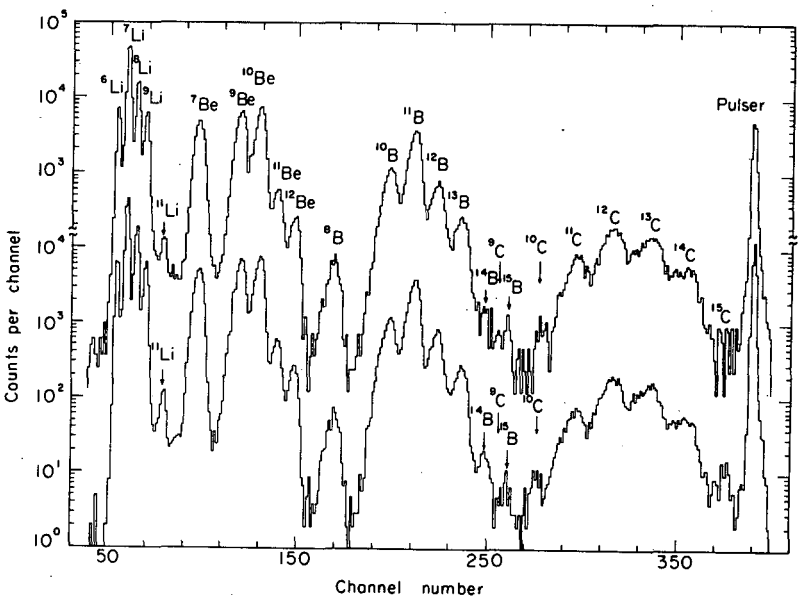

Fig. A. 11-1. Particle-identifier spectra resulting from the bombardment of uranium by 5.3 GeV protons. An energy loss from the E detector between 20 and 60 MeV was accepted. The solid angle subtended by the detectors was 0.8×10^{-4} sr for the lower curve and 1.7×10^{-4} sr for the upper curve with data collection times of 66 hours and 30 hours, respectively. The two spectra were normalized by slightly shifting the upper curve.

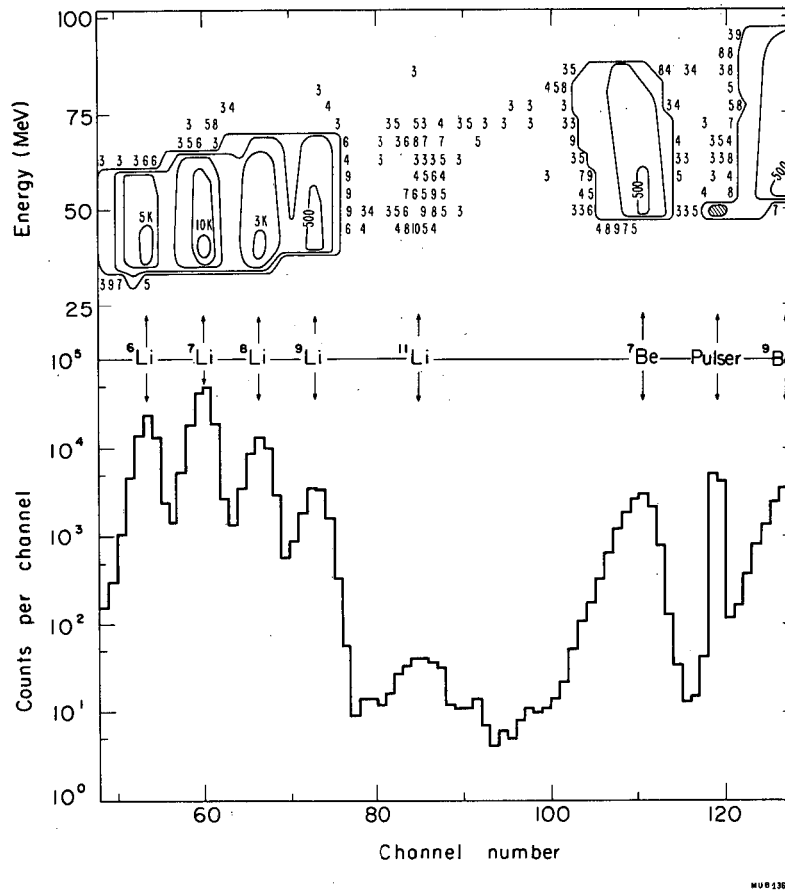

Fig. A. 11-2. The upper portion of the figure is a contour plot of counts as a function of total energy and particle-identifier signal centered in the ^{11}Li region. Unless labeled, the contour lines indicate the 10-, 100-, 500-, and 5000-count levels. Counts less than 10 are indicated, except for 1's and 2's, which have been suppressed for clarity. The cross-hatched peak is due to a pulser which was run at a slow rate throughout the experiment as a stability check. The energy loss accepted from the E detector was 10 to 87 MeV. No correction was made for energy loss in the target or in the 8.5 mg/cm^2 Al foil. The lower portion of the figure shows the projection of these data onto the particle-identifier axis. The solid angle subtended by the detectors was 0.8×10^{-4} sr and the data were collected for 41 hours.

12. A NEW CALIFORNIUM ISOTOPE, ^{242}Cf

Torbjorn Sikkeland and Albert Ghiorso

Summary

A new isotope of californium has been produced in the bombardments of ^{233}U, ^{234}U, ^{235}U, and ^{236}U with ^{12}C ions from the Hilac. It decays with a half-life of 3.4 ± 0.2 min by the emission of α particles with an energy of 7.39±0.02 MeV. From an analysis of the excitation functions, it is concluded that the isotope has the mass number 242.

Experimental

The uranium targets were made by molecular plating, from an isopropyl alcohol solution of uranyl nitrate onto 5-mg/cm^2 Be foils to a thickness of about 0.5 mg/cm^2. The nitrate was converted to the oxide by careful heating.

Beams of 124-MeV ^{12}C from the Hilac were, after magnetic deflection through 30 deg, degraded to the desired energy by the use of weighed Be foils. The range-energy curve of ^{12}C in Be as measured by Walton was used to estimate the energy.[1] The degraded energy spectrum was also measured by the use of a Li-diffused Si detector.

The collimator in front of the target had a diameter of 0.6 cm. The average beam current was about 1.5×10^{-6} A. At these intensities the degrader foils had to be water cooled.

The recoil atoms produced in the reaction were slowed down in helium at a pressure of about 700-mm Hg contained inside a cylindrical chamber of diameter 2.5 cm and length 4.4 cm. A Faraday cup for beam-intensity measurement was located at the end of the chamber. In the middle of the chamber wall and vertical to the beam axis was a 0.2-mm orifice through which the helium gas with the recoils was pumped into a target chamber. The recoils were collected on a platinum disk[2] placed in front of the orifice at a distance of about 1 cm. After the end of bombardment, the foil was flamed to remove β and α activities of volatile elements produced from the Be foils, and Pb and Bi impurities. The remaining activities were analyzed by the use of an α grid chamber in connection with a 1600-channel pulse-height analyzer. The decay of the various α groups was followed through seven preset time intervals, during each of which 200 channels of the analyzer were used for analysis of the energy spectrum. As calibration standards, the 5.80-MeV and 7.68-MeV α groups from ^{244}Cm and ^{214}Po, respectively, were used.

The time between end of bombardment and start of analysis was about 1 minute.

Results and Discussion

The α groups in the spectra obtained with the various targets were identified as follows:

1. A group at 7.05±0.02 MeV decayed with a half-life of about 10 minutes and was tentatively assigned to the previously unobserved nuclide ^{243}Cf. Further experiments are underway to confirm this assignment (see A. 12).
2. A group at 7.14 MeV and half-life of 44 min, observed with ^{236}U and ^{238}U as targets, was from the excitation functions assigned to the known[3] isotope ^{245}Cf.
3. A group at 7.21 ± 0.02 MeV decayed with a half-life of 20 min. This emitter was produced in a 3n, 4n, and 6n reaction with the targets ^{235}U, ^{236}U, and ^{238}U, respectively, and was attributed to ^{244}Cf that previously has been reported[3] to decay with a half-life of 25 ± 3 min by the emission of α particles with an energy of 7.17 ± 0.01 MeV.
4. A least-square-fit analysis of the decay for the α group at 7.39 ± 0.02 MeV gave a half-life of 3.4 ± 0.2 min. The shapes and positions of the maxima of excitation functions for the production of this α emitter corresponded to a (^{12}C, 3n), (^{12}C, 4n), (^{12}C, 5n), (^{12}C, 6n), and (^{12}C, 8n) reaction with the targets ^{233}U, ^{234}U, ^{235}U, ^{236}U, and ^{238}U, respectively,[4] and is thus the nuclide ^{242}Cf. Especially the functions of ^{234}U (^{12}C, 4n) and ^{235}U(^{12}C, 5n) were conclusive.

A more complete quantitative analysis of the functions shall be given in a later report.

The possibility that ^{242}Cf also decays by electron capture was not investigated. The half-life-energy relationship fits well the general trend for even-even Cf isotopes, indicating the dominant mode of decay for ^{242}Cf to be by α emission. The α energy of 7.39 MeV corresponds to

a Q_α of 7.54 MeV that is in excellent agreement with the value predicted by Foreman and Seaborg.[5]

We would like to thank Donald F. Lebeck for help in the analysis of the data. We also wish to thank Charles A. Corum for the design of the equipment, Thomas E. Bowman for the preparation of the targets, and the Hilac crew for excellent accelerator operations.

References

1. John R. Walton (LRL, Berkeley) unpublished results, 1960.
2. This technique was first developed by one of the authors (Albert Ghiorso) in 1959 and later applied by R. MacFarlane and R. D. Griffioen, then at the Lawrence Radiation Laboratory, who published a similar version of the experimental arrangement in Nucl. Instr. Methods 24, 461 (1963).
3. A. Chetham-Strode, Jr., G. R. Choppin, and B. G. Harvey, Phys. Rev. 102, 747 (1956).
4. T. Sikkeland, S. G. Thompson, and A. Ghiorso, Phys. Rev. 112, 543 (1958).
5. B. M. Foreman, Jr., and G. T. Seaborg, J. Inorg. Nucl. Chem. 7, 305 (1958).

13. DECAY PROPERTIES OF ^{243}Cf AND ^{244}Cf

Torbjorn Sikkeland, Albert Ghiorso, Jaromir Maly, and Matti Nurmia

Experimental Arrangement and Results

The experimental arrangement was identical to that used in the discovery of ^{242}Cf (Ref. 1) in which various uranium isotopes were bombarded with ^{12}C. We shall here discuss in some detail the α group at 7.05 MeV, that in the previous report was tentatively assigned to ^{243}Cf, and the group at 7.21 MeV that was assigned to ^{244}Cf.

^{243}Cf.

A least-square analysis of the decay of the α group at 7.05 ± 0.02 MeV gave a half-life of 10.3 ± 0.5 min. The assignment of the emitter to ^{243}Cf was based on the excitation functions of its production in ^{12}C reactions on ^{235}U and ^{236}U. In the former, the shape of the function corresponded to a (^{12}C, 4n) reaction, and in the latter to a (^{12}C, 5n) reaction. We also observed this activity in a ^{238}U(^{12}C, 7n) reaction, although here it was partly masked by the tail of an intense α group at 7.14 MeV from ^{245}Cf. Indirect experimental evidence that ^{243}Cf also has other decay modes can be obtained from cross-section systematics for (^{12}C, xn) reactions. At a particular value of x, the maximum cross section, σ_x, for such reactions is, to a good approximation, proportional to the quantity $\overline{(\Gamma_n/\Gamma_t)}^x$. Here $\overline{\Gamma_n/\Gamma_t}$ is the geometric mean of the relative level widths for neutron emission for the nuclides in the cascade of x neutrons. The quantity log (Γ_n/Γ_t) is expected to vary very nearly linearly with $\overline{A}$, the average mass number of the nuclei in that cascade. Hence one can set

$$\log \sigma_x = C_x + xC_0A , \qquad (1)$$

where C_x is a constant dependent only on x, and C_0 is independent of both $\overline{A}$ and x.

These constants were determined from the measured maximum cross sections for (^{12}C, 4n) reactions with ^{234}U, ^{236}U, and ^{238}U as targets, and for (^{12}C, 5n) reactions with the targets ^{235}U and ^{238}U. The calculated maximum cross sections for ^{235}U (^{12}C, 4n) ^{243}Cf and ^{236}U (^{12}C, 5n) ^{243}Cf were found to be larger than the measured cross sections for the 7.05-MeV 10-min α activity, by a factor of 9 ± 2 and 12 ± 2, respectively. The weighted average of these values is 10 ± 2. Hence, the partial α half-life for this group is 100 ± 20 min, which corresponds to an unhindered α decay.

The energy of the ground-state transition α's in the decay of ^{243}Cf is predicted[2] to be about 7.17 MeV. According to the energy-level diagram of Nilsson,[3] the odd neutron for the ground state of the nuclide ^{243}Cf is in the state 1/2+[631], and that of the daughter ^{239}Cm is in the state 7/2-[743], and hence the transition between these two states will be unfavored.

An excited-neutron level, 1/2+[631], in the daughter is expected, to which a favored decay will take place. The 7.05-MeV α group apparently is a manifestation of that transition, and the level 1/2+[631] in ^{239}Cm then is about 120 keV above the ground state.

It appears from our experiments that other α groups from ^{243}Cf must have intensities less than that of 7.05 MeV. Hence, we conclude the dominant mode of decay of ^{243}Cf to be by electron capture (EC) to ^{243}Bk, and the ratio EC/α to be about 10.

^{244}Cf

This nuclide was produced in ^{235}U(^{12}C, 3n), ^{236}U, (^{12}C, 4n) and ^{238}U(^{12}C, 6n) reactions. In the last system the 7.14-MeV alphas from ^{245}Cf, produced simultaneously, interfered with the α spectrum from ^{244}Cf. In the bombardment of ^{236}U with 69-MeV ^{12}C, the yield of ^{245}Cf was about two orders of magnitude less than that of ^{244}Cf, and this system was used to study the decay properties. The decay of ^{244}Cf was followed over 8 half-lives and a least-square-fit analysis gave a half-life of 19.4 ± 0.6 min.

In separate experiments, the energy spectrum of the α's from ^{244}Cf was studied in greater detail, with the 7.070-MeV α's from ^{217}At and the 7.680-MeV α's from ^{214}Po used as calibration sources.

With 2.5 keV/ch, the group at 7.21 MeV was resolved into two, one at 7.214 MeV and the other 40 ± 4 keV lower. The ratio of the intensity of the former group to that of the latter was 3.0 ± 0.3. Apparently the former consists of α's from a ground-state transition and the latter of α's from a transition to the 2+ rotational level associated with the ground state. The FWHM of the group at 7.214 MeV was measured to be 21 keV.

We would like to thank Donald F. Lebeck for help in analysis of the data.

References

1. See also T. Sikkeland and A. Ghiorso, Paper A. 12.
2. B. M. Foreman, Jr., and G. T. Seaborg, J. Inorg. Nucl. Chem. 1, 305 (1958).
3. E. K. Hyde, I. Perlman, and G. T. Seaborg, The Nuclear Properties of Heavy Elements (Prentice Hall, Englewood Cliffs, New Jersey, 1964), p. 843.

14. ISOTOPES OF ELEMENT-102 WITH MASS 251 TO 257

Albert Ghiorso, Torbjorn Sikkeland, and Matti J. Nurmia

We have used ^{12}C and ^{13}C ions accelerated by the Hilac to bombard essentially mono-isotopic targets of ^{244}Cm, ^{246}Cm, and ^{248}Cm for the production of isotopes from ^{251}102 to ^{257}102. The apparatus is an elaboration of a simple principle first observed in this laboratory some years ago.[1] Atoms recoiling from the target are stopped in a stream of helium at 450 torr and carried by this gas through an orifice about 0.5 mm in diameter into an evacuated space. The gas jet impinges a few millimeters away on the periphery of a wheel, and a large fraction (≈ 40%) of the heavy atoms attach themselves to its surface. At regular intervals the wheel is digitally pulsed about 60 deg to expose the collected atoms to Au-Si surface-barrier α-particle detectors. In this series of experiments four detectors, equally spaced around the wheel, were used simultaneously in order to obtain half-life information as well as α-particle energies. The targets, made by molecular deposition, were curium oxide (0.2 to 0.5 mg/cm^2) on beryllium metal (4 to 5 mg/cm^2). Beam currents used were typically 2×10^{12} particles/sec in an area of 0.2 cm^2. Changes in bombarding energy were made by inserting different thicknesses of Be degrader foils in the beam path so that excitation functions for the α-particle activities could be determined.

The electronic circuitry to analyze the pulse outputs from the individual detectors was conventional. After preamplification with charge-sensitive preamplifiers located near the detectors, the pulses were shaped by delay lines to one microsecond and further amplified in the counting area. They were then sorted with a multiparameter analyzer into four 200-channel

groups. The resolution of the system varied from 25- to 50-keV full-width at half-maximum, depending on the detector used. Spontaneous fissions were recorded by discriminators set to trigger on pulses greater than 30 MeV in amplitude. It was necessary to gate the system off during the beam pulse to prevent spurious signals from neutron reactions, and thus a 20% loss was suffered. The total counting efficiency, defined as the ratio of the counts observed to the α disintegrations undergone by the nuclei transmuted from the target, varied from 5 to 10%, depending on the detector size used.

Fortunately the production cross sections to form the element-102 isotopes by these reactions range from 10^{-32} to 10^{-30} cm^2, so that it was possible to make measurements of energies and half-lives with relatively good statistical accuracy. Each isotope, except for $^{251}102$, was made by more than one reaction as a check on the mass assignment obtained from the peak energy of its excitation function. Half-lives were obtained by the relative amounts of α activity in the four detectors after correcting for the individual counting efficiencies. These were obtained by measuring the α-particle decay of a known activity.

A difficulty that was encountered initially was created by the discovery that the 2.6-sec 7.14-MeV ^{214}Ra decayed slightly by electron capture to 3.9-msec 8.43-MeV ^{214}Fr. The ^{214}Ra was produced in these experiments by reactions of carbon ions with lead isotopes present in the target as impurities. This background activity interfered in some cases with the radiation from the 102 isotopes, but it was possible to adequately correct for this effect by referring to the amount of the ^{214}Ra parent activity. Similarly, corrections for the α-particle groups from ^{211m}Po were taken into account when they were a possible source of background.

Table A. 14-I summarizes these measurements. For comparison we have listed the most recent data available from G. N. Flerov's Dubna groups as published at their recent Heavy Ion Conference held at that Laboratory.

It can be seen that within the statistical errors, there is reasonable agreement between the two sets of results except in the value of $^{256}102$ for the half-life. Several attempts were made to find an α-emitting 8-sec activity that could be attributed to $^{256}102$ but were unavailing. The source of the discrepancy is unknown and thus the spontaneous fission branching ratio must be questioned. It would seem possible that an isomer may be responsible for much or all of the spontaneous fission activity observed by Kuznetsov et al.[2]

As a matter of historical interest, it is worth pointing out that the activities, both α particles and spontaneous fissions, that are now ascribed to $^{252}102$ were first observed in 1959. At that time the 3-sec 8.3-MeV alphas and spontaneous fissions were thought to be due to $^{254}102$ because this coincided with a half-life determined the year before by a milking method in which ^{250}Fm was observed. In 1961, as a part of the experiments in which element 103, lawrencium, was discovered, α particles of 8.2 MeV and 15-sec half-life were ascribed to element 102, and now it is clear that they belong to mass 257 rather than 255 as guessed at that time.

References

1. Albert Ghiorso, unpublished work, 1959.
2. V. I. Kuznetsov, Yu V. Lobanov, and V. P. Perelygin, Half-Life of an Isotope of Element 102 with Mass Number 256, Dubna preprint 2525, Dec. 28, 1965.

Table A. 14-I. Decay properties of various isotopes of element-102.

Isotope	Reaction used	Half-life (sec)	αE (MeV) ±0.02	SF/α ratio	Reaction used	Half-life (sec)	αE (MeV) ±0.03	SF/α ratio
$^{251}102$	$^{244}Cm(^{12}C, 5n)$	0.8±0.3	8.68≈20% ?	-	Not reported			
			8.60≈80%					
$^{252}102$	$^{244}Cm(^{12}C, 4n)$	2.3±0.3	8.41	$\frac{1}{2}$	$^{239}Pu(^{18}O, 5n)$	4.5±1.5	8.41	–
	$^{244}Cm(^{13}C, 5n)$	~2.5[a])	8.41	$\frac{1}{2}$				
$^{253}102$	$^{244}Cm(^{13}C, 4n)$	105±20	8.01		$^{242}Pu(^{16}O, 5n)$	95±10	8.01	–
	$^{246}Cm(^{12}C, 5n)$	~100[a])	8.01		$^{239}Pu(^{18}O, 4n)$			
$^{254}102$	$^{246}Cm(^{12}C, 4n)$	55±5	8.10		$^{243}Am(^{15}N, 4n)$		8.11	$<\frac{1}{1800}$
	$^{246}Cm(^{13}C, 5n)$	~50[a])	8.10		$^{238}U(^{22}Ne, 6n)$	50±10		
	$^{244}Cm(^{13}C, 3n)$	~50[a])	8.10		$^{242}Pu(^{16}O, 4n)$	75±15		
$^{255}102$	$^{246}Cm(^{13}C, 4n)$	185±20	8.11		$^{238}U(^{22}Ne, 5n)$	≈ 120	8.08	–
	$^{248}Cm(^{12}C, 5n)$	~180[a])	8.11		$^{242}Pu(^{18}O, 5n)$	180±10	8.09	
$^{256}102$	$^{248}Cm(^{12}C, 4n)$	2.7±0.5	8.43		$^{238}U(^{22}Ne, 4n)$	6±2	8.41	$\frac{1}{200}$
	$^{248}Cm(^{13}C, 5n)$	3.2±0.2	8.43			≈8		
	$^{246}Cm(^{13}C, 3n)$	~3[a])	8.43		$^{242}Pu(^{18}O, 4n)$	9±3	8.42	
$^{257}102$	$^{248}Cm(^{13}C, 4n)$	23±2	8.23≈50%		Not reported			
	$^{248}Cm(^{12}C, 3n)$	~20[a])	8.27≈50%					

a) No error given due to rather poor statistics.

15. THE APPLICATION OF SEMICONDUCTOR x-RAY DETECTORS TO THE STUDY OF HEAVY-ION REACTIONS

H. R. Bowman, J. B. Wilhelmy, R. L. Watson, R. C. Jared, and S. G. Thompson

The recent development of high-resolution semiconductor detectors at this laboratory[1] has stimulated their application to a variety of nuclear reactions and nuclear spectroscopy research problems. One such application is the study of x-ray emission from radioactive products of reactions induced by complex nuclear projectiles in the heavy-ion accelerator. Many of the products of these reactions are highly neutron-deficient and hence decay by orbital electron capture accompanied by the emission of x rays.

A straightforward application of these detectors is shown in Fig. A. 15-1, which displays the K x-ray energy distribution from a gold target bombarded with 70- and 60-MeV carbon ions. It is known from previous work[2] that the predominant reaction at these energies is $^{197}Au(^{12}C, 4n)^{205}At$. The main product, ^{205}At, decays by orbital electron capture with a 26-min half-life to produce ^{205}Po, and emits an x ray in the process. The two x-ray peaks to the left of the Po x rays in Fig. A. 15-1 are from gold (target) x rays caused by fluorescent excitation of the target. The increase in x-ray intensity as the bombarding energy is increased from 60 to 70 MeV reflects the reaction cross section very well. As the energy was increased in steps up to the full energy of the beam (125 MeV), it was possible to identify the onset of the 5n, 6n, and 7n reactions by simply observing the change in the x-ray intensities. The measurements were usually taken 2 min after a 2-min bombardment.

Other x-ray measurements were taken with various choices of projectile and target, and the results were compared with compound nucleus reactions detected by more conventional means. In the case of the heavy ion ^{40}Ar, we observed some rather unexpected results.

Consider Fig. A. 15-2 which shows the x-ray spectrum observed in a thorium target at various times after a bombardment with 416-MeV ^{40}Ar ions. In this case even a partial transfer of projectile particles to the target nuclei would have produced elements that have a high fission probability. Hence one might expect to see mainly fission products symmetrically distributed around some maxima in the region between rhodium and xenon. Instead, what is revealed in Fig. A. 15-2 is a very complex yet rather regular distribution of products in the region of dysprosium to polonium. The separation of the spectrum into clearly defined x-ray peaks is the result of the detector's high resolution and the circumstance that the $K\alpha_1$ and $K\alpha_2$ energies of adjacent elements reinforce each other in this particular region. Figure A. 15-2 strongly suggests that a variety of reactions occurs when thorium is bombarded with argon ions. One possibility would be the transfer of particles from the target to the projectile. It is highly improbable that the observed distribution of products could be the result of de-excitation of products above thorium by emission of many nucleons or α particles.

The low-energy x-ray spectrum region below dysprosium also led to interesting results. Figure A. 15-3 shows this region (4 to 60 keV), examined with a silicon detector, for the cases of 416-MeV argon ions on gold, lead, thorium, and uranium targets. The target L x rays (self-induced fluorescence) appear at the left for each spectrum. The heavy vertical arrow in each spectrum points to the K x-ray energy that would correspond to symmetrical division of the reaction products if no charged particles were emitted. One surprising feature is the absence of any clear evidence of the symmetrical distribution of fission products. Another striking feature is the close similarity of the x-ray distribution from all targets.

These x-ray results clearly indicate that heavy-ion reactions have many complex and interesting features not adequately explored in previous work. Various possibilities for making these measurements more precise by the identification of the isotopes produced have been proposed. One which is under investigation is the simultaneous measurement of K x rays and γ rays. If these radiations are measured and recorded digitally on magnetic tape, they can later be sorted to reveal those γ rays in coincidence with x rays of a given element and thereby identify the isotope.

References

1. Harry R. Bowman, Earl K. Hyde, Stanley G. Thompson, and Richard C. Jared, Science 151, 562 (1966).

2. T. Darrah Thomas, Glen E. Gordon, Robert M. Latimer, and Glenn T. Seaborg, Spallation-Fission Competition in Astatine Compound Nuclei Formed by Heavy-Ion Bombardment, UCRL-9950, November 1961.

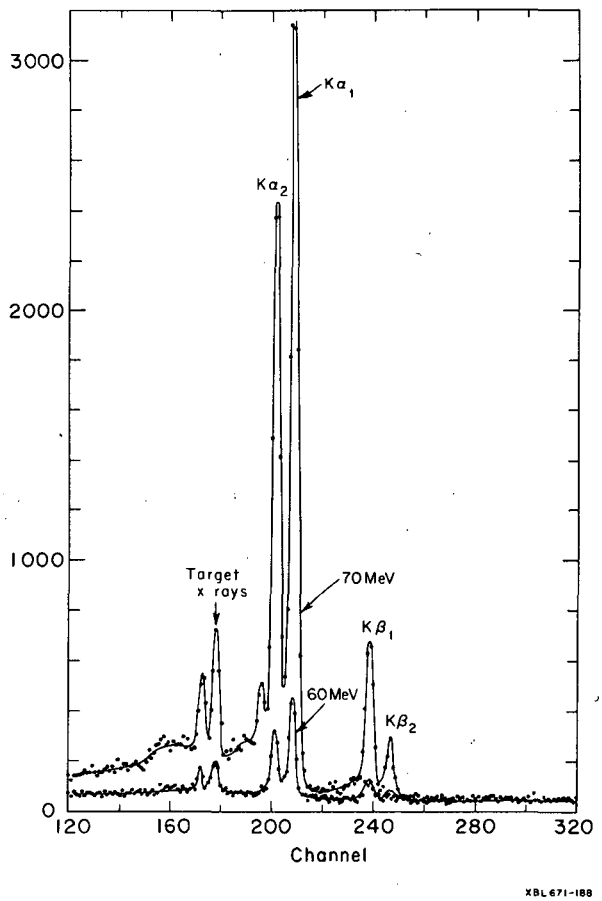

Fig. A. 15-1. The K x-ray energy distribution from a gold target bombarded with 70- and 60-MeV carbon ions. The prominent reaction is $^{197}Au(^{12}C, 4n)^{205}At$.

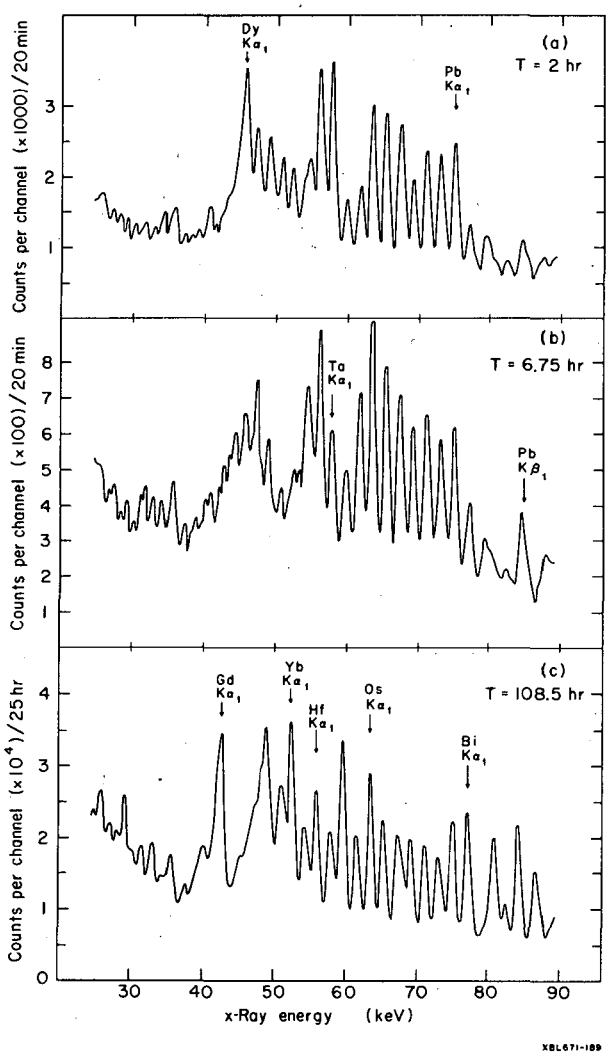

Fig. A. 15-2. The x-ray spectrum observed in a thorium target at (a) 2 h, (b) 6.75 h, and (c) 108.5 h after a bombardment of 416-MeV argon ions.

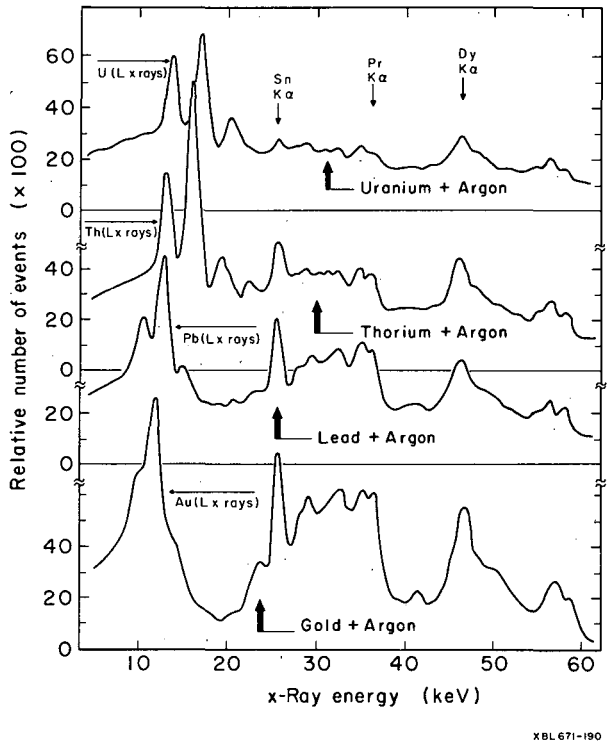

Fig. A. 15-3. The low-energy x-ray spectrum (4 to 60 keV) of gold, lead, thorium, and uranium after a bombardment of 416-MeV argon ions.

16. GROUND-STATE (QUASI-) ROTATIONAL LEVELS IN LIGHT Os, Pt, AND Hg NUCLEI†

J. Burde, R. M. Diamond, and F. S. Stephens

The present work represents a continuation of studies of the γ-ray cascade de-exciting the final nucleus produced in heavy-ion nuclear reactions. In a previous work,[1] reactions were studied in which the final nuclei (of Yb, Hf, and W) all had stable equilibrium deformations and consequently well-defined rotational spectra. The aim of the present work was to extend the region of study upward in atomic number (to Os, Pt, and Hg), and thus come into a region where the product nuclei do not have stable equilibrium deformations in their ground states.

A difference in technique between this and our previous study is that we now have available reasonably large Ge(Li-drifted) detectors, so that for all the nuclei reported, both electron and high-resolution γ-ray spectra were taken. This has permitted us to assign multipolarities to the observed transitions, and thus to establish our partial-level schemes with considerably greater certainty.

Self-supporting metallic foils of ^{165}Ho, ^{169}Tm, ^{175}Lu, and ^{181}Ta, 1 to 5 mg/cm^2 thick, provided the targets used in this work; they were bombarded by 10^{-3} to 10^{-1} μA beams of ^{11}B, ^{14}N, or ^{19}F accelerated by the Hilac. The beam energies were measured using a solid-state counter and were expected to be accurate to about 2%. The Hilac is a pulsed machine, producing 3-msec beam bursts 15 times per second (subsequent modifications have made much larger duty cycles available). The presently reported data on the prompt de-excitation of the final nuclei were, of course, taken during the 3-msec beam burst. However, the targets were also observed in the interval between beam pulses, and two metastable states thus observed during the course of this work have been reported elsewhere.[2] For each product nucleus studied, electron spectra were taken at three or four projectile energies 5 to 10 MeV apart (centered around the expected optimum energy). This limited excitation function enabled us to group the conversion lines by

nuclide, and also established the optimum bombarding energy for that particular product nucleus.

The electron and γ-ray spectra of ^{178}Os, ^{188}Pt, and ^{190}Hg are shown in Figs. A. 16-1, -2, and -3, as more or less typical of the group. In general, we found here, as in the previous work, that the cleanest spectra are associated with those reactions in which the fewest neutrons are emitted. The assignment of the lines to a given element could be immediately proposed according to the simple rule that charged particles are not emitted (at these excitation energies and distances from β stability) in sufficient intensity that their product nuclei can give rise to strong lines. For most of the low-energy transitions, the K- to L-conversion line separation could be measured sufficiently accurately to confirm this. The mass assignments could be rather unambiguously made from the very regular behavior of the excitation functions. Thus in both this and the previous work, using the β-stable, odd-Z, even-N targets, we found that the optimum (best peak-to-background ratio) bombarding energy was within about 5 MeV of the following values: (^{11}B, 4n), 55 MeV; (^{11}B, 6n), 85 MeV; (^{14}N, 5n), 93 MeV; and (^{19}F, 6n), 120 MeV. In many cases cross checks were possible, when a given product was made by two or even three reactions.

In each nucleus the K/L ratio of one of the two lowest cascade transitions could be measured with sufficient accuracy to identify it unambiguously as E2. This transition then served as the basis for normalizing the γ-ray and electron spectra, so that multipolarities for all the transitions seen in both spectra could be deduced.

Almost all the intense lower energy transitions were found to be E2, to behave very regularly in their energy spacings, and to decrease monotonically (but sometimes not very regularly) in intensity with increasing energy. In the deformed nuclei these transitions undoubtedly comprise the ground-state rotational band, and in the nondeformed nuclei, they define a "quasi-rotational" band, which, in the harmonic oscillator limit, would become just the highest spin member of each vibrational multiplet. In this work we have been primarily interested in these transitions, and they are summarized in Table A. 16-I. The classification, A or B, following the energy indicates a confidence of 95 or 75%, respectively, in the assignment of the transition to the (quasi) rotational sequence. We have also listed in Table A. 16-I the relative intensities of the transitions in each nucleus. These are expected to be accurate to about 20%.

Although spin determinations are in general absent, they were made in two cases up through the 8+ state. These cases were the 106-neutron nuclei, ^{182}Os, and ^{184}Pt, where weakly populated 8- isomers exist with half-lives of around one millisecond. These isomers, discussed in detail elsewhere,[2] de-excite predominantly to the 8+ member of the ground-state rotational band, and then on down the ground-state band. Angular-distribution measurements established reasonably unambiguously the spin sequence in the isomers, and the ground-state rotational band transitions thus identified in the isomers coincided with the first four strong E2 transitions observed in the prompt in-beam spectra of these nuclei. Thus, in at least these two cases, the expected spin sequence can be considered independently established up through the 8+ state.

In the group of nuclei reported here, the occurrence of prominent nonrotational-band transitions was much more frequent than in the previously studied group of Yb, Hf, and W nuclei. Some of these transitions have been summarized in Table A. 16-II, together with their intensities and probable multipolarities. This list is by no means complete; only a few of the most intense transitions whose mass assignments are unambiguous have been included.

One of the reasonably clear results of this study is that we could generally not identify states of so high a spin in these transition- and vibrational-region nuclei as in the previous study of rotational nuclei. This is most apparent in the mercury isotopes, for which spins no higher than six could be found. At least for ^{190}Hg the spectra are reasonably good, and it is clear (Fig. A. 16-3) that the higher transitions are not simply obscured. Since we are able to identify a state only if it is populated heavily (at least 10 to 20% of the time), the above result suggests only that whereas the high-spin (14 to 20) rotational states do receive this much population in regions of well-deformed nuclei, no single high-spin state receives this much population in the vibrational nuclei.

It seems likely to us that this change is due to the rather dramatically different level structure of the vibrational nuclei rather than to any sudden change in the reaction mechanism. Nevertheless, at present we have to conclude that we do not have enough information to establish even the most important causes of the observed populations. It is clear that direct experimental information is needed on the kind of levels feeding the ground band.

Our main interest in this work had to do with the structure of the light Os, Pt, and Hg nuclei. This has been discussed in some detail in another publication.[3] Stated briefly in terms of the nuclear potential energy, we tentatively conclude that in moving out of the deformed region, the potential barrier in the γ direction is a function of both proton and neutron number (the latter being more apparent); whereas the deformation (controlled by the central bump in the potential) is mainly a function of proton number; and it, in fact, changes dramatically between osmium and platinum over most of the region for which there is information.

Footnote and References

†Shortened version of UCRL-17067, submitted to Nucl. Phys.

1. F. S. Stephens, N. L. Lark, and R. M. Diamond, Phys. Rev. Letters 12, 225 (1964); Nucl. Phys. 63, 82 (1965).
2. J. Burde, R. M. Diamond, and F. S. Stephens, Nucl. Phys. (in press).
3. J. Burde, R. M. Diamond, and F. S. Stephens, UCRL-17067; Nucl. Physics (in press).

Table A. 16-I. Ground-state (quasi-) rotational band transitions[a]

Transition (rel. inten.)	^{178}Os	^{180}Os	^{182}Os	^{182}Pt	^{184}Pt	^{186}Pt	^{188}Pt	^{188}Hg	^{190}Hg
2 → 0	131.6 A (100)	132.2 A (100)	126.9 A (100)	153.7 A (b)	162.1 A (100)	191.1 A (100)	265.9 A (100)	412.6 A (100)	416.4 A (100)
4 → 2	266.1 A (94)	276.3 A (88)	273.3 A (92)	262.5 A	272.7 A (87)	298.5 A (98)	405.4 A (84)	489.9 A (84)	625.1 A (108)
6 → 4	363.1 A (89)	386.6 A (74)	393.7 A (70)	355.2 A	362.5 A (66)	387.2 A (65)	513.3 A (53)		730.2 A (91)
8 → 6	432.9 A (79)	462.2 A (72)	483.0 A (63)	431.0 A	431.6 A (58)	464.3 A (51)	597.7 B (27)		
10 → 8	488.0 A (43)	510.2 A (42)	532.7 A (44)	493 B	475.8 A (55)	514.6 A (43)	654.0 B (18)		
12 → 10	536.8 B (28)	541.0 A (34)		543 B	496.6 B (43)	551 B (9)			
14 → 12		566.4 B (25)			521.5 B (47)				
16 → 14					554 B (29)				

a. Energies are expected to be accurate to ±0.25% and intensities to ≈ 20%.
b. This spectrum was not sufficiently clean to give intensities accurate to 20%.

Table A. 16-II. Prominent nonrotational transitions.

Nucleus	Energy	Intensity[a]	Probable multipolarity
^{178}Os	623	45	E2
^{180}Os	365	35	E1
	618	30	E1
	643	17	M1
^{182}Os	493	15	E2
^{186}Pt	477	37	E2
	489	21	E2
^{188}Pt	412	11	M1
	417	18	E2
	582	20	E1
	892	27	E1
^{190}Hg	661	30	E2

a. Relative to the intensities of Table A. 16-I.

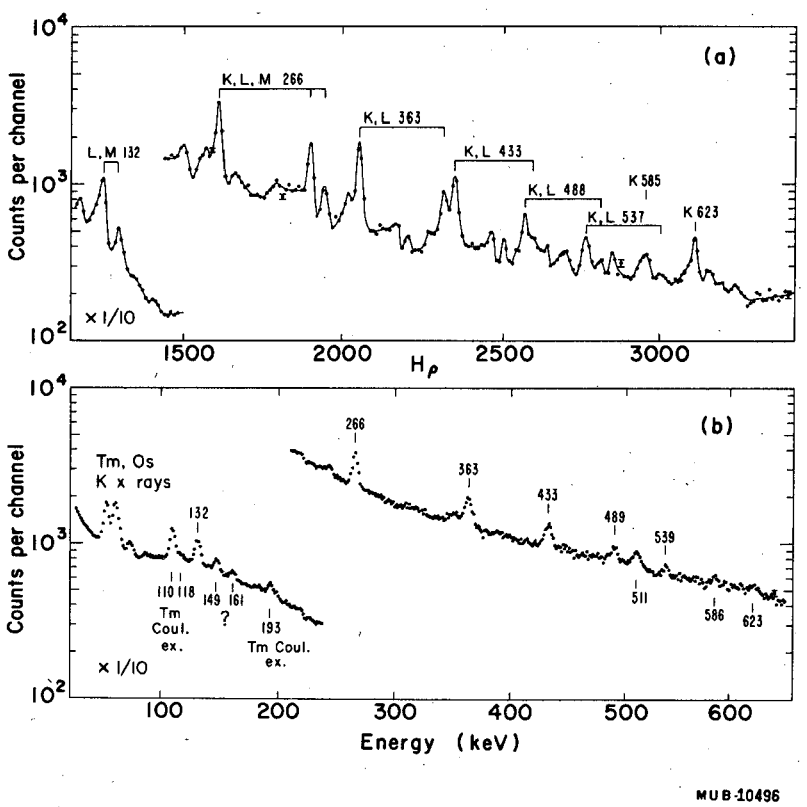

Fig. A. 16-1. Conversion electron (a) and γ ray (b) spectra of ^{178}Os observed following the ^{169}Tm(^{14}N, 5n)^{178}Os reaction at 93-MeV bombarding energy.

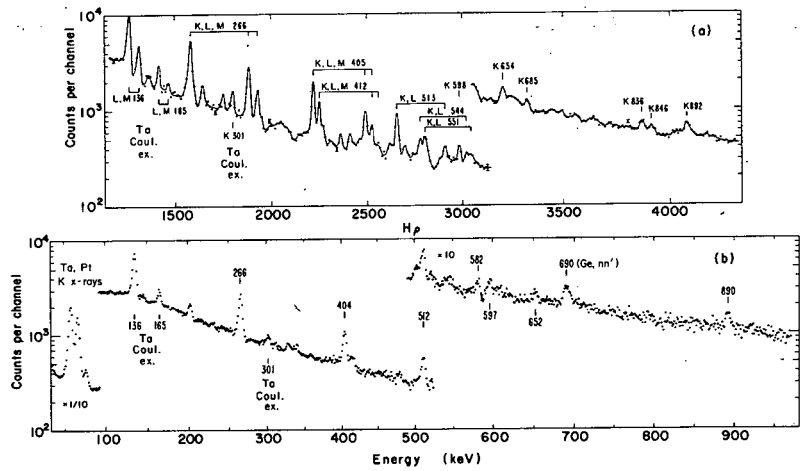

Fig. A. 16-2. Conversion electron (a) and γ ray (b) spectra of ^{188}Pt observed following the $^{181}Ta(^{11}B, 4n)^{188}Pt$ reaction at 56-MeV bombarding energy.

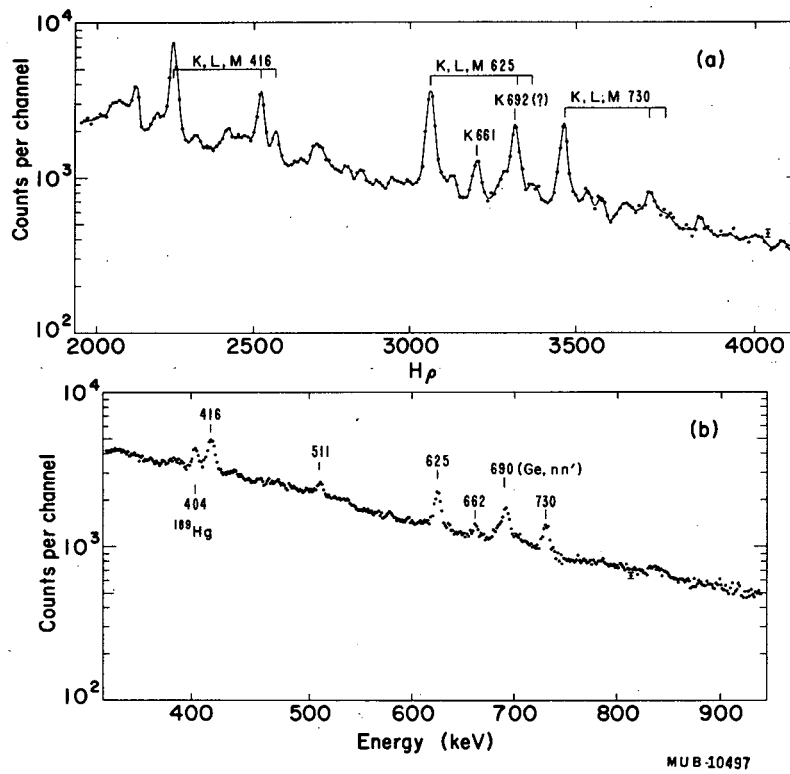

Fig. A. 16-3. Conversion electron (a) and γ ray (b) spectra of ^{190}Hg observed following the $^{181}Ta(^{14}N, 5n)^{190}Hg$ reaction at 93-MeV bombarding energy.

17. COLLECTIVE EXCITATIONS IN NEUTRON-DEFICIENT BARIUM, XENON, AND CERIUM ISOTOPES

Jack E. Clarkson, R. M. Diamond, F. S. Stephens, and I. Perlman

The existence of three regions in the periodic table where deformed nuclei exist is now well established. The properties of these nuclei have been surveyed by several authors.[1,2] Experimental evidence concerning a fourth region of deformation where N and Z both lie between 50 to 82 was first given by Sheline et al.,[3] who observed the first-excited states in ^{130}Ba, ^{128}Ba, and ^{126}Ba. These isotopes were subsequently studied by Chanda,[4,5] who proposed partial-level schemes for the three barium nuclei. The evidence suggesting that the nuclei in this region might be deformed consisted mainly of (a) systematics of the first-excited state energies, and (b) the ratio of the energy levels observed in relation to that expected for rotational bands in even-even deformed nuclei.

The study of the collective energy levels of nuclei in this new region of deformation is also the subject of the present work; in particular, we have studied the levels of ^{126}Ba, ^{124}Ba, ^{122}Xe, ^{120}Xe, and ^{134}Ce. The systematic investigation of collective levels following radioactive decay is not always possible, so that the "in-beam" method has been used in most of this work.

The Hilac was used to accelerate beams of ^{14}N, ^{12}C, ^{11}B, and ^{10}B to the energies required to produce ^{126}Ba, ^{124}Ba, ^{122}Xe, ^{120}Xe, ^{134}Ce, and ^{134}Pr from the appropriate targets (Table A. 17-I). The experimental setup for the in-beam γ-ray detection (Fig. A. 17-1) consisted of: (a) a retractable gold scatter foil and a beam-energy detector for beam-energy measurements; (b) a collimator of approximately 3/8-in. diameter connected to an electrometer that measured the beam hitting the collimator, and facilitated focusing of the beam; (c) the target assembly which included the target on a retractable paddle and Lucite windows which allowed viewing of the target while in the beam location; (d) the Faraday cup, connected to an electrometer which measured the beam intensity; and (e) the lithium-drifted germanium counter which was usually placed a few millimeters from the Lucite window at 90° to the beam direction.

Since the Hilac "partial-energy" beam was used, no degradation of the beam by absorbers was necessary. The desired energy was achieved by changing the tilt of the gradient in the post-stripper tank, and by adjusting the tank tuners. The beam was magnetically analyzed by deflection through 52 deg, and then it traveled through a quadrupole focusing magnet into the experimental area. The beam-pulse repetition rate was 12 pulses per second in the early part of this work, and was later increased to 40 pulses per second. The beam-pulse length was ≈ 3 milliseconds.

Thin (about 5 mg/cm^2) self-supporting metallic targets of indium and separated tin isotope were used in the γ-ray apparatus as previously described (see Fig. A. 17-1). Thick targets of indium and lead iodide were used in a terminating target holder, where the target holder itself served as the Faraday cup.

A method used for measuring the lifetime of the first-excited state of ^{126}Ba was essentially that of Novakov et al.[3] The equipment, set up by Burde, Diamond, and Stephens, made use of a small wedge-gap electron spectrometer. The diagram of the high-voltage target arrangement is shown in Fig. A. 17-2. As the reaction products were made, they were given a recoil energy of about 5 MeV. Conversion electrons were given off before the recoiling nuclei reach the negative high-voltage grid, which was placed at a distance depending on the mean lifetime of the level. The electrons were then slowed down by the negative-voltage gradient by an amount depending on their distance of emission from the grid. After passing the grid, the electrons were accelerated by the full-voltage gradient to an energy greater than their original energy. In this manner an electron was given an additional amount of energy, the magnitude of which depended on the recoil distance before electron emission, and therefore on the lifetime of the nuclear state involved. By comparing the electron energy with the high voltage off to that when it is on, and knowing the recoil velocity and applied voltage, one can obtain the mean lifetime of the state. In order for a reference-peak position to be obtained, the negative voltage was applied only to every other Hilac pulse; as the information was thus stored separately, a perturbed and unperturbed peak were recorded during the same magnet sweep. A target thickness of ≈ 200 μg/cm^2 was used. A description of the calculations and uncertainties involved has been given elsewhere.[7]

In the study of the energy levels of ^{134}Ce, radiochemical separation and study of the radioactive decay of ^{134}Pr were employed as well as the in-beam technique. The former procedure was similar to that used by Chanda.[5] The copper iodide target was prepared by evaporating

the copper iodide in vacuum and depositing it on 2.7 mg/cm^2 nickel foil. Target thickness varied from 1 to 2 mg/cm^2. A beam of carbon ions, with a beam current of about 150 nA, was used. The praseodymium nuclei produced were chemically separated from the other products present. A crude excitation function was measured, and ^{134}Pr was produced with maximum yield by selecting the beam energy as ≈ 90 MeV. A detailed description of the procedures used here has been given elsewhere.[7]

The mass assignments of the nuclei considered in this work were based on several criteria. The peak of the calculated-excitation function for a product formed in a given reaction was used as a starting point for investigation of the nuclides studied. The assignment of the γ rays from ^{126}Ba and ^{122}Xe was in agreement with the values previously found by Chanda[4] (^{126}Ba) and Morinaga and Lark[8] (^{122}Xe). The results of the ^{134}Pr radiochemical study and the in-beam method both support the assignment of the ^{134}Ce levels. Since ^{124}Ba was produced by two reactions, with different targets and projectiles, both giving the same transitions, this mass assignment is also considered to be quite certain.

The spin and parity assignments were made from the systematic behavior of the observed lines. This includes (a) the regular spacing of the transition energies, approaching in some cases the I(I+1) rotational spacing; (b) the outstanding intensity of the lines which decreased monotonically with increasing transition energy, and (c) the knowledge that in all cases for which the spins and parities were known, the ground-state rotational band was the most prominent (or only) band populated by the method used. For ^{126}Ba, the E2 assignment for the lowest energy transition was also supported by its lifetime and the measured K/L intensity ratio.

An example of the electron spectra observed in the lifetime study of the first-excited state of ^{126}Ba is shown in Fig. A. 17-3. The mean lifetime (τ) for the 256-keV transition was $2.7 \pm 0.5 \times 10^{-10}$ seconds. The limits of error quoted are due mainly to the statistical uncertainty in the calculation of the centroids of the peaks in the electron distributions. (In the determination of the lifetime of the 2+ level, an approximate upper limit for the lifetime of the 455-keV 4+ transition was also measured. This value, $\leq 8 \times 10^{-11}$ seconds, has been subtracted from $2 \rightarrow 0$ lifetime to allow for the effect of the decay from the $4 \rightarrow 2$ level.) The value for the lifetime as determined above gives a deformation (β) of ^{126}Ba of 0.24±0.02, where β is the deformation parameter of a spheroid given by $\beta = 4/3(\pi/5)^{1/2}(\Delta R/R_0)$, with R_0 the mean nuclear radius and ΔR the difference between the major and minor semiaxis of the spheroid. Unfortunately the experiment does not distinguish between an rms value of β resulting from oscillations about a spherical shape and a stable equilibrium value of β.

The Ge γ-ray spectra of the nuclei studied here are shown in Figs. A. 17-4 through A. 17-8.

A summary of the ground-state rotational band transitions as determined in this work is shown in Table A. 17-II. The classification system of the transitions has the following meanings: A, definite peak, definite assignment; B, definite peak, rather indefinite assignment; and C, indefinite peak, indefinite assignment. The nuclei studied in this work are probably at the edge of a region of deformation, and hence the transitions and deformation determined in this work are of interest in extending the knowledge of nuclear shapes in this region.

It is clear that there is no sharp discontinuity of nuclear properties in this region (such as is found in the region above the 82-neutron shell) would indicate the definite onset of stable equilibrium deformations in the ground states of nuclei. Furthermore, it has been pointed out that the existence of a stable equilibrium deformation cannot be established from a knowledge of the energy of the first 2+ state and its E2 transition probability to the ground state (rms value of β) alone. Thus, to make definite statements concerning nuclear shapes, one would have to know considerably more about higher collective (vibrational) excitations. In the absence of such information, we can compare only the ground-state band properties of these nuclei with those of other nuclei, lying in regions of the periodic table where there is more knowledge about the nuclear shapes. This has been done in some detail in a separate publication.[9] We will very briefly state the results of that comparison here.

Nuclei like the light Ba and Xe nuclei studied here, are probably easily deformed (low β vibration) and are likely to be stretched under rotation to become deformed nuclei. Whether they are deformed in their ground states, however, is not really clear. To decide this point on the basis of the present data, one would have to carry out model calculations of the type done by Kumar and Baranger,[10] and when the known characteristics of the levels are reproduced, the ground-state wavefunction can be examined. Perhaps other experimental indications of the

ground-state shape can be found; however, this is not so easy if one does not assume that the shapes of the ground and lowest 2+ states are necessarily the same.

References

1. R. K. Sheline, Rev. Mod. Phys. 32, 1 (1960).
2. E. Eichler, Rev. Mod. Phys. 36, 809 (1964).
3. R. K. Sheline, T. Sikkeland, and R. N. Chanda, Phys. Rev. Letters 7, 446 (1961).
4. R. Chanda, J. Clarkson, and R. K. Sheline, in Proceedings of the Third Conference on Reactions between Complex Nuclei, Asilomar, California, April 1963 (University of California Press, Berkeley, 1963).
5. R. N. Chanda, Evidence for a New Region of Deformation with Less Than 82 Neutrons (Ph. D. Thesis), UCRL-10798, April 1963.
6. T. Novakov, J. M. Hollander, and R. L. Graham, Nucl. Instr. Methods 26, 189 (1964).
7. J. E. Clarkson, Collective Excitation of Neutron-Deficient Barium, Xenon, and Cerium Isotopes: Centrifugal Stretching Treatment of Nuclei (Ph. D. Thesis), UCRL-16040, May 1965.
8. H. Morinaga and N. L. Lark, Nucl. Phys. 67, 315 (1965).
9. Jack E. Clarkson, R. M. Diamond, F. S. Stephens, and I. Perlman, UCRL-16974; Nuclear Physics (in press).
10. K. Kumar and M. Baranger, unpublished work; K. Kumar, Collective Potential Energy, Quantum Mechanical Fluctuations, and Tunnelling Effects in Even Nuclei I, UCRL-16768, May 1966; K. Kumar, Michigan State University Technical Report, MSPT-101 (1966).

Table A. 17-I. Nuclear reactions employed.

Isotope	Reaction	Heavy-ion bombarding energy (approx) (MeV)
^{126}Ba	$^{115}In(^{14}N, 3n)^{126}Ba$	52
^{124}Ba	$^{115}In(^{14}N, 5n)^{124}Ba$	84
	$^{116}Sn(^{12}C, 4n)^{124}Ba$	80
^{122}Xe	$^{115}In(^{10}B, 3n)^{122}Xe$	37
	$^{115}In(^{11}B, 4n)^{122}Xe$	57
^{120}Xe	$^{115}In(^{10}B, 5n)^{120}Xe$	67
^{134}Ce	$^{127}I(^{11}B, 4n)^{134}Ce$	57
^{134}Pr	$^{127}I(^{12}C, 5n)^{134}Pr$	90

Table A. 17-II. Ground-state rotational band transitions[a] (keV).

Transition	^{120}Xe	^{122}Xe	^{124}Ba	^{126}Ba	^{134}Ce
2 → 0	321.8 A	331.1 A	229.5 A	256.1 A	409.5 A
4 → 2	472.6 A	497.5 A	420.6 A	455.5 A	638.9 A
6 → 4	601.4 A	638.2 A	573 B	621.4 A	814.6 A
8 → 6	701 C	749.9 A	634 C	757.1 A	871.4 B
10 → 8	773 C	819 B		829 C	

a. The accuracy of these transitions is expected to be ± 1 keV.

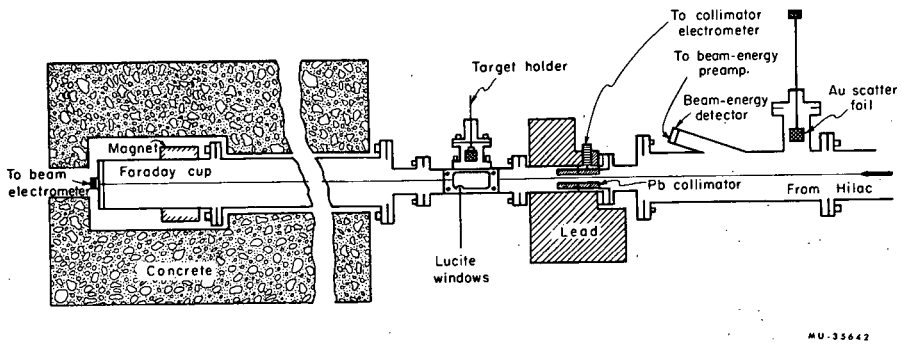

Fig. A. 17-1. Vertical cross section of the experimental setup for γ-ray detection.

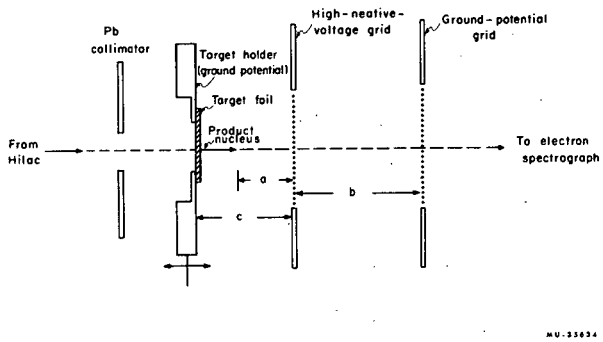

Fig. A. 17-2. Drawing of the target high-voltage assembly used to measure the lifetime of the first-excited state of ^{126}Ba. The distance c could be varied, but the distance b was fixed.

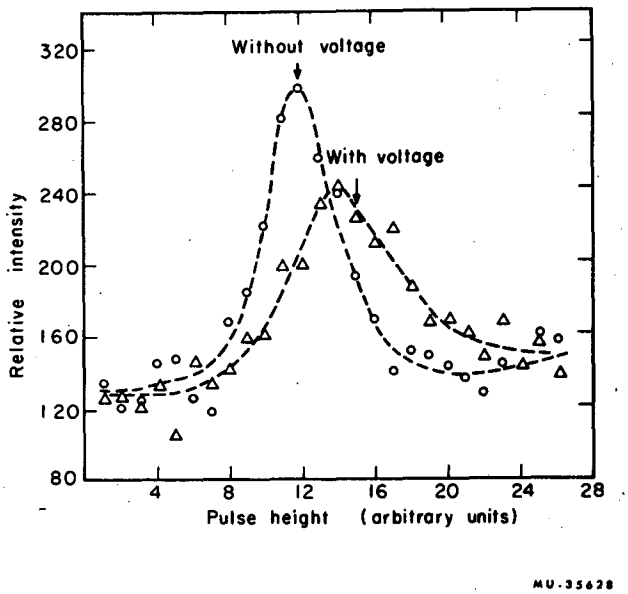

Fig. A. 17-3. The electron spectra in the region of the K line of the 256-keV transitions from an ^{115}In target bombarded with 52-MeV ^{14}N as found by using the lifetime apparatus.

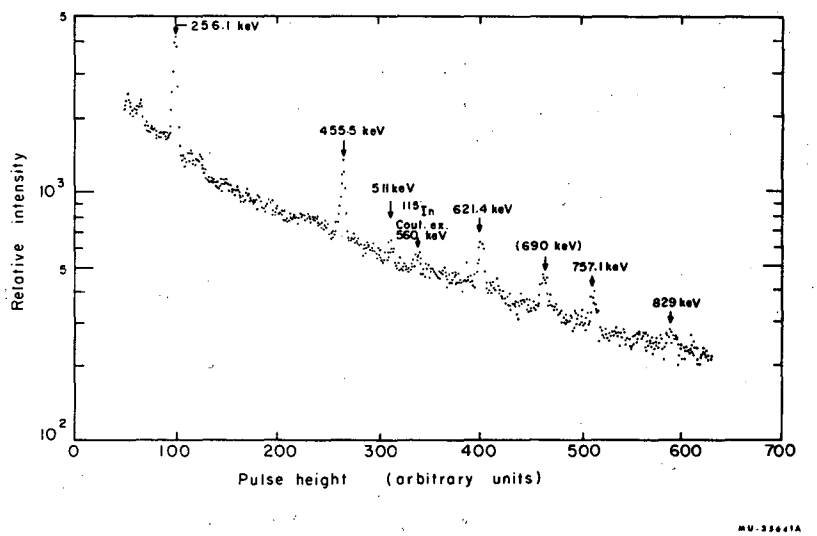

Fig. A. 17-4. Pulse-height spectrum of ^{126}Ba as observed from an ^{115}In target bombarded by 52-MeV ^{14}N ions.

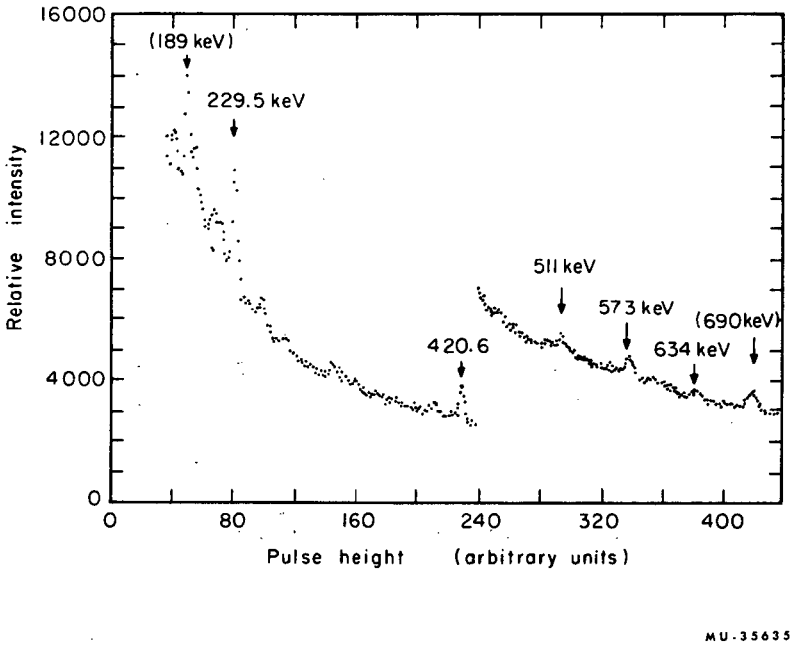

Fig. A.17-5. Pulse-height spectrum of ^{124}Ba as observed from a ^{116}Sn target bombarded with 80-MeV ^{12}C ions.

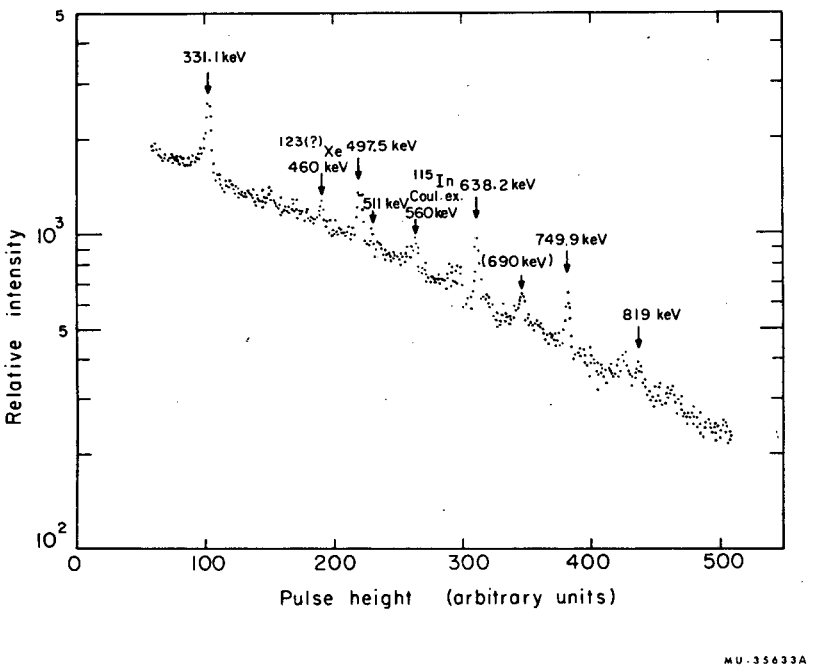

Fig. A.17-6. Pulse-height spectrum of ^{122}Xe as observed from an ^{115}In target bombarded with 57-MeV ^{11}B ions.

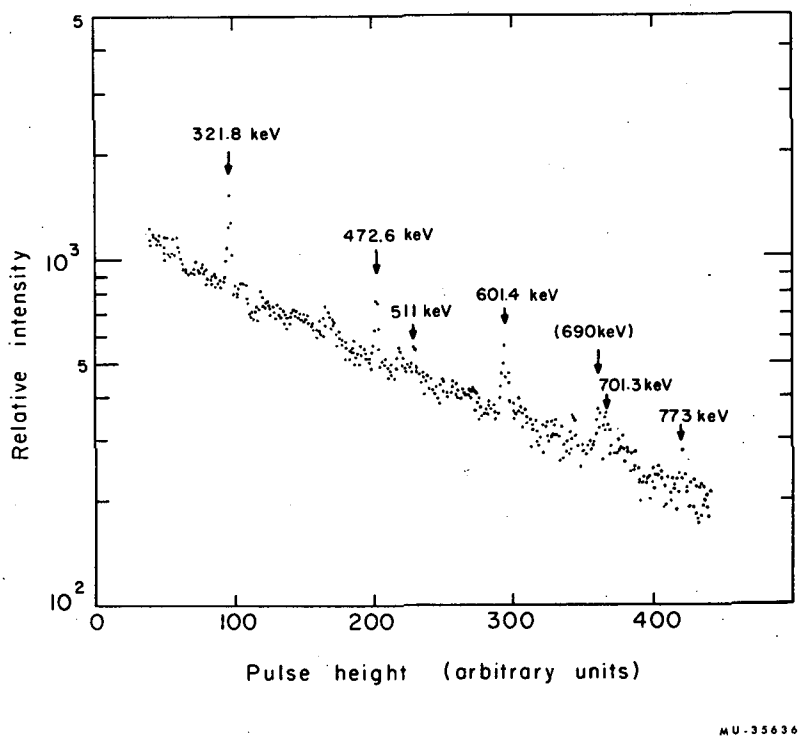

Fig. A. 17-7. Pulse-height spectrum of ^{120}Xe as observed from an ^{115}In target bombarded with 67-MeV ^{10}B ions.

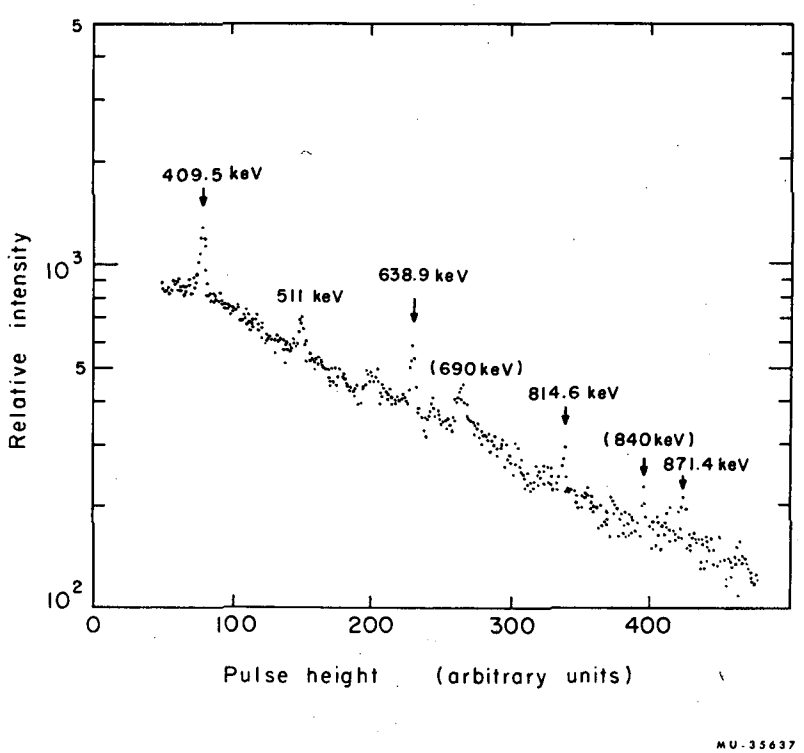

Fig. A. 17-8. Pulse-height spectrum of ^{134}Ce as observed from an ^{127}I target bombarded with 57-MeV ^{11}B ions.

18. THE ROTATIONAL STATES OF ^{184}Os, ^{186}Os, AND ^{188}Os†

J. O. Newton, F. S. Stephens, and R. M. Diamond

New data on the ground-state rotational bands of ^{184}Os, ^{186}Os, and ^{188}Os have been obtained from studies of the γ rays following the reactions ^{182}W(^{4}He, 2n)^{184}Os, ^{184}W(^{4}He, 2n)^{186}Os, and ^{186}W(^{4}He, 2n)^{188}Os. The method of measurement is fully described in an earlier paper.[1]

The Nucleus ^{186}Os

From the decay of ^{186}Ir (Refs. 2, 3) and the ^{187}Re(p, 2n)^{186}Os reaction (Refs. 4–6), it has been previously thought that a 584.4-keV γ ray was the 8→6 transition. Lark and Morinaga[7] have also studied the (^{4}He, 2n) reaction leading to ^{186}Os, but their resolution was too poor to give reliable results when, as in this case, there are many γ rays.

In our measurements on the γ rays from the ^{184}W(^{4}He, 2n)^{186}Os reaction (see Fig. A. 18-1), we also saw a γ ray of energy 584.4 keV and measured its angular distribution. We obtained values of $A_2 = 0.17 \pm 0.08$ and $A_4 = 0.05 \pm 0.09$. These values are not very precise, but they are consistent with the 584.4-keV transition's being a stretched E2 transition, which it must be if it is the 8→6 transition. Further, we observed a γ ray of 551.8-keV energy, which had an intensity comparable to that of the 584.4-keV γ ray. The angular distribution of the 551.8-keV γ ray, with $A_2 = 0.22 \pm 0.09$ and $A_4 = -0.14 \pm 0.09$, is consistent with that of a stretched E2 transition. This γ ray was not seen in the ^{187}Re(p, 2n)^{186}Os reaction.

On the above evidence alone, it would be possible to assign either the 584.4-keV or the 551.8-keV γ ray to the 8→6 transition. We shall demonstrate here, considering first experimental evidence and then the systematics of rotational states in osmium nuclei, that the 551.8-keV γ ray is likely to be the correct assignment.

The excitation functions of the 2→0, 4→2, 584.4-keV, and 551.8-keV transitions, relative to that for the 6→4 transition, are shown in Fig. A. 18-2. It can be seen that the yields of the 2→0 and 4→2 γ rays decrease with increasing bombarding energy, relative to the yield of the 6→4 transition. Such behavior is generally observed in (^{4}He, 2n) reactions, which occur at bombarding energies only a little above the potential barrier for the incident helium ions. From the discussion of the reaction mechanism in a previous paper,[1] one can see qualitatively the main reason for this. When the target has spin zero, as here, a significant yield of γ rays from a final state of spin I will be expected only if a sizeable fraction of the total reaction cross section corresponds to incoming angular momenta ℓ of about I or greater. Since with increasing bombarding energy above the potential barrier, the cross sections for high ℓ values increase relatively more rapidly than those for low ℓ values, it will be expected that the yields of γ rays from final states of high I will increase relatively more rapidly than those of low I. Figure A. 18-3 shows theoretical cross sections for forming particle stable states in ^{186}Os with spin greater than I, divided by the cross sections for spin greater than 6, as functions of incident energy. These curves were calculated with a computer program described elsewhere.[1] It can be seen that the behavior of these curves is similar to that observed in our experiment. Referring again to Fig. A. 18-2, one can see that the excitation function of the 584.4-keV γ ray is similar to that for the 4→2 and 2→0 transitions, that is, like a γ ray arising from a state of spin less than 6. On the other hand, the 551.8-keV γ ray has an excitation function which could be consistent with a rise in its relative cross section with energy, as expected for a γ ray from a state of spin 8.

A second piece of evidence for the assignment of the 551.8-keV γ ray to the 8→6 transition, comes from a comparison of the ^{187}Re(p, 2n)^{186}Os data with those from the ^{184}W(^{4}He, 2n)^{186}Os reaction. The 584.4 keV γ ray was seen in both (p, 2n) and (^{4}He, 2n) reactions, whereas the 551.8 keV γ ray was seen only in the (^{4}He, 2n) experiment. Table A. 18-I shows the relative intensities of the various transitions observed in both types of reaction. As expected, the high angular momentum states are relatively more populated in the (^{4}He, 2n) reaction. Nevertheless, the intensity of 584.4-keV transition relative to that of the 4→2 transition is approximately the same for both reactions. Thus again the evidence suggests that the 584.4-keV γ ray comes from a state having relatively low angular momentum and the 551.8-keV γ ray from one having rather high angular momentum.

The third piece of evidence, supporting the assignment of the 551.8-keV γ ray to the 8→6 transition, arises from the systematics of the rotational states of the osmium nuclei, shown in Fig. A. 18-4. This type of plot shows deviations from systematic behavior very sensitively,

since it removes the general I(I + 1) energy dependence of the levels of spin I. We have plotted the ratio of successive rotational constants A_I against the intermediate spin I. The quantity A_I is defined by

$$A_I = \frac{h^2}{2J_I} = \frac{\Delta E(I \rightarrow I - 2)}{4I - 2} .$$

It is very apparent that the energy of 584.4 keV for the 8→6 transition in ^{186}Os fits with the systematics very badly indeed, whereas 551.8 keV fits in very well (the 8 → 6 transition corresponds to intermediate spin 6 in Fig. A. 18-4). Although no one piece of evidence in itself is entirely conclusive, we feel that these three taken together suggest strongly that the 551.8-keV γ ray does rise from the 8→6 transition and that the 584.4-keV γ ray has previously been incorrectly assigned.

Harmatz and Handley[3] have given an alternative assignment for the 584.4-keV transition, based on energy sums only. This assignment, to a transition from a 4+ state at 1352 keV to the 2+ state at 767 keV, would not be in conflict with the data reported here.

We observed another γ ray of energy 647.6 ± 0.5 keV, which might be very tentatively assigned to the 10→8 transition. Its angular distribution coefficients, $A_2 = 0.55 \pm 0.3$, and $A_4 = -0.3 \pm 0.3$, are consistent with its being a stretched E2 transition and its energy fits very well with the systematics, as shown in Fig. A. 18-4. Its excitation function, shown in Fig. A. 18-2, was measured, but the results are not precise enough for one to draw any firm conclusions. The intensity of this γ ray is nearly equal to that of the 551.8-keV transition, whereas one might have expected the 10→8 transition to be rather weaker.

The Nucleus ^{184}Os

States up to the 8+ state in ^{184}Os have been assigned from the (p, 2n) reactions,[4, 6] the 8→6 transition being given as 504 keV. In these experiments this transition has about the same intensity relative to that of the 6→4 transition as does the 584-keV transition in ^{186}Os. In view of our remarks on the ^{186}Os case, we note that the difference between their value of 504 keV and ours of 500.7 ± 0.4 keV for the 8→6 transition may be significant. It is possible that the 8→6 transition is very weak in the (p, 2n) reaction and that the 504-keV transition is not seen in our (^{4}He, 2n) experiment, because it is masked by the strong 500.7-keV transition. A γ ray of 596.6 ± 1 keV might be assigned tentatively to the 10→8 transition. Its values for $A_2 = 0.20 \pm 0.1$ and $A_4 = -0.06 \pm 0.1$ are not very precise, but are probably not inconsistent with the value of $A_2 \approx 0.32$, expected for the 10→8 transition, from those for the 8→6 and 6→4 transitions in this nucleus. Note that the peak corresponding to this γ ray is broad. Its energy is in good accord with the systematics, as can be seen from Fig. A. 18-4.

The Nucleus ^{188}Os

Apart from the work of Lark and Morinaga,[7] the levels in the ground-state rotational band of ^{188}Os have been given only up to the 4+ state.[3, 8] We find γ rays of 461.9 ± 0.3 keV and 573.8 ± 0.4 keV, whose angular distributions are consistent with those expected for the 6→4 and 8→6 transitions. These energies are not in agreement with those of 470 ± 7 and 640 ± 10 keV, given by Lark and Morinaga. Another γ ray of 655.9 ± 1 keV energy might be very tentatively assigned to the 10→8 transition, on the basis of systematics only. A point corresponding to this is shown in Fig. A. 18-4.

Conclusion

The energies which seem to us to be most likely for the members of the ground-state rotational bands in the three osmium isotopes are shown in Table A. 18-II. We feel that the assignments up to the 6+ states are likely to be good, those for the 8+ states fairly good, and those for the 10+ states very tentative.

Footnote and References

†Shortened version of UCRL-17205.

1. J. O. Newton, F. S. Stephens, R. M. Diamond, K. Kotojima, and E. Matthias, Nucl. Phys. (to be published in 1967).
2. G. T. Emery, W. R. Kane, M. McKeown, M. L. Perlman, and G. Scharff-Goldhaber,

Phys. Rev. 129, 2597 (1963).
3. B. Harmatz and T. H. Handley, Nucl. Phys. 56, 1 (1964).
4. M. Sakai, T. Yamazaki, and H. Ejiri, Nucl. Phys. 74, 81 (1965).
5. H. Ejiri, M. Ishihara, M. Sakai, T. Inamura, and K. Katori, J. Phys. Soc. Japan, 21, 1021 (1966).
6. T. Yamazaki and D. L. Hendrie, Gamma Vibrational Bands in ^{182}Os and ^{184}Os, UCRL-16986, Sept. 1966.
7. N. L. Lark and H. Morinaga, Nucl. Phys. 63, 466 (1965).
8. R. L. Graham, J. S. Geiger, R. A. Naumann, and J. P. Prospero, Can. J. Phys. 40, 296 (1962).
9. J. Burde, R. M. Diamond and F. S. Stephens, Nucl. Phys. (in press).

Table A. 18-I. Relative intensities of transitions in ^{186}Os observed in two reactions. Those for the 551.8-keV transition were estimated from the published spectra for the ^{187}Re + p reaction.[5,6]

Reaction	Type of observation	2→0	4→2	6→4	551.8	584.4
^{187}Re + 14 MeV p	conv. el.	270	100	39	< 6[a]	27
	γ rays				< 8	24
^{182}W + 27 MeV ^{4}He	γ rays	175	100	46	16	20

a. E2 assumed.

Table A. 18-II. Energies of rotational states. The data for the 2+, 4+, and 6+ states of ^{186}Os are taken from Ref. 2 and those for the 2+ and 4+ states of ^{188}Os from Ref. 8. The brackets round the 10+ transitions indicate that these assignments are tentative.

	^{184}Os	^{186}Os	^{188}Os
2+	119.8 ± 0.3	137.15 ± 0.03	155.03 ± 0.03
4+	383.6 ± 0.4	433.90 ± 0.06	477.94 ± 0.05
6+	773.9 ± 0.6	868.7 ± 0.1	939.8 ± 0.3
8+	1274.6 ± 0.7	1420.5 ± 0.3	1513.6 ± 0.5
10+	(1871.2 ± 1.2)	(2068.1 ± 0.6)	(2169.5 ± 1.1)

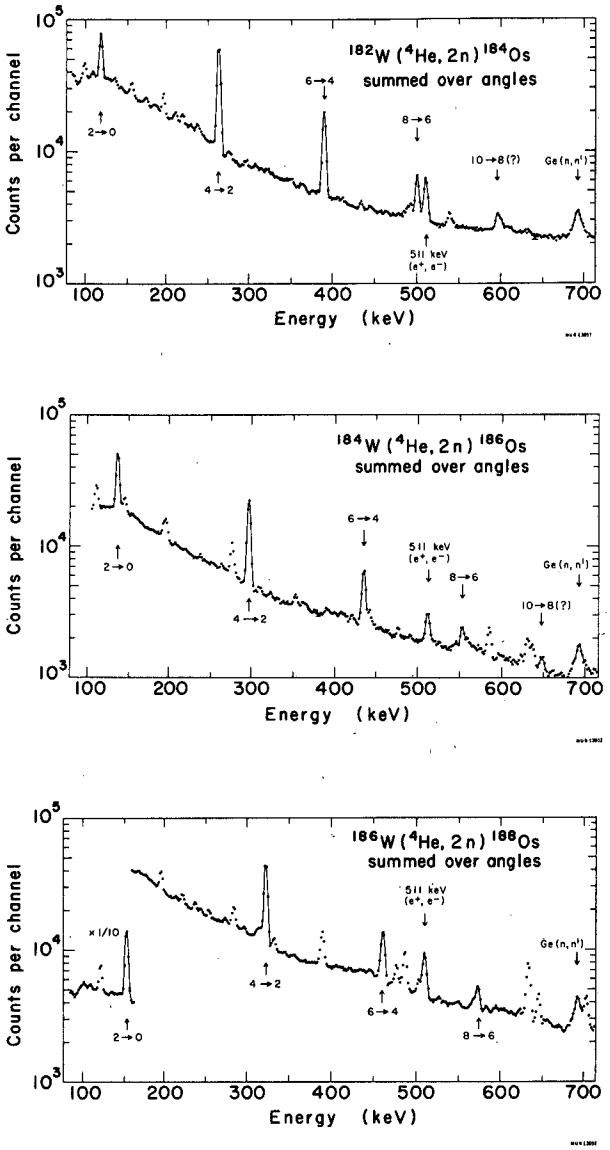

Fig. A. 18-1. Gamma-ray spectra from the bombardment of ^{182}W, ^{184}W, and ^{186}W with 27-MeV ^{4}He ions.

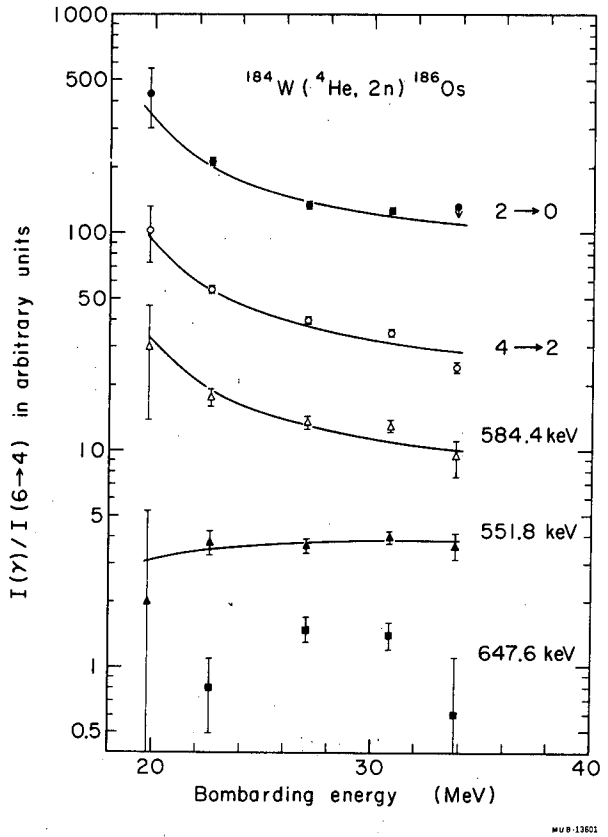

Fig. A. 18-2. Relative excitation functions of γ rays seen in the ^{184}W(^{4}He, 2n)^{186}Os reaction. The full lines have no theoretical significance.

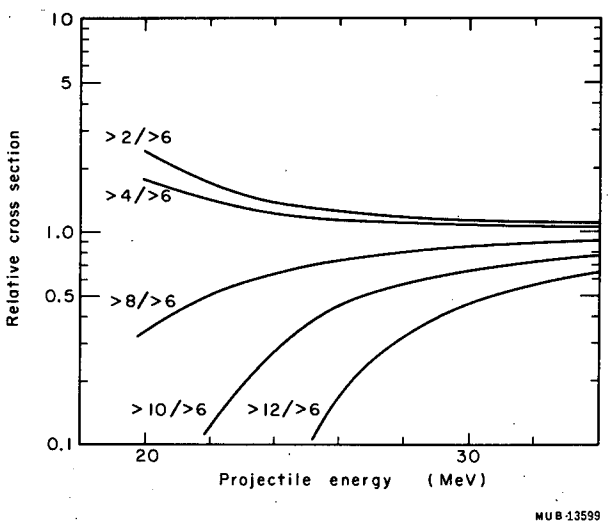

Fig. A. 18-3. Calculated cross sections for forming particle-stable states in ^{186}Os with spin greater than I, relative to those for forming states with spin greater than 6.

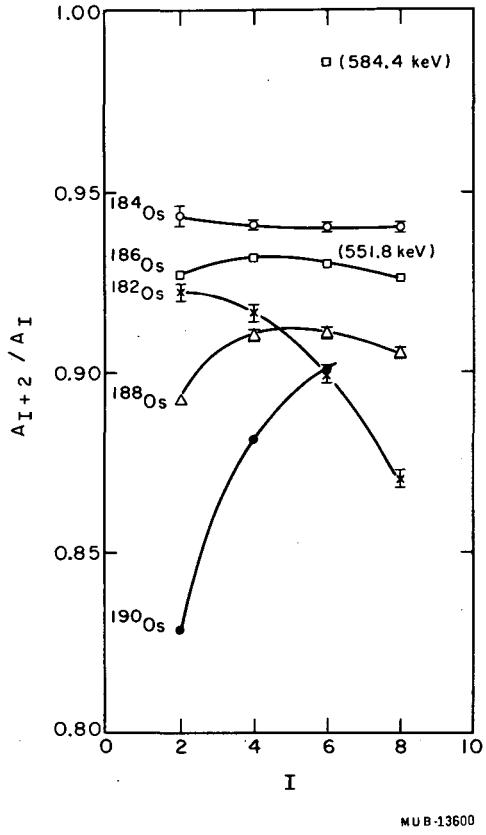

Fig. A. 18-4. Systematics of rotational-state energies in osmium nuclei. Data were obtained from the present work and the following references: ^{182}Os, Ref. 9; ^{186}Os, Ref. 2; ^{188}Os, Ref. 8; ^{190}Os, Ref. 3.

19. NUCLEAR ALIGNMENT IN HEAVY-ION REACTIONS*

R. M. Diamond, E. Matthias, J. O. Newton, and F. S. Stephens

It is well-known that in compound-nucleus reactions the incoming particle brings orbital angular momentum to the compound system but only in the m = 0 substates, taking the beam direction as the axis of quantization.[1] Thus the compound nuclei have their spins aligned in the plane perpendicular to the beam axis; the only deviations are caused by the spins of the target nucleus and projectile. With heavy ions as projectiles, the amount of orbital angular momentum brought in far exceeds the usual nuclear spins, and the resulting compound nuclei should be highly aligned. The evaporation of a few neutrons will leave the initial spin distribution of the compound system largely unaltered and will broaden the distribution in m. However, since evaporated neutrons do not carry off much angular momentum, the nuclei with high angular momenta will be expected to remain highly aligned even after the evaporation process. Thus the final γ rays (or particles) emitted between discrete states of the residual nuclei will show angular distributions with respect to the beam direction, provided that the alignment is not destroyed by some interaction with extranuclear fields.

Angular distributions of the stretched E2 γ-ray transitions cascading from rotational and vibrational states, populated by heavy-ion xn reactions, have been measured with lithium-drifted Ge detectors. The reactions were induced by ^{4}He, ^{11}B, ^{14}N, and ^{19}F ions on targets in the mass range from 159 to 186.

Very pronounced angular distributions were observed for all these stretched E2 cascades. Using the expression $W(\theta) = 1 + A_2P_2(\cos\theta) + A_4P_4(\cos\theta)$, we have summarized the results of that work in Fig. A. 19-1, where A_4 vs A_2 has been plotted for the observed transitions

other than the 2→0. The line in Fig. A. 19-1 represents the relationship between A_4 and A_2 expected with a Gaussian distribution, centered at m=0, for the population of magnetic substates. Figure A. 19-1 shows that: (a) the population can be approximately represented by a Gaussian about m=0, although significant deviations from this appear; and (b) the A_2 values are large, and both A_2 and A_4 are reasonably well-clustered about particular values (all data, $I > 2$, fall within $A_2 = +0.30 \pm 0.09$, and $A_4 = -0.09 \pm 0.05$). The latter result shows that this alignment will be an extremely useful tool, since it generally persists throughout the entire neutron and γ-ray cascade.

The γ decay of nuclei formed in heavy-ion xn reactions offers a very general method of studying the decay schemes of neutron-deficient nuclei over a wide range of the periodic system. We feel that the strong alignment produced in these reactions is a very important feature which will be of great value, particularly in the study of these more complex level schemes. One of the most obvious ways to exploit the alignment is the measurement of angular distributions of the de-excitation γ rays with respect to the beam direction. We would like to illustrate this with an example taken from a general study of the levels of the neutron-deficient odd-mass Tl nuclei.[2] In the reaction $^{197}Au(^{4}He, 2n)^{199}Tl$, we have found, among others, three transitions of 331, 370, and 701 keV which lie above the 9/2- isomeric level at 749 keV. From the energies and intensities of these transitions, we believe they connect two higher levels with the isomeric one in a cascade arrangement with a crossover (see insert in Fig. A. 19-2). We have measured the angular distributions of these radiations with respect to the beam direction and find large anisotropies for each transition. From these angular distributions, shown in Fig. A. 19-2, definite conclusions about a particular spin sequence can be based both on the signs of A_2 and A_4 and on their magnitudes, whenever the experimental values exceed that for complete alignment ($|m| = 1/2$). Also, if two transitions come from the same level, both distributions must be consistent with the same alignment of the state. In the present example, where we know initially only the arrangement of the levels (Fig. A. 19-2) and that the transitions must be dipole, quadrupole, or a mixture, the distributions alone unambiguously reduce the possible spin sequences from 19 to 5. It is then possible to go further and make probable conclusions based on the expected alignment of the state obtained from the range of A_2 and A_4 values observed above for the even-even nuclei. These considerations reduce the probable number of spin sequences to 3; these probable spins are shown in Fig. A. 19-2. Conversion coefficient and other data can provide the basis for a choice among these remaining spin sequences. The E2-M1 amplitude mixing ratio for the mixed transitions can then be derived when the alignment of the initial state can be deduced (e. g., when there is also a pure transition coming from the same state), or probable ranges can be defined in less favorable cases. It can be seen that in this example a considerable amount of spectroscopic information can be obtained from the measurement of the angular distributions of these three transitions.

This high degree of alignment can also be used in the measurement of electromagnetic moments and hyperfine interactions of nuclear states by the method of perturbed angular distributions. This type of experiment requires a target structure which preserves the spin orientation of the reaction product for a period longer than the lifetime of the nuclear state of interest. In these studies, the large recoil velocity of the product nucleus is very valuable in getting the nucleus quickly into a suitable environment for the experiment.

Footnote and References

*From UCRL-16889, in Phys. Rev. Letters 16, 1205 (1966), and UCRL-17204.

1. L. C. Biedenharn, Angular Correlations, in Nuclear Spectroscopy, Ed., F. Ajzenberg-Selove (Academic Press, New York, 1960), Chap. V. C. and references therein.
2. S. Cirilov, R. M. Diamond, J. O. Newton, and F. S. Stephens, Phys. Rev. Letters 16, 1205 (1966).

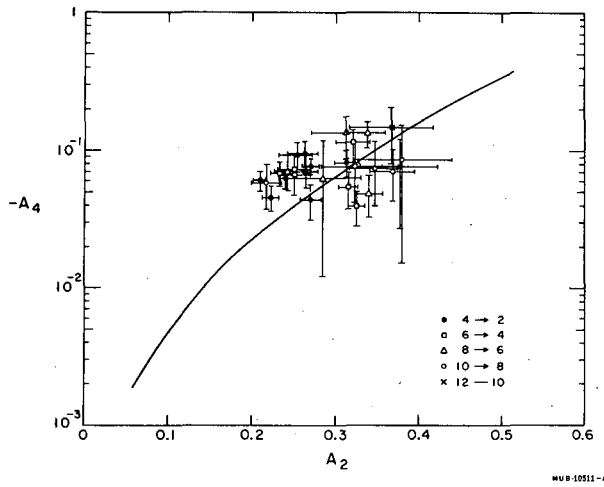

Fig. A. 19-1. The A_4 vs A_2 coefficients (see text) are plotted for a number of rotational or vibrational γ rays observed as the last step of heavy-ion (^{4}He-^{19}F) nuclear reactions. The coefficients for the 2→0 transitions have not been included since they can be attenuated by extranuclear effects. The line represents the relationship between A_4 and A_2 expected for a Gaussian population of magnetic substates centered around m-0.

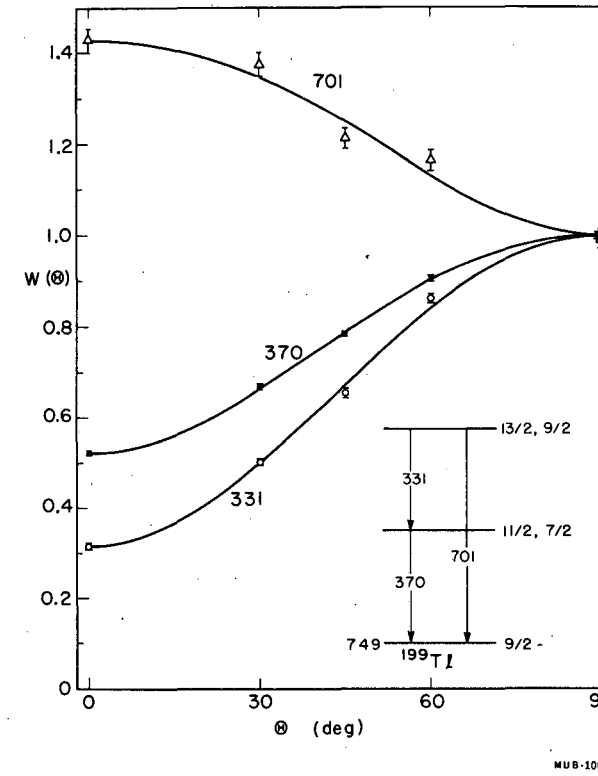

Fig. A. 19-2. The curves are the observed angular distributions with respect to the beam direction of three γ rays produced in the reaction ^{197}Au(^{4}He, 2n)^{199}Tl. The placement of these γ rays above the 749-keV, 9/2- isomeric level in ^{199}Tl is shown in the insert along with the probable spins based on the angular distributions. The measured coefficients are: 331 keV, A_2 = -0.58±0.03, A_4 = -0.02±0.03; 370 keV, $-A_2 \geqslant 0.36\pm0.02$, $-A_4 \geqslant 0.03\pm0.02$; 701 keV, A_2 = +0.26±0.04, A_4 = -0.03±0.04.

20. ANGULAR DISTRIBUTIONS OF GAMMA RAYS EMITTED IN $^{197}Au(p, 2n)^{196}Hg$ AND $^{197}Au(p, 4n)^{194}Hg$ REACTIONS†

T. Yamazaki and D. L. Hendrie

The angular distributions of γ rays emitted in $^{197}Au(p, 2n)^{196}Hg$ and $^{197}Au(p, 4n)^{194}Hg$ were measured using Ge(Li) detectors in the beam of the Berkeley 88-inch cyclotron.

The γ-ray spectrum at $E_p = 12 \approx 16$ MeV revealed γ rays in ^{196}Hg involving the $^12^+$, $^22^+$, 4^+, 5^-, and 6^+ levels (see Fig. A.20-1). The 0^+ - $^12^+$ - 4^+ - 5^- sequence was recently found by Petry et al.[1] in the decay of ^{196m}Tl. The angular distributions are illustrated in Fig. A. 20-2 and are also tabulated in Table A. 20-I. All of these are consistently explained by the assumption of the level scheme and spins and parities given in Fig. A. 20-1. The A_2 value of the $6^+ \rightarrow 4^+$ γ ray is very large, being close to the average value ≈ 0.3 observed in heavy-ion-induced reactions,[2] whereas those of other transitions decrease appreciably as the spin decreases because of many possible processes of population that smear out the alignment. The negative value of $A_2(695)$ uniquely assigns the $5^-(E1)4^+$ sequence. The present results agree with the anisotropy measurements on γ rays and conversion electrons carried out by the Tokyo group.[3] The γ-ray spectrum at $E_p = 35$ MeV showed predominantly γ rays of ^{194}Hg associated with the level scheme presented in Fig. A. 20-1. The 2^+, 4^+, 5^-, and 7^- levels were also studied by Petry et al. from the decay of ^{194m}Tl. In Table A. 20-II are shown A_2 values which were deduced from $I_\gamma(158°)/I_\gamma(90°)$ by assuming $A_4 = 0$. These values are consistent with the given level scheme.

Further experiments and analyses are in progress. It is apparent that study of angular distributions of γ rays in nuclear reactions of this kind is a powerful tool to determine level spins and transition multipolarities.

Footnote and References

†UCRL-16987, presented at the International Conference on Nuclear Physics, Gatlinburg, Tennessee, September 12 through 17, 1966.

1. R. F. Petry, R. A. Naumann, and J. S. Evans, preprint, May 1966.
2. R. M. Diamond, E. Matthias, J. O. Newton, and F. S. Stephens, Phys. Rev. Letters 16, 1205 (1966).
3. H. Ejiri, M. Ishihara, M. Sakai, K. Katori, and T. Inamura, Phys. Letters 18, 314 (1965); INS-Report 94 (to be published); H. Ejiri, M. Ishihara, K. Katori, and T. Inamura, private communication.

Table A. 20-I. Angular distribution of γ rays of ^{196}Hg emitted in $^{197}Au(p, 2n)$ reaction at $E_p = 16$ MeV.

Transition	Energy (keV)	Angular distribution A_2	Angular distribution A_4
$^12^+ \rightarrow 0^+$ E2	425	0.073±0.009	0.007±0.014
$^22^+ \rightarrow ^12^+$ E2 + M1	610	0.068±0.041	0.051±0.063
$4^+ \rightarrow ^12^+$ E2	635	0.121±0.008	-0.003±0.012
$5^- \rightarrow 4^+$ E1	695	-0.120±0.011	0.004±0.017
$6^+ \rightarrow 4^+$ E2	725	0.235±0.056	-0.045±0.085

Table A. 20-II. Angular anisotropy of γ rays of ^{194}Hg emitted in ^{197}Au(p, 4n) reaction at E_p = 35 MeV.

Transition		Energy (keV)	$I_\gamma(158°)/I_\gamma(90°)$	A_2 [a]
$2^+ \rightarrow 0^+$	E2	426	1.24	0.14±0.02
$4^+ \rightarrow 2^+$	E2	635	1.24	0.14±0.02
$6^+ \rightarrow 4^+$	E2	734	1.51	0.25±0.05
$5^- \rightarrow 4^+$	E1	747	0.86	-0.10±0.03
$7^- \rightarrow 5^-$	E2	99	1.27	0.15±0.02
$7^- \rightarrow 6^+$	E1	112	0.90	-0.07±0.02

a. Deduced from $I_\gamma(158°)/I_\gamma(90°)$ by assuming A_4 = 0.

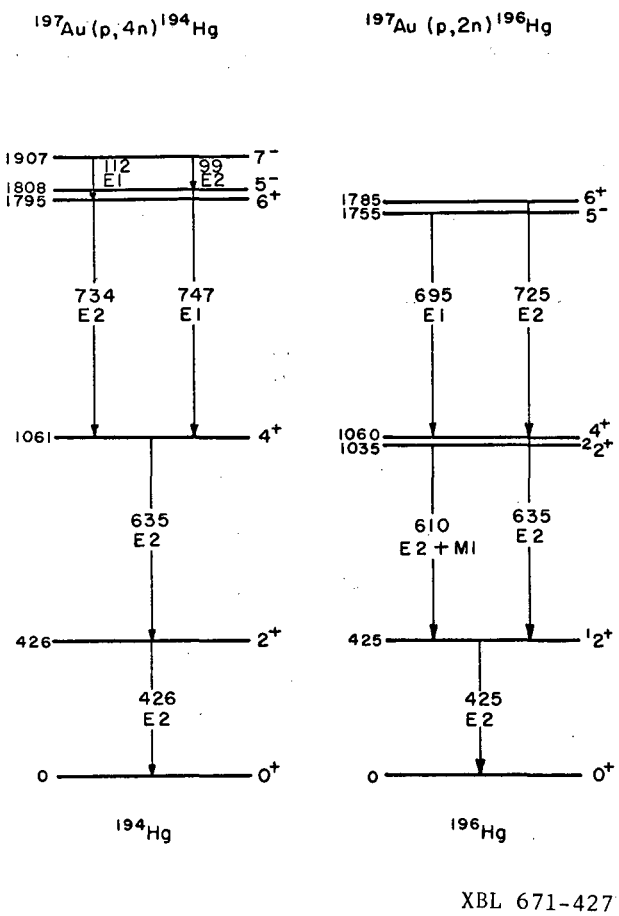

XBL 671-427

Fig. A. 20-1. The levels and transitions of ^{194}Hg and ^{196}Hg populated in ^{197}Au(p, xn) reactions.

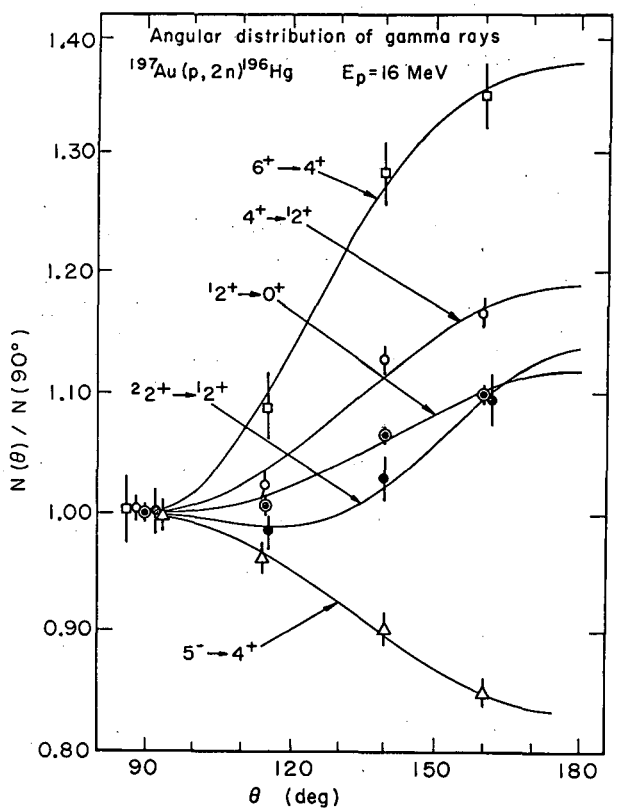

XBL 671-428

Fig. A. 20-2. Angular distributions of γ rays of ^{196}Au(p, 2n)^{196}Hg reaction at E_p = 16 MeV.

21. TABLES OF COEFFICIENTS FOR ANGULAR DISTRIBUTION OF γ RAYS FROM ALIGNED NUCLEI*

T. Yamazaki

Study of the angular distribution of γ rays emitted from aligned states which are formed by nuclear reactions permits assignments of multipolarities of the γ rays, and spins and parities of the levels involved. This method, in conjunction with the angular correlation technique, has been applied to nuclear spectroscopy for many years, as reviewed by Ferguson.[1]

Recently, particular interest has been focused on (particle, xn)-type reactions, which were first utilized by Morinaga and Gugelot[2] to study ground-state rotational bands of deformed nuclei, and are extensively applied in the search for any low-lying levels. It has been found that a wide range of excited states populated in these reactions are well aligned,[3-6] so that γ rays exhibit angular distributions depending upon the multipolarities and the spin sequences. The simplest method of analyses of the experimental data is to regard the degree of alignment as a parameter, which may be determined experimentally, estimated empirically, or evaluated on the basis of a specific model.

The present report has been prepared to provide a simplified formulation of angular distribution functions and tables of coefficients for the angular distribution of γ rays; the author hopes this will be useful in the analyses of experimental data. The theory has been well established. One may refer to the review article by de Groot et al.[7]

The statistical tensor for the complete alignment is

$$B_k(J) \equiv \begin{cases} \sqrt{2J+1}\,(-)^J (J0J0|k0) & \text{for integral spin,} \\ \sqrt{2J+1}\,(-)^{J-\frac{1}{2}} (J\tfrac{1}{2}J{-}\tfrac{1}{2}|k0) & \text{for half-integral spin,} \end{cases}$$

which is presented in Table 1 of Ref. 9. Then, for this ideal case,

$$A_k^{max}(J_iL_1L_2J_f) = \frac{1}{1+\delta^2}\left[f_k(J_fL_1L_1J_i) + 2\delta f_k(J_fL_1L_2J_i) + \delta^2 f_k(J_fL_2L_2J_i)\right],$$

where

$$f_k(J_fL_1L_2J_i) \equiv B_k(J_i)F_k(J_fL_1L_2J_i)\ .$$

In Tables 2a and 2b of Ref. 9, F_k and B_kF_k ($\equiv f_k$) are tabulated.

In actual cases, where the alignment is partial, we see that

$$A_k(J_iL_1L_2J_f) = \alpha_k(J_i)A_k^{max}(J_iL_1L_2J_f)\ ,$$

where $\alpha_k(J_i)$ is the attenuation coefficient of the alignment

$$\alpha_k(J_i) \equiv \frac{\rho_k(J_i)}{B_k(J_i)}$$

The population parameters of a state depend on the formation process of this state, which is in general complicated. However, if we assume that the population parameters are represented by a distribution function involving only one parameter, then α_4 and α_6 will be uniquely related to α_2. Therefore, we regard α_2 as the only free parameter that represents the population of substates. The parameter α_2 may be determined experimentally, estimated empirically, or evaluated on the basis of a specific model.

Figure A.21-1 illustrates $\alpha_4(J)$ and $\alpha_6(J)$ versus $\alpha_2(J)$, under the assumption of the Gaussian distribution

$$P_m(J) = \frac{\exp\left(-\frac{m^2}{2\sigma^2}\right)}{\sum_{m'=-J}^{J} \exp\left(-\frac{m'^2}{2\sigma^2}\right)} .$$

[The case that $\sigma = 0$ corresponds to the complete alignment $\alpha_k(J) = 1$.] In addition, Fig. A. 21-2 shows $\alpha_k(J)$ versus σ/J. These figures indicate: (a) α_4 decreases very rapidly as α_2 decreases, and (b) α_6 is negligible in most cases of interest.

Footnote and References

*Condensed from UCRL-17086.

1. A. J. Ferguson, Angular Correlation Methods in Gamma-Ray Spectroscopy (North-Holland Publishing Co., Amsterdam, 1965).
2. H. Morinaga and P. C. Gugelot, Nucl. Phys. 46, 210 (1963).
3. H. Ejiri, M. Ishihara, M. Sakai, K. Katori, and T. Inamura, Phys. Letters 18, 314 (1965); H. Ejiri, M. Ishihara, M. Sakai, T. Inamura, and K. Katori, INS-Report 94 (Institute for Nuclear Study, University of Tokyo, April, 1966).
4. C. F. Williamson and B. J. Shepherd, Bull. Am. Phys. Soc. 10, 428 (1965).
5. R. M. Diamond, E. Matthias, J. O. Newton, and F. S. Stephens, Phys. Rev. Letters 16, 1205 (1966).
6. T. Yamazaki and D. L. Hendrie, Angular Distributions of Gamma Rays Emitted in ^{197}Au(p, 2n)^{196}Hg and ^{197}Au(p, 4n)^{194}Hg Reactions, in Contribution to the International Conference on Nuclear Physics in Gatlinburg, Tenn., UCRL-16987, July 1966.
7. S. R. de Groot, H. A. Tolhoek, and W. J. Huiskamp, Alpha-, Beta- and Gamma-Ray Spectroscopy (North-Holland Publishing Co., Amsterdam, 1965), Ed. K. Siegbahn, p. 1199.
8. T. Yamazaki, Tables of Coefficients for Angular Distribution of Gamma Rays from Aligned Nuclei, UCRL-17086, September 1966.

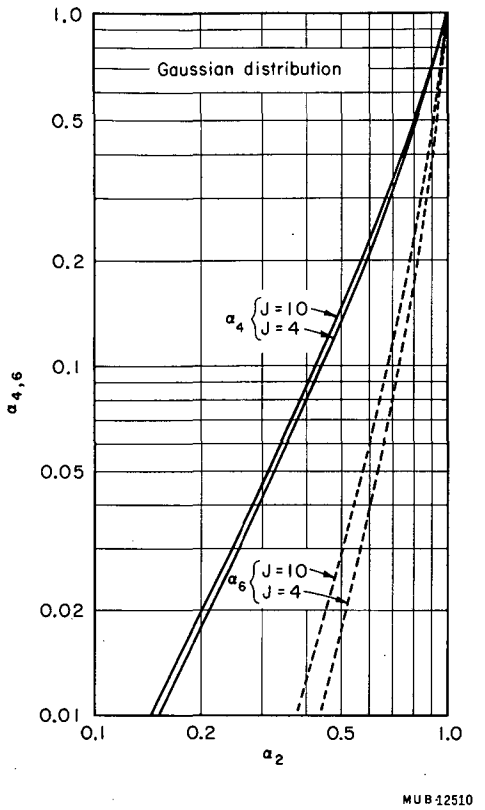

Fig. A. 21-1. The $\alpha_4(J)$ and $\alpha_6(J)$ versus $\alpha_2(J)$ under the assumption of the Gaussian distribution of substates.

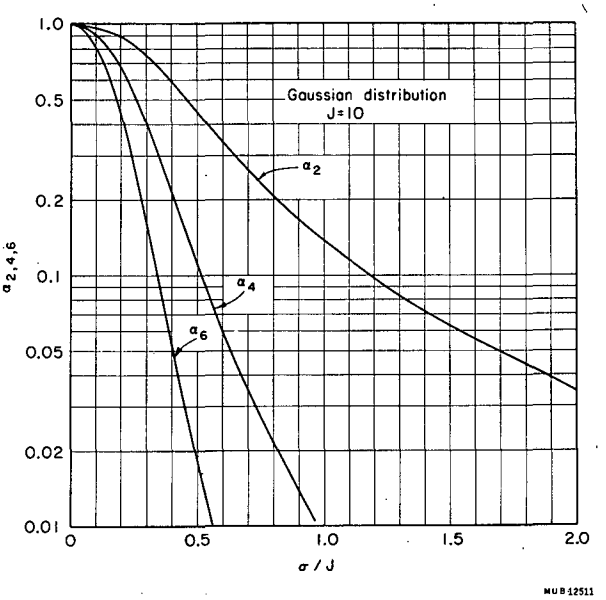

Fig. A. 21-2. Dependence of $\alpha_k(J)$ on the distribution parameter σ/J.

22. GAMMA-VIBRATIONAL BANDS IN ^{182}Os AND ^{184}Os†

T. Yamazaki and D. L. Hendrie

The γ-vibrational bands in neutron-deficient even Os nuclei have been studied by observing interband γ rays in ^{185,187}Re(p, 2n)^{184,186}Os and ^{185,187}Re(p, 4n)^{182,184}Os reactions. The previously known γ-vibrational band of ^{186}Os, which was studied by Emery et al.[1] from the decay of ^{186}Ir, is considerably populated up to the 5+ level in the ^{187}Re(p, 2n)^{186}Os reaction [see the spectrum in Fig. A. 22-1(a)]. This information was utilized to assign γ rays in the ^{185}Re(p, 2n)^{184}Os reaction [Fig. A. 22-1(b)]. The assignment given in Fig. A. 22-1(b) seems to be suspicious, because in the strong-coupling limit the $2_\gamma \rightarrow 2_g$ line and $2_\gamma \rightarrow 0_g$ lines should agree with the $4_\gamma \rightarrow 4_g$ and $3_\gamma \rightarrow 2_g$ lines, respectively. If we regard the 840-keV peak as the $2_\gamma \rightarrow 2_g$, $4_\gamma \rightarrow 4_g$ doublet, and the 936-keV peak as the $2_\gamma \rightarrow 0_g$, $3_\gamma \rightarrow 2_g$ doublet, then the 822- and 942-keV lines must be associated with another level at 942 keV. However, if they were so, such a level should also be populated in ^{186}Os as well as the γ-vibrational levels. Therefore we have made the assignments as shown in Fig. A. 22-1(b), although they are still doubtful.

After having established the γ-vibrational band in ^{184}Os, the population of the same states was examined in the ^{187}Re(p, 4n)^{184}Os reaction at E_p = 35 MeV, which showed lower population of the γ-vibrational band than the ground band and relatively higher population of higher spin γ-vibrational states. Subsequently this information was utilized to identify γ rays in the ^{185}Re(p, 4n)^{182}Os reaction.

The systematics of the ground and the γ-vibrational bands has been obtained, as shown in Fig. A. 22-2. Remarkable facts are:

1. The energy of γ vibration is uniquely correlated with the moment of inertia. As the neutron number decreases, the moment of inertia and the γ-vibrational energy increase until they reach maxima at A = 184 (N = 108), then both start decreasing.

2. There is appreciable difference in the moment of inertia between the ground band and the γ-vibrational band. The level spacing $\Delta^{\gamma}_{32} \equiv E(3_{\gamma}) - E(2_{\gamma})$ should be equal to $\Delta^{g}_{20} \equiv E(2_{\gamma})$ in the strong-coupling limit. The differences are presented in Table A. 22-I. The quantity $\Delta^{\gamma}_{32} - \Delta^{g}_{20}$ is negative in ^{164}Er, ^{168}Yb, and ^{180}W (according to a recent experiment by Graetzer et al. [2]), whereas in Os nuclei it is always positive. This quantity is roughly evaluated by perturbation as follows:

$$\frac{\Delta^{\gamma}_{32} - \Delta^{g}_{20}}{\Delta^{g}_{20}} = -\frac{4}{3}\left(\frac{E(2_g)}{E_{\beta}}\right)^2 + \frac{4}{9}\left(\frac{E(2_g)}{E_{\gamma}}\right)^2$$

The first term arises from the β-vibration-rotation interaction. When only the interaction between the ground band and the K = 2 γ-vibrational band is taken in account, the second term should vanish. This is why in the Davydov-Chaban model this quantity is always negative. The second term appears when the interaction between the K = 2 γ-vibrational state and the K = 0 (two-phonon) γ-vibrational state is taken into account. Therefore, the positive value of $\Delta^{\gamma}_{32} - \Delta^{g}_{20}$ may imply the presence of the two-phonon γ-vibrational band which plays an important rôle in the Os region.

Footnote and References

†UCRL-16986.

1. G. T. Emery, W. R. Kane, M. McKeown, M. L. Perlman, and G. Scharff-Goldhaber, Phys. Rev. 129, 2597 (1963).
2. R. Graetzer, G. B. Hagemann, K. A. Hagemann, and B. Elbek, Nucl. Phys. 76, 1 (1966).

Table A. 22-I. Energy spacings of γ vibrational bands.

Nucleus	$E(2_g)$ (keV)	$E(2_{\gamma})$ (keV)	$(\Delta^{\gamma}_{32}-\Delta^{g}_{20})/\Delta^{g}_{20}$ (%)	$(\Delta^{\gamma}_{42}-\Delta^{g}_{42})/\Delta^{g}_{42}$ (%)
^{182}Os	128	892	14.9	9.7
^{184}Os	122	942	17.2	7.6
^{186}Os	137	768	3.7	1.7
^{188}Os	155	633	1.3	2.8
^{190}Os	187	557	6.4	10.2
^{192}Os	206	489	-1.9	
^{158}Dy	98.7	945	1.3	1.0
^{164}Er	91.3	858	-3.6	-4.8
^{168}Yb	87.9	986	-4.4	-5.5
^{180}W	103.6	828	-9.3	-11.1

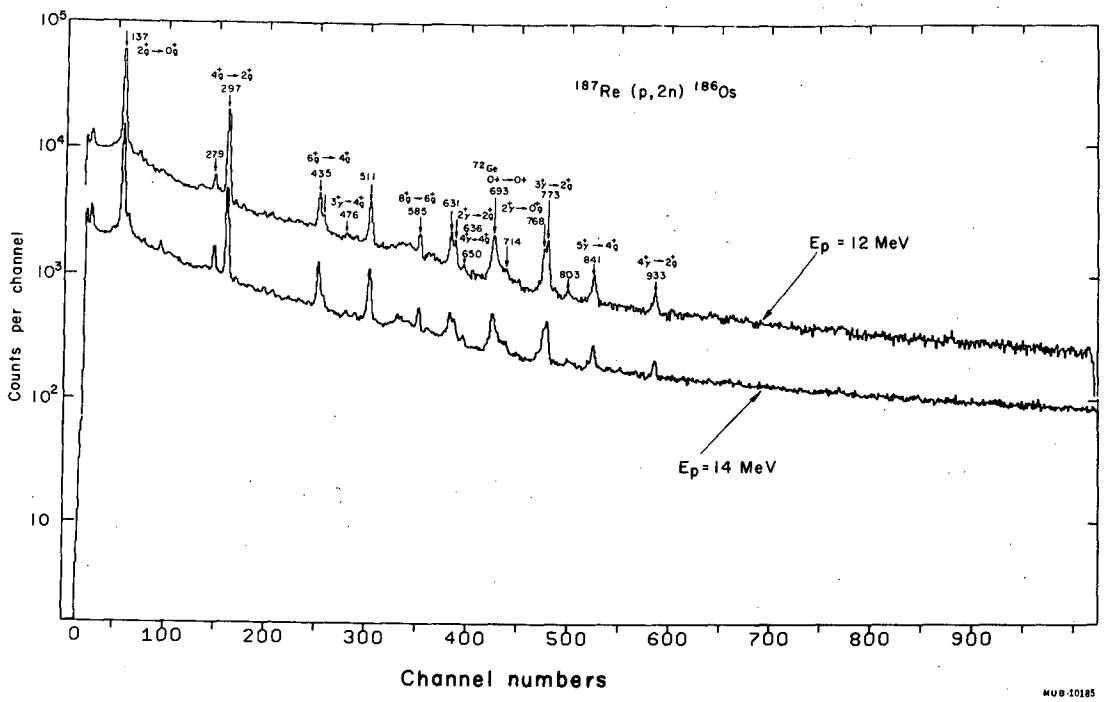

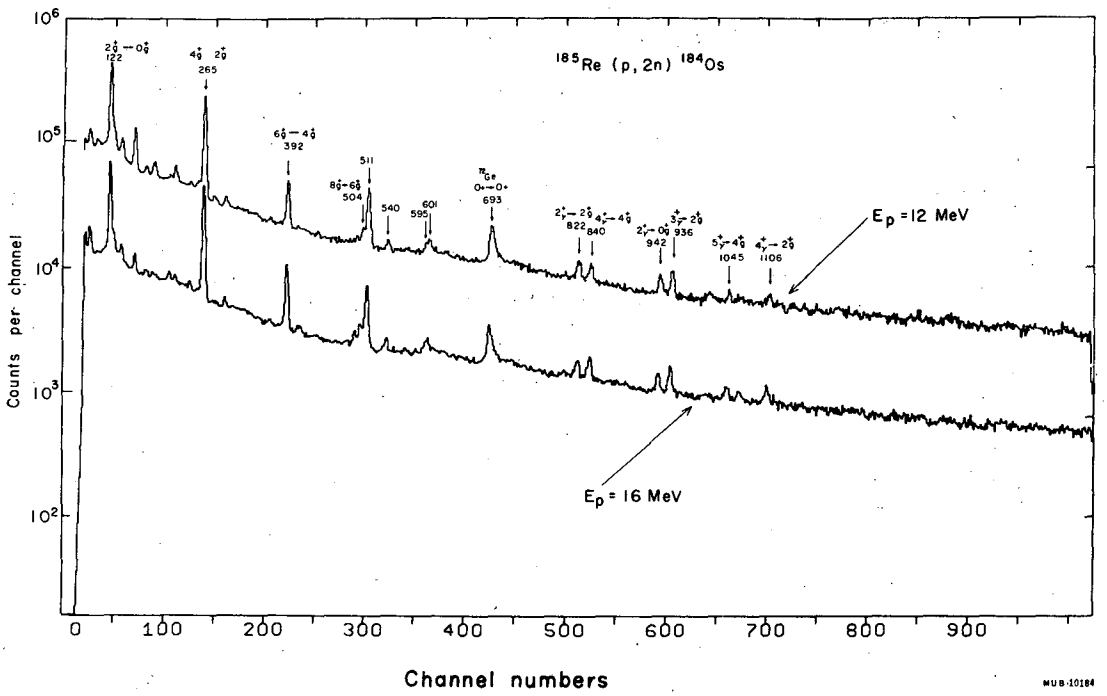

Fig. A. 22-1(a) (above). Gamma-ray spectra in ^{187}(p, 2n)^{186}Os reaction.
(b) (below). Gamma-ray spectra in ^{185}(p, 2n)^{184}Os reaction.

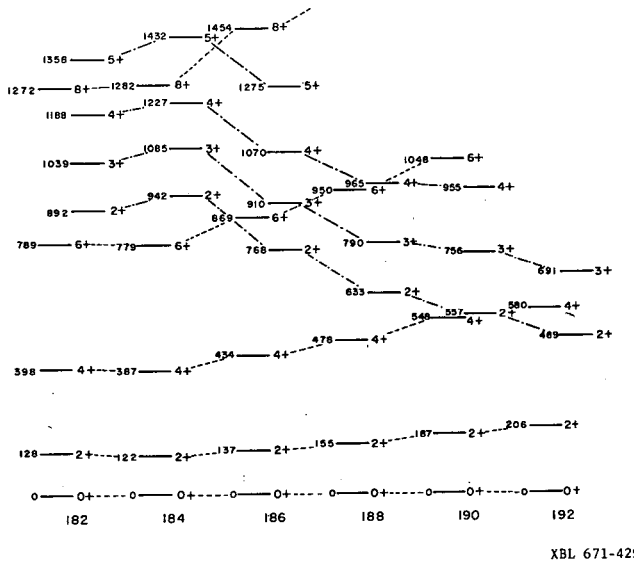

Fig. A. 22-2. Systematics of the ground band and the γ-vibrational bands in even Os nuclei.

23. LEVELS OF ^{188}Os POPULATED BY ^{188}Re AND ^{188}Ir†

T. Yamazaki, J. Sato,* Y. Yokoyama,* S. Baba,‡ H. Ikegami,** and M. Sakai††

The decay of ^{188}Re and ^{188}Ir was studied using electron spectrometers, Ge(Li) detectors, and coincidence and angular correlation apparatus. Conversion coefficients of almost all transitions were determined from electron and γ-ray intensities. The decay scheme, as shown in Fig. A. 23-1, was proposed. Comparison of γ-ray spectra from both parents was very useful and interesting. We will discuss some of the remarkable features observed in this study.

The Lowest K = 2 Band

This band is interpreted as the γ-vibrational state of an axially symmetric rotor, which is intrinsically different from the ground-state band. On the other hand, in the asymmetric rotor model it is regarded as a kind of rotational state of an asymmetric rotor generated by a rotation with respect to the nearly symmetric axis. In other words, the wavefunction of the K = 2 state is intrinsically the same as that of the ground state. The β decay of ^{188}Re (1-) to the ^{1}2+ and ^{2}2+ states provides the most crucial test to distinguish between these models. The experimental values reveal great deviation from the asymmetric-rotor prediction.

A similar discussion can be made on the γ-transition rates from the K = 1 states. If we take the asymmetric rotor model, the B(M1) ratio from any K = 1, I = 1 state should approximately follow the simple expression

$$\frac{B(M1,\ 1+ \rightarrow {}^{2}2+)}{B(M1,\ 1+ \rightarrow {}^{1}2+)} = \left| \frac{\langle I111|22\rangle}{\sqrt{2}\ \langle I11\text{-}1|20\rangle} \right|^{2} = 3.$$

The small band mixing between the ground and the K = 2 bands changes these values only slightly. On the other hand, as seen in Table A. 23-I, the experimental values are quite different from this prediction, showing the dependence of experimental values on the individual initial state. These facts mean that the intrinsic state of the K = 2 band is different from the ground state, which contradicts the basic idea of the asymmetric rotor model.

Beta Decays to Quasi-Particle States

If we assume the independent quasi-particle model, the β decay can take place only when either the quasi-proton or the quasi-neutron in the parent odd-odd state changes its charge and

configuration. In other words, one of two quasi-particle configurations in the final even-even state should be the same as in the initial state. This explains the fact that there are only a few quasi-particle states commonly populated by both parents. This also explains the remarkable experimental fact that we do not see many negative-parity states in the decay of ^{188}Re and ^{188}Ir, both of which have negative parity, so that they could feed negative-parity states by allowed β decay, if any occurred. Experimentally, there is no negative-parity state well populated by ^{188}Re except the 1463-keV 2- state. This 1463-keV 2- state may be interpreted as a K = 2- collective state because its energy is so low, and therefore it must be composed of many two-quasi-particle states, some of which are responsible for the β decay from the parent nuclei. As for the ^{188}Ir decay, we observed only one negative-parity state at 2350 keV in addition to the 1463-keV state.

Decoupled Rotational Bands

From the decay scheme of Fig. A. 23-1, it seems difficult to identify a rotational band for each intrinsic excited state. Two-quasi-particle states are located so close to each other that the Coriolis coupling among those states is supposed to destroy the regular rotational pattern. One of the most significant effects should be coupling between the state of $K = \Omega_1 + \Omega_2$ and the state of $K = \Omega_1 - \Omega_2$ in the case of $\Omega_2 = 1/2$. This effect is compared with the decoupling phenomena in odd-A nuclei. The irregularity of rotational bands, which is exhibited by the 1+ and 2+ states above 2 MeV, may be partly due to this Coriolis admixture. However, because of missing 3+ states, we cannot correctly identify these states.

The Excited 0+ States

The well-known 0+ states at 1087 and 1765 keV are interpreted as the two-phonon γ-vibrational and the β-vibrational state. However, the most surprising fact is that the 1087-keV 0+ state has no 2+ state based on it; such a 2+ state should exist and be populated 50% as well as the 0+ state is, insofar as we assume collective models. Therefore the conventional interpretation of this 0+ state seems to be quite doubtful. These 0+ states are not populated by the ^{188}Ir decay. On the other hand, in the ^{188}Ir decay we found an almost pure E0 transition (1812 keV). This fact suggests the presence of an 0+ state at 1812 keV, or a 2+ state at 1969 keV which deexcites to the 155-keV state via a large E0 component. If the latter case is true, then this new state may be interpreted as the β-vibrational state.

Footnotes

† Condensed from UCRL-16996.

*Department of Chemistry, University of Tokyo, Tokyo, Japan.

‡ Japan Atomic Energy Research Institute, Ibaraki, Japan.

**Tokyo Institute of Technology, Tokyo, Japan.

††Institute for Nuclear Study, University of Tokyo, Tokyo, Japan.

Table A. 23-I. B(M1) ratios from K = 1, I = 1 states to the ^{1}2+ and ^{2}2+ states in ^{188}Os.

Initial state (keV)	B(M1, i → ^{2}2+)/B(M1, i → ^{1}2+)
1620.7	> 3.4
1843.3	37
2099.3	< 1.2
2216.7	< 0.037

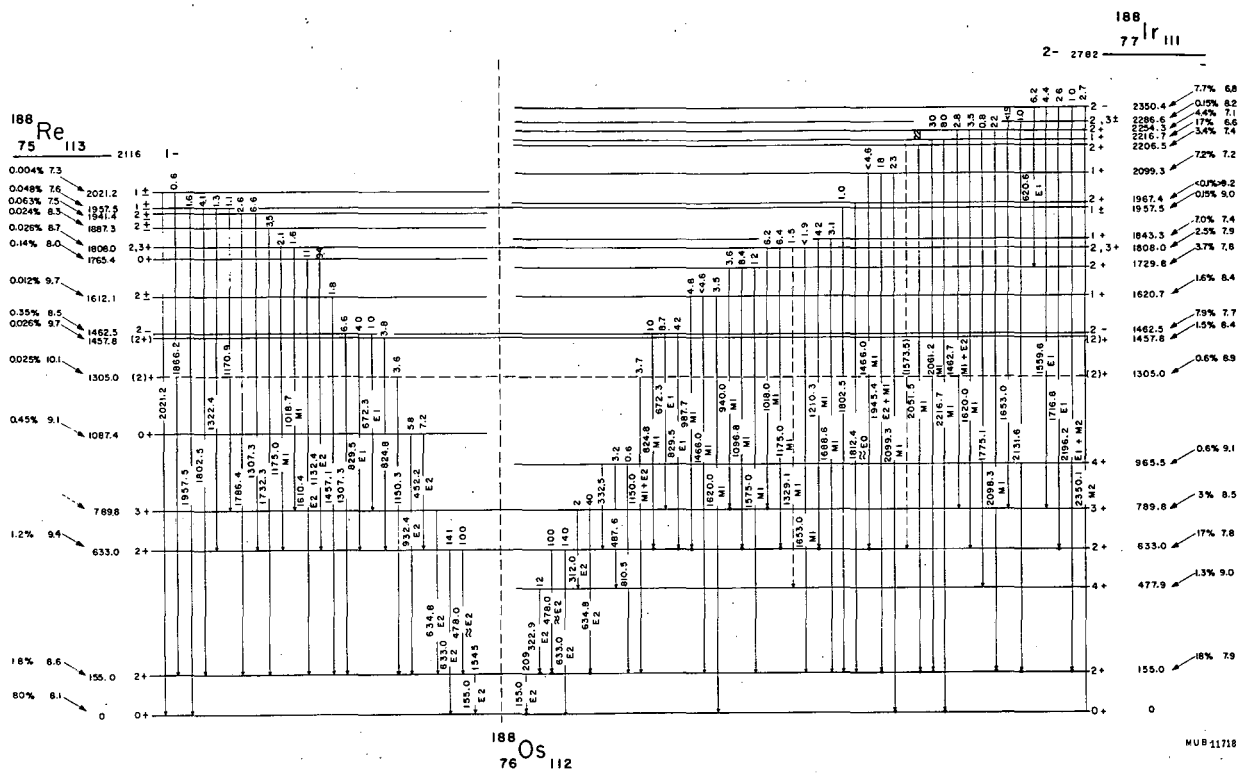

Fig. A. 23-1. Proposed decay scheme of ^{188}Re and ^{188}Ir.

24. THE PULSED BEAM METHOD FOR THE SYSTEMATIC OBSERVATION OF ISOMERIC STATES IN THE 3 — 500 nsec RANGE POPULATED BY (PARTICLE, xn) REACTIONS

T. Yamazaki and G. T. Ewan

Using a pulsed beam, one can study isomeric states populated by nuclear reactions. The natural beam characteristics of the Berkeley 88-inch cyclotron (repetition period is 100 to 170 nsec and time spread of each bunch is approx 5 nsec, depending on the particle and energy) and the fast rise time of the Ge(Li) spectrometer have made it possible to search for unknown short-lived isomers and to determine a lifetime as short as a few nsec. A block diagram of our apparatus is shown in Fig. A. 24-1. The fast signal from a Ge(Li) spectrometer is used as a starting signal of the time-to-height converter, and the rf signal from the cyclotron stops the converter. The energy signal and the time signal are analyzed in a two-dimensional pulse-height analyzer.

A part of the 256-channel (energy) by 16-channel (time) spectrum in the ^{208}Pb(α, 4n)^{208}Po reaction, taken with a 2 cm^2 × 5 mm thin window Ge(Li) detector, is shown in Fig. A. 24-2. The Pb $K\alpha_2$, $K\alpha_1$, $K\beta_1$, $K\beta_2$ x rays are seen in the prompt spectrum, but disappear in the delayed spectrum, whereas the Po x rays, which are predominantly associated with the delayed 176-keV transition, remain in the delayed spectrum. The 145-keV peak and other weak peaks disappear promptly, but the 147-keV peak decays slowly ($T_{1/2}$ = 8 nsec). The 176-keV peak decays much slower ($T_{1/2}$ = 390 nsec), but is not the isomeric transition itself because of its prompt component (see time distribution curves in Fig. A. 24-3). A tentative level scheme is shown in Fig. A. 24-3. We surveyed $^{206,\,208}$Pb(α, xn)Po and $^{110-116}$Cd(α, xn)Sn reactions, in each of which we observed at least one isomer. Specific cases will be described in Paper A. 25.

In summary, we point out some remarkable features of this method.

1. Since (particle, xn) reactions populate many varieties of states of almost all neutron-deficient nuclei, this method is the most systematic and powerful means to search for the nuclear isomerism in this time range.

2. Since there is no loss of counts by making the time analysis, one can survey a nucleus within only an hour.

3. The lower limit for the lifetime is set essentially by the beam width and shape. The time characteristics of a Ge(Li) detector depend on its size and the energy of interest. In good cases, the width (FWHM) of the prompt peak, which includes the beam spread and overall crystal and electronics width, was about 5 nsec and the overall instrumental half-life (slope of the prompt curve on the delay side) was 1.5 nsec, indicating that we may be able to determine lifetimes as short as a few nsec.

4. Since the nuclear states formed in these reactions are highly aligned, this time analysis system becomes immediately a device for observing the perturbed angular distribution by applying an extranuclear field.

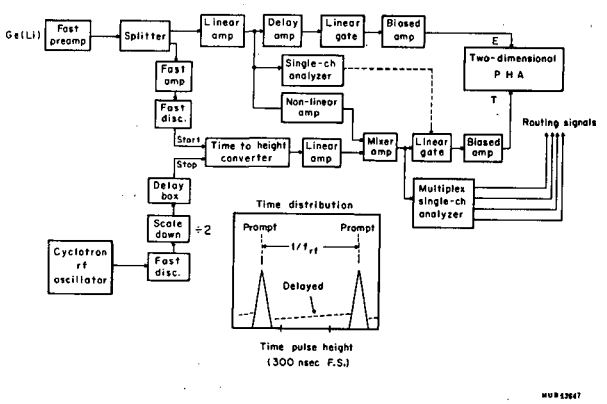

Fig. A. 24-1. Block diagram of the electronics.

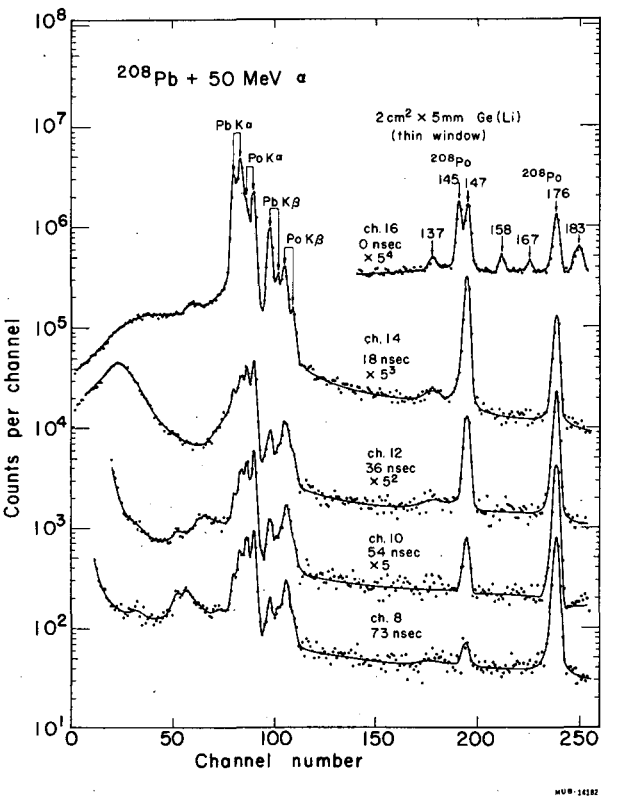

Fig. A. 24-2. Part of the 256-channel (energy) by 16-channel (time) spectrum in the $^{208}Pb(\alpha, 4n)^{208}Po$ reaction, taken with a 2 cm^2 by 5 mm thin-window Ge(Li) detector.

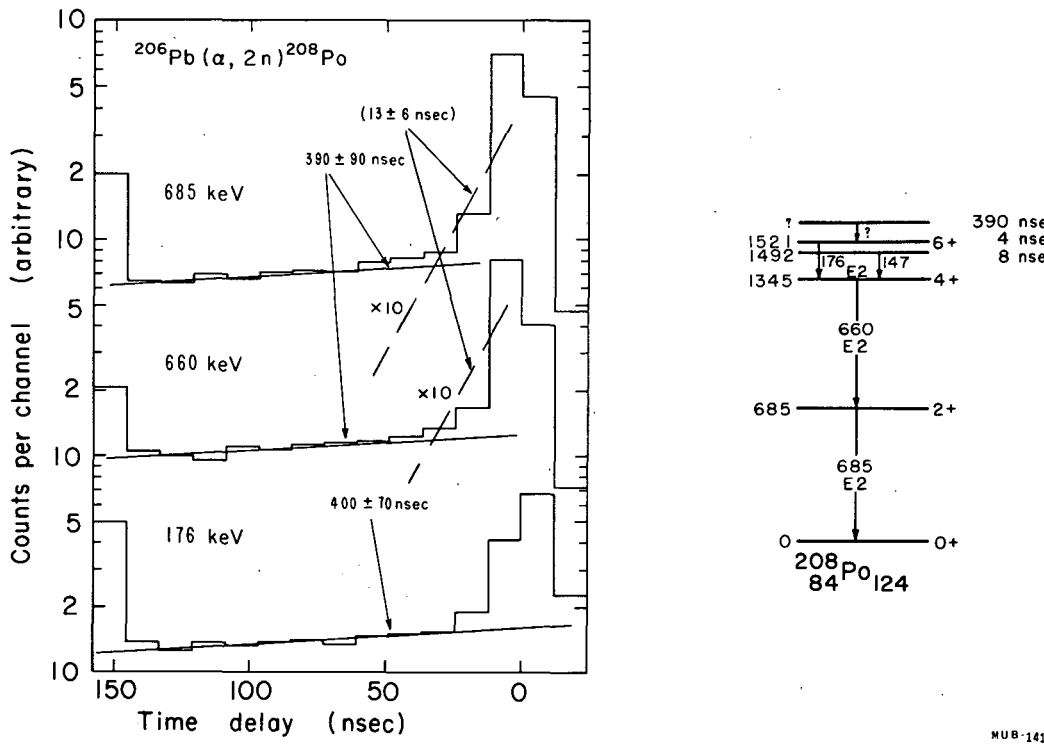

Fig. 24-3. (Left) Time-distribution curves of transitions in ^{208}Po. (Right) Tentative level scheme.

25. ISOMERIC STATES IN Po AND Sn ISOTOPES

T. Yamazaki, G. T. Ewan, and S. G. Prussin

A survey of short-lived isomeric states has been carried out by employing the pulsed-beam method in (α, xn) reactions, as described in Paper A. 24.

At first we took full-range energy spectra for the prompt component and for a few delayed components (for example, see Fig. A. 25-1). When the delayed spectrum exhibited delayed γ rays, two-dimensional pulse-height analysis was performed. The CDC-6600 computer analyzed the data to give time distribution for each γ ray.

In general, there are many γ rays involved in an isomeric decay. Since a reaction also populates any state directly, any of those γ rays exhibits a prompt component as well as a delayed component except when it deexcites the isomeric state directly. In many cases, such an isomeric transition is missing because of too low energy or too much conversion process. The intensities of prompt and delayed components were taken into account in establishing a reasonable decay scheme.

As a first example, we discuss the ^{208}Pb(α, 2n)^{210}Po reaction. The nucleus ^{210}Po, consisting of two protons outside of the double-closed shell ^{208}Pb, is one of the most typical nuclei which exhibit pure shell-model configurations. Since in the past it was studied only from the decay of ^{210}At, the levels of the ground-state configuration $(h_{9/2})^2$ are known up to the 6+ member, the half-life of which is 38 nsec according to the delayed coincidence experiments. The missing 8+ member was expected to be highly populated in (α, 2n) reactions, and also to be isomeric. Figure A. 25-2 shows decay curves of each transition, and a partial-level scheme we have established based on the experiment. The 1180-keV 2+→0+ and 245-keV 4+→2+ transitions follow a half-life of 150±3 nsec, which clearly indicates the presence of a 150-nsec isomer above

the 6+ level. However, the 8+→6+ isomeric transition itself (as well as the 46-keV 6+→4+ transition) was not seen in the energy spectrum because of too-high conversion coefficients. On the other hand, the new 1292-keV transition seems to be an isomeric transition, itself, with a half-life of 24±1 nsec. This lifetime is compatible with an E3 multipolarity. Therefore, the only possibility is to place this transition between an unknown 11- level, which must be the lowest of all the negative parity states, and the 8+ level. This fact agrees with the prediction of Kim and Rasmussen[1] that the 11- member of the $h_{9/2}i_{13/2}$ configuration is the lowest of all.

The nucleus ^{208}Po, studied by means of ^{206}Pb(α, 2n) and ^{208}Pb(α, 4n), has three prominent transitions, all of which follow a 390-nsec half-life and show prompt components. A tentative decay scheme is shown in Fig. A. 25-3 of Paper A. 24, but the isomeric transition is missing.

There are many other isomers, which are presented in Table A. 25-I, but are not well studied at the moment.

The even Cd isotopes (A = 110 to 116) were bombarded with 28-MeV α particles, which yielded many Sn isomers. Time-distribution curves are presented in Fig. A. 25-3. Tentative level schemes in $^{112, 114, 116, 118}$Sn are shown in Fig. A. 25-4.

Reference

1. Y. E. Kim and J. O. Rasmussen, Nucl. Phys. 47, 184 (1963).

Table A. 25-I. Observed isomers in Po isotopes.

Nucleus	Half-life (nsec)	Main transitions (energy in keV)
^{206}Po	long	390, 475, 698, 805
^{207}Po	long	268, 301, 577, 622, 813
^{208}Po	8	147
	390±90	176, 660, 685
^{209}Po	130± 8	545, 780
^{210}Po	24± 1	1292
	150± 3	245, 1180

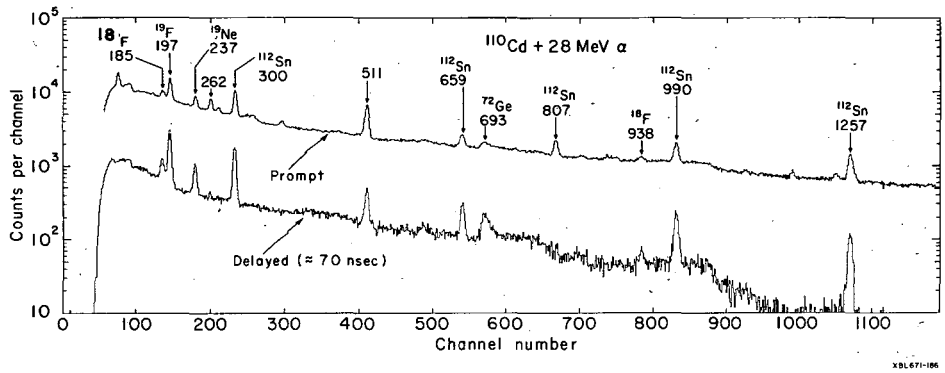

Fig. A. 25-1. Prompt and delayed spectra of γ rays in ^{110}Cd + 28-MeV α reactions. Some peaks come from the Mylar backing. Predominant reaction is ^{110}Cd(α, 2n)^{112}Sn.

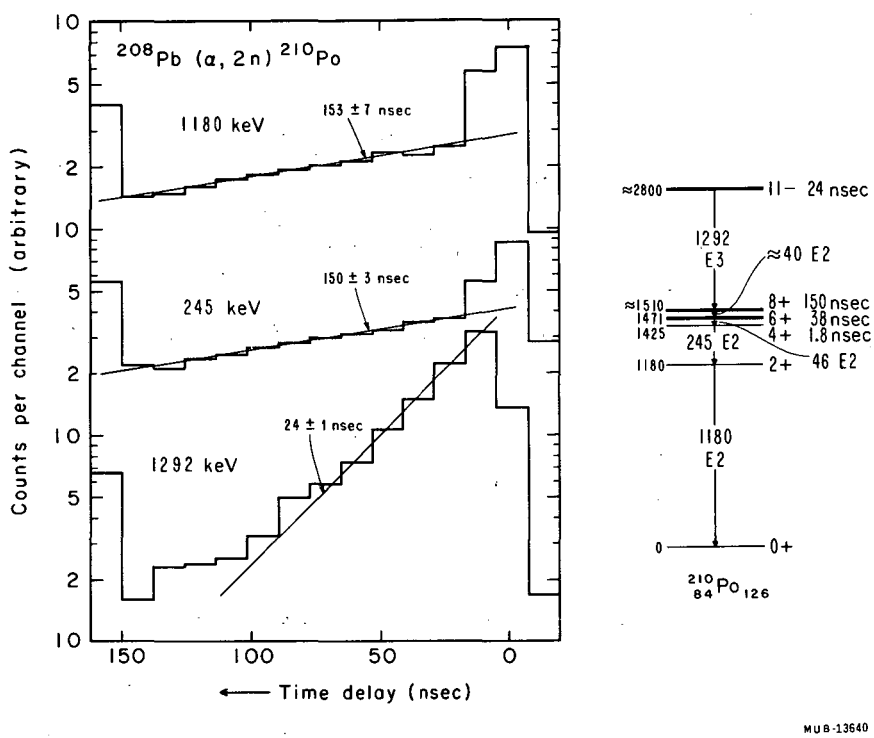

Fig. A.25 2. (Left) Time distribution curve of γ rays in the ^{208}Pb(a, 2n)^{210}Po reaction. (Right) Partial level scheme of ^{210}Po.

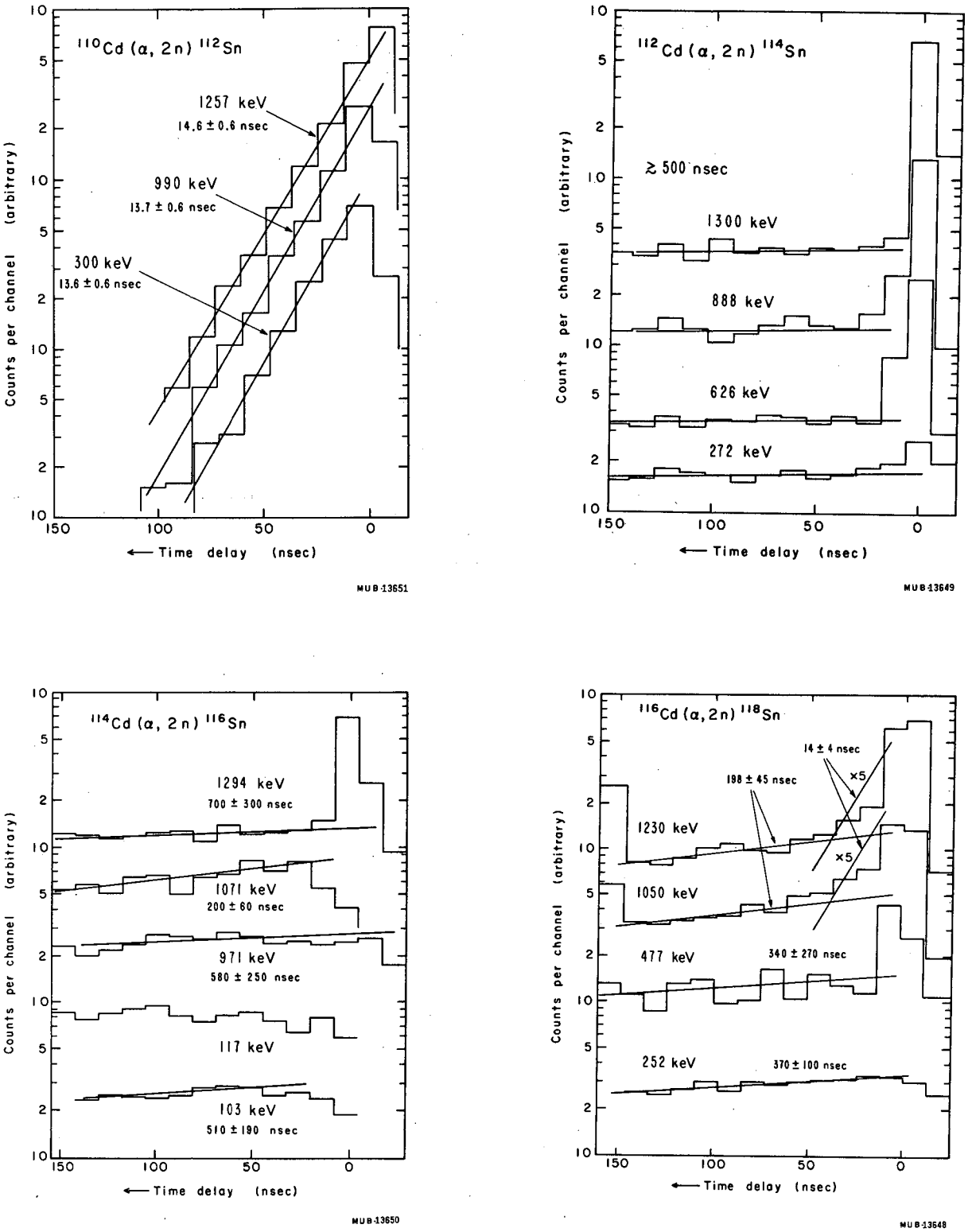

Fig. A.25-3. Time-distribution curves of transitions in even Sn isotopes.

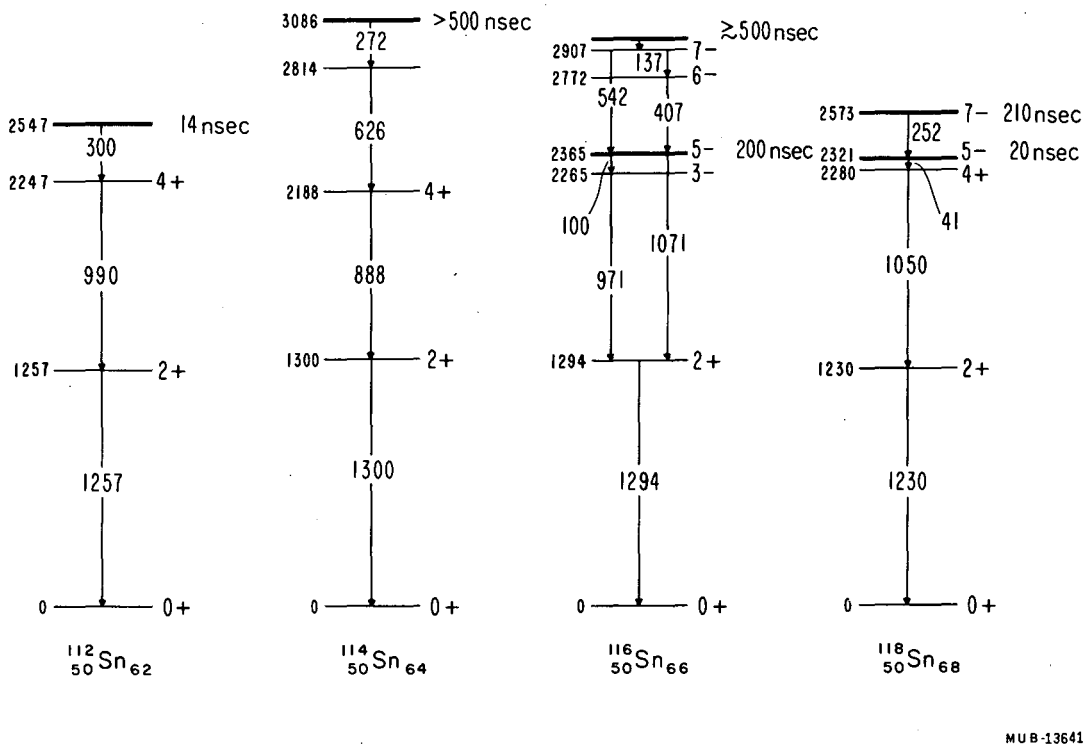

Fig. A. 25-4. Tentative-level schemes in even Sn isotopes.

B. NUCLEAR REACTIONS AND SCATTERING

1. POLARIZATION IN p-^{3}He SCATTERING BETWEEN 10 AND 20 MeV

W. F. Tivol, D. J. Clark, H. E. Conzett, J. S. C. McKee,†
E. Shield, and R. J. Slobodrian

Until the present series of experiments, knowledge of the polarization in p-^{3}He scattering was limited to a few points of energies below 10 MeV.[1] The present experiments have resulted in angular distributions at five energies between 10 and 20 MeV. These new data allow an extension of a phase-shift analysis into the region where inelastic parameters differ from those of Ref. 1 and provide more accurate values for the splittings of the phase shifts. Triple-scattering experiments are necessary, however, to provide a unique phase-shift solution.

These experiments were performed by using the polarized beam facility of the 88-inch isochronous cyclotron.[2] A beam of α particles incident upon a hydrogen target produced a beam of recoil protons whose polarization was more than 99%. This proton beam was collimated and focused upon a gas cell containing ^{3}He. At the higher energies the cell was operated at 60 psia; at the lower energies it was operated at 20 psia. Along the path of the polarized beam was a solenoid magnet which was used to reverse the spins of the protons. Use of the solenoid eliminates the necessity of exchanging detectors to correct for geometric asymmetries and counter efficiencies. Each angle was measured in three separate runs. In two of the runs the solenoid was operated with equal and opposite currents; in the third the solenoid was off. The run with the solenoid off was twice as long as each of the other two. In this way both the small effects on the beam due to the solenoid and the instrumental asymmetries are canceled out. The resulting left-right asymmetry is due only to the polarization of the scattering being measured, except for negligible second-order effects. The gas cell used had a 1.9-mil Dural window at the higher pressure and a 1-mil Dural window at the lower pressure.[3] At 13 MeV points were taken with both high and low pressures.

The scattered protons were detected with crystals of CsI, mounted on DuMont 6363 phototubes, whose thickness varied from 10 to 80 mils. In all cases the ranges of the protons were less than 2/3 the thickness of the crystal. The signals produced by the phototubes were amplified and routed to two pulse-height analyzers.[2] In all cases the spectra from the analyzers contained so few background counts that an unambiguous subtraction could be made and the asymmetries determined with confidence.

Figure B.1-1 shows the values of the polarizations obtained in these experiments. The values for the five energies are plotted on overlapping scales to facilitate comparisons between them. The minimum of the polarization shifts from 83 deg at 10.9 MeV to 101 deg at 20.9 MeV, and a second maximum seems to be developing at small angles at 20.9 MeV. The results of the present experiments agree well with the few previously determined points.[1]

Work is in progress on a phase-shift analysis of these data.

Footnote and References

†. On leave from the University of Birmingham.

1. A review of previous work can be found in the paper by T. A. Tombrello, Phys. Rev. 138, 1B, 12 April 1965.
2. Howard S. Goldberg, Elastically Scattered Polarization of 40-MeV Protons from Deuterium (Ph.D. Thesis), UCRL-11526, Aug. 1964.
3. The gas cell is that pictured in Goldberg's thesis except that the window is glued on the inside with epon rather than clamped to the outside.

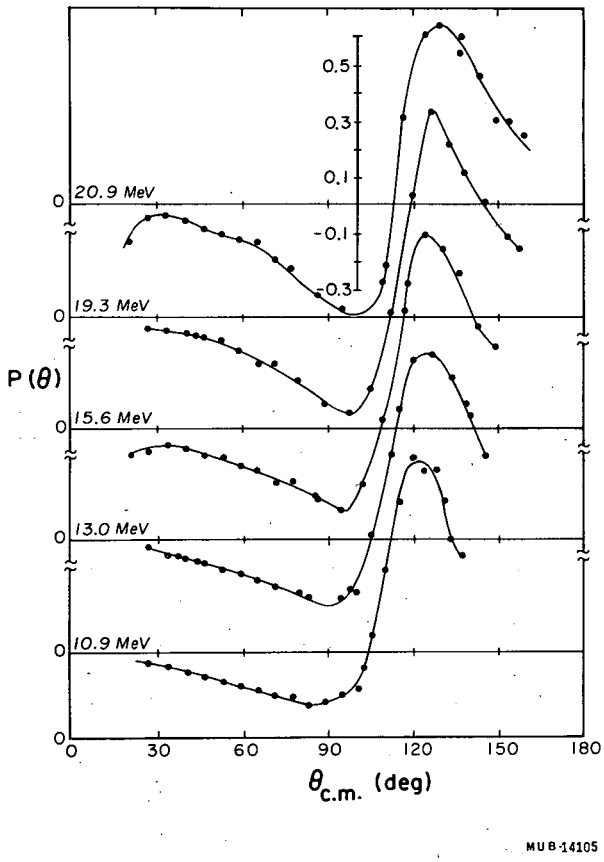

Fig. B. 1-1. Plot of polarization versus center-of-mass angle for incident proton energies of 20.9, 19.3, 15.6, 13.0, and 10.9 MeV.

2. SCATTERING OF POLARIZED PROTONS BY DEUTERIUM IN THE ENERGY REGION 10 TO 20 MeV

J. S. C. McKee, D. J. Clark, R. J. Slobodrian, and W. F. Tivol

Recent measurements of proton polarization in elastic proton-deuteron scattering at incident particle energies of 22 MeV,[1] 30 MeV,[2] 40 MeV,[3] and 50 MeV,[4] have provided angular distributions for the scattered particles, each characterized by a considerable negative polarization in the region of the minimum of the elastic scattering cross section. Lower-energy data, on the other hand, from the Wisconsin[5] and Washington[6] laboratories in the range 1 to 10 MeV, exhibit positive polarization at all angles, and show double peaking of the angular distribution about a shallow minimum.

The purpose of the work presented here was to investigate the intermediate region between these two sets of results, and to examine in some detail the behavior of the polarization at large angles, as a function of energy.

Protons with a polarization in the region of 100% are produced as recoil protons from the bombardment of liquid-nitrogen-cooled hydrogen by the α-particle beam of the 88-inch cyclotron at Berkeley. Polarized protons of energies up to 60 MeV are readily available, but for this experiment energies of only 11.0, 13.2, 15.7, and 19.5 MeV were required. At each energy the protons were scattered from a gaseous deuterium target held at a pressure of around 2 atm, and the observed asymmetries in the angular distribution of scattered particles allowed the polarizations due to the scattering process itself to be calculated, once the polarization of the impinging beam was known.

For each separate experiment eight detectors consisting of CsI crystals mounted on

Dumont 6363 photomultiplier tubes were available to record simultaneously asymmetries at four scattering angles. For the lowest energy considered, however (11.0 MeV), only the four forward counters were used because of the limited angular range over which particles are received in the laboratory system. Pulses from the detectors were routed to separate quadrants of two 400-channel pulse-height analyzers, and from these final spectra were obtained. Sample spectra obtained at 15.7 MeV incident proton energy and at an angle of 20 deg are shown in Fig. B.2-1. It will be seen that the proton peak is clearly resolved from that due to recoil deuterons. At the highest energies considered, the recoil deuterons allow asymmetries of the associated backward protons to be deduced, thus providing consistency checks on some experimental data at backward angles. Such points are shown on the 15.9-MeV data, and on the 19.5-MeV data plotted in Fig. B.2-2. A spin-precession solenoid was used to rotate proton spins through 180 deg at each of the energies mentioned.

Although no theoretical analysis of the final data has as yet been attempted, certain qualitative features of the results can be noted from an examination of Fig. B.2-2. The first observation is that the polarization around 120 deg c.m. goes negative for the first time in the region of 19 MeV incident proton energy. This is evident from a comparison of the earlier 22-MeV data with these results. It will be seen that the angular distribution as a whole dips in the middle, and rises at both forward and backward angles with increasing energy. The minimum in the asymmetry, when it occurs, does so in the vicinity of the deep minimum of the elastic differential cross section in each case;[7] a phenomenon which has been observed on previous occasions, in other scattering experiments.

At forward angles the polarization is seen to go negative at the lowest energies considered. The detailed behavior of the polarization in this region is worth further study, and it is intended to carry out such experiments in the near future.

In the absence of a complete theory of the three-nucleon system, and in the knowledge that the impulse approximation can have no applicability to this energy region, these results are presented as raw data in the hope that they may help to illustrate at least the energy dependence of the polarized nucleon-deuteron scattering process.

Throughout this series of experiments, the uncertainties in the measurement of any particular point are seldom greater than a few per cent, after consideration of both background and statistics. Background was reduced to a minimum, and at backward angles crystals as thin as 0.005 in. were made for this purpose. These thin crystals efficiently reduced the background from γ conversion, despite being thick enough to stop low-energy protons at those angles for which they were designed.

References

1. H. E. Conzett, G. Igo, and W. J. Knox, Phys. Rev. Letters 12, 222 (1964).
2. S. J. Hall, A. R. Johnston, and R. J. Griffiths, Phys. Letters 14, 212 (1965).
3. H. E. Conzett, H. S. Goldberg, E. Shield, R. J. Slobodrian, and S. Yamabe, Phys. Letters 11, 68 (1964).
4. A. R. Johnston, W. N. Gibson, J. H. N. C. Megaw, R. J. Griffiths, and R. M. Eisberg, Phys. Letters 19, 289 (1965).
5. W. Bruebler, W. Haeberli, and P. Exterman, Nucl. Phys. 77, 394 (1966).
6. W. Trachslin and L. Brown, Scattering of Polarized Protons by Deuterium from 1 to 3 MeV (preprint, Carnegie Institute, Washington, D.C.).
7. W. T. H. Van Oers and K. W. Brockman, and references therein. Phase Shift Analysis of Elastic Nucleon-Deuteron Scattering (preprint).

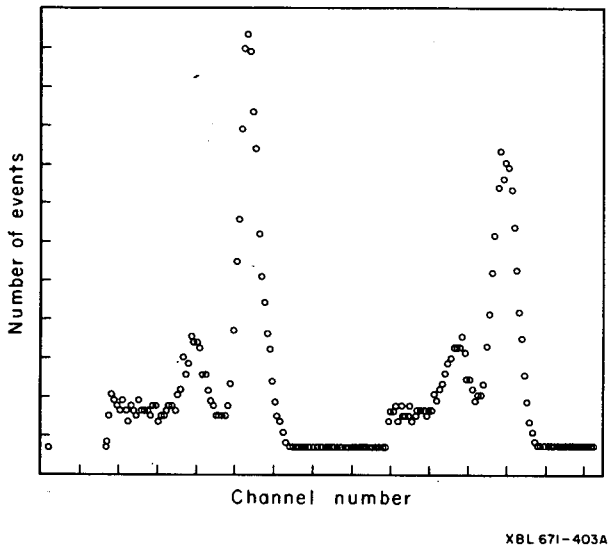

Fig. B.2-1. Sample spectra from counters 1 and 2 taken for 15.7-MeV protons. The angles of scattering are shown. The right-hand peak in each case corresponds to elastically scattered protons and the lower one to recoil deuterons. The peaks are cleanly resolved.

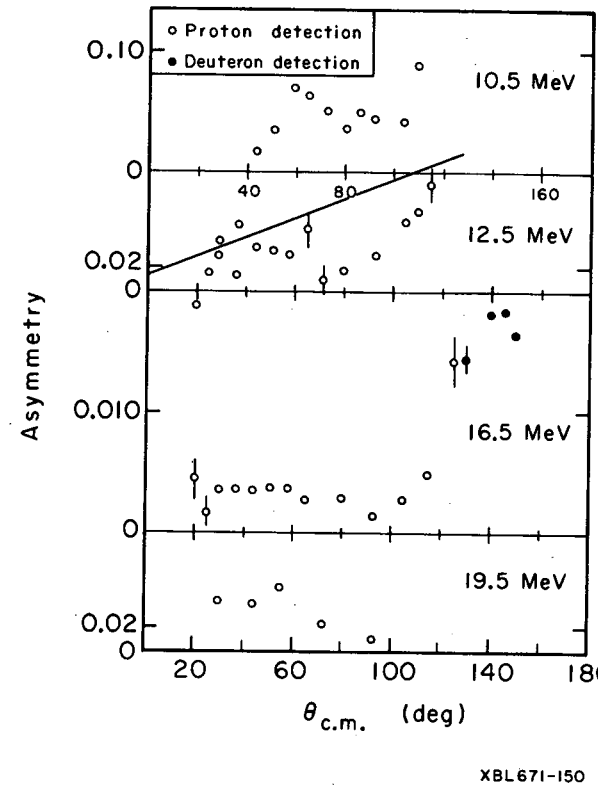

Fig. B.2-2. Data from 88-inch cyclotron on p-d asymmetries; the variation in asymmetry with angle at various incident proton energies is shown.
o proton detection, • deuteron detection

3. THE 2p FINAL-STATE INTERACTION IN THE ^{3}He(^{3}He, α)2p REACTION

R. J. Slobodrian, D. J. Clark, J. S. C. McKee,†
W. F. Tivol, and T. A. Tombrello††

The ^{3}He(^{3}He, α)2p reaction has been previously studied by Artjomov et al.[1] at a bombarding energy of 26 MeV for laboratory-system angles between 6 and 15 deg. At 6 deg there was some indication of the proton-proton interaction, whereas at 15 deg the spectrum resembled phase space.

There is continued interest in the study of reactions leading to the singlet dinucleon state, particularly with respect to the possible distortions of the observed third-particle spectra due to interactions with the nucleons.

We have studied this reaction at 44 and 54 MeV laboratory-system energy, measuring the α-particle spectra with a solid-state detector telescope and an electronic-particle identifier.[2] Our spectra were taken between 5 and 42 deg lab, and show a pronounced peak near the high-energy end of the spectrum from the 2p interaction, similar to the ones observed from the ^{3}He(d, t)2p reaction.[1,3] The angular distribution of this peak exhibits a very pronounced diffraction pattern. Figure B.3-1 shows the energy spectra at θ_L = 10 deg, near the first minimum, and θ_L = 18 deg

taken at 54 MeV lab (the latter angle corresponding to the second maximum of the angular distribution). Figure B.3-2 shows the angular distribution of the peak at 44 MeV lab.

The deep minima of the angular distribution seem to indicate that a simple-minded single-nucleon transfer theory may account for it. Nevertheless a PWBA fit[4] is inadequate because it does not account for the relative values of the successive maxima, and it gets out of phase with respect to the minima. Clearly the reaction amplitude has to be symmetrized, but the PWBA is out of the question except for the forward peaking. A fit with a cylindrical Bessel function[5] is somewhat more successful but it is far from perfect.

The energy spectra agree qualitatively with predictions of the Watson-Migdal final-state interaction theory,[6] and quantitative calculations are in progress.

Footnotes and References

† On leave from the University of Birmingham.
†† Summer visitor from California Institute of Technology.

1. K. P. Artjomov, V. I. Chuev, V. Z. Goldberg, A. A. Ogloblin, V. P. Rudakov, and J. N. Serikov, Phys. Letters 12, 53 (1964).
2. F. S. Goulding, D. A. Landis, J. Cerny III, and R. H. Pehl, IEEE Trans. Nucl. Sci. 11, 388 (1964).
3. O. M. Bilaniuk and R. J. Slobodrian, Phys. Letters 7, 77 (1963); H. E. Conzett, E. Shield, R. J. Slobodrian, and S. Yamabe, Phys. Rev. Letters 13, 625 (1964); T. A. Tombrello and A. D. Bacher, Phys. Letters 17, 37 (1965).
4. M. H. Macfarlane and J. B. French, Rev. Mod. Phys. 32, 567 (1960).
5. A. Dar, Nucl. Phys. 55, 305 (1964) and references therein.
6. K. M. Watson, Phys. Rev. 88, 1163 (1952), A. B. Migdal, Zh. Eksperim. i Teor. Fiz. 28, 3 (1955) [translation: Soviet Phys.-JETP 1, 2 (1955)].

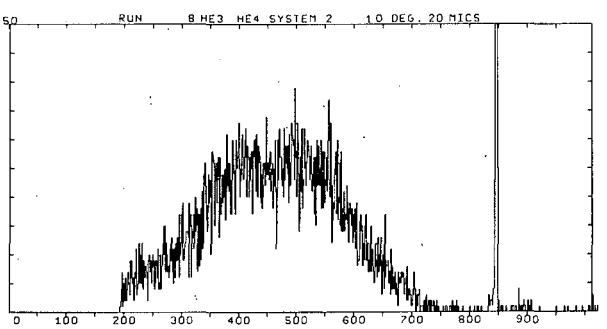

XBL 672-1152

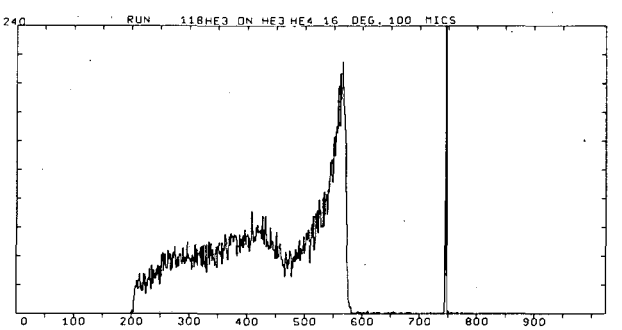

XBL 672-1153

Fig. B.3-1. α-Particle energy spectrum (a) at θ_L = 10 deg near the first minimum of the differential cross section; (b) at θ_L = 18 deg, near the second maximum of the differential cross section. Abscissas are channel numbers, ordinates are number of counts.

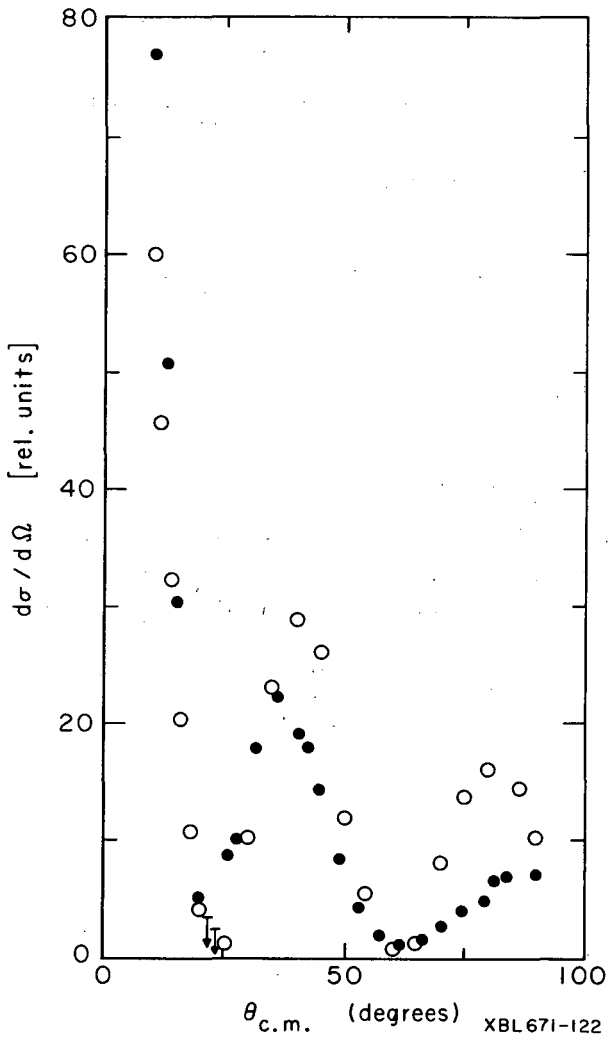

Fig. B.3-2. Angular distribution of the peak at 44 MeV lab energy.
● Experimental points;
o cylindrical Bessel function "fit," r_i = 4.6 F

4. PROTON-PROTON SCATTERING BETWEEN 4.2 AND 10 MeV AND THE $^1S_0$ SHAPE-DEPENDENT SCATTERING PARAMETERS†

R. J. Slobodrian, H. E. Conzett, E. Shield, and W. F. Tivol

Low-energy proton-proton scattering has been the object of very accurate experimental investigation, and of refined and sophisticated theoretical analyses in recent years.[1] Particularly fruitful was the research carried out at Wisconsin, where the energy range between 1.397 and 4.203 MeV (laboratory system) was covered by two separate experimental groups.[2,3] An accurate value of the $^1S_0$ phase shift was obtained recently at 0.3825 MeV through measurements of the interference minimum.[4] The $^1S_0$ phase shift at 0.3825 MeV has been used in conjunction with the KMBND data in order to attempt a determination of the shape parameter P,[5] in the expansion

$$C^2 k \cot \delta_0 + \frac{1}{R} h(\eta) = -\frac{1}{a_p} + \frac{1}{2} r_e k^2 - P r_e^3 k^4 + Q r_e^5 k^6 + \cdots ,$$

where the symbols have the usual meaning. Several objections were raised concerning the certainty of the determination of P.[6-8] Gursky and Heller[7] reported an attempt to produce a four-parameter fit, which resulted in unreasonable values for the shape-dependent parameters P and Q.[9]

Additional difficulties arise due to the uncertainty of the accuracy of the vacuum polarization correction[10] for S waves, since this correction dominates the curvature of the low-energy limit of the expression.

It can be shown[11] that the WMF data reduce the ambiguities quite considerably, notwithstanding the reservations voiced by KMBND[3] concerning some systematic errors contained in the data and the shortcomings of early analyses of them. Between 4.203 and 10 MeV there is an additional accurate experiment at 9.69 MeV,[12] consistent with the trend indicated by the WMF data, but inconsistent with a set of data that will be called OC[1] (old cyclotron data), that range from 4.2 to 8 MeV. Such OC data are inaccurate for the purpose of a determination of shape-dependent parameters, but their trend could be interpreted as consistent with the KMBND data at 1.855, 2.425, and 3.037 MeV.

The experiment presented here and its analysis were undertaken with the hope of providing clues to determine the shape parameters of the p-p interaction. The parameterization provided by the expansion of k cot δ_0 is particularly suitable for visualizing the degree of relevance of the information between 4.2 and 10 MeV, and also because predictions of P[1,13] and Q[1,14] are readily available in the literature.

The Berkeley 88-inch spiral-ridge cyclotron was used to produce a beam of 6.141, 8.097, and 9.918 MeV at the center of the target, which consisted of 99.99% pure H_2 at about 0.1, 0.075, and 0.05 atm, contained in a 20-inch scattering chamber. The pressure was measured to within ±0.1% accuracy with a silicon oil manometer. The temperature was measured to ±0.1°K, and the total variation throughout the experiment was within ±0.25°K. The beam was accelerated as H_2^+ ions and conveyed through an analyzing magnet and quadrupole magnet lenses onto the scattering chamber. The beam was defined by Ni slits and carbon antiscatter baffles. The charge collection was accomplished with a Faraday cup and an integrating electrometer, accurate to within ±0.1%. Calibrations of the integrating system were performed at regular intervals during the experiment. The beam direction was aligned to better than 2.5 minutes of arc. The beam energy was determined through its range in aluminum, and converted by use of Bichsel's experimental ranges;[15] such energy determination should therefore be accurate to about 0.1%. The detection of the scattered protons was accomplished with two lithium-drifted silicon detectors, one on either side of the beam. The positioning was accurate to within 1 minute of arc. The gas geometry factor was approximately 6.7×10^{-6} cm-sr. Counting statistics were kept in the range of 0.3%. Dead-time losses were kept below 1% and corrected by means of fast scalers. The spectra were stored in two RIDL 400-channel analyzers. Two monitor detectors were also used, one at 8 deg and the other at 25 deg, off the azimuthal plane. Their spectra were routed to a Nuclear Data 4096-channel PHA, into separate quadrants. Coincidences (prompt and delayed) between both detectors on the azimuthal plane were also recorded to obtain an indication of inelastic events. The net difference between real and accidental coincidences sets a limit on inelastic events at about 0.1% of the elastic cross sections. The background subtraction on the spectra is in the order of 1%. The peak due to impurities is separated from the proton-hydrogen peak at angles larger than 7 deg. The absolute error of the cross sections is 0.5%, resulting from the above mentioned sources, as well as from the geometrical factor.

A phase-shift analysis was accomplished by using a CDC 6600 computer and a version of the program developed by Knecht[16] for the analyses of the KMBND data. Table B.4-I contains the results, which should be considered preliminary because some more exhaustive searches will be undertaken in the future. The limit of error on the $^1S_0$ phase shift can be set at 0.2 deg.

A discussion of the scattering parameters that can be obtained from the experimental phase shifts, without and with extended electromagnetic structure corrections,[17] is beyond the scope of this paper. Nevertheless Fig. B.4-1 presents a plot of the nonlinear part of the expansion

$$K = \sum_{i=0}^{n} A_i E^i,$$

where E is the laboratory-system energy. The nonlinear part is obtained as $\Delta K = K_{exp} - (A_0+A_1E)$. The function K_{exp} is calculated from the experimental phase shifts, and is corrected for vacuum polarization effects;[10] A_0 and A_1 were obtained through a least-squares fit effected on the WMF, the KMBND, and our data, without performing extended electromagnetic structure corrections. The resulting shape-dependent parameters are P = 0.102 and Q = 0.014. If Q is set equal to zero one obtains P = 0.072. Such values may not be inconsistent with a Yukawa well. The above-

mentioned values are also to be understood as preliminary.

Figure B.4-1 illustrates the dramatic improvement over the old cyclotron data accomplished by the 88-inch variable-energy cyclotron and its instrumentation.

There is an apparent discrepancy, beyond experimental error, with the phase shift obtained from the Minnesota data[11] by MacGregor (also reproduced by a calculation performed here with the CDC 6600 computer). It will require further clarification.

Acknowledgments

It is a pleasure to thank T. Chan for his assistance in mechanical designs, John Meneghetti in the mechanical instrumentation, D. Landis with electronic circuits, and B. Lothrop, who made the silicon detectors.

Footnote and References

† Presented at International Conference on Nuclear Physics, Gatlinburg, Tennessee, Sept. 1966.

1. A summary of the work prior to 1950 is contained in J. D. Jackson and J. M. Blatt, Rev. Mod. Phys. 22, 77 (1950).
2. H. R. Worthington, J. N. McGruer, and D. E. Findley, Phys. Rev. 90, 899 (1953), hereafter referred to as WMF.
3. D. J. Knecht, S. Messelt, E. D. Berners, and L. C. Northcliffe, Phys. Rev. 114, 550 (1959); D. J. Knecht, P. F. Dahl, and S. Messelt, Phys. Rev. 148, 1031 (1966), hereafter referred to as KMBND.
4. J. E. Brolley, J. D. Seagrave, and J. D. Berry, Bull. Am. Phys. Soc. 8, 604 (1964).
5. H. P. Noyes, Phys. Rev. Letters 12, 171 (1964).
6. G. Breit, as quoted by D. Amati in Comptes Rendus du Congrès International de Physique Nucléaire (Centre National de la Recherche Scientifique, Paris, 1964), Vol. I, p. 60.
7. M. L. Gursky and L. Heller, Phys. Rev. 136, B1693 (1964).
8. R. J. Slobodrian, Nuovo Cimento 40B, 443 (1965).
9. An inversion of curvature is induced by the point at 3.037 MeV; see Refs. 8 and 11.
10. L. L. Foldy and E. Eriksen, Phys. Rev. 98, 775 (1955); M. deWit and L. Durand, Phys. Rev. 111, 1597 (1958).
11. R. J. Slobodrian, Nucl. Phys. 85, 33 (1966).
12. L. H. Johnston and D. E. Young, Phys. Rev. 116, 989 (1959), analyzed by M. H. MacGregor, Phys. Rev. 113, 1559 (1959). See also B. Cork and W. Hartsough, Phys. Rev. 94, 1300 (1954).
13. V. V. Babikov, Sov. J. Nucl. Phys. 1, 567 (1965); J. Nucl. Phys. (USSR) 1, 793 (1965).
14. L. Hulthén and M. Sugawara, in Encyclopedia of Physics, Vol. 39, ed. by S. Flügge (Springer-Verlag, Berlin, 1957) and references therein.
15. H. Bichsel, Phys. Rev. 112, 1089 (1958); H. Bichsel and E. A. Uehling, Phys. Rev. 119, 1670 (1960).
16. D. J. Knecht, Least-Squares Method for the Analysis of Proton-Proton Scattering Data, Technical Documentary Report No. WL TDR-64-78 (unpublished). One of the authors of this paper (RJS) is indebted to Dr. Knecht for sending a preprint of the second paper of Ref. 3 prior to publication, and a copy of the above-mentioned report.
17. R. J. Slobodrian, Phys. Rev. 145, 766 (1966).

Table B.4-I. Values of the S, P, and D phase shifts, resulting from the analysis of the experimental data.

E_{lab} (MeV)	Phase shifts (degrees)				
	$^1S_0$	$^3P_0$	$^3P_1$	$^3P_2$	$^1D_2$
6.141	56.55	1.53	-1.85	-0.50	-0.56
8.097	57.27	2.39	-1.81	-0.13	-0.17
9.918	56.39	3.14	-2.13	-0.02	-0.12

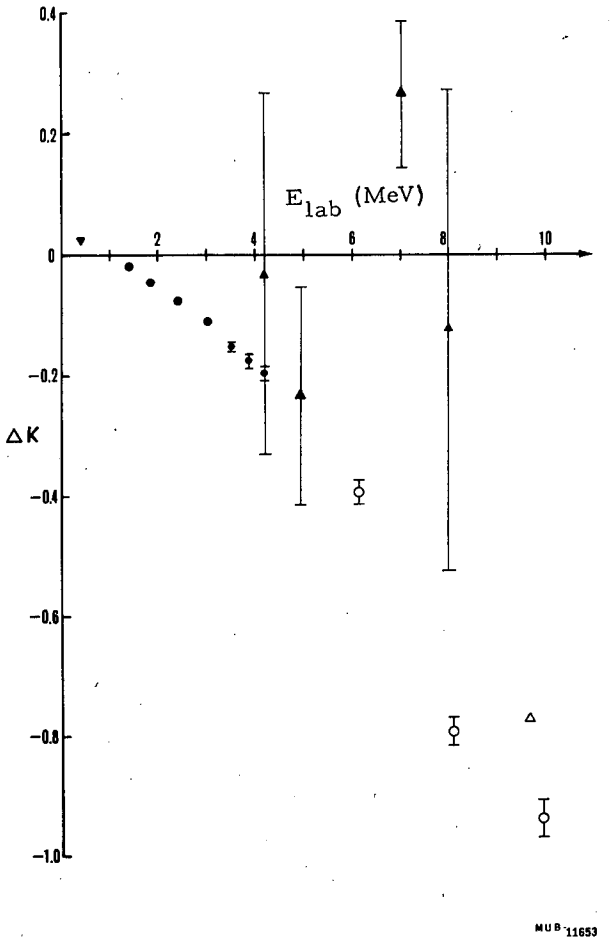

Fig. B.4-1. Plot of $\Delta K = K_{exp} - (A_0+A_1E)$ as a function of laboratory-system energy. The solid dots are the Wisconsin data (Refs. 2, 3). The open triangle is the Minnesota datum (Ref. 12). The solid triangles are the OC data contained in Ref. 1. The inverted solid triangle is the interference minimum datus (Ref. 4). The open circles correspond to the work reported here.

5. DETERMINATION OF THE NEUTRON-NEUTRON SCATTERING LENGTH FROM THE REACTION $T(d, {}^3He)2n$†

E. Baumgartner,* H. E. Conzett, E. Shield, and R. J. Slobodrian

Recent papers[1] have reemphasized the need for an accurate determination of the neutron-neutron $^1S_0$ scattering length a_n, since comparison with the pp and np scattering lengths, a_p and $^1a_{np}$, provides a test of charge symmetry and charge independence in the nucleon-nucleon interaction.

Several determinations of a_n have recently been reported.[2-5] The reactions studied experimentally fall into two categories: (a) the reaction $\pi^-d \rightarrow 2n\gamma$, with only two strongly interacting particles in the final state, and (b) the reactions D(n, p)2n and T(n, d)2n, which have three particles that may interact strongly in the final state. The most recent investigation[4] of the π^-+d reaction has resulted in the preliminary value $a_n = -16.4 \pm 1.3$ F, where the sign was assumed and the error introduced by the theoretical uncertainties[6] was not included in the quoted probable error. In contrast, analyses of the data from the D(n, p)2n reactions at 14 MeV have given the values[2, 3]

$$a_n = -21 \pm 2F \qquad \text{and} \qquad a_n = -23.6^{+2.0}_{-1.6}\ F,$$

which are consistent within themselves but which do not agree with the π^-+d result. Finally, the T(n, d)2n reaction has provided the value[5] $a_n = -18 \pm 3$ F. Neither the D(n, p)2n nor the T(n, d)2n

spectra could be interpreted in terms of the final-state neutron-neutron interaction alone.[7-9] The discrepancies among the values obtained for a_n clearly indicate the need for a test of the theory used to determine a_n from experiments other than that of neutron-neutron scattering.

We report here a determination of a_n from analysis of ^{3}He spectra from the T(d, ^{3}He)2n reaction. Also, triton spectra were obtained from the mirror reaction ^{3}He(d, T)2p. Analysis of these spectra for a determination of a_p, which is well established[10] ($a_p = -7.719 \pm 0.008$ F) from low-energy proton-proton scattering data, provides a direct test of the theory used to deduce a_n.

The ^{3}He(d, T)2p reaction has been investigated by several groups,[11-16] and it has been shown that there is a good semiquantitative agreement between the final-state-interaction calculations and the measured triton spectra.[12,15] The T(d, ^{3}He)2n reaction was first studied several years ago.[17]

The experiment presented here was carried out at the Berkeley 88-inch variable-energy cyclotron. The T(d, ^{3}He)2n reaction was studied at deuteron energies (E_d) of 32.5 and 40.2 MeV. The ^{3}He spectra were obtained with a resolution of 240 keV at several laboratory-system angles between 6 and 25 deg. The ^{3}He(d, t)2p was studied at $E_d = 29.8$ MeV (to match the final-state c.m. energy of the previous reaction at 32.5 MeV) with a resolution of 140 keV. The experimental techniques were essentially the same as described in an earlier paper.[12]

Figure B. 5-1(a) contains the triton spectrum measured at a lab angle of 8 deg, and Fig. B. 5-1(b) exhibits the ^{3}He spectrum taken at 6 deg. The fitted curves were calculated from the Watson-Migdal theory. At these angles, no effects of p-T or n-^{3}He final-state interactions were seen. It has been established that both reactions proceed through a direct reaction mechanism at small angles,[11,13,14,17] consistent with an $\ell = 0$ nucleon transfer. The peripheral nature of the reaction then implies a small overlap of the outgoing T or ^{3}He wave function with the wave function of the nucleon pair, and thus a suitable description should be provided by a dominant nucleon-nucleon final-state interaction.

In the studied rearrangement collisions the differential cross section can be expressed as

$$\frac{d^2\sigma}{dEd\Omega} = \frac{2\pi}{\hbar}\frac{1}{v_d}|T_{if}|^2\rho(E), \tag{1}$$

where T_{if} is the transition matrix element and $\rho(E)$ is the phase-space factor. The general form of T_{if} is $T_{if} = \int\psi^\dagger_f V_I \psi_i \, d\tau$, where V_I is the interaction causing the rearrangement. For the T(d, ^{3}He)2n reaction at small angles we can write[7] $\psi_f = \Psi_{^3He}\phi_R f(r)(e^{i\delta}\sin\delta)/k$, and therefore

$$T_{if} = \frac{e^{-i\delta}\sin\delta}{k}\int[f(r)\,\Psi_{^3He}\,\phi_R]^\dagger V_I\,\psi_i\,d\tau = g(\theta)\frac{e^{-i\delta}\sin\delta}{k}. \tag{2}$$

The term $(e^{-i\delta}\sin\delta)/k$ comes in simply through the S-wave function of the neutron pair in the final state, δ is the singlet S-wave phase shift, $\hbar k$ is the relative nucleon-nucleon momentum, $\Psi_{^3He}$ is the internal wave function of ^{3}He, and ϕ_R describes the relative motion between the ^{3}He nucleus and the neutron pair. The function $g(\theta)$ depends on the reaction mechanism, θ being the c.m. angle of the observed particle (i.e., ^{3}He).

For the T(d, ^{3}He)2n reaction we have used

$$|T_{if}|^2 = |g(\theta)|^2 \; 1/[E_{2n} + \frac{\hbar^2}{m_n}(-\frac{1}{a_n} + \gamma_n E_{2n})^2], \tag{3}$$

and for the ^{3}He(d, T)2p reaction[8]

$$|T_{if}|^2 = |g(\theta)|^2 \; C(\eta)/\{C^2(\eta)\,E_{2p} + \frac{\hbar^2}{m_p}[-\frac{1}{a_p} - \frac{h(\eta)}{R} + \gamma_p E_{2p}]^2\}, \tag{4}$$

where $C(\eta) = 2\pi\eta/e^{2\pi\eta - 1}$, a_p is the scattering length, $\eta = e^2/\hbar v$, $h(\eta) = \mathrm{Re}[\Gamma'(-i\eta)/\Gamma(-i\eta)] - \ln\eta$, $R = \hbar^2/m_p e^2$, $\gamma_n = 3.19\times10^{11}$ MeV^{-1} cm^{-1} corresponding to an effective range $r_e = 2.65$ F, $\gamma_p = 3.40\times10^{11}$ MeV^{-1} cm^{-1}, and E_{2n} (E_{2p}) is the relative nucleon-nucleon energy. In both cases $\rho(E) = CE^{1/2}(E_{max} - E)^{1/2}$, where E is the c.m. energy of the

observed particle with a maximum value E_{max}.

Using expression (3) and (4) converted to the laboratory system with the Jacobian transformation, we have obtained fits for the spectra of both reactions. Experimental values for $|g(\theta)|^2$ were used and the instrumental resolution was folded in. The section of the spectrum of the ^{3}He(d, T)2p reaction shown in Fig. B. 5-1(a) contains 21 798 events. It is roughly equivalent to the section of the T(d, ^{3}He)2n spectrum shown in Fig. B. 5-1(b) (E_{2n} = 0 to 1.57 MeV), which was used to extract a_n. From the ^{3}He(d, T)2p reaction we obtained, for 11 268 events, the value $a_p = -7.69^{+0.61}_{-0.67}$ F, and for 21 798 events, $a_p = -7.41^{+0.39}_{-0.49}$ F, using a minimum χ^2 criterion. The errors are the probable errors determined from a normal χ^2 distribution.

For the T(d, ^{3}He)2n reaction at E_d = 32.5 MeV the best fit for 17 782 events yields $a_n = -16.1 \pm 1.0$ F. Also, the value of a_n is stable to within 0.2 F irrespective of the section of the spectrum (up to E_{2n} = 1.57 MeV) employed for the fit. Even though we estimate from the comparicon between our a_p result and its established value that 0.6 F is the upper limit of error due to theoretical uncertainties, we consider this stability of a_n to be a good indication that this error is in fact smaller. A fit with a positive scattering length yielded $a_n = 18.4 \pm 1.1$ F.

We have made a determination of the sign of a_n, assuming that in both reactions $|g(\theta)|^2$ in expressions (3) and (4) are the same to within a few percent. Then the ^{3}He(d, T)2p reaction can be used to determine $|g(\theta)|^2$, which in turn can be used to predict the T(d, ^{3}He)2n absolute yield for both signs of a_n. Fig. B. 5-2 contains the pertinent plots, and it is seen that the comparison with the experimental spectrum is consistent with the negative sign. The spectrum calculated with the positive scattering length does not include the contribution[3,8] from the resulting bound state. This contribution would increase the discrepancy between the calculated and experimental spectra. In fact, a bound-state contribution given by $(d\sigma/d\Omega)_{bound} \approx 0.4 \int (d^2\sigma/d\Omega dE)dE$ would make it impossible to fit the shape of the measured spectrum. This independent evidence for negative a_n would provide support for the assumption of near equivalence of $|g(\theta)|^2$ for the mirror reactions.

Our determination of $a_n = -16.1 \pm 1.0$ F compares well with the π^-d result and with the value -16.4 to -16.9 F predicted by Heller, Signell, and Yoder[1] from a_p on the basis of a charge-symmetric nucleon-nucleon interaction.

We wish to thank J. Meneghetti, J. Downen, D. Landis, and R. Lothrop for their considerable assistance with the experimental equipment.

Footnotes and References

† Shortened version of paper published in Phys. Rev. Letters 16, 105 (1966).

* Present address: University of Basel, Switzerland.

1. Michael J. Moravcsik, Phys. Rev. 136, B624 (1964); L. Heller, P. Signell, and N. R. Yoder, Phys. Rev. Letters 13, 577 (1964).
2. M. Cerineo, K. Ilakovac, I. Šlaus, P. Tomaš, and V. Valković, Phys. Rev. 133, B948 (1964).
3. V. K. Voitovetskii, I. L. Korsunskii, and Y. F. Pazhin, Phys. Letters 10, 109 (1964); V. K. Voitovetski, I. L. Korsunskii, and Yu. F. Pazhin, Nucl. Phys. 64, 513 (1965).
4. R. P. Haddock, R. M. Salter, Jr., M. Zeller, J. B. Czirr, and D. R. Nygren, Phys. Rev. Letters 14, 318 (1965), and references therein.
5. V. Ajdačić, M. Cerineo, B. Lalović, G. Paić, I. Šlaus, and P. Tomaš, Phys. Rev. Letters 14, 442 (1965).
6. Myron Bander, Phys. Rev. 134, B1052 (1964). His estimate of ≈1 F is considered to be somewhat optimistic by Moravcsik, Ref. 1.
7. Kenneth M. Watson, Phys. Rev. 88, 1163 (1952).
8. A. B. Migdal, Zh. Eksperim. i Teor. Fiz. 28, 3 (1955) [translation: Soviet Phys. JETP 1, 2 (1955)].
9. R. J. N. Phillips, Nucl. Phys. 31, 643 (1962) and 53, 650 (1964).
10. R. J. Slobodrian, Nuovo Cimento 40, 443 (1965). The quoted value is obtained from very accurate phase shifts at five low energies, excluding the vacuum polarization correction.
11. O. M. Bilaniuk and R. J. Slobodrian, Phys. Letters 7, 77 (1963).
12. H. E. Conzett, E. Shield, R. J. Slobodrian, and S. Yamabe, Phys. Rev. Letters 13, 625 (1964).
13. M. Jakobson, J. H. Manley, and R. H. Stokes, Nucl. Phys. 70, 97 (1965).
14. E. M. Henley, F. C. Richards, and D. U. L. Yu, Phys. Letters 15, 331 (1965).
15. T. A. Tombrello and A. D. Bacher, Phys. Letters 17, 37 (1965).

16. R. W. Zurmühle, Nucl. Phys. 72, 225 (1965) reports an apparent discrepancy with Refs. 11 and 12 in an experiment detecting the two protons in coincidence. His published spectrum corresponds to $\langle\theta_{c.m.}\rangle \cong 38°$ for low relative momenta of the pp system, whereas the relevant spectra reported here and in Ref. 12 correspond to $\theta_{c.m.} \approx 12$ deg and $\theta_{c.m.} \approx 16$ deg, and therefore a marked difference is to be expected (see Refs. 13 and 14).
17. J. E. Brolley, Jr., W. S. Hall, L. Rosen, and L. Stewart, Phys. Rev. 109, 1277 (1958). Although these authors did not extract a value for a_n from their data, it is interesting to note that fits to their histograms at 10 deg lab give 12 F $< -a_n <$ 18 F.

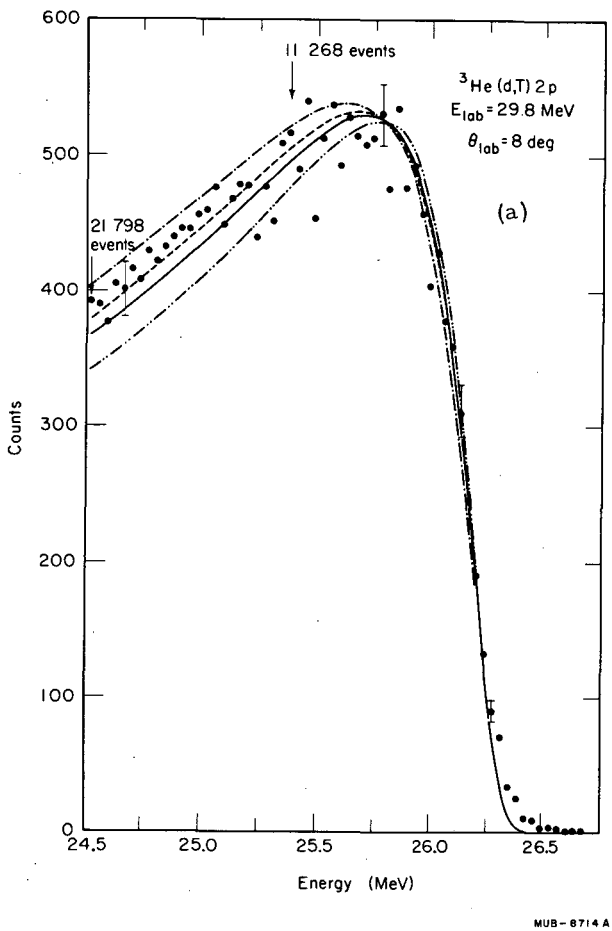

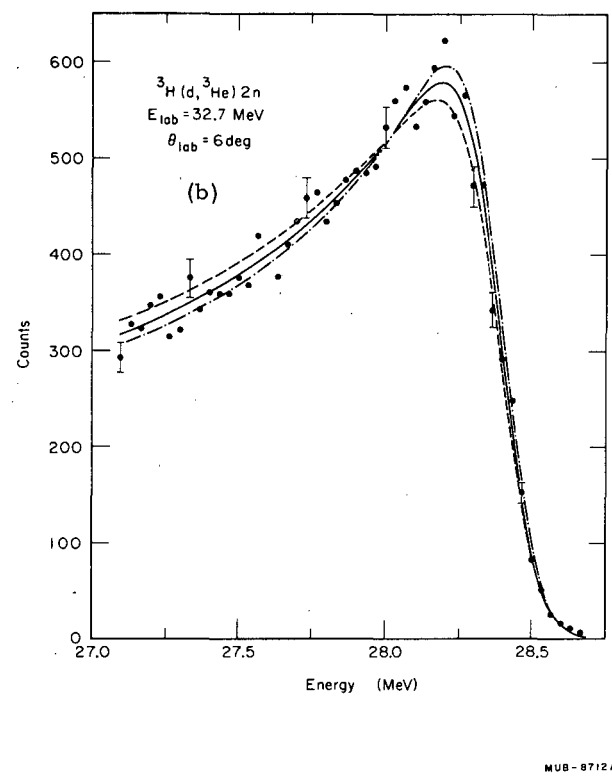

Fig. B. 5-1. (a) Triton spectrum at 8 deg lab of the reaction ^{3}He(d, T)2p at 29.8 MeV, with theoretical fits calculated for 11 268 events and for 21 798 events. The dots are experimental points. The solid line is the best fit for 11 268 events with a_p = -7.69 F. The dashed line is the best fit for 21 798 events with a_p = -7.41 F. The dash-dot line is obtained with a_p = -6.90 F for 11 268 events, and the dash-double-dot line is obtained with a_p = -8.33 F; they indicate the sensitivity of the theoretical curve to variation of a_p. (b) ^{3}He spectrum at 6 deg lab of the reaction T(d, ^{3}He)2n at 32.5 MeV with theoretical fits calculated for 17 782 events. The solid line is the best fit for a_n = -16.1 F. The dashed line is obtained with a_n = -14.0 F, and the dash-dot line corresponds to a_n = -18.0 F.

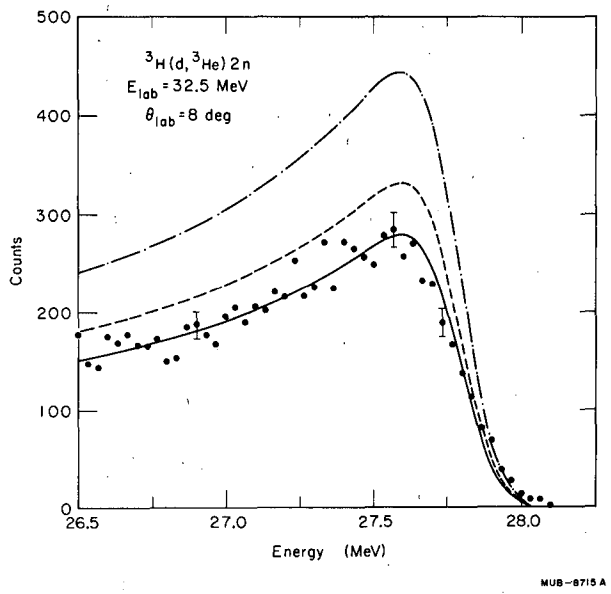

Fig. B. 5-2. ^{3}He spectrum at 8 deg lab of the reaction T(d, ^{3}He)2n at 32.5 MeV together with the theoretical fit for a_n = -16.0 F, shown with solid line. The fit is consistent with the value determined for the 6-deg spectrum. The dashed line is a prediction for a_n = -16.0 F using the $|g(\theta)|^2$ determined from the ^{3}He(d, T)2p reaction, and the dash-dot line for a_n = +18.4 F.

6. PROTON-NEUTRON TWO-PARTICLE EXCITED STATES OF $(d_{5/2})^2_{5+}$ CONFIGURATIONS IN LIGHT NUCLIDES

C. C. Lu and B. G. Harvey

In previous investigation of (α, d) reactions on light nuclides, it was shown that a few levels are populated with cross sections much larger than average.[1,2] These levels were assigned to the configuration $[(d_{5/2})^2_{5+} + J_c]_J$, where the captured neutron-proton pair in the 1 $d_{5/2}$ shell couples to an angular momentum of 5. The pair then couples to the unexcited core J_c to give J, the total angular momentum of the final state. For nonzero values of J_c, multiplets, $2J_c + 1$, of strongly excited levels are observed. In the (^{11}B, ^{9}Be) reactions, similar preference for strong population of these same states has been observed.[3] The reasons for favoring such assignment have been discussed in detail before.[2]

In the work reported here, ^{15}N(α, d)^{17}O, ^{20}Ne(α, d)^{22}Na, ^{14}C(α, d)^{16}N, and ^{13}C(α, d)^{15}N reactions were studied with helium ion energies of 45.4, 44.5, 46.0, and 40.1 MeV, respectively. The Berkeley 88-inch cyclotron was used to produce the incident α particles. A dE/dx-E counter-telescope, which consisted of two lithium-drifted silicon detectors, was used to identify and also to measure the energy of the outgoing particles. The particle-identifying system and the mechanical setup have been previously described.[4,5] The ^{15}N, ^{20}Ne, and ^{13}C targets were gases. The isotopic purity of the ^{15}N was 99.71%.[6] The ^{20}Ne was 98.1% pure.[7] The $^{13}CH_4$ was 93.7% pure.[8] The ^{14}C target was a solid target with 2 mg/cm^2 gold backing.[9]

Table B. 6-I summarizes the properties of the levels believed to be of $(d_{5/2})^2_{5+}$ configuration found in the previous work as well as in this work. The Q values for formation, Q_f, of these states show a systematic variation with mass number, as shown in Fig. B. 6-1. The monotonically decreasing character of $-Q_f$ as a function of A is to be expected if the binding energy of a nucleon in the 1 $d_{5/2}$ shell to the target core increases with A. For A>18, the target already has one or more nucleons in the 1 $d_{5/2}$ shell. The residual interaction of these nucleons with the captured "deuteron" will tend to lower the binding energy of the latter to the target. This is presumably why the $-Q_f$ tends to decrease less rapidly with A for A>18.

The residual interaction energy between the captured proton and neutron of $(d_{5/2})^2_{5+}$ configuration can be calculated for ^{18}F and ^{14}N by assuming that the total binding energy released when a proton, a neutron, and target nucleus form the $(d_{5/2})^2_{5+}$ state is equal to the sum of the

single $d_{5/2}$ proton and neutron binding energies plus the residual interaction energy between the proton and the neutron. The total binding energy released is also equal to the mass difference between (neutron + proton + target nucleus) and the product nucleus in the $(d_{5/2})^2_{5^+}$ state. Using the atomic mass tables[13] to obtain the odd $d_{5/2}$ nucleon binding energies to ^{16}O, one finds the calculated interaction energy of a neutron and a proton in the $(d_{5/2})^2_{5^+}$ configuration for ^{18}F to be 3.89 MeV. If the 3.85-MeV level of ^{13}C and the 3.56-MeV level of ^{13}N are assumed to be the single-particle 1 $d_{5/2}$ levels,[14] the interaction energy between a neutron and a proton in the $(d_{5/2})^2_{5^+}$ configuration in ^{14}N is found to be 4.05 MeV. The above simple calculation cannot be done for ^{16}N because of lack of knowledge about the position of the excited state of ^{15}N with the configuration of pure $[^{14}C_{gs} + d_{5/2}\ \text{proton}]_{5/2}$. For odd-A target nuclides, because the targets have $J_c \neq 0$, the above kind of calculation is not applicable. Calculation involving decoupling of the proton and neutron in $(d_{5/2})^2_{5^+}$ configuration and then recoupling to the spin of the target probably should be used.

The work presented here confirms the earlier conclusion that the states highly populated by the (α, d) reaction in light nuclei belong to the $(d_{5/2})^2_{J=5}$ configuration. The correct multiplicity was again observed in those cases in which the target nucleus had nonzero spin.

References

1. B. G. Harvey, J. Cerny, R. H. Pehl, and E. Rivet, Nucl. Phys. 39, 160 (1962).
2. E. Rivet, R. H. Pehl, J. Cerny, and B. G. Harvey, Phys. Rev. 141, 1021 (1966).
3. J. E. Poth, Boron Induced Transfer Reactions (Ph.D. Thesis), Yale University, 1966.
4. F. S. Goulding, D. A. Landis, J. Cerny, and R. H. Pehl, Nucl. Instr. Methods 31, 1 (1964).
5. B. G. Harvey, E. Rivet, A. Springer, J. R. Meriwether, W. B. Jones, J. H. Elliott, and P. Darriulat, Nucl. Phys. 52, 465 (1964).
6. Obtained from Isomet Corporation.
7. Obtained from Mound Research Corporation.
8. Obtained from Monsanto Research Corporation.
9. The ^{14}C target was kindly loaned to us by Brookhaven National Laboratory.
10. The nuclear reaction Q value is from C. Maples, G. W. Goth, and J. Cerny, UCRL-16964, July 1966.
11. R. W. Detenbeck, J. C. Armstrong, A. S. Figuera, and J. B. Marion, Nucl. Phys. 72, 552 (1965). Previous value for this state in Ref. 2 is 9.00 ± 0.05 MeV.
12. S. Hinds and R. Middleton, Proc. Phys. Soc. 73, 721 (1959).
13. From appendix of Ref. 10.
14. W. W. True, Phys. Rev. 130, 1530 (1963).

Table B.6-I. The $(d_{5/2})^2_{5^+}$ levels identified in the (α, d) reaction.

Final nucleus	Energy level (MeV)	Ref.	Q_f (Ref. 10) (MeV)	J	π	T
^{14}N	8.963 ± 0.002	11	-22.54	5	+	0
^{15}N	11.96 ± 0.03		-19.65	(9/2, 11/2	-)	(0)
	13.03 ± 0.03		-20.72	(11/2, 9/2	-)	(0)
^{16}N	5.75 ± 0.03		-19.13	(5	+)	(0)
^{16}O	14.33 ± 0.10	2	-17.44	(4	+)	0
	14.74 ± 0.10	2	-17.85	(6	+)	0
	16.16 ± 0.10	2	-19.27	(5	+)	0
^{17}O	7.74 ± 0.03		-17.54	(11/2, 9/2	-)	0
	9.14 ± 0.03		-18.94	(9/2, 11/2	-)	0
^{18}F	1.119 ± 0.01	12	-17.44	5	+	0
^{22}Na	1.53 ± 0.03		-14.10	(5	+)	0
^{26}Al	0.0		-12.43	5	+	0

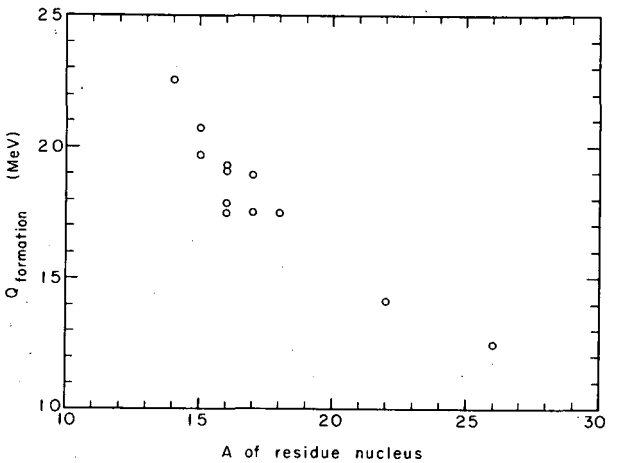

XBL671-142

Fig. B.6-1. Relationship between the mass number A of the residue nucleus and the Q-value of formation of the $(d_{5/2})^2_{5+}$ levels preferentially populated by the (α, d) reactions.

7. THE $^{12}C(^3He, p)^{14}N$ REACTION AT $E(^3He) = 20$ MeV

Nolan F. Mangelson and Bernard G. Harvey

In a paper dealing with two-nucleon transfer, Glendenning[1] has shown that the cross sections of states populated by such reactions are influenced by details of the wave functions for the states. A calculation of cross sections for the two-nucleon process could therefore be used as a test of correctness of assumed wave functions. The (α, d) reaction has been shown to yield spectroscopic information by an empirical analysis of the data.[2-5] The study presented here was undertaken in the hope that the (^{3}He, p) reaction could be exploited as was the (α, d) reaction. In addition, the (^{3}He, p) reaction seemed to be a good case to which to apply a detailed two-nucleon stripping calculation. Carbon was chosen as a target because of the availability of wave functions for the states of ^{14}N and because of an interest in the spectroscopy of ^{14}N.

For E(^{3}He) greater than 12 MeV several studies[6-8] have been made of the reaction $^{12}C(^3He, n)^{14}O$. The states of ^{14}O populated are analog states to T = 1 states of ^{14}N. Priest, et al.[9] and Rivet[10] have studied the $^{12}C(^3He, p)^{14}N$ reaction at 13.9 and 31.5 MeV respectively. Both obtained angular distributions for the ground state and first two excited states of ^{14}N. In addition Rivet obtained an angular distribution for a composite of levels centered at about 9.0 MeV excitation energy.

The mechanical and electronic arrangement for the experiment was essentially the same as has been reported previously.[11] A ^{3}He beam accelerated in the Berkeley 88-inch cyclotron to an energy of 20.1 MeV was used for the experiment. An energy spectrum taken at a laboratory-system angle of 30.4 deg is shown in Fig. B.7-1. Below channel 400 the energy resolution is about 85 keV FWHM (full width at half maximum). For larger channel numbers the FWHM becomes gradually larger. Table B.7-I contains a listing of all the known levels of ^{14}N up to 13 MeV in excitation energy. In the table are also included the known values of JπT, the excitation energy, and total cross section from this experiment, and two major components of the wave function of each level as suggested by calculations or experiment.

Angular distributions for a number of levels are shown in Fig. B.7-2 through Fig. B.7-6. The levels arising from a given pure or dominant angular momentum (L) transfer are plotted together in one figure. The L = 0 transitions (Fig. B.7-2) are characterized by a sharp rise in cross section at small angles and a pronounced first maximum. L = 1 transitions (Fig. B.7-3) are characterized by a gradual rise in cross section with decreasing angle, starting at about 100 deg and continuing to angles at least as small as 12 deg. There is also present the suggestion of a broad maximum at about 120 to 130 deg. L = 2 transitions (Fig. B.7-4) are characterized by a maximum in the region of 20 deg. There seem to be two types of L = 2 transitions. The ground-state and

7.029-MeV states [both $(p)^2$ states] show a very broad first maximum and a backward angle cross section which rises higher than the forward angle cross section. Other L = 2 transitions have a narrower first maximum and a steeper, less structured angular distribution in the forward direction with no back angle rise. L = 3 transitions (Fig. B.7-5) are characterized by their nearly flat angular distributions. The 8.96-MeV level (Fig. B.7-6) is a composite of levels, as indicated in Table B.7-I.

The 9.388-MeV level (Fig. B.7-3) has been assigned 2^-, 3^- by Latorre et al.[17] Either spin assignment allows a transfer of L = 3. Only an assignment of 2^- allows L = 1 transfer. The 9.388-MeV angular distribution in Fig. B.7-3 clearly indicates a strong contribution for L = 1 transfer. Therefore the 9.388-MeV level can be assigned $J = 2^-$. Negative parity states in this region are expected to arise from $(p_{3/2})^{-1}(p_{1/2})^2(s,d)$ type configurations.[16,19] An examination of the coupling coefficients for a jj to LS transformation show that only $s_{1/2}$ or $d_{5/2}$ major components are consistent with the L = 1 transfer observed. The 10.85-MeV level is known to be T = 0,[3,5] but its $J\pi$ are unknown. The angular distribution for this level (Fig. B.7-5) indicates an $L \geq 3$ transfer. This level is strongly populated in the (α, d) reaction,[3,5] which suggests its interpretation in terms of single-particle states. The calculations by True[1,16] of ^{14}N states suggest a maximum L value of 4 for major components of states in this energy region. Tentative J assignments for the 10.85-MeV level are 2^-, $3^{\pm}$, $4^{\pm}$, and 5^-, with L = 3 or 4.

The Glendinning[1] two-nucleon transfer theory was used as a basis for an analysis of this experimental work. The Glendenning DWBA code employs a truncated harmonic oscillator well for the captured particles in the zero-range approximation. Wave functions for ^{14}N as calculated by Cohen and Kurath[15] and True[16] were used in the analysis. The Cohen and Kurath wave functions consider only p shell states (four levels below 9 MeV), and thus account for $(p_{3/2})^{-1}$ character in these states. The True wave functions assume only $p_{1/2}$ configuration in the p shell but also allow $d_{5/2}$, $2s_{1/2}$, $d_{3/2}$, and $f_{7/2}$ configurations as well. Inasmuch as the $(p_{3/2})^{-1}$ character is neglected, wave functions by True containing p-shell character may be expected to give poor results when used in calculations sensitive to the details of wave functions.

A 2^+ T = 0 state of dominant $(s_{1/2}, d_{5/2})$ character calculated by True[16] at an energy of 8.8 MeV was formerly assigned to the 10.096-MeV level of ^{14}N. This level is now thought to be 1^+.[12] Latorre and Armstrong[17] have shown that the 8.979-MeV state is 2^+ and give evidence suggesting a state of s, d character. The calculated 2^+ state under discussion is therefore assigned to the 8.979-MeV state of ^{14}N.

Proton elastic scattering on ^{14}N at proton energies of 20 MeV[23] and 30 MeV[24] was fitted with the optical model. It was found that a reasonable fit could be obtained with the same parameters at both energies except the real well depth, which varied slightly with energy. The parameters are shown in Table B.7-II. The dependence of the real-well depth on energy was assumed to be linear, and the proper depth for the scattered proton was determined from this relationship. Three sets of ^3He optical-model parameters tried are listed in Table B.7-II. Set 1 gave a general fit to ^3He elastic scattering from ^{12}C at 20 MeV; however, the goodness of fit was poor. It was found necessary to use a cutoff radius of 3.2 f in the DWBA calculation in order to fit the $(^3He, p)$ data with set 1. Set 2 fitted the scattering data well. By use of set 2 a reasonable fit to the $(^3He, p)$ data was obtained for the low-lying levels. Most of the higher levels (near 9 MeV) were poorly fitted.

There is theoretical reason to believe that the optical-model potential of complex particles used in DWBA calculations should be approximately a sum of single-nucleon potentials.[25,26] Proton-scattering potentials suggested by Perey[27] and neutron potentials suggested by Bjorklund and Fernbach[28] were assumed to hold at 7-MeV scattering on carbon, and were combined to give parameter set 3. The well depths were summed and the other parameters were averaged.

Two of the possible reaction mechanisms which may be competing with the direct stripping reaction assumed in these calculations are compound nuclear effects and a two-step process whereby the 2^+ level of carbon is first excited by inelastic scattering followed by two-nucleon transfer. A comparison of angular distributions and cross sections from the work of Priest et al.[9] and Rivet[10] with this work shows that the angular distributions at these three energies are nearly identical. The cross sections are decreasing as a function of energy. The work of Manley and Stein[8] for the $(^3He, n)$ reaction indicates that the total reaction cross section for neutrons of energy greater than 12 MeV arises about 10:1 from direct reaction vs compound nuclear. These data therefore indicate a small contribution from compound nuclear effects. There is good evidence to suspect that a two-step process proceeding through the 2^+ level of carbon may contribute to reactions involving carbon.[29,30]

The solid-line curves in Figs. B.7-2 through B.7-6 are the DWBA fits using parameter set 3. The curves are arbitrarily normalized to the data. The solid-line curves for the ground state (Fig. B.7-4) and first excited state (Fig. B.7-2) were calculated by using the wave functions of Cohen and Kurath.[15] The first excited-state transition is pure L = 0. The shape of the angular distribution calculated by using the wave function by True[16] is nearly identical to the fit shown. The ground-state transition is a mixture of L = 0, 2. The calculation using the wave function of True[16] is shown as the broken line in Fig. B.7-4. The rise at small angles indicates that the wave function of True predicts too much L = 0 character for the ground state. The solid-line fit for the composite level at 9.6 MeV is a sum of the calculations for the 8.906-, 8.963-, and 8.979-MeV levels, each properly weighted by its (2J+1) value. The 8.979-MeV level contributed most of the cross section and the 8.906-MeV one contributed least. The broad maximum at about 20 deg seen in L = 2 transfer is also seen in the angular distribution of this level, confirming the dominant L = 2 character suggested by the calculations.

The DWBA fits to the experimental angular distributions are generally good up to about 70 deg c.m. In this region all the general features of the experiment are reproduced by the fits. Beyond 70 deg the fits fall off in cross section faster than the experimental angular distributions.

The correct reaction theory and wave functions should combine to give calculated total cross sections that are in proper proportion to one another. Total cross sections between 10 and 70 deg c.m. were calculated for both experiment and theory. The experimental cross sections were divided by the experimental ground-state cross section. These ratios are listed in Table B.7-III. Similar ratios are also shown for calculations using Cohen and Kurath[15] and True[16] wave functions.

Calculations based upon the wave functions of Cohen and Kurath are in good agreement with experiment. Calculations based upon the wave functions of True do not agree with experiment. Perhaps the most interesting failure is lack of agreement for the 2.311-MeV state. It was suggested above that the True calculations may be in error for states of p character. For this reason calculations based upon True wave functions were also normalized to the 6.44-MeV state, a state of dominant (s, d) character. In this case the relative cross sections of (s, d) states differ by an average of only 9% from the experiment. The p-character states do not agree with experiment.

The results of this work seem to indicate that the (^{3}He, p) reaction can yield spectroscopic information both by an empirical treatment of the data and by a detailed analysis of the reaction.

References

1. N. K. Glendenning, Phys. Rev. 137, B102 (1965).
2. B. G. Harvey, J. Cerny, R. H. Pehl, and E. Rivet, Nucl. Phys. 39, 160 (1962).
3. R. H. Pehl, E. Rivet, J. Cerny, and B. G. Harvey, Phys. Rev. 137, B114 (1965).
4. E. Rivet, R. H. Pehl, J. Cerny, and B. G. Harvey, Phys. Rev. 141, 1021 (1966).
5. C. D. Zafirators, J. S. Lilley, and F. W. Slee, Isospin Conservation in the Reaction ^{12}C(α, d)^{14}N, in preparation.
6. J. H. Manley, Phys. Rev. 130, 1475 (1963).
7. H. C. Bryant, J. G. Berry, E. R. Flynn, and W. T. Leland, Nucl. Phys. 53, 97 (1964).
8. J. H. Manley and W. E. Stein, Phys. Rev. 144, 956 (1966).
9. J. R. Priest, D. J. Tendam, and E. Bleuler, Phys. Rev. 119 1295 (1960).
10. E. J. Rivet, Investigation of Highly Populated Levels of the $(d_{5/2})_5{}^2$ and $(f_{7/2})_7{}^2$ Configurations by the (α, d) Reaction, UCRL-11341, March 1964.
11. N. Mangelson, F. Ajzenberg-Selove, M. Reed, and C. C. Lu , Nucl. Phys., 88, 137 (1966); B-8, UCRL-17299.
12. T. Lauritsen and F. Ajzenberg-Selove, Nuclear Data Sheets, compiled by K. Way et al. (Printing and Publishing Office, National Academy of Sciences–National Research Council, Washington, D. C., 1962) NRC-61-5, 6.
13. E. K. Warburton and W. T. Pinkston, Phys. Rev. 118, 733 (1960).
14. I. Talme and I. Unna, Ann. Rev. Nucl. Sci. 10, 353 (1960).
15. S. Cohen and D. Kurath, Nucl. Phys. 73, 1 (1965).
16. W. W. True, Phys. Rev. 130, 1530 (1963); private communication to N. K. Glendenning.
17. V. A. Latorre and J. C. Armstrong, Phys. Rev. 144, 891 (1966).
18. G. C. Ball and J. Cerny, The ^{14}N(^{3}He, t)^{14}O Reaction and Excited Isospin Triads in Mass 14, UCRL-17038, October 1966.
19. R. W. Detenbeck, J. C. Armstrong, A. S. Figuera, and J. B. Marion, Nucl. Phys. 72, 552 (1965).

20. H. J. Rose, F. Riess, and W. Trost, Nucl. Phys. 52, 481 (1964).
21. G. C. Ball and J. Cerny, Phys. Letters 21, 551 (1966).
22. C. P. Swann, Phys. Rev. 148, 1119 (1966).
23. R. H. Chow and B. T. Wright, Can. J. Phys. 35, 184 (1957); R. H. Chow, Absolute Angular Distributions of 20-MeV Protons Elastically Scattered by Oxygen and Nitrogen (Thesis), University of California-Los Angeles, 1955.
24. C. C. Kim. S. M. Bunch, D. W. Devins, and H. H. Forster, Nucl. Phys. 58, 32 (1964).
25. K. R. Greider and L. R. Dodd, Phys. Rev. 146, 671 (1966).
26. J. R. Rook, Nucl. Phys. 61, 219 (1965).
27. F. G. Perey, Phys. Rev. 131, 745 (1963).
28. F. Bjorklund and S. Fernbach, Phys. Rev. 109, 1295 (1958).
29. M. Chabre, D. L. Hendrie, H. G. Pugh, and C. Detraz, in Chemistry Division Annual Report, UCRL-16580, Jan. 1966, p. 68.
30. D. Kurath, International Conference on Nuclear Physics, Gatlinburg, Tennessee, Sept. 1966.
31. H. J. Rose, W. Trost, and F. Riess, Nucl. Phys., 44, 287 (1963).

Table B.7-I. Levels of nitrogen-14.

Energy (MeV)	JπT	This work (MeV ± keV)		Cross section[a] (mb)	Dominant configurations	References[b]
0.0	1+0	0.0	19	1.73	$0.975(p\ 1/2)^2-0.208(p\ 3/2, p\ 1/2)^{-1}$	15
					$-0.951(p\ 1/2)^2-0.217(d\ 5/2)^2$	16
2.311	0+1	2.31	22	1.27	$0.914(p\ 1/2)^2-0.405(p\ 3/2)^{-2}$	15
					$-0.931(p\ 1/2)^2+0.298(d\ 5/2)^2$	16
3.945	1+0	3.94	32	2.45	$0.932(p\ 3/2, p\ 1/2)^{-1}-0.318(p\ 3/2)^{-2}$	15, 21
4.91	0-0	4.93	33	1.78	$1.00\ (p\ 1/2, s\ 1/2)$	16
5.10	2-0	5.12	36	5.25	$0.960(p\ 1/2, d\ 5/2)-0.220(d\ 3/2, f\ 7/2)$	16
5.69	1-0	5.65	30	2.99	$0.985(p\ 1/2, s\ 1/2)+0.140(p\ 1/2, d\ 3/2)$	16
5.83	3-0	5.84	30	3.32	$0.989(p\ 1/2, d\ 5/2)-0.120(d\ 3/2, f\ 7/2)$	16
6.21	1+0	6.21	20	4.98	$0.834(s\ 1/2)^2+0.365(d\ 3/2, d\ 5/2)+0.348(d\ 5/2)^2$	16
6.44	3+0	6.46	18	14.9	$0.810(s\ 1/2, d\ 5/2)+0.440(d\ 5/2)^2$	16
7.029	2+0	7.01	42	1.70	$1.000(p\ 3/2, p\ 1/2)^{-1}$	15, 21, 22
7.97	2-0	7.95	26	1.85	$-0.980(p\ 1/2, d\ 3/2)-0.160(d\ 5/2, f\ 7/2)$	16
8.060	1-1	8.05	35	1.12	$-0.987(p\ 1/2, s\ 1/2)+0.132(p\ 1/2, d\ 3/2)$	16, 17
8.489	4-0	8.47	30	3.76	$(p\ 3/2)^{-1}(p\ 1/2)^2(d\ 5/2)$	19
8.617	0+1	8.61	34	1.09	$-0.907(s\ 1/2)^2-0.308(d\ 5/2)^2$	16, 17
8.71	0-1				$1.000(p\ 1/2, s\ 1/2)$	17, 18
8.906	3-1				$-0.994(p\ 1/2, d\ 5/2)-0.086(d\ 5/2, f\ 7/2)$	16, 17
8.963	5+0	8.96	19	28.4	$-0.995(d\ 5/2)^2+0.098(f\ 7/2)^2$	3, 16, 19
8.979	2+0				$-0.850(s\ 1/2, d\ 5/2)+0.420(s\ 1/2, d\ 3/2)$	16, 17
9.129	2-0	9.15	18	5.39	$(p\ 3/2)^{-1}(p\ 1/2)^2(s;d)$	19
9.17	2+1				$\approx 0.5\ (s\ 1/2, d\ 5/2), \approx 0.5(p\ 3/2, p\ 1/2)^{-1}$	15, 16, 20, 21
9.388	2-0[c]	9.39	26	4.26	$(p\ 3/2)^{-1}(p\ 1/2)^2(s\ 1/2;d\ 5/2)$	17
9.508	2-1				$-0.9997(p\ 1/2, d\ 5/2)+0.026(p\ 1/2, d\ 3/2)$	16, 17
9.702	1+0	9.70	22	2.25[a]	$0.695(d\ 5/2)^2-0.532(s\ 1/2)^2$	16, 17
10.096	(1+)0	10.08	18	2.40		17
10.213	1+0					17, 31
10.431	2+1	10.43	20	3.28	$\approx 0.5\ (s\ 1/2, d\ 5/2), \approx 0.5(p\ 3/2, p\ 1/2)^{-1}$	15, 16, 17, 20, 21
10.55	1-	10.56	28	0.75		
10.85	d 0	10.81	23	1.57		5
11.06	1+0	11.06	50	1.29[a]		
11.23	3-1	11.27	50			17
11.299	2-0					
11.39	(1+)0	11.39	40			
11.51	3+0	11.51	30			17
11.66		11.66	40			
11.74	1+	11.79	110			
11.80	(2+)					
11.97	(2-)	11.95	30			
12.05						
12.21	3-					
12.29						
12.41	4-0	12.40	18	3.41[a]		5
12.52		12.50	6	2.18		
12.61	3+	12.63	12	1.51		
12.69	3-					
12.80	4+	12.74	22	8.90		
12.83	4-0					5
12.95	(4+)	12.90	10	5.74		
13.05	0					5
13.17	0-0	13.15	40			5
		14.91	60			
		15.8	200			
		17.4	200			

a Limits of integration are as follows:
levels 0.0 to 9.388, 10 - 130 deg c.m.
levels 9.702 to 10.85, 10 - 100 deg c.m.
level 11.06 15 - 95 deg c.m.
levels 12.41 to 12.95 10 - 70 deg c.m.

b References used, other than 12-14

c 2^- and configuration assigned this work

d 2^-, $3^{\pm}$, $4^{\pm}$, 5^- suggested by this work

Table B.7-II. Optical-model parameters.

Particle	Target	Set	V (MeV)	r_1 (F)	a (F)	W (MeV)	W_d (MeV)	r_2 (F)	b (F)	r_c (F)
^{3}He (20 MeV)	^{12}C	1	150.0	1.54	.55		25.4	1.54	.40	1.3
"	"	2	135.0	1.19	.644	7.9		1.92	.904	1.4
"	"	3	146.5	1.25	.65		36.5	1.25	.47	1.25
P (30 MeV)	^{14}N	4	42.0	1.25	.65		6.0	1.25	.50	1.25
P (20 MeV)	"	5	47.0	1.25	.65		6.0	1.25	.50	1.25

Table B.7-III. Comparison of cross section ratios for levels of ^{14}N.

Level (MeV)	JπT	Ratio of total cross section/2J+1) to the Ground State[a]						
		Experiment	Cohen and Kurath		True			
			Ratio	F[b]	Ratio	F[b]	Ratio	F[b]
0.0	1+0	1.0	1.0	0.0	1.00	0.0	0.70	0.30
2.311	0+1	2.40	2.86	0.19	0.98	0.59	0.69	0.71
3.945	1+0	1.47	2.06	0.40				
4.91	0-0	4.21			3.04	0.28	2.14	0.49
5.10	2-0	2.10			1.84	0.12	1.29	0.39
5.69	1-0	1.92			2.63	0.37	1.85	0.03
5.83	3-0	0.71			1.36	0.92	0.96	0.35
6.21[c]	1+0	2.96			3.47	0.17	2.44	0.18
6.44[c]	3+0	4.83			6.87	0.42	4.83	0.0
7.029	2+0	0.52	0.79	0.52				
7.97	2-0	0.57			2.58	4.40	1.81	2.18
8.06	1-1	0.73			2.19	2.00	1.54	1.11
8.617[c]	0+1	2.13			3.41	0.60	2.40	0.13
8.906	3-1 [d]							
8.963[c]	5+0	49.8			66.5	0.34	46.8	0.06
8.979[c]	2+0							
			Average:	0.28	Average[c]:	0.38		0.09
					Average[e]:	1.09		0.69

(a) Cross sections integrated from 10 to 70 deg c.m.
(b) $F = |R_{exp} - R_{th}|/R_{exp}$
(c) States of (s, d) configurations.
(d) This composite level is not corrected for (2J+1).
(e) States of configurations containing p particles.

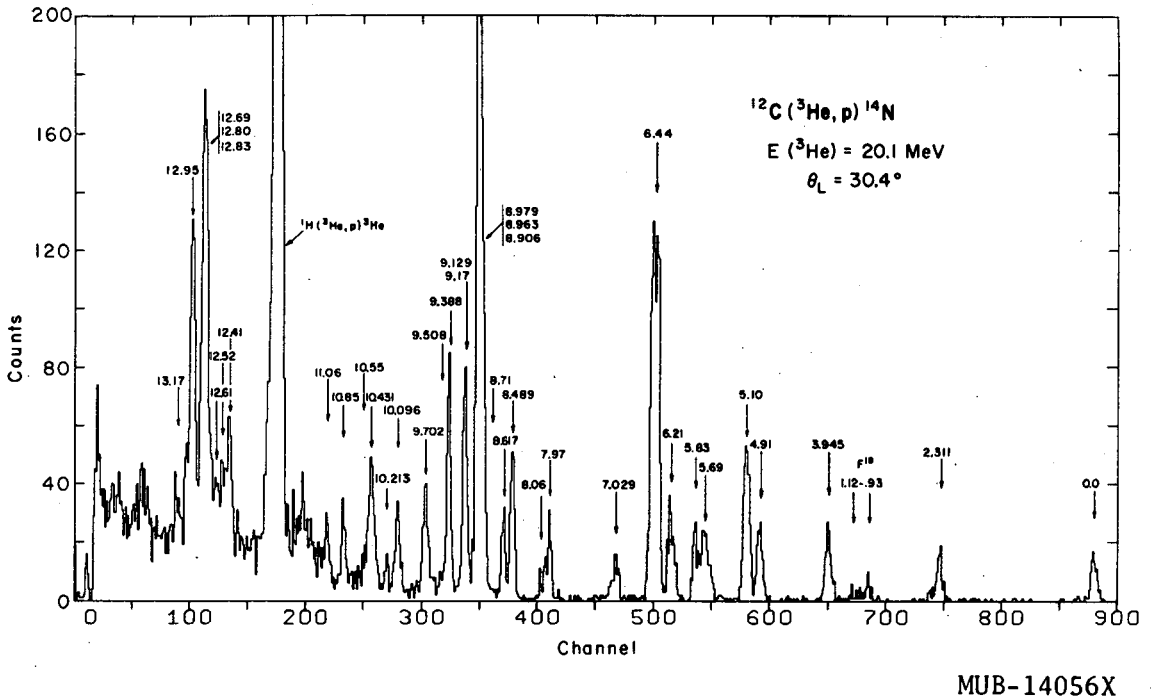

Fig. B. 7-1. Proton energy spectra for the reaction $^{12}C(^3He, p)^{14}$ at $E(^3He)$ = 20.1 MeV taken at θ(lab) = 30.4 deg. Impurity peaks for the reactions $^{16}O(^3He, p)^{18}F$ and $^1H(^3He, p)^3He$ are indicated.

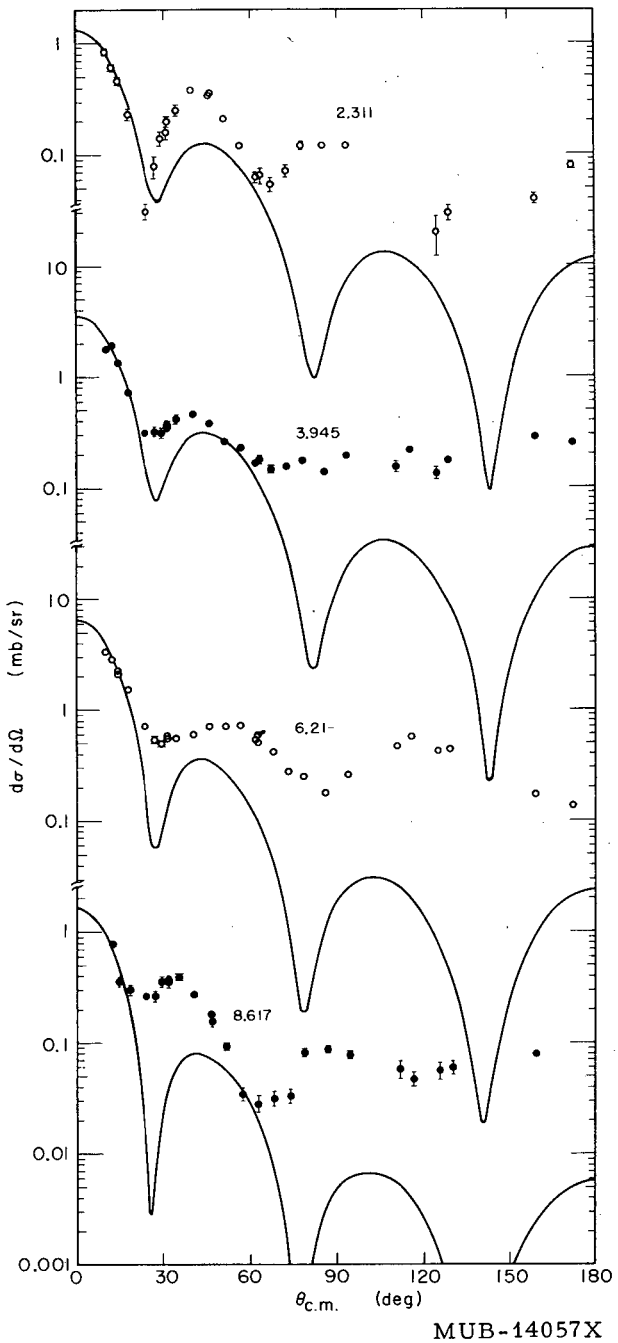

Fig. B.7-2. Angular distributions for pure or dominant L = 0 transitions in the reaction $^{12}C(^{3}He,p)^{14}N$. Solid lines are DWBA fits arbitrarily normalized to the data. Fits to the 2.311- and 3.945-MeV states are based on wave functions by Cohen and Kurath (Ref. 15). Fits to the 6.21- and 8.617-MeV states are based on True wave functions (Ref. 16). Error bars on the experimental points indicate statistical error only. The absence of error bars indicates a statistical error smaller than the symbol.

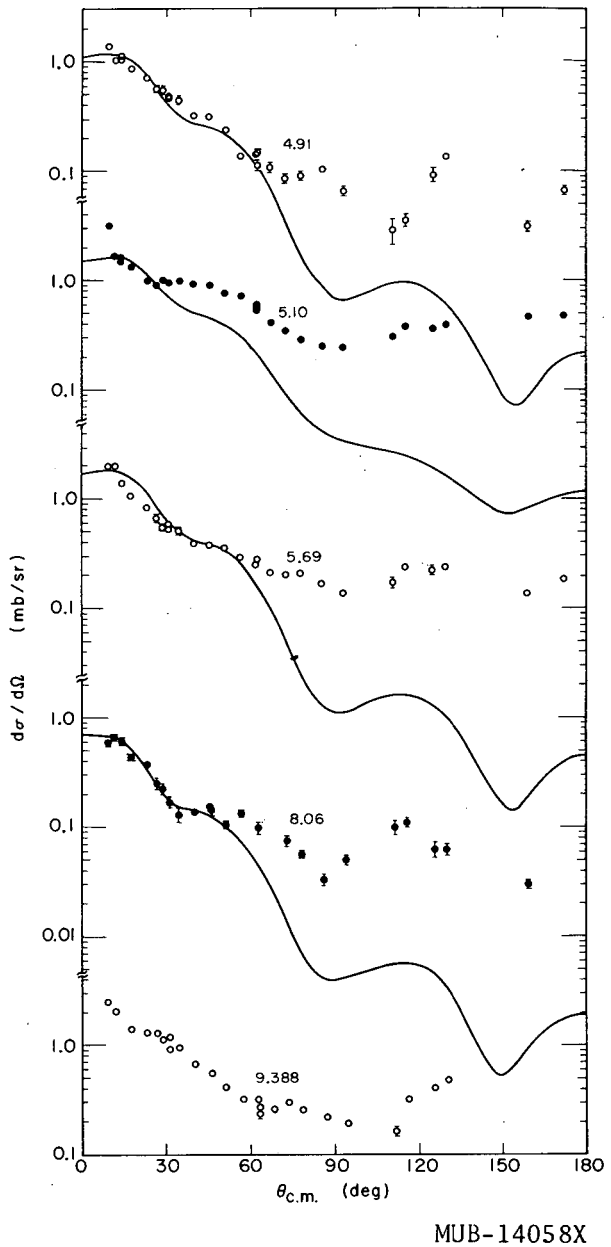

Fig. B.7-3. Angular distributions for pure or dominant L = 1 transitions. All fits are based on the wave functions by True (Ref. 16). See caption of Fig. B.7-2.

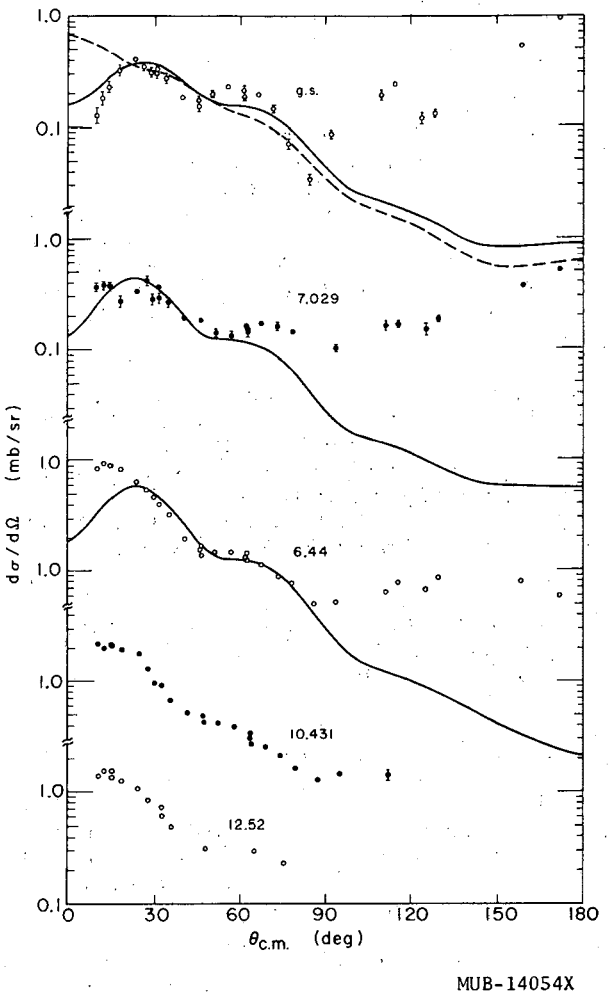

Fig. B. 7-4. Angular distributions for pure or dominant L = 2 transitions. The solid-line fit to the g. s. and the solid line fit to the 7.029-MeV state are based on wave functions by Cohen and Kurath (Ref. 15). The remaining fits are based on the wave functions of True (Ref. 16). See caption of Fig. B. 7-2.

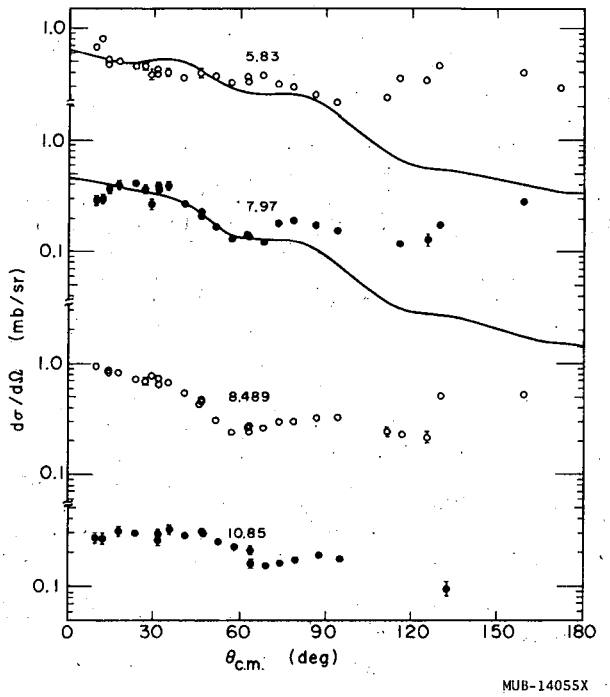

Fig. B. 7-5. Angular distributions for pure or dominant L = 3 transitions. Fits are based on wave functions by True (Ref. 16). See caption of Fig. B. 7-2.

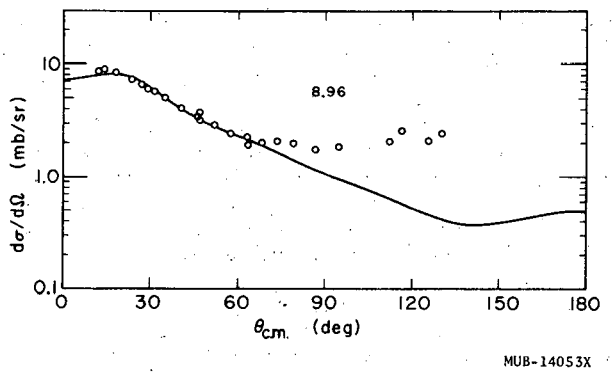

Fig. B. 7-6. Angular distribution as a sum of three levels: 8.906, 8.963, and 8.979 MeV. The fit is a sum of calculations for these same three levels based on wave functions by True (Ref. 16). See caption of Fig. B. 7-2.

8. EXCITED STATES IN ^{6}Be AND ^{10}C†

Nolan F. Mangelson, Fay Ajzenberg-Selove,†† Mary F. Reed, and Chi Chang Lu

Experimental evidence on the level structure of the A = 6 isobaric triad is rather sparse.[1] In ^{6}He only one excited state (E_x = 1.797 ± 0.025 MeV, Γ = 113 ± 20 keV) has been located with any degree of certainty. In ^{6}Li, the corresponding T = 1 state has probably been observed (E_x = 5.36 ± 0.015 MeV, Γ = 320 ± 50 keV), but no other T = 1 states have been found at higher excitations. The experimental results for levels of ^{6}Be[2-6] are not all consistent. Recently studies[7] of the ^{4}He(^{3}He, n)^{6}Be and ^{6}Li(p, n)^{6}Be reactions have shown that below E ≈ 5.7 MeV, there is only one excited state, at E_x = 1.6 ± 0.1 MeV and Γ = 1.1 ± 0.2 MeV. The study of the ^{6}Li(^{3}He, t)^{6}Be reaction reported here permits a redetermination of the energy parameters of this state, and permits an investigation of the level structure of ^{6}Be up to E_x ≈ 13 MeV.

The structure of the A = 10 isobaric triad is much better known[1] than that for A = 6. Below E_x = 12 MeV, eleven T = 1 states have been located in ^{10}Be, and approximately eight such states have been located in the corresponding excitation region in ^{10}B: see Table B.8-I. On the other hand, in ^{10}C--which, until now, has been studied only through the ^{10}B(p, n)^{10}C (Q_m = -4.388) and ^{12}C(p, t)^{10}C (Q_m = -23.319) reactions--only one excited state (E_x = 3.360 ± 0.017 MeV[10, 11]) has been located with any certainty. States at 5.6 ± 0.1, (7.2 ± 0.2) and 10.2 ± 0.2 MeV (Γ ≈ 1.5 MeV) have also been reported.[12] We will report on a preliminary study of the ^{10}B(^{3}He, t)^{10}C reaction (Q_m = -3.624 MeV) and on the location of excited states of ^{10}C.

The incident beam of ^{3}He particles was accelerated in the Berkeley 88-inch cyclotron. The mechanical and electronic systems are described in published works.[13-15] The ^{6}Li and ^{10}B targets were self-supporting foils. Both were separated isotopes: the lithium was 99.3% ^{6}Li and the boron was 96% ^{10}B.

Figure B.8-1 shows a part of the triton spectrum at E(^{3}He) = 39.4 MeV, θ = 40 deg, from the ^{6}Li(^{3}He, t)^{6}Be reaction. Additional spectra have also been obtained at E(^{3}He) = 30.6 MeV (θ = 35 and 55 deg), 39.4 MeV (θ = 20, 50, and 70 deg), and 40.1 MeV (θ = 30 deg). The spectra all show the triton groups corresponding to the (92 ± 6)-keV-wide[1] ground state of ^{6}Be and to the broad first excited state.[7] These groups are observed over a smooth many-particle continuum. In Table B.8-II, our values for the energy parameters of the first excited state of ^{6}Be are compared with recently reported values. The agreement is good among these four measurements.

Figure B.8-2 shows a portion of the triton spectrum at E(^{3}He) = 30.6 MeV, θ = 30 deg from the ^{10}B(^{3}He, t)^{10}C reaction. Peaks due to the reaction[16] ^{11}B(^{3}He, t)^{11}C are marked on the spectrum. We observe clearly the triton groups to the bound ground state and 3.36-MeV first excited state of ^{10}C.[10, 11] We also observe the excitation of unbound states analogous to the 6- to 7-MeV states in ^{10}Be, although we are not able to resolve the analogs of all these six states. This is hardly surprising, since two of the ^{10}Be states are separated[1] by only 1.1 keV. The known information on the analog T = 1 states in the A = 10 isobaric triad are summarized in Table B.8-I. It is not clear whether the structure we observe at E_x = 5.28 and 6.58 MeV is due to two broad levels or to composite groups of levels. There is some suggestion that the level structure centered at E_x = 5.28 MeV is due to three partially resolved states at E_x = 5.03, 5.28, and 5.60 MeV. However, neither the resolution nor the intensity of the two "shoulder" peaks warrants definite assignment of the 5.03- and 5.60-MeV states to ^{10}C.

Some preliminary work with the reaction ^{12}C(p, t)^{10}C at this Laboratory[17] shows spectra similar in character to those reported here. Values of excitation energy in the ^{12}C(p, t)^{10}C reaction are in good agreement with the E_x = 5.3- and 6.6-MeV structure reported here. Consideration of the work of Bachelier et al.,[12] suggests that the 5.6-MeV level reported there may be a composite of the structure at E_x = 5.28 and 6.58 MeV.

Footnotes and References

† Shortened version of Nucl. Phys. 88, 137 (1966).
†† J. Simon Guggenheim Fellow 1965-1966; now at Haverford College, Haverford, Pennsylvania.

1. T. Lauritsen and F. Ajzenberg-Selove, Nucl. Phys. 78, 1 (1966).
2. F. Ajzenberg-Selove, C. F. Osgood, and C. P. Baker, Phys. Rev. 116, 1521 (1959).
3. H. C. Bryant, J. G. Beery, E. R. Flynn, and W. T. Leland, Nucl. Phys. 53, 97 (1964).
4. W. Whaling, Bull. Am. Phys. Soc. 9, 627 (1964); Phys. Rev. 150, 836 (1966).

5. J. L. Honsaker, Ph.D. Thesis, California Institute of Technology, 1965.
6. C. J. Batty, E. Friedman, P. C. Rowe, and J. B. Hunt, Phys. Letters 19, 35 (1965).
7. S. F. Eccles, C. Wong, and J. D. Anderson, Phys. Letters 20, 190 (1966).
8. P. C. Rogers and H. E. Wegner, Phys. Rev. Letters 17, 148 (1966).
9. M. Grelyamov, B. V. Rybakov, and V. A. Sidorov, Translated from IAE-835.
10. L. G. Earwaker, J. G. Jenkin, and E. W. Titterton, Nucl. Phys. 42, 521 (1963).
11. R. E. Segel and P. P. Singh, Bull. Am. Phys. Soc. 10, 426 (1965).
12. D. Bachelier, M. Bernas, I. Brissaud, P. Radvanyi, and M. Roy, Phys. Letters 16, 304 (1965).
13. B. G. Harvey, E. Rivet, A. Springer, J. R. Meriwether, W. B. Jones, J. H. Elliott, and P. Darriulat, Nucl. Phys. 52, 465 (1964).
14. E. S. Goulding, D. A. Landis, J. Cerny, and R. H. Pehl, Nucl. Instr. Methods 31, 1 (1964).
15. R. H. Pehl, E. Rivet, J. Cerny, and B. G. Harvey, Phys. Rev. 137, B114 (1965).
16. T. Lauritsen and F. Ajzenberg-Selove, Nucl. Phys. (to be published) (1967).
17. Donald Fleming and Joseph Cerny, III, (LRL), private communication.

Table B.8-I. Known[1] analog T = 1 states in the A = 10 triad.

^{10}Be			^{10}B			^{10}C	
E_x (MeV ± keV)	J^π	Γ (keV)	E_x (MeV ± keV)	J^π	Γ (keV)	Previous work E_x (MeV ± keV)	This work[a] E_x (MeV ± keV)
0	0^+	b	1.740 ± 2	0^+	c	0^d	0
3.366 ± 3	2^+	c	5.166 ± 4	2^+	0.003	3.360 ± 17[c]	3.37 ± 30
5.958 ± 5	2^+	c				5.6 ± 100	(5.03 ± 60)[e]
5.959 ± 5	1^-	c	7.479 ± 2	(2^-)	72		5.28 ± 60
6.178 ± 9	0^+	c	7.561 ± 1	0^+	3.3		(5.60 ± 60)[e]
6.262 ± 9	2^-	c	7.77 ± 30	2^-	210		6.58 ± 60
7.377 ± 10	3^-	16	8.892 ± 6	3(-)	84	(7.2 ± 200)	
7.548 ± 10	2^+	6	8.896 ± 2	2^+	36		
f			f				

a. The 5- and 6-MeV levels listed below are not uniquely assigned corresponding analog states in ^{10}Be and ^{10}B.
b. $\tau_{1/2} = (2.7 \pm 0.4) \times 10^6$ years.
c. These states are sharp.
d. $\tau_{1/2} = 19.41 \pm 0.04$ sec.
e. Assignment to ^{10}C not certain: see text.
f. Higher excited states have also been observed.

Table B.8-II. Comparison of energy parameters for the first excited state of ^{6}Be.

Reaction	E_x (MeV)	Γ (MeV)	Reference
^{6}Li(^{3}He, t)^{6}Be	1.67 ± 0.08	1.13 ± 0.08	This work
^{6}Li(^{3}He, t)^{6}Be and ^{4}He(^{3}He, n)^{6}Be	1.6 ± 0.1	1.1 ± 0.2	7
^{6}Li(^{3}He, t)^{6}Be	1.63 ± 0.10	1.20 ± 0.1	8
^{4}He(^{3}He, n)^{6}Be	1.73 ± 0.1	1.7 ± 0.3	9

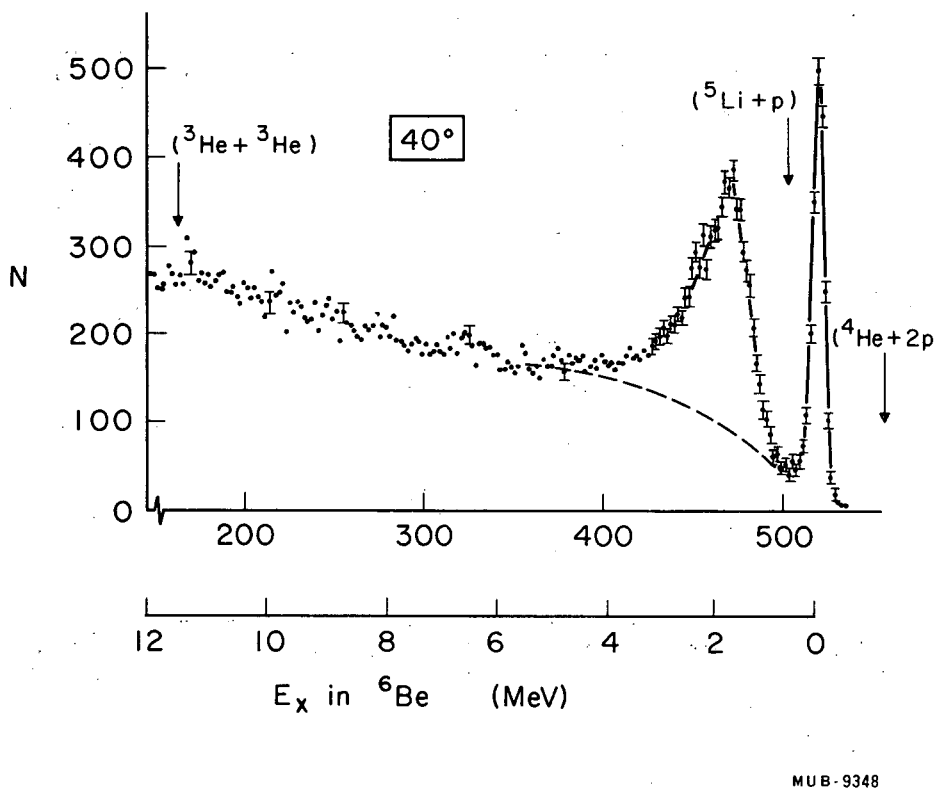

Fig. B.8-1. Spectrum from the ^{6}Li(^{3}He, t)^{6}Be reaction at E(^{3}He) = 39.4 MeV, θ = 40 deg. N represents the average number of counts in a two-channel-wide window, at the corresponding average value of the abscissa channel. The E_x scale gives the excitation energy in ^{6}Be. The binding energies (E_b) for breakup into ^{4}He + 2p, ^{5}Li + p, and 2^{3}He are also shown.

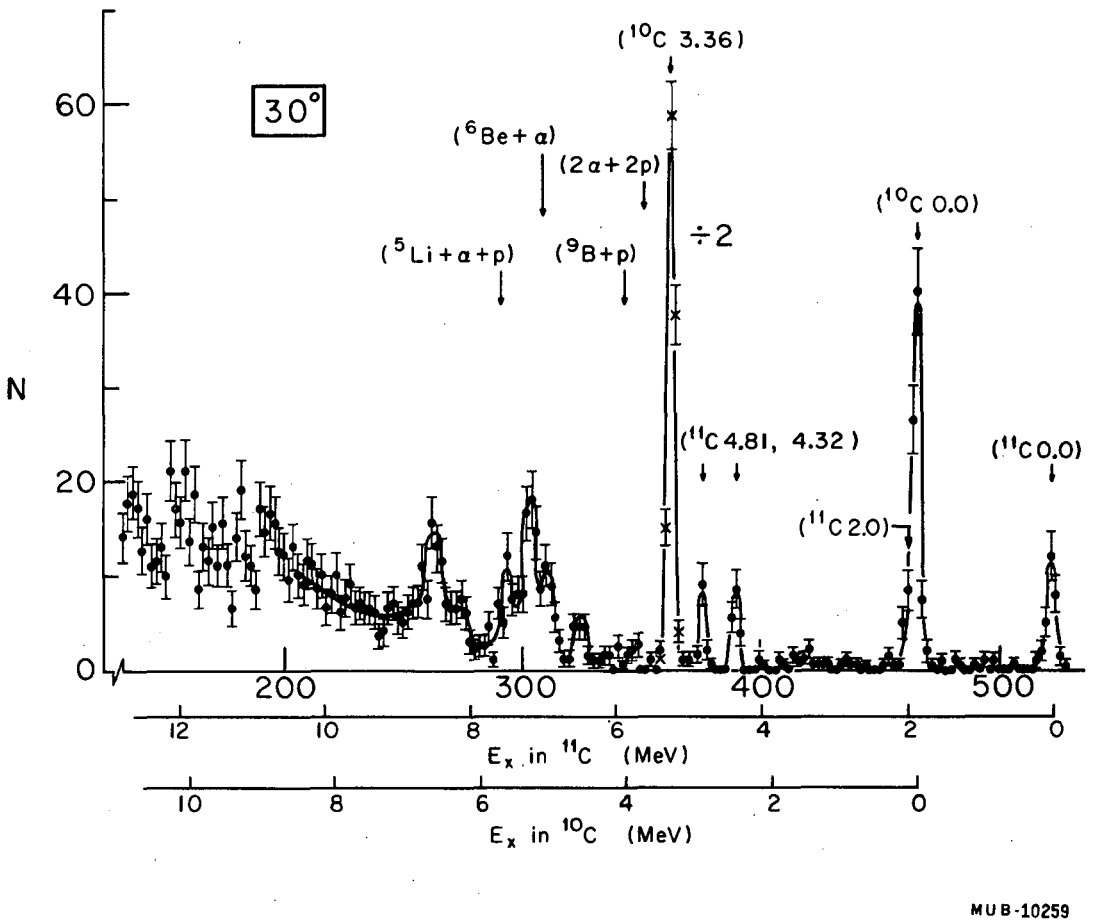

Fig. B.8-2. Spectrum from the $^{10}B(^{3}He,t)^{10}C$ reaction at $E(^{3}He) = 30.6$ MeV, $\theta = 30$ deg. (See also caption of Fig. B.8-1.)

9. THE MASSES AND EXCITED STATES OF ^{24}Al AND ^{28}P†

Nolan F. Mangelson, Mary F. Reed, Chi Chang Lu, and
Fay Ajzenberg-Selove††

Very little is known[1,2] about the proton-rich nuclei $^{24}_{13}Al$ and $^{28}_{15}P$. The positron decay has been observed[1,3,4] to various states in the corresponding $T_z = 0$ nuclei, $^{24}_{12}Mg$ and $^{28}_{14}Si$. Using the Q values of the positron decay[1] and the masses of the ^{24}Mg and ^{28}Si,[5] one finds the atomic mass excesses of ^{24}Al and ^{28}P are 0.09 ± 0.3 MeV and -7.69 ± 0.3 MeV. If the ^{24}Al maximum positron energies[4] are assumed to be due to transitions to the ^{24}Mg states at 4.12 MeV[1] and 8.44 MeV,[5,6] the atomic mass excess of ^{24}Al is -0.01 ± 0.13 MeV. Recently Bromley et al.[7] have used (p, n) threshold reactions to obtain mass excesses of -0.051 ± 0.007 MeV and -7.152 ± 0.008 MeV for ^{24}Al and ^{28}P, respectively.

No energy levels other than the ground state of ^{24}Al and ^{28}P have been reported. By analogy with the mirror nucleus ^{24}Na, the ground state of ^{24}Al should have $J\pi = 4^+$. The corresponding $T = 1$ state in ^{24}Mg has been located[4] at $E_x = 9.512 \pm 0.008$ MeV. The ground state of ^{28}P is possibly a $J\pi = 3^+$ state, by analogy with the 3^+, first $T = 1$ state[1] in ^{28}Si at $E_x = 9.324 \pm 0.011$ MeV,[4] although the close spacing of the next $T = 1$ state ($\Delta E_x = 31$ keV in ^{28}Al, $\Delta E_x \approx 60$ keV in ^{28}Si,

between the $J\pi = 3^+$ and 2^+ states) would permit $J\pi = 2^+$ as an alternative.

In this experiment the $^{24}Mg(^3He, t)^{24}Al$ and $^{28}Si(^3He, t)^{28}P$ reactions[8] were studied at $E(^3He) \approx 40$ MeV by using a beam of ^3He particles from the Berkeley 88-inch spiral-ridge cyclotron. The experimental procedures were identical to those described in another paper.[9] The ^{24}Mg and Si targets were self-supporting foils, 270 ± 3 μg/cm^2 and 160 ± 15 μg/cm^2 thick, respectively. The magnesium target was enriched to 99.96% ^{24}Mg. For the other target natural silicon (92.2% ^{28}Si) was used.

Figure B.9-1 shows part of the triton spectrum for the $^{24}Mg(^3He, t)^{24}Al$ reaction at $E(^3He) = 39.3$ MeV, $\theta_{lab} = 20$ deg. Additional spectra were also obtained at this energy for $\theta_{lab} = 25$, 30, 50, 55, and 60 deg and at $E(^3He) = 40.1$ MeV at $\theta_{lab} = 30$ deg. The full width at half maximum of peaks corresponding to single states is ≈ 85 keV. The Q value for the ground-state reaction was determined to be -13.88 ± 0.06 MeV. From this and the masses of ^{24}Mg, ^3He, and t,[5] the mass excess of ^{24}Al is determined to be -0.07 ± 0.06 MeV. The excitation energies of the observed states of ^{24}Al are shown in Table B.9-I. It is clear that some of our triton groups correspond to unresolved levels. The differential cross section for the formation of the ground state decreases from 67 ± 15 μb/sr at 23.4 deg c.m. to 6 ± 2 μb/sr at 68.4 deg c.m.

Figure B.9-2 shows part of the triton spectrum for the $^{28}Si(^3He, t)^{28}P$ reaction at $E(^3He) = 37.8$ MeV, $\theta_{lab} = 20$ deg. Additional spectra were obtained at this energy for $\theta_{lab} = 35$ deg and for $E(^3He) = 40.1$ MeV, $\theta_{lab} = 30$ and 35 deg. The Q value for the ground-state reaction was determined to be -14.38 ± 0.06 MeV. From this the mass excess of ^{28}P was determined to be -7.12 ± 0.06 MeV. The excitation energies of the observed ^{28}P states are also shown in Table B.9-I. The ground state and first excited state were resolved by fitting the triton peaks with two Gaussian peaks. It is clear that many of these triton groups are due to unresolved states. The differential cross section for the ground state falls from 70 ± 15 μb/sr at 22.8 deg c.m. to 25 ± 6 μb/sr at 39.7 deg c.m.

Footnotes and References

† Shortened version of Phys. Letters 21, 661 (1966).

†† J. Simon Guggenheim Fellow 1965-1966; now at Haverford College, Haverford, Pennsylvania.

1. P. M. Endt and C. Van der Leun, Nucl. Phys. 34, 1 (1962).
2. M. Rickey and R. G. Matlock, Bull. Am. Phys. Soc. 10, 463 (1965).
3. A. Scott and R. Polichar, Bull. Am. Phys. Soc. 8, 85 (1963).
4. M. Rickey, E. Kashy, and D. Knudsen, Bull. Am. Phys. Soc. 10, 550 (1965).
5. J. H. E. Mattauch, W. Thiele, and A. H. Wapstra, Nucl. Phys. 67, 1 (1965).
6. E. L. Haase, H. A. Hill, and D. B. Knudsen, Phys. Letters 4, 338 (1963).
7. D. A. Bromley, J. C. Overly, and P. D. Parker, Phys. Rev. Letters 17, 705 (1966).
8. These reactions have been observed, but no results have been published: see Ref. 2.
9. N. Mangelson, F. Ajzenberg-Selove, M. Reed, and C. C. Lu, Paper B.8.

Table B.9-I. Energy levels of ^{24}Al and ^{28}P.

Levels of ^{24}Al		Levels of ^{28}P	
Group no.	E_x [a]	Group no.	E_x [a]
1	0	1	0
2	0.47 ± 30	2	0.125 ± 30
3	1.12 ± 30	3	1.14 ± 40
4	1.28 ± 50	4	1.31 ± 30
5	1.62 ± 40	5	1.54 ± 40
6	2.38 ± 40	6	2.12 ± 30
7	2.88 ± 30	7	2.65 ± 100
8	3.06 ± 40	8	3.24 ± 30
9	3.35 ± 50	9	3.59 ± 30
10	3.71 ± 50	10	3.84 ± 30
11	3.92 ± 30	11	4.17 ± 70
12	4.34 ± 40	12	4.53 ± 50
13	4.53 ± 40	13	4.94 ± 30
14	4.77 ± 50		
15	5.48 ± 60		
16	5.93 ± 40		
17	6.81 ± 40		
18	7.07 ± 50		
19	(8.25 ± 50) [b]		

a. Energies given in MeV ± keV.
b. Assignment of ^{24}Al not certain.

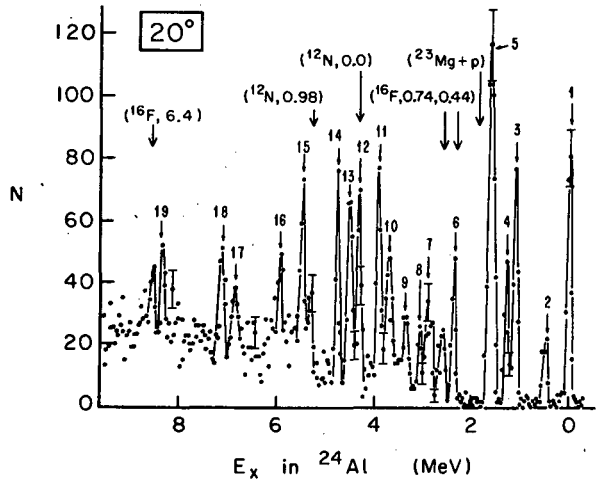

Fig. B.9-1. Spectrum from the $^{24}Mg(^3He, t)^{24}Al$ reaction at $E(^3He)$ = 39.3 MeV and θ_{lab} = 20 deg. N is the number of counts per channel. The E_x scale gives the excitation energy in ^{24}Al. The binding energy (1.88 MeV) for breakup into ^{23}Mg + p is indicated. The locations of possible contaminant groups from the $^{12}C(^3He, t)^{12}N$ and $^{16}O(^3He, t)^{16}F$ reactions are also shown.

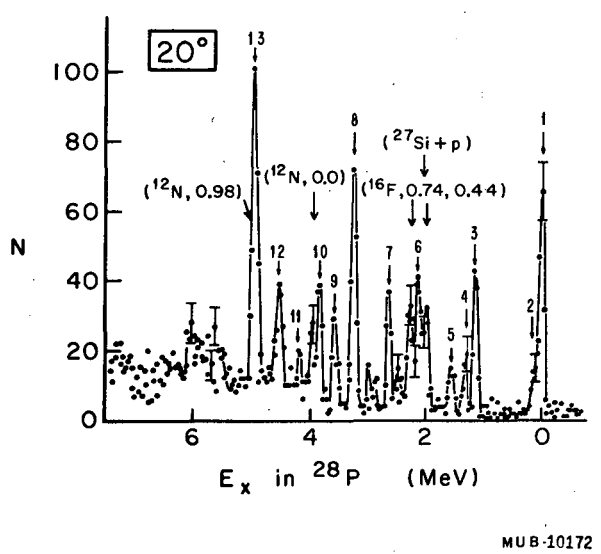

Fig. B.9-2. Spectrum from the $^{28}Si(^3He, t)^{28}P$ reaction at $E(^3He)$ = 37.8 MeV and θ_{lab} = 20 deg. The binding energy (2.03 MeV) for breakup into ^{27}Si + p is shown. (See also legend for Fig. B.9-1.)

10. A STUDY OF MASS 5 AND 7 NUCLEI BY (p, t) AND (p, ^{3}He) REACTIONS ON ^{7}Li AND ^{9}Be†

J. Cerny, C. Détraz,‡ and R. H. Pehl

Simultaneous observation of direct (p, t) and (p, ^{3}He) reactions has been shown[1] to be a very useful tool for locating states with $T = |T_Z(\text{target})| + 1$ in the lighter nuclei. Several further spectroscopic advantages of such comparisons remain to be explored. If one considers these two-nucleon pickup reactions, in first order, on targets with $T_Z \neq 0$ leading to final states with $T = |T_Z(\text{target})|$, then the (p, t) reaction requires S = 0 for the transferred pair whereas the (p, ^{3}He) reaction may proceed by both S = 0 and S = 1 transfer. This restriction on (p, t) transitions as compared to (p, ^{3}He) transitions may cause some (p, t) transitions to be "S-forbidden." Particularly in the lower part of the p shell, where LS coupling of the target and final nuclei is appropriate, one can have transitions in which, though the relevant L transfer is allowed, the configuration of the final state requires a change of S incompatible with the restrictions on S of the transferred pair in the (p, t) reaction. An example would be a $^2P_{3/2} \rightarrow {}^4P_{5/2}$ transition—forbidden in the (p, t) but allowed in the (p, ^{3}He).

We have investigated the (p, t) and (p, ^{3}He) reactions on ^{7}Li and ^{9}Be. Observation of the T = 3/2 states in ^{7}Li-^{7}Be has been previously reported.[2] Transitions to several T = 1/2 final states have been observed, some of which permit us to explore and then exploit spectroscopically the S-forbidden behavior of the (p, t) reaction in these light p-shell nuclei.

The (p, t) and (p, ^{3}He) reactions were induced by a beam of 43.7-MeV protons from the 88-in. cyclotron. Particles were detected and identified[3] by utilizing a counter telescope that consisted of two semiconductor detectors: a 25.5-mg/cm^2 phosphorus-diffused silicon transmission counter backed by a 755-mg/cm^2 lithium-drifted silicon stopping counter.

Typical ^{9}Be(p, t)^{7}Be and ^{9}Be(p, ^{3}He)^{7}Li spectra are presented in Fig. B.10-1. On the basis of their dominant LS coupling, the ground and first four excited states of ^{7}Be-^{7}Li are described as $^2P_{3/2}$, $^2P_{1/2}$, $^2F_{7/2}$, $^2F_{5/2}$, and $^4P_{5/2}$, respectively.[4] Angular distributions were obtained but are not discussed herein.

A striking difference between the (p, t) and (p, ^{3}He) spectra of Fig. B.10-1 is the strong excitation of the 5/2-, 7.48-MeV ^{7}Li level, whereas the mirror 7.19-MeV level of ^{7}Be is not appreciably populated. This absence of the ^{9}Be[$^2P_{3/2}$](p, t) ^{7}Be[7.19 MeV, $^4P_{5/2}$] transition is an example of an S-forbidden reaction; the change of S required by the nuclear wave function is forbidden by the S = 0 requirement on the transferred two-neutron pair in the (p, t) reaction. However, the greater flexibility of the (p, ^{3}He) reaction permits the analogous ^{9}Be[$^2P_{3/2}$](p, ^{3}He) ^{7}Li[7.48 MeV, $^4P_{5/2}$] transition through the additional allowed S = 1 for the transferred neutron-proton pair.

Figures B.10-2 and B.10-3 show, respectively, a typical energy spectrum for the ^{7}Li(p, t)^{5}Li and for the ^{7}Li(p, ^{3}He)^{5}He reactions. At high excitation a marked difference again appears in comparing the (p, t) and (p, ^{3}He) spectra—namely the absence in the ^{5}Li excitation spectrum of the two energy levels clearly apparent in the ^{5}He data. The first of these levels, known to be $3/2^+$ and located at 16.70 MeV in ^{5}He and 16.65 MeV in ^{5}Li, is due to an S-wave interaction in d-t or d-^{3}He scattering. Transitions to this $^4S_{3/2}$ state[5] from the $^2P_{3/2}$ ground state of ^{7}Li require S = 1 for the transferred pair. As already observed in the transitions to the mass-7 final nuclei, such a (p, t) transition is S-forbidden.

The same argument holds for the broad state near 20 MeV. A definite state at 20.0 ± 0.5 MeV in ^{5}Li was recently observed[6] as a D-wave d-^{3}He interaction with a tentative spin assignment of $3/2^+$ or $5/2^+$; the mirror level in ^{5}He has only tentative support.[5] Comparative (p, t) and (p, ^{3}He) data permit us to distinguish between the two possible total spin configurations for this state, ^2D and ^4D. The appearance of a state at 19.9 ± 0.4 MeV in the ^{7}Li(p, ^{3}He)^{5}He data and the absence of transitions to the presumed mirror level at 20 MeV in the ^{7}Li(p, t)^{5}Li data imply that the latter transition is S-forbidden and that the state is $^4D_{3/2}$ or $_{5/2}$.

Footnotes and References

† Condensation of article in Phys. Rev. 152, 950 (1966).

‡ CNRS and NATO fellow, visitor (1964-1965) from Institut de Physique Nucléaire, Orsay, France.

1. J. Cerny, R. H. Pehl, and G. T. Garvey, Phys. Letters 12, 234 (1964).
2. C. Détraz, J. Cerny, and R. H. Pehl, Phys. Rev. Letters 14, 708 (1965).
3. F. S. Goulding, D. A. Landis, J. Cerny, and R. H. Pehl, Nucl. Instr. Methods 31, 1 (1964).
4. D. Kurath, Phys. Rev. 101, 216 (1956); S. Meshkov and C. W. Ufford, Phys. Rev. 101, 734 (1956); V. V. Balashov, At. Energ. (USSR) 9, 48 (1960) [translation: Soviet J. At. Energy 9, 544 (1961)].
5. T. Lauritsen and F. Ajzenberg-Selove, Nucl. Phys. 78, 1 (1966).
6. T. A. Tombrello, A. D. Bacher, and R. J. Spiger, Bull. Am. Phys. Soc. 10, 423 (1965).

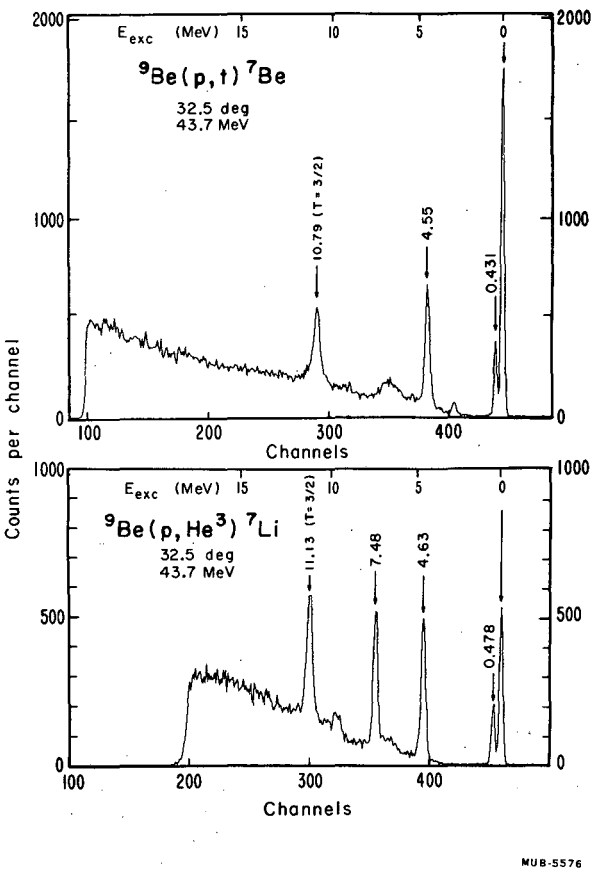

Fig. B.10-1. Energy spectra for the reactions $^9Be(p,t)^7Be$ and $^9Be(p,^3He)^7Li$ at 32.5 deg.

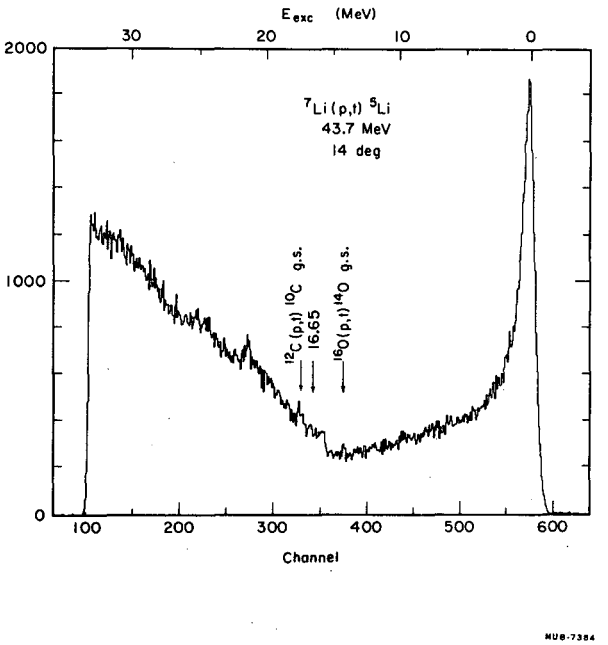

Fig. B.10-2. The energy spectrum of the $^7Li(p,t)^5Li$ reaction at 14 deg.

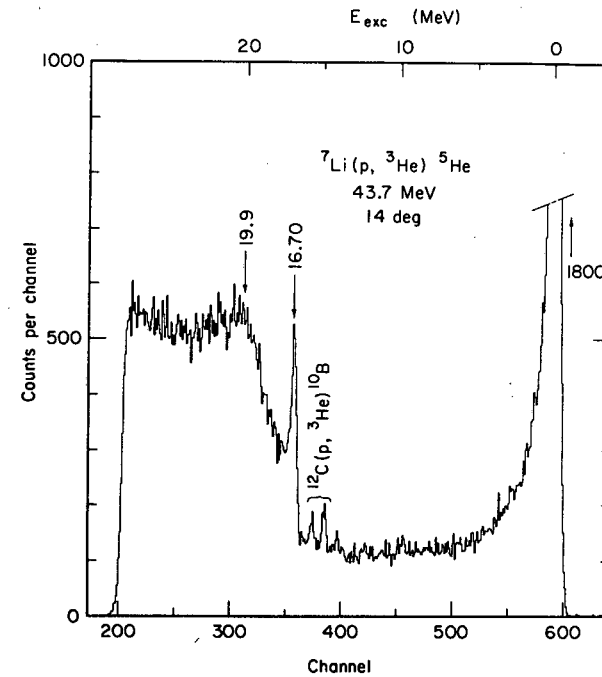

Fig. B. 10-3. The energy spectrum of the ^{7}Li(p, ^{3}He)^{5}He reaction at 14 deg.

11. MASS OF ^{8}He FROM THE FOUR-NEUTRON TRANSFER REACTION ^{26}Mg(α, ^{8}He)^{22}Mg†

J. Cerny, S. W. Cosper, G. W. Butler, R. H. Pehl,
F. S. Goulding, D. A. Landis, and C. Détraz*

The existence and mass of ^{8}He have been determined from the four-neutron transfer reaction ^{26}Mg(α, ^{8}He)^{22}Mg. The accurate mass of ^{8}He may serve as a guide among the various prescriptions[1-3] which predict the many yet unobserved high-T states in the very light nuclei, while the development of a technique for measuring ^{8}He as a reaction product permits an exploration of nuclear masses bracketing the predicted[4] neutron-deficient edge of stability in the light elements (e.g., the masses of ^{12}O and ^{16}Ne—nuclei which are also candidates for double proton decay). While the experiment presented here was in progress, two other definite observations of the existence of ^{8}He were made. Cosper, Cerny, and Gatti[5] observed ≈1100 ^{8}He nuclei as third fragments in ^{252}Cf fission (≈1 in 10^6 fissions) utilizing counter telescope techniques similar to those described below, while Poskanzer, Esterlund, and McPherson,[6] in experiments with the Brookhaven Cosmotron, reported the decay properties and 122-msec half-life of ^{8}He.

It was first necessary to redetermine the masses of the ground and low excited states of ^{22}Mg, since various systematics[7] implied that the reported data[8] were in error. By utilizing the reaction ^{24}Mg(p, t)^{22}Mg, the mass excess of ^{22}Mg was found to be -0.38 ± 0.05 MeV on the ^{12}C scale with excited states at 1.22 ± 0.03 and 3.24 ± 0.05 MeV.[9, 10]

The 88-inch cyclotron provided an analyzed beam of 80-MeV α particles which impinged on a ^{26}Mg target in an evacuated scattering chamber. Preliminary experiments indicated two problems which required an advance in particle-identifier technique. One was the necessity of identifying 32- to 36-MeV ^{8}He particles (depending on the correct mass prediction[1-3]) with a $d\sigma_{g.s.}$ (lab) of ≈50 nb/sr, or about 1 ^{8}He per 10^7 particles traversing a counter telescope. The other was the fact that the chance coincidence of an α particle and a deuteron traversing the telescope within the resolving time of the system can produce an energy loss and hence identification pulse almost identical to that of a ^{8}He particle, thereby introducing a difficult background problem. The major features of the final system[11, 12] are indicated in Fig. B. 11-1.

We wish to present the results of two runs at 14 deg lab of length 52 hours (Run 1) and 60 hours (Run 2) and of alpha-particle energies 78.4 and 80.0 MeV, respectively. Run 2 is considered in more detail, since it employed the pile-up rejector and the on-line computer; otherwise, the runs were essentially identical. The complete particle-identifier spectrum for Run 2 is shown in Fig. B. 11-2 along with the spectrum for the region above ^{8}He from Run 1. The tailing on the ^{6}Li peak during Run 2, which was not present during Run 1 (dashed lines in Fig. B. 11-2), was due to relaxed single-channel-analyzer settings on ΔE2 and ΔE1 which permitted storage of ^{8}Li pulses as a further calibration but failed to reject ^{6}Li ions of marginal behavior. Complete data on particles whose identification pulse appeared in region A-B were stored in the computer and later analyzed in detail. This analysis revealed that no ^{6}Li ions were present in region A-B. Otherwise, this region encompassed the ^{8}He peak as predicted from range-energy systematics and most of two other peaks due to alpha-proton chance coincidences and alpha-triton chance coincidences, which simulate ^{7}He and ^{9}He particles, respectively. [^{7}He has been predicted to be particle unstable from calculations based on the T = 3/2 states in mass seven,[13] and Ref. 5 places an upper limit for its emission in ^{252}Cf fission as <1 per 12 ^{8}He fragments. ^{9}He would not be expected to be stable on general systematics.] The observed alpha-proton and alpha-triton chance coincidences agreed within statistics with those predicted from the appropriate singles rates, and led us to expect 12 ± 4 alpha-dueteron chance coincidences among the 26 events in the ^{8}He identifier peak. No significant grouping of the alpha-proton or alpha-triton energy spectra was observed.

Figure B. 11-3 presents energy spectra from both runs arising from the same identifier region. The energy range over which valid events could have been observed is indicated; no ^{8}He events from the minor target impurities (^{12}C, ^{16}O, ^{24}Mg) were energetically possible. The noticeable reduction of "background" events in Run 2 was due primarily to the pile-up rejector. Further, 8 of the 26 possible ^{8}He events in Run 2 can be excluded, having been shown through analysis of their losses in the ΔE2 and ΔE1 detectors to be alpha-deuteron coincidences and not real ^{8}He nuclei. [Only some of the chance coincidences can be eliminated in this manner; the excluded events, which do not affect our mass arguments, are the shaded ones in Fig. B. 11-3.]

The last problem that must be discussed is the likelihood of obtaining distorted spectra from the presence of correlated alpha-deuteron coincidences from the breakup of any ^{6}Li* ions in the exit channel.[14] Only breakup of ^{6}Li ions excited to the 2.18-MeV level could be observed as correlated coincidences due to the restrictions imposed by kinematics, geometry, and detector thicknesses. Since the population of this level is not known, we assumed as an upper limit[15] that it is of the same order as the average ^{6}Li g. s. continuum cross section; with this assumption, at most three correlated alpha-deuteron coincidences would be present in the data of Run 2.

Figure B. 11-3 clearly indicates two ^{26}Mg(α, ^{8}He)^{22}Mg transitions common to the runs whose spacing is that between the ground and first excited states of ^{22}Mg. Run 1 could not have observed transitions to the second excited level of ^{22}Mg and Run 2 apparently did not; it is of interest that this second level is only weakly populated in the reaction ^{24}Mg(p, t)^{22}Mg at the observed forward angles. The ground-state peaks in both spectra agree in absolute value to 60 keV and determine a mass excess for ^{8}He of 31.65 ± 0.12 MeV on the ^{12}C scale. A mass excess of 32.4 ± 1.5 MeV for ^{8}He was calculated from the decay experiment of Poskanzer, Esterlund, and McPherson.[6] The lightest particle-unstable channel of ^{8}He is ^{6}He + 2n with a mass excess of 33.7 MeV.

Three theoretical predictions of the mass of ^{8}He are of current interest, and that of Goldanskii[1] agrees best with these results. His prediction is based on the assumption that the pairing energy of the last two neutrons in ^{8}He is less than that in ^{6}He (2.86 MeV) and greater than that in ^{9}Li (2.02 MeV); based on the ^{7}He mass calculated in Ref. 13, a mass excess for ^{8}He of 32.0 ± 0.4 MeV would be predicted. The expression of Garvey and Kelson[2] predicts $29.7^{+\approx 1.5}_{-\approx 0.5}$ MeV, while Jänecke's systematics[3] predict 34.2 ± ≈2 MeV.[16]

Footnotes and References

† Condensed from Phys. Rev. Letters 16, 469 (1966).

* Centre National de la Recherche Scientifique and NATO Fellow, visitor from Laboratoire Joliot-Curie de Physique Nucléaire, Orsay, France.

1. V. I. Goldanskii, Zh. Eksperim. i Teor. Fiz. 38, 1637 (1960) [translation: Soviet Phys.-JETP 11, 1179 (1960)].
2. G. T. Garvey and I. Kelson, Phys. Rev. Letters 16, 197 (1966).
3. J. Jänecke, Nucl. Phys. 73, 97 (1965).
4. A. I. Baz, V. I. Goldanskii, and Ya. B. Zeldovich, Usp. Fiz. Nauk 72, 211 (1960) [translation: Soviet Phys.-Usp. 3, 729 (1961); J. Jänecke, Nucl. Phys. 61, 326 (1965).

5. S. W. Cosper, J. Cerny, and R. Gatti, Long-Range Particles of Z = 1 to 4 Emitted During the Spontaneous Fission of ^{252}Cf, Phys. Rev. (in press).
6. A. M. Poskanzer, R. A. Esterlund, and R. McPherson, Phys. Rev. Letters 15, 1030 (1965).
7. We wish to thank Paul C. Rogers for first bringing this to our attention.
8. F. Ajzenberg-Selove, L. Cranberg, and F. S. Dietrich, Phys. Rev. 124, 1548 (1961).
9. We wish to thank Gerald T. Garvey for participating in this measurement.
10. This ^{22}Mg mass compares well with measurements of -0.33 ± 0.03 MeV (private communication, R. W. Kavanagh) and -0.34 ± 0.05 MeV (private communication, W. Whaling and C. Moss).
11. F. S. Goulding, D. A. Landis, J. Cerny, and R. H. Pehl, IEEE Trans. Nucl. Sci. NS-13, 514 (1966).
12. F. S. Goulding, D. A. Landis, J. Cerny, and R. H. Pehl, Nucl. Instr. Methods 31, 1 (1964).
13. C. Détraz, J. Cerny, and R. H. Pehl, Phys. Rev. Letters 14, 708 (1965).
14. No contribution from ^{6}Li g.s. dissociation, as reported by R. W. Ollerhead, C. Chasman, and D. A. Bromley, Phys. Rev. 134, B74 (1964), is possible.
15. The population of the ^{7}Li*(0.478 MeV) level is at most one-third that of the ^{7}Li g.s. in (α, ^{7}Li) reactions induced on light targets at these beam energies.
16. It is of interest to note that Jänecke's prediction of 15.9 ± 2 MeV for $\Delta T_{3/2,1/2}$ in mass seven also does not agree with the experimental value (see Ref. 13) of 10.96 ± 0.22 MeV.

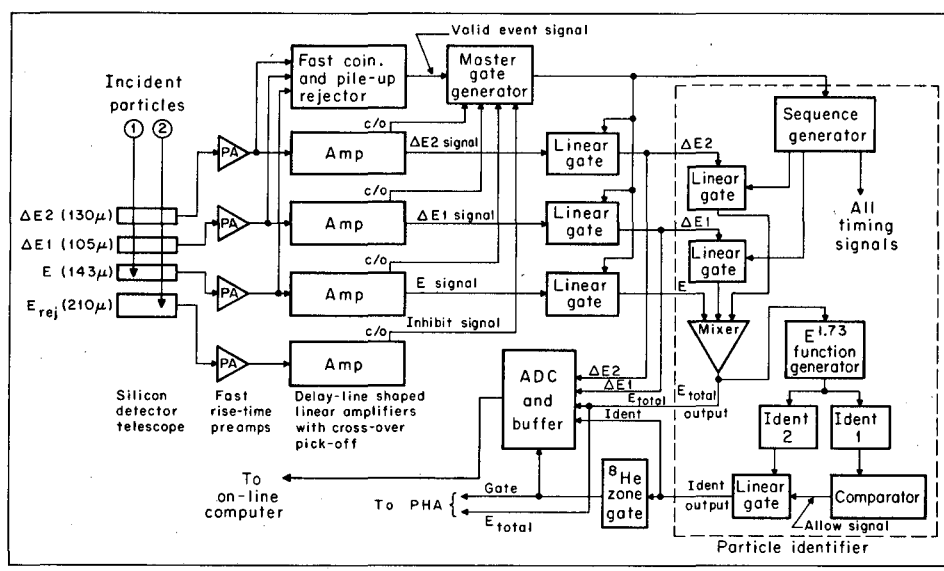

Fig. B. 11-1. An abbreviated block diagram of the electronic equipment.

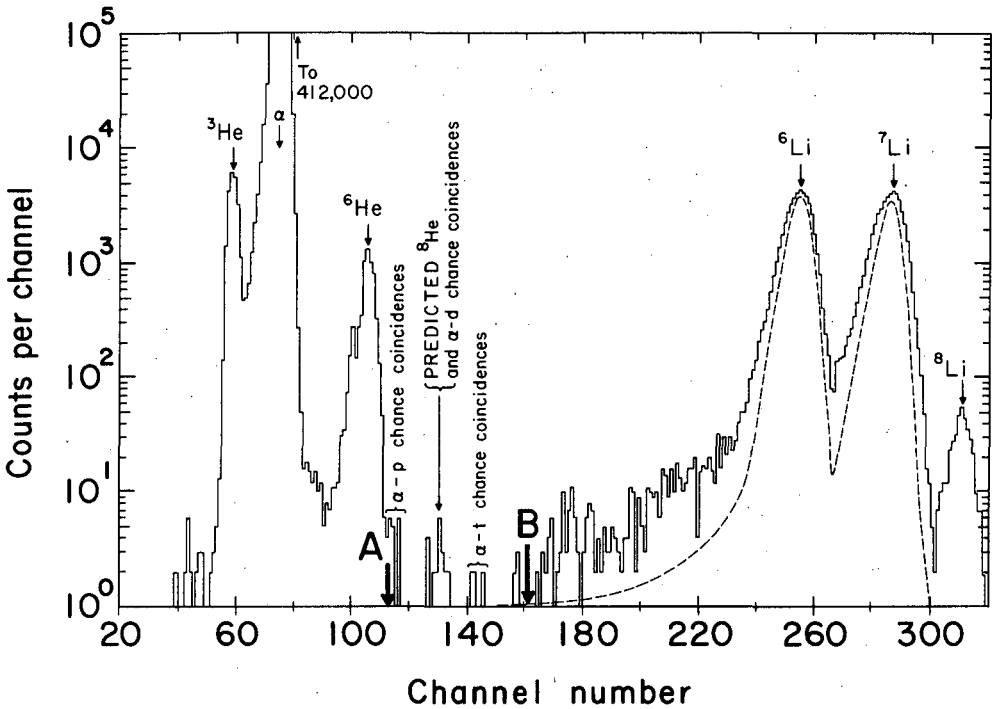

Fig. B.11-2. A complete particle-identifier spectrum for Run 2. Single-channel analyzers were set so that only α particles of energy between 22.7 and 26.6 MeV were identified. Counts in the region between A and B were stored in the on-line computer. The dotted lines represent the complete particle-identifier spectrum of Run 1 for channels 150 and higher.

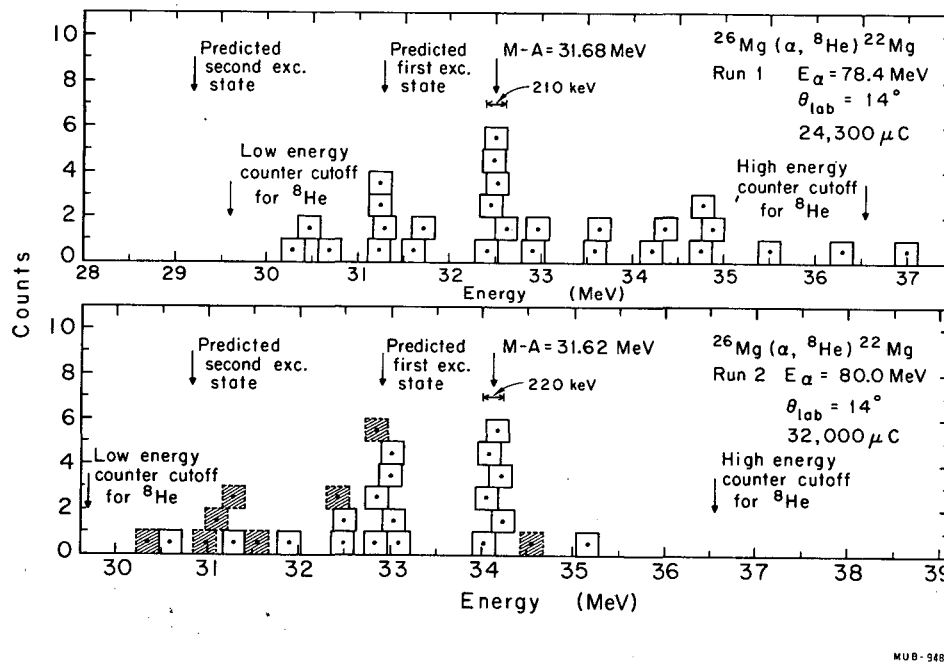

Fig. B.11-3. The energy spectra from the reaction ^{26}Mg(α, ^{8}He)^{22}Mg at 14 deg for both Runs 1 and 2. The block width of each count corresponds to the expected full width of a ^{8}He peak, and the central dot represents the exact energy of each event. Shaded counts in the Run-2 spectrum can be excluded from consideration as true ^{8}He particles through an analysis of their energy losses in the ΔE detectors. The predicted ^{8}He energies for leaving ^{22}Mg in its first and second excited states are indicated.

12. A J DEPENDENCE IN THE (^{3}He, α) REACTION CONFIRMING NEW SPECTROSCOPIC ASSIGNMENTS IN ^{14}N AND ^{13}C†

Gordon C. Ball and Joseph Cerny

In an investigation of the p-shell hole states of ^{14}N and ^{13}C through the ^{15}N(^{3}He, α)^{14}N and ^{14}C(^{3}He, α)^{13}C reactions, we have found that the shapes of the angular distributions are sensitive to the J of the picked-up neutron, an effect observed in other reactions.[1] States with the configurations $(p_{1/2})^{-2}$ and $(p_{3/2}, p_{1/2})^{-1}$ were observed in ^{14}N, and it was possible to identify all six of these states, including the $(p_{3/2}, p_{1/2})^{-1}_{1^+, T=1}$ state which had not been assigned previously. Of particular interest in the ^{13}C spectrum was the measurement of the lowest T = 3/2 state. An accurate measurement of the excitation of this state was necessary as one component of a rigorous test of the isobaric multiplet mass equation.[2]

The ^{15}N(^{3}He, α)^{14}N and ^{14}C(^{3}He, α)^{13}C reactions were carried out at energies of 39.8 and 44.8 MeV, respectively, using the ^{3}He beam from the Berkeley 88-inch cyclotron. Particles were detected by using a (dE/dx)-E counter telescope which fed a particle identifier;[3] the energy resolution (FWHM) in both reactions was around 200 keV.

If we assume that ^{15}N and ^{14}C contain a closed neutron shell and then consider a pure pickup mechanism, we can expect to populate only certain p-shell hole states in ^{14}N and ^{13}C. It is observed experimentally that these are the only states made with a large cross section.

Intermediate-coupling shell-model calculations[4-7] have shown that the six lowest p^{-2} states in ^{14}N are those with the configurations $(p_{1/2})^{-2}_{1^+,T=0}$, $(p_{1/2})^{-2}_{0^+,T=1}$, $(p_{3/2},p_{1/2})^{-1}_{1^+,T=0}$, $(p_{3/2},p_{1/2})^{-1}_{2^+,T=0}$, $(p_{3/2},p_{1/2})^{-1}_{2^+,T=1}$, and $(p_{3/2},p_{1/2})^{-1}_{1^+,T=1}$. Of the seven large peaks observed in the $^{15}N(^3He,\alpha)^{14}N$ reaction, six correspond to the first five p^{-2} configurations, which have already been well established.[8-10] The 9.17- and 10.43-MeV 2^+, T=1 levels are populated almost equally, in good agreement with the calculations by Rose et al.,[10] who found that the contributions from the p^{-2} and (s,d) configurations to these levels must be approximately equal. The seventh peak, at 13.72 ± 0.04 MeV, has been assigned the configuration $(p_{3/2},p_{1/2})^{-1}_{1^+,T=1}$. Calculations[4-7] have predicted values for the energy of this state which range from 10 to 15 MeV.

Angular distributions for the $^{15}N(^3He,\alpha)^{14}N$ reaction are shown in Fig. B. 12-1. The two distributions which correspond to the pickup of a $p_{1/2}$ neutron are similar in shape but differ from those corresponding to the pickup of a $p_{3/2}$ neutron. The main difference occurs in the angular region from $\theta_{c.m.}$ = 15 to 45 deg. As compared to the $p_{3/2}$ pickup shape, the cross section for $p_{1/2}$ pickup drops off much more quickly after the first maximum, and the second maximum is almost nonexistent. Another difference occurs in the region $\theta_{c.m.}$ = 55 to 75 deg., where the $p_{1/2}$ pickup states are at a maximum while the $p_{3/2}$ pickup states all reach a minimum. (The transitions to the 3.95-MeV level and, to a much lesser extent, to the ground state do show an intermediate character which can be attributed to the known[4-7] mixing between the dominant configurations of these states.) Artemov et al.[11] have recently studied the $(^3He,\alpha)$ reaction on ^{14}N and ^{16}O at energies from 17.4 to 36.6 MeV. Their data at 36.6 MeV seem to show some of the trends reported here.

In ^{13}C three levels were populated as expected. A sharp state at 15.108 ± 0.014 MeV was attributed to the T = 3/2 ground-state analog. An accurate determination of the energy of this level, in good agreement with previously reported results,[2,12,13] was possible because of the large amount of ^{12}C impurity in the ^{14}C target.

The angular distributions for the $^{14}C(^3He,\alpha)^{13}C$ reaction are shown in Fig. B. 12-2. A similar J dependence is observed in this reaction in the region $\theta_{c.m.}$ = 15 to 45 deg, where the $1/2^-$ ground state has a very deep minimum which is not observed in the $3/2^-$ states. For additional comparison the $^{12}C(^3He,\alpha)^{11}C$ ground-state transition is shown in Fig. B. 12-2. Its angular distribution shows the expected J dependence corresponding to $p_{3/2}$ pickup.

Footnote and References

† Condensed from Phys. Letters 21, 551 (1966).

1. L. L. Lee, Jr. and J. P. Schiffer, Phys. Rev. Letters 12, 108 (1964); L. L. Lee, Jr. and J. P. Schiffer, Phys. Rev. 136, B405 (1964).
2. J. Cerny, R. H. Pehl, G. Butler, D. G. Fleming, C. Maples, and C. Detraz, Phys. Letters 20, 35 (1966).
3. F. S. Goulding, D. A. Landis, J. Cerny, and R. H. Pehl, Nucl. Instr. Methods 31, 1 (1964).
4. D. R. Inglis, Rev. Mod. Phys. 25, 390 (1953).
5. J. P. Elliott, Phil. Mag. 1, 503 (1956).
6. W. M. Visscher and R. A. Ferrell, Phys. Rev. 107, 781 (1957).
7. A. N. Boyarkina, Izv. Akad. Nauk. SSSR, Ser. Fiz., 28, 337 (1964).
8. E. K. Warburton and W. T. Pinkston, Phys. Rev. 118, 733 (1960).
9. H. J. Rose, Nucl. Phys. 19, 113 (1960).
10. H. J. Rose, F. Riess, and W. Trost, Nucl. Phys. 52, 481 (1964).
11. K. P. Artemov, V. Z. Goldberg, B. I. Islamov, V. P. Rudakov, and I. N. Serikov, Soviet J. Nucl. Phys. 1, 726 (1965).
12. J. Cerny, R. H. Pehl, D. G. Fleming, and C. C. Maples, Bull. Am. Phys. Soc. 9, 704 (1964).
13. D. C. Hensley and C. A. Barnes, Bull. Am. Phys. Soc. 10, 1194 (1965); Richard G. Miller and G. W. Kavanagh, Bull. Am. Phys. Soc. 11, 315 (1966).

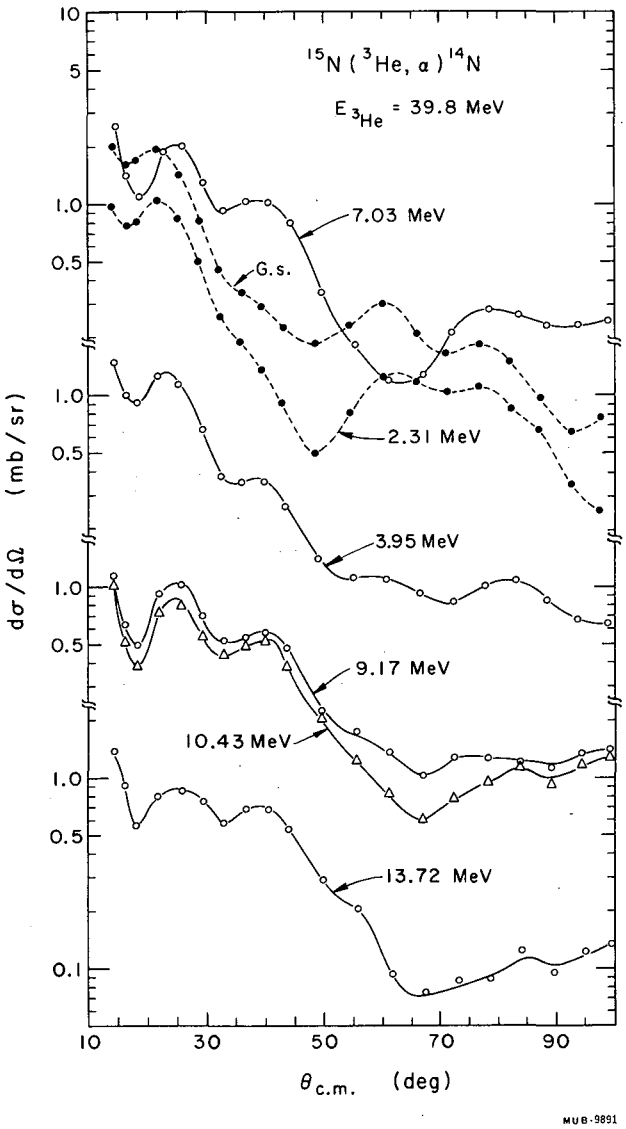

Fig. B. 12-1. Angular distributions from the $^{15}N(^3He,\alpha)^{14}N$ reaction; $p_{1/2}$ pickup states are indicated with broken lines; $p_{3/2}$ pick-up states are shown as solid lines.

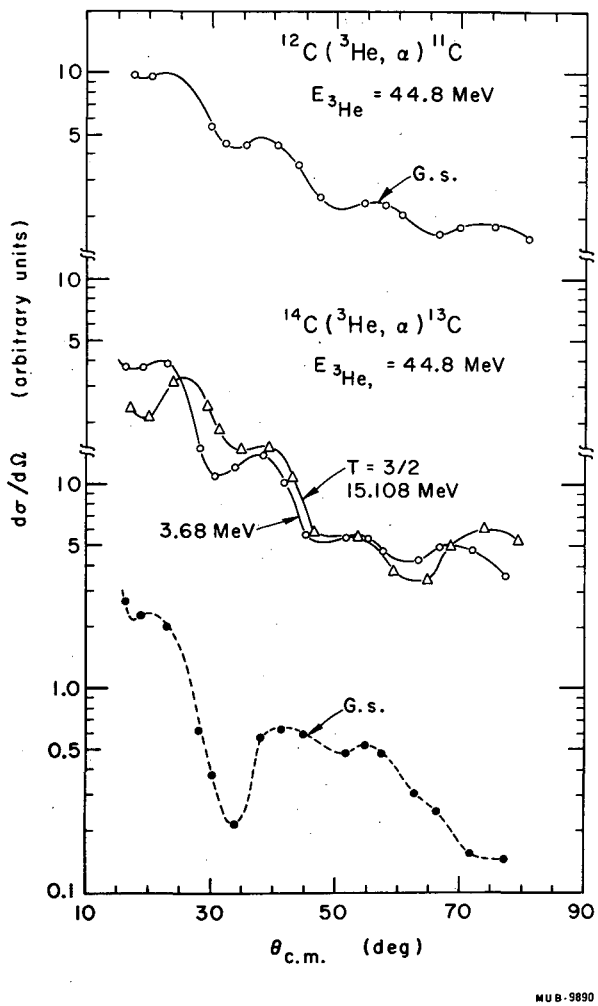

Fig. B. 12-2. Angular distributions from the $^{14}C(^3He,\alpha)^{13}C$ and $^{12}C(^3He,\alpha)^{11}C$ reactions; $p_{1/2}$ pickup states are indicated with broken lines; $p_{3/2}$ pickup states are shown as solid lines.

13. THE $^{14}N(^{3}He,t)^{14}O$ REACTION AND EXCITED ISOSPIN TRIADS IN MASS 14†

Gordon C. Ball and Joseph Cerny

At present, very little experimental evidence exists for complete correspondences among excited states in isobaric multiplets of $T > 1/2$. The mass-14 triad is an especially attractive system to investigate, since more is known about the $T = 1$ levels of ^{14}N than of any other $T_z = 0$ nucleus. In addition, the energy levels of ^{14}C have been extensively studied. All that is necessary to complete this triad is a knowledge of the levels of ^{14}O, which can now be investigated through the $^{14}N(^{3}He,t)^{14}O$ reaction. In an investigation of the $(^{3}He,t)$ reaction on several other nuclei in the 1p shell, notably ^{14}C and ^{15}N, we have found that the shapes and relative magnitudes of the angular distributions arising from single-particle transitions appear to fall into groups characterized by the specific shell-model transition involved. By utilizing this effect in conjunction with other available data, it was possible to make spin and parity assignments of (1-), (0+), (3-), 2+, (2-), and 2+ for the levels observed in ^{14}O at 5.17, 5.91, 6.28, 6.60, 6.79, and 7.78 MeV, respectively. In this manner a correspondence has been established for six excited $T = 1$ levels in all three members of the mass-14 triad.

The $^{14}N(^{3}He,t)^{14}O$ reaction was carried out at an energy of 44.6 MeV with a ^{3}He beam from the Berkeley 88-inch cyclotron. Particles emitted from both a N_2 gas target and a solid adenine ($C_5H_5N_5$) target were detected using a (dE/dx-E) counter telescope which fed a particle identifier.[1] Typical energy spectra are shown in Fig. B. 13-1; an energy resolution (FWHM) of 190 ± 10 keV was observed using the gas target; the adenine target gave a resolution of 155 ± 10 keV. Several new energy levels were observed up to an excitation energy of 18 MeV, and angular distributions were obtained from $\theta_L = 12$ to 60 deg for all levels observed below 9 MeV (see Fig. B. 13-2).

Several different single-particle transitions are expected in the $^{14}N(^{3}He,t)^{14}O$ reaction below an excitation of 9 MeV. In particular $p_{3/2} \rightarrow p_{1/2}$, $p_{1/2} \rightarrow d_{5/2}$ and $p_{1/2} \rightarrow s_{1/2}$ transitions should be readily observed. In Fig. B. 13-2 it can be seen that the transitions to the 6.60- and 7.78-MeV levels in ^{14}O have almost identical angular distributions whose shape is characteristic of several known $p_{3/2} \rightarrow p_{1/2}$ transitions. These levels have been assigned as the analogs to the 9.17- and 10.43-MeV 2+, $T = 1$ levels in ^{14}N. Another pair of strongly populated levels which have similar and quite distinct angular distributions are those at 6.28 and 6.79 MeV. These distributions are characteristic of $p_{1/2} \rightarrow d_{5/2}$ transitions, and it was possible to assign these levels as the analogs to the 3- and 2-, $T = 1$ levels in ^{14}N at 8.91 and 9.51 MeV, respectively. In a similar manner the ^{14}O level at 5.17 MeV was determined to arise from a $p_{1/2} \rightarrow s_{1/2}$ transition.

An energy-level diagram shown in Fig. B. 13-3 summarizes the available information on the $T = 1$ levels in ^{14}C, ^{14}N, and ^{14}O. It can be seen that all levels in ^{14}N are shifted downward relative to their position in ^{14}C, with the 0- and 1- levels undergoing a stronger shift. Since all levels in ^{14}C below 8.176 MeV are bound, whereas all but the lowest $T = 1$ level in ^{14}N (and ^{14}O) are unbound (see Fig. B. 13-3), a major component of these strong shifts, in addition to the Coulomb displacement, is certainly the Thomas-Ehrman effect, which would be most pronounced for an s-state proton. A similar general shift is observed for all levels in ^{14}O relative to their positions in ^{14}N, with the 5.17-MeV 1- level the most strongly shifted, as expected.

Tombrello[2] has recently proposed a simple two-body model for relating levels within an isobaric multiplet. This model was applied to the 0-, 1-, 2-, and 3- levels in ^{14}C, ^{14}N, and ^{14}O;[3] good agreement with our assignments was obtained.

Footnote and References

† Condensation of article in Phys. Rev. (in press).

1. F. S. Goulding, D. A. Landis, J. Cerny, and R. H. Pehl, Nucl. Instr. Methods 31, 1 (1964).
2. T. A. Tombrello, Phys. Letters 23, 134 (1966).
3. T. A. Tombrello, private communication.

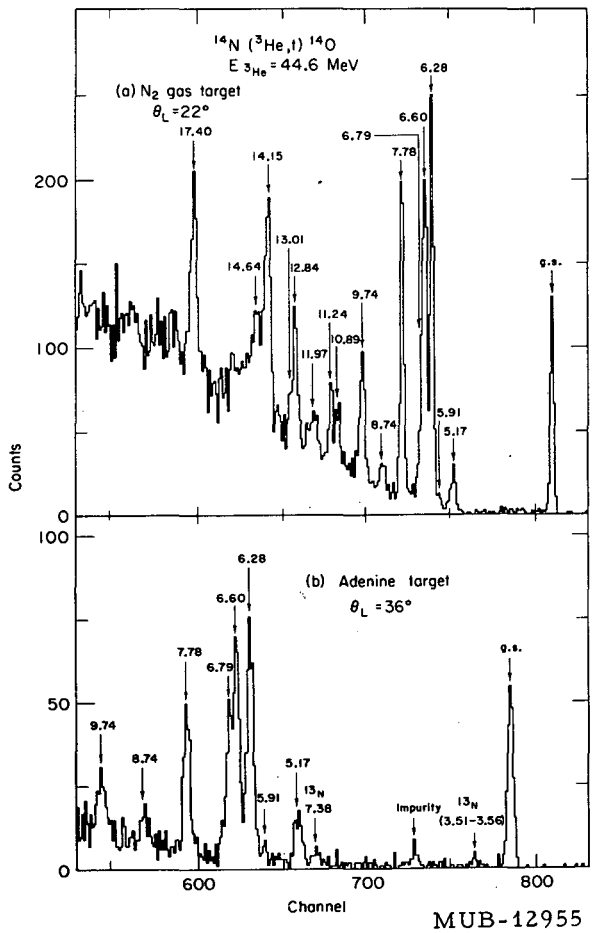

Fig. B.13-1. Energy spectra for the ^{14}N(^{3}He, t)^{14}O reaction at a ^{3}He energy of 44.6 MeV obtained with (a) a N_2 gas target and (b) a solid adenine target.

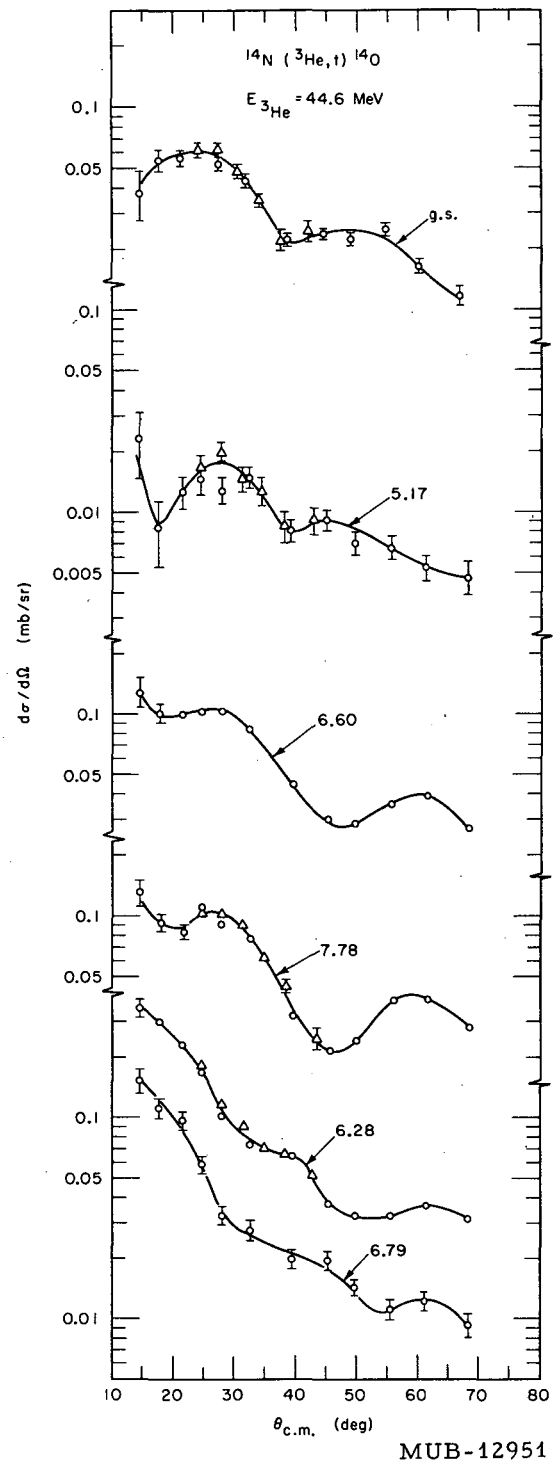

Fig. B.13-2. Angular distributions from the ^{14}N(^{3}He, t)^{14}O reaction. Δ, gas target data; O, solid adenine target data. When no error bars are shown the statistical error is contained within the point.

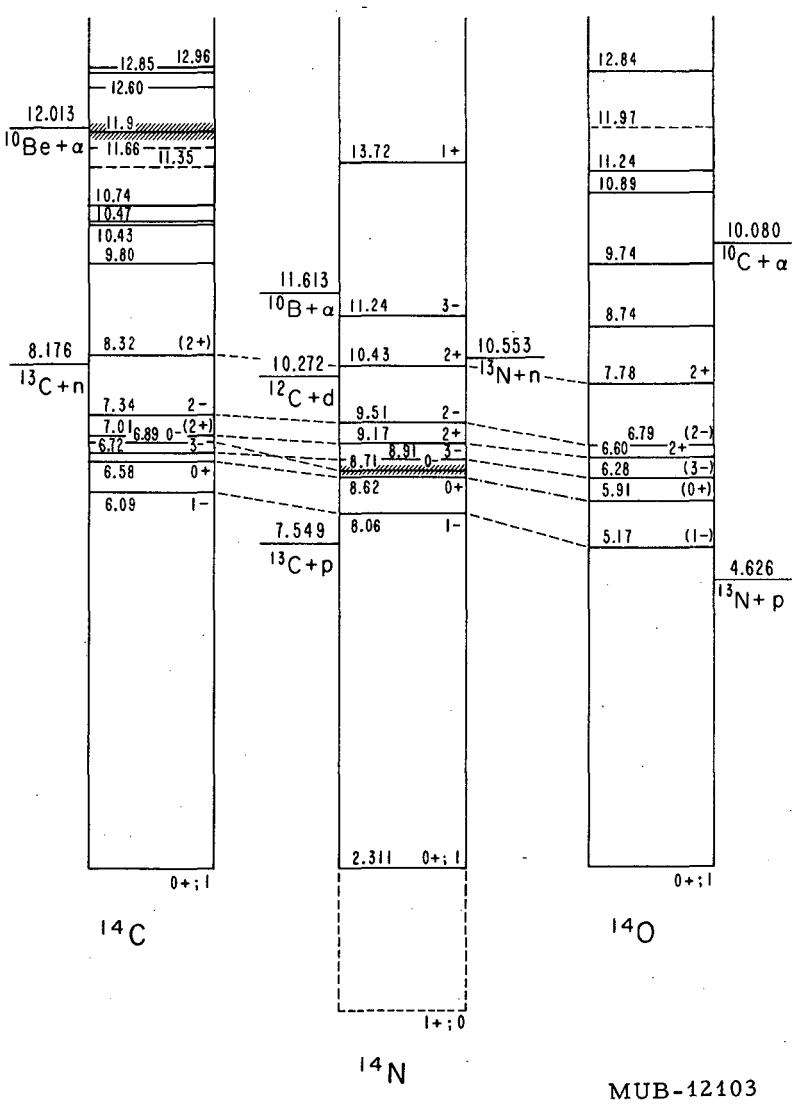

Fig. B. 13-3. Energy-level diagram for the T = 1 levels in ^{14}C, ^{14}N, and ^{14}O. Uncertain J^{π} assignments are enclosed in parentheses. The levels are connected by a dashed line if the correspondence is considered well established and by a dot-dash line if the correspondence is considered tentative.

14. NUCLEAR REACTION Q VALUES

C. Maples, G. W. Goth, and J. Cerny

Tables of Q values for nuclear reactions have been calculated from the currently available mass data on the nuclides. The calculations were carried out on all stable and naturally occurring radioactive isotopes from a Z of 2 to 92, as well as on a few common long-lived isotopes. The tabulated reactions involve the following:

Isotope	Incoming particles	Outgoing particles
$5 \leq Z \leq 22$	γ, n, p, d, t, ^{3}He, ^{4}He, ^{6}Li, ^{7}Li, and ^{12}C	γ, n, p, d, t, ^{3}He, ^{4}He, ^{6}He, ^{6}Li, ^{7}Li, ^{8}Li, ^{9}Li, ^{7}Be, ^{9}Be, ^{10}Be, ^{8}B, ^{10}B, and ^{11}B
$2 \leq Z \leq 4$ and $23 \leq Z \leq 92$	γ, n, p, d, t, ^{3}He, ^{4}He, ^{6}Li, ^{7}Li, and ^{12}C	γ, n, p, d, t, ^{3}He, ^{4}He, ^{6}He, and ^{6}Li

The computations were carried out with the FORTRAN IV program SHADRACH on an IBM 7094 computer. This program (which will be made available on request) contains all the stored mass information and permits the calculation of Q-value matrices for any set of incident and exit particles.

15. THE ^{24}Mg(α, α') REACTION AT 50 MeV

D. L. Hendrie, B. G. Harvey, J. Mahoney, and J. R. Meriwether†

In the continuing program of investigation of collective levels by inelastic scattering of α particles, an obvious choice of target nuclei in the light element region is ^{24}Mg. In addition to the well-known ground-state rotational band, there is also an apparent K = 2 gamma band with experimentally accessible higher members.[1] However, the closeness of the 4.118-MeV 4^+ member of the ground-state band and the 4.236-MeV 2^+ member of the gamma band have, up to now, prevented α-particle angular distribution from being obtained for the two states separately.

The experimental arrangement was as usual for this work, four lithium-drifted silicon detectors cooled to -25°C and spaced 2 deg apart looked at a 350 μg/cm^2 self-supporting evaporated magnesium foil isotopically enriched in ^{24}Mg. Pulses were stored in four quadrants of a 4096-channel Nuclear Data analyzer and transferred to a PDP-5 computer for analysis and permanent storage at the end of each run. A typical spectrum, shown in Fig. B.15-1 has about 60-keV resolution, sufficient to resolve the 4.118- and 4.236-MeV levels and reveal a large number of separated states above 7 MeV.

The elastic scattering differential cross sections were used to generate a four-parameter optical potential by use of an adaptation of the program SEEK;[2] the parameters were: V = 196.6 MeV; W = 53.5 MeV; $r_0 = r_c = r_i = 1.336$ F; $a = a_i = 0.58$ F. These parameters were then used in the DWBA program JULIE[3] to obtain spins, parities, and transition strengths of the excited states. Several of the cross sections and fits are shown in Figs. B.15-2 and B.15-3, and a resumé of the data is listed in Table B.15-I.

The cross sections to the first and second 2^+ levels show the usual Blair[4] phase rule patterns, and the strength of the 1.37 level agrees with previous alpha-scattering results,[5] but is lower than Coulomb-excitation and electron-scattering results.[6] See Ref. [7], however, for a possible explanation of the overestimate of strengths by those experiments.

The 4^+ state at 4.12 MeV shows the reversed phase and flatter angular distribution expected[4] for excitation of a second rotational state. The 3^+ state at 5.22 MeV is weak and featureless at these angles at 50 MeV (see, however, the contribution of M. Reed to this report). The 4^+ level at 6.01 MeV shows a strong direct $\ell = 4$ transition, which disagrees with the expected results for assignment of this level to a K = 2 rotational band. Further work on this nucleus is planned in order to investigate the rotational aspect of ^{24}Mg.

Footnote and References

† Present address: University of Southwestern Louisiana, Lafayette, Louisiana.

1. P. M. Endt and C. Van Der Leurs, Nucl. Phys. 34, 1 (1962).
2. M. A. Mekanoff, J. Raynal, and T. Sawada, UCLA report 66-10, 1966.

3. R. H. Bassel, R. M. Drisko, and G. R. Satchler. The Distorted-Wave Theory of Direct Nuclear Reactions. I. "Zero-Range" Formalization Without Spin-Orbit Coupling, and the Code SALLY, ORNL-3240, Feb. 1962.
4. N. Austern and J. S. Blair, Ann. Phys. (N. Y.) 33, 15 (1965).
5. See, for example, I. M. Nagib, Ph.D. Thesis, University of Washington, 1962.
6. P. H. Stelson and L. Grodzins, Nucl. Data 1, 21 (1965).
7. L. W. Owen and G. R. Satchler, Nucl. Phys. 51, 155 (1964).

Table B.15-I. Resumé of data.

Level	Energy (MeV	J^{π}	δ_I	$\frac{B(EI)}{Bsp}$	Remarks
A	ground state	0^+			
B	1.365 ± 0.004	2^+	1.68	10.9	Ref. 6: δ = 2.25, B/Bsp = 16.6; Ref. 5: δ = 1.66
C	4.118 ± 0.007	4^+			Double excitation
D	4.236 ± 0.007	2^+	0.49	0.93	Ref. 5: δ = 0.43
E	5.233 ± 0.010	3^+			Weak
F	6.010 ± 0.007	4^+	0.68	2.0	
G	6.433 ± 0.007	0^+	0.35	0.9	
H	7.353 ± 0.007	2^+	0.53	1.1	
I	7.603 ± 0.010	3^-	0.65	1.7	
J	7.800 ± 0.020				Isotropic
K	8.122 ± 0.010	(-)			Weak
L	8.382 ± 0.010	3^-	0.79	2.5	
M	8.64 ± 0.02	4^+	0.26	0.3	
N	8.85 ± 0.02	0^+	0.25	0.4	
O	8.99 ± 0.02	(3^-)	0.26	0.3	
P	9.12 ± 0.02	4^+	0.42	0.8	
Q	9.30 ± 0.02	(4^+)	0.52	1.1	
R	9.52 ± 0.02				Isotropic
S	10.03 ± 0.02	4^+	0.59	1.5	
T	10.34 ± 0.03	--			
U	10.63 ± 0.03	--			
V	10.72 ± 0.03	--			
W	11.18 ± 0.03	(3^-)	0.55	1.2	
X	11.32 ± 0.03	--			
Y	12.02 ± 0.03	(4^+)			
Z	12.54 ± 0.03	--			
AA	12.88 ± 0.03	--			
BB	13.48 ± 0.03	--			

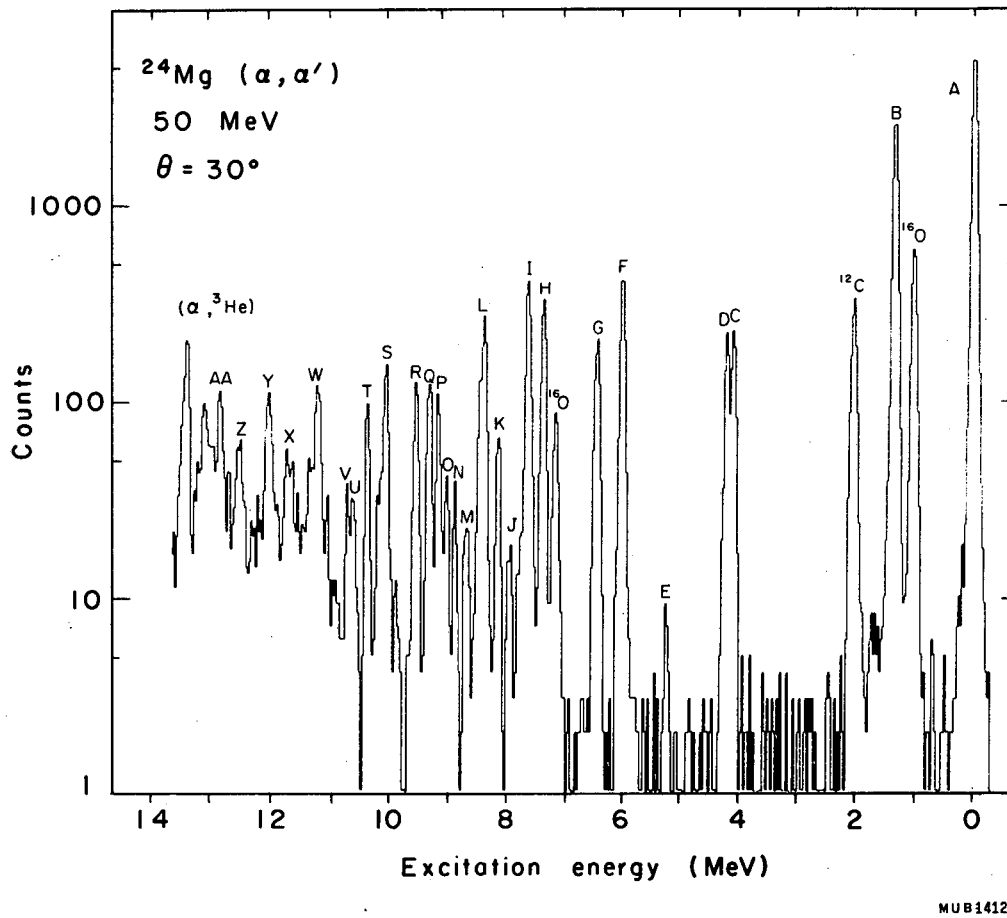

Fig. B. 15-1. The energy spectrum for scattering of 50-MeV α particles from ^{24}Mg. The letters indicating the levels are interpreted in Table B. 15-I.

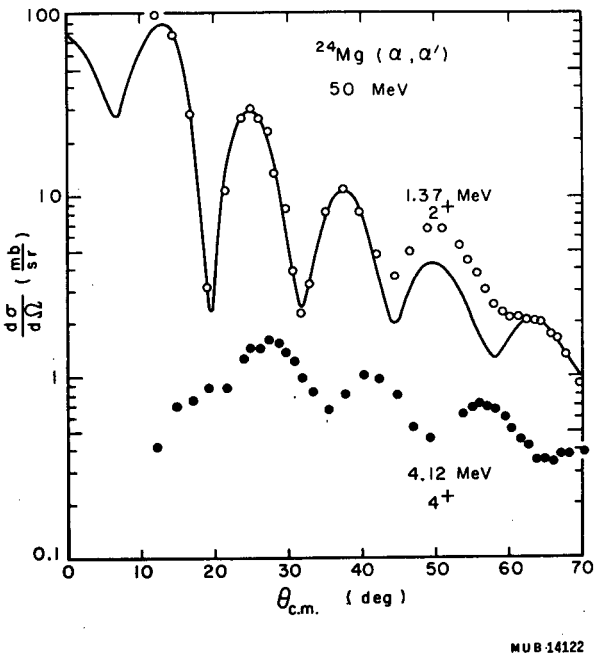

Fig. B. 15-2. Angular distributions of the 1.37- and 4.23-MeV 2^+ levels of ^{24}Mg. The solid line is a DWBA fit with $\ell = 2$.

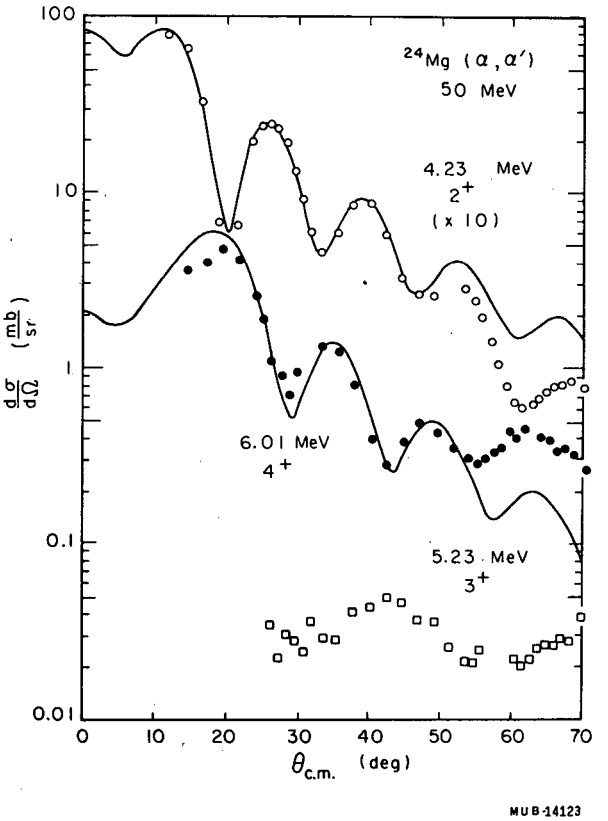

Fig. B. 15-3. Angular distributions of the 4.12- and 6.01-MeV 4^+ levels of ^{24}Mg. The solid line is a DWBA fit with $\ell = 4$.

16. PRODUCTION OF THE 3^+ UNNATURAL-PARITY STATE IN ^{24}Mg BY INELASTIC α SCATTERING

Mary F. Reed, Bernard G. Harvey, and David L. Hendrie

In the past few years the nuclear reaction mechanism leading to the production of unnatural parity states ($\pi \neq (-1)^J$ in even-even nuclei by inelastic α scattering has been the subject of much research.[1-7] The interest in these energy levels stems from the fact that they cannot be excited in this reaction by simple direct mechanisms.[1] Thus, they afford a unique opportunity to study more complicated nuclear interactions between spinless projectiles and targets.

In previous studies of 2^- states in ^{16}O and ^{20}Ne and 3^+ states in ^{24}Mg and ^{28}Si using low- and medium-energy α particles (to E_α = 65 MeV), the results were inconclusive and led to various speculations about the reaction mechanisms. In all cases the angular distributions for the unnatural-parity states showed oscillatory behavior with periods approximately the same as those of the oscillations in the elastic and natural-parity-state angular distributions, although the phase relationships were, in general, not clear or consistent at all angles.

In particular, previous work on the 3^+ state at 5.22 MeV in ^{24}Mg by Braithwaite et al.[2]

indicated possible compound-nucleus contributions to the reaction mechanism at low incident α-particle energies (15.0 to 24.5 MeV). At E_α = 22.5 MeV, the angular distribution taken by Eidson and Cramer[1] indicated interference effects, suggesting contributions from both multiple phonon excitation and exchange processes. Work by Kokame et al.[3] at 28.5 MeV incident energy also indicated multiple phonon excitation in the production of the 3^+ level. At E_α = 42 MeV, Vincent, Boschitz, and Priest[7] found a diffraction pattern in the angular distribution and an enhanced cross section for large-angle scattering, indicating that exchange effects may play a role in this excitation. The only theoretical treatment of this state has been a coupled-channel approach by Tamura[8] using the 28.5-MeV data of Kokame et al.[3] He found reasonably good agreement with experiment, and concluded that the multiple excitation process can account for the excitation. However, the assumptions necessary to obtain this agreement still leave some doubt that this is in fact the mechanism of the reaction at this α-particle energy.

A study of the excitation of this level at higher bombarding energies was undertaken at the 88-inch variable-energy cyclotron in hope of shedding further light on the mechanism of the reaction. In this series of experiments, α particles of 50, 65.7, 81, and 119.7 MeV were scattered from isotopically enriched (99.96%) self-supporting ^{24}Mg targets. Energy spectra of the scattered α particles were obtained by using lithium-drifted silicon detectors and 1024-channel pulse-height analyzers. In these spectra the 3^+ level was well separated from the other ^{24}Mg levels; however, ^{16}O and ^{12}C impurities masked some of the ^{24}Mg levels at forward angles.

The experimental angular distributions for the elastic, first 2^+ and 3^+ levels are shown in the Figs. B. 16-1 through B. 16-3. Here they have been plotted versus momentum transfer times the interaction radius, $|\vec{k}_i - \vec{k}_f| \times R$, to eliminate kinematic shifts in the positions of the oscillations and make it possible to compare the different α-particle energy results directly. The relative errors in the differential cross sections are approximately ±10%, and the absolute errors about ±15%. The effective interaction radius used for each energy is given in Fig. B. 16-1. They were obtained by matching the positions of the oscillations in the elastic and 2^+ angular distributions at the different α-particle energies. Figures B. 16-1 and B. 16-2 show that the oscillations line up very well. Similar agreement in the positions of the oscillations in the angular distributions was also found for the other low-lying natural-parity states studied, e.g., the 4^+ at 6.00 MeV and the 0^+ at 6.44 MeV. However, for the 3^+, Fig. B. 16-3, no such agreement is found. The 42-MeV data of Vincent, Boschitz, and Priest[7] are also included here.

It can be seen that the rather pronounced large-angle oscillations at 42 MeV tend to become damped out and then two very broad oscillations appear as the α-particle energy increases. These broad oscillations appear at large values of $|\vec{k}_i - \vec{k}_f| \times R$, where the elastic and natural-parity states are only weakly excited at the lower energies and move toward smaller values as the energy increases. This behavior is entirely different than has been seen before for any nuclear energy level in inelastic α scattering.

The integrated cross sections for the 2^+ and 3^+ levels were calculated, and they were found to fall off with increasing α-particle energy; however, the 3^+ cross section falls off more slowly.

The reaction mechanism is obviously not simple! The experimental angular distributions do not suggest a specific mechanism. Possibly there are competing mechanisms that interfere at some angles and add coherently at others, giving rise to the broad oscillations. Or there may be a single mechanism that is inhibited at certain scattering angles and not at others, giving rise to this behavior. The different results found at lower energies make it seem unlikely that the same mechanism is dominant for both lower- and higher-energy α particles. Since other unnatural parity states have not been investigated at higher bombarding energies, it is not known whether this behavior and the mechanism involved are peculiar to ^{24}Mg or common to all unnatural-parity states.

It is hoped that further theoretical study of the data for ^{24}Mg and further experimentation on other unnatural-parity states will bring about better understanding of these reaction mechanisms and of inelastic α scattering in general.

References

1. W. W. Eidson and J. G. Cramer, Phys. Rev. Letters 9, 497 (1962).
2. W. J. Braithwaite, J. G. Cramer, and R. A. Hinrichs, University of Washington Nuclear Physics Laboratory Annual Report, 1966, p. 18.

3. J. Kokame, K. Fukunaga, N. Inoue, and H. Nakamura, Phys. Letters 8, 342 (1964).
4. J. S. Blair, N. Cue, and D. Shreve, University of Washington Nuclear Physics Laboratory Annual Report, 1965, p. 3.
5. F. W. Bingham, Phys. Rev. 145, 901 (1966).
6. B. G. Harvey, E. J-M. Rivet, A. Springer, J. R. Meriwether, W. B. Jones, J. H. Elliott, and P. Darriulat, Nucl. Phys. 52, 465 (1964).
7. J. S. Vincent, E. T. Boschitz, and J. R. Priest, Bull. Am. Phys. Soc. 11, 333 (1966).
8. T. Tamura, Nucl. Phys. 73, 241 (1965).

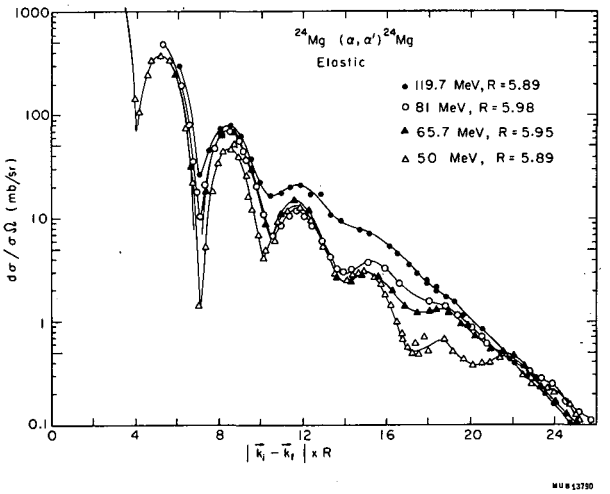

Fig. B. 16-1. The ^{24}Mg elastic angular distributions plotted versus momentum transfer times R for E_α = 50, 65.7, 81, and 119.7 MeV. The lines are drawn to connect the points, and serve only as visual aids.

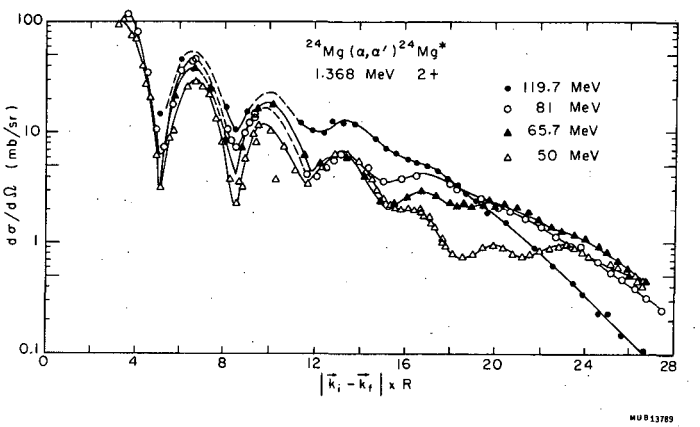

Fig. B. 16-2. The ^{24}Mg, 1.368-MeV, 2^+ angular distributions.

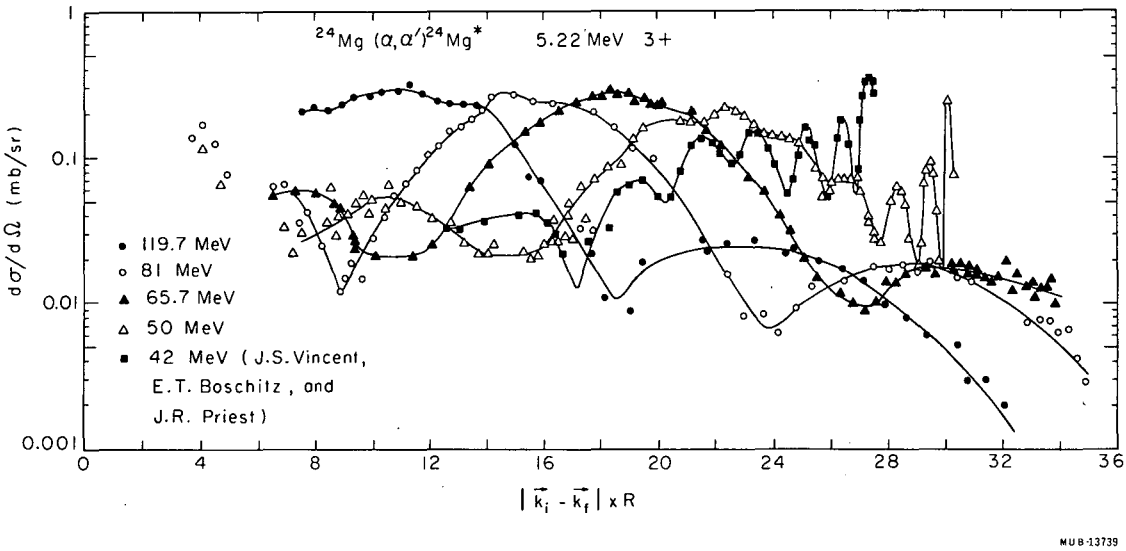

Fig. B. 16-3. The ^{24}Mg, 5.22-MeV, 3^+ angular distributions. The 42-MeV data are taken from Ref. 7.

17. EXCITATION OF ROTATIONAL LEVELS IN ^{152}Sm AND ^{154}Sm†

B. G. Harvey, D. L. Hendrie, O. N. Jarvis,* J. Mahoney, and J. Valentin‡

The location of diffraction maxima in the angular distributions of inelastically scattered α particles has led to the Blair phase rule,[1] BPR I. The mechanism is assumed to be a simple direct excitation of a collective level. However, several cases are known[2] in which the phase is reversed and the distribution is flatter than in BPR I distributions. These characteristics, denoted by BPR II, have been explained as being due to double excitation of two surfon levels in a model by Austern and Blair.[3] However, the character of the states giving rise to such distributions has not been well established.

In order to investigate the validity of the correspondence between double excitation and BPR II, we chose to look at the inelastic scattering of 50-MeV α particles from ^{152}Sm and ^{154}Sm. The requirement of experimentally accessible pure two-surfon states are well met by the rotational levels of the rare earths. The deformations, β, of these two nuclei are known to be 0.304 and 0.351 respectively.[4]

Self-supporting samarium target foils about 300 μg/cm^2 thick were obtained by heating isotopic samarium oxide in the presence of lanthanum metal.[5] Scattered α particles were detected in four cooled lithium-drifted silicon detectors, and stored in a multichannel analyzer. The total beam passing through the target was collected and measured with a Faraday cup and checked with a fixed-angle monitor counter. Target thicknesses were obtained by normalizing the elastic cross section to Rutherford scattering at small angles. Total experimental resolutions were about 45 keV, sufficient to resolve the 2^+ from the ground state at most angles. Particular care was taken to reduce backgrounds and low-energy tails by using a highly polished cylindrical-edged gold plated analyzing slit located far from the target area. Similar care was taken with the counter collimators. Nevertheless, backgrounds proved to be our most severe experimental problem, and tails from the large elastic peaks at forward angles obscured much of the inelastic data below about 25 deg. Extraction of the inelastic cross sections was aided by use of a computer program which approximated the spectra by a series of Gaussian peaks plus background.[6] Sample samarium spectra at larger angles are shown in Fig. B. 17-1.

The inelastic differential cross sections to the 2^+, 4^+, and 6^+ levels of ^{152}Sm and ^{154}Sm are shown in Figs. B. 17-2 and B. 17-3. These levels were all clearly resolved from adjacent

inelastic levels except for the 6^+ level of ^{152}Sm. This level could not be separated from the 0^+ level at 920 keV, but we do not expect significant contribution from the 0^+ level. Inspections of the 2^+ and 4^+ distributions for both target nuclei shows the expected BPR I distributions for the 2^+ levels and BPR II distributions for the 4^+ levels. Both the reversed phase and the flatter angular distribution of the 4^+ levels are apparent. In addition, the cross sections are roughly in the ratio to be expected from the additional factor β^2, which would multiply the double excitation cross section. Therefore we can establish a definite correspondence between known two-surfon levels and BPR II distributions for these nuclei.

We consider next the angular distributions of the 6^+ levels. These distributions have still another reversal of phase. The envelopes of their oscillations are even flatter than those of the 4^+ levels. The magnitude of their cross sections is reduced from that of the 4^+ levels again by about a factor of β^2. In addition, the ^{154}Sm data at about 25 deg indicate a minimum where one would not be expected for a direct $\ell = 6$ transition. We denote these characteristics by BPR III and, by analogy with the 4^+ levels, relate them to "triple excitation" of the previously known 6^+ three-surfon members of the ground-state rotational bands.

Extension of the Austern-Blair model[3] to include triple excitation in the Fraunhofer limit provides qualitative agreement with our results. However, the Austern-Blair model does not include Coulomb excitation, which is certainly important for the excitation of the 2^+ level but probably not for the other states. More important, deformations as large as those in the samarium isotopes lead to such strong coupling of the 2^+ and elastic channels that the DWBA approach is inappropriate. A coupled-channels program with Coulomb excitation is indicated for more quantitative calculations.

Footnotes and References

† A brief version of UCRL-17303.
* Visitor from Nuclear Physics AERE, Harwell, Didcot, Berks., England.
‡ Present address: Laboratoire de Physique Nucleaire, Institut Fourier, Grenoble, France.

1. J. S. Blair, Phys. Rev. 115, 928 (1959).
2. R. Beurtey, P. Catillon, R. Chaminade, M. Crut, H. Faraggi, A. Papineau, J. Saudinos, and J. Thirion, Compt. Rend. 252, 1756 (1961).
3. N. Austern and J. S. Blair, Ann. Phys. 33, 15 (1965).
4. P. H. Stelson and L. Grodzins, Nuclear Data 1, 21 (1965).
5. L. Westgaard and S. Bjørnholm, Nucl. Instr. Methods 42, 77 (1966).
6. Arthur Springer, Scattering of 50.9-MeV Particles From ^{20}Ne and ^{40}Ca (Ph.D. Thesis), UCRL-11681, May 1965.

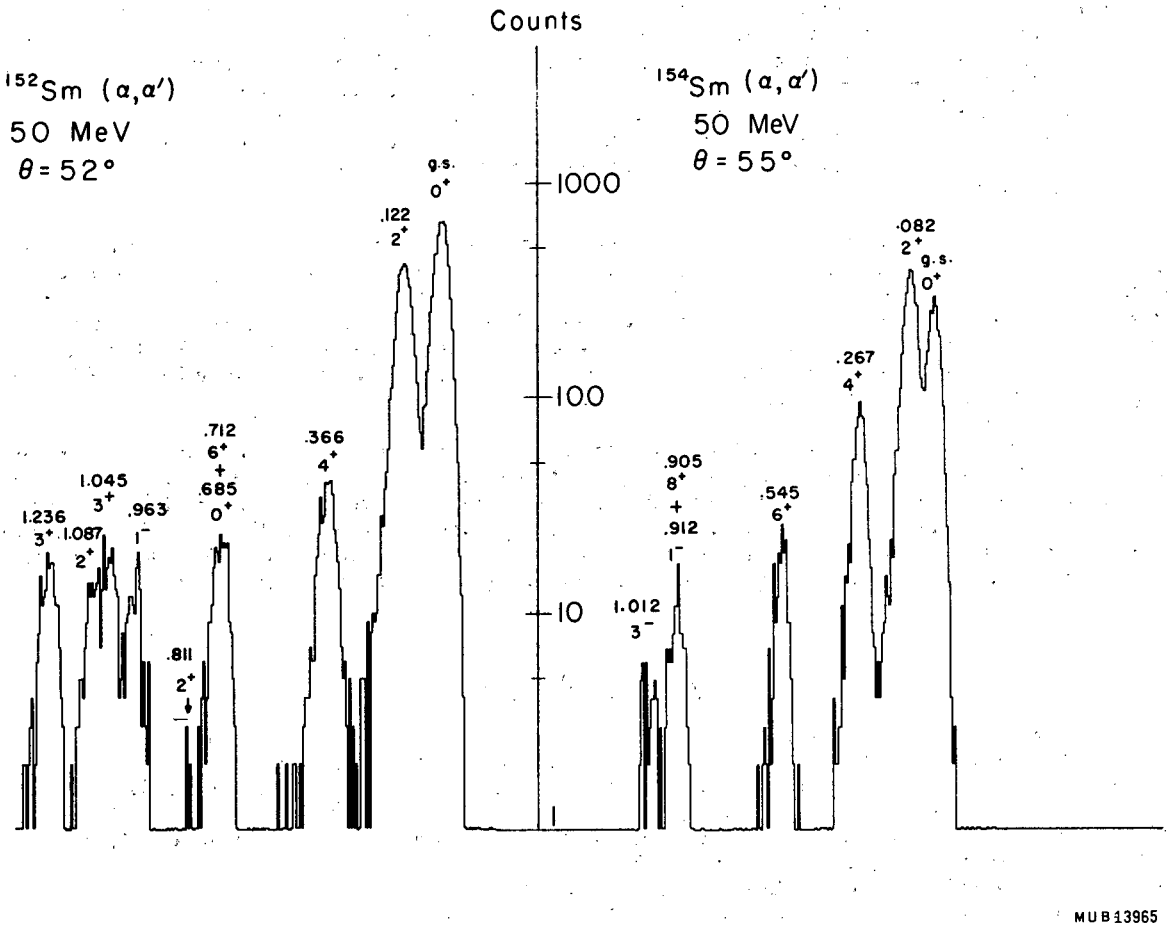

Fig. B. 17-1. Energy spectra for the inelastic scattering of 50-MeV alphas from ^{152}Sm and ^{154}Sm plotted on a logarithmic scale. Positions of excited states are indicated.

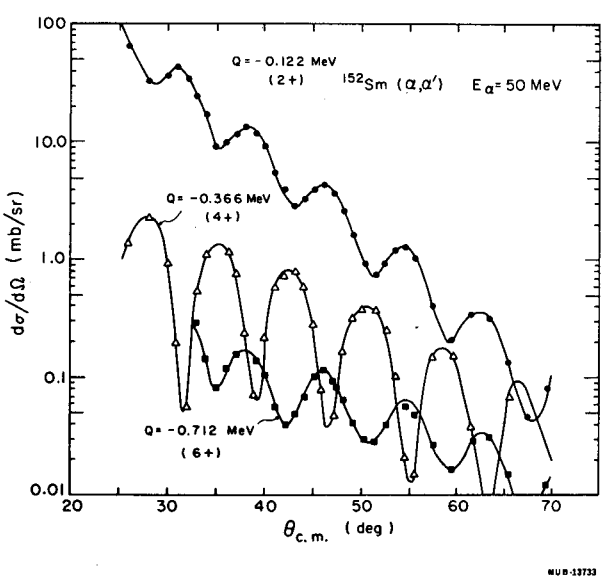

Fig. B. 17-2. Differential cross sections for the 2^+, 4^+, and 6^+ members of the ground-state rotational band of ^{152}Sm. Relative errors are, in general, smaller than the data points.

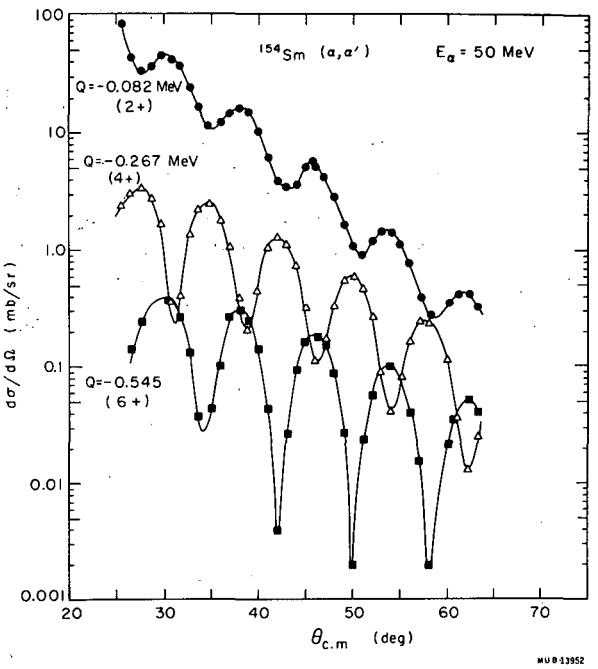

Fig. B. 17-3. Differential cross sections for the 2^+, 4^+, and 6^+ members of the ground-state rotational band for ^{154}Sm. Relative errors are, in general, smaller than the data points. We did not find excitation of the 0^+ state at 1.012 MeV.

18. ELASTIC SCATTERING OF 55-MeV PROTONS FROM ^{3}He

D. L. Hendrie, B. G. Harvey, O. N. Jarvis,† J. Mahoney, and W. Tivol

In recent work at this Laboratory the quasi-elastic scattering process of 55-MeV protons off two- and three-nucleon clusters in the lithium isotopes has been investigated.[1] Analysis of this reaction requires knowledge of the differential cross sections for the scattering of protons from the free nucleon cluster. Since such experiments have not been reported above 31.5 MeV[2] for the three-nucleon clusters, such an experiment was performed for our relevant energy of 55-MeV.

The proton beam (of up to 1 μA) was analyzed to about 100 keV and directed through a gas target and into a magnetically shielded Faraday cup, where it was collected and integrated for each run. The charge integration was checked with a monitor counter located 20 deg from the beam direction. The gas target consisted of a 3-in.-diameter cylinder with a continuous 0.1-mil Havar[3] foil window covering over 75% of its circumference. The pressure and temperature of the 99.73% isotopically pure ^{3}He gas were monitored throughout the experiment.

Two detector telescopes were used with all counters cooled to -25°C. Three 0.5-cm lithium-drifted silicon detectors were stacked and the outputs added to obtain data at forward angles. The second telescope, located 20 deg from the first and on the same scattering table, consisted of a 0.5-cm E detector and 0.06-cm diffused junction ΔE detector. The pulses from these two detectors were summed and protons were selected by use of the Goulding-Landis particle identifier.[4] This enabled us to eliminate contributions to the spectra of recoil ^{3}He and deuterons from the (p, d) reaction. This also greatly reduced backgrounds, mostly due to neutrons produced in the target and Faraday cup. The geometry of the telescopes has been described previously;[5] the total angular acceptance, including beam divergence, was about 0.5 deg. Total final energy resolutions, due mostly to kinematical effects, were about 350 keV for telescope #1, and 300 keV for telescope #2. Pulser signals, random in time, were fed into the preamplifiers during each run to monitor the electronic stability and to measure effects of dead time and pile-up losses.

The resulting differential cross section is shown in Fig. B. 18-1. The distribution is comparable to that obtained by extrapolation from lower energies. Excited states of ^{3}He at 10.2 and 12.6 MeV have been reported recently in which a similar reaction at 31.5 MeV was studied.[2] Investigation of our spectra show no evidence for excitation of such states, which an upper limit

of about 1/40 of the elastic cross section.

Footnote and References

† Permanent address: AERE, Harwell, Berks., England.

1. D. L. Hendrie, Marc Chabre, and H. G. Pugh, The ^{6}Li(p, pd)^{4}He and ^{7}Li(p, pt)^{4}He Reactions at 55 MeV, Chemistry Division Annual Report UCRL-16580, Jan. 1966.
2. C. C. Kim, S. M. Bunch, D. W. Devins, and H. H. Forster, Phys. Letters 22, 314 (1966).
3. Obtained from Hamilton Watch Company, New York
4. F. S. Goulding, D. A. Landis, J. Cerny, and R. H. Pehl, Nucl. Instr. Methods 31, 1 (1964).
5. B. G. Harvey, E. J.-M. Rivet, A. Springer, J. R. Meriwether, W. B. Jones, J. H. Elliott, and P. Darriulat, Nucl. Phys. 52, 465 (1964).

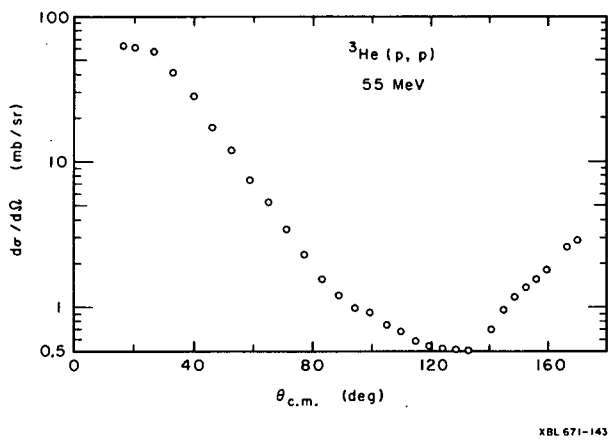

Fig. B.18-1. Differential cross section for the elastic scattering of 55-MeV protons on ^{3}He. The relative errors are about 3% and absolute error is estimated to be less than 5%.

C. NUCLEAR STRUCTURE THEORY

1. THE $^1S_0$ p-p SCATTERING PARAMETERS OBTAINED FROM A REANALYSIS OF EXPERIMENTAL DATA†

R. J. Slobodrian

There are at present several models describing the nucleon-nucleon interaction below 1 GeV. The low-energy S-wave proton-proton scattering should provide a test for the singlet-even interaction predicted by the models. Between 0 and 10 MeV, the S-wave scattering can be represented by a convergent power series,[1] and therefore it can be approximated by a polynomial

$$K = \sum_0^n A_n E^n, \tag{1}$$

where E is the laboratory-system energy, usually expressed in MeV. The explicit relation of Eq. 1 to the $^1S_0$ p-p phase shifts and currently used scattering parameters is obtained through the equation K = RF,

$$F = C^2 k \cot \delta_0 + \frac{1}{R} h(\eta) = -\frac{1}{a_p} + \frac{1}{2} r_e k^2 - P r_e^3 k^4 + Q r_e^5 k^6 - \cdots , \tag{2}$$

where $C^2 = \frac{2\pi\eta}{e^{2\pi\eta}-1}$, $k^2 = \frac{M_p E}{2\hbar^2}$, $R = \frac{\hbar^2}{M_p \epsilon^2}$, and $h(\eta) = \mathrm{Re}\,\frac{\Gamma'(-i\eta)}{\Gamma(-i\eta)} - \ln \eta$.

Here E is again the lab energy; M_p is the proton mass; $\eta = \epsilon^2/\hbar v_{lab}$, usually called Coulomb parameter (ϵ is the proton charge, $\hbar$ is Planck's constant divided by 2π, v_{lab} is the relative velocity); a_p is the proton-proton scattering length; r_e is the effective range; and P and Q are shape-dependent parameters. Existing calculations of Q for different well shapes[2] do indicate that the term in k^6 (Eq. 2) is small compared with the term in k^4, for energies between 0 and 4 MeV lab. Correspondingly, Eq. 1 can be approximated by $K = A + BE + CE^2$. Noyes[3] has calculated the scattering parameters from recent, very accurate experimental phase shifts[4,5] at five low energies between 0.3825 and 3.037 MeV, with the aim of comparing theoretical predictions of the shape parameter P with the experimental value. Such calculations have been repeated by different authors,[6,7] and the results are substantially in agreement, except for fluctuations well within the experimental errors. Nevertheless, some of the problems pointed out a long time ago by Foldy and Eriksen[8] in relation to the empirical evidence for the accuracy of the vacuum polarization correction (from now on called VPC) still remain unresolved if the analysis is restricted to the five above-mentioned experimental points. It can be shown that the determination of the parameter P depends critically on the experimental point at 0.3825 MeV and also on the correctness of the VPC.[7] On the other hand, Gursky and Heller[6] have reported that the Yale[9] and Hamada-Johnston[10] potentials predict a k^6 term in the expansion 2, or correspondingly a cubic term DE^3 in Eq. 1 of "comparable importance" to the quadratic term at 3 MeV lab energy.[11] Gursky and Heller[6] attempted a cubic fit for the five data points between 0.3825 and 3.037 MeV. Figure C.1-1 shows the cubic fit as calculated by the present author, in agreement with their calculation. The values obtained for P and Q are completely unreasonable. An inversion of curvature is produced by the point at 3.037 MeV. The function K thus determined is unacceptable because it diverges strongly from experimental values at higher energies, calculated from the data of Worthington, McGruer, and Findley[12] (from now on called WMF data). The WMF data have been subjected to a phase-shift analysis originally by Hall and Powell[13] and subsequently by de Wit and Durand,[14] who also discussed the VPC with regard to the calculation of proton-proton scattering parameters, as well as relativistic effects, in S and P waves. The singlet S-phase shifts themselves were substantially in agreement in both analyses, within statistics.

Table C.1-I contains 12 experimental values of K between 0.3825 and 4.203 MeV, and also the values K' arrived at after correction for electromagnetic structure effects obtained with models without a static core, with a hard core of radius r_c = 0.4 F, and with a soft core.[15]

The purpose of this note is to report results of least-squares fits to the values of the functions K and K' of Table C. 1-I, and compare the scattering parameters thus obtained with predictions for the shape-dependent parameters P (Refs. 2 and 15) and Q (Ref. 2). For convenient reference to the theoretical predictions of the scattering parameters, Table C. 1-II gives a list of them.

Table C. 1-III contains four-parameter fits to the 12 values of K, together with several others. The fits after the electromagnetic corrections (EMC) are made in a model without a core (NC) is slightly better than the fit to the uncorrected function. In both cases the pair P and Q acquires values not predicted by any existing model. The exclusion of the experimental point at 0.3825 MeV does not alter this conclusion, because P remains small and Q varies within the probable errors. This result is thus fairly independent of the accuracy of the VPC. In order to allow comparison of this result with current fits[3, 6, 7] to the five recently measured experimental points[4, 5] Table C. 1-III lists fits to the 12 values of K given in Table C. 1-I, with the assumption that Q = 0. There is a drift of all the scattering parameters towards higher values than in the five-point fit, and, in particular, P is almost doubled.

Table C. 1-III contains also the function $\chi^2 - \chi^2_{3.037}$ resulting from the subtraction of the χ^2 due to both values at 3.037 MeV. The WMF measurement,[12] as well as the recent measurement,[4] is in good mutual agreement, but both values induce an inversion of curvature, apparently unwarranted by the higher-energy values. The minimum of the function $\chi^2 - \chi^2_{3.037}$ yields values for a_p, r_e, and P in remarkable agreement with values that can be easily interpolated between calculations of Babikov,[16] in the context of a soft-core model due to Babikov et al.[17]

If the values of P predicted by the hard-core potential models of Hamada-Johnston[10] and Yale[9] are used to calculate the remaining parameters, the coefficient D of the cubic term of the polynomial 1 is only 1/400th and 1/20th (respectively) as big as the coefficient C. Thus the experimental data in conjunction with such models do not favor a cubic term of comparable importance to the quadratic term, over the investigated energy range, at variance with the conclusion of Ref. 6.

The results of the present reanalysis are to a certain extent ambiguous, particularly because of the strong contribution to the χ^2 function of the experimental values at 3.037 MeV. Nevertheless the 12 values of K restrict the possible final solutions to two, so that the quadratic term CE^2 is small and the cubic term DE^3 is large, or vice versa. The latter alternative is in excellent agreement with a soft-core model, like the one proposed by Babikov et al.[17] On the theoretical side it would be desirable to have available the prediction of Q for the models currently in vogue, as well as an exploration of core effects on it. It is already known[18] that P varies rapidly as a function of the core parameters, and can be zero. Therefore, a solution with P = 0, or a very small value, cannot be discarded, although presumably in such a case Q would also be small because of core effects.

Footnote and References

† Shortened version of paper published in Nucl. Phys. 85, 33 (1966).

1. J. S. Schwinger, Hectographed Notes on Nuclear Physics, Harvard (1947); Phys. Rev. 72, 742A (1947).
2. J. D. Jackson and J. M. Blatt, Rev. Mod. Phys. 22, 77 (1950).
3. H. Pierre Noyes, Phys. Rev. Letters 12, 171 (1964).
4. D. J. Knecht, S. Messelt, E. D. Berners, and L. C. Northcliffe, Phys. Rev. 114, 550 (1959); P. F. Dahl, D. J. Knecht, and S. Messelt, private communication to H. Pierre Noyes, Ref. 3.
5. J. E. Brolley, J. D. Seagrave, and J. G. Berry, Bull. Am. Phys. Soc. 8, 604 (1963).
6. M. L. Gursky and L. Heller, Phys. Rev. 136, B1693 (1964).
7. R. J. Slobodrian, Nuovo Cimento 40 B, 443 (1965).
8. L. L. Foldy and E. Eriksen, Phys. Rev. 98, 775 (1955).
9. K. E. Lassila, M. H. Hull, Jr., H. M. Ruppel, F. A. McDonald, and G. Breit, Phys. Rev. 126, 881 (1962).
10. T. Hamada and L. D. Johnston, Nucl. Phys. 34, 382 (1962).
11. The conclusion was based on "some low-energy S-wave phase shifts computed by Signell," private communication to M. L. Gursky and L. Heller, Ref. 6.
12. H. R. Worthington, J. M. McGruer, and D. E. Findley, Phys. Rev. 90, 899 (1953).
13. H. H. Hall and J. L. Powell, Phys. Rev. 90, 912 (1953).
14. M. de Wit and L. Durand III, Phys. Rev. 111, 1597 (1958).
15. R. J. Slobodrian, Phys. Rev. 145, 766 (1966).

16. V. V. Babikov, Yadern. Fiz. (USSR) 1, 793 (1965) [translation: Soviet J. Nucl. Phys. 1, 567 (1965)].
17. V. V. Babikov, I. Bystritskii, anf F. Legar, in Twelfth International Conference on High Energy Physics, Dubna, Russia, 1964 (Atomizdat, Moscow, 1966).
18. L. Hulthèn and M. Sugawara, Encyclopedia of Physics, Ed., S. Flügge, Vol. 39 (Springer Verlag, Berlin, Göttingen, Heidelberg, 1957), and references therein.

Table C. 1-I. Experimental values of the function K and of K', corrected for electromagnetic-structure effects in a model without a static core (NC), with a hard core (HC) of radius r_c=0.4 F, and with a soft core (SC) (Ref. 15).

E_{lab} (MeV)	K	K'		
		NC	HC	SC
0.3825[a]	3.86501 ± 0.00274	3.88899	3.84631	3.84042
1.397[a]	4.35428 ± 0.00156	4.37810	4.33517	4.32914
1.855[a]	4.57406 ± 0.00219	4.59780	4.55479	4.54864
1.855[b]	4.57398 ± 0.00243	4.59772	4.55471	4.54856
1.858[b]	4.57232 ± 0.00294	4.59606	4.55305	4.54690
2.425[a]	4.84212 ± 0.00155	4.86575	4.82263	4.81637
2.425[b]	4.84104 ± 0.00320	4.86467	4.82155	4.81529
3.037[a]	5.13318 ± 0.00237	5.15670	5.11347	5.10708
3.037[b]	5.13418 ± 0.00473	5.15770	5.11448	5.10808
3.527[b]	5.35126 ± 0.00575	5.37469	5.33139	5.32488
3.899[b]	5.52449 ± 0.00744	5.54785	5.50449	5.49790
4.203[b]	5.66355 ± 0.01093	5.68687	5.64343	5.63680

a. Data of several authors, Refs. 4 and 5.
b. Data of Worthington, McGruer, and Findley, Refs. 12, 13, and 14.

Table C. 1-II. The $^1S_0$ scattering parameters as calculated by several authors for various models describing the proton-proton interaction.

No.	Model	Parameter			
		$-a_p$ (F)	r_e (F)	P	Q
1	Yukawa[a]	7.6512	2.6756	0.05540	0.019
2	Hamada-Johnston[b] (x_0 = 0.343)	7.729	2.749	0.0478	-
3	Hamada-Johnston[b] (x_0 = 0.341)	8.542	2.664	0.0499	-
4	Breit et al.[b] (x_0 = 0.350)	7.078	2.829	0.0372	-
5	Babikov et al.[b] ($g_\omega^2 - 2f_\omega^2 = 29.2$)	8.710	2.721	0.0371	-
6	Babikov et al.[b] ($g_\omega^2 - 2f_\omega^2 = 29.6$)	7.572	2.840	0.0357	-
7	CSF[c]	7.8426	2.853	0.0612	-
8	PWDR[c]	7.8259	2.786	0.024	-
9	BC[c]	7.8009	2.687	-0.036	-
10	Gaussian well[a]	7.7797	2.6055	-0.01936	-0.00073

a. Values taken from Table VIII of Ref. 2
b. Values taken from Ref. 16
c. Values taken from Table I of Ref. 3

Table C. 1-III. Experimental values of the $^1S_0$ proton-proton scattering parameters, obtained from fits to the function K of Table C. 1-I. The probable errors of the fits that were considered more relevant are given.

EMC	$-a_p$ (F)	r_e (F)	P	Q	χ^2	$P(\chi^2>\chi^2_{fit})$	$\chi^2-\chi^2_{3.037}$	Remarks
	7.8320 ± 0.0035	2.7869 ± 0.0042	-0.0015 ± 0.0035	-0.084 ± 0.024	5.61	0.69	2.98	
	7.8353	2.7970	0.0054	-0.074	-	-	-	11 points fit[a]
	7.8404 ± 0.0035	2.8391 ± 0.0058	0.049 ± 0.003	0	7.08	0.63	2.45	
	7.8603	2.8789	0.059	0	-	-	-	11 points fit[a]
no	7.7939	2.7087	0	0	53.7	~0	39.5	SI fit
	7.8424 ± 0.0034	2.8515 ± 0.0037	0.061 ± 0.002	0.019 ± 0.008	7.86	0.44	2.75	Q of Yukawa well
	7.8402	2.8379	0.0478	-0.0014	7.24	0.52	2.64	P of Hamada-Johnston[b]
	7.8384	2.8267	0.0372	-0.018	6.63	0.57	2.51	P of Breit-Babikov[c]
	7.8381 ± 0.0038	2.8247 ± 0.0019	0.0357 ± 0.0025	-0.021 ± 0.0011	6.53	0.59	2.50	P of Babikov[d]
	7.8365	2.8148	0.026	-0.037	6.22	0.62	2.58	P of Ref. 3[e]
yes NC	7.7790 ± 0.0039	2.7746 ± 0.0051	-0.0124 ± 0.0036	-0.102 ± 0.013	5.47	0.71	3.08	
" HC	7.8808	2.8399	0.0518	0.0042	7.47	0.48	2.96	
" SC	7.8930 ± 0.0030	2.8254 ± 0.0034	0.0365 ± 0.0047	-0.022 ± 0.009	5.98	0.65	2.06	
" NC	7.7888 ± 0.0035	2.8364 ± 0.0058	0.0487 ± 0.0025	0	7.25	0.61	2.54	
" HC	7.8802	2.8368	0.0491	0	7.35	0.60	2.70	errors as in NC
" SC	7.8957	2.8420	0.0510	0	7.42	0.59	3.11	errors as in NC
" NC	7.7908	2.849	0.0602	0.019	7.47	0.48	2.54	Q of Yukawa well
" NC	7.7859	2.8181	0.0315	-0.028	6.30	0.62	2.36	min of $\chi^2-\chi^2_{3.037}$

a. The point at 0.3825 MeV was excluded. Such fits are less dependent on the correctness of the VPC, with regard to P and Q.
b. See Table C. 1-II, No. 2.
c. See Table C. 1-II, No's 4 and 5.
d. See Table C. 1-II, No. 6. This value also furnishes the minimum of $\chi^2-\chi^2_{3.037}$.
e. This value of P is consistent with fits to the more recent experimental values by several authors (Refs. 3, 6, and 7).

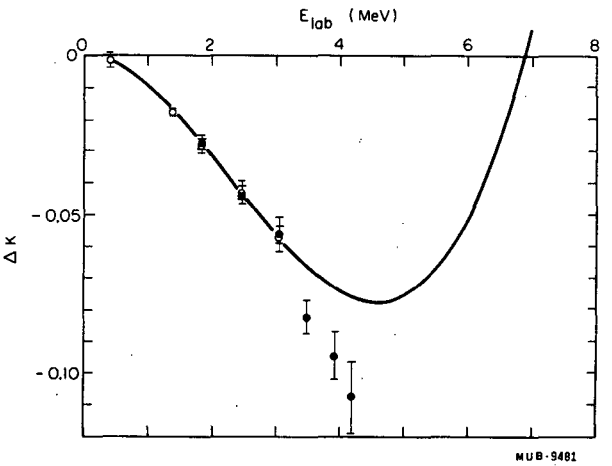

Fig. C. 1-1. Values of the function $\Delta K = K - (A + BE)$ obtained from the experimental phase shifts. The solid line results from the four-parameter fit, $K = A + BE + CE^2 + DE^3$, to the five recent measurements between 0.3825 MeV and 3.037 MeV. The open circles correspond to the data of Refs. 4 and 5. The solid dots are plotted from the WMF data.

2. SMALL-ANGLE HIGH-ENERGY SCATTERING BY DEUTERONS†

Victor Franco

The analysis of interferences between nuclear and Coulomb scattering in pp and pd collisions has become an important means for obtaining information regarding the real parts of the nucleon-nucleon (NN') elastic scattering amplitudes.[1,2] Several experimental and theoretical studies of small-angle high-energy scattering by deuterons have been recently carried out.[1-6] The theoretical analyses are based upon the Glauber diffraction approximation and have treated both single and double interactions. Such investigations are also of current interest because of questions recently raised[7] concerning the applicability of this approximation to high-energy scattering by deuterons, and the suggestion[7] that double-interaction effects may vanish much more rapidly at high energies than is inferred from this approximation. Recent calculations[5] have indicated, however, that even for incident momenta up to 18 GeV/c, this approximation yields results for deuteron total cross sections that agree fairly well with measurements. In this note we compare the theory with high-energy pd differential-cross-section measurements of elastic scattering $(d\sigma/d\Omega)_{e\ell}$, and of the sum of inelastic (i.e., $p + d \rightarrow p + n + p$) plus elastic scattering $(d\sigma/d\Omega)_{sc}$. Since we shall consider small-angle collisions we shall explicitly include the single- and double-scattering effects due to the Coulomb interaction.

By means of the closure approximation, $(d\sigma/d\Omega)_{sc}$ may be approximated by[5] the expectation value of the squared modulus of an operator $F(\vec{q}, \vec{s})$ taken with respect to the deuteron ground state, $(d\sigma/d\Omega)_{sc} = \langle |F(\vec{q}, \vec{s})|^2 \rangle$, where $\hbar\vec{q}$ is the momentum transferred by the incident particle, and $\vec{s}$ is the projection of the internal coordinate $\vec{r}$ of the deuteron on the plane perpendicular to the direction of the incident beam. The differential cross section for elastic scattering is given by $(d\sigma/d\Omega)_{e\ell} = |\langle F(\vec{q}, \vec{s}) \rangle|^2$. In the Glauber approximation, $F(\vec{q}, \vec{s})$ takes the form

$$F(\vec{q}, \vec{s}) = (ik/2\pi) \int e^{i\vec{q}\cdot\vec{b}} \, \Gamma_{tot}(\vec{b}, \vec{s}) d^{(2)}\vec{b}, \tag{1}$$

where the integration is over the plane of impact parameters $\vec{b}$ perpendicular to the direction of the incident beam. The function Γ_{tot} is given by

$$\Gamma_{tot}(\vec{b}, \vec{s}) = 1 - \exp[i\chi_n(\vec{b} - \vec{s}/2) + i\chi_p(\vec{b} + \vec{s}/2)], \tag{2}$$

where χ_n and χ_p represent phase shifts produced by the neutron and proton in their instantaneous positions.

To exhibit the effects of the Coulomb interaction, we write

$$\chi_p(\vec{b}) = \chi_C(\vec{b}) + \chi_{ps}(\vec{b}), \tag{3}$$

where $\chi_C(\vec{b})$ is due to the Coulomb interaction alone, and χ_{ps} is attributed to the pp strong interaction. Putting

$$\Gamma_j(\vec{b}) = 1 - \exp[i\chi_j(\vec{b})], \qquad j = C,\ ps,\ n, \tag{4}$$

we have the identity

$$\Gamma_{tot}(\vec{b},\vec{s}) = \Gamma_C(\vec{b}+\vec{s}/2) + \exp[i\chi_C(\vec{b}+\vec{s}/2)][\Gamma_{ps}(\vec{b}+\vec{s}/2) + \Gamma_n(\vec{b}-\vec{s}/2) - \Gamma_{ps}(\vec{b}+\vec{s}/2)\,\Gamma_n(\vec{b}-\vec{s}/2)]. \tag{5}$$

This identity is to be used in Eq. 1. For high-energy pp scattering, $\chi_C(0)$ is typically small[8] and $\chi_C(\vec{b})$ varies slowly over a range of values for b which does not greatly exceed the range a of the nucleon-incident-particle strong interaction plus the average n-p separation r_d in the deuteron. In addition, for $b \gg a + r_d$, both Γ_n and Γ_{ps} are negligibly small and therefore do not contribute to the integral Eq. 1. Thus for calculating differential cross sections, it is a good approximation to replace the last three terms in Eq. 5 by $\exp(i\chi_1)\Gamma_{ps} + \exp(i\chi_2)\Gamma_n + \exp(i\chi_3)\Gamma_{ps}\Gamma_n$, where the constants χ_1, χ_2, and χ_3 are appropriate "average" values of χ_C. For example, χ_1 is given by $\chi_1 = \int \chi_C\Gamma_{ps}\, d^{(2)}\vec{b} / \int \Gamma_{ps}\, d^{(2)}\vec{b}$.

In Fig. C.2-1 we show the calculations for $(d\sigma/d\Omega)_{sc}$ at 19.3 GeV/c as a function of -t, the negative of the squared four-momentum transfer, together with the data.[1] The measurements present clear evidence for the influence of double scattering, and indicate a rather large effect. In Fig. C.2-2 we compare calculations for $(d\sigma/d\Omega)_{e\ell}$ at several momenta with measured values[3] and with fits[2] to more recent measurements. Our calculations contain no adjustable parameters and use NN' data as input.

Footnote and References

† Condensed from Phys. Rev. Letters 16, 944 (1966).

1. G. Bellettini et al., Phys. Letters 19, 341 (1965).
2. L. S. Zolin et al., Zh. Eksperim. i Teor. Fiz.-Pis'ma Redakt. 3, 75 (1966) [translation: JETP Letters 3, 8 (1966)].
3. L. F. Kirillova et al., Yadern Fiz. 1, 533 (1965) [translation: Soviet J. Nucl. Phys. 1, 379 (1965)]; Z. Korbel, Czech. J. Phys. 14, 741 (1964); Z. M. Zlatanov et al., Izv. Fiz. Inst. s Aneb, Bulgar. Akad. Nauk. 11, 101 (1963).
4. R. J. Glauber, Phys. Rev. 100, 242 (1955).
5. V. Franco and R. J. Glauber, Phys. Rev. 142, 1195 (1966); V. Franco, Deuteron Cross Sections and Stripping Processes at High Energies, (Ph. D. Thesis), Harvard University, 1963.
6. D. R. Harrington, Phys. Rev. 135, B358 (1964); 137, AB3(E) (1965).
7. E. S. Abers et al., Nuovo Cimento 42A, 365 (1965).
8. This property does not hold in the limit of infinite momentum. However, it is true for presently available energies.

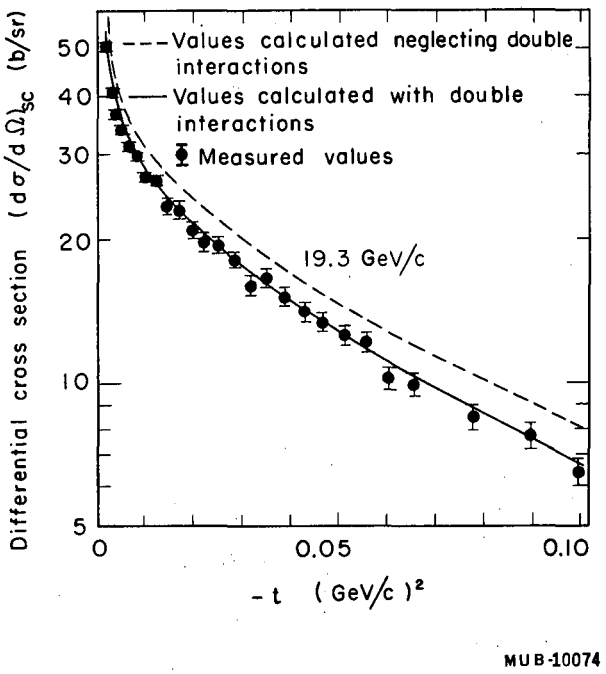

Fig. C.2-1. Differential cross sections for pd elastic plus inelastic scattering as a function of the squared four-momentum transfer t, at an incident proton momentum of 19.3 GeV/c.

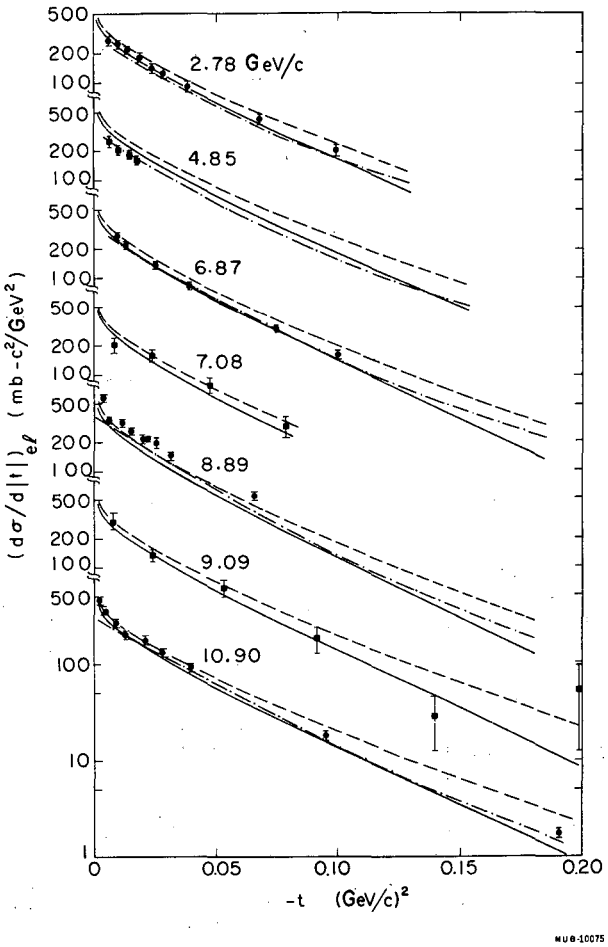

Fig. C.2-2. Differential cross sections for pd elastic scattering between 2.78 and 10.9 GeV/c. Measurements (●, ■) and fits to measurements (dash-dot lines) are compared with calculations which neglect (dashed lines) and which include (solid lines) double scattering. The points (■) for the momentum 4.85 GeV/c are from measurements at 4.67 GeV/c.

3. HIGH-ENERGY DEUTERON-DEUTERON CROSS SECTIONS†

Victor Franco

The deuteron-deuteron cross section is expressed in terms of nucleon-nucleon elastic scattering amplitudes and the deuteron ground-state wave function. Single, double, triple, and quadruple interactions are treated. Calculations are compared with experiment.

The dd total cross section at momentum $\hbar k$ is written in terms of nucleon-nucleon total cross sections as $\sigma_{dd}(k) = \sigma_{nn}(k/2) + \sigma_{np}(k/2) + \sigma_{pn}(k/2) + \sigma_{pp}(k/2) + \delta\sigma_2 + \delta\sigma_3 + \delta\sigma_4$, where $\delta\sigma_2$, $\delta\sigma_3$, and $\delta\sigma_4$ are contributions arising from double, triple, and quadruple interactions, respectively. Expressions are derived for these contributions.

Calculations for σ_{dd} at 2.8 GeV/c yield $\delta\sigma_2 = 21.0$ mb, $\delta\sigma_3 = 1.8$ mb, $\delta\sigma_4 = 0.2$ mb, and $\sigma_{dd} = 145$ mb. This might be compared with measurements[1] at 3 GeV/c which yield a value of 122 ± 7 mb for σ_{dd}.

Footnote and Reference

† Material condensed from UCRL-16694.

1. J. Debaisieux et al., Nucl. Phys. 70, 603 (1965).

4. HIGH-ENERGY DEUTERON CROSS SECTIONS: CHARGE-EXCHANGE EFFECTS†

Victor Franco and Roy J. Glauber‡

The effects of charge exchange in collisions of high-energy particles of isotopic spin 1/2 with deuterons are investigated. The diffraction approximation is used to express the deuteron charge-exchange cross section in terms of the elastic scattering amplitudes of the neutron and proton, and the deuteron ground-state wave function. Examinations are also made of the influence of the charge-exchange mechanism on the total cross section of the deuteron, the elastic differential cross section, and the summed angular distribution of scattering (elastic plus inelastic scattering with initial charges preserved). The important role played by double scattering processes in shaping the differential cross sections of the deuteron is illustrated in a discussion of proton-deuteron elastic scattering at 2 GeV. Double scattering is shown to be the dominant collision mechanism at scattering angles which are not too close to the forward direction. The effect of the double charge-exchange process on the elastic differential cross section is shown to be small but of some significance in the angular range that is dominated by double scattering. The theory developed for charge-exchange reactions is applied to the K^0 angular distribution which has been observed from K^+-deuteron collisions at 2.27 GeV/c. Estimates are found for the differential and integrated K^+-neutron charge-exchange cross sections, and for some related parameters. The effects of double collisions on these cross sections are relatively small and are easily evaluated. The effect of the charge-exchange mechanism on the vlaues of the pn, $\bar{p}n$, and $K^{\pm}n$ total cross section which are reached indirectly via measurements on the deuteron is shown to be exceedingly small for momenta above ~ 2 GeV/c.

We apply our description of deuteron charge-exchange processes to the reaction $d(K^+, K^0)2p$ at 2.27 GeV/c, and illustrate the way in which the cross section for the K^+n charge-exchange reaction $n(K^+, K^0)p$ may be estimated from observations of the K^+d reaction and of K^+p collisions. In so doing, we obtain estimates for the ratio of the real part of the forward K^+n elastic scattering amplitude to its imaginary part, and for the slope of the forward diffraction peak in K^+n elastic scattering.

The differential cross section for the K^+d charge-exchange reaction may be expressed in terms of the K^+p and K^+n elastic scattering amplitudes, f_p and f_n, and the np charge-exchange amplitude $f_c = f_p - f_n$. If we take advantage of the circumstance that the K^+p scattering amplitude varies much more slowly with increasing momentum transfer than does the deuteron form factor, the expression for the charge-exchange cross section reduces to the form

$$(d\sigma/d\Omega)_{ex} = [1 - S(q)]\,|f_c(\vec{q})|^2 - 2k^{-1}\langle r^{-2}\rangle_d \,\mathrm{Im}\{f_c^*(\vec{q})[f_p(\vec{q})f_n(0) - f_n(\vec{q})f_p(0)]\}$$
$$+[\langle r^{-2}\rangle_d/4\pi k^2]\int[\,|f_p(\tfrac{1}{2}\vec{q}+\vec{q}\,')f_n(\tfrac{1}{2}\vec{q}-\vec{q}\,') - f_n(\tfrac{1}{2}\vec{q}+\vec{q}\,')f_p(\tfrac{1}{2}\vec{q}-\vec{q}\,')|^2$$
$$+\,|f_c(\tfrac{1}{2}\vec{q}+\vec{q}\,')f_c(\tfrac{1}{2}\vec{q}-\vec{q}\,')|^2\,]\,d^{(2)}\vec{q}\,',$$

where S(q) is the form factor of the deuteron ground state, and $\langle r^{-2}\rangle_d$ is the mean-inverse-square neutron-proton separation in the deuteron ground state.

The observed[1] angular distribution of the K^0 meson in the laboratory system is shown in Fig. C.4-1 for $\cos\theta_{lab} \gtrsim 0.85$. The calculation is represented by the solid curve. To illustrate the magnitude of the double-scattering correction, we have calculated $(d\sigma/d\Omega)_{ex}$ with double-

scattering effects neglected. The results, shown by the dashed line in Fig. C.4-1, indicate that double-scattering effects are small within the angular region $\theta_{lab} \lesssim 30$ deg. The differential cross section for the reaction $K^+n \rightarrow K^0p$ is simply $|f_c|^2$. Over the angular range $\theta_{lab} \gtrsim 10$ deg, where $|S(q)| << 1$, the form $|f_c|^2$ is very nearly the angular distribution for $K^+d \rightarrow K^0pp$ given without treating double-scattering effects, and is therefore represented by the dashed line in Fig. C.4-1. At smaller angles the effects of the exclusion principle must be accounted for and the K^+n charge-exchange angular distribution extrapolates to 0 deg along the dotted curve.

The differential cross section $(d\sigma/d\Omega)_{ex}$ for K^+d charge exchange may be analyzed in terms of single scattering, interference between single and double scattering, and pure double scattering. In Fig. C.4-2 we show the angular distributions of these three components of the differential cross section. The contribution arising from the interference term is negative; the curve shown corresponds to its absolute value. The magnitude of the interference term is always considerably smaller than the single-scattering term, and for $\cos\theta_{lab} \lesssim 0.9$ has an angular distribution rather similar in form to the single-scattering term. The pure double-scattering term gives the only nonzero contribution in the forward direction.

Footnotes and Reference

† Material condensed from article (UCRL-17142) submitted to Phys. Rev.
‡ Present address: Harvard University, Cambridge, Massachusetts.

1. I. Butterworth, J. L. Brown, G. Goldhaber, S. Goldhaber, A. A. Hirata, J. A. Kadyk, B. M. Schwarzschild, and G. H. Trilling, Phys. Rev. Letters 15, 734 (1965).

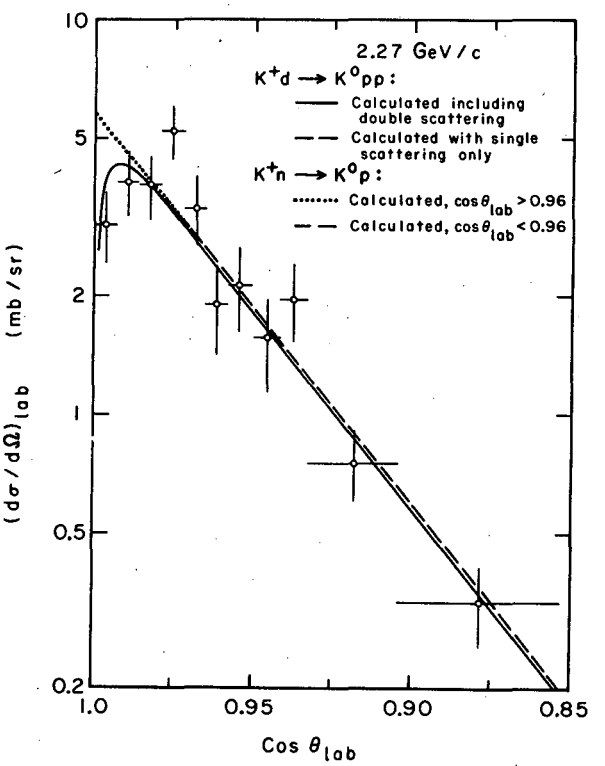

MUB-13003

Fig. C.4-1. Differential cross sections in the laboratory system for K^+d and K^+n charge-exchange scattering at 2.27 GeV/c as a function of $\cos\theta_{lab}$, the cosine of the K^0 scattering angle. The data for $K^+d \rightarrow K^0pp$ are from Ref. 1. The solid curve is calculated for $K^+d \rightarrow K^0pp$ with double scattering taken into account. The broken curve is calculated for $K^+d \rightarrow K^0pp$ with double scattering neglected, and coincides with the solid curve for $\cos\theta_{lab} \gtrsim 0.98$. The dotted curve, which coincides with the broken curve for $\cos\theta_{lab} \lesssim 0.96$, is the calculated angular distribution for $K^+n \rightarrow K^0p$.

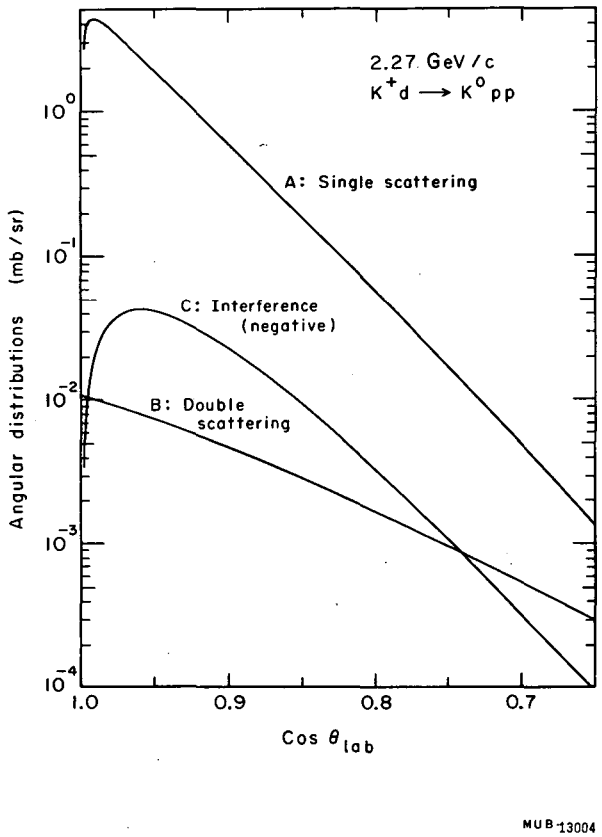

Fig. C.4-2. Angular distribution of the components of the K^+d charge-exchange intensity as a function of cos θ_{lab}. The incident K^+-meson lab momentum is 2.27 GeV/c. Curve A represents the single-scattering contribution and curve B the double-scattering contribution. Curve C represents the contribution from the interference between the single- and double-scattering processes, and is negative in sign.

5. DOUBLE SCATTERING IN HIGH-ENERGY ELASTIC COLLISIONS WITH DEUTERONS†

Victor Franco and Ernest Coleman‡

In this note we suggest an explanation for the broad shoulder observed in recent measurements[1] of pd elastic scattering at 2 GeV, and propose an experiment to establish clearly whether or not double-scattering effects in deuterons persist at high energies. Analyses[2,3] of a variety of particle-deuteron cross sections suggest that these effects persist at least up to energies of 18 GeV. The influence of double scattering on the cross sections which have been considered up to now, however, has been considerably smaller than that of single scattering. We suggest that high-energy pd elastic scattering at $0.5\ (\mathrm{GeV}/c)^2 \lesssim -t \lesssim 1.5\ (\mathrm{GeV}/c)^2$, where t is the squared four-momentum transfer, consists mainly of double scattering. A test of this suggestion at high energies could have a bearing on the question of Regge-pole dominance, since it has been argued that if the nucleon-nucleon (NN) scattering amplitudes near the forward direction can be represented as a sum of Regge poles, double-scattering effects should vanish much more rapidly at high energies than is inferred from the Glauber approximation.

The differential cross section $d\sigma/d\Omega$ for xd elastic scattering may be written in the Glauber approximation in terms of the xp and xn elastic-scattering amplitudes f_{xp} and f_{xn} as

$$d\sigma/d\Omega = \left|S(\tfrac{1}{2}\vec{q})[f_{xn}(\vec{q}) + f_{xp}(\vec{q})] + (\tfrac{1}{2}\pi k)\int S(\vec{q})\langle f_1(\tfrac{1}{2}\vec{q} + \vec{q}\,')f_2(\tfrac{1}{2}\vec{q} - \vec{q}\,')\rangle d^{(2)}\vec{q}\,'\right|^2, \qquad (1)$$

where f_1 and f_2 are scattering matrices for collisions between particle x and target nucleon 1, and between particle x and target nucleon 2. The product f_1f_2 is an operator in the composite isotopic-spin space of particle x and nucleons 1 and 2. The brackets $\langle\ \rangle$ denote the expectation

value with respect to the deuteron ground state, which is an isotopic singlet (I = 0) state, and with respect to the initial isotopic-spin state of the incident particle. This expression does not violate the charge independence of nuclear forces, and it includes elastic double-charge-exchange processes, i.e., processes in which the incident proton undergoes a charge exchange with the target neutron, and the resulting scattered neutron then undergoes a charge exchange with the target proton, with the final state of the target being the deuteron ground state. At momentum transfers larger than approximately 0.5 GeV/c, this expression differs rather dramatically from that in which the integral--i.e., double scattering term--is neglected.[4] We shall be concerned here with t in the range $0 \leq -t \lesssim 1.5\ (\mathrm{GeV}/c)^2$, where NN measurements are fairly well represented by elastic-scattering amplitudes of the form $f_{xN}=(i+\alpha_{xN})(k\sigma_{xN}/4\pi)\exp(\frac{1}{2}a_x t+\frac{1}{2}b_x t^2)$, where N = n, p.

The calculations (shown by the solid curve in Fig. C. 5-1), together with the measurements,[1,5] present evidence for the importance of double scattering at 2 GeV. The predicted minimum and secondary maximum, the existence of which is perhaps suggested by the measurements, result from the destructive interference between the single- and double-scattering amplitudes, and from the relatively large amount of double scattering at $-t \gtrsim 0.5\ (\mathrm{GeV}/c)^2$. Our calculations indicate that the shoulderlike departure of the -t data between 0.4 and 1.5 $(\mathrm{GeV}/c)^2$ from the exponential trend of the diffraction peak is not of the same nature as the secondary peaks observed in recent $\pi^{\pm}p$ and K^-p elastic scattering. Note that this calculation contains no adjustable parameters and that the input was determined from NN measurements. It should be clear that changes within the quoted statistical errors for the input could yield even better agreement with the pd data, but that no such changes would yield very large qualitative differences.

Footnotes and References

† Condensed from Phys. Rev. Letters 17, 827 (1966).

‡ Present address: The University of Michigan, Ann Arbor, Michigan.

1. E. Coleman et al., Phys. Rev. Letters 16, 761 (1966).
2. V. Franco and R. J. Glauber, Phys. Rev. 142, 1195 (1966).
3. V. Franco, Phys. Rev. Letters 16, 944 (1966).
4. V. Franco, Deuteron Cross Sections and Stripping Processes at High Energies, (Ph. D. Thesis), Harvard University, 1963, p. 67.
5. L. S. Zolin et al., Zh. Eksperim. i Teor. Fiz.-Pis'ma Redakt. 3, 15 (1966)[translation: JETP Letters 3, 8 (1966)].

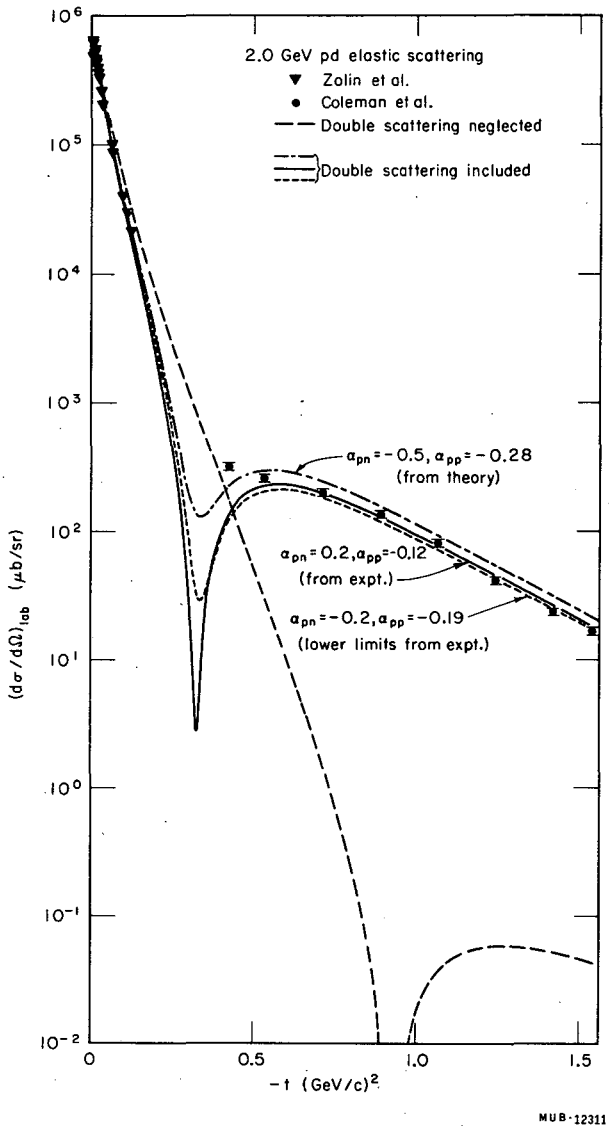

Fig. C. 5-1. Differential cross sections in the laboratory system for elastic pd scattering at 2 GeV. The solid curve is the theoretical prediction, based on nucleon-nucleon data, when double scattering is treated, the broken curve when it is neglected. The dotted and dot-dashed curves are calculated with the experimental lower limits for α_{pn} and α_{pp} and with theoretical predictions for α_{pn} and α_{pp}, and include double scattering.

6. INELASTIC SCATTERING

Norman K. Glendenning

Interest in inelastic scattering of nucleons and light nuclides by nuclei was concentrated on the strong collective transitions until the energy resolution, through a succession of improvements, permitted the beginning of a study of the other levels. By their nature, collective excitations, involving as they do the coherent participation of many nucleons, are amenable to a macroscopic description, as given by Bohr and Mottelson. This is not true of the weaker transitions, which are weak either because they correspond to the promotion of a single nucleon (in which case the particular single-particle states involved are crucial), or, if the state is of a complicated structure, because the many nucleons participate destructively (in which case the details of the destructive interference are crucial).

Concurrent with the improvements in the experiments, advances in theoretical techniques have brought a better understanding of nuclear states in terms of their microscopic structure.

Thus interest has been revived in the microscopic description of inelastic scattering since it can handle both the collective and hindered excitations on the same footing, in terms of the elementary nucleon excitations.[1]

There is another motive for exploring such detailed nuclear descriptions, and that is the expectation that the higher energy spectrum may contain additional types of collective states. Such states are believed to exist because the nucleon-nucleon force is a complicated one, depending as it does on the state of the interacting pair. There is a tendency for many particle systems to form states that exploit one component or other of the force by means of appropriate correlations. It is hoped that model calculations which explore the role of the different parts of the force in determining the nuclear structure, together with a calculation of the resulting inelastic cross sections and polarizations, may help in identifying and suggesting in what way some of these states can be observed.

The most accurate method of calculating inelastic cross sections and polarizations is provided by the coupled-channel method. This method takes into account both the direct excitations from the ground state and the multiple excitations through the other excited states of the system. A computer program has been prepared which solves this problem, using a detailed microscopic description of the nuclear states. A detailed discussion of the physical assumptions and the mathematical formulation is given elsewhere.[2]

References

1. N. K. Glendenning and M. Veneroni, Phys. Rev. 144, 839 (1966).
2. N. K. Glendenning, Coupled-Channel Calculation of Inelastic Scattering Based on a Microscopic Nuclear Description, UCRL-16841, April 1966.

7. TEST OF A MICROSCOPIC DESCRIPTION OF NICKEL ISOTOPES BY INELASTIC PROTON SCATTERING*

Norman K. Glendenning, B. G. Harvey, D. L. Hendrie,
O. N. Jarvis, and J. Mahoney

The main thrust of the theory of nuclear structure in recent years has been directed towards obtaining a detailed understanding of the microscopic structure of nuclei. At this level all nuclear phenomena, the collective as well as the single-particle aspects, are described in terms of the underlying nucleon motions and their correlations. The theoretical methods developed for this purpose have proven capable of explaining the energy-level systematics and some of the prominent features of transition rates. A still more stringent test is provided by the analysis of inelastic nucleon scattering.

Protons of about 17.7 MeV were scattered from targets of ^{58}Ni and ^{60}Ni. Some of the experimental angular distributions are shown in Fig. C.7-1. Unfortunately there is some uncertainty about the spin and parity assignments of the low-lying states of ^{58}Ni. Table C.7-I shows the assignments that can be deduced from a study of inelastic scattering of 50-MeV helium ions[1] and from (p,p'γ) measurements.[2] Figure C.7-1 shows no experimental angular distribution for an excited 0^+ state of ^{58}Ni because the candidate level at 2.934 MeV was not sufficiently well resolved from the 2.899-MeV level.

Angular distributions (solid lines of Fig. C.7-1) were calculated by the coupled-channel method,[3] with the wave functions of Arvieu, Salusti, and Veneroni used.[4] These authors diagonalized the nuclear Hamiltonian in a subspace of two quasi-particle configurations. This treatment can describe the collective states that correspond to the one-phonon states of the vibrational model. Comparing the calculated and observed cross sections shown in Fig. C.7-1 for the 2_1 and 4_1 states suggests that the microscopic description of these states is fairly good. For ^{58}Ni (but not for ^{60}Ni), the microscopic theory describes quite well the cross section to the second 2^+ level. However, the calculated cross section for the 2_3 levels is much smaller than observed. Evidently there is a good deal more strength going into these 2^+ levels than the theory describes. This suggests that there is some two-phonon character in these states, or possibly distributed over several of the 2^+ states in this region. Such an admixture would probably enhance the total transition

strength by virtue of the strong coupling between the one- and two-phonon states.

The inelastic scattering of helium ions suggests, moreover, that there should be some two-phonon admixture to the 2.772-MeV level of ^{58}Ni. This level has been assigned spin 2 or 3 (Ref. 5). The helium-ion angular distribution is in phase with the elastic angular distribution. A spin of 3^- would give such a result, but negative parity states should not be so low in ^{58}Ni. The only possibility remaining is that this is a 2^+ state made by a double excitation.

Although the coherent collective states seem to be reasonably well described by the two-quasi-particle approximation, the inclusion of four-quasi-particle configurations seems highly desirable for a more complete description of the higher states.

Footnote and References

* Based on paper presented at International Conference on Nuclear Physics, Gatlinburg, Tennessee, 1966.

1. O. N. Jarvis, D. L. Hendrie, J. Mahoney, and B. G. Harvey (LRL), unpublished work, 1966.
2. P. F. Hinrichsen, G. T. Wood, and S. M. Shafroth, Nucl. Phys. 81, 449 (1966).
3. N. K. Glendenning, Phys. Letters 21, 549 (1966).
4. R. Arvieu, E. Salusti, and M. Veneroni, Phys. Letters 8, 334 (1964); N. K. Glendenning and M. Veneroni, Phys. Rev. 144, 839 (1966).
5. L. W. Swenson and R. K. Mohindra, in Proceedings of a Topical Conference on the Basis for Nuclear Spin Assignments, Gatlinburg, Tennessee, 1965.

Table C.7-I. Excited levels of ^{58}Ni consistent with Refs. 1 and 2 and with the present work.

J^π	2_1^+	4^+	(2_2^+)	(1^+)	0^+	2_3^+	2_4^+
E(MeV)	1.452	2.458	2.772	2.899	2.934	3.035	3.260

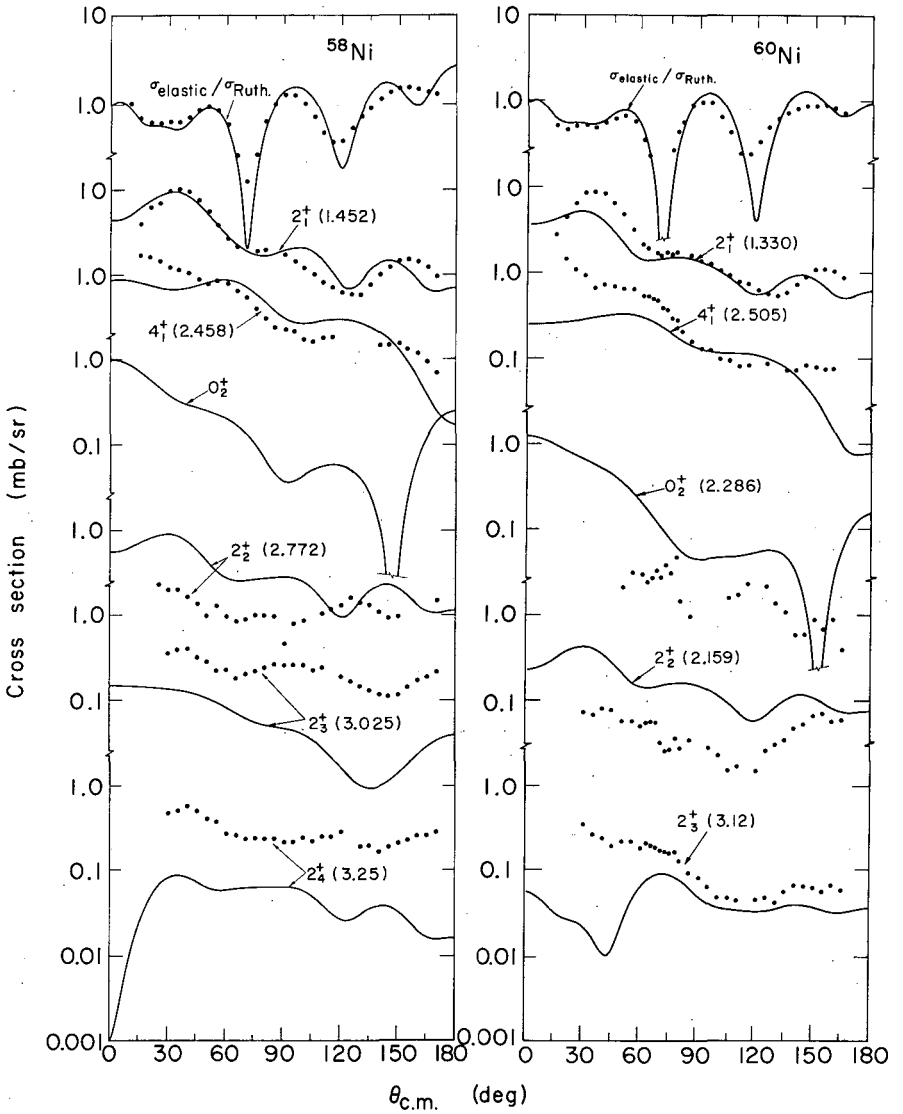

Fig. C.7-1. Observed proton cross sections for low-lying prominent levels of ^{58}Ni and ^{60}Ni are compared with calculations based on a microscopic nuclear description obtained by the coupled-channel method.

8. ANALYSIS OF THE ^{208}Pb(p,t) REACTION*

Norman K. Glendenning

Introduction

Two-nucleon transfer reactions, as has already been emphasized, are highly sensitive to the type of correlations that exist between the transferred pair in their nuclear state. For this reason they should provide a very important means of testing detailed nuclear descriptions. The theory of these reactions can be formulated in such a way as to concentrate their dependence on the nuclear structure in one set of amplitudes, and the dynamical description of the reaction in

another.[1] Before the full potential of this type of reaction can be realized, one has to know that the dynamic part can be handled satisfactorily. There has been little opportunity to investigate this point so far. Recently, however, differential cross sections for the reaction ^{208}Pb(p, t) leading to a number of states in ^{206}Pb were reported.[2] Not only are the nuclear wave functions in these cases known as well as, or better than, in any other nuclei, but the dependence of some of the transitions on the nuclear description is minimal, as we explain in the next section. In addition, and of vital importance, is the absence of strongly enhanced transitions in the inelastic scattering channels. This permits an interpretation of the transfer reaction in terms of the simple direct mechanism as contrasted with the complication attendant on core excitation.

This note is devoted first to the question concerning the dynamics of the two-nucleon transfer reaction. It is found in fact that the probability for a direct transfer, calculated in the distorted-wave Born approximation, gives a very good account of the angular distributions. Thus encouraged to trust the calculation of the dynamical parts of the transfer amplitude, we proceed to a detailed calculation of the cross sections implied by the shell-model description of ^{206}Pb given by True and Ford.[3]

Theory

For each transition multipole (L, S, J), the information carried in the nuclear wave functions that is relevant to the reaction can be concentrated into a set of structure amplitudes G_{NLSJ} in a way described in our earlier work.[1] Here N refers to the number of nodes in the radial function describing the center of mass of the transferred pair, and L, S, and J refer to the orbital, spin, and total angular momentum of the pair with respect to the nuclear center. In general, several multipoles (L, S, J) can contribute to a given transition. However, for (p, t) transitions connecting even-even nuclei, only one is allowed, the one with S = 0 and L = J equal to the spin of the excited state. Thus for each transition we need to specify one set of G_N, $N = 1, 2, \cdots$. From our knowledge of the ^{207}Pb spectrum, we know the single-particle spectrum.[4] From it we can conclude fairly safely that for the low-lying positive parity states of ^{206}Pb, the dominant configurations will involve only the $3p_{1/2}$, $2f_{5/2}$, and $3p_{3/2}$ single-particle states, which all belong to the same oscillator shell. The significance of this is that for a state having the favored correlations, one member of the set of amplitudes, G_N, will dominate.[5] For such a state that value of N will be $N = [(2\mathcal{N} - L)/2] + 1 = 6 - L/2$ (for Pb), where the oscillator quantum number ℓ of the single-particle state n, ℓ is defined as $\mathcal{N} = 2(n-1)+\ell$. We have thus argued that, for a strong transition to any low-lying positive parity level of ^{206}Pb, we know the radial state from which the pair is taken and therefore can calculate the angular distribution (though not the magnitude) without a detailed knowledge of the nuclear wave function. Thus transitions to the lowest $J = 0^+$, 2^+, and 4^+ levels are characterized as 6s, 5d, and 4g respectively. This is the meaning of our statement in the Introduction that the nuclear structure enters the description of some of the ^{208}Pb(p, t) transitions in a minimal way.

Results

Enhanced Transitions: Test of the Reaction Theory

For each lowest state of spin $J = 0^+$, 2^+, and 4^+, the angular distribution for the (p, t) reaction has been calculated. In each case the radial function, as we argued in the previous section, is essentially known, aside from its normalization. Its asymptotic behavior should be determined by the energy required to remove the pair, leaving the residual nucleus in the energy state under consideration. In the interior region we represent it by a harmonic oscillator function. If the single-particle states have the oscillator parameter $\nu (= m\omega/\hbar)$, then the center of mass of a pair of nucleons has the parameter 2ν. We use the same value as True and Ford,[3] $\nu = 0.185\ F^{-2}$. In Ref. 1 we suggested two possible ways of handling the bad asymptotic behavior of the harmonic oscillator functions. One is that used here. The other consists in using single-particle states of a Woods-Saxon potential. This will yield a wave function for the center of mass of the pair which is improved over a pure harmonic oscillator function in the sense that it does not decay so rapidly, and hence will yield improved results for the calculated angular distribution, as was emphasized recently by Drisco and Rybicki.[6] However, this function still does not have the asymptotic behavior associated with the separation energy of the pair. We therefore prefer our first prescription.

We calculate cross sections using the distorted-wave Born approximation with an interaction between the proton and center of mass of the neutrons having zero range. The optical-model parameters are taken from the literature.[7] They are shown in Table C.8-I.

The calculated angular distributions for the lowest state of each spin J = 0^+, 2^+, and 4^+ are compared in Fig. C. 8-1 with the data of Reynolds, Maxwell, and Hintz. The agreement in each case is excellent and tends to confirm the theoretical description of the two-nucleon transfer reaction. (Note that some authors have used a point-triton approximation.[8] This is not equivalent to our assumption of a zero-range interaction, but is additional to it and in particular leads to quite different radial functions for the center of mass of the transferred pair. This fact has also been emphasized by Broglia and Riedel.[9] However, the reaction is concentrated at the surface to such an extent that both radial functions would yield almost the same angular distribution, though they would, in general, lead to different cross sections.)

Cross Sections: Test of the Nuclear Model

Having confirmed the theory of the reaction mechanism for those levels for which the nuclear structure enters in a minimal way in determining the angular distribution, we now consider the cross sections of transitions to all levels. The wave functions for ^{206}Pb have been obtained through a shell-model calculation by True and Ford.[3] Since ^{208}Pb is doubly magic, its ground-state wave function, to excellent approximation, will be the pure closed-shell wave function. The structure amplitudes based on these wave functions were calculated by Reynolds, Maxwell, and Hintz. Even without a calculation of the transfer amplitudes, one is able, as these authors did, to draw conclusions about some relative intensities. However, we have proceeded to calculate the cross sections to all levels computed by True and Ford to lie below about 3 MeV. Some of these have small cross sections and were not observed. Of the observed levels, angular distributions to the higher-lying levels are shown in Fig. C. 8-2. In two cases, the observed peak was known to contain a doublet, and for these we compare the summed computed angular distributions. Also shown are the separate angular distributions in case subsequent experiments resolve the levels. The integrated cross sections for all natural-parity levels (which alone can be excited in this reaction), predicted to be in the energy range considered, are listed in Table C. 8-II, together with the observed cross sections. Our calculation does contain for each level a common factor which we do not calculate, but evaluate by normalizing to the 4_1^+ level.

Surveying the angular distributions shown in Fig. C. 8-1 and C. 8-2 reveals excellent agreement in most cases, the most notable exception being the unresolved doublet at 2 MeV, thought to contain the 4_2^+ and 7_1^- states. As is well known, however, the angular distribution for a process in which the transfer of angular momentum occurs mainly in the surface region is not particularly sensitive to the details used to describe the reaction, when a single multipole alone is allowed. Of course, each multipole generally has its own angular distribution. Therefore the angular distribution, when several multipoles are allowed, will depend upon the details, since they determine the weight with which the individual multipoles contribute. However, that is not the situation for the reaction considered here, so we have to look to the absolute cross sections to provide a more stringent test of the nuclear wave functions. Table C. 8-II shows that levels for which small cross sections are calculated are either not observed or are only weakly excited. Of the more strongly excited levels, the agreement is generally good. Undoubtedly some uncertainty should be attached to the calculated cross sections because of factors such as ambiguities in the optical model parameters, or neglect of finite-range effects. An uncertainty of 30% is often quoted for single-nucleon transfer reactions, although relative cross sections should be better determined. There is also an uncertainty of ±20% in the measured cross sections. The experiment and theory agree within the combined errors in all cases. Agreement within such a large error is perhaps more significant than one would at first consider, inasmuch as transition rates are a rather sensitive probe of the wave functions.

The greatest discrepancy seen in Table C. 8-II occurs for the ground-state transition. It is actually to this transition that the neglected ground-state correlations consisting of excited pairs in the neutron shell above N = 126 would make their contribution. Although such admixtures may be small, they are coherent.

The 9^- level, calculated to be at 2.6 MeV, was not seen in the experiment. Since its calculated cross section is of an easily observed magnitude and since the calculated cross section for the near-lying 5^- level falls short of what is measured, we suggest that the group at 2.8 MeV actually contains both the 9^- and 5^- levels. Similarly the 4_3^+ level calculated to be at 3.01 MeV probably contributes to the groups observed at 3.1 MeV, as well, possibly, as does the 7_2^-.

In connection with Table C. 8-II, note also that almost the entire transition strength for each multipole is gathered into a single state. This is of course a reflection of the sensitivity of the reactions to certain correlations between the pair (in this case ^{1}S), so that states possessing the favored correlations are favored. That the lowest state of each spin is the one that possesses

the favored correlations is a reflection of the importance of the attractive singlet-even part of the interaction in binding that state.

Summary

Differential cross sections to all levels below about 3 MeV in ^{206}Pb that can be excited by the (p, t) reaction have been calculated with the distorted-wave method, under the assumption of a simple direct transfer as distinguished from sequential transfers or excitation of the core. The angular distributions of several of the transitions are insensitive to the details of the nuclear wave functions, and these were used to provide a test of the reaction mechanism assumed. These angular distributions are in near-perfect agreement with experiment. The integrated cross sections for many levels, calculated with True and Ford's wave functions, were compared with the experimental data. The agreement at worst was about a factor 2. Since transition rates provide a quite stringent test of the nuclear description, it is felt that the True-Ford wave functions provide a quite accurate description of most of the states, particularly since some or all of the discrepancy could be blamed on the summed errors of the experiment and reaction calculation.

Of more general interest, we conclude that when there is good reason to believe that the simple direct process dominates a double-transfer reaction, an analysis in terms of the theory employed here[10] can be used to test the nuclear wave functions. Such programs have already been reported by several authors.[9,11]

Footnote and References

* Abbreviated version of UCRL-17199 (to be submitted to Phys. Rev.).

1. N. K. Glendenning, Phys. Rev. 137, B102 (1965); Ann. Rev. Nucl. Sci. 13, 191 (1963); ANL-6848, 1964.
2. G. M. Reynolds, J. R. Maxwell, and Norton M. Hintz, Phys. Rev. (in press).
3. W. W. True and K. W. Ford, Phys. Rev. 109, 1675 (1958).
4. D. E. Alburger and A. W. Sunyar, Phys. Rev. 99, 695 (1955); N. H. Lazar and E. D. Klema, Phys. Rev. 98, 710 (1955).
5. For a given configuration, the G_N are generally monotonic, increasing to the maximum allowed N. [This follows from the behavior of the overlap integral on the relative motion contained in G_N (see Ref. 1)]. When all configurations belong to the same oscillator shell, each has the same maximum N. A correlated state will have such phases that the contribution of all configurations to this last G_N will be coherent.
6. R. M. Drisco and F. Rybicki, Phys. Rev. Letters 16, 275 (1966). All publications based on our work since 1963 have treated the asymptotic region properly, and consequently are not subject to the criticism implied by Drisco and Rybicki.
7. The proton parameters are taken from M. P. Fricke and G. R. Satchler, Phys. Rev. 139, B567 (1965). The triton parameters are attributed to G. R. Satchler by S. Hinds et al., Nucl. Phys. 83, 17 (1966).
8. J. R. Rook and D. Mitra, Nucl. Phys. 51, 96 (1964); R. N. Glover, A. D. W. Jones, and J. R. Rook, Nucl. Phys. 81, 289 (1966).
9. R. A. Broglia and C. Riedel, preprint (Niels Bohr Institute, Copenhagen, Denmark).
10. See Ref. 1 and also E. M. Henley and D. V. L. Yu, Phys. Rev. 133, B1445 (1964); C. L. Lin and S. Yoshida, Progr. Theoret. Phys. (Kyoto) 32, 885 (1964); and B. Bayman, ANL-6878, 1964.
11. J. J. Wesolowski, L. F. Hansen, J. G. Vidal, and M. L. Stelts, Phys. Rev. 148, 1063 (1966); J. Vervier, Phys. Letters 22, 82 (1966), and Proceedings of the International Conference on Nuclear Physics, Gatlinburg, Tennessee, September, 1966 (to be published); see also C. H. Hoot, ibid., who uses a diffraction model for the calculation of the transfer amplitudes and our formulation for the structure amplitudes; C. L. Lin, Progr. Theoret. Phys. (Kyoto) 36, 251 (1966).

Table C. 8-I. Optical-model parameters (energy in MeV; length in fermis)

	V	W	W_D	r_v	r_w	r_c	a_v	a_w
p	51	8	0	1.2	1.428	1.2	0.65	0.704
t	160	20	0	1.1	1.6	1.4	0.75	0.75

Table C. 8-II. Natural-parity states of ^{206}Pb that lie below about 3 MeV. Values for experimental cross sections are compared with calculated values. Also listed are total calculated cross sections.

Level (MeV)		Spin	Cross section (mb)		
			Integrated over observed range[b]		Total calculated[c]
Calc.	Obs.[a]		Obs.[a]	Calc.	
0	0	0_1^+	140	94	131
0.725	0.8	2_1^+	500	410	550
1.36		0_2^+	≤ 15	10	14
1.39		2_2^+	≤ 15	23	31
1.68	1.68	4_1^+	300	300	650
1.77		2_3^+	small	2	6
2.06		0_3^+	not seen	11	32
2.01	2.	4_2^+	180	49	110
2.17		7_1^-		230	550
2.19		2_4^+	not seen	6	18
2.53		2_5^+	not seen	10	27
2.53[d]		3_1^-	not seen	--	--
2.60		9_1^-	?	98	530
2.81	2.8	5_1^-	210	120	250
2.98		7_2^-	?	16	42
3.01		4_3^+	?	58	120
3.06	3.1	5_2^-	450	76	150
3.15		6_1^+		280	570

a. Groups observed in Ref. 2.
b. The first four entries are results of integrating from 10 to 60 deg and the rest from 10 to 30 deg. Theory is normalized to the 4_1 state.
c. Calculated cross section integrated from 0 to 180 deg with normalization to the 4_1 state.
d. Not seen in experiment of Ref. 2, nor calculated by True and Ford. See Nuclear Data Sheets (National Academy of Sciences).

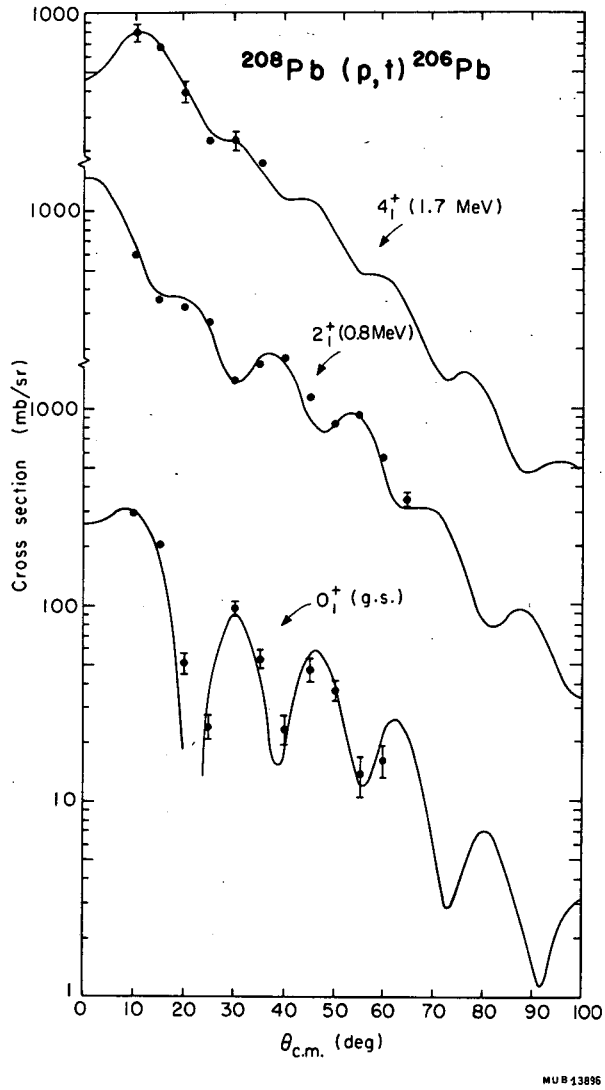

Fig. C. 8-1. Differential cross sections for the first 0^+, 2^+, and 4^+ states in ^{206}Pb excited by 40-MeV protons in the (p, t) reaction. Solid lines are calculated as described in text. Data are from Ref. 2.

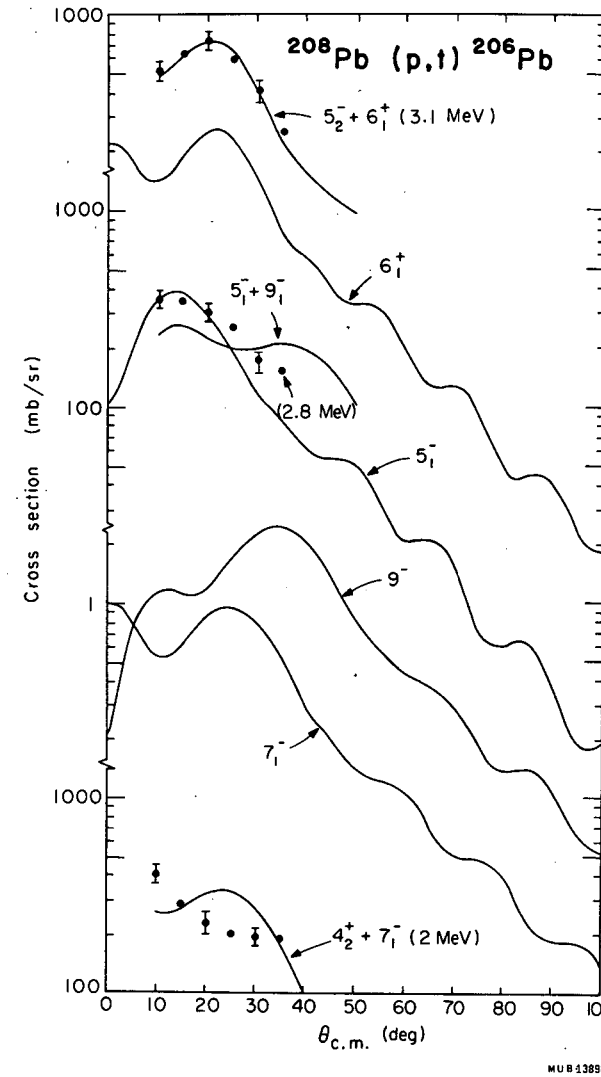

Fig. C. 8-2. Differential cross sections for higher levels in ^{206}Pb excited by 40-MeV protons in the (p, t) reaction. Solid lines are calculated as described in text.

9. CALCULATIONS OF THE FLATTENING OF IDEALIZED NUCLEI DURING HEAD-ON COLLISIONS

Jaromir Maly and James Rayford Nix

When two charged liquid drops closely approach each other, they tend to flatten as a result of their mutual electrostatic forces. The amount of flattening depends upon the relative strengths of the electrostatic and surface forces, and in addition upon the drops' vibrational periods relative to their collision period (the amount of time during which the drops are separated by distances less than a few nuclear radii). The vibrational period of a drop is a function not only of its restoring forces against deformation, but also of its vibrational effective mass (inertia)[1-3] and

of the viscosity of the fluid flow.

The dependence of the amount of flattening upon the effective mass and the viscosity suggests an experimental method for determining information regarding these quantities: Bombard a variety of nuclei throughout the periodic table, observing the energies at which they first begin to interact through nuclear forces in head-on collisions. If either the effective inertia for flattening or the viscosity of nuclear matter were exceptionally large, the nuclei would remain essentially spherical as they approached, and the required energies would correspond approximately to those in bringing two undeformed spheres from infinity to distances such that their nuclear force fields first begin to interact. If, on the other hand, both the mass and the viscosity are low, the nuclei would flatten somewhat as they approached, and a larger energy would be required to bring their nuclear force fields into contact.

As discussed, for example, in Ref. 4, the nuclear surface is not sharp but is diffuse, and in addition the nuclear force extends beyond the nuclear-matter distribution. Thus if the nuclei were to remain spherical as they approached, the distance ℓ at which their nuclear force fields would begin to interact would be given approximately by $\ell = (R_1 + t) + (R_2 + t)$. In this equation R_1 and R_2 are the radii of the target and projectile, respectively. From the Stanford electron-scattering experiments[5] we know that the radius to the point where the density of nuclear matter has decreased to one-half its central value may be related to the atomic mass number according to $R = r_0 A^{1/3}$, where $r_0 = (1.07 \pm 0.02)$F. The quantity t, which should be approximately independent of the mass number, is a characteristic thickness, so that $R + t$ is the radius at which the nuclear forces are effective. The magnitude of t would depend somewhat upon the particular experiment that is used to measure the point at which the nuclear force fields begin to interact. It would probably be smaller, for example, for the detection of the transfer of nucleons from the projectile to the target, or vice versa, than for the detection of small deviations of the angular distribution of the scattered particles from the predictions of the Rutherford formula.

We recommend that transition nuclei (nuclei that are neither deformed nor near closed shells) be used for the experiment because their properties are expected to resemble most closely those of liquid drops, and for such nuclei the results should be less affected by single-particle shell structure.[6] Closed-shell nuclei, because of their special stability against deformation, would be expected to remain nearly spherical as they approached. Deformed nuclei, because of their elongation, would be expected to require relatively less energy to bring their major axes together.

There are various limiting cases for which the flattening of drops colliding head-on can be calculated fairly easily, corresponding to either the vibrational effective mass or the coefficient of viscosity (or both) taking on limiting values. The simplest case occurs when either the mass or the viscosity (or both) is infinite, in which case the drops would not deform at all during the collision. Although physically the effective mass cannot be zero, the limiting case in which both the mass and the viscosity are zero is also fairly easy to calculate: Because the drops would be able to deform instantaneously in response to applied forces, they would undergo oblate deformations corresponding to the minimum potential energy of two droplets whose mass centers were held fixed at constant separation. Another limiting case corresponds again to zero viscosity but to irrotational fluid flow, which yields the minimum effective mass that is possible physically.[3]

For the case of irrotational fluid flow and zero viscosity, we have calculated the amount of flattening experienced by two idealized droplets whose shapes are constrained to spheroids (ellipsoids of revolution) with collinear symmetry axes. The calculations were performed exactly by integrating numerically the classical equations of motion describing the approach and deformations of the spheroids. The initial conditions used were spherical droplets initially separated a large distance (taken equal to 15 times the radius of a nucleus formed from the two colliding nuclei) and moving toward each other with various translational kinetic energies. The appropriate formulas are given in Ref. 2.

We present in Figs. C. 9-1, C. 9-2, and C. 9-3 some illustrative results of the calculations. Figure C. 9-1 refers to a ^{197}Au target, and gives as a function of the atomic mass number A_2 of the projectile the total c. m. kinetic energy E required during head-on collisions to bring the nuclear force fields of the target and projectile into contact. The kinetic energy E is plotted in units of the energy V that would be required if the drops remained spherical, viz, $V = Z_1 Z_2 e^2/[r_0(A_1^{1/3} + A_2^{1/3}) + 2t]$, where Z_1 and Z_2 are the atomic numbers of the target and projectile, respectively, and where e denotes the electronic charge. Figure C. 9-2 is an analogous plot, but gives the results as a function of the mass number A_1 of the target for an ^{40}Ar projectile. In Fig. C. 9-3 the results refer to identical targets and projectiles and are presented as functions of their common mass number A. In each of the three figures, the five curves give the results of

the calculations for irrotational flow and zero viscosity for values of t/r_0 = 0.0, 0.5, 1.0, 1.5, and 2.0. The base line at E/V = 1 gives the result (independent of t) for the limiting case of either an infinite effective mass or infinite viscosity. (Note that Fig. C.9-2 is plotted on a different relative scale than Figs. C.9-1 and C.9-3.)

As discussed earlier, the amount of flattening depends upon the relative strengths of the surface and Coulomb forces; our calculations were performed for a ratio of twice the surface-energy constant to the Coulomb-energy constant [commonly referred to as $(Z^2/A)_{crit}$ in fission theory], equal to 50.13 (Ref. 7). It is also clear that the results are functions not only of the mass numbers given as abscissas in the three figures, but also of the corresponding atomic numbers; the results presented here are for the case in which these quantities are approximately related according to the course of the line of β stability.

We have also made some estimates of the amount of flattening for the nonphysical case of zero effective mass for flattening (and zero viscosity); these indicated that the amount of flattening is not an extremely sensitive function of the magnitude of the effective mass. Thus, provided that the effective masses for the transition nuclei that are used experimentally are not several times as large as their irrotational values, our calculations for irrotational flow would give the approximate amount of flattening such nuclei should experience if their viscosity were zero. In this way the experimental information concerning the flattening could be used for inferring a value for the coefficient of nuclear viscosity. This is a very old and fundamental question which is likely to take on increased importance in the coming years, since nuclear viscosity should play a crucial role in attempts to form an extremely heavy stable nucleus by fusing together two lighter nuclei. We plan further work that should put the extraction of the coefficient of viscosity from the experimental data on a more quantitative basis.

Acknowledgments

We are indebted to several individuals, particularly Wladyslaw J. Swiatecki, for valuable suggestions and discussions concerning this work, and to Joan Phillips for assistance in preparing the figures.

Footnote and References

1. The effective mass, which is in general a function of deformation, is the proportionality factor relating one-half the square of the time rate of change of the deformation coordinate to the vibrational kinetic energy. The effective mass corresponding to the irrotational fluid flow of a spheroid is given, for example, in Refs. 2 and 3.

2. James Rayford Nix, Studies in the Liquid-Drop Theory of Nuclear Fission (Ph.D. Thesis), UCRL-11338, April 1, 1964.
3. Sir Horace Lamb, Hydrodynamics, 6th Ed. (Dover Publications, New York, 1945), Sec. 382, pp. 719-721, and Sec. 45, pp. 47-48.
4. David L. Hill, Matter and Charge Distribution Within Atomic Nuclei, in Encyclopedia of Physics, S. Flügge, Ed., Vol. 39, Structure of Atomic Nuclei (Springer-Verlag, Berlin, 1957), p. 178.
5. Beat Hahn, D. G. Ravenhall, and Robert Hofstadter, High-Energy Electron Scattering and the Charge Distributions of Selected Nuclei, Phys. Rev. 101, 1131 (1956).
6. William D. Myers and Wladyslaw J. Swiatecki, Nuclear Masses and Deformations, Nucl. Phys. 81, 1 (1966).
7. Alex E. S. Green, Coulomb Radius Constant from Nuclear Masses, Phys. Rev. 95, 1006 (1954).

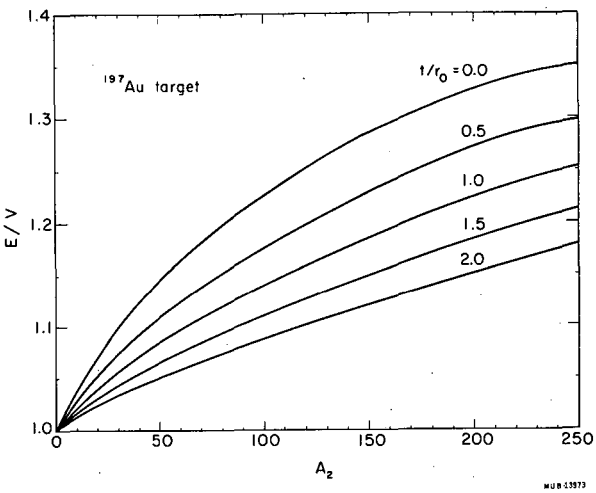

Fig. C. 9-1. The energy E required for the case of irrotational mass flow and zero nuclear viscosity to bring into contact the nuclear force fields of a ^{197}Au target and a projectile of mass number A_2, as a function of A_2. The five curves refer to different values of the ratio of the thickness t to the nuclear radius parameter r_0. The energy E is measured in units of the energy V that would be required if the nuclei were to remain spherical.

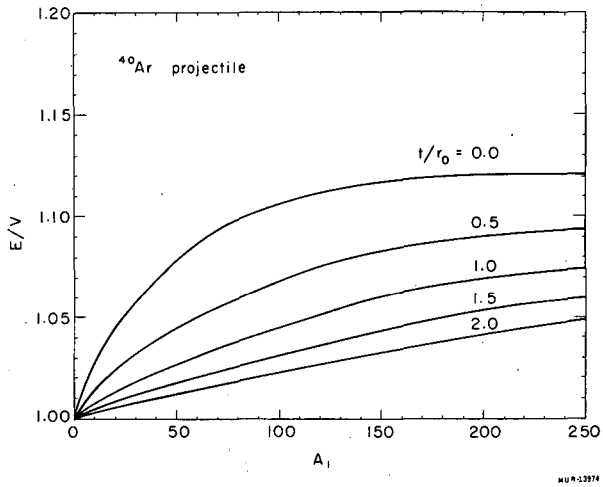

Fig. C. 9-2. The energy E required for the case of irrotational mass flow and zero nuclear viscosity to bring into contact the nuclear force fields of an ^{40}Ar projectile and a target of mass number A_1, as a function of A_1. The quantities t/r_0 and V have the same meaning as in Fig. C. 9-1.

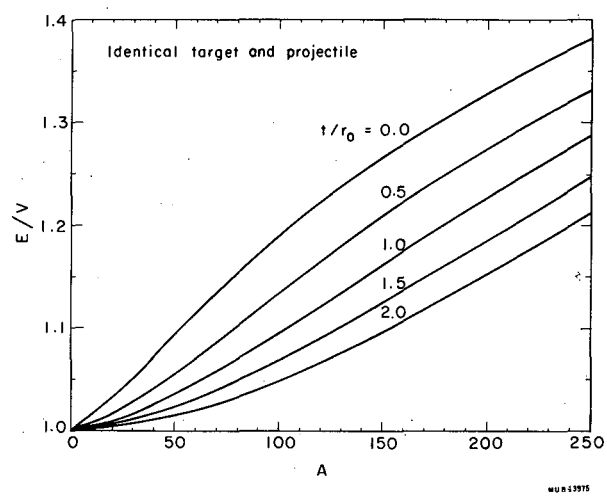

Fig. C. 9-3. The energy E required for the case of irrotational mass flow and zero nuclear viscosity to bring into contact the nuclear force fields of an identical target and projectile, as a function of their common mass number A. The quantities t/r_0 and V have the same meaning as in Fig. C. 9-1.

10. PREDICTIONS OF NEW MAGIC REGIONS AND MASSES FOR SUPERHEAVY NUCLEI FROM CALCULATIONS WITH REALISTIC SHELL-MODEL SINGLE-PARTICLE HAMILTONIANS*

Heiner Meldner

The single-particle part of a realistic shell-model Hamiltonian is considered to contain a nonlocal potential similar to the classic Van Vleck nuclear potential. Using an ansatz for the Hamiltonian suggested by rather general treatments of many-fermion systems, we found it possible to get a consistent fit to (a) nuclear-charge density distribtuions including isotope effects, (b) 1s proton levels as measured in (e, e'p) scattering, and (c) total binding energies or nuclear mass

defects, while (d) reproducing the shell-model level sequences, i.e., spin assignments. Extrapolations to nuclei off the stability valley and to superheavy nuclei appear to be reasonable. In the latter case, some evidence was found for a double magic nucleus at proton number 114 and neutron number 184 with a total binding energy around 2200 MeV. There is no indication of a double magic nucleus with $Z = 126$, $N = 184$ close to the line of β stability. However, some support was found for a relatively long-lived compound nucleus with these nucleon numbers by investigating metastable proton states.

In an attempt to obtain self-consistency, a crude fit was obtained with a certain set of input data. For some nuclei on the line of β stability, one gets the neutron levels shown in Fig. C. 10-1 and the proton levels of Fig. C. 10-2. The experimental points in the latter figure refer to recent (e, e'p) scattering measurements.[1] The extrapolations shown in these figures suggest closed shells at $N = 184$ and $Z = 114$. The same result was obtained in simpler calculations with local potentials two years ago.[2] The hypothetical superheavy nucleus with these nucleon numbers was investigated in more detail by varying within their reasonable limits the parameters of importance for level sequences. The computer program in addition allows an approximate calculation of metastable levels or resonances (shown as dashed lines in the figures).

In this fit, the calculated total binding energies agree with nuclear mass defects to within 5%. The charge-density distributions reproduce recent electron-scattering data[3] on Ca and Pb with a χ^2 of the same order of magnitude as is obtained in a fit with local potentials.[4] The Johnson-Teller effect,[5] i.e., larger rms radii for neutron than for proton densities, is exhibited for the heavier nuclei in spite of the decreasing central density of protons.

Since this report was first written, the proton shell at $Z = 114$ has been found in independent investigations.[6]

Footnote and References

* Resumé of UCRL-16843 presented at the conference: Why and How Should We Investigate Nuclides Far Off the Stability Line? Lysekil, Sweden, August 21-27, 1966 (to be published in Arkiv. Fysik).

1. U. Amaldi, Jr., G. Campos Venuti, G. Cortellessa, G. Fronterotta, A. Reale, P. Salvadori, P. Hillman, Phys. Rev. Letters 13, 341 (1964); U. Amaldi, Jr., G. Campos Venuti, G. Cortellessa, E. De Sanctis, S. Frullani, R. Lombard, P. Salvadori, Phys. Letters 22, 593 (1966); and private communication with Professor G. Cortellessa.
2. H. Meldner and P. Roeper, see Ref. 23 of W. D. Myers and W. J. Swiatecki, Nucl. Phys. 81, 1 (1966).
3. K. J. van Oostrum, R. Hofstadter, G. K. Noeldecke, M. R. Yearian, B. C. Clark, R. Herman, and D. G. Ravenhall, Phys. Rev. Letters 16, 258 (1966); et loc. cit. and private communication with Dr. K. J. van Oostrum on ^{208}Pb data.
4. B. F. Gibson, and K. J. van Oostrum, Charge Structure of the Calcium Isotopes (to be published in Nucl. Phys.). See also L. R. B. Elton, The A-Dependence of Nuclear Charge and Mass Distributions, preprint (University of Surrey, London, SW11).
5. M. H. Johnson and E. Teller, Phys. Rev. 93, 357 (1954).
6. S. G. Nilsson (University of Technology, Lund, Sweden), private communication; A. Sobiczewski, F. A. Gareev, B. N. Kalinkin, Phys. Letters 22, 500 (1966); B. I. Strutinskii (JINR, Dubna, USSR), private communication.

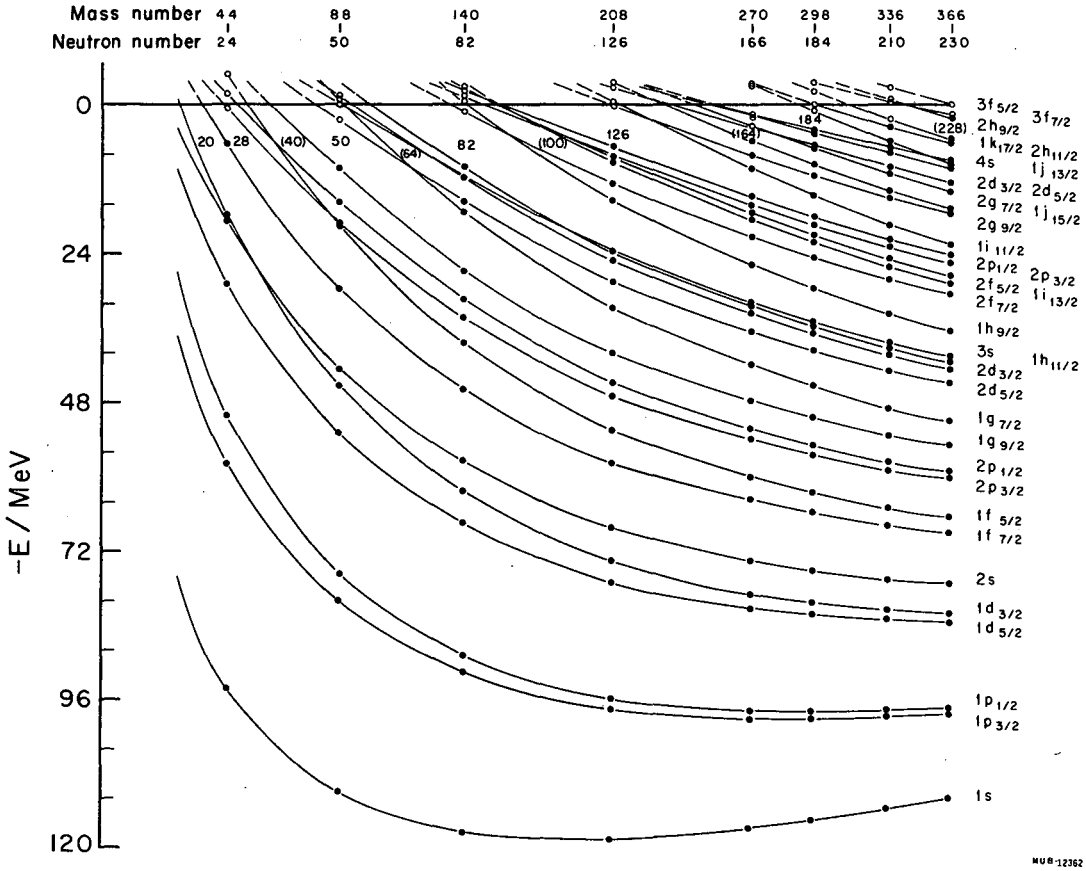

Fig. C. 10-1. Neutron single-particle levels for spherical nuclei close to the line of β stability. For explanation, see text.

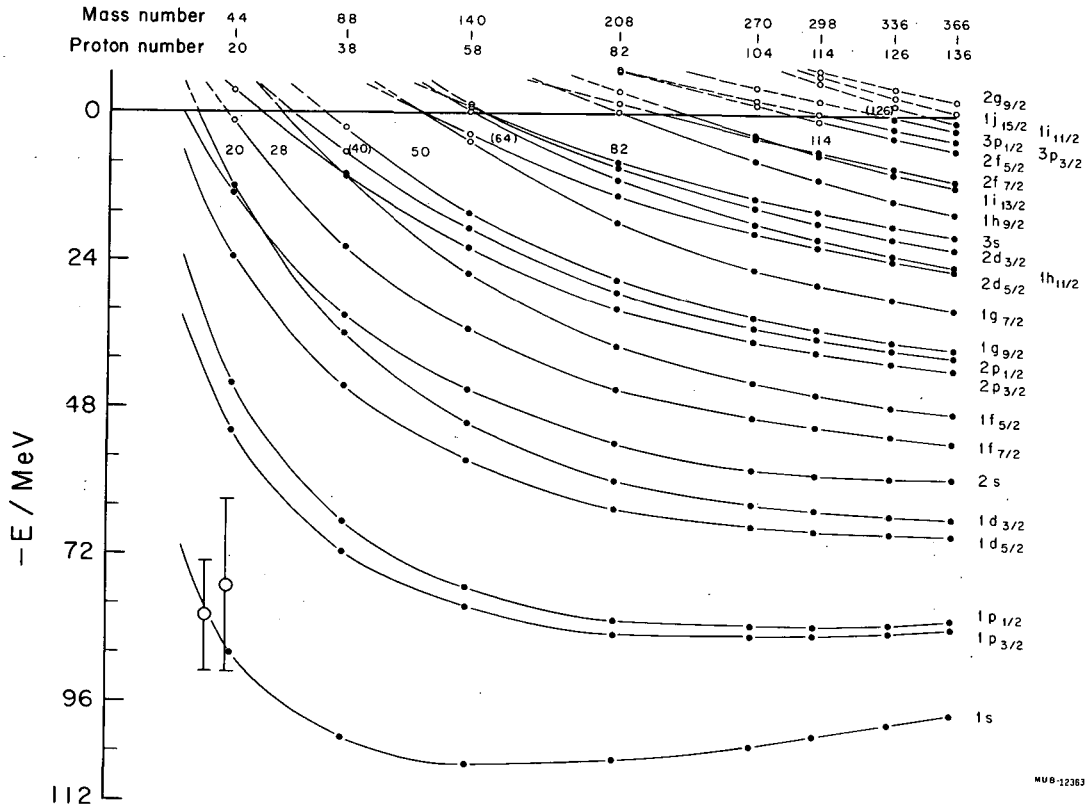

Fig. C. 10-2. Proton single-particle levels for spherical nuclei close to the line of β stability. The two experimental points give the 1s levels found in (e, e'p) scattering on ^{32}S and ^{40}Ca. For explanation, see text.

11. SHELL STRUCTURE AND NUCLEAR LEVEL DENSITIES

Arnold Gilbert

It has been known for a long time that the independent-particle model fails in certain basic respects;[1] it cannot give saturation, and therefore it does not predict the correct sequence of nuclear ground-state energies. However, the recent successes of the shell model for spherical nuclei and the unified model for deformed nuclei indicate that an independent-particle formulation may be able to give the deviations of actual nuclei from some average "liquid drop" behavior. Myers and Swiatecki[2] have used this idea to obtain shell corrections to liquid-drop masses. The object of the work presented here is to see whether such a picture will also work for nuclear level densities.

In the independent-particle model, the nuclear level density can be calculated by the standard methods of statistical mechanics. This has been done many times (see, for example, Ericson's review article[3]).

Consider a system with N neutrons, Z protons, and total energy E. Let $g_n(\epsilon)$, and $g_z(\epsilon)$ be the densities of single-particle states for neutrons and protons, respectively. The total level density $\rho(E)$ is given by

$$\rho(E) = \exp\,(\Omega - a_n N - a_z Z + \beta E/(2\pi)^{3/2}\, D^{1/2},$$

where $\Omega = \int_0^\infty d\epsilon\; g_n(\epsilon)\, \log(1 + e^{a_n - \beta\epsilon}) + \int_0^\infty d\epsilon\; g_z(\epsilon)\, \log\,(1 + e^{a_z - \beta\epsilon})$

and

$$D = \begin{vmatrix} \frac{\partial^2\Omega}{\partial \alpha_n^2} & \frac{\partial^2\Omega}{\partial \alpha_n \partial \alpha_z} & \frac{\partial^2\Omega}{\partial \alpha_n \partial \beta} \\ \frac{\partial^2\Omega}{\partial \alpha_n \partial \alpha_z} & \frac{\partial^2\Omega}{\partial \alpha_z^2} & \frac{\partial^2\Omega}{\partial \alpha_z \partial \beta} \\ \frac{\partial^2\Omega}{\partial \alpha_n \partial \beta} & \frac{\partial^2\Omega}{\partial \alpha_z \partial \beta} & \frac{\partial^2\Omega}{\partial \beta^2} \end{vmatrix}$$

The quantities N, Z, and E are determined by

$$N = \frac{\partial\Omega}{\partial \alpha_n}, \qquad Z = \frac{\partial\Omega}{\partial \alpha_z}, \text{ and } \qquad E = -\frac{\partial\Omega}{\partial \beta}.$$

The angular momentum dependence is calculated essentially as indicated by Bloch.[4] Let $\rho(E, J)$ be the level density at energy E and angular momentum J. Then

$$\rho(E, J) = \rho(E)\,(2J+1)\,\exp\left[-\frac{(J+1/2)^2}{2\sigma^2}\right]/2\sqrt{2\pi}\,\sigma^3 ,$$

where $\sigma^2 = \langle m_n^2\rangle \int_0^\infty d\epsilon\, g_n(\epsilon)\, \frac{e^{\alpha_n-\beta\epsilon}}{(1+e^{\alpha_n-\beta\epsilon})^2} + \langle m_z^2\rangle \int_0^\infty d\epsilon\, g_z(\epsilon)\, \frac{e^{\alpha_z-\beta\epsilon}}{(1+e^{\alpha_z-\beta\epsilon})^2}$.

The quantities $\langle m_n^2\rangle$ and $\langle m_z^2\rangle$ are the mean square magnetic quantum numbers for neutrons and protons, respectively. In this work the Jensen-Luttinger estimate[5] is used, $\langle m_n^2\rangle = \langle m_z^2\rangle = 0.146\, A^{2/3}$, A being the nucleon number. The odd-even effect is taken into account by subtracting from the energy E the pairing energy Δ for odd-A nuclei, and twice that for even-even nuclei. Here Δ is taken to be $11/A^{1/2}$, following the convention of Myers and Swiatecki.[2]

The outstanding feature of the shell model is the existence of gaps in the single-particle spectrum at the magic numbers. The form chosen for $g(\epsilon)$ [referring to either $g_n(\epsilon)$ or $g_z(\epsilon)$] is a simple one that incorporates this feature; it is illustrated in Fig. C. 11-1. The density of single-particle states is obtained from its average value G by "bunching" some of the single-particle states together, creating gaps at the magic numbers; between the gaps we have $g(\epsilon) = G'$.

This is essentially the same form as the one used by Myers and Swiatecki,[2] but some simplifications have been introduced:

(a) whereas Myers and Swiatecki take G, the average density of single-particle states, to be a Fermi gas spectrum, proportional to $\epsilon^{1/2}$, here G is considered uniform,

(b) we have taken $g(\epsilon)$ to be periodic in energy, with period d.

The bunching is done in such a way that there are the same number of particles in a shell before and after bunching, i.e., $G\,d = G'(d - \delta)$, δ being the size of the shell gap. The degree of bunching b (same as that of Myers and Swiatecki) is defined by $\delta = db$. One reason we can make the above-mentioned simplifications is that the level density depends only on the behavior of $g(\epsilon)$ in a small region around the Fermi level. Another reason for using the periodic model is that at high energies the level density goes over into the Fermi gas expression, with a shift in the energy scale. This energy shift is the same as the shell correction to the liquid-drop mass, aside from a possible additive constant.

We are thus in a position to compare calculated and experimental shell corrections and level densities. Preliminary calculations have been made on nuclei near ^{208}Pb for which there are neutron resonance data. Here d and b were taken to be the same for neutrons and protons; we also set $G_n = c\,N$ and $G_z = c\,Z$ (as would be the case for a Fermi gas in a square well of radius $R = r_0\,A^{1/3}$). The results are shown in Tables C. 11-I and C. 11-II.

The comparison of theory with experiment shows that:

(a) There are values of the parameters b, c, and d which give reasonably good fits to the data. As it turned out, it was not necessary to put an additive constant on the calculated energy shifts to get agreement with the shell corrections. The fit to the experimental data determines fairly well the value of c; there seems to be somewhat more latitude in the choice of the quantities b and d.

(b) There is somewhat of a problem than with the chosen value of c. The normal Fermi gas-level density formula is

$$\rho(E) = \frac{\sqrt{\pi}}{12} \frac{e^{2\sqrt{aU}}}{a^{1/4}\, U^{5/4}},$$

where U is the excitation energy and $a = (\pi^2/6)(G_n + G_z)$. The present value of c would give $a \approx A/11$. This is somewhat lower than the value of a required to fit the neutron resonances in the rare-earth and uranium regions, namely $a \approx A/8$. The reason for this discrepancy is not clear at present.

References

1. J. M. Blatt and V. F. Weisskopf, Theoretical Nuclear Physics (John Wiley and Sons, 1952), Ch. III.
2. W. D. Myers and W. J. Swiatecki, Nucl. Phys. 81, 1 (1966).
3. T. Ericson, Advan. Phys. 9, 425 (1960).
4. C. Bloch, Phys. Rev. 93, 1095 (1954).
5. J. H. D. Jensen and J. M. Luttinger, Phys. Rev. 86, 907 (1952).

Table C. 11-I. Comparison between calculated energy shifts and Myers-Swiatecki shell corrections (the experimental shell-force corrections are the differences between actual nuclear masses and liquid-drop masses).

Compound nucleus	Shell correction (MeV)		Energy shifts (MeV)	
	Theory	Experiment	c = 0.055 d = 8 MeV b = 0.20	c = 0.055 d = 7 MeV b = 0.25
^{198}Au	-1.97	-3.43	- 3.13	- 2.92
^{199}Hg	-2.60	-4.09	- 3.88	- 3.43
^{200}Hg	-3.23	-4.72	- 4.51	- 4.04
^{201}Hg	-3.88	-5.26	- 5.19	- 4.69
^{202}Hg	-4.57	-5.93	- 5.92	- 5.38
^{204}Tl	-5.94	-7.39	- 7.50	- 6.89
^{206}Tl	-7.46	-9.08	- 9.18	- 8.50
^{207}Pb	-8.13	-9.55	-10.07	- 9.34
^{208}Pb	-8.94	-9.96	-10.98	-10.22
^{210}Bi	-7.21	-7.61	- 9.36	- 8.66

Table C. 11-II. Comparison between calculated and experimental densities of neutron resonances.

Compound nucleus	Neutron resonance densities (MeV^{-1}) Experiment	Theory c = 0.055 d = 8 MeV b = 0.20	Theory c = 0.055 d = 7 MeV b = 0.25
^{198}Au	63 000	77 000	75 000
^{199}Hg	12 000	6 500	6 400
^{200}Hg	17 000	20 000	17 000
^{201}Hg	800	2 000	1 600
^{202}Hg	11 000	13 000	11 000
^{204}Tl	500	3 500	2 900
^{206}Tl	100	930	700
^{207}Pb	18	90	80
^{208}Pb	20	60	50
^{210}Bi	150	270	200

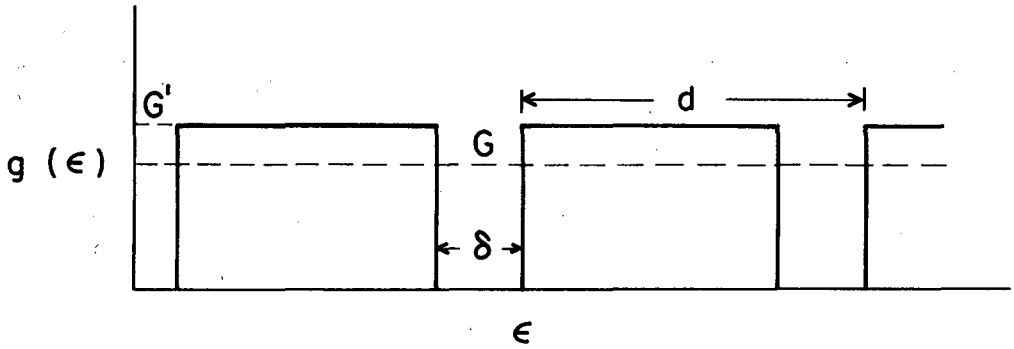

XBL671-300

Fig. C. 11-1. The density of single-particle states, $g(\epsilon)$, as a function of the energy ϵ. Here G is the average value of $g(\epsilon)$, and d is its period; G' is the value of $g(\epsilon)$ between shell gaps, and δ is the gap size.

D. FISSION

1. CALCULATIONS IN THE LIQUID-DROP THEORY OF NUCLEAR FISSION

James Rayford Nix

In working out the implications of the liquid-drop theory of nuclear fission an essential difference in the degree of difficulty arises between the fission of elements lighter than about radium and those heavier than about radium. The lighter elements have dumbbell-like saddle-point shapes that are fairly close to the scission shape itself. In such cases it is a fairly good approximation to neglect the dynamical descent from the saddle point to scission, and this approximation has been used recently to work out the predictions of the liquid-drop model for the lighter elements.[1] These calculations were found to reproduce, without the use of any adjustable parameters, the magnitudes of the most probable values and the widths of experimental distributions in the masses and kinetic energies of the fragments, as well as some, but not all, of the finer details of the distributions.

At the conclusion of this study, it was decided to work out in an analogous way the predictions of the liquid-drop model for the fission of the heavier elements. This is a far more difficult task because the heavier elements have cylinder-like saddle-point shapes that are far removed from scission shapes, and it is consequently necessary to treat explicitly the difficult stage of the dynamical descent from the saddle point to scission.

A parameterization was chosen in which the shape of the drop is described by three overlapping or separated collinear spheroids (actually quadratic surfaces of revolution, since the middle quadratic surface of revolution can be either a spheroid or a hyperboloid of one or of two sheets). Since three numbers are required to specify each of the three spheroids, a drop parameterized in this way has eight degrees of freedom (volume conservation eliminates one). Such a parameterization permits the drop to divide into either two or three fragments, so that ternary fission can be discussed as well as binary fission.

The study of this parameterization of the liquid-drop model has proceeded in systematic steps. The first step was the derivation of formulae and the writing of computer programs to calculate the drop's potential energy (a sum of surface and Coulomb energies) and the partial derivatives of the potential energy with respect to the eight generalized coordinates describing the shape of the drop. The surface energy and its derivatives were expressed in closed forms, but the evaluation of the Coulomb energy and its derivatives involves performing a double integral numerically.

In the second step the saddle point corresponding to our parameterization was determined as a function of the fissility parameter x. This included writing a computer program to solve the system of nonlinear equations obtained by equating to zero the first partial derivatives of the potential energy. Detailed comparisons were made between the saddle-point properties corresponding to this parameterization and those that have recently been calculated by other methods.[2-4] The comparisons indicated that the three-spheroid parameterization is capable of reproducing the more important known saddle-point properties with amazing accuracy over the entire range of x from 0 to 1, and that for values of $x < 0.50$ it is more accurate in many respects than a parameterization in which the radius vector is expanded in terms of the first 18 Legendre polynomials.[2]

The third step was the derivation of the formula and the writing of a computer program to calculate the kinetic energy of the drop as a function of its eight generalized coordinates and their time derivatives. At present the kinetic energy is calculated by use of the approximate method of Werner and Wheeler,[5] in which the flow of matter is assumed to occur within infinitesimally thin slices perpendicular to the drop's symmetry axis. By use of this approximation it was possible to arrive at a closed expression for the kinetic energy.

In the fourth step a study was made of the small oscillations of the drop about its saddle-point shape, including the calculations as functions of x of the frequencies and eigenvectors of

the normal modes of motion. These results were compared with those previously calculated on the basis of a parameterization in which the drop's radius vector is expanded in terms of the first 18 Legendre polynomials.[6] The frequencies and eigenvectors of the two lower symmetric modes (fission and stretching) and of the two lower asymmetric modes (center-of-mass shift and mass asymmetry) were reproduced with good accuracy by the three-spheroid parameterization (with the kinetic energy calculated in the Werner-Wheeler approximation). The properties of the remaining four higher modes were reproduced less accurately.

The fifth and current step in the study is the development of a program to integrate numerically the classical equations of motion describing the division of the drop and the separation of the fragments to infinity. The preliminary results of a few test cases indicate that for small values of x the descent from the saddle point to scission consists primarily of a contraction of the drop's neck, with the ends of the drop remaining at almost constant separation. On the other hand, for large values of x the descent from the saddle point proceeds through a fairly large initial elongation of the drop.

A question of central importance that will be answered by these dynamical calculations is whether, for large values of x, the small initial asymmetric components of motion in the neighborhood of the symmetric saddle-point shape will be "amplified" into a large mass asymmetry during the dynamical descent from saddle to scission. To shed light on this question a study was made of the criterion for the stability of small asymmetric motion superimposed on symmetric motion. The results of the study are currently being applied to the calculations of the dividing drops to see if there is a point along the path from saddle to scission at which stability against asymmetric deformations is lost.

The final step will involve a study of the solutions of the equations of motion for a large number of initial conditions. This will permit conversion of the known probability distributions for the initial states of motion at the saddle point into probability distributions for observable properties of fission fragments at infinity—their relative masses (including division into three fragments), their kinetic energies, and their excitation energies. The subsequent comparison of these predicted distributions with the corresponding experimental distributions for the heavier elements should permit a more definitive conclusion regarding the applicability of the liquid-drop model for discussing fission.

Acknowledgments

It is a pleasure to acknowledge numerous discussions with Wladyslaw J. Swiatecki and Stanley G. Thompson concerning this work. I am further indebted to Esther Coleman for writing the computer programs used in this study, and to Joan Phillips for assistance with various hand calculations.

References

1. James Rayford Nix and Wladyslaw J. Swiatecki, Studies in the Liquid-Drop Theory of Nuclear Fission, Nucl. Phys. 71, 1 (1965); James Rayford Nix, Studies in the Liquid-Drop Theory of Nuclear Fission (Ph. D. Thesis), UCRL-11338, April 1, 1964.
2. Stanley Cohen and Wladyslaw J. Swiatecki, The Deformation Energy of a Charged Drop, Part V: Results of Electronic Computer Studies, Ann. Phys. (N. Y.) 22, 406 (1963).
3. V. M. Strutinskii, N. Ya. Lyashchenko, and N. A. Popov, Symmetrical Equilibrium Shapes in a Sharp Surface Nucleus Model (The Liquid Drop Model), Soviet Phys. JETP 16, 418 (1963) [English translation of Zh. Eksperim. i Teor. Fiz. (USSR) 43, 584 (1962)]; similar article published as Symmetrical Shapes of Equilibrium for a Liquid Drop Model, Nucl. Phys. 46, 639 (1963).
4. James N. P. Lawrence, Static Fission-Barrier Calculations of a Two-Parameter Liquid Drop, Phys. Rev. 139, B1227 (1965).
5. Frederick G. Werner (University of Cincinnati) and John Archibald Wheeler (Princeton University), Superheavy Nuclei and the Kolesnikov-Larkin-Mottelson Effect in Spontaneous Fission, Appendix III, Approximate Procedure Used to Evaluate Inertial Deformation Parameter (unpublished, no date).
6. James Rayford Nix, The Normal Modes of Oscillation of a Uniformly Charged Drop About Its Saddle-Point Shape (UCRL-16786, April 1, 1966), to be published in Ann. Phys. (N. Y.), 41 [1], Jan. 1967.

2. THE NORMAL MODES OF OSCILLATION OF A UNIFORMLY CHARGED DROP ABOUT ITS SADDLE-POINT SHAPE†

James Rayford Nix

A study was made of the normal modes of oscillation of an idealized uniformly charged axially symmetric liquid drop about its saddle-point shape. For the calculation of the normal modes and their frequencies as functions of the fissility parameter x, both expansions to first order in 1-x and formulas appropriate for numerical evaluations were derived. For the range $0.7 \leq x \leq 1.0$ numerical results for the four lowest symmetric and the four lowest asymmetric modes were tabulated at intervals of 0.02 in x for the frequencies, normal-coordinate stiffness and inertia constants, and eigenvectors (with respect to the coefficients a_n in an expansion of the drop's radius vector in Legendre polynomials). For $0.3 \leq x < 0.7$ the results obtained were of limited accuracy, and in this range only graphs of the frequencies of the three lowest symmetric modes were given.

The results obtained for the frequencies of the six lowest modes are shown as functions of the fissility parameter in Fig. D.2-1 and D.2-2. In each figure the portions of the curves indicated by the short dashed lines are of questionable accuracy, and the dot-dashed lines give for $x \leq 0.5$ the results previously obtained for n = 4 and n = 5 in the two-spheroid approximation.[1] The solid points give the locations of the known zeros of the n = 3 curve. Shown in Fig. D.2-3 are the distortions from the saddle point associated with the six lowest modes for x = 0.9, 0.8, and 0.7. In each case the saddle-point shape is indicated by a dashed line; the shapes obtained by displacing the appropriate normal coordinate by a designated amount in the positive and the negative direction are indicated respectively by dark and by light solid lines.

Various applications of the results were discussed in connection with the theory of nuclear fission. These include the transition-state energy levels of collective oscillations, the probability distributions for the saddle-point states of motion, and the penetration of the fission barrier. In order to obtain an improved description of fission-barrier penetration at very low excitation energies, the formula for the penetrability of a cubic barrier was derived by use of the WKB approximation. In Fig. D.2-4 the calculated (purely imaginary) frequency for motion in the fission direction, which affects the penetrability of the fission barrier, is compared as a function of x with existing experimental data on fission widths, spontaneous-fission lifetimes, and the variation of fission cross sections with excitation energy. This comparison, which is made without the use of any adjustable parameters, indicates that the calculations are capable of reproducing the correct order of magnitude of the fission-direction frequency. Most of the data are at present not sufficiently accurate to provide a sensitive test of the theory, but the points derived from spontaneous-fission lifetimes suggest that possibly 2.8 times as much mass is displaced in the fission mode as would correspond to irrotational motion.

Footnote and References

†Resume of UCRL-16786, to be published in Ann. Phys. (N. Y.), 41 [1], Jan. 1967.

1. James Rayford Nix and Wladyslaw J. Swiatecki, Studies in the Liquid-Drop Theory of Nuclear Fission, Nucl. Phys. 71, 1 (1965); James Rayford Nix, Studies in the Liquid-Drop Theory of Nuclear Fission (Ph. D. Thesis), UCRL-11338, April 1, 1964.
2. Alex E. S. Green, Nuclear Physics (McGraw-Hill Book Company, Inc., New York, 1955), pp. 185, 250.
3. William D. Myers and Wladyslaw J. Swiatecki, Nuclear Masses and Deformations, Nucl. Phys. 81, 1 (1966).

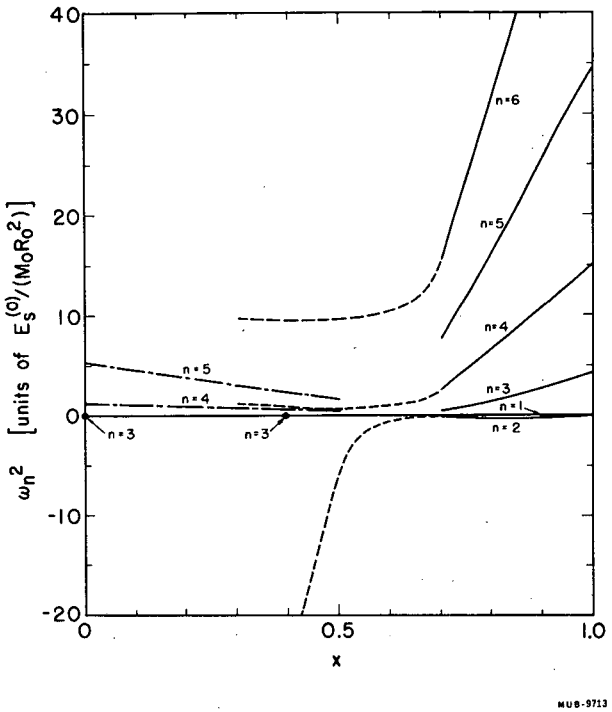

Fig. D.2-1. Squares of the six lowest frequencies in natural liquid-drop units of $E_s^{(0)}/(M_0R_0^2)$ as functions of the fissility parameter x.

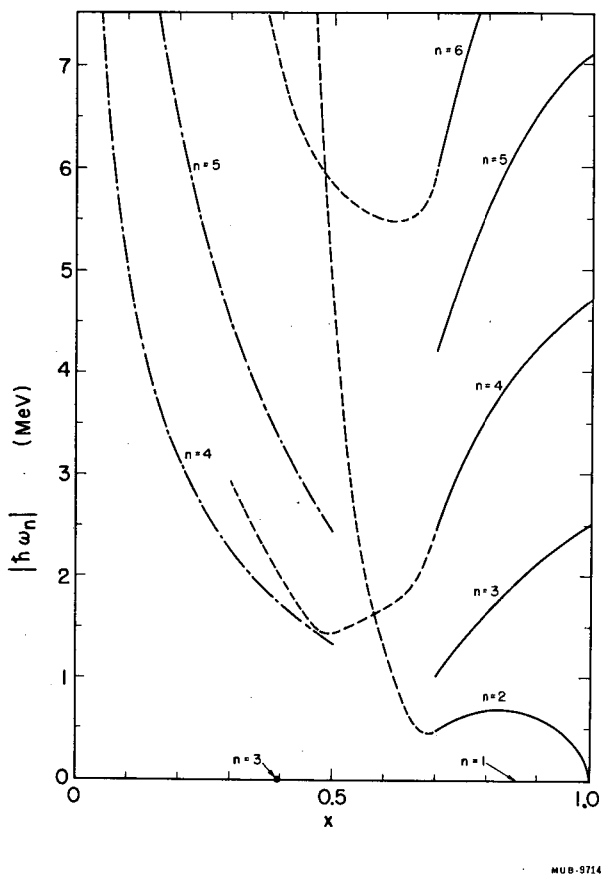

Fig. D.2-2. Magnitudes of the six lowest frequencies in MeV for nuclei along Green's approximation (Ref. 2) to the line of beta stability as functions of the fissility parameter x. The values used for the constants of the semiempirical mass formula are those of Myers and Swiatecki (Ref. 3).

MUB-9720

MUB-9721

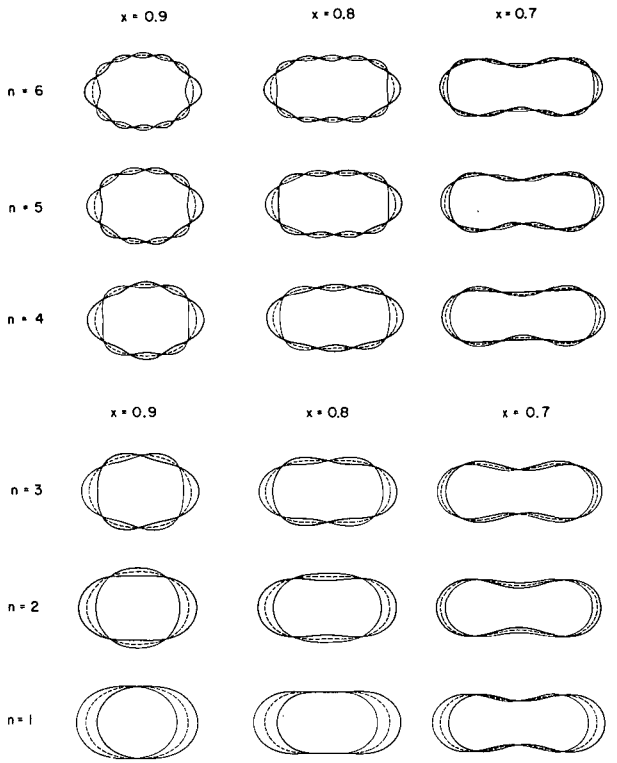

Fig. D.2-3. Distortions associated with the six lowest normal modes for x = 0.9, 0.8, and 0.7.

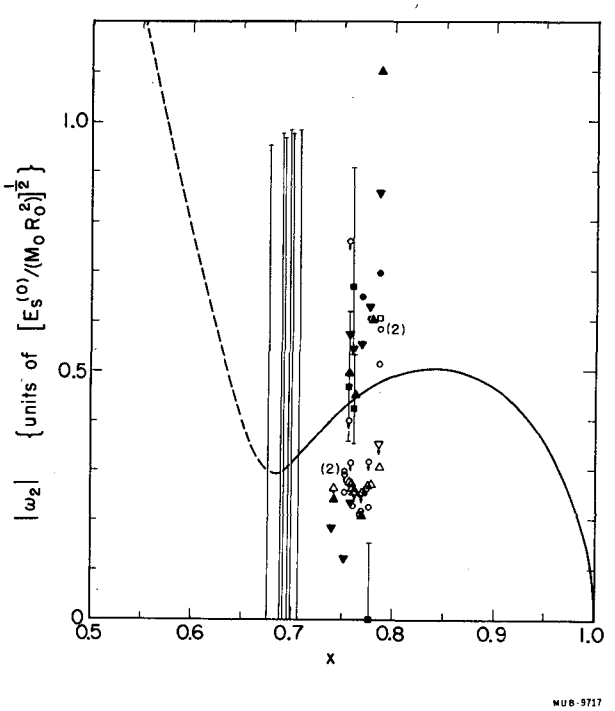

Fig. D.2-4. A comparison of the calculated and experimental values of the magnitude of the purely imaginary frequency ω_2 that is relevant for penetration of the fission barrier, as a function of the fissility parameter x. In converting the experimental values of $|\hbar\omega_2|$ from MeV to the natural liquid-drop units of $[E_s^{(0)}/(M_0 R_0^2)]^{\frac{1}{2}}$ the values of Myers and Swiatecki (Ref. 3) have been used for the constants of the semi-empirical mass formula. No arbitrary parameters have been adjusted; the calculated curve has not been normalized to the experimental points in any way. The portion of the calculated curve indicated by the dashed line is of questionable accuracy. The data are derived from experimental measurements of slow-neutron fission widths (O and □), spontaneous-fission lifetimes (▽ and △), and the variation of fission cross sections with excitation energy (●, ▼, ■, ▲ and tall error bars with no symbol). Arrows pointing downward denote upper limits, and a numeral 2 in parentheses indicates two identical data points.

3. LONG-RANGE PARTICLES OF Z = 1 TO 4 EMITTED DURING THE SPONTANEOUS FISSION OF ^{252}Cf

S. W. Cosper, J. Cerny, and R. C. Gatti

Several investigators have reported the observation of long-range protons,[1,2] deuterons,[1] tritons,[1-3,8] ^{3}He particles,[1] α particles[1-7] and ^{6}He particles[2] emitted during the spontaneous fission of ^{252}Cf. Since all the known hydrogen isotopes which are stable to nucleon emission are emitted during the fission process, it seems reasonable to assume that all nucleon-stable helium isotopes could be observed during the fission of ^{252}Cf. The observation of ^{3}He, ^{4}He, and ^{6}He along with the absence of ^{5}He, which is known to be particle unstable, tends to support this assumption. Hence, a detailed study of the long-range helium isotopes emitted during the spontaneous fission of ^{252}Cf might be expected to yield information concerning the particle stability of He isotopes of mass number >6. Additionally, a knowledge of the various light fragments emitted during the spontaneous fission of ^{252}Cf, along with their relative intensities and energy distributions, might be of help in better understanding the mechanism of the fission process itself.

Two- and three-counter particle identification techniques[9,10] have been used to investigate the long-range particles emitted from ^{252}Cf, confirming the emission of ^{1}H, ^{2}H, ^{3}H, ^{3}He, ^{4}He, and ^{6}He. In addition it was found that ^{8}He, ^{6}Li, ^{7}Li, ^{8}Li, ^{9}Li, ^{9}Be, ^{10}Be, and probably other isotopes of Be are also emitted.

A three-counter particle identification (PI) spectrum for the hydrogen and helium isotopes is presented in Fig. D.3-1, and shows the nearly complete separation obtained for these isotopes. Three methods of accumulating data were used during the course of this investigation:

MODE 1: To investigate relatively low-yield particles in detail, the two ΔE, E_{total}, and PI pulses from the three-counter PI system were fed into a 4096-channel ADC-Buffer system which was gated by the appropriate region of the PI spectrum. These four pulse heights were recorded in an on-line computer and were later individually analyzed by using the known detector thicknesses and range-energy relations in silicon for the particles of interest.

MODE 2: To collect the energy spectra of the more populous particles in their higher energy ranges, the PI output was fed to a four-channel router whose outputs were used to route the energy signals into the appropriate quadrant of a 4096-channel pulse-height analyzer.

MODE 3: To investigate energy spectra at low energies, the PI pulse and the total energy pulse were fed to a 4096-channel pulse-height analyzer operating in a two-parameter (64×64 channels) mode.

Two- and three-counter particle identifier spectra of Li and Be ions detected from ^{252}Cf fission are shown in Fig. D.3-2. The two-counter PI (Fig. D.3-2b) was obtained by using a somewhat nonuniform 15-μ ΔE detector, and hence separation of the various isotopes of Li and Be was not possible.

To investigate in detail the emission of helium isotopes with mass number ≥7, the three-counter identification system[10] was used to take data in Mode 1. Detector profiles were obtained for the ΔE detectors by observing the energy loss distributions of natural α particles and selected narrow bands of long-range α particles and ^{6}He particles from ^{252}Cf fission. The two ΔE, E_{total}, and PI pulses were then individually recorded for 100 events whose identifier signal was contained in the ^{7}He→^{9}He region of the identifier spectrum. The percentage deviation of each ΔE detector pulse from that expected for a ^{6}He, ^{7}He, ^{8}He, or ^{9}He particle of incident energy E_{total} was calculated for each event by using range-energy relationships and the average detector thickness. Taking into account the detector profiles, the probability of that event's being a ^{6}He, ^{7}He, ^{8}He, or ^{9}He particle was calculated for each of the two ΔE detectors. The overall probability that a particular event was either a ^{6}He, ^{7}He, ^{8}He, or ^{9}He was assumed to be the product of the respective probabilities for that particle in each detector; the event was finally classified according to its dominant probability. This study, combined with a 220-hour investigation of the ^{9}He→ ^{10}He region of the PI spectrum (in Mode 1), indicated that ^{7}He, ^{9}He, and ^{10}He are particle-unstable.

Energy spectra for all the observed hydrogen and helium isotopes (with the exception of ^{3}He) and for the Li and Be ions were obtained, and the most probable energy for each determined. Relevant numerical data resulting from the "measured" and "extrapolated" energy spectra are explained and summarized in Table D.3-I, and the relative intensities of emission of the various long-range particles are shown in Fig. D.3-3.

References

1. H. E. Wegner, Bull. Am. Phys. Soc. 6, 307 (1961).
2. S. L. Whetstone, Jr., and T. D. Thomas, Phys. Rev. Letters 15, 298 (1965).
3. J. C. Watson, Phys. Rev. 121, 230 (1961).
4. R. A. Nobles, Phys. Rev. 126, 1508 (1962).
5. M. L. Muga, H. R. Bowman, and S. G. Thompson, Phys. Rev. 121, 270 (1961).
6. Z. Fraenkel and S. G. Thompson, Phys. Rev. Letters 13, 438 (1964).
7. J. A. Coleman, A. W. Fairhall, and I. Halpern, Phys. Rev. 133, B724 (1964).
8. D. L. Horrocks, Phys. Rev. 134, B1219 (1964).
9. F. S. Goulding, D. A. Landis, J. Cerny, and R. H. Pehl, Nucl. Instr. Methods 31, 1 (1964).
10. F. S. Goulding, D. A. Landis, J. Cerny, and R. H. Pehl, IEEE Trans. Nucl. Sci. NS-13, 514 (1966).

Table D.3-I. Summary of numerical data obtained from this investigation of the long-range particles emitted during the fission of ^{252}Cf.

Particle detected	Measured energy range (MeV)	Intensity relative to emission of 100 α particles[a]		Most probable energy (MeV)	HWHM (MeV)	High-energy cutoff (MeV)
		Measured[b]	Extrapolated[c]			
Proton	7.3 - 18.8	1.10 ±0.15	1.75 ±0.30	7.8±0.8	3.4±0.8	18.8
Deuteron	5.3 - 21.5	0.63 ±0.03	0.68 ±0.03	8.0±0.5	3.6±0.5	22.4
Triton	6.5 - 24.3	6.42 ±0.20	8.46 ±0.28	8.0±0.3	3.1±0.3	24.5
^{3}He	14.2 - 21.3	≤0.075	---	---	---	---
^{4}He	8.3 - 37.7	---	---	16.0±0.2	5.1±0.2	37.9
^{6}He	10.0 - 33.3	1.95 ±0.15	2.63 ±0.18	12.0±0.5	4.0±0.5	32.6
^{8}He	9.3 - 27.7	0.062 ±0.008	0.090±0.012	10.2±1.0	4.0±1.0	28.7
^{6}Li	24.0 - 33.2	0.0011±0.0005	---	---	---	---
^{7}Li	25.4 - 38.3	0.0081±0.0012	---	---	---	37.5
^{8}Li	26.8 - 37.5	0.0015±0.0006	---	---	---	---
^{9}Li	28.1 - 37.1	0.0009±0.0004	---	---	---	---
Li ions	15.2 - 37.3	0.126 ±0.015	0.132±0.016	20.0±1.0	3.3±1.0	38.0
^{9}Be	39.3 - 43.9	~0.0002	---	---	---	---
^{10}Be	41.0 - 45.6	~0.0004	---	---	---	---
Be ions	23.0 - 49.1	0.156 ±0.016	0.201±0.020	~26.0	~5.5	45.0

a. 299 fissions per α particle is the best available value for ^{252}Cf.

b. Numerical values under this column were obtained by using only those portions of the energy spectra which were determined experimentally.

c. Numerical values under this column were obtained by using energy spectra extrapolated to zero energy.

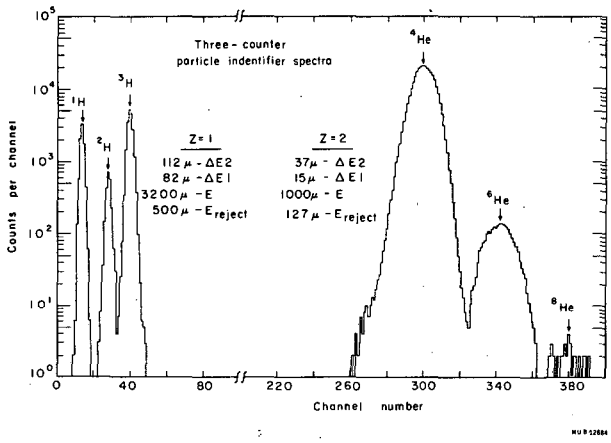

Fig. D.3-1. Typical spectra from the three-counter particle identifier resulting from long-range particles emitted during ^{252}Cf fission. The thicknesses of the detectors which were used to accumulate these data are indicated on the figure.

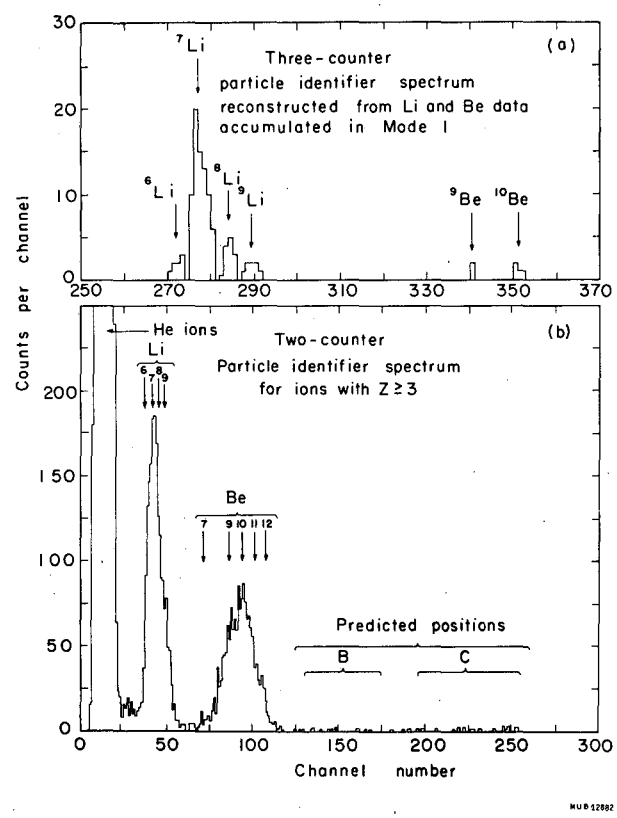

Fig. D.3-2. (a) A three-counter particle-identifier spectrum reconstructed from Li and Be ion individual events (data accumulated in Model), and (b) a two-counter particle-identifier spectrum (for ions with Z≥3) showing Li and Be ion separation and predicted positions of B and C groups.

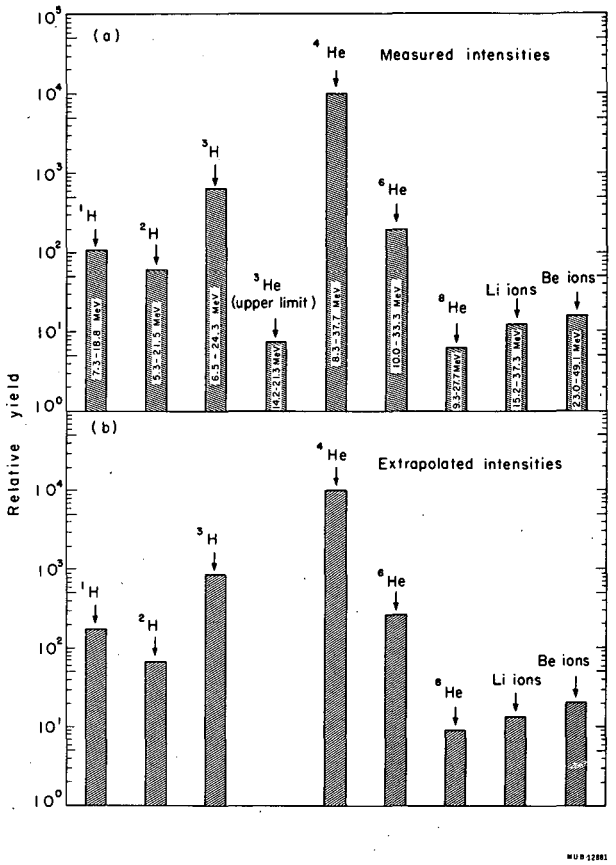

Fig. D.3-3. Relative intensities of particles emitted from ^{252}Cf fission. The (a) measured and (b) extrapolated values are explained in Table D.3-I.

4. EXPERIMENTAL DETERMINATION OF FIRST-CHANCE-FISSION PROBABILITY IN ^{4}He-INDUCED FISSION OF SOME TUNGSTEN ISOTOPES

Luciano G. Moretto,* Raymond C. Gatti, and Stanley G. Thompson

For intermediate and heavy nuclei at moderate excitation energies, the total reaction cross section is mainly due to fission and neutron emission. It is therefore a good approximation to put the total decay width Γ_{total} equal to $\Gamma_f + \Gamma_n$. Fission not only can occur for the produced compound nucleus, but also competes at every stage of neutron evaporation. The Γ_f/Γ_n ratio as a function of energy can give very useful information on the level densities at the ground and saddle-point states and provides a check for different theoretical models.

The main difficulty in the analysis of the experimental data is to obtain the first-chance-fission probability $P_{f,1}$ from the total-fission-probability $P_{f,total}$, which also contains the probability of fission after multiple neutron emission. A very simple way of determining $P_{f,1}$ is to measure $P_{f,total}$ for isotopes, differing by one neutron, as a function of energy. In fact, assuming that neutron emission is weakly affected by the total angular momentum, we can write

$$P^A_{f,total}(E) = P^A_{f,1}(E) + [1 - P^A_{f,1}(E)] \int_0^\infty P^{A-1}_{f,total}(E - B_n - \epsilon)\, g(\epsilon)\, d\epsilon,$$

where

$$P^{A}_{f,\,total}(E) = \frac{\sigma_f(E)}{\sigma_R(E)} \quad \text{for the isotope of mass A,}$$

$$P^{A}_{f,\,total}(E) = \frac{\sigma_f(E)}{\sigma_R(E)} \quad \text{for the isotope of mass A-1,}$$

$$P^{A}_{f,\,1} = \Gamma_f/(\Gamma_f + \Gamma_n),$$

$$B_n = \text{neutron binding energy,}$$

$$\epsilon = \text{neutron kinetic energy,}$$

and $g(\epsilon)$ = normalized distribution in neutron kinetic energy;

$P^{A}_{f,\,total}$ and $P^{A-1}_{f,\,total}$ can be obtained from the experimental fission cross sections, by using the optical-model calculated total cross sections, and thus $P^{A}_{f,\,1}$ can be deduced.

The ^{4}He-ion induced fission cross sections of ^{182}W, ^{183}W, and ^{184}W have been measured between 60 and 110 MeV bombarding energy. Some results are shown in Fig. D.4-1. The experimental equipment consists of a fission chamber that allows the measurement of the fission-fragment angular distribution; mica was used as the fission detector. The position of the beam was defined by a collimator; any small displacement of the beam from the center of the target can be corrected by using the ratio of counts at 90 and 270 deg from the beam axis. The total beam charge was measured by using a Faraday cup connected with a current integrator. By integrating over the angular distribution of the fission fragments, the total fission cross section was calculated.

The evaluation of the fission-fragment angular distribution allows a highly accurate measurement of the total fission cross section. The accurate determination of $P_{f,\,1}$ requires knowledge of the function $g(\epsilon)$. A reasonable choice seems to be of the form $g(\epsilon) = k\,\epsilon\, e^{-\epsilon/T}$, as proposed earlier by Weisskopf from the evaporation model. With the available data and work in progress, the $P_{f,\,1}$ and $P_{f,\,2}$ for ^{184}W + ^{4}He and $P_{f,\,1}$ for ^{183}W will in the near future be available from the fission threshold up to 110 MeV.

Footnote

*Visitor from the Laboratorio di Radiochimica, Università di Pavia, Pavia, Italy.

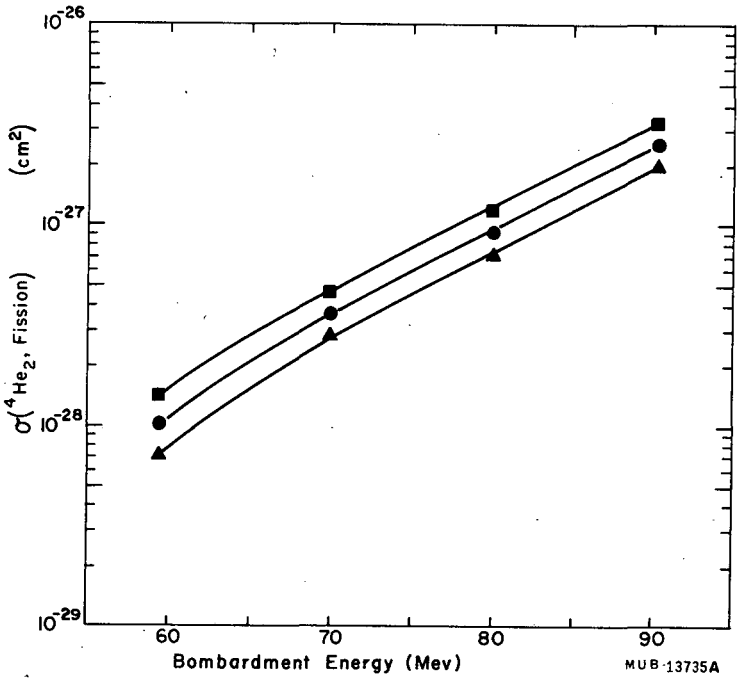

Fig. D.4-1. Fission cross sections of tungsten isotopes vs bombardment energy.

■ $^{182}_{74}W + ^{4}_{2}He \rightarrow ^{186^*}_{76}Os \rightarrow$ fission

● $^{183}_{74}W + ^{4}_{2}He \rightarrow ^{187^*}_{76}Os \rightarrow$ fission

▲ $^{184}_{74}W + ^{4}_{2}He \rightarrow ^{188^*}_{76}Os \rightarrow$ fission

5. POSSIBLE EVIDENCE OF LARGE PAIRING EFFECTS AT THE SADDLE POINT OF SOME Po AND At ISOTOPES

Luciano G. Moretto,* Raymond C. Gatti, John R. Huizenga,†
John O. Rasmussen, and Stanley G. Thompson

The saddle point in nuclear fission has been treated successfully as a quasi-stationary state to which the unified model can be applied.[1] Some recent experiments[2,3] seem to show that in very heavy nuclei the superfluid effects at the saddle point are somewhat larger than at the ground state. In particular, for ^{240}Pu, a pairing gap $2\Delta_0$ of 2.7 MeV has been reported.[3] This value was obtained from an analysis of the fission-fragment angular distribution observed in the ^{239}Pu (d, p fission) reaction. It seemed desirable to obtain experimental evidence in a different region of the periodic table and to use a different reaction in order to check the dependence of the results on the reaction involved. A systematic study was therefore undertaken of the possible superfluid effects at the saddle point of nuclei in the region $200 < A < 213$, through the (α, fission) reaction.

Fission-fragment angular distributions were measured for helium-ion-induced fission of ^{206}Pb, ^{207}Pb, and ^{209}Bi targets, starting at an energy of $\approx$ 3 MeV over the saddle point. Since the fission cross section is remarkably small in the energy region of interest, mica was used to detect the fission fragments. A schematic diagram of the fission chamber and the mica holders is shown in Fig. D.5-1. The radius of the chamber is 28.40 mm, the diameter of the collimator is 1.59 mm, and its length is 22.35 mm.

The position of the beam on the target is assured by the low convergence of the incoming beam, controlled by a quadrupole focusing lens positioned about 7 m away from the collimator. The high-intensity ^4He-ion beam was provided by the 88-inch variable-frequency cyclotron. The target consists of a water-cooled copper block on which more than 20 mg/cm^2 of high purity silver

has been evaporated in order to stop any possible fission fragments coming from copper impurities. The extremely pure target material is deposited over the silver layer by partial evaporation.

The experimental angular distribution is transformed to the center-of-mass system, and, by using the standard Halpern-Strutinskii theory, the parameter $p = \langle I^2 \rangle / 2K_0^2$ is deduced. The quantity K_0^2 is the standard deviation of the assumed Gaussian distribution of the component of the total angular momentum I on the nuclear elongation axis. The $\langle I^2 \rangle$ used to calculate K_0^2 is obtained from an optical-model program. It should be noted that in the Halpern-Strutinskii theory, the assumption is made that the magnitude of the projection M of the total angular momentum along the beam direction is 0 or << K.

Curves of K_0^2 vs bombarding energy for the compound nuclei ^{210*}Po, ^{211*}Po, and ^{213*}At are shown in Figs. D.5-2, D.5-3 and D.5-4. It can be observed that in ^{210*}Po, K_0^2 is very low for energies near the top of the barrier, and that at energies exceeding the barrier height by about 4 MeV it increases to a constant value of ≈19. At about 8 MeV over the barrier, K_0^2 rises again up to a value of 37 to 38. At still higher energies, the curve presents only minor structure. In ^{211*}Po there is the same general trend, with the difference that K_0^2 flattens out at a value of ≈ 28 to 29. These features can be explained reasonably well if one accepts a gap parameter Δ_0 of about 2 or 2.5 MeV and therefore a gap $2\Delta_0$ somewhere between 4 and 5 MeV. A BCS calculation[4] for a finite superfluid system, using a fixed-energy ensemble, chosen to resemble the neutron or proton component of a highly deformed even-even nucleus, shows that the average number of quasi particles (and, in the first approximation, K_0^2) as a function of energy presents discontinuities at excitation energies of approximately $2\Delta_0$ and $4\Delta_0$ and a less evident structure at about $6\Delta_0$ (see Fig. D.5-5). At higher energies, the statistical competition between two contiguous configurations washes out any structure. Essentially the same structures seem to be reproduced by the ^{210*}Po experiment. The two steepest parts of the curve should represent the onset of the two- and four-quasi-particle configurations. Since K_0^2 is proportional to the average number of quasi particles, and since for the same energy over the saddle point ^{211*}Po has one quasi particle more than ^{210*}Po, the ratio $K_0^2(^{210*}\text{Po})/K_0^2(^{211*}\text{Po})$ should be n/(n+1), where n is the number of quasi particles present in ^{210*}Po. Thus for two and three quasi particles, respectively, one would expect a ratio of 2/3. Since the experimental ratio of 2/3 occurs between 4 and 8 MeV over the barrier,[5] this should imply that in this region, ^{210*}Po and ^{211*}Po have respectively only two and three quasi particles. This evidence supports the idea of a pairing gap of the order of 4 or 5 MeV. The ^{213*}At data have not been corrected for the average M component introduced by the 9/2 target.

The properties observed for ^{213*}At differ from those for ^{211*}Po: the first flat region in K_0^2 is both higher and wider for ^{213*}At. The higher value of K_0^2 can be explained if one considers the effect of the M component, while the larger width could be explained if the possibly larger proton gap parameter is reduced by the extra-proton blocking effect to a value equal to the neutron gap parameter. In this way the neutron and proton quasi-particle transitions are brought in phase, thus keeping K_0^2 flat for a larger energy interval.

Similar experiments have been started for ^{208}Pb, ^{204}Pb, and ^{197}Au with helium-ion-induced fission.

Footnotes and References

*Visitor from the Laboratorio di Radiochimica, Università di Pavia, Pavia, Italy.
†Present address: Argonne National Laboratory, Argonne, Illinois.

1. A. Bohr, Paper No. P/911, in Proceedings of the International Conference on the Peaceful Uses of Atomic Energy, Geneva, 1955, Vol. 2 (United Nations, New York, 1956), p. 151.
2. James J. Griffin, Phys. Rev. 132, 2204 (1963).
3. H. C. Britt, R. Stokes, W. Gibbs, and J. Griffin, Phys. Rev. Letters 11, 393 (1963).
4. M. Rich and J. J. Griffin, Phys. Rev. Letters 11, 19 (1963).
5. The ^{210*}Po and ^{213}At barriers are taken from a private communication of Khodai, Gatti, and Thompson. The ^{211}Po barrier has been taken from William D. Myers and Wladyslaw J. Swiatecki, Nucl. Phys. 81, 1 (1966).

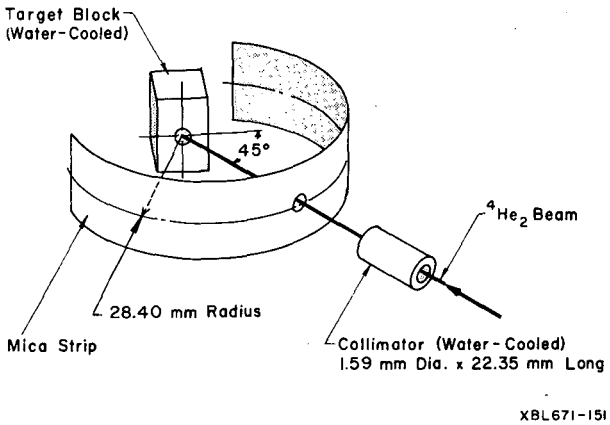

Fig. D.5-1. Schematic drawing of the apparatus used in measuring angular distributions of fission fragments.

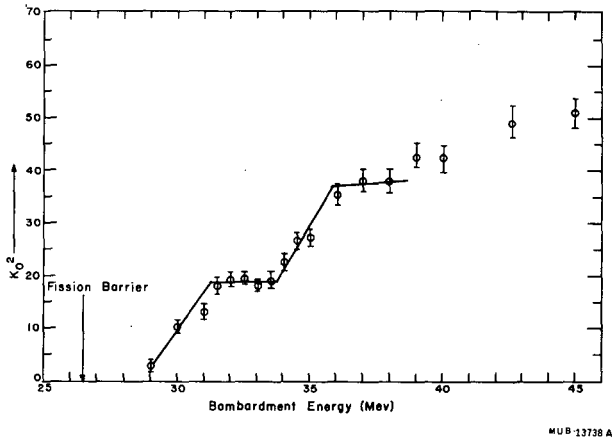

Fig. D.5-2. K_0^2 for $^{210*}_{84}Po$ at the saddle point vs bombardment energy; $^{206}_{82}Pb + ^4_2He \rightarrow ^{210*}_{84}Po \rightarrow$ fission.

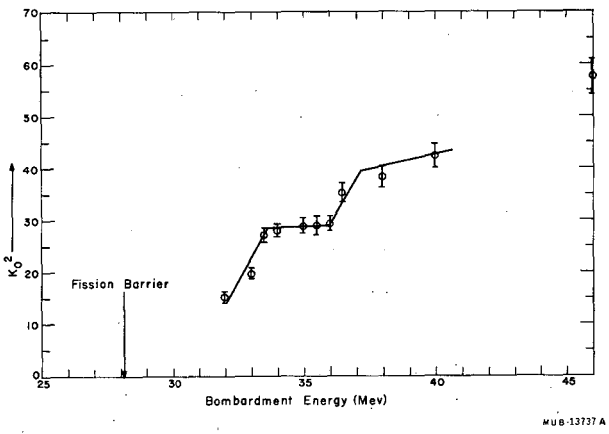

Fig. D.5-3. K_0^2 for $^{211*}_{84}Po$ at the saddle point vs bombardment energy; $^{207}_{82}Pb + ^4_2He \rightarrow ^{211*}_{84}Po \rightarrow$ fission.

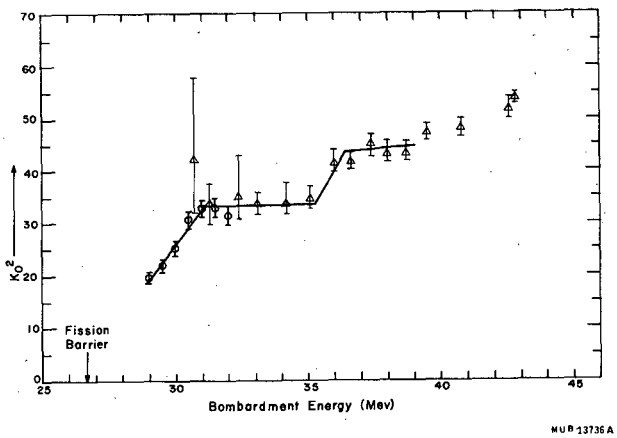

Fig. D.5-4. K_0^2 for $^{213*}_{85}At$ at the saddle point vs bombardment energy; $^{209}_{83}Pb + ^4_2He \rightarrow ^{213*}_{85}At \rightarrow$ fission.

Φ This work; ▲ Chaudhry et al., Phys. Rev. 126, 220 (1962).

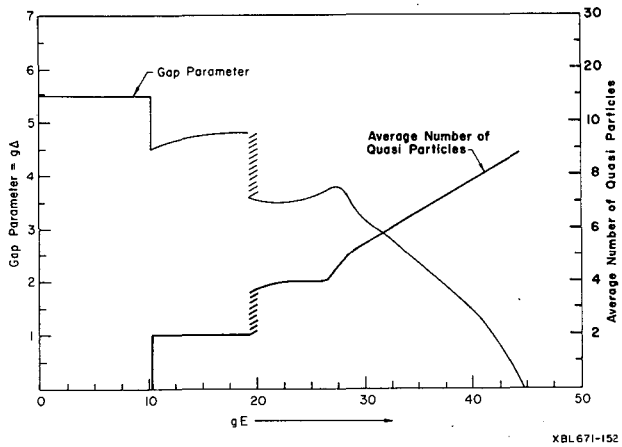

Fig. D.5-5. The dependence of the gap parameter and the average number of quasi particles on excitation energy for the fixed-energy ensemble.

6. STUDIES OF FRAGMENT ANGULAR DISTRIBUTIONS IN THE FISSION OF ^{209}Bi AND ^{238}U INDUCED BY α PARTICLES OF ENERGIES UP TO 115 MeV†

S. S. Kapoor,* H. Baba,‡ and S. G. Thompson

By use of semiconductor detectors, we have measured the fragment angular distributions in fission of ^{209}Bi and ^{238}U induced by α particles of various energies ranging from 23 to 115 MeV obtained from the Berkeley 88-inch variable-energy cyclotron. The center-of-mass angular distributions were analyzed by a least-squares fitting code to obtain the value of K_0^2 corresponding to the saddle-point excitation energy E_x^s for each bombarding energy. Examples of such angular distributions are shown in Fig. D.6-1. The transmission coefficients T_ℓ and the mean square of the orbital angular momentum $\langle \ell^2 \rangle$ of the fissioning nucleus required for deducing K_0^2 were determined from optical-model calculations. Figure D.6-2 shows the dependence of K_0^2 upon E_x^s for ^{209}Bi + ^{4}He, and Fig. D.6-3 shows the dependence of $K_0^2/(E_x^s)^{1/2}$ upon E_x^s for ^{238}U + ^{4}He. For the cases of compound nuclei of both ^{213}At and ^{242}Pu, it was found that the values of K_0^2 increase more rapidly with E_x^s than expected on the basis of the Fermi-gas model, irrespective of the assumptions made about multiple-chance fissions. The fission cross sections of ^{238}U for α-particle energies up to 110 MeV, also measured in this work and shown in Fig. D.6-4, enabled us to check the accuracy of the optical-model calculations. The presence of direct interactions and their effects on the deduced values of K_0^2 were also investigated in detail for the target nucleus ^{238}U. By use of the standard expression for Γ_n/Γ_f, the first-chance values of K_0^2 have been obtained and further corrected for the estimated direct-interaction effects, for the target nucleus ^{238}U. These results are shown in Fig. D.6-5. Even after allowance is made for the direct-interaction effects, the energy dependence of K_0^2 appears to be significantly different from that expected on the basis of the simple Fermi-gas model. These results can be explained within the framework of the Fermi-gas model if it is assumed that $J_{eff}/a_f^{1/2}$ increases significantly with the bombarding energy. It appears likely that these results suggest a rapid increase in the effective moment of inertia J_{eff} with the angular momentum, as can be expected on the basis of the observed steep variation in the saddle shapes with Z^2/A.

Footnotes and References

†Resumé of article in Phys. Rev. 149, 965 (1966).

*Present address: Nuclear Physics Division, Atomic Energy Establishment, Trombay, Bombay, India.

‡Present address: Japan Atomic Energy Research Institute, Tokaimura, Ibaraki-ken, Japan.

1. I. Halpern and V. M. Strutinskii, in Proceedings of the Second United Nations International Conference on the Peaceful Uses of Atomic Energy, Geneva, 1958 (United Nations,

Geneva, 1958), Vol. 15, p. 408.
2. R. Chaudhry, R. Vandenbosch, and J. R. Huizenga, Phys. Rev. 126, 220 (1962).
3. J. E. Simmons, R. B. Perkins, and R. L. Henkel, Phys. Rev. 137, B809 (1965).
4. V. E. Viola, Jr., J. M. Alexander, and A. R. Trips, Phys. Rev. 138, B1434 (1965).

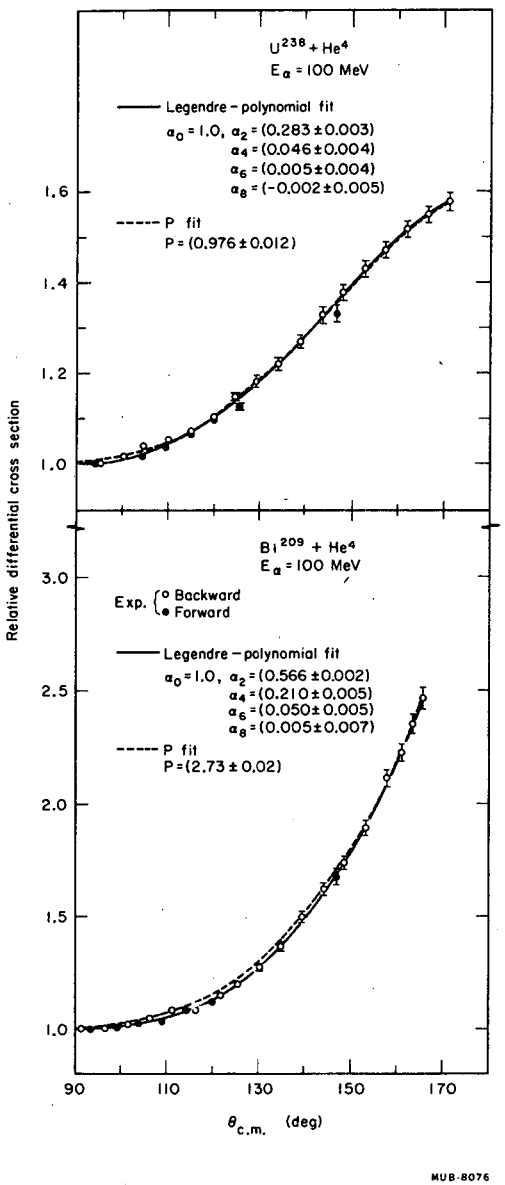

Fig. D.6-1. Relative differential cross sections as functions of the c.m. angle in degrees. The open and the closed points represent the experimental data taken in the backward and the forward directions, respectively. The solid curves are the Legendre-polynomial fits to the data. The dashed curves represent least-squares fits of the data to the result of the Halpern-Strutinskii theory.

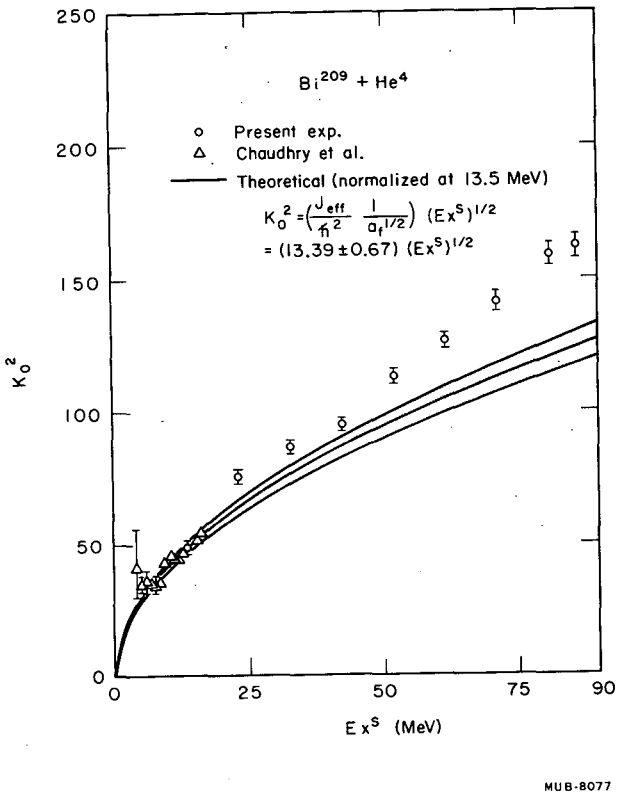

Fig. D.6-2. The deduced values of K_0^2 as a function of the excitation energy E_x^s above the fission barrier for the case of alpha-induced fission of ^{209}Bi. The values of K_0^2 obtained by Chaudhry et al. for the relatively low energy region are also shown. The region between the heavy lines represents the dependence expected on the Fermi-gas model as obtained by normalizing to the value of K_0^2 for 40-MeV α bombarding energy, where essentially all the observed fissions correspond to the first-chance fissions.

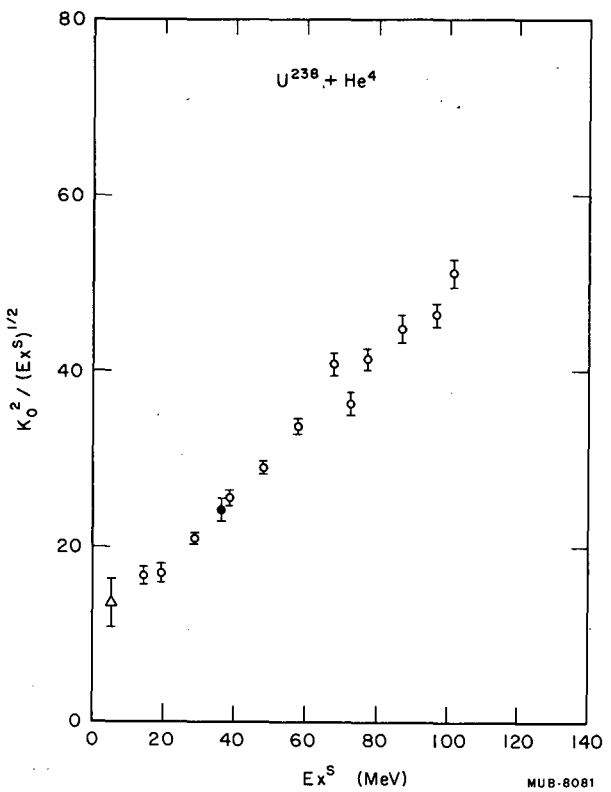

Fig. D.6-3. A plot of $K_0^2/(E_x^s)^{1/2}$ versus E_x^s for α-induced fission of ^{238}U. The two points shown by triangle and closed circle represent the values obtained by Simmons et al. and Viola et al., respectively.

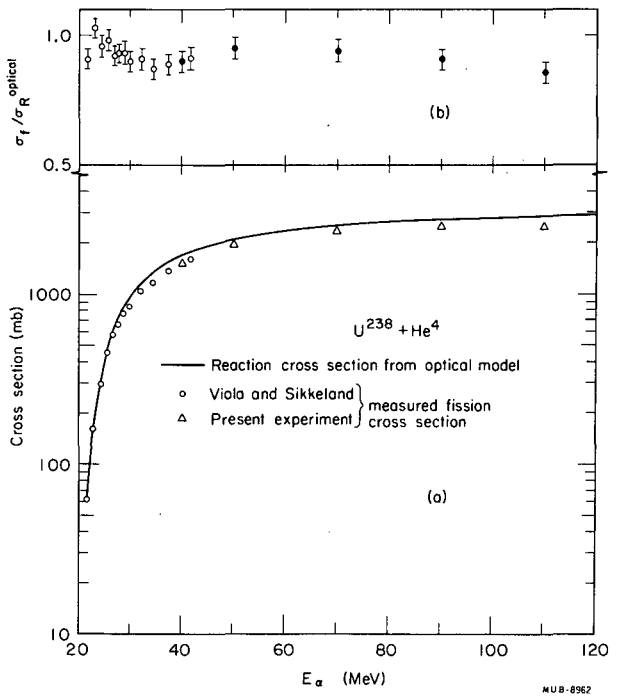

Fig. D.6-4. (a) Measured fission cross sections at different α-bombarding energies for α-induced fission of ^{238}U. The reaction cross sections calculated from an optical-model code are shown by the solid-line curve. (b) The ratio of the measured fission cross sections to the calculated reaction cross sections for different α bombarding energies. The closed circles represent the measurements carried out in this work.

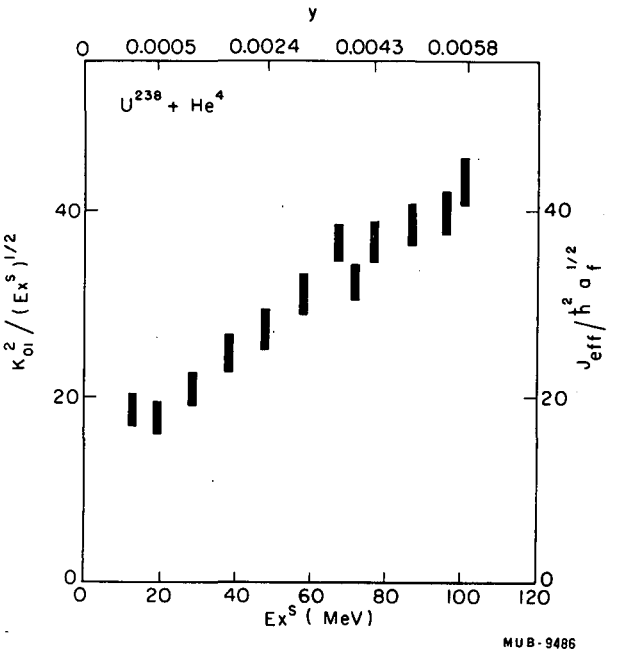

Fig. D.6-5. A plot of $K_{01}^2/(E_x^s)^{\frac{1}{2}}$ vs E_x^s. K_{01}^2 are values of K_0^2 extracted for first-chance fission at saddle-point excitation energy E_x^s. These values of K_{01}^2 have been further corrected for the estimated maximum direct-interaction effects. On the Fermi-gas model, this can also be written as a plot of $J_{eff}/(\hbar^2 a_f^{1/2})$ versus E_x^s. The values of the average angular momenta of the fissioning nucleus are shown on the top abscissa in terms of rotational parameter y, where y is the ratio of the rotational energy E_R^0 to the surface energy E_s^0 for the initial spherical shape of the nucleus. The surface energy E_s^0 is taken as equal to 17.8 $A^{2/3}$(MeV).

7. KINETIC ENERGY AND MASS DISTRIBUTIONS FROM THE FISSION OF NUCLEI LIGHTER THAN RADIUM†

F. Plasil,* D. S. Burnett,‡ H. C. Britt,** and S. G. Thompson

The distributions in masses and total kinetic energies of fission fragments from a number of elements ranging from erbium to bismuth have been measured. The nuclei undergoing fission were produced by bombarding a variety of targets with projectiles ranging from ^4He to ^{16}O. The energies of coincident fission fragments were measured by use of solid-state counters. The energy data were transformed to give mass-total kinetic energy density-of-events distributions. These distributions were compared with those calculated from an approximate version of the liquid-drop model which applies to this region of elements.[1] Examples of the comparisons, which were made without the use of any adjustable parameters, are shown in Figs. D.7-1 and D.7-2. General agreement in the shapes and widths of the distributions was found, particularly in the cases which involved small angular momenta and small nuclear temperatures. Some, but not all, of the finer details of the distributions were reproduced by the theory. As can be seen in Figs. D.7-3 and D.7-4, the dependence of the widths of the experimental distributions on the nuclear

temperature was found to differ somewhat from that predicted by the theory, but uncertainties in the evaluation of nuclear temperatures for the reactions investigated may be large. Analysis of these uncertainties indicated that they were not large enough to alone account for the discrepancy, although this analysis was subject to some error. Angular momentum effects were studied by using certain combinations of targets and projectiles to give the compound nucleus ^{186}Os at the same excitation energy but with different angular momenta. The effect of increasing angular momentum was to broaden and change the shape of the experimental distributions.

Footnotes and References

†Resumé of article in Phys. Rev. 142, 696 (1966).
*Present address: Brookhaven National Laboratory, Upton, Long Island, New York.
‡Present address: California Institute of Technology, Pasadena, California.
**Present address: Los Alamos Scientific Laboratory, Los Alamos, New Mexico.

1. J. R. Nix and W. J. Swiatecki, Nucl. Phys. 71, 1 (1965).

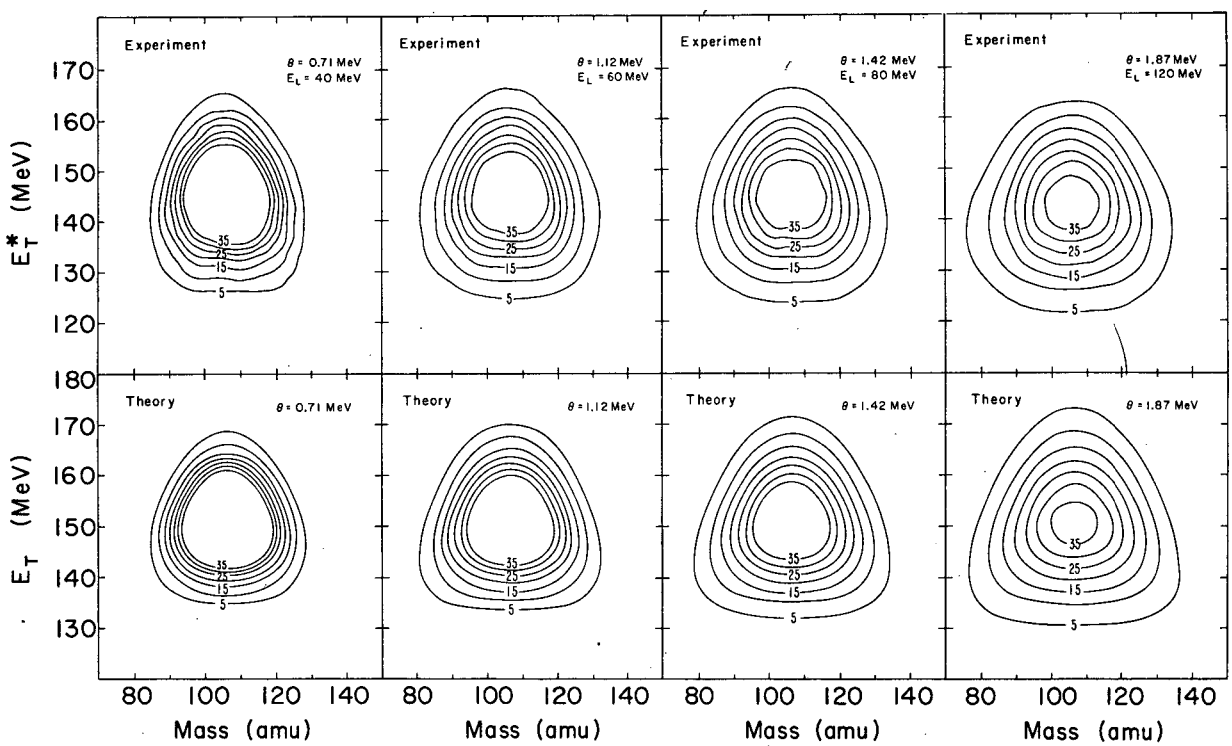

MUB-5352

Fig. D.7-1. Experimental and theoretical contour diagrams for the probability distributions, $P(E_T, A_1)$, of fragment total kinetic energy, E_T, and mass, A_1, for the reaction $^4He + {}^{209}Bi = {}^{213}At \rightarrow$ fission. Several values of the nuclear temperature of the compound nucleus, θ, and corresponding laboratory-system bombarding energies, E_L, are shown. The labels on the lines of constant probability have the following significance: a contour labeled 10, for example, would pass through those regions of the E_T versus A_1 plane where an area of 6 MeV by 3 amu contains 1% of the total number of events. Seven contours are shown at all values of θ; higher contours are present in narrow distributions at low θ values, but are not shown.

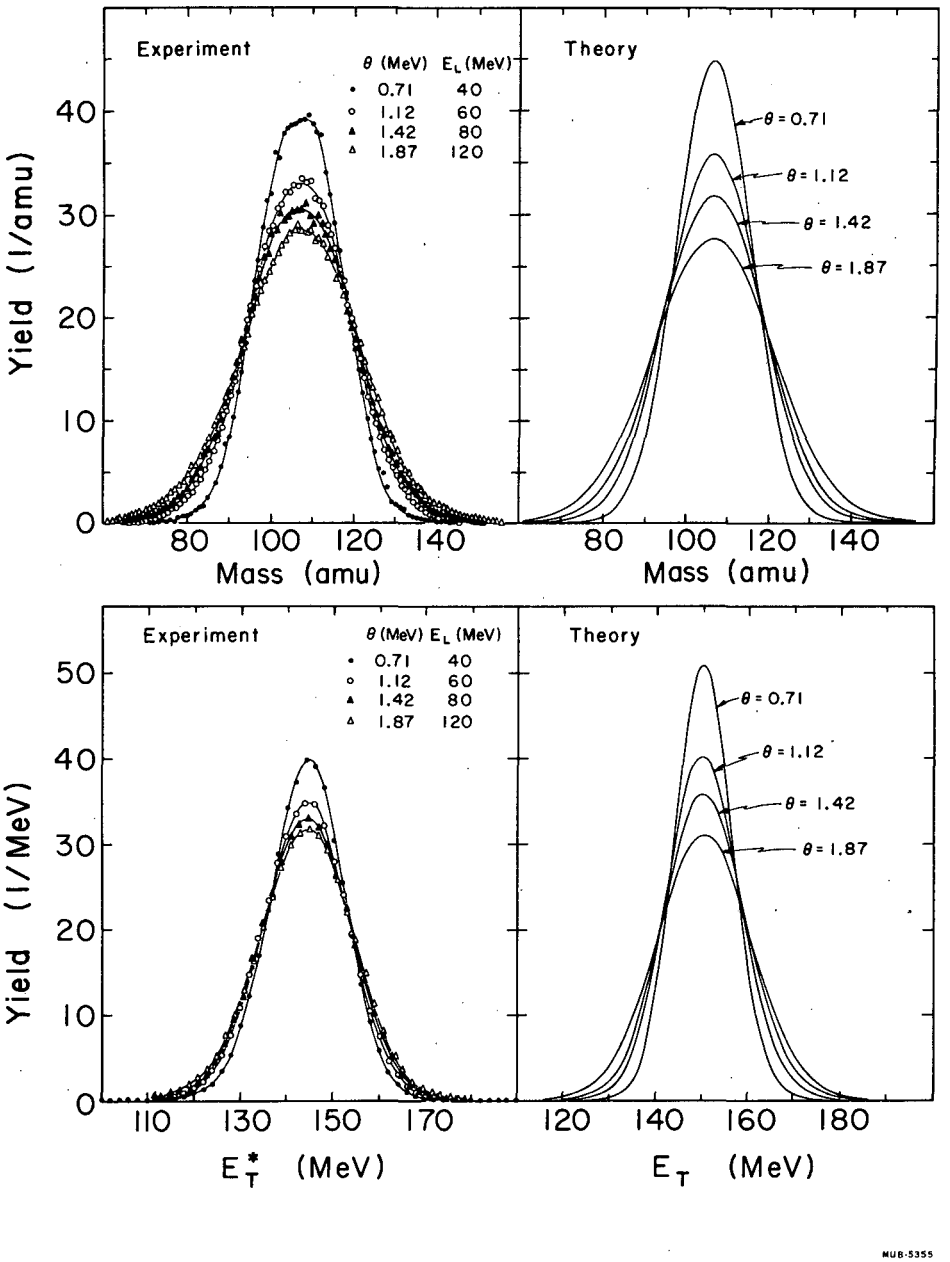

Fig. D.7-2. Mass-yield and total kinetic energy-yield distributions (experimental and theoretical) for the fission of the ^{213}At compound nucleus produced by ^{4}He bombardments of ^{209}Bi at several bombarding energies. The units of yield are arbitrary. The E_T^* scale given is that for θ = 0.71 MeV. Other experimental energy-yield distributions shown were normalized in such a way as to make their average total kinetic energy $\langle E_T \rangle$ equal to $\langle E_T \rangle$ of the θ = 0.71-MeV distribution.

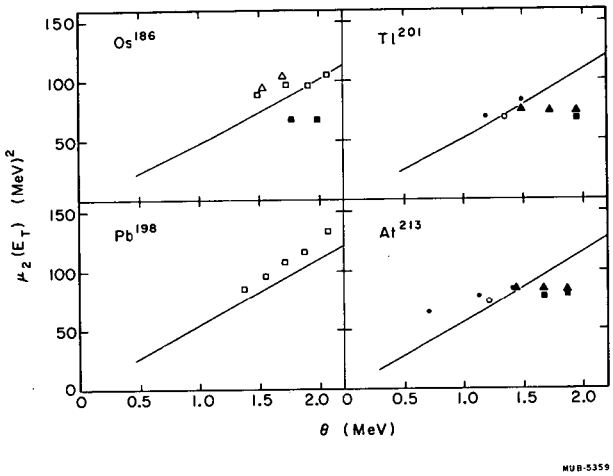

Fig. D.7-3. Variances of the overall total kinetic energy distributions, $\mu_2(E_T)$, as a function of the nuclear temperature θ, for several compoiund nuclei. The open triangles in the ^{186}Os case refer to the reaction $^{174}Yb + {}^{12}C = {}^{186}Os$. The open squares refer to $^{170}Er + {}^{186}Os$, while the closed squares refer to $^{182}W + {}^{4}He = {}^{186}Os$. The ^{198}Pb was produced by ^{16}O bombardments of ^{182}W. The ^{201}Tl and ^{213}At were obtained by ^{4}He bombardments of ^{197}Au and ^{209}Bi, respectively. The different symbols in these two cases represent different experiments. The solid line shows the theoretical result. The experimental points have been corrected for neutron emission effects. The size of the symbols is not to be taken as representative of the errors involved.

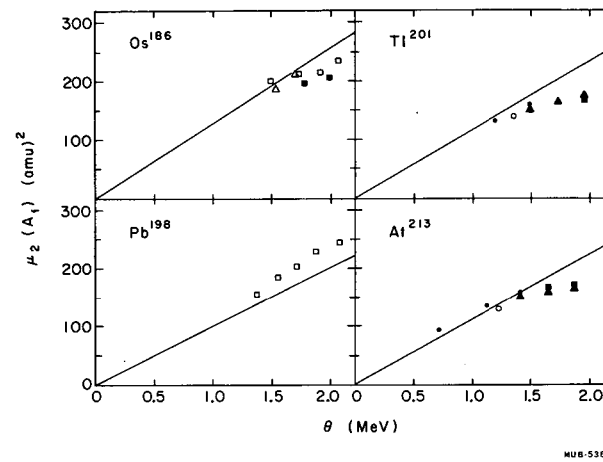

Fig. D.7-4. Variance of the overall mass-yield distributions, $\mu_2(A_1)$, as a function of the nuclear temperature θ. The symbols have the same meaning as in Fig. D.7-3. The solid line gives the theoretical calculations. The experimental results have been corrected for prompt neutron emission effects. The size of the symbols is not representative of the errors in measurement.

8. ELECTRON BINDING ENERGIES FOR HIGHLY IONIZED FISSION FRAGMENT ATOMS

R. L. Watson and J. O. Rasmussen

Recent experiments involving the measurement of γ rays and their associated internal-conversion electrons emitted from primary ^{252}Cf fission fragments have demonstrated that it is now possible to resolve discrete line spectra for many fragments.[1] The energy resolution presently attainable in this work is sufficiently precise to allow the observation of numerous individual nuclear transitions. Although the energies of the fragments undergoing the observed nuclear transitions are simultaneously measured in these experiments and may be related to their mass numbers, no direct means exists for determining their atomic numbers. It may be possible, however, to ascertain the atomic numbers of the specific isotopes responsible for many of the nuclear transitions by correlating γ-ray and internal-conversion electron energies, the difference in these two energies being equal to the electron binding energy.

It has long been known that primary fission fragments are formed in high states of ionization.[2] Due to the large velocities attained by fission fragments ($\approx 10^9$ cm/sec) very soon after fissioning, they are unable to carry along many of their outer orbital electrons and hence become highly ionized. Measurements of ^{235}U fission-fragment initial ionic charges have indicated that states of ionization ranging from +20 to +24 are commonly attained.[3,4] Since the electron binding

energies are directly affected by the state of ionization in an atom, it therefore becomes important to know how the electron binding energies vary as a function of ionic charge before attempting to determine the nuclear charges of fission fragments on the basis of measurements of electron binding energy. For this reason, we have undertaken to calculate the binding energies of several atoms which span the region of ^{252}Cf fission products (namely Sr, Pd, Xe, and Sm) as a function of ionic charge.

The binding energy calculations were carried out by using a computer program designed by Roothaan and Bagus[5] employing a nonrelativistic Hartree-Fock self-consistent field (SCF) method. The program utilizes an LCAO expansion procedure developed by Roothaan.[6]

The K binding energies were obtained by computing the total energies of both the ion in question and the ion with one 1s electron removed. The difference between these two computed total energies, then, is the K binding energy of the ion. In all cases, the total energies were calculated with minimal basis sets (one basis function for each occupied orbital) using fully optimized orbital exponents.

The K binding energies for the neutral atoms are well known.[7] The K binding energies for the single-electron atoms (ionic charge of Z-1) are easily calculable from the Sommerfeld relativistic hydrogen atom equation[8] given by

$$E_{n,\ell} = -\frac{2\pi^2\mu e^4}{h^2}\,\frac{Z^2}{n^2}\left[1 + \frac{\alpha^2 Z^2}{n}\left(\frac{1}{J+\frac{1}{2}} - \frac{3}{4n}\right)\right],$$

$$E_{1,0} = -ChR_\infty\left(\frac{M}{M+m}\right)Z^2\left[1 + 0.25\,\alpha^2 Z^2\right], \tag{1}$$

where α is the Sommerfeld fine-structure constant and R_∞ is the Rydberg constant for an infinitely heavy nucleus. When the approriate values are inserted, this equation reduces to

$$E_{1,0} = -13.606\times10^{-3}\,Z^2\,(1 + 13.314\times10^{-6}\,Z^2)\ \text{keV}. \tag{2}$$

By comparing the calculated values for the neutral and single-electron cases with the values obtained from Ref. 7 and Eq. (2), the error in the calculated values was found to range from 1.8% for strontium to 4.9% for samarium. This error was attributed to calculational error arising from the use of minimal basis sets, and to correlation and relativistic energy effects not taken into consideration by the computation.

The relative error was very nearly the same for both the neutral and the single-electron cases. On this basis, the relative error in the calculated values was assumed to be constant with respect to ionic charge state, and a linear adjustment was made on all calculated K binding energy values such that the two extremes of ionic charge states (neutral and single electron) agreed with the values obtained from Ref. 7 and Eq. (2). These values were then plotted as a function of ionic charge, and a smooth curve was fitted through the points.

Using the calculated binding energy curves for Sr, Pd, Xe, and Sm, we determined an empirical formula for computing the K binding energies of atoms from Z = 34 to Z = 66 in any state of ionization:

$$E_{ion} = E_{neut}\left[1 + f(n_e/Z)\,e^{-aZ}\right], \tag{3}$$

where E_{ion} = K binding energy of the ion,
E_{neut} = K binding energy of the neutral atom,
Z = atomic number,
n_e = ionic charge of the ion,
a = 1.8484×10^{-2} (empirical constant).

The function $f(n_e/Z)$ is a seventh-degree polynomial in $(n_e/Z)^{3/2}$:

$$f\left(\frac{n_e}{Z}\right) = \sum_{k=1}^{7} C_k \left[\left(\frac{n_e}{Z}\right)^{3/2}\right]^k , \tag{4}$$

where

$C_1 = 0.2491,$
$C_2 = -0.6131,$
$C_3 = 4.001,$
$C_4 = -10.28,$
$C_5 = 14.88$
$C_6 = -11.55,$
$C_7 = 3.861.$

Equation 3 reproduces the calculated binding energy curves with a maximum deviation of ±0.04 keV for all states of ionization except the single-electron state (which is easily calculable from Eq. 4) and is believed to give values that are accurate to ±0.08 keV. Binding energy curves resulting from the SCF calculations are given in Figs. D.8-1 and D.8-2 for the 2s and 2p orbitals of Sr, Pd, Xe, and Sm. The values of the single orbital eigenvalues (orbital energies) were taken as the unadjusted binding energies of all orbitals other than the 1s orbitals (Koopman's theorem[9]).

The calculated K and L electron binding energies as well as the Kα x-ray energies for the neutral atoms and for the probable ionic charge states formed in fission are listed in Table D.8-I, and K binding energy increase is plotted as a function of atomic number for these charge states in Fig. D.8-3. On the basis of the available measurements of ionic charge states of fission fragments, we have estimated the most probable initial charges for Sr, Pd, Xe, and Sm fission fragments arising from the spontaneous fission of ^{252}Cf to be +21, +23, +24, and +26 respectively. It is interesting to note in Fig. D.8-3 that the present calculations yield K binding energy increases of approximately 0.9 keV (ΔE_{ave} = 0.93 keV) for each of these ions, and hence tend to indicate that this increase is nearly constant over the whole region of fission products.

Recently, determinations of the distribution of nuclear charge formed in fission, based upon measurements of K x-ray energies, have been reported by Glendenin and Griffin[10] and by Kapoor, Bowman, and Thompson.[11] These studies have raised the question of whether or not the effect of ionization on the x-ray energies may be neglected. The present calculations indicate, as may be seen from Table D.8-I, that the Kα x-ray energies of typical fission fragments are shifted by 50 eV or less. Hence, the neglect of corrections for the effect of ionization in the above-mentioned experiments was indeed justified.

In Fig. D.8-4 a plot is shown of the relative increase in K binding energy versus the relative ionization for Sr, Pd, Xe, and Sm. On the enlarged section of this figure are shown several experimentally measured energy shifts made in conjunction with a recent study of the fission-fragment conversion electrons.[12] The horizontal error bars represent the statistical uncertainty associated with the energy determination, and the vertical error bars extend over an arbitrary 1 charge unit on either side of the estimated fragment ionic charge. Although the points for Z = 44 and Z = 54 tend to indicate somewhat different ionic charges than expected, the measurements are too rough to use for anything other than an illustration of experimentally observed binding energy shifts. (A number of experimental uncertainties may have contributed a significant amount of systematic error to these measurements.)

It is interesting to note that utilization of the binding energy shifts experienced by atoms as a result of ionization or perturbation of their outer electrons has already been reported by Hagstrom, Nordling, and Siegbahn[13] in determinations of chemical valence states. They have detected K binding energy shifts between the 0 and 4+ and the 0 and 6+ valence states in sulfur of 4.3 and 5.5 eV respectively, with an accuracy within 0.2 eV.

Conceivably, the relatively large shifts in binding energies between adjacent charge states in highly ionized fission fragments (≈ 70 eV) could be used to study in detail the distribution of ionic charge resulting from fission. Hypothetically, internal conversion electrons arising from nuclear transitions offer a direct means of measuring these binding energy shifts. The application is obscured, however, by a number of experimental difficulties stemming from the fact that the fragments are traveling at relatively high velocities, which for any single isotope may vary by as much as 15%.

References

1. H. R. Bowman, S. G. Thompson, R. L. Watson, S. S. Kapoor, and J. O. Rasmussen, in Physics and Chemistry of Fission (IAEA, Austria, 1965), p. 125.
2. N. Bohr, Kgl. Danske Videnskab. Selskab, Mat.-Fys. Medd. 18, 8 (1940).
3. B. L. Cohen, Phys. Rev. 104, 1046 (1956).
4. H. Opower, E. Konecny, and G. Siegert, Z. Naturforsch. 20, 131 (1965).
5. C. C. J. Roothaan and P. S. Bagus, Methods in Computational Physics (Academic Press, New York, 1963), Vol. II, p. 85.
6. C. C. J. Roothaan, Rev. Mod. Phys. 32, 179 (1960).
7. S. Hägström, C. Nordling, and K. Siegbahn, In Alpha-, Beta-, and Gamma-Ray Spectroscopy, Vol. I, edited by K. Siegbahn (North-Holland Publishing Co., Amsterdam, 1965), p. 845.
8. R. M. Eisberg, Fundamentals of Modern Physics (John Wiley and Sons, New York, 1964), p. 356.
9. T. Koopmans, Physica 1, 104 (1933).
10. L. E. Glendenin and H. C. Griffin, Phys. Letters 15, 153 (1965).
11. S. S. Kapoor, H. R. Bowman, and S. G. Thompson, Phys. Rev. 140, B1310 (1965).
12. R. L. Watson, A Study of the Internal Conversion Electrons Emitted Within Three Nanoseconds after the Spontaneous Fission of ^{252}Cf (Ph. D. Thesis), UCRL-16798, July 1966.
13. S. Hagström, C. Nordling, and K. Siegbahn, Z. Physik 178, 439 (1964).

Table D.8-I. K, L, and Kα energies for Sr, Pd, Xe, and Sm fission fragment ions.

	Electron binding energy (keV)			Kα x-Ray
	1S	2S	2P	Energy (keV)
Sr neutral	16.11	2.21	1.97	14.14
Sr^{+20}	16.94	3.02	2.76	14.18
Sr^{+21}	17.02	3.10	2.84	14.18
Sr^{+22}	17.10	3.18	2.92	14.18
Pd neutral	24.35	3.61	3.26	21.09
Pd^{+22}	25.22	4.49	4.14	21.08
Pd^{+23}	25.30	4.57	4.22	21.08
Pd^{+24}	25.39	4.65	4.30	21.09
Xe neutral	34.58	5.45	4.94	29.64
Xe^{+23}	35.42	6.25	5.74	29.68
Xe^{+24}	35.49	6.32	5.81	29.68
Xe^{+25}	35.56	6.38	5.88	29.68
Sm neutral	46.86	7.74	7.02	39.84
Sm^{+24}	47.67	8.51	7.80	39.87
Sm^{+25}	47.74	8.57	7.85	39.89
Sm^{+26}	47.81	8.63	7.92	39.89

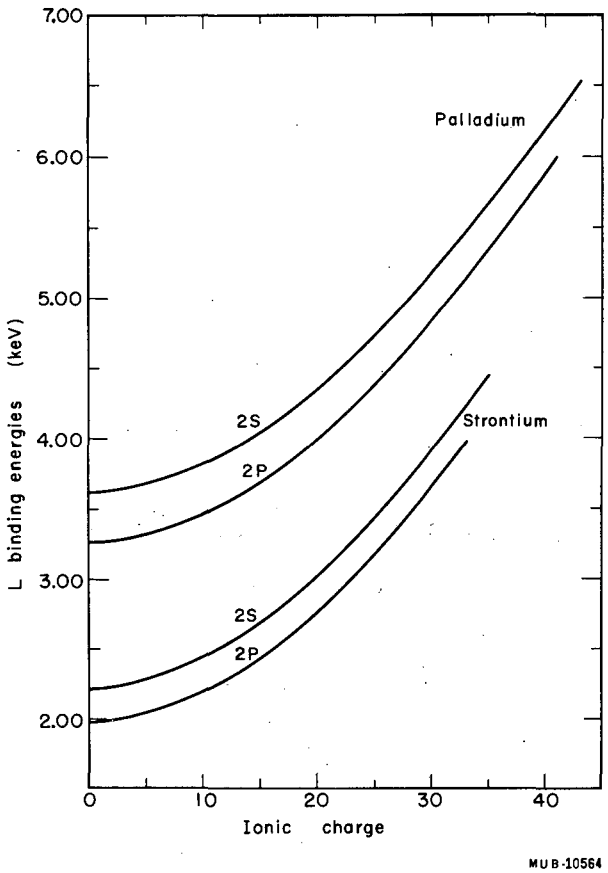

Fig. D.8-1. Calculated L binding energies of a strontium and a palladium atom as a function of their ionic charges.

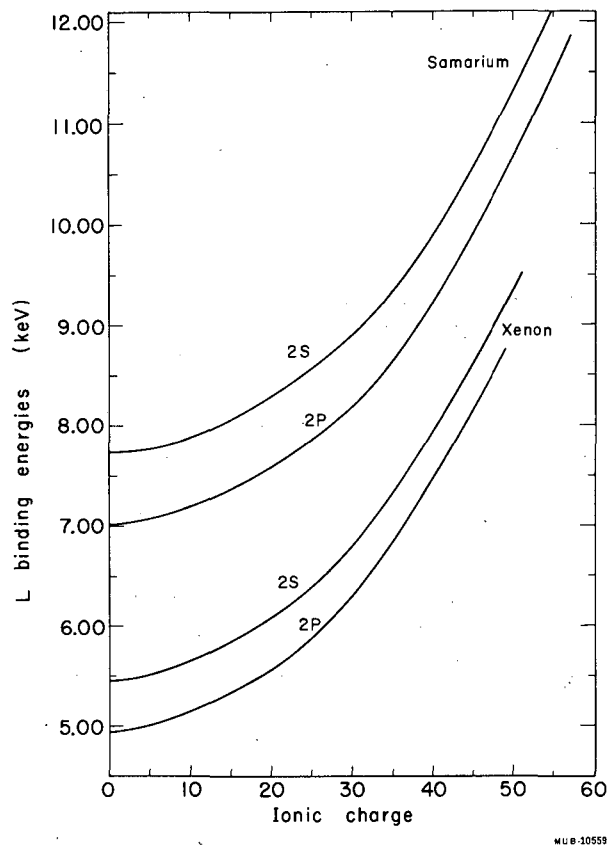

Fig. D.8-2. Calculated L binding energies of a xenon and a samarium atom as a function of their ionic charges.

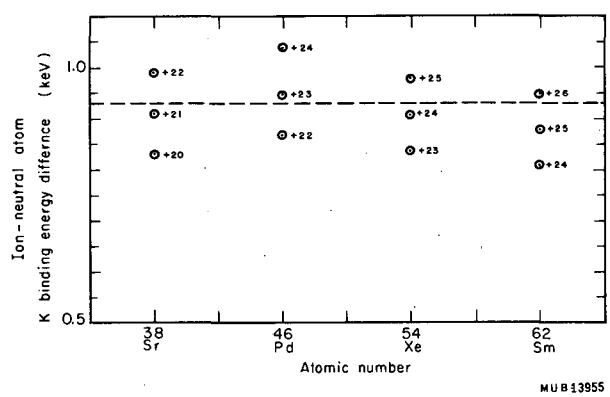

Fig. D.8-3. The calculated increase in K binding energy for several probable fission-fragment ionic charge states as a function of nuclear charge. The dashed line indicates the approximate constancy of the K binding energy increase for the proable charge states of +21, +23, +24, and +26 spanning the whole region of fission product isotopes.

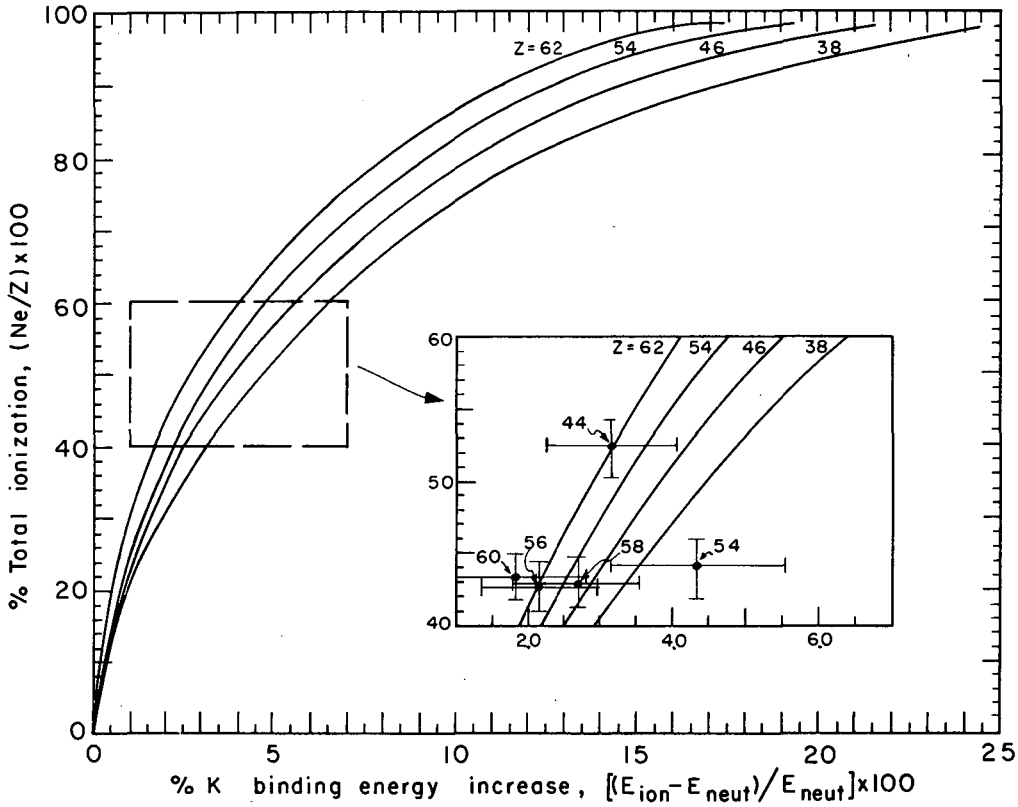

Fig. D.8-4. Comparison of the relative increase in K binding energy as a function of total ionization for Sr, Pd, Xe, and Sm. Enlarged section contains several experimentally measured points taken from Ref. 13.

9. x-RAY, γ-RAY COINCIDENCE MEASUREMENTS ON FISSION PRODUCTS

J. B. Wilhelmy, S. G. Thompson, and J. O. Rasmussen

Recent experiments[1-6] have demonstrated the feasibility of obtaining discrete spectroscopic information for individual isotopes from the prompt fission products. The method consisted of sorting the emitted radiation (x rays, γ rays, or conversion electrons) with respect to the masses of the particles. With the advent of high-resolution lithium-drifted silicon and germanium detectors it has become possible to perform x-ray, γ-ray coincidence measurements on unseparated fission products. This technique allows the determination of the element from which the radiation is being emitted without performance of any chemical or physical separations.

The experimental apparatus consists of a 6-cm^3 lithium-drifted germanium detector for γ rays and a 1-cm by 3-mm-deep lithium-drifted silicon detector for x rays. They are placed in a standard fast-slow coincidence circuit. The coincident analog signals from these detectors are stored event by event in a multidimensional pulse-height analyzer. To prevent long-term energy drift in the system, digital gain stabilization is used.[7] The coincidence data are subsequently sorted on a computer to give γ-ray spectra with respect to x-ray energy intervals or, conversely, x-ray spectra with respect to γ-ray energy intervals. Fission products from the spontaneous fission of ^{252}Cf were collected for approximately 3 months. These were allowed to cool for 5 hours and then were counted for 12 days. During this period 2.5×10^6 coincidence events were recorded.

Since the fission products are all β^- emitters, in order to obtain an x-ray, γ-ray coincidence, it is necessary that there be a cascade of γ rays with at least one of the members undergoing internal conversion in the K electron shell. This requirement forbids the observation of γ rays coming from the de-excitation of levels which are not members of a prompt cascade. This also means that the observed intensity of the γ rays does not necessarily follow their isotopic abundances. Although this is a restriction for obtaining total information on all isotopes, it is an aid in obtaining information on some weakly abundant isotopes which have a favorable decay scheme.

The figures shown below demonstrate the type of information obtainable by this method. Figure D.9-1(a) is the γ-ray spectrum which is in coincidence with the total x-ray energy interval (5 to 60 keV). Some well-defined peaks can be seen. These are coded and identified in Table D.9-I. Figure D.9-1(b) shows the γ-ray spectrum that is in coincidence with the 26.5- to 29.0-keV portion of the x-ray energy interval. This energy interval includes the $K\alpha_1$ and the $K\alpha_2$ x-ray energies of I (28.6 and 28.3 keV, respectively). It is seen in this figure that the most intense γ ray is greatly enhanced with respect to its relative intensity in Fig. D.9-1(a). Figure D.9-1(c) shows the γ-ray spectrum in coincidence with the x-ray energy range from 37.5 to 40.0 keV. This interval contains the $K\alpha_1$ and $K\alpha_2$ x rays of Pm (38.7 and 38.2 keV, respectively). The indicated peaks in the spectrum come from the decay of $^{147}Nd \rightarrow {}^{147}Pm$. The correct assignment of the element emitting the radiation can be determined by observing the x-ray energy at which the γ ray is the most intense. The assignment can then be confirmed, as shown in Fig. D.9-2, by sorting the x-ray spectrum with respect to the γ ray of interest. Figure D.9-2(a) shows the overall x-ray spectrum sorted with respect to the total γ-ray energy interval (100 to 650 keV). Again, some discernible peaks appear above the general background. Figure D.9-2(b) is the x-ray spectrum in coincidence with the most intense γ ray of Fig. D.9-1(b). This spectrum shows the $K\alpha$ and $K\beta$ x rays of I and the 50-keV transition in ^{132}I. From this information it is possible to assign the γ ray to a transition in an I isotope. From its energy, the γ ray is known to originate from the β^- decay of $^{132}Te \rightarrow {}^{132}I$. By a similar procedure the indicated γ rays shown in Fig. D.9-1(c) are found to originate from the decay of $^{147}Nd \rightarrow {}^{147}Pm$. By this technique it has been possible to identify γ radiation from the decay of the isotopes ^{44}Mo, ^{103}Ru, ^{132}Te, ^{131}I, ^{140}Ba, ^{140}La, ^{143}Ce, and ^{147}Nd.

As seen from the figures, the most prominent peak in the spectrum comes from the decay of $^{132}Te \rightarrow {}^{132}I$. Since in the spontaneous fission of ^{252}Cf the mass yield of the mass-132 chain is only 2.0%, this at first appears inconsistent. From the simple decay scheme for the decay of ^{132}Te (Fig. D.9-3), it is evident that this is a strongly favored case for the required coincidence. The 50-keV transition in ^{132}I is highly converted and therefore gives many x rays. This, of course, enhances the coincidence requirement and the 228-keV γ ray appears very intense.

These results were for isotopes with relatively long half-lives (30 hr $\leq t_{1/2} \leq$ 40 days). It is felt that the great utility of this method will lie in the areas where short half-lives make it impractical to do chemical separations. With this objective, investigations are currently underway to use this procedure on gross fission isotopes with short half-lives (0.1 sec $< t_{1/2} <$ 1 hr).

References

1. H. R. Bowman, S. G. Thompson, and J. O. Rasmussen, Phys. Rev. Letters 12, 195 (1964).
2. R. L. Watson, H. R. Bowman, S. G. Thompson, and J. O. Rasmussen, Phys. Rev. Letters 14, 183 (1965).
3. H. R. Bowman, S. G. Thompson, R. L. Watson, S. S. Kapoor, and J. O. Rasmussen, in Proceedings of the International Symposium on the Physics and Chemistry of Fission, Salzburg, Austria, 1965 (IAEA, Austria, 1965).
4. R. L. Watson, H. R. Bowman, S. G. Thompson, and J. O. Rasmussen, Internal Conversion Processes (Academic Press, New York, 1955) p. 443.
5. S. S. Kapoor, H. R. Bowman, and S. G. Thompson, Phys. Rev. 140, B1310 (1965).
6. R. L. Watson, A Study of the Internal Conversion Electrons Emitted Within Three Nanoseconds After the Spontaneous Fission of ^{252}Cf (Ph. D. Thesis), UCRL-16798, July 1966.
7. M. Nakamura and R. L. La Pierre, Nucl. Instr. Methods 32, 277 (1964).

Table D. 9-I. Coding and identification of peaks in γ-ray spectra.

Figure	Code	Energy (keV)	Assignment
1	A	120	^{147}Nd
	B	141	^{99}Mo
	C	162	^{140}Ba
	D	228	^{132}Te
	E	275	^{147}Nd
	F	284	^{131}I
	G	291	^{143}Ce
	H	305	^{140}Ba
	I	319	^{147}Nd
	J	329	^{140}La
	K	400	^{147}Nd
	L	424	^{140}Ba
	M	440	^{147}Nd
	N	487	^{140}La
	O	537	^{140}Ba
	P	555	^{103}Ru
2	A	18.3	Kα Tc
	B	20.2	Kα Rh
	C	28.5	Kα I
	D	30.0	^{140}Ba
	E	32.3	Kβ I
	F	35.9	Kα Pr
	G	38.6	Kα Pm
	H	41.0	^{99}Mo
	I	50.0	^{132}Te

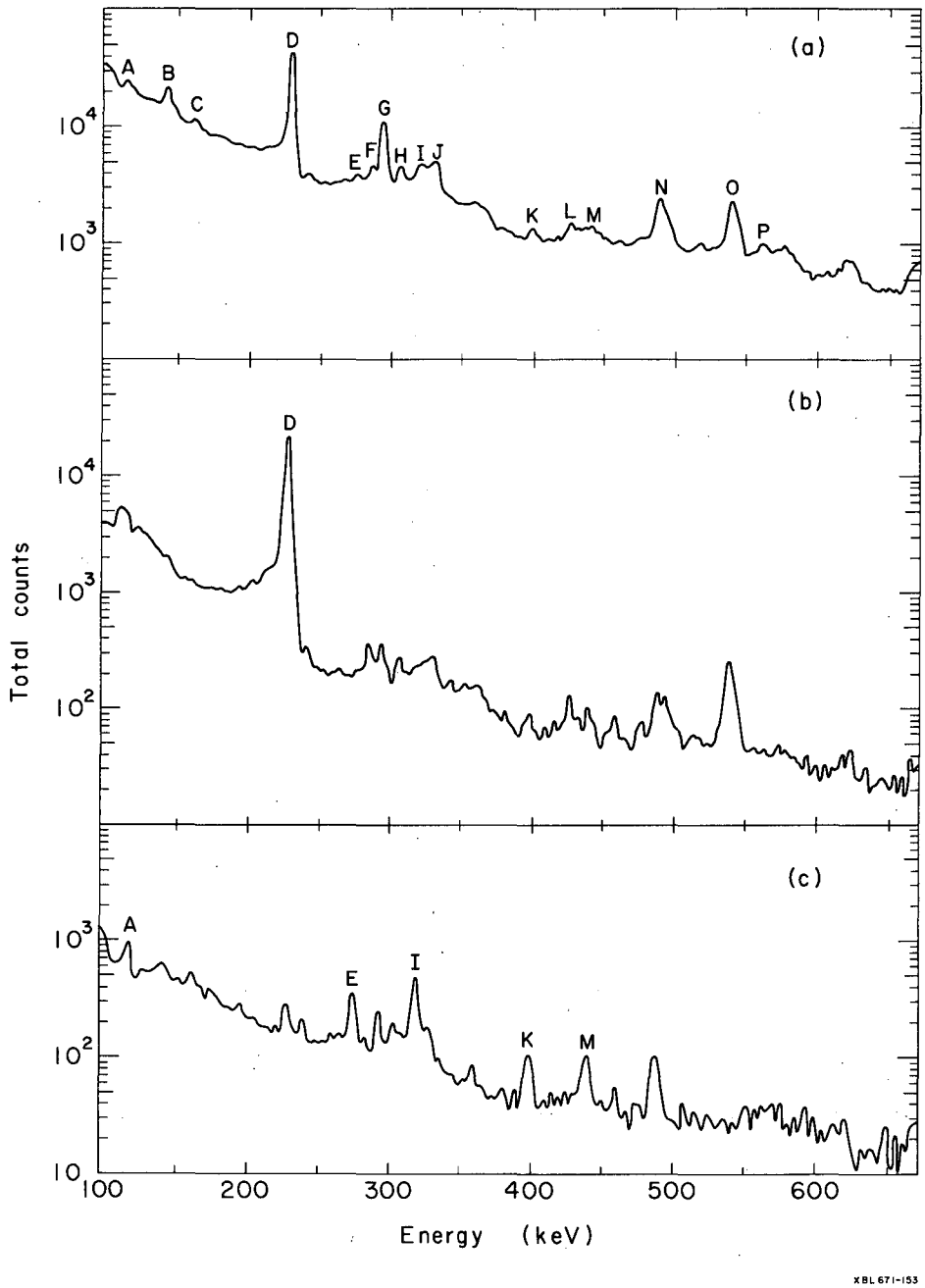

Fig. D.9-1. Gamma-ray spectrum in coincidence with x-ray intervals of (a) 5 to 60 keV, (b) 26.5 to 29.0 keV, and (c) 37.5 to 40.0 keV.

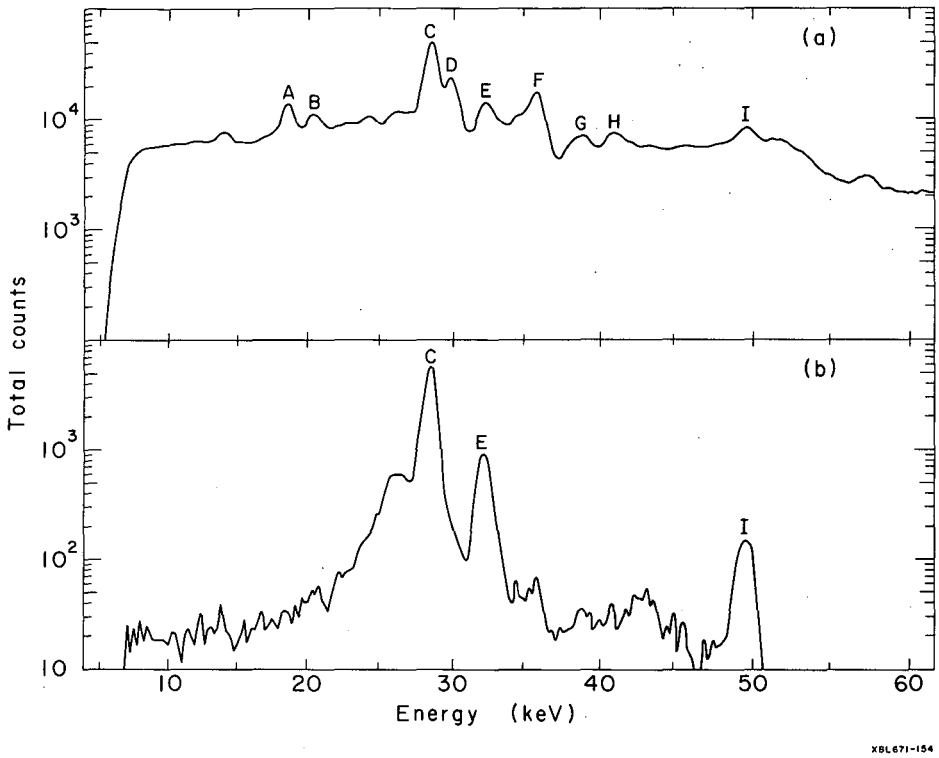

Fig. D.9-2. x-Ray spectrum in coincidence with γ-ray intervals of (a) 100 to 650 keV and (b) 227 to 229 keV.

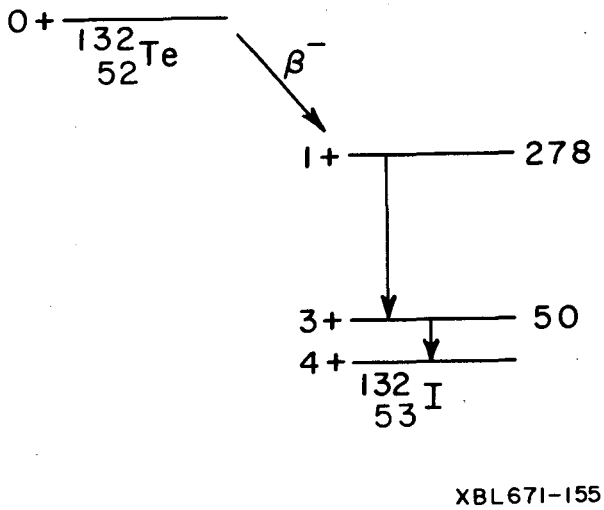

Fig. D.9-3. Decay scheme of ^{132}Te.

10. AN EMPIRICAL FORMULA FOR THE NUMBER OF ^{252}Cf SPONTANEOUS-FISSION NEUTRONS AS A FUNCTION OF THE FISSION MASS PAIR AND THE TOTAL KINETIC ENERGY

Eiko Takekoshi[†*] and Stanley G. Thompson

Properties of the prompt neutrons associated with the spontaneous fission of ^{252}Cf have been reported by H. R. Bowman et al.[1] The numbers of neutrons emitted and the neutron angular distributions were analyzed as a function of fission-fragment mass and total kinetic energy. They presented graphically a number of their results, such as the variation of the number of neutrons per fragment with fragment mass, the total number of neutrons per fission as a function of mass pair, the average number of neutrons per fragment as a function of fragment mass for selected total kinetic energy intervals, and the number of neutrons versus total kinetic energy for selected fragment masses.

Although their graphs can be used directly to analyze ^{252}Cf spontaneous-fission experiments, in order to evaluate the number of neutrons ν emitted as a function of fragment mass and total kinetic energy, it is sometimes more convenient to use an empirical expression that will yield the same results. With this goal in mind, the original experimental data[1] were fitted to the empirical formula

$$\nu(M, E_T) = A(M)e^{-B(M)(E_T-150)} , \qquad (1)$$

where M designates the fission-fragment mass pair and E_T the total kinetic energy in MeV. The parameters A(M) and B(M) were obtained by means of least-squares fits of Eq. 1 to the above-mentioned data for selected fragment pairs (one of which is shown in Fig. D.10-1 for the fragment mass pair 104.5–147.8). The parameters A(M) and B(M) are tabulated in Table D. 10-I and are also plotted as functions of fragment mass in Figs. D. 10-2 and D. 10-3, respectively.

As can be seen in Fig. D.10-1, the fitting of the empirical expression to the data is very good. Therefore, if the formula were also applicable to the fission of other elements, its use might help resolve some of the essential problems associated with the fission mechanism, particularly those connected with total kinetic energy, excitation energy, and total energy released.

Footnotes and Reference

[†]Postdoctoral physicist, February 1965 to February 1966.
[*]Present address: Japan Atomic Energy Research Institute, Tokaimura, Naka-gun, Ibaraki-ken, Japan.

1. H. R. Bowman, J. C. D. Milton, S. G. Thompson, and W. J. Swiatecki, Phys. Rev. 129, 2133 (1962).

Table D.10-I. A(M) and B(M) values with standard deviations associated with mass pairs fragment, M.

M	A(M)	B(M)	± ΔA(M)	± ΔB(M)
90.6-162.0	1.051142E 01	3.175789E-02	1.145673E 00	5.587937E-03
93.3-159.1	1.298356E 01	4.047030E-02	1.119826E 00	4.320221E-03
96.0-156.1	1.036345E 01	3.418736E-02	1.062659E 00	2.219159E-03
98.9-153.2	1.059153E 01	3.551356E-02	1.073524E 00	2.417977E-03
101.7-150.4	1.411688E 01	4.568359E-02	1.049548E 00	1.557781E-03
104.5-147.8	1.548740E 01	4.709535E-02	1.043418E 00	1.295249E-03
107.1-145.3	1.711756E 01	4.757485E-02	1.045976E 00	1.306369E-03
109.6-142.8	1.908681E 01	4.711096E-02	1.040042E 00	1.105750E-03
112.3-140.2	1.613277E 01	3.966645E-02	1.072244E 00	1.902963E-03
114.9-137.7	2.186056E 01	4.468517E-02	1.084261E 00	2.137312E-03
117.4-135.3	1.961045E 01	4.037683E-02	1.075005E 00	1.855199E-03
119.7-133.0	1.978643E 01	3.740538E-02	1.096399E 00	2.375969E-03
123.8-128.5	1.607475E 01	2.703174E-02	1.099831E 00	2.607426E-03

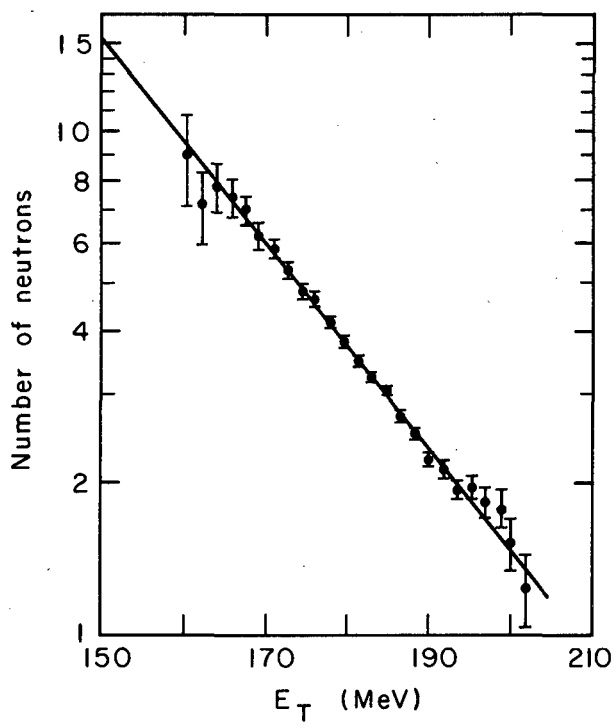

XBL671-191

Fig. D.10-1. Number of prompt neutrons as a function of the total kinetic energy associated with fragment mass pair 104.5–147.8. The points with standard deviations were calculated from Tables I and IV of Ref. 1, and the straight line in the semi-logarithmic graph was obtained by means of a least-squares fit to the formula

$$\nu(M, E_T) = A(M)\, e^{-B(M)(E_T - 150)} .$$

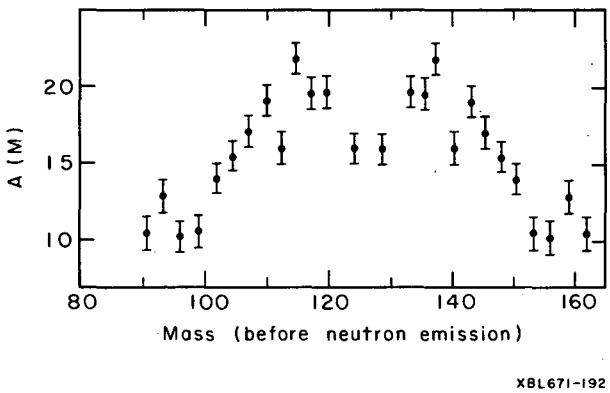

Fig. D. 10-2. A(M) values with standard deviations as a function of fragment mass pairs.

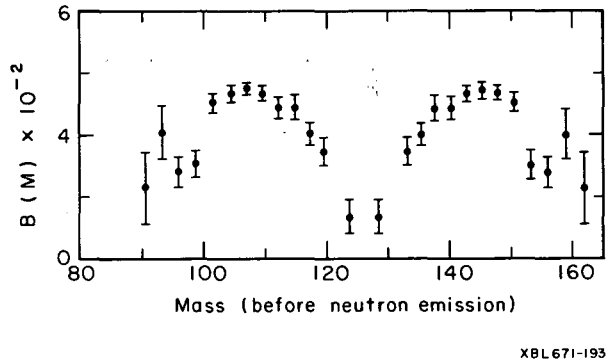

Fig. D.10-3. B(M) values with standard deviations as a function of fragment mass pairs.

E. HYPERFINE INTERACTIONS

1. NUCLEAR MAGNETIC RESONANCE IN POLARIZED NUCLEI†

E. Matthias and R. J. Holliday

The nuclear ferromagnetic resonance of ^{60}Co in Fe has been detected by observing the effect of a rf field on the angular distribution of the γ radiation emitted by polarized ^{60}Co nuclei at temperatures of about 0.03°K. At resonance, rf-induced transitions partially randomize the Boltzmann distribution, which is set up by the low temperature and the large hyperfine field for Co in Fe, in the ^{60}Co ground state. This has a highly disturbing effect on the angular distribution of the emitted γ rays, which can be detected by observing the counting rate at a specific angle as a function of frequency. The enhancement of the rf amplitude in a ferromagnet[1] was necessary to keep the rf power at a sufficiently low level to avoid a rapid warm-up of the sample.

An experiment of this type was suggested in principle by Bloembergen and Temmer[2] in 1953, but to our knowledge, no successful experiment has been carried out along this line. The reason for the lack of success was probably the large heating effect of the rf field.

The low temperature (0.02°K) was reached by adiabatic demagnetization of a chrome-alum-glycerine slurry. The sample was a thin ($\approx 10^{-4}$ cm) Fe foil about 3×3 mm^2 onto which the activity was electroplated. The activity was then diffused (alloy I at 950°C for 80 hr, alloy II at 950°C for 48 hr) into the foil. The polarizing field, H_0, was parallel to the plane of the foil and was produced by a pair of Nb rings located on either side of the foil. The rf field, H_1, was oriented parallel to the plane of the foil but perpendicular to the polarizing field H_0.

The effect can be seen in the upper part of Fig. E. 1-1, where the warm-up curve for $\theta = 0$ deg is shown as a function of frequency, which was varied at constant time intervals. The resonance effect is clearly visible at about 165.8 MHz. To check whether this peak is really a frequency effect we measured the warm-up curve for the same temperature interval and the same rf amplitude but at a fixed frequency off resonance. The result was negative, as shown in the lower part of Fig. E. 1-1. To improve statistics we added together the results of different demagnetizations, and the final result for two different alloys is shown in Fig. E. 1-2. The data in the left part of this figure (alloy I) are the sum of four demagnetizations, in which the frequency range was scanned twice per demagnetization. The data on the right (alloy II) are the result of two demagnetizations with one frequency scan after each. Although the effect at 90 deg is smaller, it is quite apparent that at 0 deg the sign is opposite. The observed line widths of about 0.8 MHz (alloy I) and 0.5 MHz (alloy II) are of the same order of magnitude as observed in nuclear ferromagnetic resonance.

The average value of the resonance frequency taken from both alloys is 165.75 ± 0.15 MHz. With a magnetic moment of $\mu = 3.754 \pm 0.008$ nm[3] this gives an effective magnetic field of $|H_{eff}| = 289.6 \pm 0.7$ kG. Assuming that the demagnetization factor for a thin foil is negligible, we obtain, after correcting for the polarizing field (1.0 ± 0.5 kG) the value $|H_{hf}| = 290.6 \pm 0.9$ kG for the magnetic hyperfine field of very dilute Co in Fe (less than 1 in 10^3 atoms) at 0.03°K. This agrees with the value of 289.7 kG measured by NMR for 1% Co in Fe[4] and 4 to 17% Co in Fe.[5]

To conclude, it can be said that the radiative detection of NMR in polarized nuclei is proved possible. Compared with conventional nuclear polarization measurements[6] this method offers at least an order of magnitude higher accuracy, which also makes it possible to determine the nuclear g factor directly by varying the external polarizing field. Further, it is independent of any precise knowledge of the temperature scale. It should be noted that the conventional nuclear orientation technique using γ rays measures an energy $|\mu H_{eff}|$, whereas the method described here gives a frequency $|g H_{eff} \mu_N/h|$. Combining both techniques would determine the spin of the nuclear state.[7] Also, with regard to magnetic hyperfine fields of impurities in ferromagnetic lattices, this technique will prove very valuable; in addition to being accurate, it measures to a good approximation the hyperfine field at 0 deg, and is capable of working with extremely small concentrations. A great number of radioactive isotopes and isomeric levels are accessible to this technique, in particular in connection with isotope separators, which provide a way to shoot isotopes

into a lattice in cases for which chemical procedures fail.

Footnote and References

† Condensed version of Phys. Rev. Letters 17, 897 (1966).

1. A. M. Portis and R. H. Lindquist, in Magnetism, Ed. by G. T. Rado and H. Suhl (Academic Press, Inc., New York, 1965), Vol. II A, p. 357.
2. N. Bloembergen and G. M. Temmer, Phys. Rev. 89, 883 (1953).
3. I. Lindgren, in Perturbed Angular Correlations, Ed. by E. Karlsson, E. Matthias, and K. Siegbahn (North-Holland Publishing Company, Amsterdam, 1964), p. 385.
4. Y. Koi, A. Tsujimura, T. Hihara, and T. Kushida, J. Phys. Soc. Japan 16, 1040 (1961).
5. E. Simanek and Z. Sroubek, Czech. J. Phys. B12, 202 (1962).
6. D. A. Shirley, Thermal Equilibrium Nuclear Orientation (UCRL-16764, March 1966), published in Ann. Rev. Nucl. Sci. 16, 89 (1966).
7. We are grateful to Dr. D. A. Shirley for calling this to our attention.

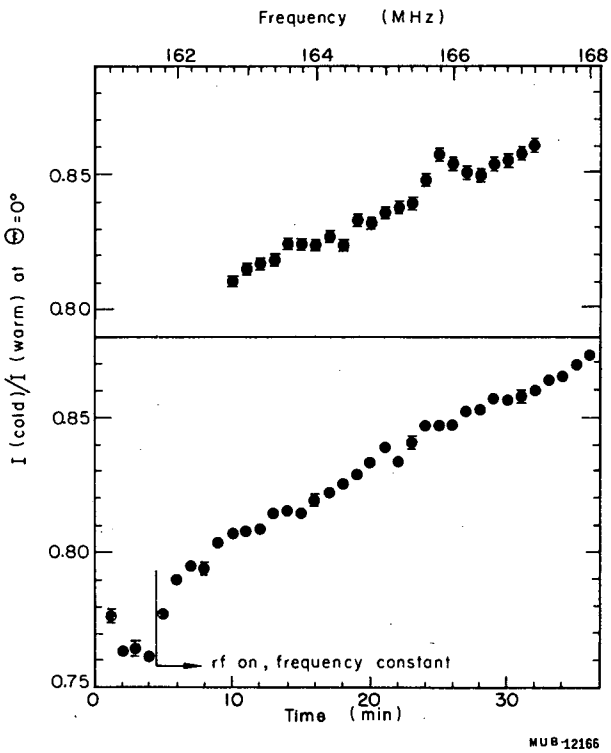

Fig. E. 1-1. Warm-up curves for ^{60}Co in Fe (alloy II) at θ = 0 deg. In the upper part the frequency was varied with time, and the resonance effect appears at 165.8 MHz. The lower curve was taken with a fixed frequency off resonance but with the same rf amplitude as for the upper one.

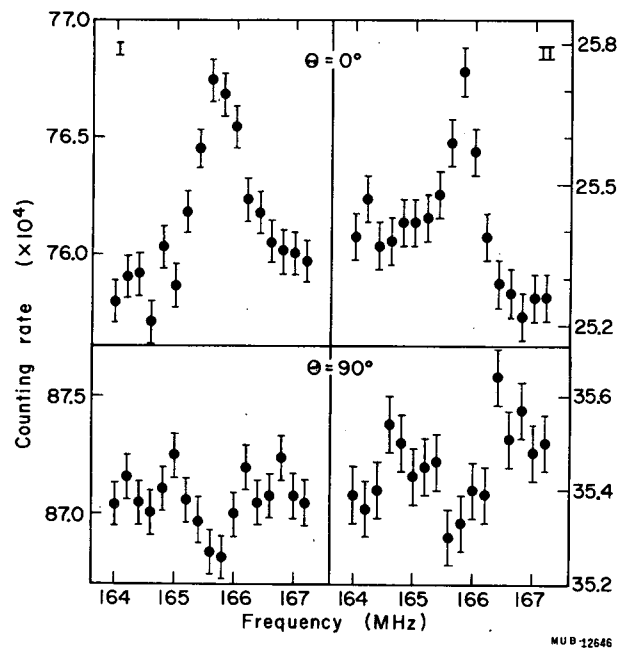

Fig. E. 1-2. Resonance effects at 0 and 90 deg for two different alloys (I and II) of ^{60}Co in Fe.

2. NUCLEAR MAGNETIC RESONANCE DETECTED BY PERTURBED ANGULAR CORRELATIONS

E. Matthias and B. A. Olsen

The nuclear magnetic resonance (NMR) in the 75-keV, 235-nsec state of ^{100}Rh has been observed by means of perturbed angular correlations (PAC).[1] The experiment was possible by making use of the enhancement of the rf amplitude in ferromagnetic lattices, where the NMR is not driven directly by the applied rf field but rather through the large hyperfine field acting on the nuclei.[2] Experimentally, the resonance was detected by a change in the coincidence counting rate between γ_1 and γ_2 at an angle of 180 deg. The polarizing dc field, H_0, was parallel to the emission direction of γ_1 and γ_2 (z axis), and the rf field with amplitude H_1 and frequency ω is applied perpendicular to H_0.

Triggered by these recent experimental results, some theoretical investigations have been undertaken to obtain a quantitative understanding of the observed effects. It is obvious that the angular correlation method of detecting the resonance introduces an additional direction not encountered in NMR experiments. As a consequence, the form of the resonance depends upon the angle between γ_1 and γ_2.

The formalism to describe the resonance destruction has to be developed from the general expression for a perturbed angular correlation,[3]

$$W(\vec{k}_1,\vec{k}_2,t) = \sum_{\substack{k_1k_2\\N_1N_2}} A_{k_1}(1)A_{k_2}(2)\, G^{N_1N_2}_{k_1k_2}(t)\,[(2k_1+1)(2k_2+1)]^{-1/2}\; Y^{N_1*}_{k_1}(\theta_1,\phi_1)Y^{N_2}_{k_2}(\theta_2,\phi_2), \tag{1}$$

with the usual definition of $A_{k_1}(1)$ and $A_{k_2}(2)$. The perturbation factor is defined as

$$G^{N_1N_2}_{k_1k_2}(t) = [(2k_1+1)(2k_2+1)]^{\frac{1}{2}} \sum_{\substack{m_am_b\\m_a'm_b'}} (-1)^{2I+m_a+m_b} \begin{pmatrix} I & I & k_1\\ m_a' & -m_a & N_1\end{pmatrix}\begin{pmatrix} I & I & k_2\\ m_b' & -m_b & N_2\end{pmatrix} \tag{2}$$

$$\times\langle m_b|e^{-(i/\hbar)\mathcal{H}(t)\cdot t}|m_a\rangle\langle m_b'|e^{-(i/\hbar)\mathcal{H}(t)\cdot t}|m_a'\rangle^*.$$

The interaction Hamiltonian is time-dependent and has the form well-known from NMR theory,[4]

$$\mathcal{H}(t) = -\gamma\hbar[H_0I_Z+H_1(I_x\cos\omega t + I_y\sin\omega t)], \tag{3}$$

where $\gamma = g\cdot\mu_N/\hbar$ and g is the nuclear g factor. The time dependence of $\mathcal{H}(t)$ can be eliminated by transforming to a coordinate system which rotates about H_0 (z axis) with frequency ω. With H_1 along the x axis we get a transformed (effective) Hamiltonian[4]

$$\mathcal{H} = -\gamma\hbar[(\omega/\gamma + H_0)I_Z + H_1I_x]. \tag{4}$$

For an experimental setup with $\theta_1 = 0$ deg and $\theta_2 = 180$ deg we obtain $N_1 = N_2 = 0$ and, consequently, $m_a = m_a'$ and $m_b = m_b'$. With these simplifications, we find the time-integrated perturbation factor from Eq. 2,

$$\hat{G}^{00}_{k_1k_2} = [(2k_1+1)(2k_2+1)]^{1/2} \sum_{m_am_b} (-1)^{2I+m_a+m_b} \begin{pmatrix} I & I & k_1\\ m_a & -m_a & 0\end{pmatrix}\begin{pmatrix} I & I & k_2\\ m_b & -m_b & 0\end{pmatrix} \tag{5}$$

$$\times\frac{1}{\tau}\int_0^\infty e^{-t/\tau}|\langle m_b|e^{-(i/\hbar)\mathcal{H}t}|m_a\rangle|^2\,dt.$$

The transformation into a rotating coordinate system affects only the interaction Hamiltonian, and not the angular correlation function, since the axis of rotation is chosen parallel to the emission direction of the γ rays. The square of the matrix element is the probability $P_{m_b m_a}$ of finding the spin I at time t in the state m_b when it was at time $t = 0$ in the state m_a. The matrix elements are nondiagonal, which means that the perturbation factor $\hat{G}^{00}_{k_1 k_2}$ is best calculated by numerical methods. It is interesting to note that the interference term for $k_1 \neq k_2$ in Eq. 5 is not zero. From Eqs. 1 and 5 it follows that the time-integrated angular correlation function at 180 deg exposed to a destructive rf field is described by

$$\hat{W}\,(180°) = \sum_{k_1 k_2} A_{k_1}(1)\, A_{k_2}(2) \cdot \hat{G}^{00}_{k_1 k_2}, \tag{6}$$

with

$$\hat{G}^{00}_{k_1 k_2} = [(2k_1+1)(2k_2+1)]^{1/2} \sum_{\substack{m_a m_b \\ n n'}} (-1)^{2I+m_a+m_b} \begin{pmatrix} I & I & k_1 \\ m_a & -m_a & 0 \end{pmatrix} \begin{pmatrix} I & I & k_2 \\ m_b & -m_b & 0 \end{pmatrix}$$

$$\times \langle n\,|m_b\rangle^* \langle n\,|m_a\rangle \langle n'\,|m_b\rangle \langle n'\,|m_a\rangle^* \{1 + [(E_n - E_{n'})\tau/\hbar]^2\}^{-1}. \tag{7}$$

In this equation E_n are the eigenvalues and $\langle n\,|m\rangle$ the corresponding eigenvectors of the interaction Hamiltonian given in Eq. 4.

To illustrate the behavior of the resonance, the attenuation factor in Eq. 7 has been calculated for several experimental conditions. In the figures the factor $a^{N_1 N_2}_{k_1 k_2}$ is displayed, which is connected with the perturbation factor in Eq. 2 by the relation[3]

$$G^{N_1 N_2}_{k_1 k_2} = \frac{[(2k_1+1)(2k_2+1)]^{1/2}}{2I+1}\, a^{N_1 N_2}_{k_1 k_2}. \tag{8}$$

Figure E.2-1 shows the typical resonance effect for spin I = 2 and some realistic values of the parameters $\omega_0\tau$ and H_1/H_0. It is apparent that the perturbing effect of the rf vanishes for $-\omega \ll \omega_0$ and H_1 and H_0 constant. Further, the effect is measurable only for $|\omega_0\tau| \gg 1$. In Fig. E.2-2 the influence of the rf power is illustrated. After the angular correlation is reduced to the "hard core value,"[5] any increase in rf amplitude results in a broadening of the resonance. A comparison between the resonance width $\Delta y = \Delta\omega/\omega_0$ and the natural line width $\Gamma = \hbar/\tau$ is very interesting even if there is no direct connection. While for $H_1/H_0 = 10^{-2}$ the theoretical width of the resonance is 4×10^{-2}, about 40 times the natural line width, it is only 4×10^{-3} for $H_1/H_0 = 10^{-3}$, or about 4 times the natural line width. It can be seen from Fig. E.2-3 that in case of $-\omega_0\tau = 10^3$ a resonance width smaller than the natural line width will be observed for $\hat{a}^0_{22} > 0.9$ ($H_1/H_0 < 2.5\times10^{-4}$), although the effect is very small. This figure (Fig. E.2-3) also shows the power dependence at the resonance point ($\omega = -\omega_0$). Even for large power levels the anisotropy cannot be wiped out completely, but remains at a certain "hard core."[5] For k_1 and $k_2 > 2$ interference terms with $k_1 \neq k_2$ occur, as shown in Fig. E.2-4. Also displayed is the line shape of the resonance for a pure K = 4 term.

In connection with Figs. E.2-1 through E.2-4, only that part of the total perturbation factor was discussed that enters the angular correlation function if the measurement is carried out with the detectors at 180 deg. If the detectors are located at 90 or 270 deg with respect to each other, the phase factors $e^{-i\omega t I_z}$, coming from the transformation into the rotating coordinate system, have to be taken into account when the perturbation factor in Eq. 2 is calculated. Numerical results indicate, however, that the shape of the resonance is still symmetric and is determined mainly by the factor $\hat{a}^{00}_{k_1 k_2}$.

References

1. E. Matthias, D. A. Shirley, M. P. Klein, and N. Edelstein, Phys. Rev. Letters 16, 974 (1966).
2. A. M. Portis and R. H. Lindquist, in Magnetism, Ed. by G. T. Rado and H. Suhl (Academic Press, Inc., New York, 1965), Vol. IIA, page 357.

3. R. M. Steffen and H. Frauenfelder, in Perturbed Angular Correlations, Ed. by E. Karlsson, E. Matthias, and K. Siegbahn (North-Holland Publishing Company, Amsterdam, 1964), Chapter 1.
4. C. P. Slichter, Principles of Magnetic Resonance (Harper's Physics Series, Harper and Row, New York, 1963).
5. The hard core value is given by $\hat{a}^{N_1N_2}_{k_1k_2}\ \delta_{nn'}$.

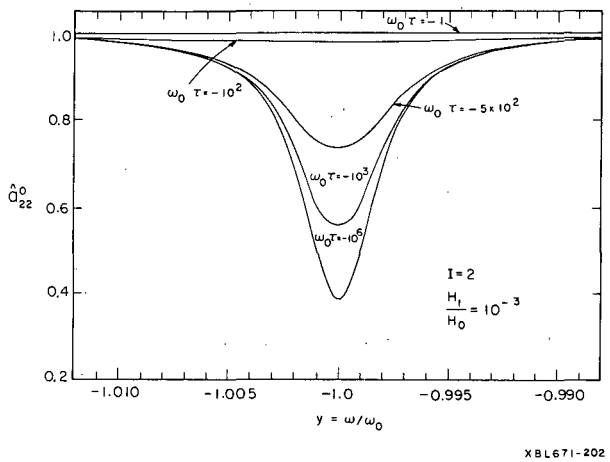

Fig. E.2-1. Typical resonance curves for some realistic parameters H_1/H_2 and $\omega_0\tau$ in the case of a spin I = 2.

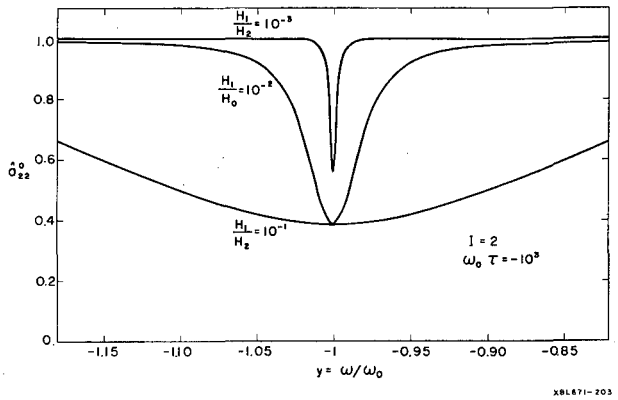

Fig. E.2-2. Dependence of the resonance effect on the power of the rf field.

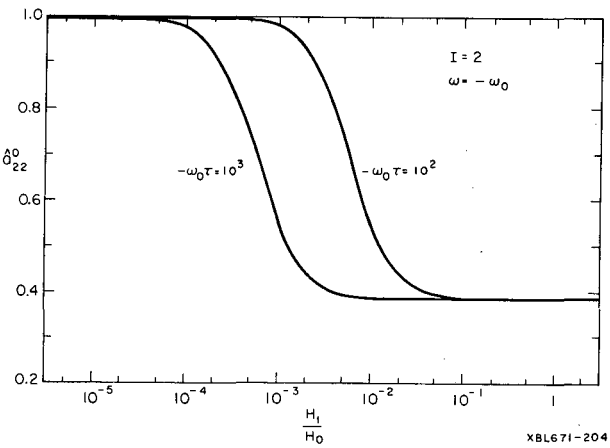

Fig. E.2-3. Power dependence of the signal at the resonance point ($\omega = -\omega_0$).

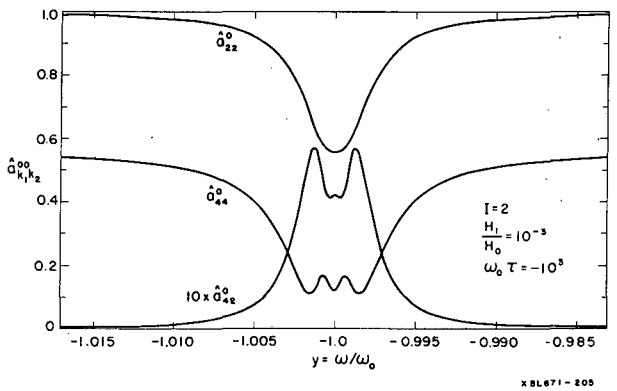

Fig. E.2-4. Example of the form of the attenuation factor for θ = 180 deg and k_1 and $k_2 \geq 2$. The interference term is ten times enhanced.

3. TEMPERATURE DEPENDENCE OF HYPERFINE FIELDS OF ^{111}Cd AND ^{99}Ru IN NICKEL

S. S. Rosenblum, E. Matthias, and D. A. Shirley

The method of perturbed angular correlation of γ radiation has been used to measure the hyperfine fields at nuclei of ^{99}Ru and ^{111}Cd in a nickel lattice as a function of temperature. Time-differential perturbed angular correlation was used for all measurements on ^{111}Cd whereas, for ^{99}Ru, the time-differential method was used below the Curie temperature (T_C), but above T_C it

was necessary to use the less accurate integral method. Both demagnetized[1] and polarized samples were used below T_C. Above T_C, polarizing fields of 19.5 kG were applied to the sample.

Results Below T_C

In Fig. E. 3-1 is shown a selection of typical data for ^{111}Cd below T_C. No external polarizing field was used. In Fig. E. 3-2 are shown typical data for ^{99}Ru in Ni below T_C. The large size of the effects, combined with temperature independence of the anisotropy, makes the angular correlation technique a very powerful one for this type of investigation.

Figure E. 3-3 shows the temperature dependence of the hyperfine field induced at ^{111}Cd nuclei in Ni. Figure E. 3-4 shows a similar plot for ^{99}Ru in Ni. The solid curve in both figures is that of the spontaneous magnetization for pure nickel. As can be easily seen, the hyperfine field of Cd follows the host lattice magnetization very closely, whereas the ^{99}Ru hyperfine field deviates from it a good deal. This indicates that the Ru is a local moment in the Ni lattice whereas the Cd is not.

A phenomenological model to explain local moment behavior was recently proposed by Jaccarino, Walker, and Wertheim (JWW),[2] based on the idea that the localized impurity magnetic moments are less strongly coupled to the lattice than the host atoms. The coupling strength is given by the parameter ζ times the molecular field of the host. The hyperfine field of the solute is thus proportional to the Brillouin function, $B_J(y)$, with $y = \zeta(\sigma/\sigma_0)\ (T_C/T)$. The JWW model then employs two parameters J and ζ in order to obtain the best fit to the experimental data. With this model, the authors were able to obtain an excellent fit to the NMR data of Koi and coworkers[3] for Mn in Fe, using $\zeta = 0.731$ and $J = 3/2$, and less satisfactory fits for other spins.

The major fault of this model is its failure to account for the important effect of nonlocal conduction electron spin polarization (cesp). Recent work by Rubinstein, Dweck, and Stauss,[4] using NMR spin echo techniques, indicates that the changes in the hyperfine fields at nuclei near an Mn impurity in Fe arise predominantly from induced changes in the cesp. Since the temperature behavior of the hyperfine field of Ru in Ni is similar to that of Mn in Fe, we would also expect that cesp is predominant here too.

The JWW model can be extended to account for cesp by considering a third parameter $(1-f) = H_N(0)/H_{hf}(0)$, which describes the fraction of $H_{hf}(0)$, the hyperfine field on the impurity at absolute zero, that arises from nonlocalized conduction electrons. We assume that the nonlocal part of the hyperfine field varies directly with lattice magnetization, and write

$$H_{hf}(T) = H_N(0)\,\frac{\sigma_T}{\sigma_0} + H_L(0)\,B_J(y) \tag{1}$$

or

$$\frac{H_{hf}(T)}{H_{hf}(0)} = (1-f)\,\frac{\sigma_T}{\sigma_0} + f\,B_J(y), \tag{2}$$

where y is as defined previously. The broken lines in Fig. E. 3-4 are the best fits to the data of Eq. 2 for $J = 1/2$ and $J = 5/2$ when ζ and f are used as parameters.

Results Above T_C

No simple independent test of the predictions of this model seems to be available below the Curie point, as can be readily seen by examining the structure of Eq. 1. In the ferromagnetic state σ_T depends on T alone; thus, for a particular set of values of ζ, f, and J, each term in Eq. 1 is completely specified by T. Above T_C this restriction is removed and we may vary σ_T, H_{ext} and T independently over a wide range by controlling the applied magnetic field (H_{ext}) and employing the known dependence of magnetization of a nickel lattice on applied field and temperature.[5] The effective field experienced by the solute nucleus is then given (after correction for contributions from Lorentz and demagnetizing fields) by

$$\vec{H}_{eff} = \vec{H}_{ext} + \vec{H}_{hf}\,(\sigma_{T,H_{ext}}, T). \tag{3}$$

To calculate H_{hf} for an H_{ext} and T, we first assume that Eq. 1 is still valid in the paramagnetic region if we replace the spontaneous magnetization of the lattice, σ_T, by the induced magnetization $\sigma_{T,H_{ext}}$. Using the values of ζ, f, and J determined from the fit below the Curie point, the hyperfine field, $H_{hf}(\sigma_{T,H_{ext}}, T)$, above the Curie point can be calculated and compared with the experimental data. This provides a very sensitive test of the validity of the extended JWW model above the Curie point.

Experimentally, one expects to observe a shift, $(H_{eff}-H_{ext})/H_{ext} = \beta-1$, which is analogous to Knight shifts in NMR. The results for Ru and Cd in Ni above the Curie temperature are shown in Figs. E. 3-5 and E. 3-6, respectively. The curve in Fig. E. 3-6 is that calculated by assuming

$$H_{hf} = [\sigma_{T,H_{ext}}/\sigma_0]\, H_{hf}(0), \tag{4}$$

i. e., a completely nonlocal moment. The lower curve in Fig. E. 3-5 is also calculated by using Eq. 4 above, while curve A is calculated by using Eq. 2 for $J = 1/2$ and the same values of the parameters determined for the best fit below T_C.

Discussion

It is obvious from these results that the behavior of the hyperfine fields induced at nuclei of Ru and Cd in Ni are basically different, Ru being a largely local moment while Cd is nonlocal and follows the lattice magnetization. It is also clear that the modified JWW model (Eq. 2) is capable of describing the behavior of the hyperfine field of Ru in Ni reasonably well both above and below T_C, although the model is clearly insensitive to the value of J chosen.

Acknowledgment

The authors would like to thank Dr. Alan Cox and Mr. Nat Sherrill for their advice and for the use of their equipment in the measurement of the Curie temperatures of our alloys.

References

1. E. Matthias, S. S. Rosenblum, and D. A. Shirley, Phys. Rev. Letters 14, 46 (1965).
2. V. Jaccarino, L. R. Walker, and G. K. Wertheim, Phys. Rev. Letters 13, 752 (1964).
3. Yoshitaka Koi, Akira Tsujimura, and Tadamiki Hihara, J. Phys. Soc. Japan 19, 1493 (1964).
4. M. Rubinstein, G. H. Stauss, and J. Dweck, Phys. Rev. Letters 17, 1001 (1966).
5. P. Weiss and R. Forrer, Ann. Physique 15, 153 (1926).

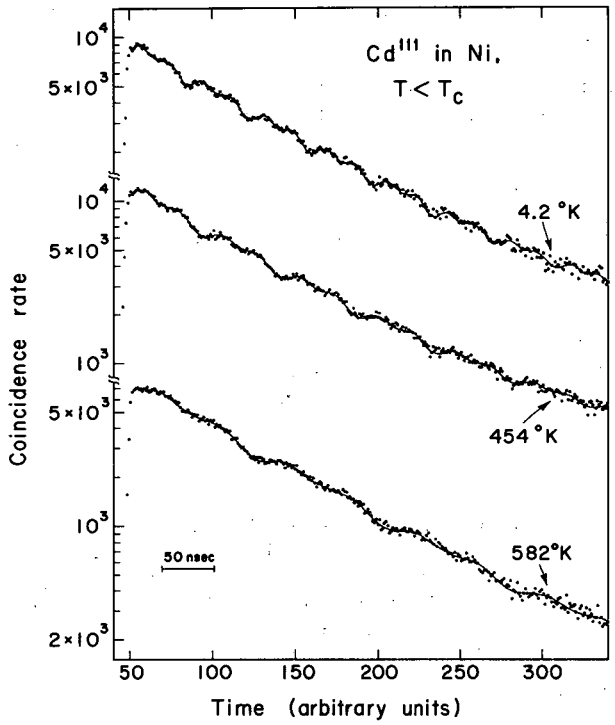

Fig. E. 3-1. Time-differential angular correlation for ^{111}Cd in Ni below the Curie point. The time spectra were recorded at an angle of 180 deg and no external polarizing field was used. The modulation pattern is characteristic of a randomly oriented magnetic interaction (Ref. 1). The solid line represents the weighted least-squares fit to the data. The interaction frequencies for the three curves are $\omega(4.2°K) = 104.37 \pm 0.21$ MHz; $\omega(454°K) = 82.55 \pm 0.21$ MHz; $\omega(582°K) = 49.77 \pm 0.20$ MHz.

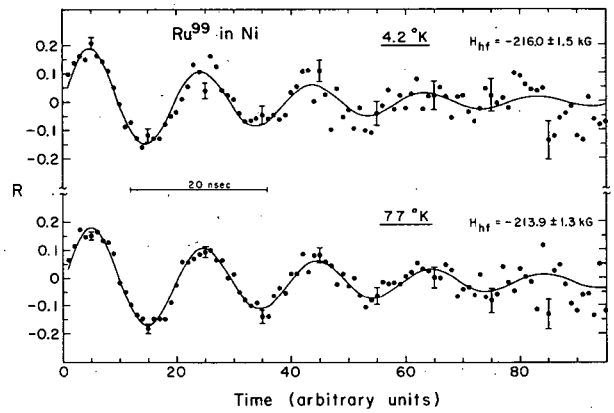

Fig. E. 3-2. Time-differential angular correlation for ^{99}Ru in Ni with a polarizing field of 5.00 kG. The indicated hyperfine field (-216.0 ± 1.5 kG at 4.2°K, -213.9 ± 1.3 kG at 77°K) has been calculated by assuming $g = 0.189 \pm 0.004$. The amplitude damping is probably caused by either a magnetic field distribution or the existence of at least two different internal fields.

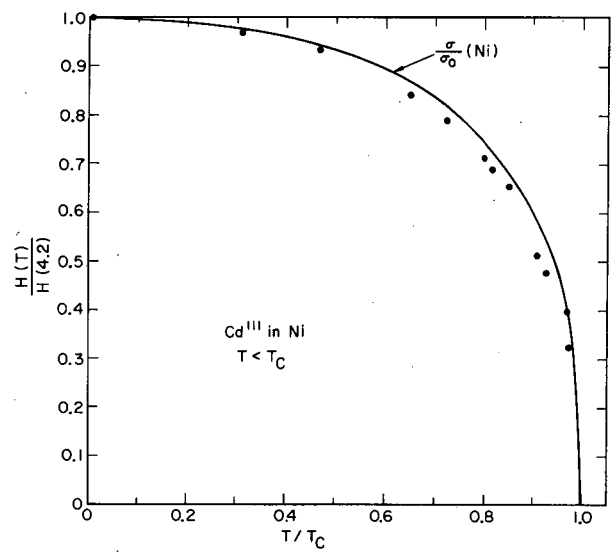

Fig. E. 3-3. Reduced hyperfine field vs reduced temperature for ^{111}Cd in Ni below the Curie point. ($T_C = 627.2°K$, the value for pure Ni.)

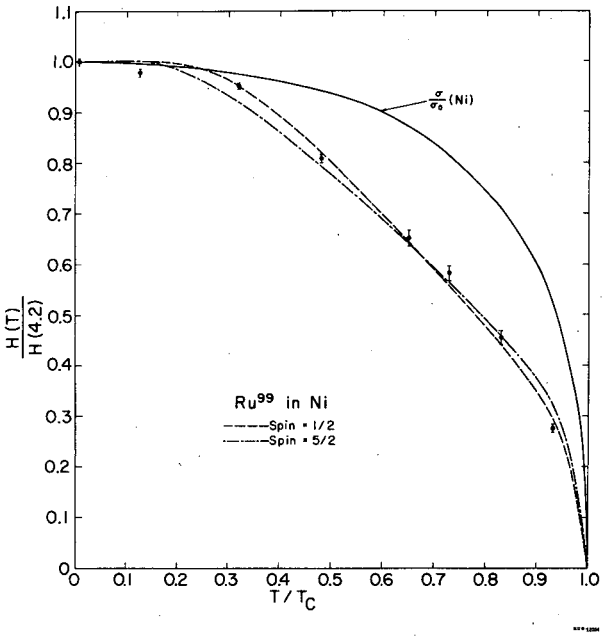

Fig. E. 3-4. Reduced hyperfine field vs reduced temperature for ^{99}Ru in Ni below the Curie temperature (T_C = 610°K for the 1 at. % alloys used) and $H_{hf}(0) = H_{hf}(4.2)$ = 217.2 kG. The broken curves are theoretical fits based on the modified JWW model (Eq. 2). The values of the parameters were
– – – – for spin 1/2,
$1.194B_{1/2}(\zeta=0.621) - 0.194\ \sigma/\sigma_0 = H_{hf}(T)/H_{hf}(0)$,
- . - . - . - for spin 5/2,
$1.958B_{5/2}(\zeta=1.757) - 0.958\ \sigma/\sigma_0 = H_{hf}(T)/H_{hf}(0)$.

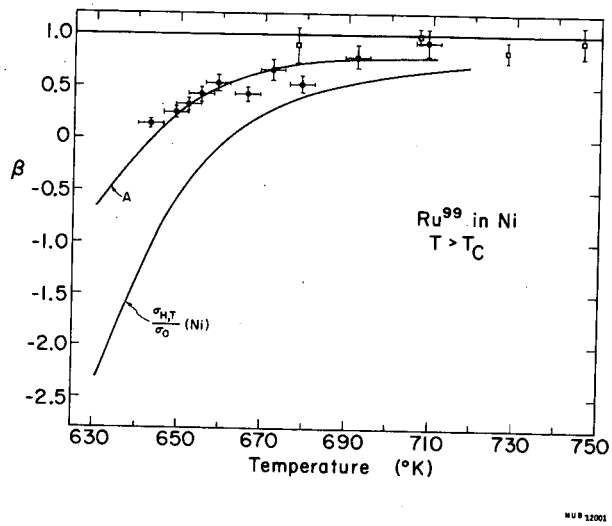

Fig. E. 3-5. ^{99}Ru above the Curie point. The temperature dependence of $\beta = H_{eff}/H_{ext}$ was measured with a polarizing field of 19.5 kG. Curve A was calculated by using $H_{hf}(T)/H_{hf}(0) = 1.194\ B_{1/2}(\zeta=0.621) - 0.194\ \sigma(H_{ext}, T)/\sigma_0$, with the values of the parameters being those calculated for the best fit below T_C. The lower curve is for $H_{hf}(T) = [\sigma_T, H_{ext}/\sigma_0]\ H_{hf}(0)$ with $H_{hf}(0)$ = 217.2 kG.

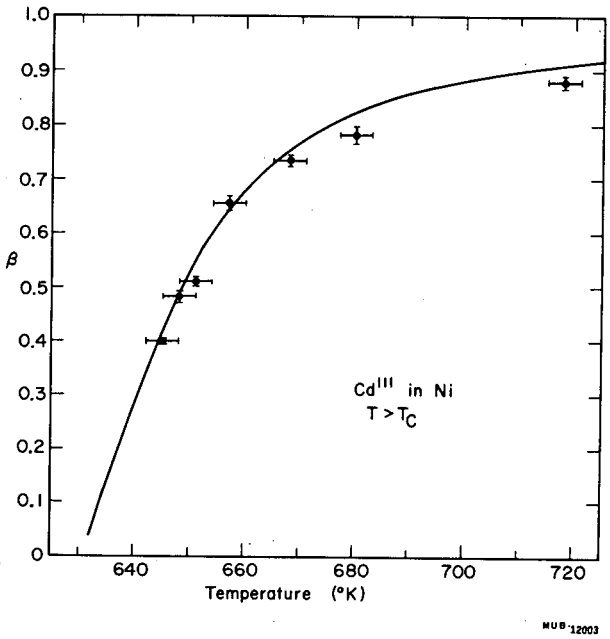

Fig. E. 3-6. ^{111}Cd in Ni above the Curie point. The temperature dependence of $\beta = H_{eff}/H_{ext}$ was measured with a polarizing field of 19.5 kG. The curve was calculated by using $H_{hf}(T) = [\sigma_T, H_{ext}/\sigma_0]\ H_{hf}(0)$, with $H_{hf}(0)$ = 68.52 kG.

4. DIGITAL ANALYSIS OF PERTURBED ANGULAR CORRELATIONS†

E. Matthias and D. A. Shirley

Until now there has been no method for measuring magnetic moments of isomeric states with half-lives between 10^{-6} sec and 1 sec. It is our concern to develop an experimental technique which allows the application of the perturbed angular correlation method up at least to the millisecond range.

When trying to use the conventional time-differential method on half-lives longer than 1 μsec, one runs into the following basic difficulties: (a) the source strength has to be reduced to keep the ratio of true to accidental coincidences acceptable; (b) the time resolution of analog converters is limited and of the order of 1% of the total time range; (c) the limited time resolution requires the use of low magnetic fields. In addition one has the usual problems with linearity, stability, and, in most instances, a memory limitation in the analyzer.

An experimental approach to overcome all the above weaknesses of the conventional technique except the ratio of true to accidental coincidences is to obtain the data directly in a digital form and to find the interaction frequency by calculating the Fourier transform of the time-spectrum.

The use of a digital time-to-height converter offers automatically the advantages[1] that the resolving time is independent of the time range used, and that there is practically no limitation in channel numbers; it has perfect linearity and a much greater stability than analog systems. Further, the necessity of an accurate time calibration is completely avoided. In our case a digital time-to-height converter with a crystal-stabilized 1000-MHz driving frequency was used.[2] The Eldorado model 793 1-nsec time interval counter provides this, together with a nine-decade scaler which allowed the use of the whole time range between 10^{-9} sec and 1 sec, or any desired part of it. The numbers occurring in the scaler and representing the time interval elapsed between γ_1 and γ_2 were dumped via a Kennedy 1500/5 incremental tape unit onto an IBM-compatible magnetic tape. The data on the tape were later put in order and analyzed by the computer.[2]

The data analysis is based on the fact that the Fourier transform of the time spectrum W(t) is a function of frequency, $f(\nu)$, with the resonance frequency given by $\nu_L = 2\,gH\,(\mu_N/h)$. After normalization for the exponential decay, the time spectrum can be described by the function $W(t) = \sum_k A_k P_k\,[\cos(\theta_0 \pm \omega_L t)]$ for the case of an oriented magnetic dipole interaction. The even and odd parts of the Fourier transform are calculated separately,

$$A(\nu) = \int_{T_{min}}^{T_{max}} W(t)\sin 2\pi\nu t\,dt, \qquad B(\nu) = \int_{T_{min}}^{T_{max}} W(t)\cos 2\pi\nu t\,dt,$$

and the absolute value $F(\nu) = [A(\nu)^2 + B(\nu)^2]^{1/2}$ is formed. The Fourier transform is usually calculated in frequency steps of $[2(T_{max} - T_{min})]^{-1}$, but smaller steps can be used. The phase of the Fourier transform is defined as $\phi(\nu) = \tan^{-1}[-A(\nu)/B(\nu)]$, and is chosen in accordance with the normal sign convention of the Fourier transform. In Table E.4-I the expected phases for the most common detector geometries and field directions are summarized.

An alternative way of treating the data is to use the autocorrelation function

$$\frac{C(\tau)}{C(0)} = \frac{\text{ave}\,\{[W(t) - \overline{W}][W(t+\tau) - \overline{W}]\}}{\text{ave}\,\{[W(t) - \overline{W}][W(t) - \overline{W}]\}}$$

in the Fourier transform

$$G(\nu) = \int_0^{\tau_{max}} \frac{C(\tau)}{C(0)} \cos 2\pi\nu\tau\,d\tau.$$

Here, τ is the lag at which the data are correlated. This autocorrelation technique smooths the discrete data carrying a statistical uncertainty at each point. Consequently, the peak-to-noise ratio is more than an order of magnitude better than that obtained by the simple Fourier transform

of the data. Thus the autocorrelation technique is extremely powerful for the analysis of small-amplitude modulations. The application of this analysis, however, is limited by the maximum possible lag τ, which is about 1/3 of the total number of channels used. The frequency steps are given by $(2\,\tau_{max})^{-1}$, which means that for shorter half-lives the frequency scale is too insensitive and the resonance is determined by too few points. This is actually the case in the following example.

A measurement of the g factor of the 74.8-keV level in ^{100}Rh will serve to demonstrate the method of digital analysis of perturbed angular correlations (DAPAC). With a half-life of $T_{1/2}$ = 235 nsec, a g factor of g = +2.15, and an anisotropy of A = +30%, the 84-to-74.8-keV cascade is a favorable test case.[3] Both the 84-keV and 74.8-keV γ rays were measured with Ge(Li) detectors. Delay gates were used to energy-select the fast pulses, which then directly served as "start" and "stop" pulses for the time interval counter. After ordering the numbers from the magnetic tape we get the usual time spectrum modulated by the rotation of the angular correlation pattern in the external magnetic field. In Fig. E.4-1 the Fourier transform of the data, $F(\nu)$, and of the autocorrelation coefficient, $G(\nu)$, are shown for a measurement in a field of 4996 gauss. The phase is $\phi = \pi/2$ in this case, in agreement with what is to be expected for $\gamma_1(135°, cw)\gamma_2$, field up, a positive anisotropy, and a positive g factor, according to Table E.4-I.

The results of all runs are listed in Table E.4-II. The resonance frequency was obtained from the derivative of the resonance peak, which is given by either the cosine or the sine transform, depending on the geometry of the experiment. This procedure is demonstrated in Fig. E.4-2. The absolute function $F(\nu)$ often gives an erroneous frequency, as the derivative is not necessarily symmetric around zero. From the resonance frequency, ν_L, the g factor can be calculated by using the relations $g = (h/2\,\mu_N)(\nu_L/H)$. In spite of the much better peak-to-background ratio we did not make any use of the Fourier transform of the autocorrelation function, because the resonance was given by too few points. The error in the frequency was defined as the reading error of the inflection point of that transform which represents the derivative. As a final result for the g factor we give the average value of all individual runs, $g = +2.160 \pm 0.004$. From Knight shift measurements on Rh in Rh-metal by Seitchik et al.[4] it is known that a correction of $\Delta H/H = 0.43\%$ has to be applied, which brings the final value to $g = +2.151 \pm 0.004$. This g factor could serve as a standard reference value in work with perturbed angular correlations, not only because of its accuracy but also because of the reproducibility of the source. No chemistry is involved and the source was simply a piece of the rhodium metal target on which a (p, 4n) reaction was induced by 42.5-MeV protons to produce the ^{100}Pd activity.

The performance of this method--its simplicity and accuracy--leaves no doubt that it will be most useful for future investigations of hyperfine interactions in isomeric states with half-lives between 10^{-8} and 10^{-3} sec. It should be noted that the measuring time for the runs listed in Table E.4-II was about 24 hours. This, together with the fact that for a pure frequency determination one needs to measure at only one field direction and angle, underlines the practical advantage of the method in addition to the other features mentioned above. Further, if even the sign of the anisotropy is unknown, this and the sign of the g factor can be unambiguously determined by a set of two measurements including one of the angles 90 or 180 deg, as can be seen from Table E.4-I.

Footnote and References

† Shortened version of UCRL-16779, April 1966, published in Nucl. Instr. Methods 45, 309 (1966).
1. See, e.g., J. K. Whittaker, Nucl. Instr. Methods 28, 293 (1964).
2. We would like to thank Dr. F. Goulding, Mr. J. Mang, and Mr. L. Robinson for designing and constructing the digital THC system, and Miss Esther Coleman for writing the computer programs and helping with the analysis of the data.
3. E. Matthias, D. A. Shirley, J. S. Evans, and R. A. Naumann, Phys. Rev. 140, B264 (1965).
4. J. A. Seitchik, V. Jaccarino, and J. H. Weruick, Phys. Rev. 138, A148 (1965).

Table E.4-I. Expected values for the phase, $\phi(\nu)$, of the Fourier transform for various detector geometries, θ_0, and magnetic field directions. All angles are counted clockwise from the γ_1 toward the γ_2 direction. The magnetic field directions "up" and "down" refer to the detector plane.

	Sign of g factor			
	+		-	
	Sign of A_2			
	+	-	+	-
135 deg up	$\pi/2$	$-\pi/2$	$-\pi/2$	$\pi/2$
135 deg down	$-\pi/2$	$\pi/2$	$\pi/2$	$-\pi/2$
225 deg up	$-\pi/2$	$\pi/2$	$\pi/2$	$-\pi/2$
225 deg down	$\pi/2$	$-\pi/2$	$-\pi/2$	$\pi/2$
90 deg up/down	π	0	π	0
180 deg up/down	0	π	0	π

Table E.4-II. Summary of g-factor measurements with a Rh-metal source. The angle θ_0 describing the geometry of the detectors is counted clockwise (cw) from γ_1 toward γ_2. The arrow indicates the field direction with respect to the detector plane. The frequency values have been obtained from the derivative of the resonance peak.

Run no.	θ_0 (deg)	Magnetic field (gauss)	Frequency (MHz)	g factor	Phase, ϕ
1	135	4996 ± 10 ↑	16.46 ± 0.05	2.161 ± 0.008	$\pi/2$
2	180	4996 ± 10 ↓	16.52 ± 0.05	2.169 ± 0.008	0
3	90	4996 ± 10 ↓	16.50 ± 0.05	2.166 ± 0.008	$-\pi$
4	180	7636 ± 7	25.17 ± 0.05	2.162 ± 0.005	0
5	180	7636 ± 7	25.04 ± 0.05	2.151 ± 0.005	0
			Weighted average:	2.160 ± 0.004	

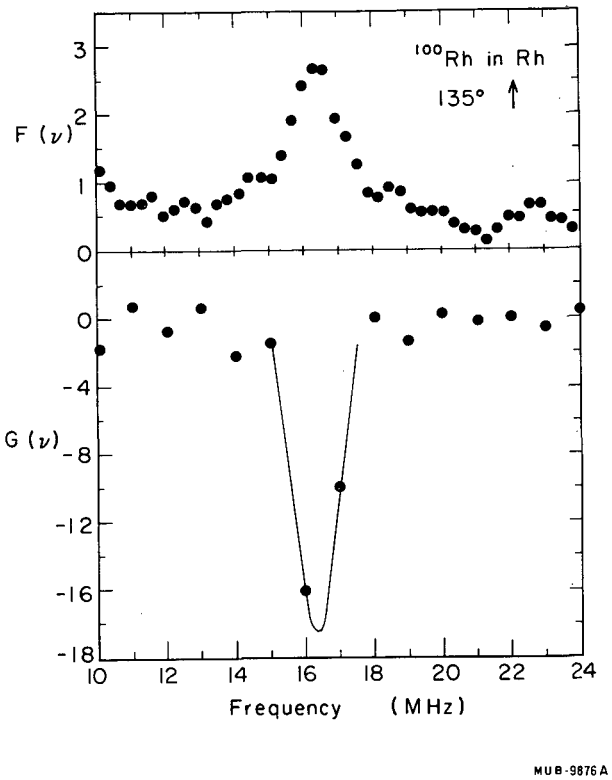

Fig. E. 4-1. Frequency spectrum of the Fourier transform, F(ν), of the normalized data and of the Fourier transform, G(ν), of the autocorrelation function. The spectrum shown represents run No. 1 in Table E. 4-II.

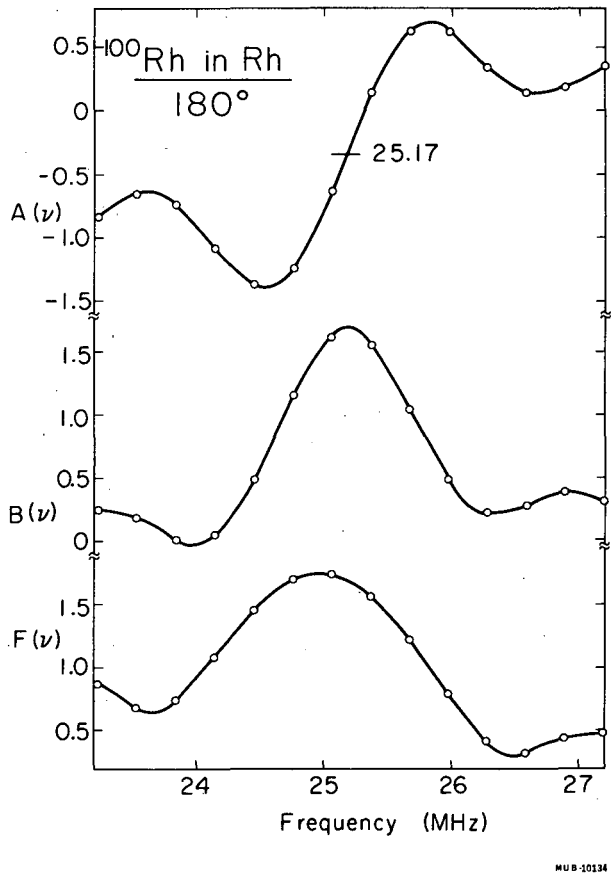

Fig. E. 4-2. Frequency spectrum of the sine, A(ν), and cosine, B(ν), transforms, and of the absolute function F(ν). The data represent run 4 of Table E. 4-II.

5. NUCLEAR MAGNETIC RESONANCE IN THE 75-keV STATE OF ^{100}Rh DETECTED BY ANGULAR CORRELATIONS

E. Matthias, N. Edelstein, H. J. Körner, and D. A. Shirley

The first successful experiment in which the large hyperfine field in a ferromagnetic lattice was used to achieve a resonance destruction of an angular correlation[1] raised many questions which demanded a further investigation of this effect. The following points are of interest:

1. Why is the observed effect smaller than the expected one?
2. What is the theoretical line width and how much of the observed width has to be attributed to relaxation broadening?
3. Under which conditions is the resonance observed in walls or domains?
4. What is the power dependence of the resonance signal?

To partly answer these questions experiments were carried out with the 84- to 74.8-keV cascade in ^{100}Rh, which has a large positive anisotropy and whose intermediate state has a half-life of 235 nsec and a g factor of +2.15. The most favorable geometry for such a resonance experiment is illustrated in Fig. E. 5-1. The detectors were placed at θ = 180 deg. It should be noted, however, that this is not the only possible geometry. A thin foil of the ferromagnetic material into which the activity has been diffused is mounted with its plane parallel to the axis of both detectors. The polarizing field, H_0, is applied parallel to this axis, which ensures, in saturation, a completely decoupled unperturbed angular correlation. The rf field, H_1, has to be applied perpendicular to

the detector plane and H_0.

The first experiment was a check on the earlier published data[1] for ^{100}Rh in Ni. As shown in Fig. E. 5-2, it was possible to resolve the earlier observed asymmetry of the resonance into two lines, which are attributed to two magnetically different lattice sites. The two resonances occur at 315.5 and 334.2 MHz, corresponding to fields of 192.5 and 203.9 kG. This discrepancy between the present result and the earlier one[1] is probably caused by a temperature shift. In the earlier measurement it was possible that the sample was at higher than room temperature.

The amplitude enhancement of the externally applied rf field,[2]

$$2\,H_1^{eff} = (1 + \frac{H_{hf}}{H_0})\,H_1,$$

indicates the advantage of large internal fields for NMR experiments of this kind. We therefore measured the resonance for ^{100}Rh in Fe. Figure E. 5-3 shows the result of a frequency scan at room temperature, yielding an interaction frequency of 882.7 ± 2.0 MHz. This result was confirmed in a second measurement, displayed in Fig. E. 5-4, which gave ν_R = 881.7 ± 1.0 MHz. For 77°K the resonance is observed at 912.5 ± 1.0 MHz, as shown in the upper part of the figure. The two curves verify the temperature shift of the hyperfine field. The final result is $H_{hf}(T = 300°K) = 538.0 \pm 0.6$ kG, $H_{hf}(T = 77°K) = 556.8 \pm 0.6$ kG. The shape of the resonance in Fe is symmetric and does not indicate more than one magnetic site for the ^{100}Rh. The line width is about 6 MHz, compared with a natural line width of 0.5 MHz. However, preliminary calculations prove that this is of the order of what is to be expected if the resonance is nearly saturated. The question whether or not the resonance is observed in walls or domains can be answered by measuring the magnetic saturation behavior of the foil. In Fig. E. 5-5 the coincidence counting rate at 180 deg is shown as a function of the polarizing field, both without and with rf field. The foil was saturated at about 400 gauss in both cases. The resonance effect is the difference between the two curves, and it is apparent that it is not largest for a saturated foil but rather in the range of approximately 200 gauss. This can be attributed to the competition between the rf enhancement, which is largest in walls, and the anisotropy, which is largest in the range of complete saturation. The dependence of the resonance effect on the rf power is illustrated in Fig. E. 5-6. The point at 2.15 V corresponds to our maximum available power of 100 W, which is sufficient to nearly saturate the resonance.

If we assume from Fig. E. 5-5 that the unperturbed angular correlation for the experimental geometry is 8%, then the results for the Fe foil are consistent with theoretical calculations, which predict that in saturation a hard-core value of approximately 0.4 of the unperturbed correlation will be reached. This corresponds to an effect of about 5%, which is in good agreement with the experimental value of 6% shown in Fig. E. 5-6. The fact that we observe only an 8% unperturbed angular correlation instead of the expected 20% is probably due to scattering because of our unfavorable geometry. We attribute the broad width and the small effect of the resonance of ^{100}Rh in Ni to a relaxation which is faster than the half-life. Such a relaxation has been observed for ^{99}Ru in Ni.[3]

References

1. E. Matthias, D. A. Shirley, M. P. Klein, and N. Edelstein, Phys. Rev. Letters 16, 974 (1966).
2. A. M. Portis and R. H. Lindquist, and Magnetism, Ed. by G. T. Rado and H. Suhl (Academic Press, Inc., New York, 1965), Vol. IIA, page 357.
3. S. S. Rosenblum, E. Matthias, and D. A. Shirley, Temperature Dependence of Hyperfine Fields of ^{111}Cd and ^{99}Ru in Nickel (to be submitted to a journal).

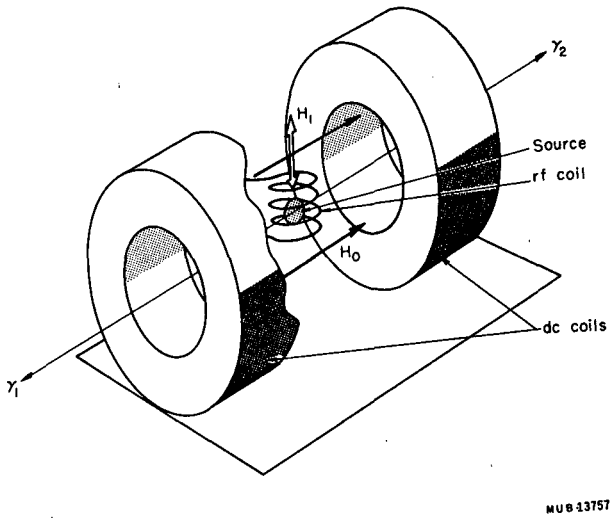

Fig. E. 5-1. Sketch of the geometry of a resonance experiment with angular correlations.

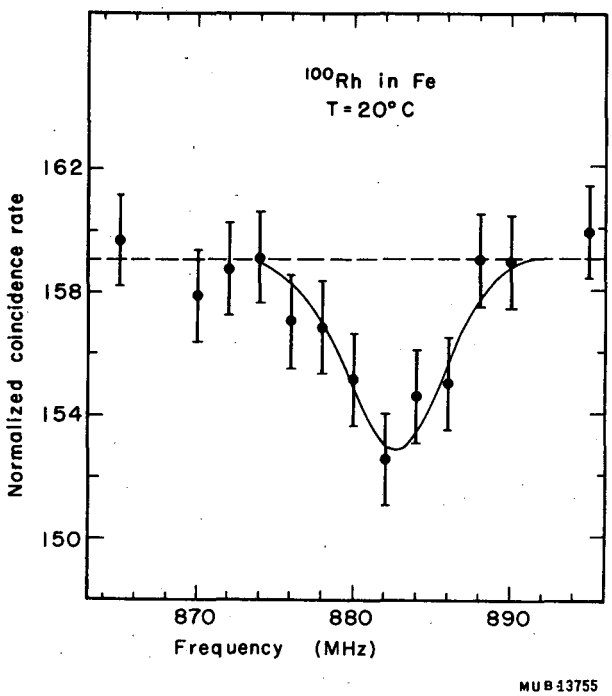

Fig. E. 5-3. Resonance effect for ^{100}Rh in Fe at room temperature. The polarizing field was 385 gauss and the average power was 80 W.

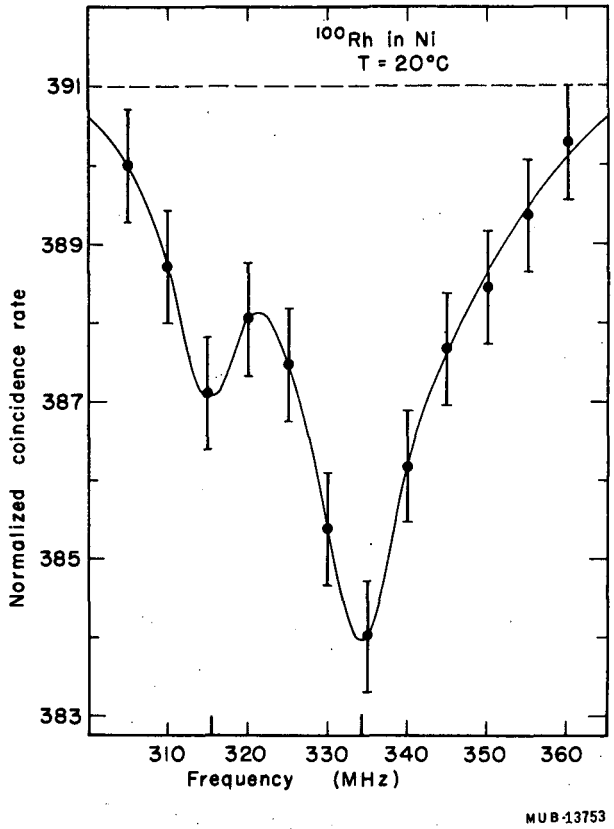

Fig. E. 5-2. Resonance effect for ^{100}Rh in Ni at room temperature. The polarizing field was 450 gauss and the average power was 35 W.

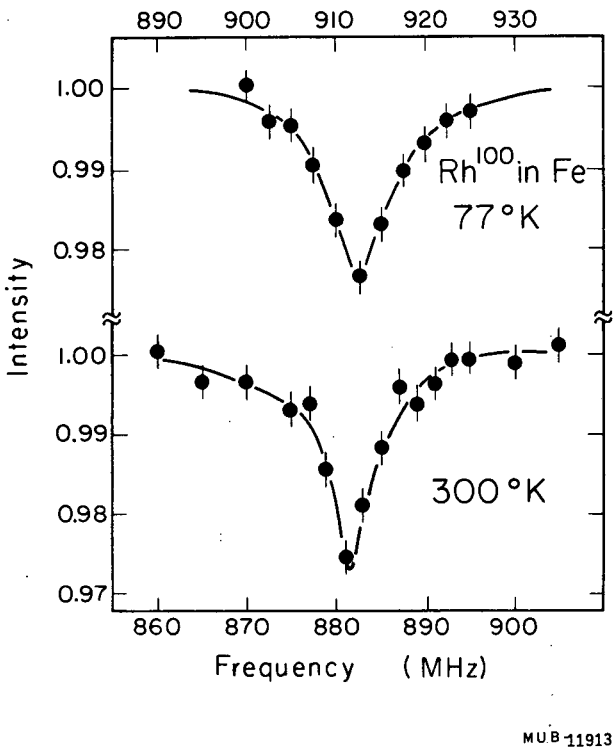

Fig. E. 5-4. Resonance effect for ^{100}Rh in Fe at two different temperatures. The polarizing field was 100 gauss and the rf amplitude was about 1.5 gauss. The data points are not corrected for accidental coincidences.

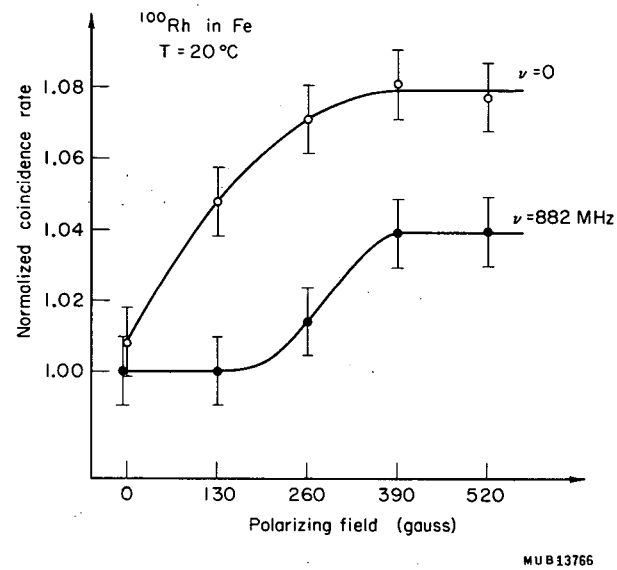

Fig. E. 5-5. Saturation behavior of the foil as a function of the polarizing field without rf field and with 100 W power at resonance frequency.

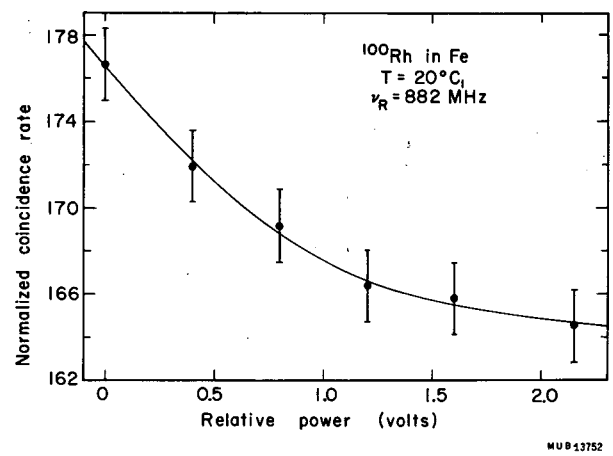

Fig. E. 5-6. Power dependence of the resonance effect at resonance. The power range extends from 0 to 100 W.

6. DETECTION OF NUCLEAR MAGNETIC RESONANCE IN A 235-nsec NUCLEAR STATE BY PERTURBED ANGULAR CORRELATIONS†

E. Matthias, D. A. Shirley, M. P. Klein, and N. Edelstein

The method of PAC has for some time provided the only way to measure precession frequencies in short-lived nuclear states, with lifetimes in the range 10^{-11} sec $< \tau < 10^{-6}$ sec. Time-differential PAC,[1] and more recently the digital analysis method (DAPAC),[2] have raised the upper

limit on lifetimes accessible to at least 10^{-3} sec and have greatly improved the accuracy possible with PAC. Still it is desirable to develop a method that combines the precision of NMR with the extremely high sensitivity of PAC in order to enjoy the advantages of both methods.

Abragam and Pound discussed, as early as 1953,[3] the possibility of detecting resonant absorption in a short-lived nuclear state by observing the angular-correlation anisotropy. They formulated the conditions for such an experiment:

(a) The splitting of the substates should be large compared with the natural nuclear linewidth; i.e., $\omega_L \tau_N >> 1$, where ω_L and τ_N are, respectively, the Larmor frequency and the nuclear lifetime.

(b) The rf field, H_1, must have sufficient amplitude to induce transitions in each nucleus in times of the order of the nuclear lifetime, $\gamma H_1 \gtrsim \tau_N^{-1}$, where γ is the nuclear gyromagnetic ratio.

(c) Other time-dependent interactions should be minimal, so that the nuclear spin-correlation time τ_c is of the order of the lifetime or larger, $\tau_c \gtrsim \tau_N$.

Conditions (a) and (c) can easily be met, but (b) is so stringent that a resonance experiment was considered not to be feasible. For a lifetime of 0.2 μsec and a g factor of 1, for example, one would have to use an rf amplitude of 1 kG, which would correspond to a power of 10^6 W in 1 cm^3 at 40 MHz.

The effective rf field, H_1^{eff}, may be greatly enhanced by performing the resonance experiment on an atom embedded in a ferromagnetic lattice.[4] The enhancement arises through the hyperfine field H_{hf}, giving

$$2\ H_1^{eff} = (1+H_{hf}/H_0)H_1,$$

where H_0 is the dc polarizing field. Thus, for typical field values H_0 = 100 G and $H_{hf} = 10^5$ G, the applied rf field is amplified by 10^3 and condition (b) can be met.

Rhodium-100 was chosen for this experiment because it is a well-understood case with a long lifetime and a large g factor, and because hyperfine fields of the order of 10^5 gauss are expected for Rh dissolved in the 3d ferromagnets. We selected a Ni lattice because nickel foil of the requisite thickness (10^{-4} cm = skin depth at 300 MHz) was available. In a recent study of the temperature dependence of H_{hf} for Ru in Ni,[5] it was found that the ratio $H_{hf}(295°K)/H_{hf}(0°K) = 0.80$; combining this with the value H_{hf}(Rh in Ni, 0°K) = -250 kG predicted from systematics,[6] we expected H_{hf}(Rh in Ni, 295°K) to have the magnitude 200 kG. This determined the frequency range selected for searching.

We have observed resonant rf absorption by 10^4 nuclei in the 74.8-keV excited state of ^{100}Rh by combining nuclear magnetic resonance in a ferromagnet with perturbed angular correlations (PAC) of the 84.0- to 74.8-keV γ-ray cascade.[7] The 4-day isotope ^{100}Pd was diffused into a nickel foil, and fed the cascade via electron-capture decay. A total of 2.8×10^6 coincidences were recorded by two 3×3-in. NaI(Tl) counters at 180 deg, while the sample was polarized in a field of 100 gauss along the counter axis. Perpendicular to the dc field an oscillating field of 3 gauss was stepped through the frequency range 289.5 to 355.5 MHz. Resonant absorption was detected by a drop in the coincidence rate centered about 322.5 MHz, as shown in Fig. E.6-1.

The essence of the experiment is very simple. The magnetization direction of the foil serves as the quantization axis and the propagation direction of the γ rays that were detected (the σ components, corresponding to $\Delta M_I = \pm 1$). For a coincidence to be recorded, σ components of the two transitions had to be registered within 2 μsec in the two counters, thus ensuring high probability that they were from the same nucleus. The coincidence counting rate under the experimental conditions varies with the angle θ between the propagation directions of γ_1 and γ_2 as $1 + 0.2\ P_2(\cos\theta)$, so with θ = 180 deg the coincidence rate is 20% larger than "average." This may be regarded as arising from the selection, by the first counter, of a certain population distribution of nuclei in the 74.8-keV state that are candidates for coincidence (i.e., those that arrived in the 74.8-keV state via a σ transition). Radiation at the resonant radio frequency tends to randomize this population, thus lowering the coincidence counting rate. This is illustrated in Fig. E.6-2, which shows rf transitions driving a nucleus that would have emitted a γ_2 σ component into a substate from which it may instead emit a π component.

Two features of Fig. E.6-1 require comment. First, the absorption is small, of the order of 2% rather than 20%, and secondly the linewidth is approximately 20 MHz, or about forty natural linewidths. These two features probably arise from the same cause, and were anticipated, because it has been found that the time-dependent correlation pattern of ^{99}Ru in Ni loses coherence in $\approx 5 \times 10^{-8}$ sec. Such behavior could be the result of fluctuating local moments, of quadrupole

interaction, or simply of the existence of different magnetic sites. This point will be explored further. The fact that we can detect resonance in spite of this problem indicates that this type of experiment is feasible for shorter-lived states.

Comparison of the resonant frequency of 322.5 ± 3 MHz with the g factor, +2.151 ± 0.004,[2] yields for H_{hf}(Rh in Ni, 290°K) a value of 197 ± 2 kG. This is in excellent agreement with the trends in this region, and quite close to the predicted value. The temperature dependence of H_{hf} is under further study. The sign of H_{hf} can be determined by radiating with circularly polarized rf radiation.

The combination of PAC and NMR should provide a method for investigating hyperfine interactions in short-lived excited nuclear states, in particular for levels with lifetimes between 10^{-6} and 1 sec, which are not accessible to other methods. For the longer lifetimes ferromagnetic enhancement should not be necessary. For longer-lived states one has to produce the nuclear levels by a reaction process, which also provides larger anisotropies for the detection of the resonance and allows singles, rather than coincidence, detection. The limit of application will be set, not by the nuclear lifetime, but by the relaxation times of the nuclei in their environments.

We thank Professor A. M. Portis for helpful discussions, Mrs. Winifred E. Heppler for the sample preparations, and Mr. R. C. Acker for devising the rf circuitry.

Footnotes and References

† Phys. Rev. Letters 16, 974 (1966).

1. This method is discussed by R. M. Steffen and H. Frauenfelder in Perturbed Angular Correlations, Ed. by E. Karlsson, E. Matthias, and K. Siegbahn (North Holland, Amsterdam, 1964), page 1.
2. E. Matthias and D. A. Shirley, Nucl. Instr. Methods (to be published).
3. A. Abragam and R. V. Pound, Phys. Rev. 92, 943 (1953).
4. A. M. Portis and R. H. Lindquist, in Magnetism, Vol. IIA, Ed. by G. T. Rado and H. Suhl (Academic Press, New York, 1965).
5. E. Matthias, S. S. Rosenblum, and D. A. Shirley, Local Moment on Ru Atoms in Ni and Giant Induced Knight Shifts Above the Curie Point, UCRL-16342, Aug. 1965.
6. D. A. Shirley, Thermal Equilibrium Nuclear Orientation, to be published in Ann. Rev. Nucl. Sci.
7. E. Matthias, D. A. Shirley, J. S. Evans, and R. A. Naumann, Phys. Rev. 140, B64 (1965).

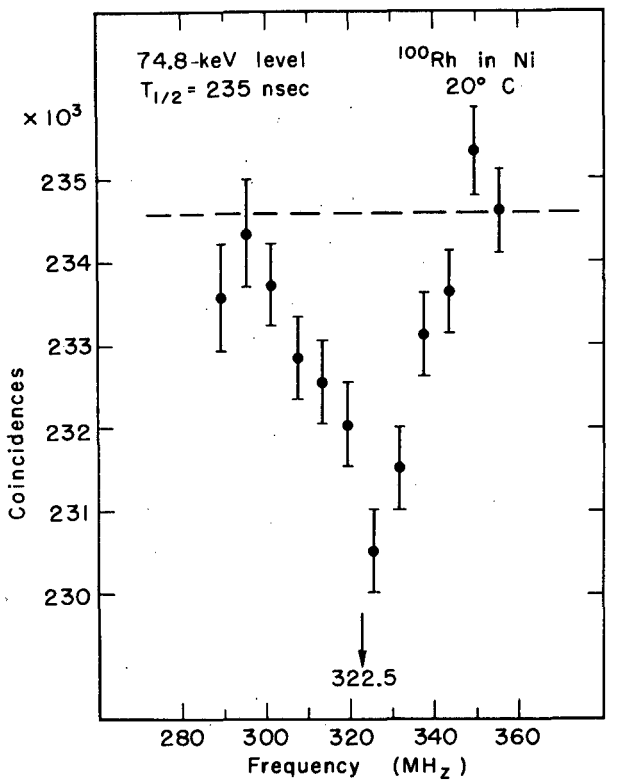

MUB-10229

Fig. E.6-1. Coincidence counting rate as a function of applied rf frequency, for the 84.0- to 74.8-keV γ-ray cascade of ^{100}Rh in nickel.

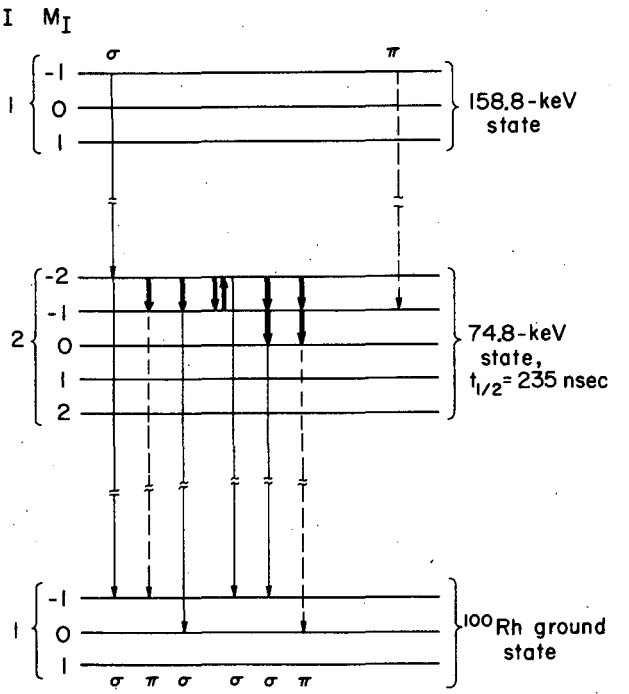

MUB-10402

Fig. E.6-2. Energy-level diagram. Three levels of ^{100}Rh, of respective spins 1, 2, 1, are quantized in a hyperfine magnetic field parallel to the counter axis. Only the σ ($\Delta M = \pm 1$) components of dipole γ radiation, with distribution $\approx (1+\cos^2\theta)$, can strike counters at $\theta = 0$ and 180 deg. For a coincidence to be registered, σ components of both the 84.0-keV (γ_1) and the 74.8-keV (γ_2) transitions must be recorded within 1 μsec. We denote σ and π components by solid and dotted lines, and ΔM_I transitions within the 74.8-keV state by heavy lines. On the left a typical σ component of γ_1 is shown, with six of the many possible fates that may befall the nucleus in the intermediate (74.8-keV) state. Four of these paths end in σ transitions and are recorded as coincidence. The other two contribute to the dip in Fig. E.6-1. Most of the possible components are omitted for clarity.

7. AN INVESTIGATION OF THE HYPERFINE STRUCTURE OF TRIVALENT ^{158}Tb BY NUCLEAR ALIGNMENT AND PARAMAGNETIC RESONANCE: DETERMINATION OF THE SPIN, DIPOLE MOMENT, AND QUADRUPOLE MOMENT OF ^{158}Tb

J. A. Barclay, W. C. Easley, and D. A. Shirley

Nuclear alignment data alone do not allow the unique determination of A, the hyperfine

structure constant, and P, the quadrupole coupling constant, which appear in the spin Hamiltonian for $^{158}Tb^{3+}$. One can set only rather broad limits on $|A|$ and P. However, the method does allow the determination of a relationship between the two parameters which is more accurate than the separate values.[1] On the other hand, electron paramagnetic resonance (EPR) measurements provide a direct measure of $|A|$ and usually give no information about P. A combination of the methods can give a complete picture of the hyperfine structure of the ion. With these points in mind, we have carried out low-temperature nuclear alignment experiments on ^{158}Tb substitutionally grown into a neodymium ethylsulfate (NES) single crystal, and we have observed the EPR spectrum of $^{158}Tb^{3+}$ ions in a single crystal of yttrium ethylsulfate (YES). The fact that we can directly compare parameters measured in a paramagnetic environment (NES) with those in a diamagnetic environment (YES) is justified elsewhere.[1]

Nuclear Alignment of ^{158}Tb in NES

The experimental procedures and apparatus have been described previously.[1] Three μC of $^{158}Tb^{3+}$ was incorporated into a 5-g NES single crystal. Although the 946-keV γ showed the largest anisotropy (≈28% at 1/T = 90), we studied the 182-keV γ, using NaI scintillation crystals (3×3 in.) in order to enhance statistics. The decay scheme of ^{158}Tb has been well studied,[2] and the relevant portion is reproduced in Fig. E.7-1. The hyperfine structure constants were related to the observed γ-ray anisotropies in the usual manner:[3] $W(\theta) = 1 + B_2U_2F_2P_2(\cos\theta)$, where the symbols have their usual meanings. Higher-order terms were found to be negligible. Since the value of U_2 for the 182-keV γ was ambiguous and that of the 946-keV γ was not, B_2 was determined by using a Ge(Li) detector on the 946-keV γ. The value found was $B_2 = +0.960 \pm 0.009$ at 1/T = 90.5. B_2 was then used to determine U_2 for the unobserved transition populating the 4+ level at 262 keV. We found $U_2(182) = +0.827 \pm 0.008$.

A plot of the experimental values of B_2 versus 1/T determined with the NaI detector along the symmetry axis of the crystal ($\theta = 0$) is shown in Fig. E.7-2. The indicated errors are statistical. The temperature was determined by using the corrected temperature scale for NES due to Blok et al.[4] The solid and dotted lines are theoretical fits to the data for the indicated values of $|A|$ and P. The curves were computed as a function of 1/T by a computer program PRIME. The resulting acceptable ranges for $|A|$ and P are given in Table E.7-I. The value of P in the adjacent column of Table E.7-I was obtained by using $|A|$ from the EPR measurements and the following equation relating $|A|$ and P derived from the alignment data:

$$P(cm^{-1}) = 0.0944\ |A| - 0.00378.$$

EPR of $^{158}Tb^{3+}$ in YES

A 10-mg single crystal of YES containing $\approx 10^{13}$ atoms of ^{158}Tb was slowly grown (4 weeks) out of 60 λ of saturated YES-D_2O solution. The crystal was placed in the bottom of a right circular cavity resonating at ≈34.5 MHz in the TE_{011} mode in such a way that the static field, the microwave field, and the C axis were all parallel.[5] The spectrum was taken at ≈1.5° K using a superheterodyne spectrometer employing low-frequency (150 cps) field modulation and synchronous detection. The spectrum consisted of four strong lines due to the ^{159}Tb resonance[5] (I = 3/2) superimposed upon a weaker seven-line spectrum which we attribute to ^{158}Tb and which verifies the nuclear spin of 3. Both sets of lines had 7-gauss widths. The results of the EPR measurements are given in Table E.7-I.

From the nuclear magnetic dipole moment given by Baker et al.[6] for ^{159}Tb (1.994 ± 0.004 nm) and the hyperfine structure constants from the EPR data, we can calculate the magnetic moment using the equation $\mu_I{}^{158} = \mu_I{}^{159} I^{158} A^{158} / I^{159} A^{159}$. The result is $\mu_I{}^{158} = 1.742(\pm 0.002)$ nm. The error includes an estimated upper limit of the uncertainty due to the hyperfine structure anomaly, which is expected to be small in this case.

For the calculation of the nuclear electric quadrupole moment we used the value of P given in Table E.7-I and the relation given by Johnson et al.,[1] which we have corrected for a revised value[6] of $\langle 1/r^3 \rangle$: $P(cm^{-1}) = 0.00227\ Q$. The result is $Q^{158} = 2.1 \pm 0.3$ barns.

Theoretical magnetic moments have been calculated using Nilsson wave functions and assuming 3/2 + [411] and 3/2 - [521] states for the odd proton and odd neutron in ^{158}Tb, respectively. The result is 2.0 nm.[7] An empirical comparison can be obtained by calculating the magnetic moment from the measured moments of odd nucleons in the two states involved, in neighboring nuclei.[7] The result, using a revised value of 1.994 ± 0.004 for the 3/2 + [411] proton state from ^{159}Tb, is +1.68 ± 0.02 nm. This estimate is in good agreement with the experimental value of

1.742(±0.005) and suggests that odd-particle correlations do not appreciably affect the magnetic moment of this type of odd-odd deformed nucleus.

References

1. C. E. Johnson, J. F. Schooley, and D. A. Shirley, Phys. Rev. 120 [6], 2108 (1960).
2. F. Schima, E. G. Funk, Jr., and J. W. Mihelich, Nucl. Phys. 63, 305 (1965).
3. R. J. Blin-Stoyle and M. A. Grace, in Handbuch der Physik, Ed. by S. Flügge (Springer-Verlag, Berlin, 1957), Vol. 42, p. 555.
4. J. Blok, D. A. Shirley, and N. J. Stone, Phys. Rev. 143, 78 (1966).
5. J. M. Baker and B. Bleaney, Proc. Roy. Soc. (London) A245, 156 (1958).
6. J. M. Baker, J. R. Chadwick, G. Garton, and J. P. Hurrell, Proc. Roy. Soc. (London) A286, 352 (1965).
7. C. A. Lovejoy and D. A. Shirley, Nucl. Phys. 30, 452 (1962).

Table E.7-I. Hyperfine structure of tripositive ^{158}Tb and ^{159}Tb ions.

Nuclear alignment ^{158}Tb		EPR ^{158}Tb	EPR ^{159}Tb
I	(3)	3	3/2
$\lvert A \rvert$ (cm^{-1})	$0.0607 < \lvert A \rvert < 0.103$	0.09109 ± 0.0002 (110.1 ± 0.2 gauss)	0.2086 ± 0.0002 (252.1 ± 0.2 gauss)
P (cm^{-1})	$0.00195 < P < 0.00602$	0.00482	

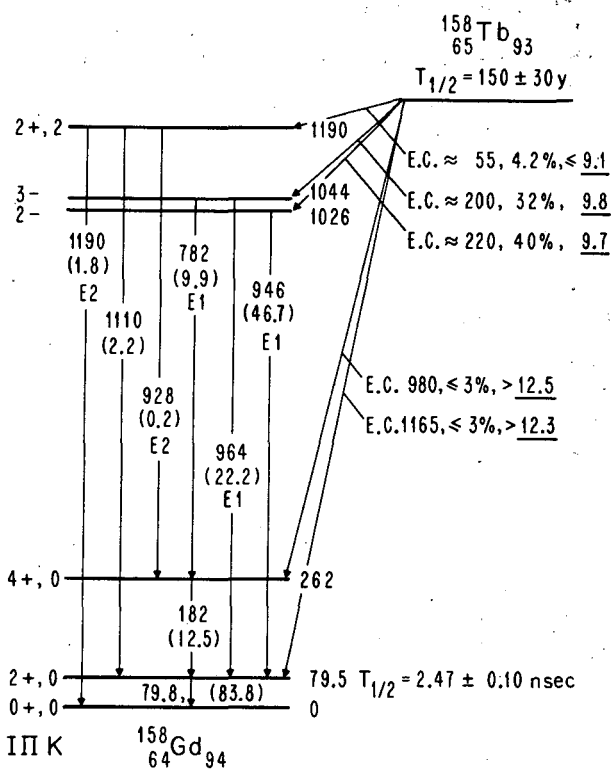

Fig. E.7-1. Portion of decay scheme of ^{158}Tb relevant to this work.

XBL671-302

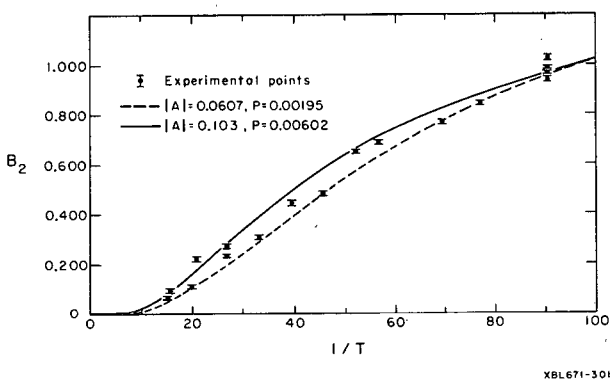

Fig. E.7-2. Plot of B_2 vs $1/T$ for the 182-keV γ ray at $\theta = 0$.

8. THE NUCLEAR SPIN OF ^{249}Bk FROM THE HYPERFINE STRUCTURE IN ITS EMISSION SPECTRUM†

Earl F. Worden,* E. K. Hulet,* Ronald Lougheed,* and John G. Conway

An electrodeless lamp containing 30 μg of Bk as the iodide was used as the source of the spectrum. The spectrograph was a 3.4 Ebert with a 60-deg blazed grating. The spectrum was photographed from 2500 to 9000 Å. There are several thousand lines on the plates and a very great percentage of them show hyperfine structure. Several show the widest hyperfine structure of any observed lines. The line at 3771 is 0.8983 Å wide, which is about twice as wide as any known line. Because of this wide spacing the hyperfine structure is easily resolved and observable, the nuclear spin can definitely be established as I = 7/2. See Fig. E.8-1.

The measurements of the lines to determine accurate wavelengths is now going on with the hope that in a year or so we will be able to search for energy levels. A calculation of the nuclear moment is not possible because the quantum-number assignments cannot be made for a line.

Footnotes

† Brief version of article (UCRL-70073) submitted to J. Opt. Soc. Am.
* LRL–Livermore

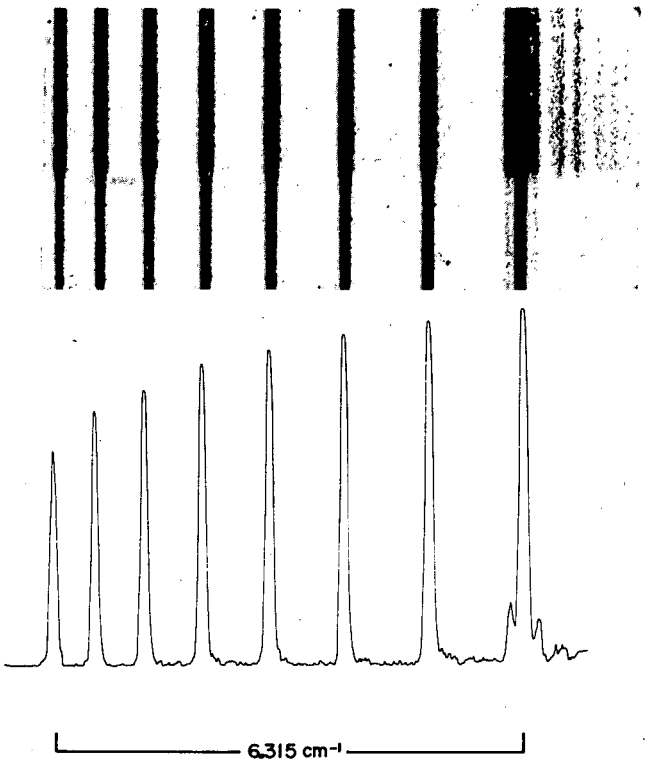

Fig. E. 8-1. Hyperfine structure of the λ 3771 line of Bk. The smallest interval is 0.560 cm^{-1} (0.080Å). The total width is 6.315 cm^{-1} (0.8983Å). The weak components near the high-wavelength side of the pattern are due to another weaker Bk line.

F. MASS SPECTROSCOPY

1. EXCITATION BY ELECTRON IMPACT OF LONG-LIVED STATES IN MOLECULES†

R. Clampitt and Amos S. Newton

Introduction

Metastable and other long-lived states of atoms have been the subjects of study for several years. One of the methods that has been successful in this Laboratory[1, 2] and elsewhere involves the use of crossed electron and molecular beams. The atom, after excitation, drifts towards a metal plate which constitutes the first dynode of an electron multiplier. If the energy of the excited electron in the atom is greater than the work function of the metal, an electron may be ejected from the metal by a process of Auger de-excitation. In this manner, and by studying the variation of ejected electron current with distance from the point of excitation, information on excitation functions, collision cross sections, and half-lives of several gases has been obtained.

In order to study, by this method, long-lived excited states of molecules in which the electronic energy levels of interest are less than 5 eV above the ground state, such as the well-known triplet states in unsaturated hydrocarbons, it is necessary to employ a detector surface that has a work function of about 1 eV. Such a surface might be cesium or cesium antimonide. Because of the difficulty of preparing and maintaining a constant efficiency in these surfaces, particularly under the level of vacuum prevailing in most molecular beam assemblies ($\approx 10^{-6}$ torr), no studies have yet been made on these excited states in hydrocarbons.

Apparatus

A new molecular beam apparatus designed specifically to investigate these states is in its final stages of assembly and testing. It is as follows.

A molecular beam is produced in the usual manner and enters the excitation chamber, which is bakable to 450°C and is pumped by a 100-liter/sec ion pump. In the absence of a beam and with minimal baking, pressures of $< 1 \times 10^{-8}$ torr can be readily obtained in this chamber. Two types of monoenergetic electron guns have been made: the first is of the Fox design, and has an energy resolution of about 0.08 eV at $\approx$ 0.5 μA electron current; the second is a more refined double 127-deg electron velocity selector capable of $\approx$0.02 eV resolution at $\approx$ 0.01 μA electron current. With the latter gun it will also be possible to study the electron energy spectrum after passage through the molecular beam. The concomitant difficulty of operating these low-current velocity selectors at 1 to 5 eV electron kinetic energy imposes a restriction on the success of this type of work.

There are facilities for mechanical chopping of the molecular beam and for electrical modulation of the electron beam in order to make use of phase- and frequency-sensitive amplification of the signal.

The detector chamber is bakable to 450°C, and is pumped by a liquid-helium-cooled surface (pumping speed $\approx$ 1000 liter/sec for H_2 at 10^{-8} torr). It is expected to achieve pressures in the ultrahigh-vacuum region in this chamber in the absence of the molecular beam. The first detector to be used is a commercial photomultiplier tube which has a cesium antimonide surface as the first dynode. The multiplier may be cooled with a liquid nitrogen finger or heated electrically. A quartz window is provided for periodic monitoring of the detector stability and efficiency by means of a chopped light beam from a monochromator. The detector is movable to facilitate measurements of lifetimes in the range from 10^{-4} to 10^{-2} sec.

Footnote and References

†Description of research in progress.

1. John Olmsted III, Amos S. Newton, and K. Street, Jr., in Nuclear Chemistry Division Annual Report, 1964, UCRL-11828, Jan. 1965, p. 207.
2. J. Chem. Phys. 42, 2321 (1965).

2. A SEARCH FOR AUTO-IONIZING STATES OF HIGHLY EXCITED IONS OF THE NOBLE GASES†

Amos S. Newton, A. F. Sciamanna, and R. Clampitt

It has recently been shown that highly excited states of noble gas ions exist which undergo transition to the next higher ionization state in collision with a surface,[1]

$$X^{+*} \rightarrow X^{++} + e^{-}. \qquad (1)$$

For those transitions occurring at the last ion source slit and appearing at an apparent mass of 1/4 the mass of the noble gas atom, it was not possible to clearly differentiate between the surface-induced transition mechanism and an auto-ionization mechanism proposed by Daly.[2]

The addition of an extra slit after the last normal ion source slit, as shown in Fig. F.2-1, has made it possible to clearly demonstrate that much of the M/4 peak in the noble gases is caused by a surface-induced transition mechanism. The added slit, S_3, was grounded. Slit S_2 was isolated from ground and a separate lead run to it from various points in the lower voltage part of the high-voltage dropping resistor string. Potentials of 3.35, 5.80, and 6.40% of the ion acceleration voltage could be applied to S_2, or it could be grounded for operation as a normal ion source.

Application of such potentials to slit S_2 resulted in the movement of a portion of the peak normally appearing at $(M/q)^* = 10$ in argon to higher mass values, as shown in Fig. F.2-2. In Fig. F.2-3 the observed apparent mass is plotted against the voltage applied to slit S_2, and it is seen that the points agree with the calculated line for a transition from singly to doubly charged ion occurring at S_2 (see Ref. 1 for calculation).

A residue of peak still remains near $(M/q)^* = 10$, but the maximum of this peak is shifted to an $(M/q)^* = 10.08 \pm 0.02$. This latter shift is unexplained, but its occurrence indicates that the residual peak may be due to an auto-ionization mechanism.

Similar shifts of the $(M/q)^* = M/4$ peak have been observed in neon and helium. In each case a peak was found at the value calculated for the shift due to a voltage on S_2 and a transition from X^{+*} to X^{++} at S_2. In both these gases the residual peak is higher than the shifted peak, and is about 0.8% higher in apparent mass than the $(M/q)^* = M/4$ observed when S_2 is grounded.

The evidence presented here shows that up to half of the $(M/4)^*$ peak in the noble gases arises from collision-induced transitions at slit S_2 of the Isatron ion source. No proof for an auto-ionization process contributing to this peak was found, and in He^{+*}, an auto-ionizing level above the appearance potential of He^{++} is manifestly impossible.

References

†Short report of work in progress. Work subsequent to that reported in Paper F. 3.

1. A. S. Newton, A. F. Sciamanna, and R. Clampitt, Surface-Induced Transitions in Highly Excited Noble Gas Ions and Quasi-Metastable Peaks in the Mass Spectra of the Noble Gases (UCRL-17187, Oct. 1966), J. Chem. Phys., in press.
2. N. R. Daly, Proc. Phys. Soc. (London) 85, 897 (1965).

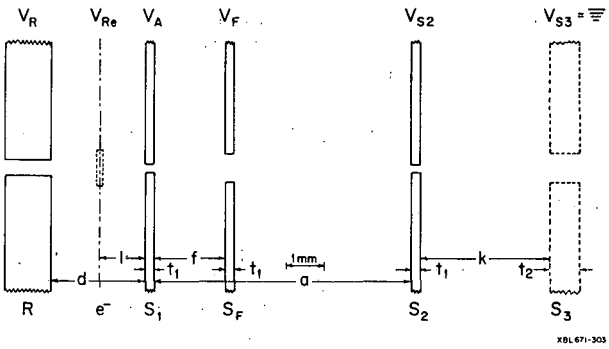

Fig. F.2-1. Modified Isatron ion source. Slit S_3 has been added and slit S_2 isolated from ground potential.
V_R = repeller potential with respect to V_A, the block potential;
V_{Re} = 0.52 V_R; V_F = potential on focus plates with respect to block potential; and V_{S_2} = potential on slit S_2 with respect to ground.
d = 2.54 mm, 1 = 1.32 mm, f = 2.03 mm, 2 = 5.08 mm.
k = 3.42 mm, t_1= 0.27 mm, t_2= 0.76 mm.

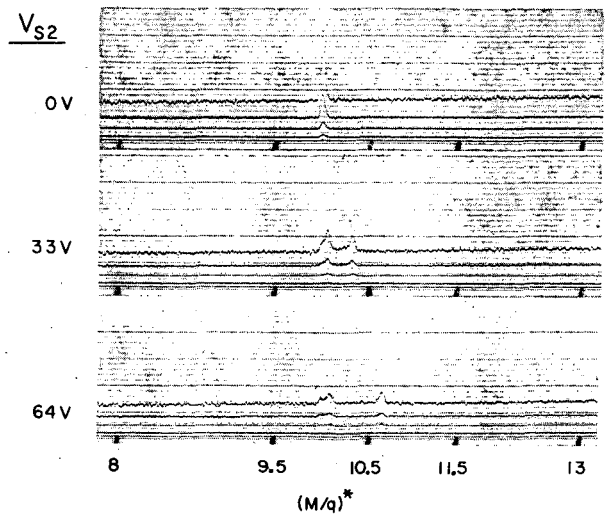

Fig. F. 2-2. Shift in $(M/q)^*$ = 10 peak in argon with potential applied to slit S_2; V_{S_2} is in V per 1000 V accelerating potential.

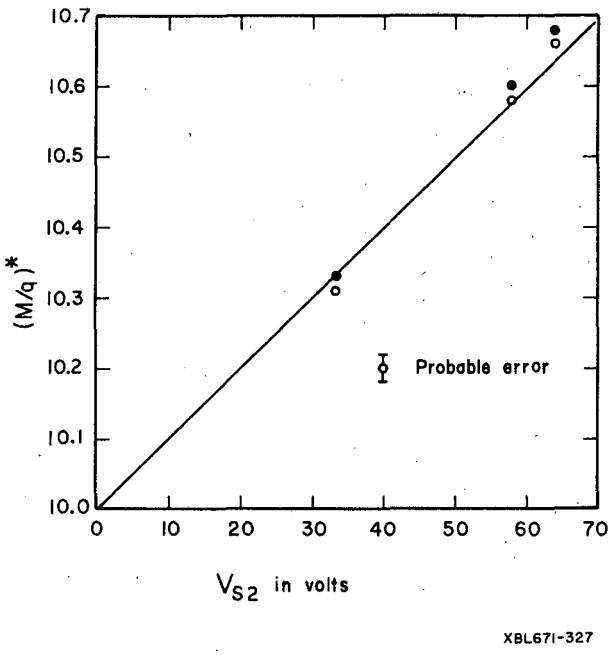

Fig. F.2-3. Observed apparent mass of shift $(M/q)^*$ = 10 peak in argon vs V_{S_2} (V per 1000 V accelerating potential). Line is calculated.

3. SURFACE-INDUCED TRANSITIONS IN HIGHLY EXCITED NOBLE GAS IONS AND QUASI-METASTABLE PEAKS[1] IN THE MASS SPECTRA OF THE NOBLE GASES†

Amos S. Newton, A. F. Sciamanna, and R. Clampitt

Introduction

Several studies made recently have established the existence of long-lived excited states of ions of the noble gases. The methods used are summarized as follows: (i) the technique of Aston bands,[2] (ii) measurements with crossed ion and electron beams,[3-5] (iii) electron ejection from metals,[6] (iv) ion-electron collisions in the potential well of an electron beam,[7-9] (v) light emission as a result of electrostatic quenching,[10] (vi) ion-molecule reactions,[11] (vii) auto-ionization,[12] and (viii) surface-induced transitions.[4,13]

In the work presented here, quasi-metastable peaks have been observed in the mass spectrum of each of the noble gases. These peaks are shown to correspond to surface-induced transitions of the type

$$X^{(q+)^*} \rightarrow X^{(q+1)+} + e^- , \qquad (1)$$

at each of the various slits of the ion source.

Experimental Procedure

All work described here was performed with a Consolidated Electrodynamics Corp. Model 103A mass spectrometer using the conventional Isatron ion source. This is shown schematically in Fig. F.3-1.

Results

In Fig. F.3-2 are shown the mass spectra of the noble gases in the region of mass of the respective doubly charged ion. A "quasi-metastable" peak occurring at about 95% of the M/q of the doubly charged ion is seen in each spectrum.

For an ion of mass M and initial charge q_1, which is accelerated through a potential V_1, then undergoes a transition to charge q_2, is further accelerated through a potential V_2, and is then magnetically analyzed as the ion M^{q_2+}, the apparent mass at which it appears in the mass spectrum is given by

$$(M/q)^* = M(q_1V_1 + q_2V_2)/q_2^2(V_1 + V_2) . \qquad (2)$$

For transitions occurring at the first slit, S_1, in the Isatron, $V_1 = 0.52\ V_R$ (where V_R = repeller potential with respect to block), and $V_2 = V_A$, the block potential. For transitions at the last slit, S_2, $V = 0.52\ V_R + V_A$, and $V_2 = 0$. Ions from transitions at both slits follow normal trajectories after the transition. At slit S_F, $V_1 = 0.52\ V_R + V_F$, where V_F is the focus potential with respect to block, and $V_2 = V_A - V_F$. The ion trajectory after collision must, in order to pass through S_2, deviate by an angle of 4° 30' from the normal trajectory, giving these ions a focus at a smaller radius than normal ions. To correct for this, the values of $(M/q)^*$ calculated from Eq. 2 are multiplied by 0.994.[14]

In Fig. F.3-3 are shown all the quasi-metastable peaks in the mass spectrum of argon caused by surface-induced transitions of Ar^{+*} and Ar^{++*}.

The apparent mass, kinetic order of formation, kinetic energy, and appearance potentials of the ions resulting in quasi-metastable peaks in argon have been investigated, and the results are shown in Fig. F.3-4 through F.3-8 and Tables F.3-I and F.3-II.

The peaks are shown to be linear with ionizing electron current, Fig. 5. The peaks resulting from transitions at each of the respective Isatron slits are shown in Figs. 5, 7, and 8 to

follow Eq. 2.

The data in these figures and the results of retarding potentials (shown in Table F.3-II) show that no loss of kinetic energy (≤ 2 eV) occurs as a result of the transition.

In Fig. F.3-9 the appearance potential (AP) of those peaks arising from Ar^{+*} are shown to be within 1 eV of the AP of Ar^{++}, and in Fig. F.3-10, the peak arising from Ne^{+*} undergoing transition at S_F to Ne^{++} is shown to have an AP within $\approx$ 1 eV of that of Ne^{++}.

Discussion

The ionization of the excited state of an atom and of ions with surfaces has been treated by Massey,[15] Shekhter,[16] Cobas and Lamb,[17] Varnerin,[18] and Hagstrum.[19] Four types of interactions have been identified: resonance ionization, resonance neutralization, Auger de-excitation, and Auger neutralization. Resonance ionization can occur only when $\phi > E^+ - E^*$, where ϕ is the work function of the surface and E^+ and E^* are respectively the ionization and excitation energies of the atom. Since $E^+ - E^*$ is small according to Figs. F.3-9 and F.3-10, it will be less than ϕ at all distances and resonance ionization can always occur. The extent to which it occurs will be the sum of the integrated transition probabilities over the whole region of approaching and leaving the vicinity of the surface.

In He^{+*} the states involved are clearly the higher Rydberg states of the helium ion. The energy of such states at each principal quantum number n can be calculated from the classical Rydberg formula for one-electron atoms. The energy difference between these states and He^{++} is shown in Fig. F.3-11. Also shown in Fig. F.3-11 is the lifetime of each level for radiative de-excitation, calculated from the total transition probabilities from each state in the H atom to all states below it, the sum multiplied by a scaling factor of Z^4; the inverse of this transition probability is the lifetime of the state.[20,21] All states in He^{+*} above n = 10 have energies within 0.5 eV of He^{++} and lifetimes larger than 10^{-7} sec. The acceleration time in the mass spectrometer is from 0.2 to 0.6×10^{-6} sec for noble gas ions under the experimental conditions used.

Daly[12] has suggested that the peaks he observed at 1/4 the mass of the respective noble gas atom were due to auto-ionization processes from a state slightly higher than the doubly charged states. Appearance potential measurements and linearity of peak height with pressure were cited as evidence of auto-ionization. Attempts to disprove the auto-ionization theory are unsuccessful, as both surface-induced transitions at S_2 and auto-ionization processes after S_2 lead to the same results. The data presented here are, however, consistent with the assumption that all the quasi-metastable peaks are due to surface-induced transitions.

Footnote and References

†Short version of paper (UCRL-17187) for publication in J. Chem. Phys.

1. The peaks described here have been labeled "quasi-metastable peaks" inasmuch as they show all the characteristics of metastable peaks, yet they are not metastable peaks as they are not formed by a gas phase unimolecular dissociation nor by an auto-ionization process. Neither are they "Aston bands," which are defined as being the result of gas phase collisions and hence follow second-order gas kinetics [for a discussion of Aston bands see J. William McGowan and L. Kerwin, Can. J. Phys. 41, 316 (1963)].
2. J. William McGowan and L. Kerwin, Can. J. Phys. 41, 1535 (1963).
3. Z. Z. Latypov, S. E. Kupriyanov, and N. N. Tunitskii, Zh. Eksperim. i Teor. Fiz. (USSR) 46, 383 (1964); Soviet Physics-JETP 19, 570 (1964).
4. S. E. Kupriyanov, Z. Z. Latypov, and A. A. Perov, Zh. Eksperim. i Teor. Fiz. (USSR) 47, 21 (1964), Soviet Physics-JETP 20, 14 (1965).
5. K. Dolder, M. F. A. Harrison, and P. C. Thonemann, Proc. Roy. Soc. (London) A264, 367 (1961); A274, 546 (1963).
6. H. D. Hagstrum, Phys. Rev. 104, 309 (1956).
7. J. Cuthbert, J. Farren, B. S. Prahallada Rao, and E. R. Preece, Proc. Phys. Soc. (London) 88, 91 (1966).
8. F. A. Baker and J. B. Hasted, Phil. Trans. Roy. Soc. A(London), 261, 33 (1966).
9. P. A. Redhead, presented at the Fourteenth Annual Conference on Mass Spectrometry and Allied Topics, Dallas, May 22-27, 1966.

10. M. F. A. Harrison, A. C. H. Smith, and D. F. Dance, in Abstracts of Proceedings of the IVth International Conference on the Physics of Electronic and Atomic Collisions, University of Laval, Quebec, 1965, p. 442.
11. R. Becker and F. W. Lampe, J. Chem. Phys. 42, 3857 (1965).
12. N. R. Daly, Proc. Phys. Soc. (London) 85, 897 (1965).
13. Florence Fiquet-Fayard, J. Chim. Phys. 63, 401 (1966).
14. J. H. Beynon, Mass Spectrometry and Its Application to Organic Chemistry (Elsevier Press, New York, 1960), p. 255.
15. H. S. W. Massey, Proc. Camb. Phil. Soc. 26, 386 (1930).
16. S. S. Shekhter, Zh. Eksperim. i Teor. Fiz (USSR) 7, 750 (1937).
17. A. Cobas and W. E. Lamb, Phys. Rev. 65, 327 (1944).
18. L. J. Varnerin, Jr., Phys. Rev. 91, 859 (1953).
19. H. D. Hagstrum, Phys. Rev. 96, 336 (1954).
20. H. A. Bethe and E. E. Salpeter, Quantum Mechanics of One and Two Electron Systems (Springer-Verlag, Berlin, 1957), p. 266.
21. W. L. Wiese, M. W. Smith, and B. M. Glennon, in Atomic Transition Probabilities, Vol. I (U. S. Government Printing Office, Washington, D. C., 1966.

Table F.3-I. Quasi-metastable peaks in the mass spectra of the noble gases arising from surface-induced transitions of the type $X^{+*} \xrightarrow{S} X^{++} + e^-$ at the Isatron focus slit. Variation of apparent mass with voltage on focus slit.

	V_{Re} [a]	V_F	V_A	$(M/q)^*_{obs}$	$(M/q)^*_{calc}$	Δ(calc-obs)
Helium	33.1	109.5	3000	1.95±0.01	1.94	-0.01
	33.1	223.5	3000	1.91±0.01	1.90	-0.01
Neon	15.6	44.5	1000	9.66±0.02	9.65	-0.01
	20.8	77.5	1000	9.48±0.02	9.46	-0.02
Argon	10.4	125.5	1000	18.57±0.02	18.56	-0.01
	10.4	37.5	1000	19.40±0.02	19.41	+0.01
Krypton [b]	(peaks from ^{84}Kr					
	5.7	53.7	1000	40.52±0.02	40.51	-0.01
	5.7	61	1000	40.37±0.02	40.36	-0.01
	5.7	66.5	1000	40.25±0.02	40.25	0.00
Xenon [b]	(peaks from ^{129}Xe					
	5.7	50.5	1000	62.40±0.05	62.33	-0.07
	5.7	79.8	1000	61.38±0.05	61.40	+0.02
	5.7	94	1000	60.93±0.05	60.88	-0.05

a. $V_{Re} = 0.52\ V_R$.
b. Owing to the multiplicity of isotopes in Kr and Xe, only peaks at a few values of $(M/q)^*$ are well resolved.

Table F.3-II. Metastable suppressor cutoff voltages of peaks from the surface-induced transition $Ar^{+*} \xrightarrow{S} Ar^{++} + e^-$.

Slit	V_{Re}	V_F	V_A	$(M/q)^*$	$\frac{(V_{mss})_{(M/q)^*}}{(V_{mss})_{(\frac{M}{q}=20)}}$	$\frac{(M/q)^*}{20}$
S_1	20.8	123	1000	19.80	0.9906	0.9900
S_F	6.1	84.5	1000	19.10	0.956	0.955
S_2	6.9	75.7	1000	10.00	0.499	0.500

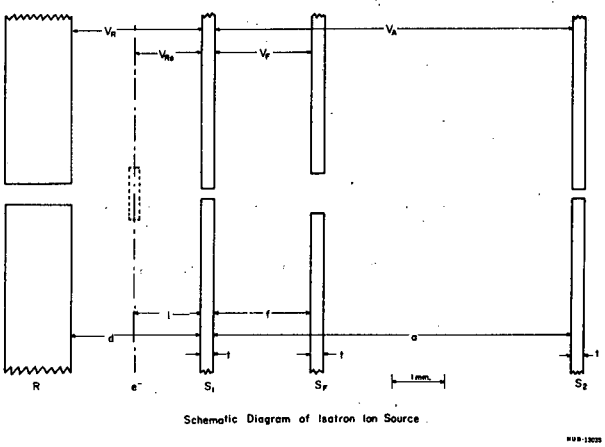

Fig. F.3-1. Schematic diagram of Isatron ion source: d = 2.54 mm, l = 1.32 mm, f = 2.03 mm, a = 5.08 mm. For normal operation, S_1 = block potential, S_2 is at ground potential. If V_A = 1000 V, then $V_R \approx$ 11 V, and $V_F \approx$ 80 V.

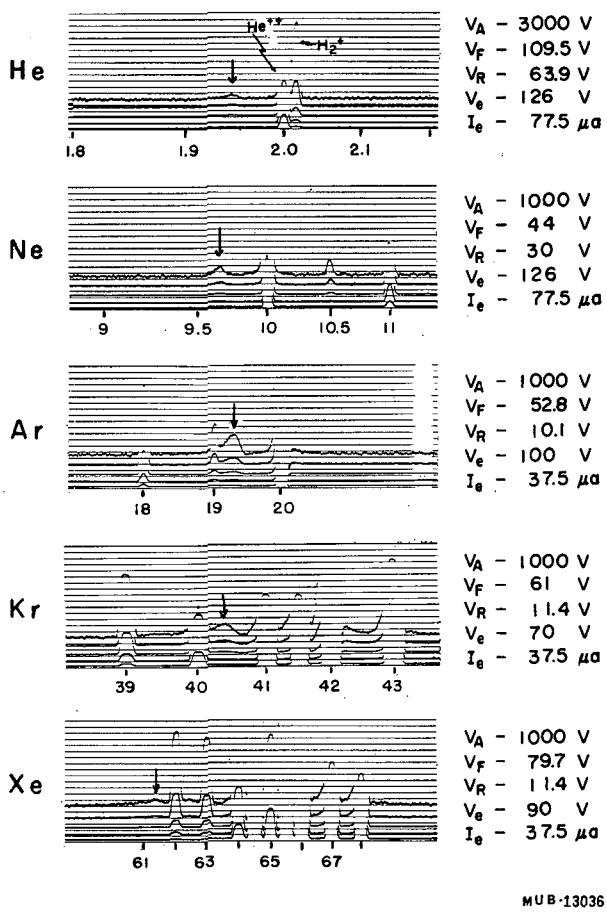

Fig. F.3-2. Quasi-metastable peaks in the mass spectra of the noble gases arising from surface-induced transitions of the type $X^{+*} \xrightarrow{S} X^{++} + e^-$. Surface for peaks marked is the Isatron focus slit. Marked peaks in Kr and Xe are from the isotopes ^{84}Kr and ^{129}Xe respectively.

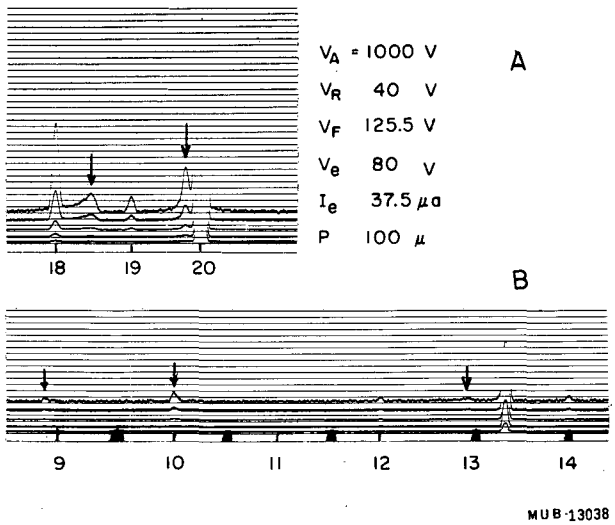

Fig. F.3-3. Quasi-metastable peaks in Ar from surface-induced transitions.
(A) $(M/q)^* = 18.46$ from $Ar^{+*} \xrightarrow{S_F} Ar^{++} + e^-$,
$(M/q)^* = 19.78$ from $Ar^{++} \xrightarrow{S_1} Ar^{++} + e^-$.
(B) Voltage scan, MV= 11 310, $V_F = 0.075$ V_A, $V_R = 0.0115\ V_A$, $V_e = 100$ V, Ie = 37.5 μA, P = 400 μ inlet pressure:
$(M/q)^* = 10.00$ from $Ar^{+*} \xrightarrow{S_2} Ar^{++} + e^-$,
$(M/q)^* = 8.90$ from $Ar^{+++*} \xrightarrow{S_2} Ar^{+++} + e^-$,
$(M/q)^* = 12.90$ from $Ar^{+++*} \xrightarrow{S_F} Ar^{+++} + e^-$.

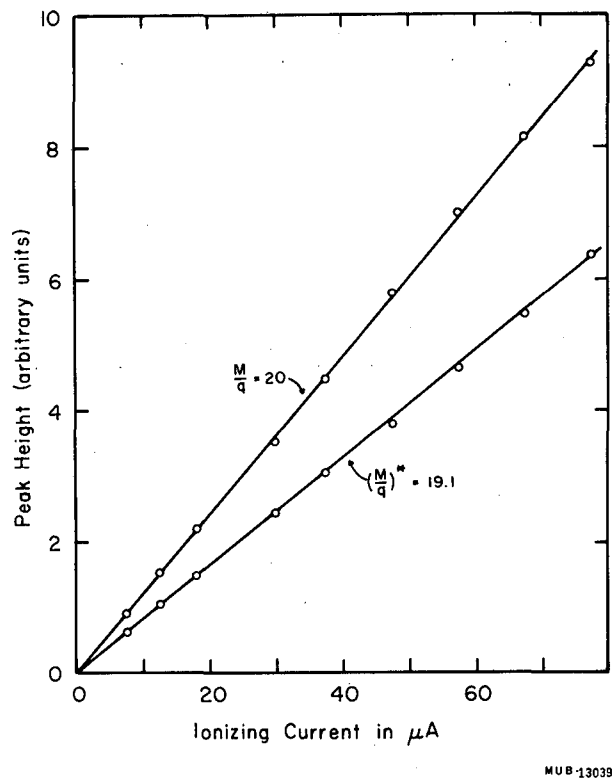

Fig. F.3-4. Linearity of M/q = 20 and $(M/q)^* = 19.1$ peaks in Ar with ionizing current.

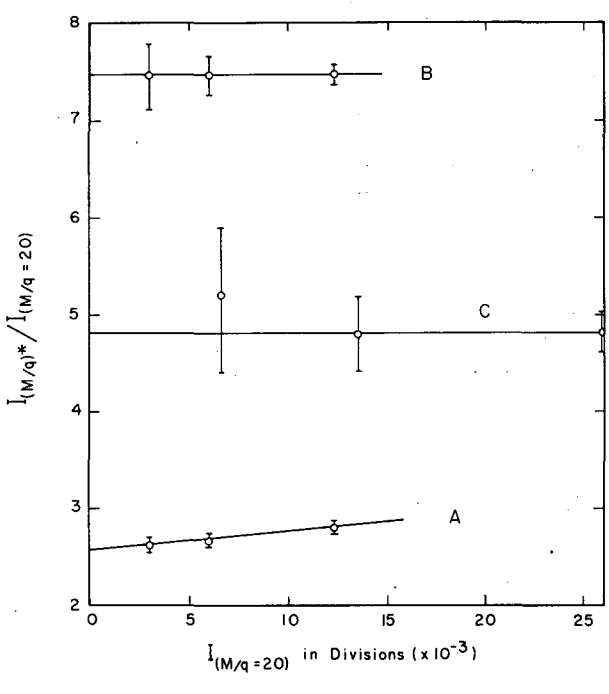

Fig. F.3-5. Linearity of quasi-metastable peaks in Ar with pressure.
(A) Peak arising at Isatron first slit: ratio $\times 10^3$,
(B) Peak arising at Isatron focus slit: ratio $\times 10^4$,
(C) $(M/q)^* = 10$ peak: ratio $\times 10^5$.

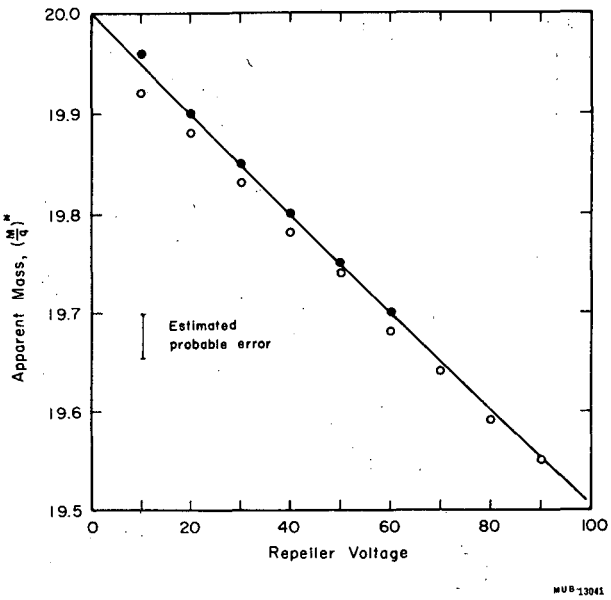

Fig. F.3-6. Variation with repeller voltage of apparent mass of quasi-metastable peak from collision of Ar^{+*} with Isatron first slit. Line is calculated from Eq. 2, V_A = 1000 V, open circles–focus voltage = 125.5 V, solid points--focus voltage = 37.5 V.

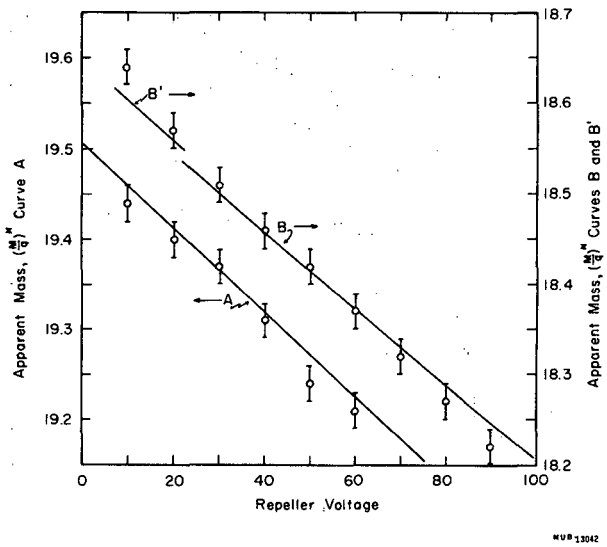

Fig. F.3-7. Variation with repeller voltage of apparent mass of quasi-metastable peak from collision of Ar^{+*} with Isatron focus slit. Lines are calculated from Eq. 2 corrected by factor for angle of emergence. V_A = 1000 V; Curve A - V_F = 37.5 V, Curve B - V_F = 125.5 V, Curve B' - V_F = 124 V.

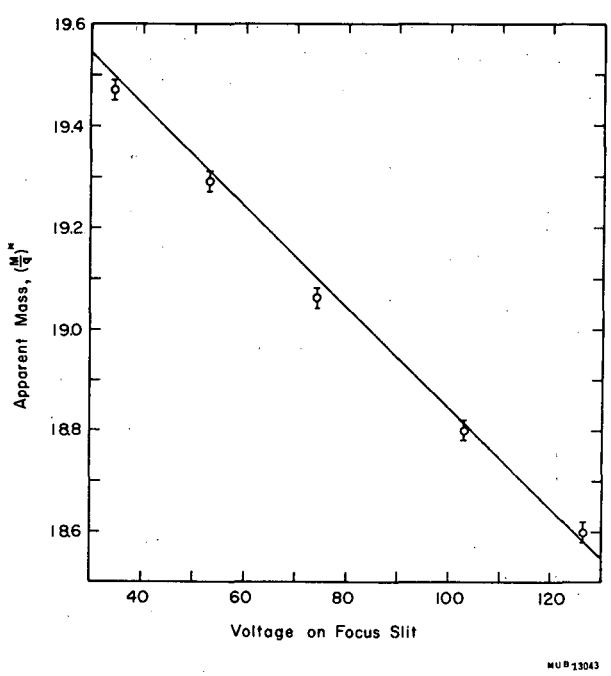

Fig. F.3-8. Variation with voltage on focus slit of apparent mass of quasi-metastable peak from collision of Ar^{+*} with Isatron focus slit. Line is calculated from Eq. 2 corrected for angle of emergence. V_A = 1000 V, V_R = 10 V.

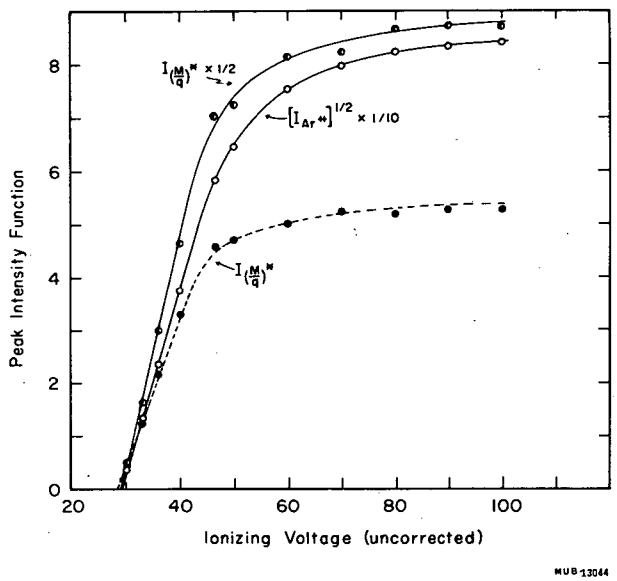

Fig. F.3-9. Appearance potential curves of Ar^{++} (open circles), and the quasi-metastable peaks from Ar^{+*} induced at the Isatron first slit (half solid points) and the Isatron focus slit (solid points), respectively. V_A = 2300 V, V_R = 27 V, V_F = 184 V, Ie = 37.5μA, P = 100 μ inlet pressure.

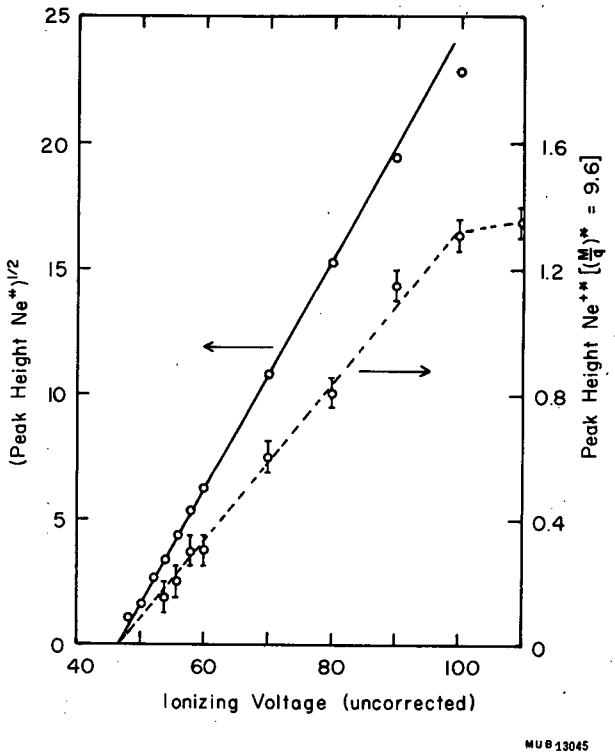

Fig. F.3-10. Appearance potential curves of Ne^{++} and quasi-metastable peak from collision of Ne^{+*} with Isatron focus slit $[(M/q)^* = 9.61]$. V_R = 30 V, V_A = 1000 V, V_F = 44.5 V.

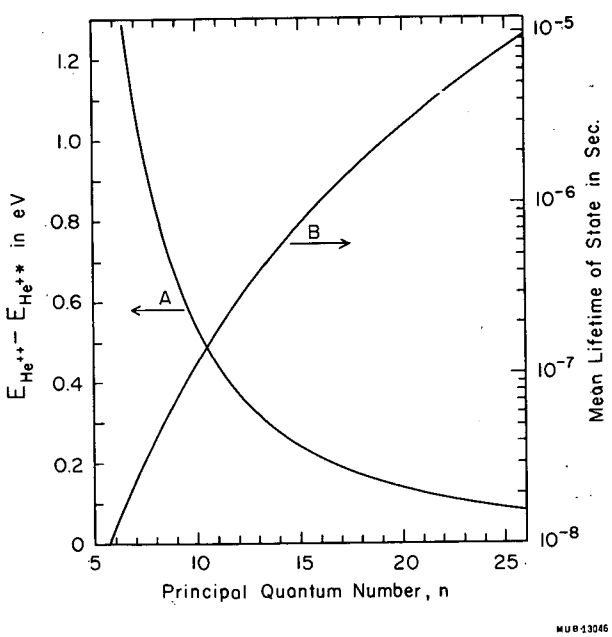

Fig. F.3-11. Curve A--Difference in energy of higher Rydberg levels of He^+ and the ionization potential of He^{++}. Curve B--mean lifetime of these levels for radiative transitions to lower levels.

G. CHEMISTRY

1. SOME CHEMICAL PROPERTIES OF ELEMENT 97

J. R. Peterson and B. B. Cunningham

As part of a continuing program at this Laboratory to investigate the chemical and physical properties of the heavy actinide elements and their compounds, a study of element 97 has been undertaken.

To date these investigations include a study of the solution absorption spectroscopy of the tripositive berkelium ion, an attempt to observe the solution absorption spectrum of the tetrapositive berkelium ion, the preparation of samples of BkO_2, Bk_2O_3, $BkCl_3$, BkOCl, and BkF_3, and the crystallographic characterization of the above compounds.

The most successful absorption experiments were carried out by using a newly-developed microabsorption cell,[1] consisting essentially of two small (100μ diam) quartz rods between which is placed a small volume (2 to 3 nl) of berkelium (4 μg) solution. The loaded cell is placed in a light-condensing apparatus which serves to focus the Cary Model 14 Spectrophotometer light beam onto the "entrance" quartz rod. An example of a typical spectrum observed is shown in Fig. G.1-1. The two main peaks at 474 and 417mμ have been noted. A final line list will be reported following additional experiments to improve transmission in the uv region and after subjecting the observed spectra to computer analysis.[2] The results of this work are in excellent agreement with similar experiments carried out by LRL-Livermore workers.[3]

An attempt was made to observe the Bk^{4+} solution absorption spectrum by electrolytically oxidizing the Bk^{3+} solution while loaded on the cell. A microsalt bridge was installed as was a 1-mil Pt anode wire. Several microamperes of current were passed through the cell while the visible region was continuously scanned, but no decrease in the Bk^{3+} absorption peaks or growth of peaks attributable to the +4 state was observed. Since the same experimental procedure had worked very well with comparable amounts of cerium, it was concluded that our failure resulted from the bulk berkelium solution's acting as a reducing medium upon the Bk^{4+} ions formed locally around the Pt anode.

About 16 μg of ^{249}Bk were recovered and purified by extraction from an aqueous nitrate solution with di-(2-ethylhexyl) orthophosphoric acid (HDEHP) followed by stripping of the organic phase with a solution of H_2O_2 in HNO_3. The aqueous berkelium solution was then subjected to further purification by the standard ion-exchange techniques so important in actinide chemistry.

A sample of the purified material was submitted for the determination by mass analysis of the total cerium and neodymium content. The results indicated 0.27 atom % total cerium and 0.063 atom % total neodymium.

This purified material was sorbed on specially washed sulfonic acid ion-exchange resin beads of approximately 200 ngram capacity each.

The technique described by Green[4] was employed for the preparation of the various compounds of berkelium. A summary of the preparation conditions is given in the flow diagram of Fig. G.1-2. Several independent samples of these berkelium compounds were characterized by use of x-ray powder techniques. All samples contained ≥95 atom % ^{249}Bk.

A list of the crystallographic properties of the dioxide, sesquioxide, trichloride, and oxychloride is given in Table G.1-I. These results represent only one sample of each type of compound, since complete analysis of all x-ray powder patterns is not yet done.

The berkelium-fluorine system seems to follow what is predicted by analogy with the lanthanide of corresponding radius (i.e., Pm). Preliminary results indicate that BkF_3 exhibits two stable modifications: the high-temperature trigonal LaF_3 type, characteristic of the light lanthanides La to Nd, and the orthorhombic YF_3 type, characteristic of the lanthanides Sm to Lu.

Complete verification will have to wait until the x-ray powder patterns are fully analyzed and their data interpreted. Further work will be geared to the preparation of BkF_4 and to the complete elucidation of the berkelium trifluoride system.

The results obtained so far provide important evidence for the continuing rare-earth-like character of the actinide elements beyond the point of the half-filled 5f subshell.

References

1. B. B. Cunningham, T. Parsons, and J. R. Peterson, (LRL), unpublished results.
2. J. T. Bell and R. E. Biggers, J. Mol. Spectroscopy 18[3], 247-75 (1965).
3. R. G. Gutmacher et al., The Absorption Spectra of Bk^{3+} and Bk^{4+} in Solution, submitted to J. Inorg. Nucl. Chem.
4. J. L. Green (Ph. D. Thesis), UCRL-16576, Nov. 1965.

Table G.1-I. Crystallographic properties of some berkelium compounds.

Compound	Sample number	Film number	Structure type	Lattice constants[a] (Å)
BkO_2	JRP-VIII	2560A	CaF_2-type fcc	a_0 = 5.334±0.001
Bk_2O_3	JRP-XV	2590A	Mn_2O_3-type bcc	a_0 =10.885±0.001
$BkCl_3$	JRP-XIV	2587A	UCl_3-type hexagonal	a_0 = 7.381±0.001 c_0 = 4.126±0.001
BkOCl	JRP-XX	2612A	PbFCl-type tetragonal	a_0 = 3.966±0.001 c_0 = 6.705±0.003

a. The error limits represent the 95% confidence level reflecting only the internal consistency of the data of this particular preparation.

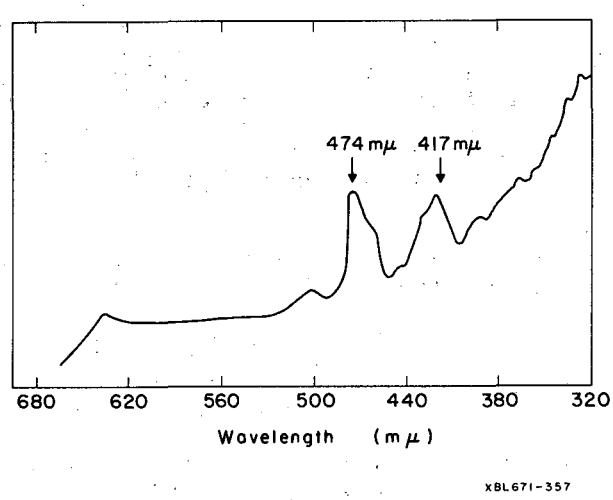

Fig. G.1-1. Absorption spectrum of Bk^{3+} in HCl solution.

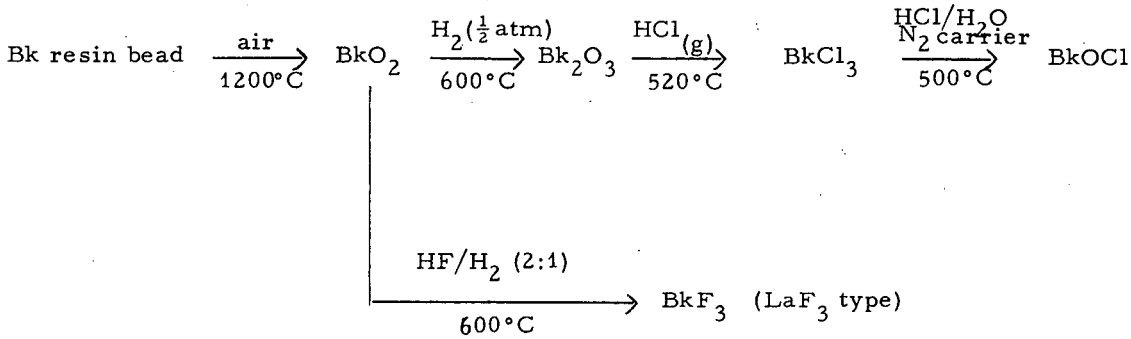

Fig. G.1-2. Flow diagram for preparation of a series of Bk compounds. The reaction with HF/H_2 was carried out in an all-Monel reaction line with a Pt rod to hold the Bk sample.

2. CHEMICAL EFFECTS ON CORE ELECTRON BINDING ENERGIES IN IODINE AND EUROPIUM†

C. S. Fadley, S. B. M. Hagstrom,* J. M. Hollander,
D. A. Shirley, and M. P. Klein

Within the last five years, an electron spectroscopic technique has been developed for the measurement of core electron binding energies.[1] The precision of this technique is sufficiently high to detect the small shifts in binding energy (of the order of 1 eV) associated with changes in the chemical environment of a given atom.[2]

We have modified the Berkeley iron-free β spectrometer to be used for such chemical-shift measurements. The experimental setup is shown in Fig. G.2-1. A nonmagnetic x-ray tube and source house are fastened in the source location on the spectrometer. Radiation from the tube is directed upon a thin flat source of the compound under investigation. The photoelectrons expelled from the source are analyzed for kinetic energy in the usual way by stepping the spectrometer current. By changing anodes in the x-ray tube the characteristic x radiation of either copper or chromium could be obtained. No attempt was made to filter the radiation, but background is very low at or near the energy of the $K\alpha_1$ and $K\alpha_2$ x rays, so these served as "monochromatic" radiation. Also the separation of these x rays is large enough (9 eV for Cr and 20 eV for Cu) that photoelectron lines from the two can be easily distinguished. Typical photoelectron lines from various compounds are shown in Fig. G.2-2 and G.2-3. The notation Eu $3d_{5/2}$ ($CrK\alpha_2$) Eu^{3+} indicates a photoelectron line due to electrons expelled from the $3d_{5/2}$ level of Eu by $CrK\alpha_2$ radiation and with the Eu in a compound where its oxidation state is +3. We also indicate just the compound in the last position as in Fig. G.2-3. Photoelectron kinetic energy increases to the right in both figures.

The method used to deduce binding energies from measurements of photoelectron kinetic energies is indicated by the energy diagram of Fig. G.2-4. Since source and spectrometer are electrically connected and presumably at chemical equilibrium, their Fermi levels coincide and the binding energy of the jth level of an atom in compound X is given by

$$E_b(j, X) = h\nu - E_{kin} - \phi_{sp}, \qquad (1)$$

where $h\nu$ is the x-ray energy, E_{kin} is the photoelectron kinetic energy and ϕ_{sp} is the work function of the spectrometer material (3.7 eV).

With the foregoing technique, we have measured chemical shifts in core electron binding energies for iodine in KI (-1 oxidation state), KIO_3 (+5), and KIO_4 (+7), and also for europium in $EuAl_2$ (+2 oxidation state) and Eu_2O_3 (+3). Such shifts are clearly visible in Fig. G.2-2 and G.2-3.

Figure G.2-2 shows spectra of a sample of Eu metal taken at two different stages of oxidation from the +2 to the +3 state, and compares these with a spectrum from pure Eu_2O_3. The shift of the $3d_{5/2}$ level of europium between $EuAl_2$ and Eu_2O_3 was found to be 9.6 eV. Figure G.2-3 shows spectra from the compounds KI and KIO_4. Within the accuracy of our measurements (±0.3 eV) all core levels in iodine are shifted by the same amount. The average core shifts relative to KI were 5.3 eV for KIO_3 and 6.3 eV for KIO_4. All the shifts found are in the direction predicted by a simple electrostatic picture. That is, electrons are bound more tightly in higher oxidation states. We also note that the shift per unit change in oxidation number is about 12 times as large in Eu as in I.

We have also made theoretical estimates of these chemical shifts in order to explain the trends and magnitudes observed. For solids with partial or total ionic character, the energy cycle of Fig. G.2-5 can be used to calculate binding energies. This cycle is a generalization of one used on valence electrons in the alkali halides.[3] Atom A in compound X is assumed to have some net charge z_x. It is removed from the lattice to form the ion A^{z_x}; the energy required is E_1. An electron is removed from the jth level of this free ion; the energy required is $E_b(j, z_x)$. Then the ion $A^{z_x 1+}$ is reinserted into the lattice, the energy requirement being E_2. Thus the binding energy of an electron in the solid is

$$E_b(j, X) = E_b(j, z_x) + E_1 + E_2, \tag{2}$$

We have calculated $E_b(j, z_x)$ with a Hartree-Fock computer program developed by Roothaan and Bagus.[4] Interpolation permitted determination of $E_b(j, z_x)$ for nonintegral z_x. The sum $(E_1 + E_2)$ is just the interaction energy of an electron in the ion of interest with all the other ions in the lattice. It can be calculated by means of Madelung sums. The chemical shift between two compounds X and Y is thus

$$\Delta E_b(j, X\text{-}Y) = E_b(j, z_x) - E_b(j, z_y) + \Delta(E_1 + E_2). \tag{3}$$

Note that $\Delta(E_1 + E_2)$ does not change with j, so that any change in $\Delta E_b(j, X\text{-}Y)$ with j must come from the two free ion terms.

Free-ion calculations on iodine in the charge range -1 to +3 showed that all core levels are shifted by the same amount (to within ± 1.5%) when a 5s or 5p electron is removed. In light of Eq. 3, this explains why all core-level chemical shifts are the same.

Calculations of $(E_1 + E_2)$ were made for all the iodine compounds. Potassium was assumed to exist as K^{1+} in all three compounds. Iodine was taken to be I^{1-} in KI, but its charge was left as a parameter in KIO_3 and KIO_4. The charge on oxygen could then be determined by invoking electrical neutrality. With the aid of previously calculated Madelung constants,[5-7] it was thus possible to calculate chemical shifts as a function of the fractional ionic character of the I-O bonds in KIO_3 and KIO_4. These results are shown in Fig. G.2-6, where they are compared with our experimental values. The experimental values correspond to the fractional ionic characters given in Table G.2-I, where we also present analogous results obtained from Mössbauer measurements.[8] The agreement is reasonably good, especially in view of some approximations made in making our Madelung calculations. Improvements in the method of making these calculations should permit much more accurate estimates of fractional ionic character solely on the basis of chemical-shift measurements.

The much larger shift per unit change in oxidation number for europium is due primarily to the larger actual charge transfer taking place in going from Eu^{2+} in $EuAl_2$ to Eu^{3+} in Eu_2O_3, which almost certainly have the electronic configurations $4f^7$ and $4f^6$, respectively. The corresponding 5p transfer in going from KIO_3 to KIO_4 is probably less than 0.4 by comparison, as can be seen from Table G.2-I.

The crystal structures of $EuAl_2$ and Eu_2O_3 are too complicated to allow a simple calculation of the Madelung sums. However, approximate estimates were made by treating the bonding process as a removal of valence electrons to a spherical shell of classical charge at radius r. Combining Hartree-Fock calculations with the repulsion due to the classical shell thus permitted a calculation of chemical shifts as a function of r. The r value required for a 9.6-eV shift was very close to the nearest-neighbor distance in both $EuAl_2$ and Eu_2O_3, thereby justifying our use of this simple model. This model also explains qualitatively why chemical shifts are always much less than predicted directly from free-ion calculations. That is, bonding electrons are not removed to infinity, as implied for the free ion, but only to a distance on the order of the nearest-neighbor separation, where they can still shield core electrons to some degree.

We have also considered in some detail the reference levels used for binding energies. Figure G.2-3 shows that experimental binding energies are referred to the Fermi level, whereas our theoretical values are referred to the vacuum level. This introduces a small uncertainty (≈1 eV) when experimental and theoretical results are directly compared, as in Fig. G.2-6. We are currently trying to develop an experimental technique which will eliminate this source of uncertainty.

The electron spectroscopic technique thus seems capable of giving very meaningful information on chemical bonding, and application of this technique to a broad range of compounds from metals to biological molecules seems possible.

Footnotes and References

†To be written up (as UCRL-17005) and submitted to J. Chem. Phys.

*Present address: Department of Physics, Chalmers Institute of Technology, Gothenburg, Sweden.

1. S. Hagstrom, C. Norling, and K. Siegbahn, Table of Electron Binding Energies in Alpha-, Beta-, and Gamma-Ray Spectroscopy, Ed. K. Siegbahn (North Holland Publishing Co., Amsterdam, 1965).
2. C. Nordling, S. Hagstrom, and K. Siegbahn, Z. Physik 178, 433 (1964).
3. N. F. Mott and R. W. Gurney, Electronic Processes in Ionic Crystals (Clarendon Press, Oxford, 1940), 1st Ed., p. 80.
4. C. C. J. Roothaan and P. Bagus, Methods in Computational Physics (Academic Press, New York, 1963), Vol. 2.
5. D. H. Templeton, J. Chem. Phys. 34, 2004 (1961).
6. F. G. Fumi and M. P. Tosi, J. Chem. Phys. 33, 1 (1960).
7. Y. Sakamoto, J. Chem. Phys. 28, 164 (1958).
8. D. W. Hafemeister, G. de Pasquali, and H. de Waard, Phys. Rev. 135, B1089 (1964).

Table G.2-I. Comparison of present results for fractional ionic character and iodine charge in KIO_3 and KIO_4 with those obtained from Mössbauer measurements in Ref. 8.

Compound	Fractional ionic character	Charge on iodine
Present work:		
KIO_3	0.67	2.99
KIO_4	0.48	2.86
Mössbauer:		
KIO_3	0.31	0.83
KIO_4	0.31	1.44

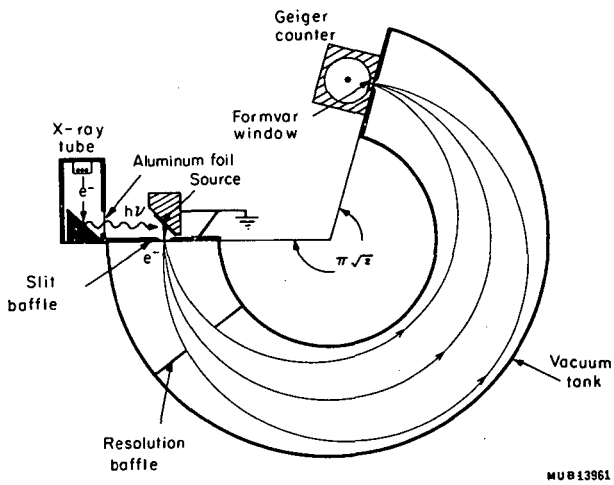

Fig. G.2-1. Schematic illustration of experimental setup.

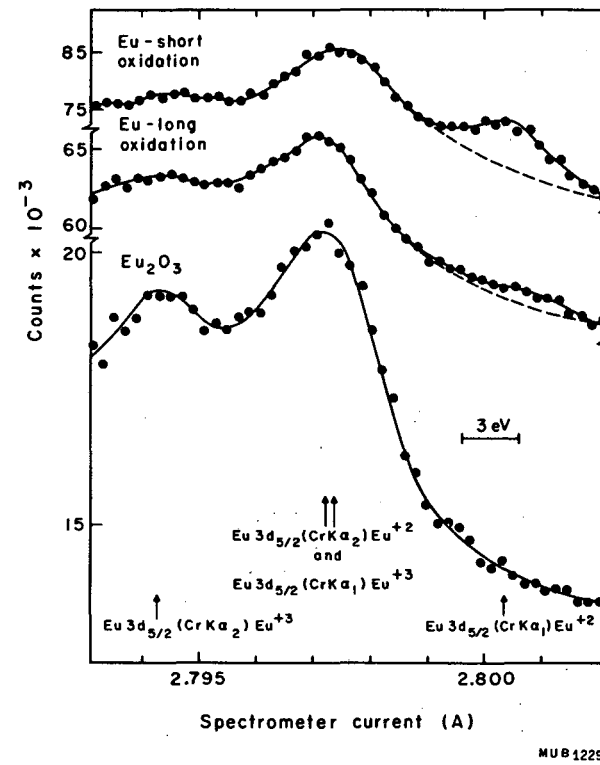

Fig. G.2-2. Photoelectron peaks from the Eu $3d_{5/2}$ level in Eu metal and in Eu_2O_3. An Eu sample was first examined with minimal oxidation and then again after prolonged exposure to air. The sources of the three peaks are noted at the bottom of the figure.

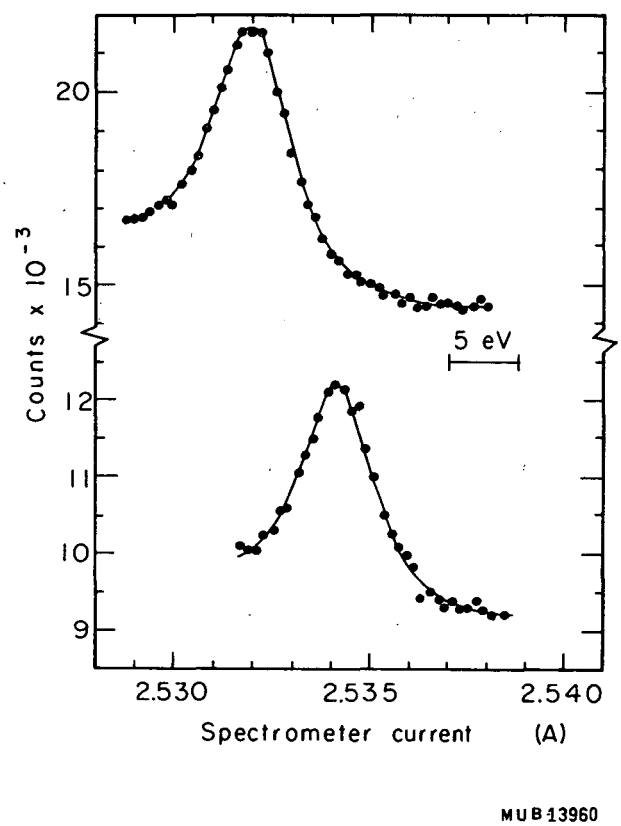

Fig. G.2-3. Photoelectron peaks from (upper) I $2p_{3/2}$(CuKα$_1$)KIO_4 and (lower) I $2p_{3/2}$ (Cu Kα$_1$) KI.

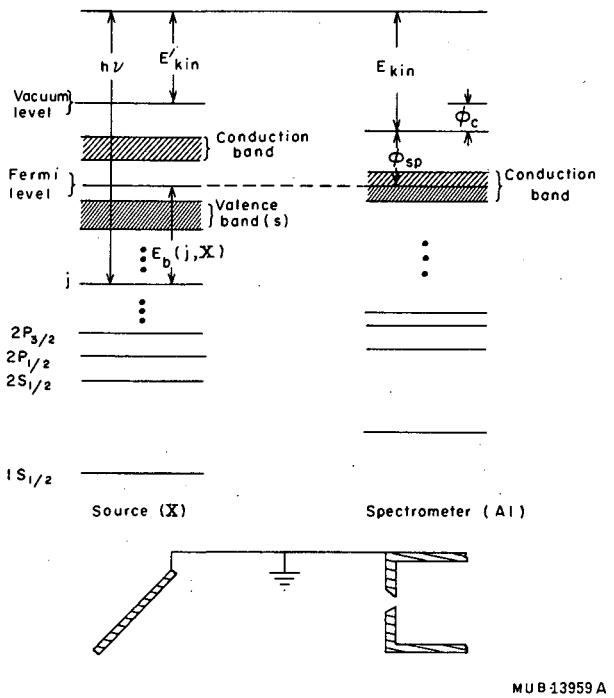

Fig. G.2-4. Energy diagram for the photoelectric process in a semiconducting or insulating source (a solid compound X). The photoemission is from some arbitrary core level j of an atom in X.

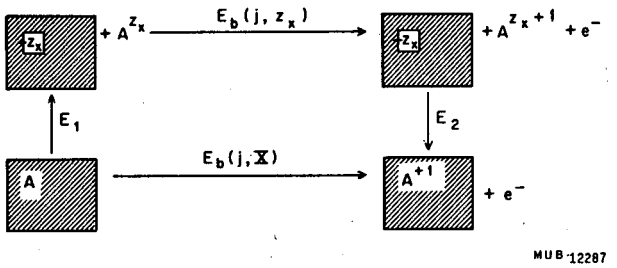

Fig. G.2-5. Energy cycle for calculating the binding energy of core electron j in atom A of the solid compound X.

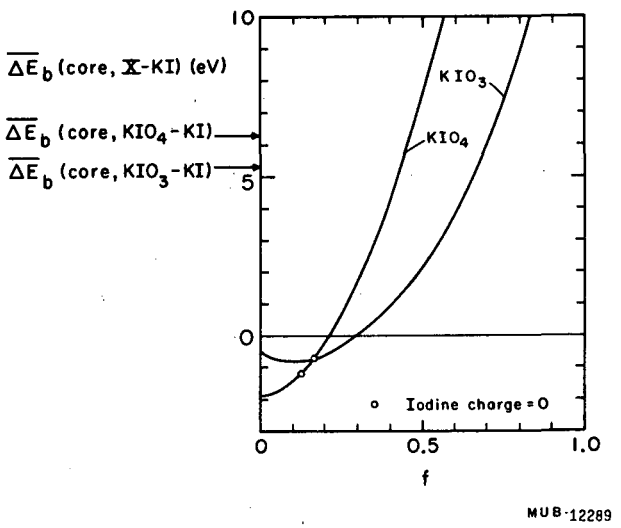

Fig. G.2-6. Calculated and experimental chemical shifts for iodine core levels in KIO_3 and KIO_4. KI is used as a reference compound. Also shown are the points on the curves at which the charge on the iodine atom is zero.

3. EXTRACTION OF METAL PYRIDINE AZIDES†

Spectrophotometric Determination of Copper, Nickel, and Palladium

Ray G. Clem and E. H. Huffman

Azide and thiocyanate ions are isoelectronic, and so it was considered to be of some interest to investigate pyridine-azide solutions as reagents for the extraction and spectrophotometric determination of transition metals, since pyridine-thiocyanate reagents had been used for this purpose.[1,2] The efficiencies of extraction into chloroform found for the pyridine azide complexes of eleven metals are given in Table G.3-I. The concentrations of pyridine and azide were 1.2 M and 0.200 M, respectively, and the initial volumes of chloroform and aqueous solution were 10 ml each. Equilibrium was attained in 30 seconds in all cases except for platinum, which required repeated shaking over a period of one half hour to finally clear the turbidity which gradually reappeared in the aqueous layer.

The details of color development were studied for only copper, nickel, and palladium, those elements for which analytical methods were developed. Spectral scans for these are shown in Fig. G.3-1. To study the effect of pH on absorbance, pyridine and azide were held at 1.12 M and 0.200 M, respectively, concentrations found sufficient to give optimum color development for all three metals. The absorbances of the organic phases after equilibrium for 30 sec are shown in Figs. G.3-2, G.3-3, and G.3-4. The absorptivity for copper in the 30- to 100-μg range is 0.0697 ± 0.0005 ppm^{-1} cm^{-1}; for nickel in the 50- to 200-μg range it is 0.0355 ± 0.0010, and for palladium in the 20- to 80-μg range it is 0.0913 ± 0.0010. The expected errors of determination for these ranges are 0.8%, 2.8%, and 1.1%, based upon the standard deviations of the absorptivities. These absorptivities are for the pH ranges from 5 to 7 for copper, from 8.5 to 11 for nickel, and from 4.57 to 4.77 for palladium, measured at 435 mμ, 320 mμ, and 325 mμ, respectively.

A spectral scan of an aqueous solution containing 1×10^{-4} M Cu^{+2} and 0.2 M N_3^- has the same shape, with maximum absorbance at 385 mμ, as has the scan of a solution which is also 1.1 M in pyridine. It thus appears that no pyridine-containing complex is present in the aqueous phase, though pyridine is necessary for the extraction of copper. A mole ratio plot using 1×10^{-3} M Cu^{+2}, with the absorbance peak at 370 mμ, shows a 1:4 copper to azide species in the presence of 4.46×10^{-2} M pyridine. Saini and Ostacoli[3] found the same ratio in a mixture of 2-ethoxyethanol and water, but containing no pyridine.

Footnotes and References

†Brief version of Anal. Chem. 38, 926 (1966).

1. G. H. Ayres and S. S. Baird, Talanta 7, 237 (1961).
2. J. H. W. Forsythe, R. J. Magee, and C. L. Wilson, Talanta 1, 249 (1958).
3. G. Saini and G. Ostacoli, J. Inorg. Nucl. Chem. 8, 346 (1958).

Table G. 3-I. Percentage extraction of various ions into chloroform as metal pyridine azides.

pH	% Extraction												$V_{aq}:V_{org}$
	Mn^a	Fe^{3+}	Co^a	Ni^{2+}	Cu^{2+}	Zn^{2+}	Pd^{2+}	Cd^{2+}	Pt^{4+}	Au^{3+}	UO_2^{2+}	N_3^-	
2	0.0	0.0	0.2	<0.1	<0.1	0.0	98.8	0.0	79.9	92.0	<0.1	47	9.5:10.5
3	0.0	0.0	0.4	0.1	1.8	0.0	98.9	0.0	92.4	98.2	<0.1	41	9.5:10.5
4	0.0	0.6	0.8	0.3	72.8	0.0	98.9	0.8	95.5	98.4	<0.1	37	9.4:10.6
5	0.0	50.0	2.5	51.6	98.1	2.9	99.4	7.4	94.6	98.9	<0.1	25	9.2:10.8
6	<0.1	ppt.	84.0	98.7	99.4	73.2	99.7	85.0	85.9	98.9	1.1	19	8.8:11.2
7	0.1	---	95.0	99.9	99.5	93.3	99.8	91.4	75.6	98.9	ppt.	2	8.7:11.3
8	0.2	---	95.7	>99.9	99.6	93.7	99.8	91.6	72.3	98.6	---	0.3	8.6:11.4
9	0.2	---	95.4	>99.9	99.8	ppt.	99.8	90.2	70.9	98.3	---	0.0	8.6:11.4
10	ppt.	---	ppt.	99.6	98.2	---	98.9	89.1	70.1	98.0	---	0.0	8.6:11.4
11	---	---	---	99.5	ppt.	---	97.6	ppt.	68.7	97.6	---	0.0	8.6:11.4
mg/10 ml	10.64	2.00	5.00	4.67	2.03	10.00	4.00	4.00	2.79	5.00	10.00 as U	84.0	

a. Oxidation state may be 2+ or higher, depending on pH and air oxidation.

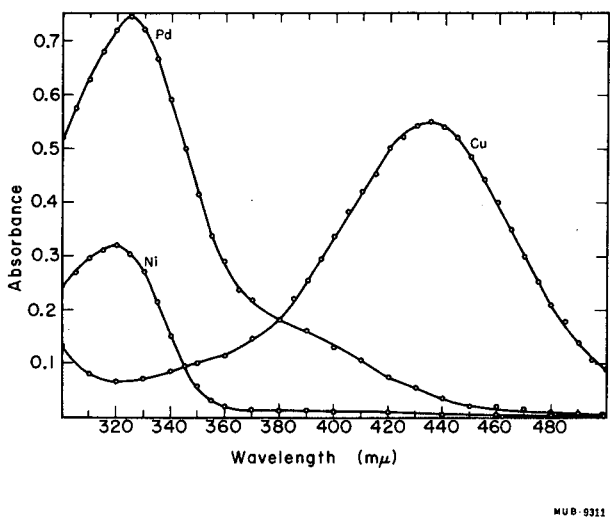

Fig. G.3-1. Absorption spectra of chloroform extracts. Aqueous phase: 0.2 M azide; 1.1 M pyridine; 70 μg Cu^{++}, 90 μg Ni^{++}, or 82 μg Pd^{++} per 10 ml. Readings vs extracts of blanks containing all reagents.

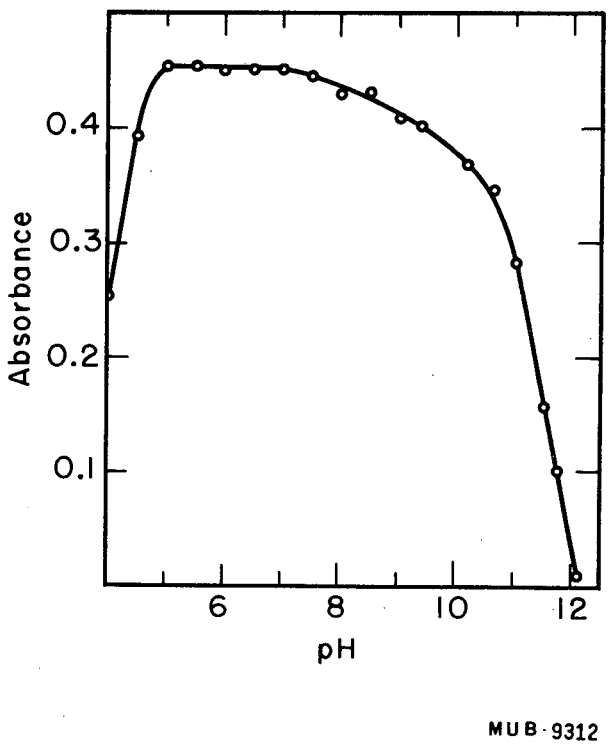

Fig. G. 3-2. Effect of pH on color development for copper at 435 mμ.

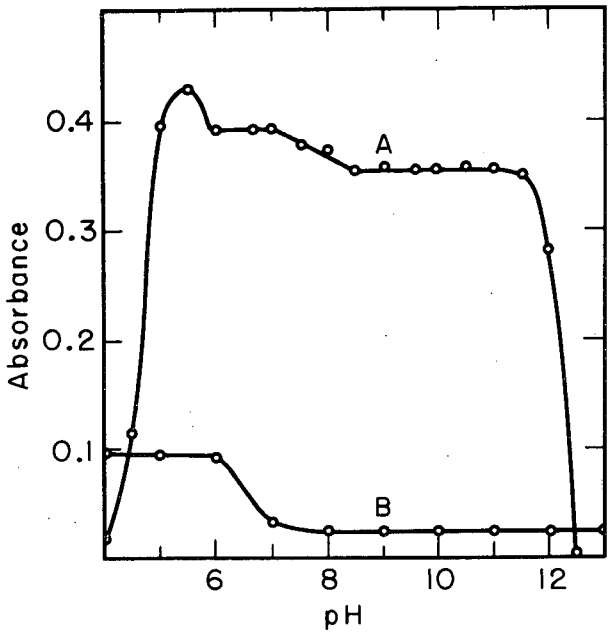

MUB-9313

Fig. G.3-3. Effect of pH on color development for nickel at 320 mμ. (A) nickel extract vs blank extract, (B) blank extract vs chloroform.

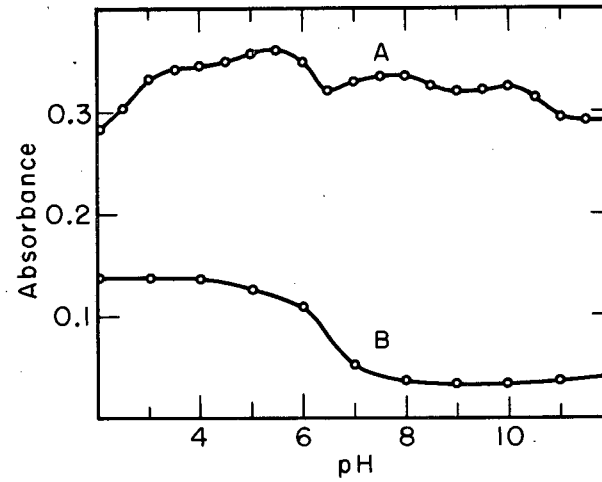

MUB-9314

Fig. G.3-4. Effect of pH on color development for palladium at 325 mμ. (A) palladium extract vs blank extract, (B) blank extract vs chloroform.

4. ISOTOPIC OXYGEN ANALYSIS BY ^{3}He ACTIVATION: EXCITATION FUNCTION FOR THE REACTION ^{18}O(^{3}He, p)^{20}F †*

J. F. Lamb, D. M. Lee, and S. S. Markowitz

Charged-particle activation analysis by ^{3}He bombardment provides a rapid, sensitive method for quantitative determination of oxygen. Markowitz and Mahony[1] have measured the excitation function for the total production of ^{18}F from ^{16}O by the reaction ^{16}O(^{3}He, p)^{18}F and by the reaction ^{16}O(^{3}He, n)^{18}Ne followed by the β^+ decay of the 1.5-sec ^{18}Ne to ^{18}F. Analyses for ^{16}O in several materials are also given.

It is often of interest to determine the ratio of ^{16}O to ^{18}O in a sample as well as the total oxygen content. This is most frequently performed by mass spectrometric analysis, which usually involves considerable chemical preparation. Activation-analysis methods, where applicable, preclude much of this prior treatment, thus saving time and involving less risk of contaminating or destroying valuable samples.

Samples* of three chemical compositions with varying atom % ^{18}O enrichment have been analyzed for % ^{18}O; these are KH_2PO_4, glycine, and Ta_2O_5. The Ta_2O_5 samples were prepared as described by Lamb, Lee, and Markowitz.[2] The KH_2PO_4 and glycine samples were finely ground and allowed to settle from a benzene suspension onto a platinum disk. The powder film was dried and fixed with 0.1 ml of a 0.1% solution of polystyrene in ethylene dichloride. The samples were then covered with platinum foils. Identical blanks were also prepared for background correction. These samples were bombarded for 10 sec with a ^{3}He beam at the Hilac. A rapid recovery system allowed counting to begin within 2 sec after bombardment. Counting was performed with NaI(Tl) scintillation detectors coupled with a 400-channel pulse-height analyzer. Immediately

following each bombardment the 10.7-sec ^{20}F activity produced from the $^{18}O(^{3}He, p)^{20}F$ reaction was determined by following the decay of the 1.63-MeV γ-ray photopeak. After a few hours' cooling, the ^{16}O was determined by following the 511-keV annihilation radiation from β^{+} decay of 110-min ^{18}F.

The excitation function for the reaction $^{18}O(^{3}He, p)^{20}F$ was measured by bombarding ^{18}O-enriched Ta_2O_5, using various aluminum absorbers to degrade the beam energy. This function is shown in Fig. G. 4-1. Figure G.4-2 is a typical spectrum showing both the 511-keV photopeak from ^{18}F and the 1.63-MeV photopeak from ^{20}F.

The analytical data shown in Table G.4-I were obtained by using an entrance ^{3}He beam energy of 10 MeV. The available beam intensity through 0.25-in. collimators was approximately 200 nA. Percent ^{18}O was determined by the comparator method, using a known standard. Counting efficiency was identical for all samples. Calculations yielded an ^{16}O: ^{18}O ratio for each bombardment so that the % ^{18}O found is independent of variations in beam intensity and sample weight. The thicknesses of the samples were sufficiently small that the reaction cross sections varied by only a few per cent as the beam traversed the sample. Errors shown in Table G.4-I represent maximum deviation from the average within triplicate analyses.

The detection limit for ^{18}O analysis by ^{3}He activation is only a few parts per thousand when the Hilac accelerated beam is used. Since the ^{3}He cyclotron now nearing completion will yield beam intensities of several μA, and since the radiation background near the cyclotron will be much less at the end of bombardment than that near the Hilac, no effort has been made to attain ultimate analytical sensitivity.

Footnotes and References

† Presented at American Chemical Society, Society for Applied Spectroscopy Joint Symposium, on Detection of Light Elements, San Francisco, Oct. 19, 1966.

*The ^{18}O-enriched samples were obtained from the Weizmann Institute of Science, Rehovoth, Israel. Values of % ^{18}O quoted are approximate values only, and are presently being checked by mass spectrometric analysis where possible.

1. S. S. Markowitz and J. D. Mahony, Anal. Chem. 34, 329 (1962).
2. J. F. Lamb, D. M. Lee, and S. S. Markowitz, Paper G.5, this report.

Table G.4-I. Results of isotopic oxygen analysis.

Sample	^{18}O found (%)	^{18}O quoted (%)
KH_2PO_4	45.7 ± 1.6	40
KH_2PO_4	7.9 ± 0.4	8.7
KH_2PO_4	2.0 ± 0.1	1.6
Glycine	12.0 ± 1.6	10
Ta_2O_5	46.8 ± 0.2	---
Ta_2O_5	3.5 ± 0.2	3.3
Ta_2O_5	0.2 ± 0.04	0.2
Ta_2O_5	10[a]	10

a. 10% ^{18}O water used as a standard.

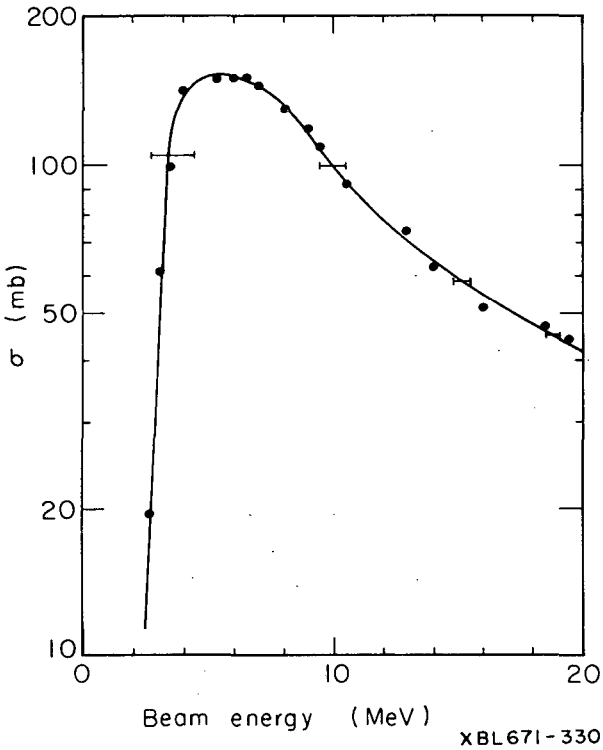

Fig. G.4-1. Excitation function for the reaction $^{18}O(^{3}He, p)^{20}F$.

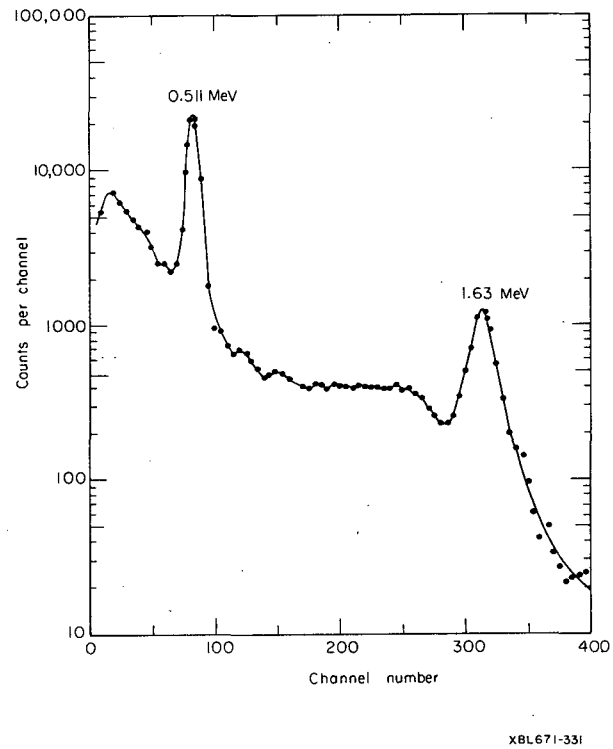

Fig. G.4-2. Gamma-ray spectrum of ^{18}F and ^{20}F produced by bombardment of ^{18}O-enriched Ta_2O_5 target. ^{3}He energy = 10 MeV.

5. PREPARATION OF OXYGEN STANDARDS FOR CHARGED-PARTICLE ACTIVATION ANALYSIS

J. F. Lamb, D. M. Lee, and S. S. Markowitz

A method has been developed for the preparation of relatively thick oxygen targets by anodic oxidation of tantalum metal foils. Theory and techniques for the formation of thin Ta_2O_5 films are discussed by Young;[1] the use of such films as standards for determination of oxide thickness by proton bombardment is described by Thompson.[2] The tantalum oxide film is particularly useful for ^{3}He activation analysis, since there are no interfering reactions to complicate the γ-ray spectra of activated products of either ^{16}O or ^{18}O, and both may be determined in a single irradiation.

The methods for forming anodic oxide coatings on tantalum utilize either constant voltage or constant current in the electrolytic cell. In the constant-voltage method, the potential applied across the electrodes and electrolyte is brought quickly to the desired value and held constant as the current reaches a maximum and then decreases to a small, almost steady-state value, at which time the oxidation proceeds only slowly. The thickness of the oxide formed depends primarily upon the voltage employed. Films prepared in this way are thin (<0.1 mg/cm^2 oxygen). In the constant-current method the potential is allowed to rise until the desired oxide thickness is obtained, limited by a breakdown point characterized by sparking and oxygen evolution. In both methods the temperature is held constant.

For maximum utility as standards for oxygen analysis by charged-particle activation, films are needed whose thicknesses vary from less than 1 mg/cm^2 to sufficient to completely stop the incident ^{3}He beam. The thickness of the oxide film must also be uniform with respect to the cross-sectional area of the beam. Anodization techniques described in the literature do not

guarantee either uniformity in oxide thickness or reproducibility of formation of the thick films of several mg/cm^2 oxygen.

The technique we have developed uses a constant current of 40 mA from a dc power supply, measured by an ammeter in the external circuit. The electrolytic cell, shown in Fig. G.5-1, has an electrolyte capacity of 7 ml. The electrolyte used was 0.1 %KCl. Temperature in the cell was adjusted to maintain gentle reflux, 90° to 100°C. The distance between the anode and the platinum cathode was 0.5 cm. The tantalum foils were chemically polished prior to use in an etching bath of 5:2:1.5 by volume H_2SO_4, HNO_3, HF, according to Tegart.[3]

Figure G.5-2 shows the oxide thickness obtained as a function of plating time. The voltage during plating was observed to rise rapidly to a maximum of 400 V at 7 min and then to fall to a 200-V plateau at 27 min. This plateau was maintained until 60 min, at which time a slight voltage rise was observed. The final voltage for the 160-min anodization was 270 V. The smooth, almost linear curve of Fig. G.5-2 allows simple preparation of an oxide standard of any thickness to match the degrading power of the sample to be analyzed. It should be noted that the thickest sample prepared, 7.15 mg/cm^2 oxygen, corresponds to a Ta_2O_5 thickness of 39.3 mg/cm^2. Figure G.5-3 is the range-energy relationship of ^3He in Ta_2O_5 calculated from data given by Williamson and Boujot.[4] It may be seen from this curve that the 39.3-mg/cm^2 Ta_2O_5 sample will degrade a 10-MeV ^3He beam to less than 1 MeV. Markowitz and Mahony[5] found negligible oxygen activation at ^3He energies less than 2.5 MeV.

In order to demonstrate the uniformity of the anodized film, the samples were bombarded for 10 sec with a 10-MeV ^3He beam at the Hilac at a beam current of approximately 200 nA. The resulting activity of ^{18}F produced at the end of bombardment, corrected for thickness of Ta_2O_5, is shown in Fig. G.5-4. The dashed line represents the maximum ^{18}F activity which could be obtained with a 10-MeV ^3He bombardment of Ta_2O_5 as calculated from the excitation function of Markowitz and Mahony.

This technique has been used for a very economical preparation of enriched ^{18}O targets for subsequent work on isotopic oxygen analysis.

References

1. L. Young, Anodic Oxide Films (Academic Press, London, 1961).
2. B. A. Thompson, Anal. Chem. 33, 583 (1961).
3. W. J. McG. Tegart, The Electrolytic and Chemical Polishing of Metals (Pergamon, London, 1956).
4. C. Williamson and J. P. Boujot, Tables of Range and Rate of Energy Loss of Charged Particles of Energy 0.5 to 150 MeV, Centre D'Etudes Nucléaires De Saclay, Report CEA-2189, 1962.
5. S. S. Markowitz and J. D. Mahony, Anal. Chem. 34, 329 (1962).

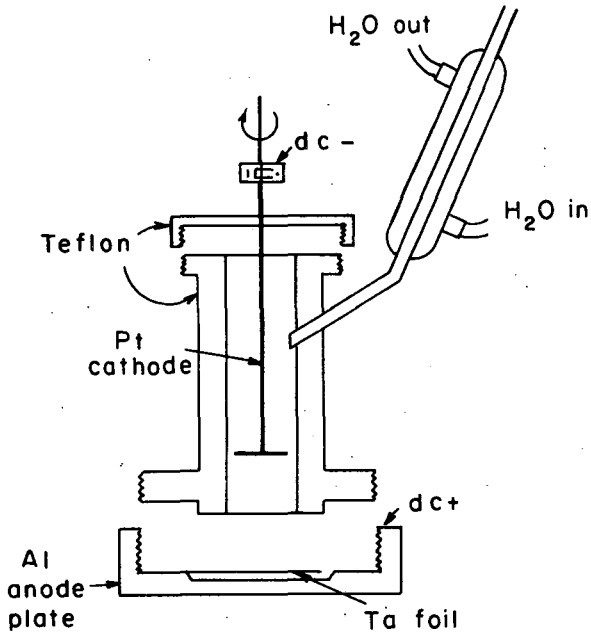

XBL671-345

Fig. G.5-1. Electrolytic cell for high-temperature anodization of Tantalum metal foils.

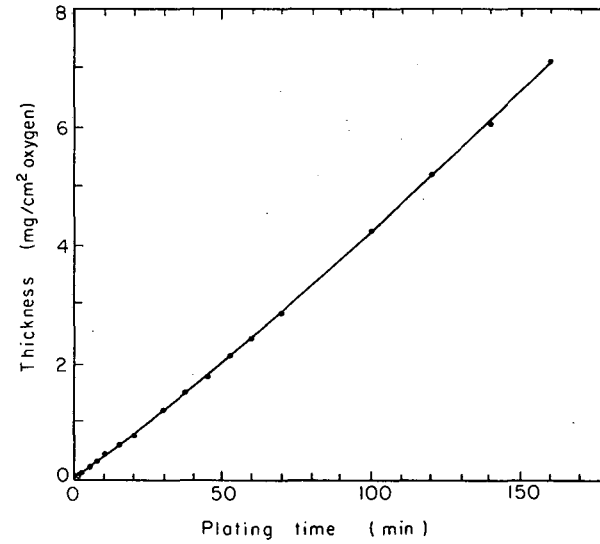

XBL671-346

Fig. G.5-2. Thickness vs plating time for the anodization of Ta metal. Current = 40 mA, electrolyte = 0.1% KCl, temperature ≈ 100°C.

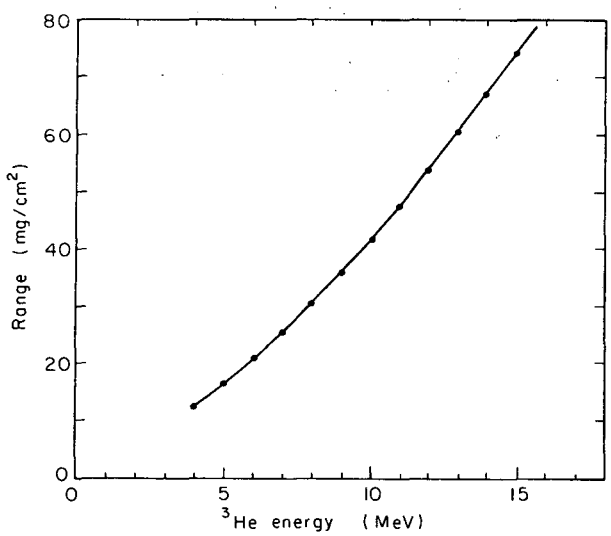

XBL671-347

Fig. G.5-3. Range-energy curve for ^{3}He ions in Ta_2O_5. The range data were calculated from data given by Williamson and Boujot.

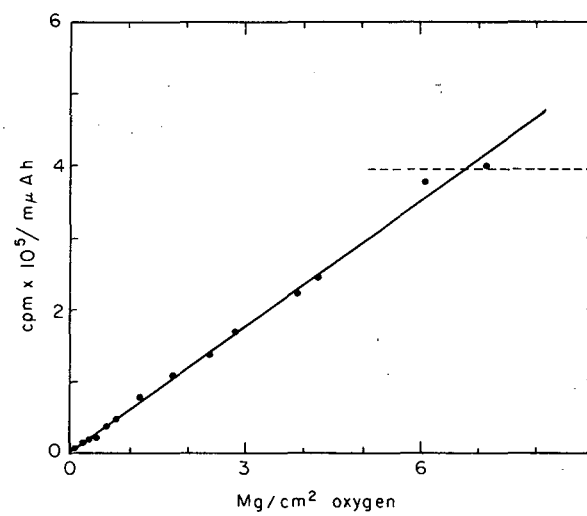

XBL671-348

Fig. G.5-4. Activation of ^{16}O by 10-MeV ^{3}He. Dashed line represents activity at the thickness at which the beam is 99.9% degraded in energy.

6. AN IMPROVED CORRELATION FOR THE HEATS OF FORMATION OF INORGANIC COMPOUNDS

Waseem Brelvi† and L. A. Bromley*

An M. S. thesis by this title was prepared by Waseem Brelvi and issued as UCRL-16865, May 1966.

An existing equation for estimating the standard heat of formation of solid inorganic compounds has been improved upon. The original equation was derived from Linus Pauling's electronegativity scale. The present form of the equation involves four characteristic parameters for each valence state of an ion present in a compound. The parameters for any ion may be correctly evaluated if experimental heats of formation of at least four of its compounds are known.

The equation has been used to correlate the known heats of formation of a large number of solid inorganic and simple metallic organic compounds. Typical compounds are metallic halides, oxides, sulfides, sulfates, silicates, tungstates, molybdates, etc. The average deviation from experimental values in correlating the heats for 611 compounds was 2.09 kcal/M. Heats of formation predicted by the correlation were estimated to be reliable to within ± 13 kcal/M.

Calculations based on the correlation led to a method of investigating any suspected errors in experimental data. Based on these calculations, it appears that the experimental heats of formation of Al_2S_3, $La(OH)_3$, and $FeCrO_4$ are seriously in error.

Footnotes

†Bechtel Corp., San Francisco.
*Department of Chemical Engineering, University of California–Berkeley, and Sea Water Test Facility, University of California–San Diego.

7. THE ABSORPTION SPECTRA OF Bk IN SOLUTION†

R. G. Gutmacher,* E. K. Hulet,* Ronald Lougheed,* John G. Conway,‡ W. T. Carnall,†† Donald Cohen,†† T. K. Keenan,** and R. D. Baybarz‡‡

Cooperative experiments, wherein several laboratories pooled their material to produce sufficient amounts of ^{249}Bk for absorption spectral, were performed at Livermore.

In all about 45 μg was collected. The spectra were investigated on a Cary 14, spectrophotometer which had automatic programming and time-averaging attachments. The spectral region 3200 to 15 000 Å was covered. Special cells and holders were used. The internal diameter was 1 mm and the path length 5 cm. Table G.7-I gives the peaks of Bk^{3+} in 1 M DCl and Table G.7-II for Bk^{4+} in 5 M $HClO_4$.

A more complete report has been submitted to J. Inorg. Nucl. Chem.

Footnotes

†Brief version of UCRL-70202.
*Lawrence Radiation Laboratory—Livermore.
‡Lawrence Radiation Laboratory—Berkeley.
††Argonne National Laboratory.
**Los Alamos Scientific Laboratory.
‡‡Oak Ridge National Laboratory.

Table G.7-I. Absorption peaks of Bk^{3+} in 1 M DCl solution.

Wavelength (Å)	Molar absorptivity	Vacuum wave numbers (cm^{-1})
3 275	1	30 530
3 350	1	29 820
3 450	1	28 990
3 670	0.5	27 300
3 744	0.5	26 700
3 910	1	25 540
3 958	0.5	25 260
4 180	4	23 900
4 300	2	23 320
4 410	1	22 680
4 600	3	21 730
4 740	7	21 090
5 040	1	19 840
6 360	3	15 730
10 470	6	9 550
12 240	13	8 160

Table G.7-II. Absorption peaks of Bk^{4+} in 5 M $HClO_4$ solution.

Wavelength (Å)	Estimated molar absorptivity	Vacuum wave numbers (cm^{-1})
3 610	a	27 690
3 690	a	27 090
3 950	8	25 310
4 240	5	23 580
4 380	3	22 820
5 950	2	16 800

a. not measurable.

8. THE SOLUTION ABSORPTION SPECTRUM OF Cf^{3+} †

John G. Conway,‡ S. Fried,‡ R. M. Latimer,‡ R. McLaughlin,‡
R. G. Gutmacher,* W. T. Carnall,†† and P. Fields††

Two separate experiments were carried out on several hundred micrograms of Cf^{3+} to determine the absorption spectrum. The largest amount used was 592 μg of Cf^{3+} in 1 M $DClO_4$. Figure G.8-1 is the absorption spectrum between 4000 and 36000 cm^{-1} (2.5 μ to 2800 Å).

Footnotes

†Submitted for publication to J. Inorg. Nucl. Chem. 28, 3064 (1966).
‡Lawrence Radiation Laboratory–Berkeley.
*Lawrence Radiation Laboratory–Livermore.
††Argonne National Laboratory.

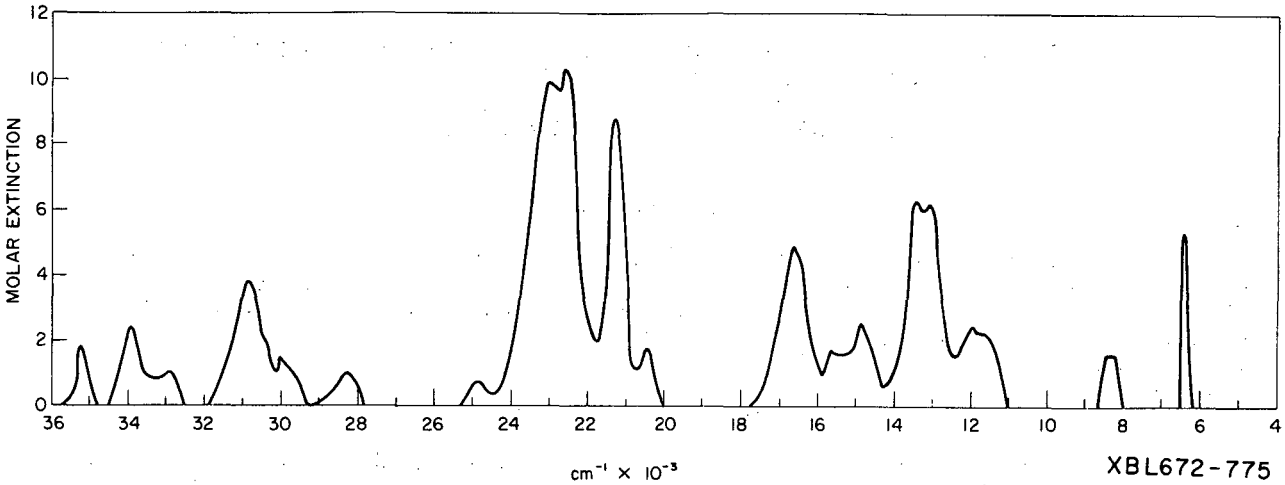

Fig. G.8-1. Absorption spectrum of Cf^{3+} in 1 M $DClO_4$.

9. ENERGY LEVELS OF SINGLE-CRYSTAL ERBIUM OXIDE†

K. Rajnak and John G. Conway

The experimental work was done by Gruber, Henderson, and Muramoto, the calculations of levels and fitting of parameters by Rajnak and Conway. The absorption spectra of large single crystals of Er_2O_3, observed at 10°, 80°, and 290°K, were analyzed in the wavelength region of 2200 to 10 000 Å. More than 600 transitions from all light crystalline Stark levels of the ground $^4I_{15/2}$ state which combined with more than 30 excited states of the Er^{3+} ion in C_2 sites were assigned. In thick crystals, evidence of vibronic spectra of ions in C_2 and S_6 sites were observed for seven J manifolds. The observed spectrum was compared with a calculation which includes configuration interaction effects on all expected "free ion" energy levels of Er^{3+} between ground and 44 000 cm^{-1}. The parameters which yield the best fit are E^1= 6844, E^2= 32.04, E^3= 635, ζ= 2354; α = 12.2, β=-590, and Y(22, 1)=-4180 cm^{-1}. The rms deviation between observed and calculated energy levels is 73 cm^{-1}.

Footnote

†A paper of this title, by J. B. Gruber, J. R. Henderson, M. Muramoto, K. Rajnak, and John G. Conway, is in J. Chem. Phys. 45, 477 (1966).

10. OPTICAL SPECTRA OF TRIPOSITIVE CURIUM-244 IN LANTHANUM TRICHLORIDE†

J. B. Gruber, W. R. Cochran, John G. Conway, and A. T. Nicol

Absorption and fluorescence spectra of Cm^{3+} in $LaCl_3$ were observed between 3000 and 8000 Å. Crystals containing 0.1 and 0.5 mole % of Cm^{3+} were studied at 77° and 4°K. In the final fitting of the data 15 levels which were clearly identified were used. The rms deviation was 120 cm^{-1}. The parameters derived from the fit are E^0 = 4939.29, E^1= 4621.47, E^2= 17.70, E^3 = 399.42, ζ = 2841.66, α = 57.08, and β =-4761.60 cm^{-1}. Three additional levels which could not be experimentally identified could be assigned because of the agreement with the calculations.

Footnote

†Short version of J. Chem. Phys. 45, 1423 (1966).

11. OPTICAL AND ELECTRON PARAMAGNETIC RESONANCE SPECTROSCOPY OF Cm IN CaF_2

N. Edelstein, W. Easley, and R. McLaughlin

Introduction

The tripositive state of Cm has a $5f^7\ ^8S_{7/2}$ electronic configuration for pure Russell-Saunders coupling. However, previous optical and electron paramagnetic resonance spectroscopy (EPR) of this ion in $LaCl_3$ has shown[1,2] that there are marked deviations from Russell-Saunders coupling. We are investigating the electronic states of Cm by optical and EPR spectroscopy in crystals of CaF_2.

Experimental Procedure

Single crystals of CaF_2 in known crystallographic orientations containing 0.1 to 0.2 wt. % Cm (^{244}Cm; half-life 18.1 years, nuclear spin I = 0) were grown by the Bridgman-Stockbarger technique.[3] EPR spectra of these crystals were examined with a conventional superheterodyne spectrometer operating at ≈ 9.1 GHz at temperatures of 1°K and 4.2°K with the magnetic field rotated in the 111 and 110 planes of the CaF_2 crystal. A plot of the magnetic field at which absorptions appeared vs the relative angle of the rotation of the magnetic field is shown in Fig. G.11-1 for the 110 plane. The solid lines are the calculated least-squares fit to the data. The dashed line is due to the resonance of Cm^{3+} ions in cubic symmetry. No resonances were seen at 77°K. Optical measurements were made at room temperature and 77°K with a Cary Model No. 14 spectrometer and a Jarrell-Ash F-6 spectrometer.

Results and Discussion

Crystals grown with Cm are initially pale yellow or almost colorless after annealing. Because of the damage due to the high radiation level they are rose-colored after 1 hour. After 3 to 4 hours the color has changed to burgundy red, and in about 15 hours the crystals are coal black. At all temperatures the characteristic orange glow of Cm^{3+} is present, which is due to emission from crystal-field levels of the first excited electronic state down to the ground electronic state. The change in color of the crystal is due to the growth of a broad absorption band centered at 5000 Å with about a 2000 Å half width. Besides this broad absorption band which grows in with time, there are a number of relatively sharp lines which start to appear after annealing. These lines have been assigned to Cm^{4+} in the CaF_2 crystal. Figure G.11-2 shows the energy-level diagram of Cm^{3+} and Cm^{4+} in the CaF_2 crystal. For comparison we show the data of Gruber and Conway on Cm^{3+} in $LaCl_3$,[2] and the data obtained by Keenan on CmF_4.[4]

Trivalent rare earth or actinide ions can be incorporated in the alkaline earth halides in sites of various symmetries. Since the crystal as a whole must be electrically neutral, charge-compensating ions must also be present. The arrangement of these charge-compensating ions about the rare earth (or actinide) ion affects the symmetry site of the impurity ion and its crystal field splittings. The most common symmetry sites present in these types of crystals are cubic, tetragonal, and trigonal.[5] The sites present are dependent on the way the crystals are grown and annealed. In our Cm-CaF_2 crystals we find trivalent Cm in the cubic site and in two different trigonal sites.

Preliminary values of the g tensor in the two trigonal sites are given in Table G.11-I. Also included is the value for the cubic site. In all three sites the crystal field splitting is large--that is, greater than 5 cm^{-1}, since at 4°K and 1°K we see only resonance lines from the ground crystal-field state. The g value for the cubic site is, within experimental error, the same as divalent Am in CaF_2,[3] and therefore the Γ_6 crystal field state is the lowest for this ion. This g value also agrees with the work of Abraham, Judd, and Wickman on Cm^{3+} in $LaCl_3$.[1]

The number of absorption lines we obtain from the Cm^{4+} depends on the temperature at which radiation damage takes place. If, after annealing, the crystal is kept at room temperature more absorption lines are found than when the crystal is placed at 77°K. More diffusion of charge-compensating ions takes place in the crystal at the higher temperature, with the consequence that more symmetry sites appear.

Further work is now in progress. From EPR measurements at 35 GHz we will obtain more accurate values of the g tensor of Cm^{3+} ions in trigonal sites. Also we will be able to

determine more accurately the splitting between the Γ_6 and Γ_8 crystal-field levels of the ground electronic state of the Cm^{3+} ions in cubic symmetry.

References

1. M. Abraham, B. R. Judd, and H. H. Wickman, Phys. Rev. 130, 611 (1963).
2. J. B. Gruber, W. R. Cochran, J. G. Conway, and A. Nicol, J. Chem. Phys. 45, 1423 (1966).
3. N. Edelstein, W. Easley, and R. McLaughlin, J. Chem. Phys. 44, 3130 (1966).
4. T. K. Keenan, J. Am. Chem. Soc. 83, 3719 (1961).
5. M. J. Weber and R. W. Bierig, Phys. Rev. 134, A1492 (1964).

Table G. 11-I. Spin Hamiltonian parameters of Cm^{3+} - CaF_2, S' = 1/2.

Cubic site
$g = 4.492 \pm 0.002$
Trigonal site I
$g_{\parallel} = 3.41 \pm 0.02$, $g_{\perp} = 6.88 \pm 0.02$
Trigonal site II
$g_{\parallel} = 2.69 \pm 0.02$, $g_{\perp} = 5.91 \pm 0.02$

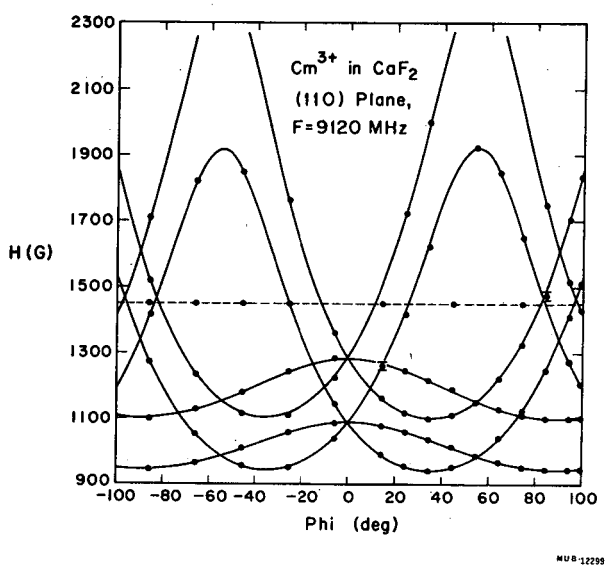

Fig. G.11-1. Variation of the EPR spectrum of Cm^{3+} in the 110 plane of CaF_2.

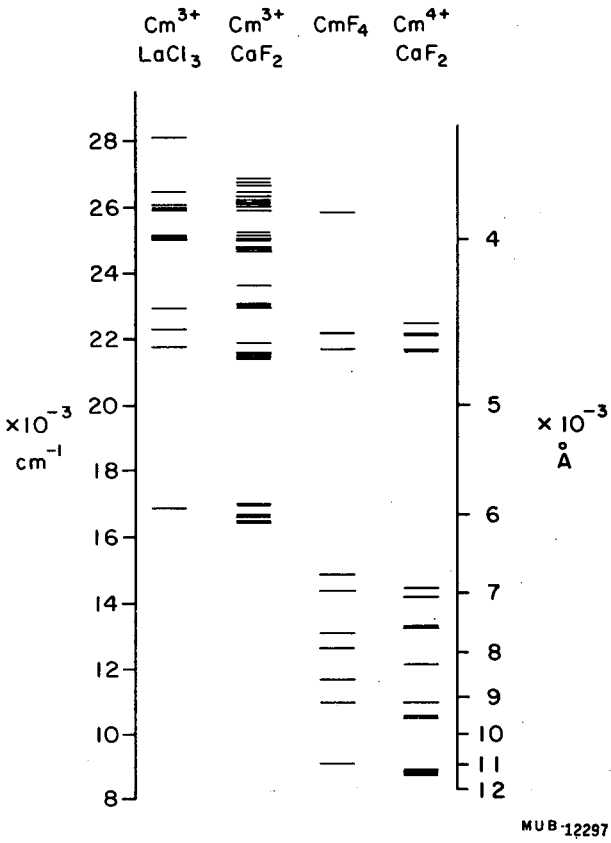

Fig. G.11-2. Energy-level diagram of Cm^{3+} and Cm^{4+} in various matrices.

12. OPTICAL SPECTRA OF Pu IN CaF_2

R. McLaughlin, R. White,† and N. Edelstein

Introduction

In the lanthanide series of the periodic table all the elements have been stabilized in the divalent state in CaF_2 crystals.[1] We have recently shown that this is also true for Am doped in CaF_2.[2] We have tried to extend this work to other actinides, and present here our results for Pu in CaF_2.

Experimental Procedure

Single crystals of CaF_2, each containing 0.1 to 0.2 wt % of ^{239}Pu (half-life 24 360 years) or ^{238}Pu (half-life 89 years) were grown as described previously.[2] The crystals were colorless or light blue when removed from the furnace, but turned to a deep blue color after a time. It required several months for the color change to occur in ^{239}Pu but only a day for ^{238}Pu.

Previous work on lanthanides and Am-doped CaF_2 suggested that under the conditions used Pu should be incorporated into the crystal in the trivalent state. Lammermann and Conway found three groups of sharp lines which shift only slightly between Pu-doped lanthanum ethylsulfate and Pu-doped lanthanum trichloride.[3] These lines were looked for and found (slightly shifted) in Pu-doped calcium fluoride, as shown in Table G.12-I. This observation confirmed the presence of trivalent Pu when the crystal was initially grown. Preliminary investigation of the fluoresence of Pu^{3+} in CaF_2 showed a band at approximately 1.3 μ.

The blue color of the crystals resulted from radiation damage caused by the α activity of the Pu. Studies were carried out to determine what spectral changes resulted from radiation

damage, since radiation in Am caused divalent Am to form. For the study the color was bleached from a ^{239}Pu crystal and a ^{238}Pu crystal by heating to ≈500°C. Blue light was emitted during this bleaching process, with band peaks at 4800 and 5800 Å. In order to determine differences due to radiation damage, spectrograms of the ^{239}Pu crystal and ^{238}Pu crystal were compared, since changes in the ^{239}Pu crystal occurred very slowly. Spectra were obtained by using a Jarrel-Ash Model 75, F/6 spectrograph and a Cary Model 14 spectrophotometer.

Results and Discussion

Two types of spectral features grew in as the radiation damage continued: broad bands of ≈ 100 Å half width, and sharp lines of ≈1 Å half width. The wavelengths of these features are listed in Table G.12-II. The ground configuration of divalent Pu would most likely be f^6. An attempt was made to predict this spectrum by interpolation between the energy levels of neutral Pu (configuration f^6s^2), Am^{3+} (configuration f^6),[4] and Cm^{4+} (configuration f^6).[5] However, no correlation was found between the observed and the predicted spectrum. Attempts were then made to correlate the observed spectrum with the solution spectrum of tetravalent Pu.[6] This correlation was suggestive but not certain. In general the spectra of actinides are more sensitive to their environment than the spectra of lanthanides; hence this kind of comparison is less positive.

The issue was resolved by obtaining the spectrum of Pu^{4+} in a CaF_2 matrix. This was accomplished precipitating Pu^{4+} and CaF_2 from an HCl solution by addition of concentrated HF. The Pu was kept in the tetravalent state by addition of $NaNO_2$ prior to precipitation.[7] In order to obtain the spectrum, the precipitate was dried with a heat lamp, mulled with mineral oil, and pressed between two quartz plates. The lines of the mull were much broader than the lines of the crystal. This is believed to be due to the presence of water incorporated into the mull. All spectra were obtained with samples immersed in liquid nitrogen. The correspondence between the spectra of the crystal and of the mull is shown in Fig. G.12-1. The broad-band features from the crystal are not included in this figure, because the lack of correspondence between the mull spectrum and crystal broad-band spectrum indicated that these features were not associated with the Pu^{4+} ion, but were probably due to color centers.

In the process of these investigations it was noted that the ^{238}Pu-doped crystal took on a different shade of blue coloration if radiation damage occurred at liquid nitrogen temperature. Close examination revealed that the sharp lines did not grow in at 77°K. Hence this new color was caused by the presence of only those features labeled as broad bands in Table G.12-II, whereas in the room-temperature damaged crystal both the sharp Pu^{4+} lines and the broad bands contributed to the color.

The difference in diffusional properties of various species in the crystal at 77°K and room temperature[8] would account for the different spectral features at these temperatures. Although we have found no evidence from the optical spectra of Pu in CaF_2 for the presence of divalent Pu, we cannot definitely say that this oxidation state is not formed.

Footnote and References

† NSF High School teachers' program, summer 1966.

1. D. S. McClure and Z. Kiss, J. Chem. Phys. 39, 3251 (1963).
2. N. Edelstein, W. Easley, and R. McLaughlin, J. Chem. Phys. 44, 3130 (1966).
3. H. Lammermann and J. Conway, J. Chem. Phys. 38, 259 (1963).
4. J. Conway, J. Chem. Phys. 40, 2504 (1964).
5. J. Conway, J. Chem. Phys. 41, 904 (1964).
6. D. Cohen, J. Inorg. Nucl. Chem. 18, 211 (1961).
7. S. Fried (Argonne National Laboratory), private communication.
8. J. L. Merz and P. S. Pershan, Bull. Am. Phys. Soc. 11, 364 (1966).

Table G.12-I. Comparison of centers of groups of sharp lines of Pu^{3+}.

		Center of group (cm^{-1})		
$La(Pu)(Et\ SO_4)_3 \cdot 9H_2O$		19635	16014	14956
$Ca(Pu)F_2$		19895	16411	15186
	Difference	260	397	230

Table G.12-II. Lines which grow into $Ca(Pu)\ F_2$ crystal due to α radiation damage.

Wave length (A)	Wave number (cm^{-1})	Intensity
	Half width ≈ 1 Å	
4 149	24 095	m
4 151	24 084	w
4 154	24 066	w
4 463	22 400	w
4 554	21 953	s
4 559	21 928	w
4 584	21 809	w
4 693	21 302	w
4 712	21 216	w
4 955	20 176	w
5 040	19 836	w
5 323	18 781	w
5 349	18 690	w
5 537	18 055	m
5 674	17 619	w
5 676	17 613	w
6 518	15 338	m
7 006	14 270	w
7 021	14 239	w
7 889	12 672	w
8 088	12 361	w
8 093	12 353	w
8 099	12 344	w
8 431	11 858	m
8 447	11 835	w
8 527	11 724	w
8 608	11 614	w
10 600	9 431	
11 440	8 739	
	Half width ≈ 100 Å	
5 998	16 670	
6 328	15 800	
6 576	15 200	
8 057	12 400	

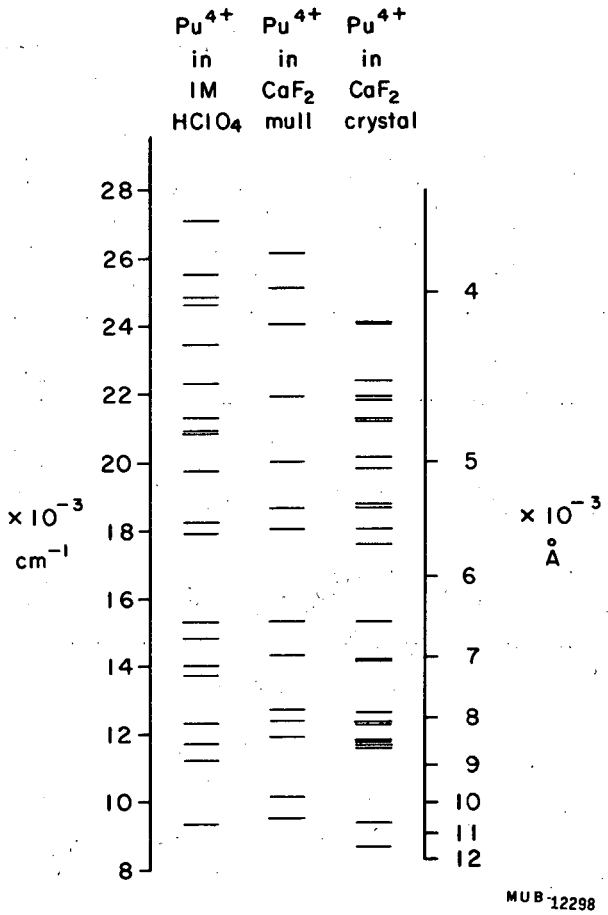

Fig. G.12-1. Energy-level diagram of Pu^{4+} in various solutions.

13. ATOMIC BEAM STUDY OF THE STARK EFFECT IN THE CESIUM AND RUBIDIUM D LINES†

Douglas McColm,* Richard Marrus, and Joseph Yellin

The atomic beam method has been applied to a study of the transitions $6^2p_{1/2,3/2} \leftrightarrow 6^2s_{1/2}$ in cesium and $5^2p_{1/2,3/2} \leftrightarrow 5^2s_{1/2}$ in rubidium. The splitting by the electric field of the $p_{3/2}$ ^2p level into two levels is observed. It is shown that the characterization of the Stark effect in the ^2p levels by a simple scalar and tensor polarizability does not hold. Fine-structure effects giving rise to differences of the $^2p_{1/2}$ and $^2p_{3/2}$ radial functions are sufficiently strong so that the Stark effect of the ^2p level must be expressed in terms of three parameters. If the polarizability $\alpha(n^2p_Jm_J)$ is defined by the relation $\Delta W(n^2p_Jm_J) = -(E^2/2)\,\alpha(n^2p_Jm_J)$, where E is the electric field and ΔW the induced energy shift, then the following values of the polarizabilities are deduced. For cesium, $\alpha(6^2p_{1/2}) = 187(29)\times10^{-24}$ cm^3; $\alpha(6^2p_{3/2}\pm3/2) = 196(30)\times10^{-24}$ cm^3; and $\alpha(6^2p_{3/2}\pm1/2) = 273(42)\times10^{-24}$ cm^3. For rubidium, $\alpha(5^2p_{1/2}) = 112(17)\times10^{-24}$ cm^3; $\alpha(5^2p_{3/2}\pm3/2) = 102(15)\times10^{-24}$ cm^3; and $\alpha(5^2p_{3/2}\pm1/2) = 148(23)\times10^{-24}$ cm^3. The polarizabilities are compared with results deduced from Stone's recent oscillator strength calculations for cesium and with values deduced from the method of Bates and Damgaard in the following tables.

Footnotes

†UCRL-16541 Abstract, Sept. 1966.

*Present address: Department of Physics, University of California-Davis.

Table G.13-I. Cesium polarizabilities $\times 10^{24}$ cm^3.

	$\alpha(6s_{1/2})$	$\alpha(6p_{1/2})$	$\alpha(6p_{3/2}\pm 3/2)$	$\alpha(6p_{3/2}\pm 1/2)$
Stone	65	187	200	273
Bates and Damgaard	56	192	191	246
Measured[a]	52.5(6.5)	187(29)	196(30)	273(42)

a. The measured value for $\alpha(6s_{1/2})$ is taken from A. Salop, E. Pollack, and B. Bederson, Phys. Rev. 124, 1431 (1961).

Table G.13-II. Rubidium polarizabilities $\times 10^{24}$ cm^3.

	$\alpha(5s_{1/2})$	$\alpha(5p_{1/2})$	$\alpha(5p_{3/2}\pm 3/2)$	$\alpha(5p_{3/2}\pm 1/2)$
Bates and Damgaard	46	116	108	151
Measured[a]	40(5)	112(17)	102(15)	148(23)

a. The measured value for $\alpha(5s_{1/2})$ is taken from A. Salop, E. Pollack, and B. Bederson, Phys. Rev. 124, 1431 (1961).

14. MOLECULAR BEAM ELECTRIC RESONANCE EXPERIMENTS ON LiF, KCl, RbF, AND CsF

Alvin J. Hebert, Craig D. Hollowell, Frank J. Lovas, and Kenneth Street, Jr.

The molecular beam electric resonance method has been used to obtain dipole moments for several diatomic molecules. The apparatus and techniques used have been discussed in detail elsewhere.[1]

Lithium Fluoride

Improvements in our voltage measuring equipment have allowed more accurate determinations for the dipole moments of $^6Li^{19}F$. The experimental error has been reduced by a factor of five below previous uncertainties.[2,3] The following values, given in debyes, are for the observed J = 1 rotational states:

Dipole moment, μ (in debyes)		
Vibrational state		
v = 0	v = 1	v = 2
6.32742(20)	6.41478(20)	6.50323(20)

$$\mu_v = \mu_e + \mu_I(v+1/2) + \mu_{II}(V+1/2)^2$$
$$\mu_e = 6.28415(25)$$
$$\mu_I = 0.08627(5)$$
$$\mu_{II} = 0.000545(20).$$

Potassium Chloride

Previous electric resonance experiments on KCl by Lee et al.[4] yielded large and unexplainable variations of dipole moment with vibrational state. The present results[2] are in agreement with the expected variation. The observed potassium quadrupole coupling constants are in

good agreement with those reported by Lee et al.[4]

The following dipole moments were obtained from observations of the J = 2 rotational state. The values obtained by Lee et al.[4] are given for comparison.

	Dipole moment, μ (in debyes)		
	Vibrational state		
	v = 0	v = 1	v = 2
$^{39}K^{35}Cl$			
This work	10.26875(100)	10.32875(150)	10.38770(220)
Lee et al.	10.48(5)		10.69(5)
	$\mu_v = \mu_e + \mu_I(v+1/2)$ $\mu_e = 10.23878(120)$ $\mu_I = 0.0600(9)$		
$^{39}K^{37}Cl$			
This work	10.26830(220)		

Rubidium Fluoride

The hyperfine interaction constants observed[5] for RbF are in good agreement with previous work on $^{85}Rb^{19}F$,[6-9] and on $^{87}Rb^{19}F$.[6-8] Intermediate field measurements on the J = 1 rotational state in conjunction with $^{6}Li^{19}F$ measurements have allowed a more accurate and complete determination of the dipole moments and their variation with vibrational state. The values, from this work, those obtained previously,[7] and some recent preliminary values by Gräff[10] are given below.

	Dipole moment, μ (in debyes)		
	Vibrational state		
	v = 0	v = 1	v = 2
This work	8.54653(90)	8.61350(110)	8.68098(130)
Reference 10	8.535(4)	8.605(4)	
Reference 7	8.80(10)		
	$\mu_v = \mu_e + \mu_I(v+1/2) + \mu_{II}(v+1/2)^2$ $\mu_e = 8.51317(115)$ $\mu_I = 0.06650(38)$ $\mu_{II} = 0.00026(12)$		

Cesium Fluoride

The observed hyperfine interaction constants for CsF were in good agreement with previous values.[9, 11-13] A more complete and accurate set of dipole moments was obtained by using a multichannel analyzer in the multiscalar mode as a detector, and frequency-modulating phase-locked signal generators to obtain the spectra.[5] The system was calibrated with $^{6}Li^{19}F$. The results of this work are for the J = 1 rotational state and are presented below with the previously reported values for comparison.

Dipole moment, μ (in debyes)

	Vibrational state			
	v = 0	v = 1	v = 2	v = 3
This work	7.8840(9)	7.9547(10)	8.0258(12)	8.0970(15)
Reference 12	7.89(17)	7.98(18)		
Reference 13	7.876(3)	7.986(3)		
Calculated from dipole moment expression below				8.0976(60)

$$\mu_v = \mu_e + \mu_I(v+1/2) + \mu_{II}(v+1/2)^2$$
$$\mu_e = 7.8487(13)$$
$$\mu_I = 0.0704(6)$$
$$\mu_{II} = 0.0002(2)$$

References

1. A. J. Hebert, A Molecular-Beam Electric-Resonance Spectrometer and the Radio-Frequency Spectra of Lithium Fluoride (Ph. D. Thesis), UCRL-10482, Sept. 1962.
2. K. Street, Jr., A. J. Hebert, C. D. Hollowell, and T. L. Story, UCRL-17256, Nov. 1966 (to be submitted to J. Chem. Phys.).
3. L. Wharton, W. Klemperer, L. P. Gold, R. Strauch, J. J. Gallagher, and V. E. Derr, J. Chem. Phys. 38, 1203 (1963).
4. C. A. Lee, B. P. Fabricand, R. O. Carlson, and I. I. Rabi, Phys. Rev. 91, 1395 (1953).
5. F. Lovas, A. J. Hebert, and K. Street, Jr. (LRL), private communication.
6. V. Hughes and L. Grabner, Phys. Rev. 79, 314 (1950).
7. H. Lew, D. Morris, F. E. Geiger, Jr., and J. T. Eisinger, Can. J. Phys. 36, 171 (1958).
8. P. A. Bonczyk and V. W. Hughes, Bull. Am. Phys. Soc. 10, 101 (1965).
9. T. English and Jens C. Zorn, private communication, Oct. 1965.
10. G. Gräff, R. Schönwasser, and M. Tonutti private communication, Aug. 1966.
11. J. W. Trischka, Phys. Rev. 74, 718 (1948).
12. J. W. Trischka, Phys. Rev. 76, 1365 (1949).
13. G. Gräff and O. Runolfsson, Z. Physik 187, 140 (1965).

15. DEPENDENCE OF LASER AXIAL BEAT-NOTE AMPLITUDE ON ZEEMAN SEPARATION

Lloyd Armstrong, Jr., Dolores Ali,* and Tetsuo Hadeishi

We here report observation of a change in the amplitude of the beat note between axial modes of a laser when the mode separation becomes equal to an integral multiple of twice the Zeeman separation of either the upper or lower lasing levels of the atoms. The magnitude of the effect decreases with increasing order, and becomes effectively zero by the fourth order.

In this experiment it was our purpose to develop a method for rf spectroscopy of excited states. In principle, this method may be extended to the measurement of g_J's and hyperfine-structure separations of any lasing states in an atom. Because the line width is to first order independent of the Doppler effect, this technique should allow the study of excited-state lifetimes under lasing conditions.

The effect was observed in both a 50-cm-long He-Ne and a 35-cm-long Ar^+ laser. These lasers had Brewster-angle windows and external spherical mirrors. The mirror separation was always much smaller than the focal length. The lasers were placed in an axial magnetic field and operated in the TEM_{00} mode. A schematic diagram of the apparatus is shown in Fig. G.15-1. Since the phototube is a square-law detector, its output is modulated at the difference frequencies between modes. The tuned receiver passes only the portion of the phototube output that contains the desired beat frequency.

Resonances were observed at a fixed cavity length by sweeping the magnetic field. Figure G.15-2 shows the beat-note amplitude for the 6328-Å transition in the He-Ne laser. The resonance takes the form of a dispersion curve because a phase-sensitive detector is used with field modulation. Because both the upper and lower lasing levels of Ne have the same g_J, only one resonance is obtained in this case. The dependence of the resonance on cavity length was verified by changing the cavity length and observing the shift in the field value of the resonance. The width of the line shown in Fig. G.15-2 is of the order of 35 MHz. Similar results were obtained for the 4880-Å transition in the Ar^+ laser. The estimated width of the resonance corresponding to an overlap of the upper levels was of the order of 70 MHz; resonances due to an overlap of lower levels were small and poorly defined because the lower levels are only partially resolved at the field values used. In both cases, no attempt was made to frequency-lock the laser, or to achieve a field homogeneous to more than approximately 10%; the line widths are therefore broader than they would be under optimum conditions.

The observed effects can be qualitatively explained by the following simple consideration. As the magnetic field is swept through the point of overlap between the Zeeman splitting and the axial-mode separation, the atom can be stimulated to emit into two modes. This has the effect of coupling the two axial modes and is analogous to the strong-coupling case in Lamb's theory.[1] At this strong-coupling point, one mode tries to quench the other, and a change in beat-note amplitude is expected.

The effect that we observed is similar to that reported by Kannelaud and Culshaw.[2] We believe, however, that our method allows easier observation of resonances and clearer determination of line shapes and widths, with corresponding gains in accuracy of spectroscopic measurements. In addition, by using a tuned receiver to select the axial modes to be studied, one no longer needs to operate the laser in a single transverse mode.

Footnote and References

*National Academy of Sciences Research Associate.

1. W. E. Lamb, Jr., Phys. Rev. 134, A1429 (1964).
2. J. Kannelaud and W. Culshaw, Appl. Phys. Letters 9, 120 (1966).

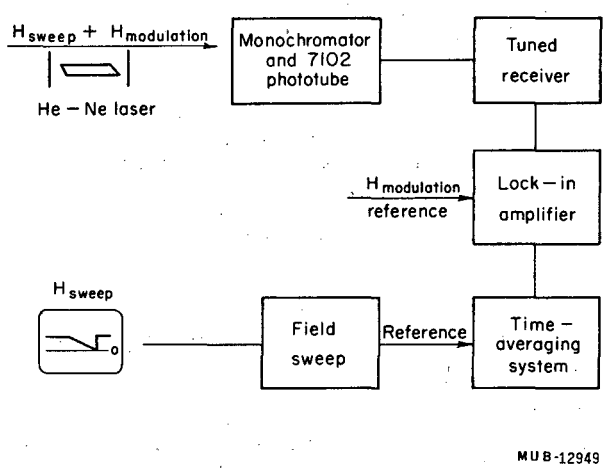

Fig. G.15-1. Schematic diagram of apparatus. The frequency of $H_{modulation}$ is about 400 Hz. The frequency of H_{sweep} equals 0.005 Hz.

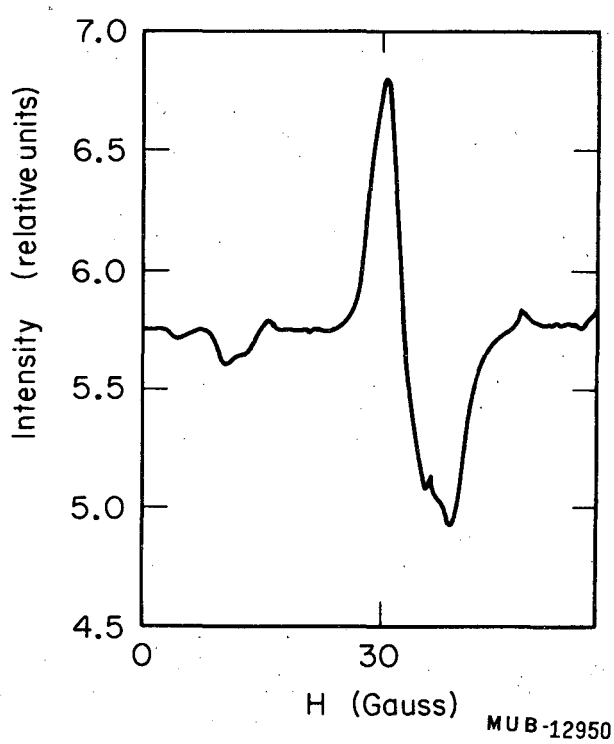

Fig. G.15-2. Intensity of beat-note amplitude vs magnetic field. The cavity is about 120 cm long; the beat frequency is 122 MHz.

16. THE CRYSTAL AND MOLECULAR STRUCTURE OF TETRAPHENYLARSONIUM cis-DIAQUOTETRACHLORO-RUTHENATE MONOHYDRATE†

Ted E. Hopkins, Allan Zalkin, David H. Templeton, and Martyn G. Adamson

The crystal structure of $(C_6H_5)_4\ AsRuCl_4(H_2O)_2 \cdot H_2O$ has been determined. The substance crystallizes from HCl solutions containing the complex ions $RuCl_4(H_2O)_2^-$ and $As(C_6H_5)_4^+$, when they are cooled to 0°C and allowed to stand for 48 hours . The structure is particularly interesting because of the possibility for cis-trans isomers involving the water molecules bonded to the ruthenium. For taking the data, a single crystal, roughly cubic, 0.15×0.17× 0.18 mm, was mounted for rotation around the b axis. Molybdenum radiation was used, with a Zr filter at the receiving slit. For Mo $K\alpha_1$, $\lambda = 0.70926$ Å.

Of the 2731 independent reflections measured ($2\theta < 41$ deg), 255 were recorded as zero intensity. Ten second counts were taken, with the crystal stationary.

The primitive cell was found to contain four formula units of $(C_6H_5)_4\ As\ RuCl_4(H_2O)_{\frac{1}{2}}H_2O$. It is monoclinic, with dimensions

$a = 15.059 \pm 0.005$, $b = 16.711 \pm 0.005$, $c = 10.996 \pm 0.005$ Å,
$\beta = 99.88 \pm 0.01$ deg.

The calculated density is 1.619 g cm^{-3}, and a rough measurement gave 1.7 g cm^{-3}.

The Weissenberg photographs showed the following reflection restrictions: $hO\ell$: $h+\ell = 2n$. Measurements with the goniostat confirmed this observation and the restriction OkO: $k = 2n$ was observed. These conditions correspond to space group $P2_1/n$. All the atoms are in general positions. 4(e): $\pm(x, y, z;\ 1/2 - x,\ 1/2 + y,\ 1/2 - z)$. The conventional R factor was reduced to 0.067, and the final values of the parameters are given in Table G.16-I. The unit cell is shown in Fig. G.16-1.

Several structures involving tetraphenylarsonium and tetraphenylphosphonium cations have been reported. No simple description is possible for the configuration of the phenyl rings in the present example of the ruthenium salt. In this case, the arsenic is situated at a point of symmetry 1, and the phenyl groups have taken correspondingly free positions around the arsenic.

The octahedral environment of the ruthenium is detailed in Table G.16-II. The most interesting aspect of the configuration is the cis-arrangement of the two water molecules in the octahedron. The average Ru-Cl and Ru-O distances of 2.34 and 2.12 Å are in agreement with the values we have found for the cesium salt[1] and with those reported by Khodashova for the potassium salt.[2] The Ru-Cl bonds opposite the oxygens in the octahedron were again found to be several hundreths of an angstrom shorter than those for which the opposite atoms were both chlorines.

The possibilities for hydrogen bonding are shown in Fig. G.16-2. The water of crystallization, designated O(3) in the figure, is probably involved in two hydrogen bonds: to water molecule O(2), and to chlorine Cl(3). The distances of 2.61 and 3.16 Å and the angle of 97 deg are acceptable evidence for bonding. In the case of the two water molecules in the octahedron surrounding the ruthenium, reasonable hydrogen bonds can be postulated for only one of the molecules, O(2). In addition to the bond to O(3), it appears to be bonded to chlorine, Cl(2), at a distance of 3.07 Å, giving an angle of about 91 deg between the bonds. The other water molecule in the octahedron, O(1), is not too distant from chlorines Cl(1) and Cl(4) of the neighboring octahedron, but the acute 66-deg angle is too small to indicate a pair of hydrogen bonds.

Water molecule O(3) appears to be vibrating quite anisotropically, with $B_{11} \approx 12$, $B_{22} \approx 4$, and $B_{33} \approx 8$. This would indicate that most of the vibration is occurring in the ac plane, or alternatively, that there is some disorder concerning the location of the oxygen atom.

It is interesting to note that the structure of this complex salt can be visualized as a series of alternating layers of ruthenium octahedra and tetraphenylarsonium ions. This is shown in Fig. G.16-1, where the alternating planes run roughly parallel to the (110) planes.

Footnote and References

†Condensation from J. Inorg. Chem. 5, 1427 (1966).

1. J. Inorg. Chem. 5, 1431 (1966).
2. T. S. Khodashova, Zh. Strukt. Khim. 1, 333 (1960).

Table G.16-I. Positional and thermal parameters in $(C_6H_5)_4As\ RuCl_4(H_2O)_2 \cdot H_2O$.[a]

Atom	x	y	z	B_{11}	B_{22}	B_{33}	B_{12}	B_{13}	B_{23}
Ru	0.4872	0.5164	0.7585	3.28	3.72	3.32	0.11	0.41	0.00
As	0.4169	0.0785	0.7332	2.56	2.75	3.38	0.23	0.12	-0.01
Cl(1)	0.3829	0.5818	0.8566	3.96	5.36	4.29	0.66	0.84	-0.43
Cl(2)	0.3813	0.4884	0.5838	3.52	6.15	3.51	-0.26	0.09	-0.45
Cl(3)	0.5308	0.6382	0.6796	4.75	3.46	5.04	0.14	0.89	0.39
Cl(4)	0.4614	0.3895	0.8391	5.75	4.02	4.39	-0.55	1.05	0.61
O(1)	0.5865	0.5358	0.9173	3.89	5.89	3.41	-0.20	0.40	0.04
O(2)	0.5884	0.4623	0.6748	3.24	4.46	3.74	0.72	0.40	-0.02
O(3)	0.0442	0.1822	0.0983	12.4	4.47	7.63	-0.66	0.01	0.17
C(I1)	0.3493	0.1309	0.5926	3.0[b]					
C(I2)	0.3189	0.0852	0.4865	4.9					
C(I3)	0.2656	0.1249	0.3866	5.9					
C(I4)	0.2489	0.2063	0.3914	6.3					
C(I5)	0.2840	0.2497	0.4922	7.3					
C(I6)	0.3338	0.2124	0.5995	5.6					
C(II1)	0.3914	0.1309	0.8793	3.6					
C(II2)	0.3130	0.1121	0.9194	5.3					
C(II3)	0.2920	0.1577	1.0226	6.2					
C(II4)	0.3530	0.2161	1.0785	5.2					
C(II5)	0.4301	0.2313	1.0359	5.1					
C(II6)	0.4502	0.1898	0.9339	4.6					
C(III1)	0.5421	0.0904	0.7312	3.6					
C(III2)	0.6046	0.0611	0.8340	5.0					
C(III3)	0.6969	0.0656	0.8253	5.4					
C(III4)	0.7249	0.0968	0.7267	6.0					
C(III5)	0.6651	0.1247	0.6252	5.4					
C(III6)	0.5707	0.1204	0.6283	4.3					
C(IV1)	0.3893	0.9670	0.7260	3.3					
C(IV2)	0.3014	-0.0579	0.7264	5.0					
C(IV3)	0.2828	-0.1419	0.7187	6.2					
C(IV4)	0.3528	-0.1957	0.7106	6.1					
C(IV5)	0.4380	-0.1698	0.7054	5.8					
C(IV6)	0.4599	-0.0871	0.7150	5.0					

a. Standard deviations of the positional parameters of Ru and As are 0.0001 or less; Cl, 0.0003 or less; and O and C, 0.001 or less. Standard deviations of the thermal parameters are 0.05 or less for Ru and As, 0.2 or less for Cl, 0.4 or less for O and C, except for O(3), which was 0.8 or less.

b. Only isotropic temperature factors were used for the carbon atoms.

Table G.16-II. Distances and angles in $(C_6H_5)_4$ As $RuCl_4(H_2O)_2 \cdot H_2O$.

Atom 1-Atom 2	bond (Å)	Bond angles (degrees)	
Ru-O(1)	2.12 ± 0.01	Cl(1)-Ru-O(2)	177 ± 1
Ru-O(2)	2.11 ± 0.01	Cl(2)-Ru-O(1)	178 ± 1
Ru-O(3)	3.92 ± 0.01	Cl(2)-Ru-O(2)	90 ± 1
Ru-Cl(1)	2.33 ± 0.01	Cl(2)-Ru-Cl(1)	93 ± 1
Ru-Cl(2)	2.32 ± 0.01	Cl(2)-Ru-Cl(3)	94 ± 1
Ru-Cl(3)	2.35 ± 0.01	Cl(2)-Ru-Cl(4)	90 ± 1
Ru-Cl(4)	2.36 ± 0.01		
As-C(1)	1.91 ± 0.01	(average of four)	
C-C	1.396±0.03	(average of twenty-four)	

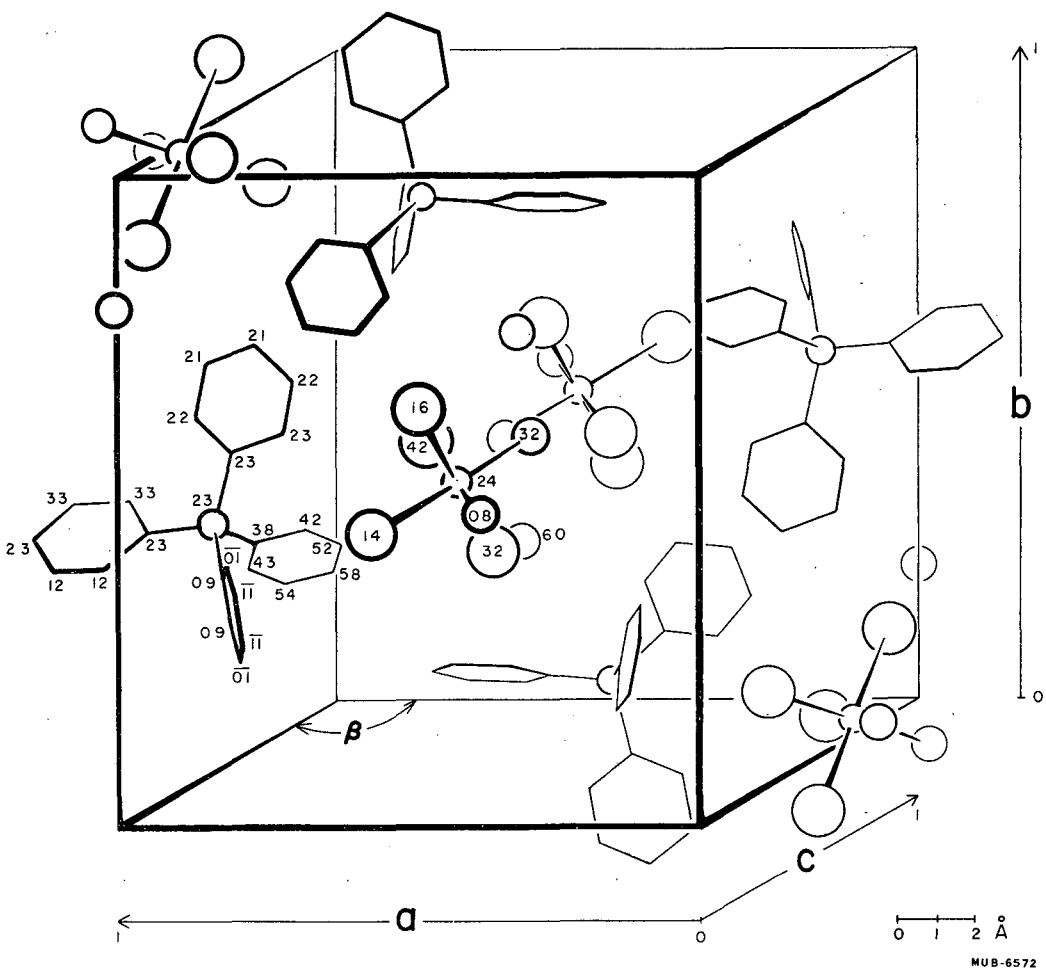

Fig. G.16-1. Unit cell of $(C_6H_5)_4$ As $RuCL_4(H_2O)_2$ H_2O. Numbers are coordinates along the c axis.

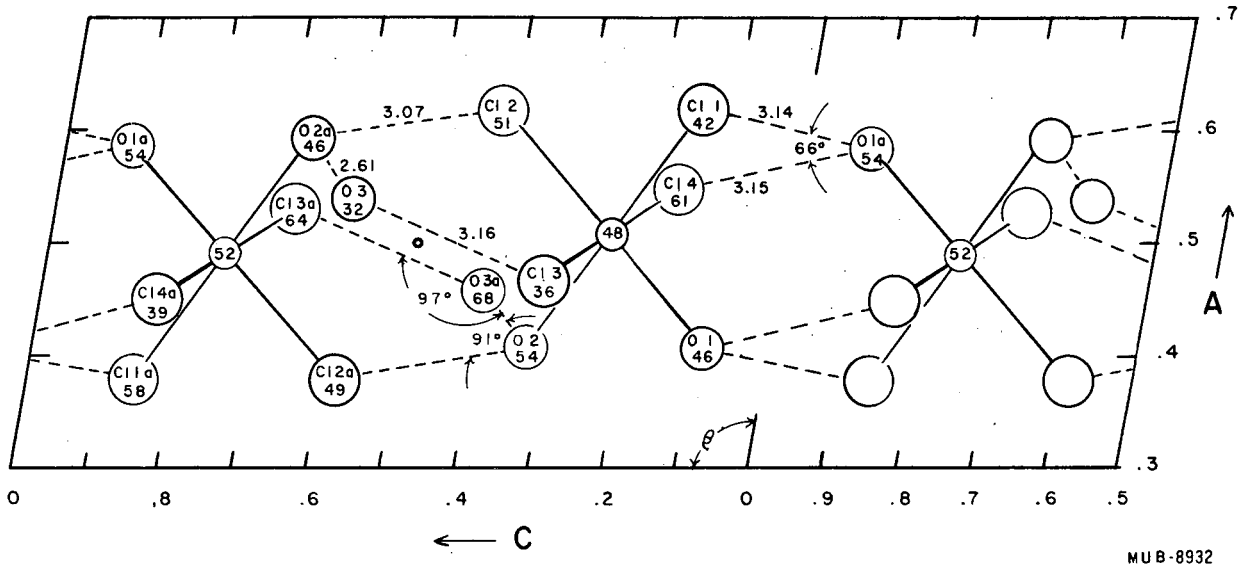

Fig. G. 16-2. Possibilities for hydrogen bonding in $(C_6H_5)_4AsRuCl_4(H_2O)_2 \cdot H_2O$.

17. THE CRYSTAL STRUCTURE OF CESIUM AQUOPENTACHLORORUTHENATE†

Ted E. Hopkins, Allan Zalkin, David H. Templeton, and Martyn G. Adamson

Small well-shaped crystals of $Cs_2RuCl_5H_2O$ were obtained from a solution of cesium chloride and ruthenium (III) in hydrocloric acid after cooling to 0°C for 48 hours. A single crystal in the form of a prism $0.14 \times 0.021 \times 0.02$ mm was used, and the cell dimensions and intensities were measured with MoKα radiation (λ = 0.70926 Å for $K\alpha_1$); 525 independent reflections were measured with counting times of 10 sec each, and 95 were recorded as zero intensity.

An A-centered orthorhombic cell was found with four formula units of $Cs_2RuCl_5H_2O$ with dimensions

$$a = 7.986 \pm 0.005, \quad b = 17.289 \pm 0.008, \quad c = 7.400 \pm 0.004 \text{ Å}.$$

The calculated density is 3.65 g cm^{-3}. The crystals sank in methylene iodide (density 3.3 g cm^{-3}).

The success of the structure determination confirmed the choice of the centro-symetric space group Amam.

Except for one set of chlorines, all the atoms are in special positons:

$$4(c): \ (1/4,\ y,\ 0;\ 3/4,\ -y, 0) + (0, 0, 0;\ 0,\ 1/2, 1/2).$$

A set of four chlorines are in the general positions

$$16(h): \pm (x,\ y,\ z;\ -x,\ -y,\ z;\ 1/2 - x,\ y,\ z;\ 1/2 + x,\ -y, z) + (0, 0, 0;\ 1/2, 1/2).$$

The atomic coordinates are listed in Table G.17-I. The final value for the conventional R factor was R = 0.07.

Figure G.17-1 is a drawing of the unit cell in a clinographic projection. The octahedral environment of the ruthenium is shown in Fig. G.17-2. A list of the distances and angles, including the estimated standard deviation, is given in Tables G.17-II and III.

The ruthenium atom lies out of the plane of the four Cl(2) atoms a distance of 0.07 Å, and the resulting Cl(1)-Ru-Cl(2) angles differ from 90 deg by several times the estimated standard deviation. In addition, the Cl(2) atoms lie on the corners of a rectangle instead of a square. Thus, the point group at the ruthenium is 2mm instead of the more symmetrical group 4mm. In the potassium salt,[1] the point group at the ruthenium is 1. The four chlorines do not lie in a plane, and the ruthenium lies on a line through two of the chlorines, rather than on the chlorine-oxygen line. The space group of the potassium salt is Pnma with Z = 4.

A review of Ru-Cl and Ru-O distances is given in the paper by Khodashova on the potassium salt. We may note here, however, that in the cesium salt the average Ru-Cl and Ru-O distances are the same as those found for the potassium salt, within the limits of the reported experimental errors: 2.10±0.03 Å, compared with 2.12±0.05 Å, and 2.34±0.005 Å compared with 2.35±0.02 Å. In both cases, the Ru-Cl bond opposite the Ru-O bond was found to be shorter by about 0.05 Å than the remaining Ru-Cl bonds.

Footnote and Reference

†Condensed from J. Inorg. Chem. 5, 1431 (1966).

1. T. S. Khodashova, Zh. Strukt. Khim 1, 333 (1960).

Table G.17-I. Atomic coordinates for $Cs_2RuCl_5H_2O$ from least-squares refinement. Standard deviations are $\sigma(y) = 0.0001$ for Cs and Ru, 0.0004 for Cl(1) and 0.002 for O. For Cl(2), $\sigma(x) = \sigma(y) = 0.0006$.

Atom	x	y	z
Cs(1)	(0.2500)[a]	0.4715	(0.0)
Cs(2)	(0.2500)	0.7534	(0.0)
Ru	(0.2500)	0.1153	(0.0)
Cl(1)	(0.2500)	0.2490	(0.0)
Cl(2)	(0.4605)	0.1112	0.2222
O	(0.2500)	0.9936	(0.0)

a. Parentheses indicate parameters subject to constraints.

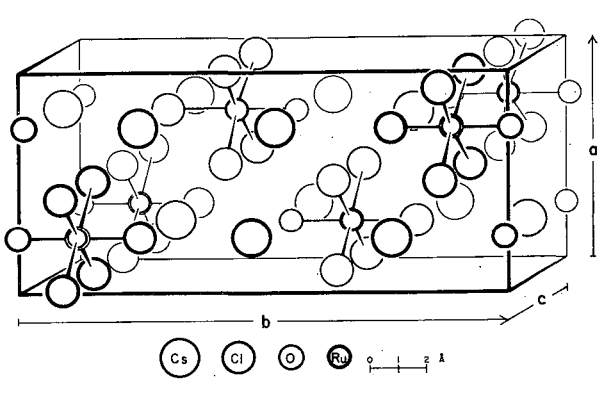

Fig. G.17-1. Unit cell of $Cs_2RuCl_5H_2O$.

Table G.17-II. Distances in $Cs_2RuCl_5H_2O$.

Atom 1 to Atom 2	Distance (Å)
Ru-O	2.104 ± 0.028
Ru-Cl(1)	2.311 ± 0.008
Ru-4 Cl(2)	2.353 ± 0.004
Ru-Cs(2)	4.404 ± 0.002
Ru-Cs(1)	4.458 ± 0.003
Cs(1)-4 Cl(2)	3.408 ± 0.004
Cs(1)-4 Cl(2)	3.590 ± 0.004
Cs(1)-2 O	3.720 ± 0.003
Cs(1)-Cl(1)	3.848 ± 0.008
Cs(1)-Cs(1)	4.113 ± 0.003
Cs(2)-4 Cl(2)	3.619 ± 0.004
Cs(2)-2 Cl(1)	3.701 ± 0.002
Cs(2)-O	4.153 ± 0.028
Cl(1)-4 Cl(2)	3.347 ± 0.007
Cl(1)-O	4.415 ± 0.028
Cl(2)-O	3.109 ± 0.018
Cl(2)-Cl(2)	3.289 ± 0.008
Cl(2)-Cl(2)	3.363 ± 0.008
O-2 O	3.999 ± 0.004

Table G.17-III. Bond angles in $Cs_2RuCl_5H_2O$.

Atom 1-Atom 2-Atom 3	Angle (degrees)
Cl(2)-Ru-O	88.3± 0.1
Cl(2)-Ru-Cl(2)	91.2± 0.2
Cl(2)-Ru-Cl(2)	88.7± 0.2
Cl(2)-Ru-Cl(1)	91.7± 0.1
Cs(1)-O-Cs(2)	84.1± 0.4
Cs(1)-O-Ru	95.9± 0.4

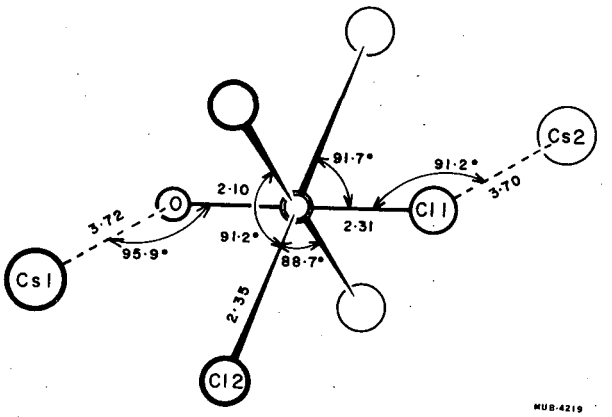

Fig. G.17-2. Ruthenium environment in $Cs_2RuCl_5H_2O$.

18. THE CRYSTAL STRUCTURE OF $(B_9C_2H_{11})Re(CO)_3Cs$ †

Allan Zalkin, Ted E. Hopkins, and David H. Templeton

π-(1)-2, 3-dicarbollylrheniumtricarbonyl was synthesized by Hawthorne and Andrews.[1] The structure work was undertaken to reaffirm the results of our previous study on the dicarbollyliron structure,[2] in $C_5H_5FeB_9C_2H_{11}$. In that study there was considerable thermal motion of the cyclopentadienyl ring, and to a lesser extent of the dicarbollyl portion, $B_9C_2H_{11}$. This thermal motion, evidenced by large thermal parameters does not permit the calculation of accurate bond distances. The $B_9C_2H_{11}Re(CO)_3Cs$ crystal does not suffer these thermal effects so badly, and the resulting structure we believe to be a more accurate description of the dicarbollyl geometry.

The work presented here confirms the geometry of this compound postulated by Hawthorne and Andrews.[1]

The crystals were sent to us by Dr. M. F. Hawthorne of the Riverside campus of the University of California. A small white crystal, ≈0.25 mm long and ≈0.08 × ≈0.08 mm in cross section, was glued to the end of a Pyrex glass fiber. All together 2452 independent intensities were measured, of which 138 were recorded as zero. A stationary-crystal stationary-counter technique using a 10-sec count for every reflection was used. The data were corrected for the Lorentz and polarization effects. No corrections were made for either absorption or extinction.

All the computations were performed on an IBM 7044 computer with a 32 K memory. Our unpublished least-squares program minimizes the function $\Sigma w(|F_o|-|F_c|)^2/\Sigma wF_o^2$, where F_o and F_c are the observed and calculated structure factors, and w is the weighting factor. All the reflections were given equal weight. The least-squares program has been modified to handle the anomalous dispersion, and these effects were included in the final set of refinements. The anisotropic temperature factors used have the form $\exp(-\beta_{11}\underline{h}^2-\beta_{22}\underline{k}^2-\beta_{33}\underline{\ell}^2-2\beta_{12}\underline{hk}-2\beta_{13}\underline{h\ell}-2\beta_{23}\underline{k\ell})$.

Unit Cell and Space Group

Four formula units of $(B_9C_2H_{11})Re(CO)_3Cs$ are contained in the monoclinic unit cell in space group $P2_1/c$ with dimensions a = 11.435±0.010 Å, b = 9.516±0.005 Å, c = 12.730±0.010 Å, and β = 92.87±0.04 deg. The errors are estimates. The calculated x-ray density is 2.57 g/cm^3. The observed extinctions correspond to the space group $P2_1/c$. The space group is centric.

The positions of the Cs and Re were easily extracted from the three-dimensional Patterson function. These heavy-atom positions were refined by least squares. A difference Fourier was calculated, and the 17 remaining atoms, excluding hydrogen, appeared as the 17 largest peaks in the patterns. The parameters of the two heavy atoms with anisotropic temperature factors, and the 17 lighter atoms with isotropic temperature factors, were refined by least squares.

A difference function was again calculated and the patterns were studied for hydrogen peaks. Among the 35 peaks whose observed electron density was greater than 0.55 electron per $Å^3$ at their peaks, 5 were close to Re, 6 were close to Cs, 7 were near the oxygen carbonyls, 10 were peaks in positions that would be suitable hydrogen atom locations, and 7 were peaks in the vicinity of the boron atoms which were either anisotropies or just spurious. The hydrogen atom near B(10) was not found. The ten hydrogen atoms were included in the ensuing refinements with these positions and an isotropic temperature factor of 4.0 $Å^2$. No attempt was made to refine the hydrogen parameters.

For the final set of refinements, all the atoms with the exception of the hydrogens were given anisotropic thermal parameters, the imaginary part of the anomalous dispersion for Cs and Re was added, and 10 hydrogen atoms were included but not refined. The final R factor was 0.042. The final results are shown in Table G.18-I.

The $B_9C_2H_{11}Re(CO)_3$ anion is shown in Fig. G.18-1. This structure was postulated by Hawthorne and Andrews[1] and has been confirmed by this work. The anion consists of the dicarbollide portion ($B_9C_2H_{11}$) to which is bonded the rhenium tricarbonyl via π bonding to the rhenium atom; the rhenium atom occupies the number 1 position in a completed icosahedron involving the dicarbollide portion. A bottom view of the structure is shown in Fig. G.18-2; this shows the orientation of the three carbonyls to the icosahedron. In the icosahedron the two carbon atoms are adjacent to each other and the Re atom. Lists of distances are shown in Table G.18-II.

The thermal motion of the atoms in the icosahedron in this structure is less than for comparable atoms in the $C_5H_5FeC_2B_9H_{11}$ structure,[2] and therefore we consider the resulting bond distances an improvement over the previous ones. In $B_9C_2H_{11}Re(CO)_3$ the average value of 18 B-B bonds, 1.78 Å, is 0.03 Å larger; the average of the 6 C-B bonds, 1.72 Å, is 0.04 larger; and the C-C bond, 1.61 Å, is 0.03 Å larger than the comparable values in the $C_5H_5FeC_2B_9H_{11}$ structure.[2] Such increases are expected, since large motions cause the observed distance to be shorter than the true average value.

In the carbonyl portion of the ion, the Re-to-C-to-O linkages are almost linear, with a slight bend of a few degrees in an outward direction away from the axis of the molecule. At the Re atom the three carbonyl carbons make very nearly right angles with respect to each other. This tricarbonyl structure is quite similar to that reported in hexamethylbenzenechromium tricarbonyl, thiophenechromium tricarbonyl, and benzenechromium tricarbonyl.[3] The carbonyl oxygens are apparently free to flop around somewhat, as their thermal parameters are larger than the carbons to which they are attached. In Table G.18-II we have included the thermally adjusted values for the C-O bond distances. These three bonds were the only bonds in the structure for which the correction due to thermal motion was larger than the estimated standard deviation of the bond length. The thermal correction is based on a calculation that assumes the oxygens are "riding on" the carbons.

The cesium ion has as its closest neighbors, at 3.2 Å, three oxygen atoms of three symmetry-unrelated carbonyls from three different anions.

The hydrogen atoms were poorly resolved in this structure determination. One hydrogen atom, H(10), was not resolved at all in the difference function.

Acknowledgment

We wish to thank Professor M. F. Hawthorne of the Riverside Campus of the University of California for providing us with the crystals which made this work possible.

Footnote and References

†Condensed from Inorganic Chemistry 5, 1189 (1966).

1. M. F. Hawthorne and T. D. Andrews, J. Am. Chem. Soc. 87, 2496 (1965).
2. A. Zalkin, D. H. Templeton, and T. E. Hopkins, J. Am. Chem. Soc. 87, 3988 (1965).
3. M. F. Bailey and L. F. Dahl, Inorg. Chem. 4, 1302, 1306, 1314 (1965).

Table G.18-I. Final positional and thermal parameters[a] in $CsB_9C_2H_{11}Re(CO)_3$.[b]

Atom	x	y	z	B11	B22	B33	B12	B13	B23
Cs	0.2766	0.1909	-0.0065	3.77	4.57	4.65	0.19	0.53	0.08
Icosahedron									
Re(1)	-0.1495	0.1406	0.2316	2.09	1.88	2.08	0.14	0.18	0.01
C(2)	-0.232	0.356	0.267	3.4	2.6	2.0	0.1	0.0	-0.2
C(3)	-0.327	0.232	0.279	2.6	2.3	2.2	0.5	0.7	0.3
B(4)	-0.342	0.138	0.164	2.3	1.9	2.8	-0.5	-0.2	-0.1
B(5)	-0.248	0.214	0.075	2.8	2.2	2.6	0.0	0.3	-0.4
B(6)	-0.176	0.358	0.145	3.3	2.2	2.3	-0.2	-0.2	0.3
B(7)	-0.377	0.404	0.269	2.8	3.6	2.2	1.0	0.0	-0.1
B(8)	-0.449	0.263	0.200	2.1	4.0	2.7	0.7	0.6	-0.1
B(9)	-0.401	0.260	0.071	2.5	3.3	3.0	0.3	0.1	-0.7
B(10)	-0.295	0.393	0.060	3.3	3.1	2.9	-0.2	0.8	1.0
B(11)	-0.282	0.483	0.180	3.6	2.9	2.8	1.2	0.2	0.6
B(12)	-0.422	0.425	0.134	3.2	4.2	2.4	0.8	0.0	0.0
Carbonyls									
C(1)-CO	-0.043	0.167	0.349	2.7	2.8	3.6	0.5	0.3	0.2
C(2)-CO	-0.021	0.092	0.153	2.4	3.3	3.0	0.4	0.4	0.5
C(3)-CO	-0.168	-0.048	0.275	4.7	2.9	2.8	0.7	0.3	0.2
O(1)-CO	0.024	0.193	0.418	4.3	6.9	4.4	1.4	-2.1	-2.2
O(2)-CO	0.057	0.065	0.102	3.6	5.0	3.6	1.5	0.7	0.3
O(3)-CO	-0.187	-0.162	0.300	7.4	2.4	7.1	-0.1	0.8	1.4
Hydrogens[c]									
H(2)	-0.20	0.40	0.34						
H(3)	-0.36	0.20	0.36						
H(4)	-0.38	0.04	0.18						
H(5)	-0.20	0.18	0.00						
H(6)	-0.10	0.42	0.12						
H(7)	-0.40	0.46	0.34						
H(8)	-0.54	0.28	0.20						
H(9)	-0.46	0.20	0.02						
H(11)	-0.26	0.60	0.20						
H(12)	-0.50	0.48	0.10						

a. Units are $Å^2$. The anisotropic values $B_{ij} = 4\beta_{ij}/a_i^* a_j^*$, where a_i^* is the ith reciprocal cell length.

b. Standard deviations of the positional parameters of Cs and Re are 0.0001 or less, and 0.001 or less for all the other atoms, excluding hydrogens. Standard deviations of the thermal parameters are 0.04 or less for Cs and Re, and 0.7 or less for all the other atoms, excluding hydrogens.

c. Hydrogen positional parameters are those from a difference Fourier, and were not refined by least squares. H(10) was not found. The labeling is parallel to the labeling in the icosahedron, i.e., H(5) is the hydrogen to B(5).

Table G.18-II. Distances in $CsB_9C_2Re(CO)_3$.[a]

Atom	Atom	Distance (Å)
Re(1)	- C(1)-CO	1.90
Re(1)	- C(2)-CO	1.88
Re(1)	- C(3)-CO	1.90
Re(1)	- C(2)	2.31
Re(1)	- C(3)	2.31
Re(1)	- B(4)	2.32
Re(1)	- B(5)	2.35
C(2)	- C(3)	1.61
C(2)	- B(6)	1.71
C(2)	- B(7)	1.72
C(2)	- B(11)	1.72
C(3)	- B(4)	1.71
C(3)	- B(7)	1.71
C(3)	- B(8)	1.74
B(4)	- B(5)	1.76
B(4)	- B(8)	1.78
B(4)	- B(9)	1.77
B(5)	- B(6)	1.81
B(5)	- B(9)	1.80
B(5)	- B(10)	1.80
B(6)	- B(10)	1.73
B(6)	- B(11)	1.78
B(7)	- B(8)	1.78
B(7)	- B(11)	1.77
B(7)	- B(12)	1.77
B(8)	- B(9)	1.76
B(8)	- B(12)	1.79
B(9)	- B(10)	1.76
B(9)	- B(12)	1.79
B(10)	- B(11)	1.76
B(10)	- B(12)	1.79
B(11)	- B(12)	1.76
C(1)-CO	-O(1)-CO	1.16(1.20)[b]
C(2)-CO	-O(2)-CO	1.16(1.18)[b]
C(3)-CO	-O(3)-CO	1.15(1.19)[b]
Cs	- O(1)-CO	3.20[c]
Cs	- O(2)-CO	3.16[c]
Cs	- O(3)-CO	3.20[c]

a. Estimated standard deviations on the distances involving Cs and Re is ≈0.01 Å; all other distances have standard deviations of ≈0.02 Å.

b. Corrected for thermal motion assuming the O rides on the C. This was the only set for which the thermal effect was larger than the estimated standard deviations.

c. Nearest neighbors to the cesium ions. Each oxygen is from a different molecule.

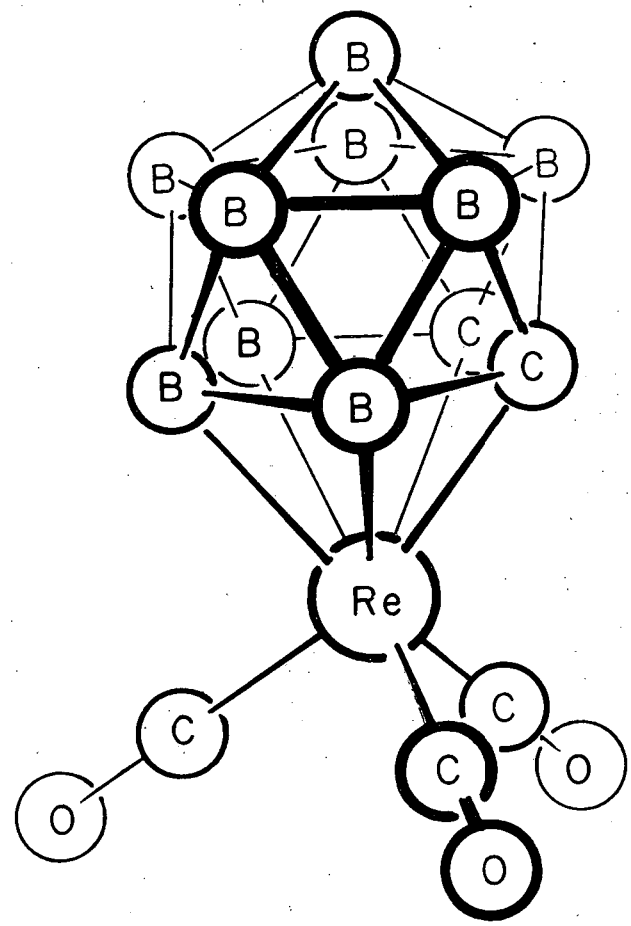

MUB-6462

Fig. G.18-1. $B_9C_2H_{11}Re(CO)_3^-$ ion (hydrogens excluded).

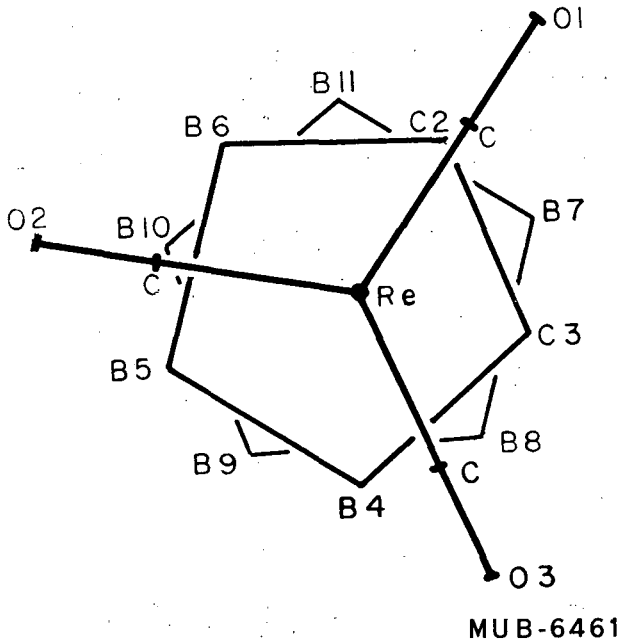

Fig. G.18-2. Bottom view of $B_9C_2H_{11}Re(CO)_3^-$ ion (hydrogens excluded), showing the orientation of the three carbonyls to the icosahedron.

19. THE CRYSTAL STRUCTURE OF CHLOROTHIODIAZYL CHLORIDE, $S_3N_2Cl_2$ †

Allan Zalkin, Ted E. Hopkins, and David H. Templeton

$S_3N_2Cl_2$ was first identified by Demarcay,[1] who prepared it by reacting SCl_2 or S_2Cl_2 with S_4N_4. Meuwsen[2] prepared $S_3N_2Cl_2$ by reacting $(NSCl)_3$ with S_2Cl_2. More recently Jolly, Maguire, and Rabinovich[3] produced the material by refluxing a suspension of ammonium chloride in S_2Cl_2. An x-ray crystal-structure analysis was undertaken to determine the molecular structure of this compound.

$S_3N_2Cl_2$ is a yellow crystalline salt which decomposes in the air. A single crystal fragment was isolated and wedged in a capillary; the fragment was an irregular plate with dimensions approximately 0.3×0.4×0.2 mm. Some decomposition of the crystal surface did occur as the crystal lost its yellow color and took on a blackish tinge; however, the crystal diffracted x rays well, and no further decomposition was encountered.

The measured monoclinic cell dimensions based on $\lambda_{K\alpha 1}$ = 0.70926 Å are a = 6.546±0.007 Å, b = 8.600±0.004 Å, c = 5.508±0.005 Å, and β = 102.37±0.03 deg. The observed density was 2.0 g/ml, suggesting two formula units per unit cell; the calculated x-ray density is 2.14±0.01 g/ml. The observed extinctions are 0k0, k = 2n+1, and the space group is $P2_1$.

One thousand twenty-two independent reflections were each counted for 10 sec, using a stationary-crystal stationary-counter technique.

All the computations were performed with an IBM 7044 computer with a 32K memory. The least-squares program used minimizes the function $\Sigma w(|F_o|-|F_c|)^2/\Sigma wF_o^2$, where w is the weighting factor, F_o and F_c are the observed and calculated structure factors. All the reflections were given unit weights with the exception of the six most intense reflections, which toward the end of the computations were given zero weight. Anistropic temperature factors have the form $\exp-(h^2\beta_{11}+k^2\beta_{22}+l^2\beta_{33}+2hk\beta_{12}+2hl\beta_{13}+2kl\beta_{23})$; however, for our convenience the program converts these thermal parameters to B_{ij} in Å^2, where $B_{ij} = 4\beta_{ij}/a_i^* a_j^*$ and a_1^* is the ith reciprocal axis length.

The "unreliability index" reported throughout this paper is $R = \Sigma||F_o|-|F_c||/\Sigma|F_o|$.

The structure was deduced from the three-dimensional Patterson function. A careful investigation of the function gave us trial positions for the three sulfur, two chlorine, and one nitrogen atoms: a Fourier based on the phases of the six-atom structure then gave the last nitrogen atom. The final identification of the sulfur and chlorine atoms was determined by studying the structure geometry and the interatomic distances. Anisotropic temperature factors were applied to all the atoms. The R was 0.0292. The introduction of the imaginary dispersion correction increased R to 0.0293; the y parameters were all reversed and R became 0.0291. This difference is so small that there may be some doubt concerning which structure is correct, but we report the one which gave the best agreement. The other structure is almost identical except that the two nitrogen atoms are shifted 0.014 Å toward zero along the y axis. The only bond lengths which are significantly different are S(1)-N(1) and S(1)-N(2), which are respectively longer and shorter by about 0.010 Å in the other structure. This relative shift of light and heavy atoms along a polar direction when refined in this manner, or "polar dispersion shift," is an effect which has also been observed in thorium nitrate pentahydrate[4] and in a diiodocyclobutene,[5] and which is explained in more detail elsewhere.[5] In this case the ambiguity is of trivial importance to the chemical interpretation.

Results

A list of the atomic and thermal parameters of $S_3N_2Cl_2$ is shown in Table G.19-I.

The most interesting result of this work is the apparent ionic nature of the material. The material consists of a $S_3N_2Cl^+$ ion and a Cl^- ion. The chloride ion is Cl(2), and its closest approaches are to S(1) at 2.90 Å, S(3) at 2.93 Å, and S(2) at 3.04 Å. Figure G.19-1 shows a sketch of the $S_3N_2Cl^+$ ion labeled with distances and angles.

The three sulfurs and two nitrogens form a slightly puckered five-membered ring with a Cl atom, Cl(1) attached to the thio sulfur, i.e., Cl-S-N-S-N-S. The puckering can be described as a chair form in the following sense: If a plane is drawn through the three sulfur atoms, the Cl (1) atom is 2.09 Å above the plane, N(1) is 0.188 Å below the plane, and the opposing N(2) atom is 0.140 Å above the plane.

The five-membered ring in $S_3N_2Cl_2$ is the smallest such ring system in a series of cyclic azyl systems. Six-membered rings are present in $(NSOCl)_3$,[6] $(NSCl)_3$,[7] and $(NSF)_3$;[8] a seven-membered ring is present in $S_4N_3NO_3$;[9] and an eight-membered ring in $N_4S_4H_4$.[10] In all these cases the nitrogens are separated by sulfur, and halogen, when present, is bonded to sulfur.

Figure G.19-2 shows the packing in the crystal as seen in projection down the c axis.

Footnote and References

†Condensed from Inorg. Chem. 8, 1767 (1966).

1. E. Demarcay, Compt. rend. 92, 726 (1881).
2. A. Meuwsen, Ber. deut. Chem. Ges. 65, 1731 (1932).
3. W. L. Jolly, K. D. Maguire, and D. Rabinovich, Inorg. Chem. 2, 1304 (1963).
4. T. Ueki, A. Zalkin, and D. H. Templeton, Acta Cryst. 20, 836 (1966).
5. G. L. Hardgrove, L. K. Templeton, and D. H. Templeton (LRL), unpublished work.
6. A. C. Hazell, G. A. Wiegers, and A. Vos, Acta Cryst. 20, 192 (1966).
7. G. A. Wiegers and A. Vos, Acta Cryst. 20, 192 (1966).
8. G. A. Wiegers and A. Vos, Acta Cryst. 14, 562 (1961).
9. A. W. Cordes, R. F. Kruh, and E. K. Gordon, Inorg. Chem. 4, 681 (1965).
10. E. W. Lund and S. R. Svendsen, Acta Chem. Scand. 11, 940 (1957).

Table G.19-I. Positional[a] and thermal[b] parameters in $S_3N_2Cl_2$.

Atom	x	y	z	B11	B22	B33	B12	B13	B23
Cl(1)	0.1017	0.0[c]	0.4844	3.32	5.33	3.63	1.18	1.51	1.24
Cl(2)	0.1975	-0.3541	0.1028	2.86	2.83	3.08	0.11	0.50	-0.09
S(1)	0.6099	0.1671	0.3235	2.37	3.48	2.81	0.37	0.37	-0.11
S(2)	0.2303	0.0264	0.1552	2.69	2.14	2.82	0.13	0.88	0.11
S(3)	0.2161	0.2734	0.1148	2.56	2.10	3.61	0.11	0.06	0.13
N(1)	0.4756	0.0105	0.2436	2.54	2.88	3.60	0.85	1.02	0.46
N(2)	0.4558	0.3039	0.2549	2.98	2.68	3.55	-0.10	0.30	-0.89

a. Estimated standard deviations of the positional parameters for S and Cl are less than 0.0003, and for N are less than 0.0008.
b. Estimated standard deviations of the thermal parameters for S and Cl are about 0.05, and for N are about 0.2. Units of Bij are $Å^2$.
c. Polar space group $P2_1$ requires that one y parameter be fixed.

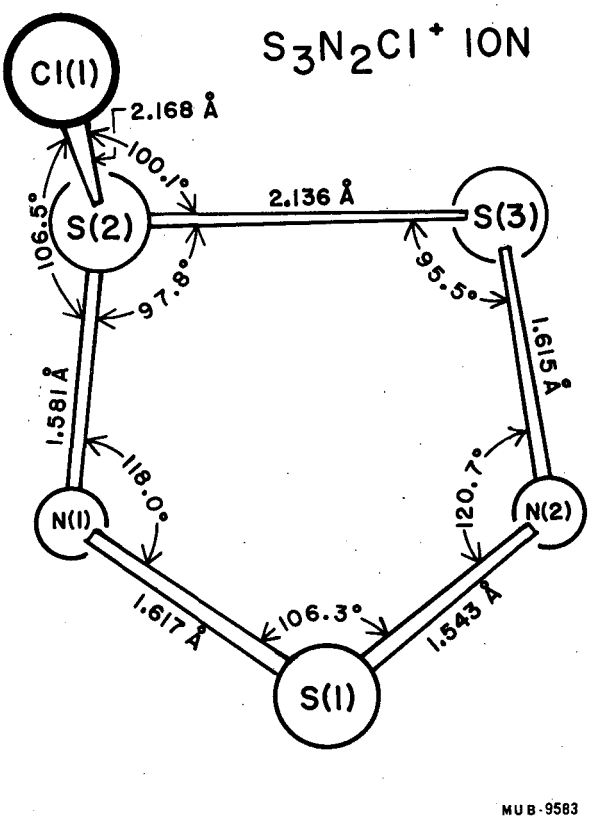

Fig. G.19-1. Distances and angles in $S_3N_2Cl^+$. The estimated standard deviations are about 0.005 Å on the distances, and about 0.3 deg on the angles.

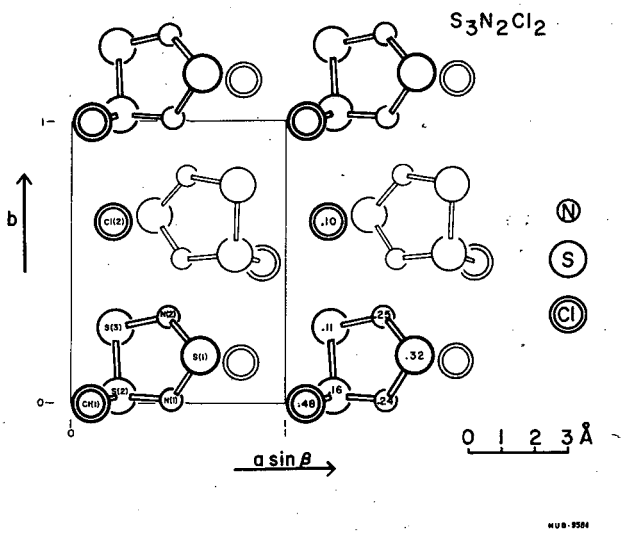

Fig. G.19-2. Projection of $S_3N_2Cl_2$ down the c axis.

20. THE ATOMIC PARAMETERS IN THE LANTHANUM TRIFLUORIDE STRUCTURE†

Allan Zalkin, David H. Templeton, and Ted E. Hopkins

Crystals of LaF_3 exhibit a structure that is typical of numerous trifluorides of lanthanide and actinide elements. In 1931 Oftedal[1] suggested a structure, based on a study of crystals of the mineral tysonite, with the assumption that the space group is $P6_3/mcm$, but with atomic coordinates which correspond almost to the symmetry $P6_3/mmc$ with a smaller unit cell. The evidence for the larger cell is the presence of weak reflections which may easily escape detection in powder diagrams. Schlyter[2] failed to see these reflections with tysonite crystals, but Templeton and Dauben[3] found them with a synthetic crystal of CeF_3. The atomic positions given by Oftedal give lanthanum a peculiar coordination geometry with five nearest neighbors and six more neighbors at a greater distance.

We were prompted to study LaF_3 again by the availability of excellent synthetic crystals and recent interest in the spectroscopic properties of ions in this structure. When we had nearly finished the determination of the structure, we learned that Mansmann[4] had independently reached the same conclusions concerning the symmetry and assignment of atoms to point sets, without reporting atomic coordinates.

We conclude that Oftedal's cell is correct and that his coordinates for La are quite accurate, but that the crystals are trigonal rather than hexagonal. Because of his failure to recognize this point symmetry, Oftedal did not consider the correct space group, and he misplaced most of the F atoms. In our structure, each La is on a twofold axis and has nine neighbors (a normal number) at nearly equal distances.

A large crystal of lanthanum trifluoride, purported to be 99.999% pure, was sent to us by Dr. Kenneth Lee of Varian Associates in Palo Alto. A fragment of this crystal, about 0.1 to 0.2 mm, was glued to the end of a Pyrex fiber with the hexagonal axis parallel to the fiber axis. The crystal was rapidly dipped into liquid nitrogen several times in an attempt to diminish extinction effects by increasing the mosaic spread by thermal shock, but no effect was observed in the intensities before and after the treatment. Diffraction angles and intensities were measured with an Eulerian cradle goniostat equipped with a scintillation counter using Mo Kα radiation [$\lambda(K\alpha_1) = 0.70926$ Å]. The cell dimensions measured at 22°C are: $a = 7.185 \pm 0.001$, $c = 7.351 \pm 0.001$ Å, in excellent agreement with the values reported by Swanson, et al.[5] The density calculated with six molecules per cell is 5.938 g/ml.

The diffraction intensities correspond to Laue symmetry $\bar{3}ml$, but there are clear violations of symmetry 6/mmm and 6/m; i.e., $I(hkl) = I(h+k, -k, l)$, but $I(hkl) \neq I(-k, h+k, l)$. Thus the crystals are trigonal rather than hexagonal (in the strict sense). The failure of previous workers to recognize the lower symmetry may be the result of twinning in their specimens, or the result of low accuracy of intensities estimated from films.

We failed to detect any pyroelectric effect when a large crystal fragment, suspended on a thread, was dipped into liquid nitrogen; when withdrawn the crystal showed no attraction for the side of the Dewar. The systematic absences, (hOl) absent if $l = 2n + 1$, correspond to space groups P3c1 and $P\bar{3}c1$. We conclude that the crystals are centric because a reasonable structure is found in space group $P\bar{3}c1$ (D_{3d}^4), No. 165 in the International Tables.[6]

The intensity measurements included 951 independent reflections (all positive hkl with $2\theta < 90$ deg) of which 65 were recorded as zero. The data were corrected for the Lorentz-polarization effects. The absorption factor μ was estimated to be ≈ 200 cm^{-1}, and the μR for the crystal was estimated ≈ 2. The data were not corrected for absorption. An empirical extinction correction was made based on an approximation suggested by Zachariasen,[7] where $F_{corrected} \approx F_{observed}(1.0 + CJ)$, where F is the scaled structure factor, J is the raw observed intensity, and C is an adjustable constant.

The structure given by Oftedal[1] can be fitted to space group $P\bar{3}c1$ by assigning the atoms to point sets as listed in Table G. 20-I. Prior to the extinction correction, we attempted to refine this structure with a full-matrix least-squares program, with trial-and-error displacements of various atoms to break the higher symmetry. The first set of refinements went poorly; i.e., the R factor, $R = \Sigma||F_o| - |F_c||/\Sigma|F_o|$, stayed high ($\approx 0.15$) and the temperature factor for the twofold fluorine "blew up." Different trial structures and the use of a noncentric space group

(P3c1) gave even worse results. We observed what appeared to be severe extinction effects, and by deleting some low-angle data which included some of the larger intensities, definite improvement in the refinement was effected. A plot of F_o/F_c (observed and calculated structure factors) versus the intensities showed a very definite extinction-type correlation. From this plot a value for C in the extinction correction was obtained, and then it was adjusted in the least-squares refinement. The extinction was so severe that the two most intense reflections were observed as one-eighth of their calculated values. In the final refinements the anomalous dispersion factors for La^{+3} were included ($\Delta f' = -0.4$, $\Delta f'' = 2.9$ electrons).[8] An anisotropic temperature factor of the form $\exp-(h^2\beta_{11}+k^2\beta_{22}+l^2\beta_{33}+2hk\beta_{12}+2hl\beta_{13}+2kl\beta_{23})$ was applied to lanthanum, with suitable constraints because of the twofold axis, and an isotropic temperature factor of the form $\exp-(B\sin^2\theta/\lambda^2)$ was applied to each fluorine. The five most intense reflections, and seven of the reflections with the worst agreement, were deleted from the final refinements. The final R factor was 0.052.

Tables G.20-I and G.20-II show the final positional and thermal parameters respectively. The standard deviations shown in these tables are estimates by the authors rather than the results of the least-squares computation, and in all cases are considerably larger than the calculated values. These estimates resulted from a study of the parameters as conditions of the refinement were modified. The parameters changed considerably more than the calculated standard deviations when just high-angle data were used or when the extinction correction was introduced. Our estimates of the standard deviations bracket these fluctuations more realistically, and because of the highly nonrandom nature of the errors here, the authors believe that an educated guess is preferable to a mathematical fiction. The thermal parameters (other than B13 and B23) are systematically lower than the true values, because of neglect of absorption, by an unknown amount estimated to be about 0.6 $Å^2$. This effect is not included in the estimated standard deviations. Table G.20-III shows a list of interatomic distances.

The structure we find has lanthanum in almost exactly the positions reported by Oftedal. The fluorine atoms have been shifted so that of the six second-nearest neighbors of each lanthanum, four have moved closer and two have moved away; thus lanthanum has a normal coordination number of nine. We have failed to find any simple description for the geometry of these neighbors. Each fluorine has three lanthanum neighbors. A sketch showing the ninefold coordination of lanthanum as viewed down the c axis is shown in Fig. G.20-1.

Footnote and References

†Inorganic Chem. 5, 1466 (1966).
1. I. Oftedal, Z. physik. Chem. [B5] B13, 190 (1931).
2. K. Schlyter, Ark. Kemi 5, 73 (1953).
3. D. H. Templeton and C. H. Dauben, J. Am. Chem. Soc. 75, 4650 (1953).
4. Von M. Mansmann, Z. anorg. Chem. 331, 98 (1964).
5. H. E. Swanson, N. T. Gilfrich, and M. I. Cook, Standard x-Ray Diffraction Patterns, National Bureau of Standards Circular 539, 7, 21 (1957).
6. International Tables for X-Ray Crystallography (Kynoch Press, Birmingham, England, 1952), p. 271.
7. W. H. Zachariasen, Acta Cryst. 16, 1142 (1963).
8. D. T. Cromer, Acta Cryst. 18, 17 (1965).

Table G. 20-I. Positional parameters in lanthanum trifluoride.

No.	Atom	Point symmetry	Positions and positional parameters
6	La	2	$\pm(x, 0, 1/4; 0, x, 1/4; \bar{x}, \bar{x}, 1/4)$
			$x = 0.3401 \pm 0.0005$
12	F(1)	1	$\pm(x, y, z; \bar{y}, x-y, z; y-x, \bar{x}, z;$
			$\bar{y}, \bar{x}, 1/2+z; x, x-y, 1/2+z; y-x, y, 1/2+z)$
			$x = 0.312 \pm 0.002$
			$y = -0.055 \pm 0.002$
			$z = 0.581 \pm 0.002$
4	F(2)	3	$\pm(1/3, 2/3, z; 1/2, 2/3, 1/2+z)$
			$z = 0.313 \pm 0.002$
2	F(3)	32	$\pm(0, 0, 1/4)$

Table G. 20-II. Temperature factors ($Å^2$)[a] in lanthanum trifluoride.

Atom	Temperature factors		
La	$B11 = 0.6 \pm 0.2$	$B22 = 0.6 \pm 0.2$	$B33 = 0.8 \pm 0.2$
	$B12 = 0.3$[b]	$B13 = -0.025$[b]	$B23 = -0.05 \pm 0.01$
F(1)	$B = 1.3 \pm 0.4$		
F(2)	$B = 1.0 \pm 0.4$		
F(3)	$B = 1.7 \pm 0.7$		

a. Anisotropic $B_{ij} = \beta_{ij}/4a_i^* a_j^*$, where a_i^* is the ith reciprocal axis length.

b. Symmetry considerations force $B22 = 2B12$ and $B23 = 2B13$.

Table G.20-III. Interatomic distances of less than 3 Å in lanthanum trifluoride.

Atom Atom	Distance (Å)	Atom Atom	Distance (Å)
La - 2 F(2)	2.416 ± 0.003	F(1) - 1 F(2)	2.69 ± 0.02
La - 1 F(3)	2.443 ± 0.004	F(1) - 2 F(1)	2.74 ± 0.02
La - 2 F(1)	2.46 ± 0.02	F(1) - 1 F(3)	2.76 ± 0.01
La - 2 F(1)	2.49 ± 0.01	F(1) - 1 F(2)	2.79 ± 0.01
La - 2 F(1)	2.64 ± 0.01	F(1) - 1 F(2)	2.87 ± 0.02
La - 2 F(1)	3.01 ± 0.01	F(2) - 3 La	2.416±0.003
F(1)- 1 La	2.46 ± 0.02	F(2) - 3 F(1)	2.69 ±0.02
F(1)- 1 La	2.49 ± 0.01	F(2) - 3 F(1)	2.79 ±0.01
F(1)- 1 La	2.64 ± 0.01	F(2) - 3 F(1)	2.87 ±0.02
F(1)- 1 La	3.01 ± 0.01	F(3) - 3 La	2.443±0.004
F(1)- 1 F(1)	2.57 ± 0.03	F(3) - 6 F(1)	2.76 ±0.01
F(1)- 1 F(1)	2.68 ± 0.03		

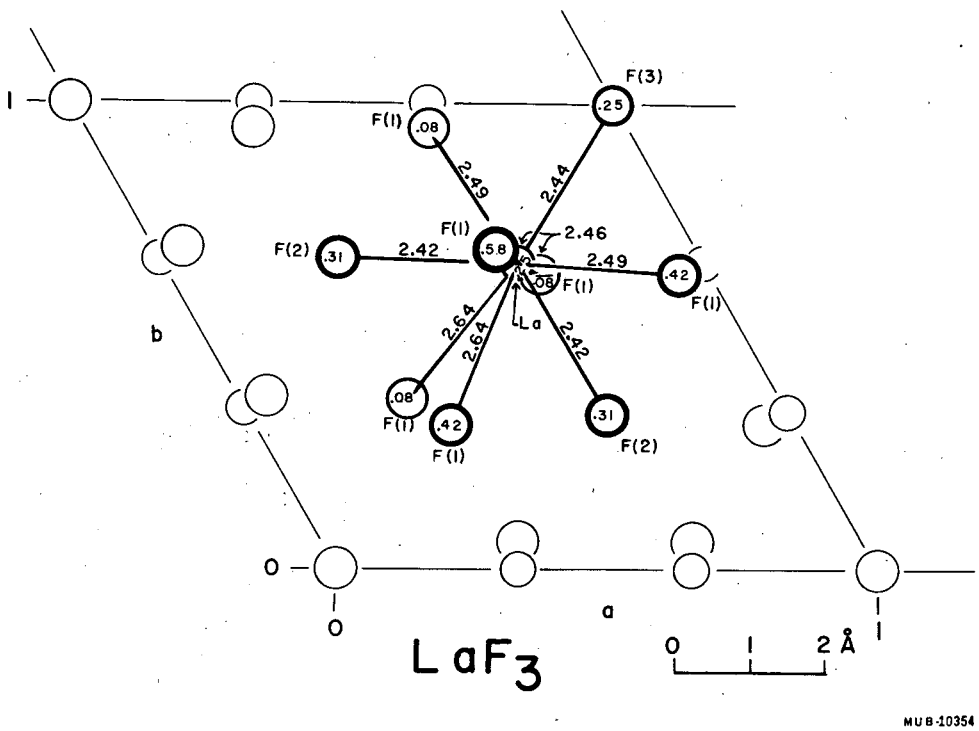

Fig. G.20-1. The ninefold coordination of La in LaF_3 as viewed down the c axis.

21. STUDIES OF OXYGEN-INITIATED PYROLYSIS OF HYDROCARBONS

Edwin D. Hausmann* and C. Judson King

Measurements have been made of the rate of pyrolysis of ethylbenzene in the presence and absence of trace amounts of oxygen.[1,2] A flow reactor system, shown in Fig. G.21-1, was employed, with residence times on the order of 0.1 sec, with a nitrogen diluent and with temperatures of 570 to 650°C.

Runs made in the absence of oxygen are summarized in Fig. G.21-2, and may be correlated by a rate expression $r = 3\times10^{13}[\exp(-70\,000/RT)][EB]^{1/2}$, where r = rate in g mole/cm^3 sec, R = 1.98 cal/g mole °K, T = temperature in °K, and [EB] is the ethylbenzene concentration in g mole/cm^3. This expression can be rationalized by a mechanism of the Rice-Herzfield variety.

The effect of traces of oxygen on the rate is shown in Fig. G.21-3. These results suggest an additional chain initiation step due to oxygen, along with an inhibiting termination reaction caused by oxygen at higher concentrations. Oxygen initiation has a lower activation energy than thermal initiation, and hence is more pronounced at lower temperatures.

The reaction selectivity is 74% to styrene in the absence of oxygen, the other aromatic products being benzene and a small amount of toluene. The selectivity to styrene increases to 81% with 10% oxygen.

Footnote and References

*Present address: Standard Oil Company of California, San Francisco, California.

1. E. D. Hausmann and C. J. King, Oxygen-Initiated Pyrolysis of Ethylbenzene, UCRL-16021, March 1965.
2. E. D. Hausmann and C. J. King, Ind. Eng. Chem. Fundamentals 5, 295 (1966).

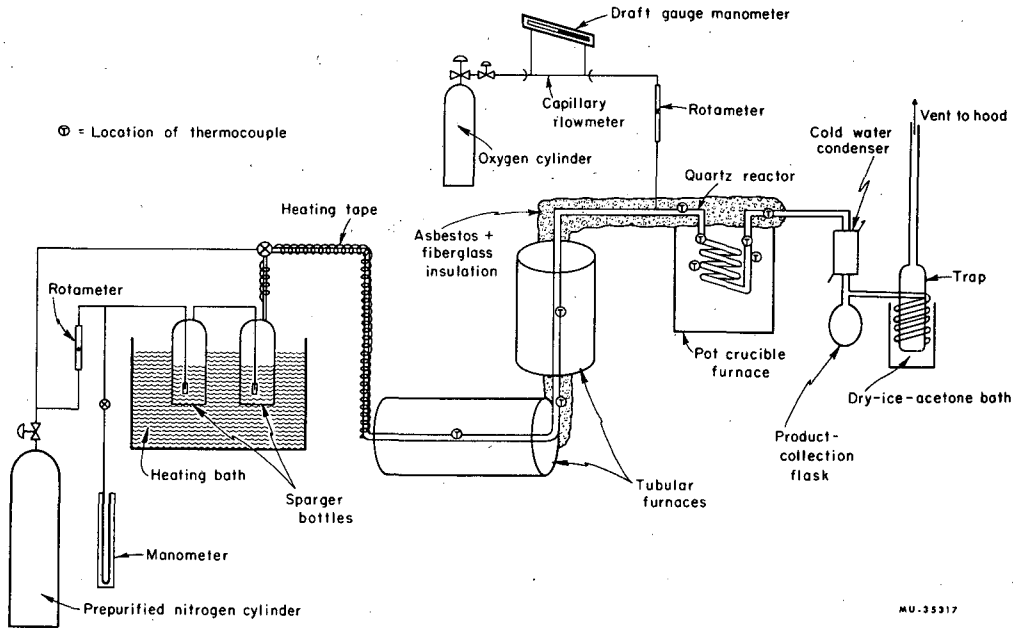

Fig. G.21-1. Schematic diagram of pyrolysis apparatus.

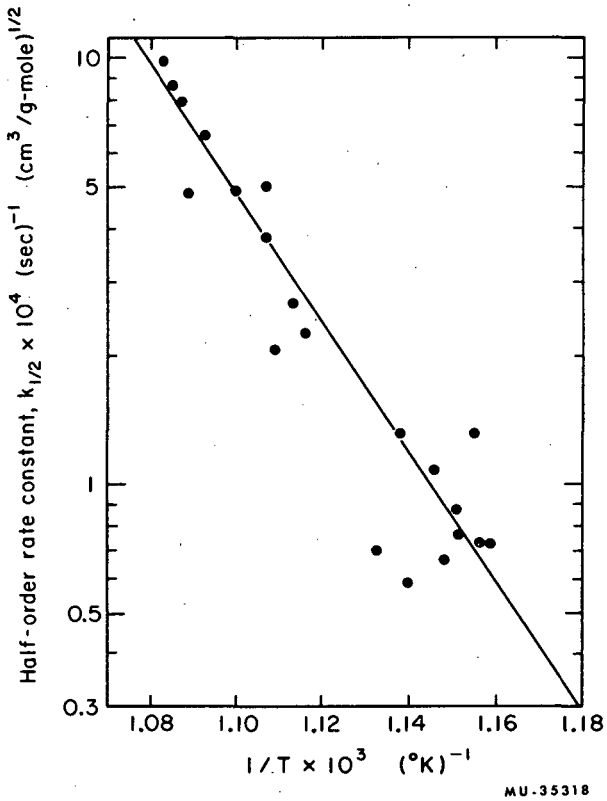

Fig. G.21-2. Arrhenius plot for pyrolysis in the absence of oxygen.

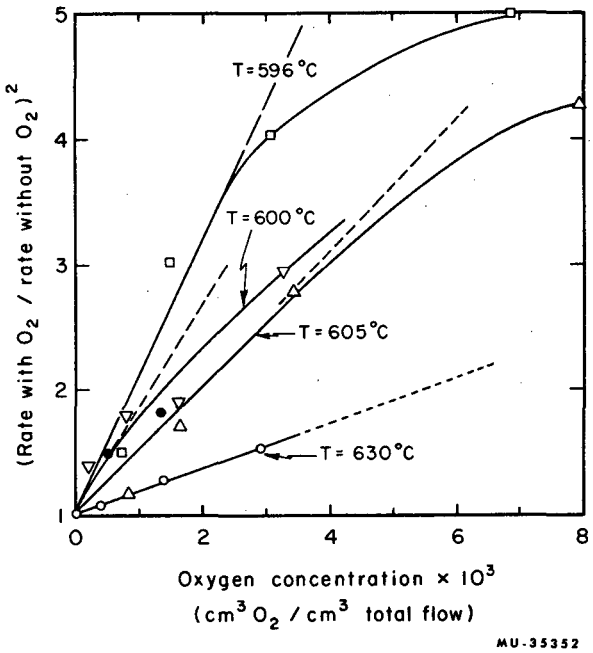

Fig. G.21-3. Increase of rate due to oxygen.

Temp. (°C)	Res. time (sec)	(EB)× 10^4 (g/cc)
▽ 600	0.08	0.7
□ 596	0.12	1.1
● 593	0.17	0.8
△ 605	0.12	1.3
○ 630	0.17	0.5

22. CHEMICAL EVIDENCE FOR MAIN-CHAIN SCISSION AS A MAJOR DECOMPOSITION MODE IN THE RADIOLYSIS OF SOLID PEPTIDES†

Warren M. Garrison, Michael E. Jayko, Boyd M. Weeks
Harvey A. Sokol, and Winifred Bennett-Corniea

We find that a major chemical effect of ionizing radiation on peptide derivatives of the aliphatic α-amino acids is the formation of labile "amidelike" products which are readily degraded to yield ammonia on mild hydrolysis. The N-acetyl derivatives of alanine, valine, and leucine, for example, give $G(NH_3)$ values of 3.8, 3.0, and 2.7 (molecules/100 eV) respectively on irradiation with ^{60}Co γ rays in vacuo; the irradiated solids were dissolved in water in the absence of oxygen and hydrolyzed for 90 min in 2 N HCl to effect a quantitative liberation of ammonia, which was then assayed after the method of Conway.[1]

A detailed study of other reaction products from N-acetylalanine has been made to obtain evidence as to the mechanism of the radiation-induced degradation. Organic acids were assayed by gas-phase chromatography[2] and by partition chromatography.[3,4] In certain runs, the acetylalanine was "spiked" with $CH_3CONHCH(CH_3)C^{14}OOH$ to facilitate product identification; the radiometric techniques have been described.[4] Carbonyl products were determined as the 2,4-dinitrophenylhydrazone derivatives.[4,5] A colorimetric method[6] was used to set a limit on the yield of lactic acid. Gaseous products were pumped off following complete dissolution of an irradiated

sample in degassed water on the vacuum line. Gases were analyzed by mass spectroscopy. A Varian EPR spectrometer, Model E-3, was used to measure the production of spin centers in the irradiated solids.

The evidence is that the observed radiolytic degradation of acetylalanine cannot be represented simply in terms of the rearrangement

$$\mathrm{RCONHCH(CH_3)R} \xrightarrow{\sim\sim} \mathrm{RCONH_2} + \mathrm{C(H)=CH_2\text{-}R}, \qquad (1)$$

since we find G(acrylic acid) < 0.2. The possibility that the N, O shift

$$\mathrm{RCONHCH(CH_3)R} \xrightarrow{\sim\sim} \mathrm{R\text{-}C(NH)\text{-}O\text{-}C(H)(CH_3)\text{-}R} \qquad (2)$$

occurs in high yield and leads to ammonia formation through subsequent hydrolysis of the labile-imino ester

$$\mathrm{2H_2O} + \mathrm{R\text{-}C(NH)\text{-}O\text{-}C(H)(CH_3)\text{-}R} \xrightarrow{\sim\sim} \mathrm{RCOOH} + \mathrm{NH_3} + \mathrm{CH_3CH(OH)R} \qquad (3)$$

is negated by the fact that G(lactic acid) ≤ 0.2. Similarly, we conclude that the production of dehydropeptide via

$$\mathrm{RCONHCH(CH_3)R} \xrightarrow{\sim\sim} \mathrm{R\text{-}C(=O)\text{-}N=C(CH_3)\text{-}R} + \mathrm{H_2(2H)} \qquad (4)$$

is relatively unimportant in view of the fact that we find G(pyruvic acid) ≈ 0.4; the dehydropeptides are hydrolyzed quantitatively to yield carbonyl and ammonia,

$$\mathrm{2H_2O} + \mathrm{R\text{-}C(=O)\text{-}N=C(CH_3)\text{-}R} \longrightarrow \mathrm{RCOOH} + \mathrm{NH_3} + \mathrm{CH_3COR}, \qquad (5)$$

under the conditions of hydrolysis employed here.[7] Additional evidence that the dehydrogenation reaction 4 occurs in low yield is given by the gas-yield data, which show $G(H_2) = 0.4$.[8]

We do find that propionic acid is produced as a major product, G(propionic acid ≈ 1.2). It is clear that main-chain scission occurs, and the simplest formulation in accord with present observations is given by

$$\mathrm{RCONHCH(CH_3)} \xrightarrow{\sim\sim} \mathrm{RCO\dot{N}H} + \mathrm{\dot{C}H(CH_3)R} \qquad (6)$$

followed by the abstraction reactions

$$\mathrm{RCO\dot{N}H} + \mathrm{RCONHCH(CH_3)R} \longrightarrow \mathrm{RCONH_2} + \mathrm{RCONH\dot{C}(CH_3)R}, \qquad (7)$$

$$\mathrm{\dot{C}H(CH_3)R} + \mathrm{RCONHCH(CH_3)R} \longrightarrow \mathrm{CH_2(CH_3)R} + \mathrm{RCONH\dot{C}(CH_3)R} \qquad (8)$$

to give amide, fatty acid and the long-lived α-carbon radicals, which have been observed in irradiated peptides at room temperatures through EPR spectroscopy.[9,10] On dissolution in water (oxygen-free), the α-carbon radicals $R\dot{C}ONHC(CH_3)R$ undergo dimerization to yield the α,α-diaminosuccinic acid derivative.[11] The formulation of reactions 6, 7, and 8 is intended only to convey the nature of the overall reaction stoichiometry.[12] Ionic or "hot" radical intermediates presumably are involved, since cage effects in the condensed medium would lead to preferential radical recombination.

We estimate from EPR measurements that the yield of the long-lived α-carbon radicals is roughly $G \approx 3$. This value and the propionic acid yield value of $G = 1.2$ are somewhat lower than would be predicted from the reaction sequence 6, 7, 8 on the basis of G(amide) ≈ 3. The apparent discrepancy may be understood if a fraction of the $\dot{C}H(CH_3)R$ radicals is removed through radical-radical interactions in the spur-regions of high radical concentration. That the "amide" type of radiolytic degradation of the peptide chain is not confined to the N-acylamino acid configuration is shown by the fact that the G values for ammonia and propionic acid from poly-D, L-alanine are almost identical with those obtained with N-acetylalanine.

It has been suggested that the long-lived α-carbon radicals are produced in peptide radiolysis through side-chain cleavage[13,14], e.g.,

$$RCONHCH(CH_3)R \longrightarrow RCONH\dot{C}(CH_3)R + H \qquad (9)$$

followed by $$H + RCONHCH(CH_3)R \longrightarrow RCONH\dot{C}(CH_3)R + H_2, \qquad (10)$$

where H formed in Reaction 9 may have excess kinetic energy. However, the low $G(H_2)$ values observed in the γ radiolysis of simple peptides, polypeptides, and protein[8] do not support the concept that Reaction 10 represents a major source of α-carbon radicals. On the other hand, Reaction 9 followed by

$$H + RCONHCH(CH_3)R \longrightarrow RCONH_2 + \dot{C}H(CH_3)R \qquad (11)$$

(or the equivalent heterolytic steps involving e^- and H^+) would satisfy the requirement of main-chain scission. Note that the stoichiometry of Reactions 9 and 11 followed by 8 is equivalent to that given by the reaction sequence 6, 7, 8.

Acknowledgment is due to Mrs. Sibyl A. Cole for assistance in some of the measurements.

Footnote and References

†To be submitted to J. Phys. Chem.

1. E. J. Conway, Microdiffusion Analysis (Crosby Lockwood and Son, Ltd., London, 1962).
2. E. M. Emery and W. E. Koerner, Anal. Chem. 33, 146 (1961).
3. C. S. Marvel and R. Rands, J. Am. Chem. Soc. 72, 2642 (1950).
4. B. M. Weeks, S. A. Cole, and W. M. Garrison, J. Phys. Chem. 69, 4131 (1965).
5. G. R. A. Johnson and G. Scholes, Ind. Eng. Chem., Anal. Ed. 79, 217 (1954).
6. F. Feigl, Spot Tests in Organic Analysis (Elsevier Publishing Co., 1956), p. 346.
7. J. P. Greenstein and M. Winitz, Chemistry of Amino Acids (John Wiley & Sons Inc., New York, N. Y., 1961).
8. Hydrogen yields from compounds containing the peptide bond are uniformly low. We have found initial $G(H_2)$ values of 0.45, 0.85, and 0.22 for polyalanine, nylon, and gelatin respectively. See M. E. Jayko and W. M. Garrison, Abstract 465, Abstract of Papers, Third International Congress of Radiation Research, Cortina, Italy, June 26 to July 2, 1966.
9. R. C. Drew and W. Gordy, Radiation Res. 18, 552 (1963).
10. N. C. Box, H. G. Freund, and K. Lilga, in Free Radicals in Biological Systems, Ed. by M. Blois et al. (Academic Press, New York, 1961).
11. W. M. Garrison and B. M. Weeks, Radiation Res. 17, 341 (1962).
12. The propionic acid yield from acetylalanine increases linearly with dosage up to 10^{21} eV/g and the dose-yield plot extrapolates through the origin. We conclude from this that propionic acid is not produced through the reduction by e^- or H of acrylic acid formed in reactions akin to 1. However, we cannot rule out the possibility that acrylic acid establishes a steady state at a concentration level below that detectable by our present

analytical techniques.
13. R. Braams, Nature 200, 152 (1966).
14. P. Riesz, F. N. White, Jr., and H. Kon, J. Am. Chem. Soc. 88, 872 (1966).

23. IDENTIFICATION OF A SPECIFIC MODE OF OXIDATION IN THE RADIOLYSIS OF THE PURINE BASES IN OXYGENATED AQUEOUS SOLUTION†

John Holian and Warren M. Garrison

The pyrimidine and purine moieties represent major sites of chemical degradation in the radiolysis of nucleic acids in aqueous solutions containing molecular oxygen.[1,2] Radiation chemical studies of representative pyrimidines such as cytosine, uracil, and thymine in dilute aqueous solution have shown that OH radicals formed in the radiation decomposition of water add preferentially to the 5, 6 carbon-carbon double bond to form the hydroxypyrimidyl radical.[1,3-5] In oxygenated solution, this radical is scavenged by oxygen and in subsequent steps yields the 5, 6 glycol as one of the radiolysis products.[1,3,4]

Reaction stoichiometries in the radiolysis of the purines in oxygenated solution are yet to be established.[2,6] Adenine has received the most attention and is reported by Scholes and Weiss[1,6] to yield ammonia with $G(NH_3) = 0.5$ (molecules/100 eV) on radiolysis with γ rays in dilute aqueous solution; they suggest that such deamination arises as a consequence of OH addition to the central 5, 6 double bond.[7] Miss Conlay[8] has isolated organic products from the same system and finds 8-hydroxyadenine and 3, 4, 5-triaminopyrimidine in yields corresponding to $G \approx 0.1$. The latter products provide evidence for OH attack at the 7, 8 position of the imidazole ring. Such reaction is in accord with the Pullmans' molecular-orbital calculations,[9] which indicate that the 7, 8 bond of the purine nucleus has the highest mobile bond order. However, since the yield for OH production in the radiation decomposition of water corresponds to $G_{OH} = 2.4$ for γ rays,[10] it follows that no conclusions regarding the major locus of reaction of OH with the purine nucleus can be made on the basis of the reported experimental yields.

Now, if glycol formation at the central 5, 6 position is involved in the radiolytic oxidation of the purines, it is clear that such products on mild hydrolysis would liberate a reactive carbonyl function. Uric acid and xanthine, for example, would yield alloxan, whereas the corresponding products from hypoxanthine and adenine would be expected to undergo further hydrolysis with liberation of free mesoxalic acid.[11]

Oxygen-saturated solutions of uric acid, xanthine, hypoxanthine, and adenine (Calbiochem, A grade, chromat. homogeneous) were irradiated with ^{60}Co γ rays at dosages in the range 2.8 to 5.6×10^{18} eV/ml. The irradiated solutions were made 2 N in hydrochloric acid, treated with 2, 4-dinitrophenylhydrazine reagent at 70°C for 1 hour, cooled, and extracted with chloroform. The hydrazones were then transferred to filter paper and chromatographed with a butanol-ammonia solvent system.[12] Control solutions containing known amounts of alloxan and mesoxalic acid were similarly treated and the authentic hydrazone derivatives were chromatographed in parallel with the irradiation products. Appropriate areas of the chromatogram were eluted and assayed spectrophotometrically. The indicated carbonyl products are formed in the yields given in Table G.23-I.

In xanthine the evidence is that OH radicals are quantitatively removed at the 5, 6 double bond to give $G(\text{alloxan}) = 2.0 \approx G_{OH}$. The carbonyl yields from hypoxanthine and uric acid indicate that although the 5, 6 position of these compounds also represents the major locus of OH attack, other competing sites are involved. Adenine, on the other hand, appears to be essentially unreactive at the 5, 6 position. That adenine is, nevertheless, undergoing chemical change is evidenced by the fact that the yield for base destruction under the conditions of Table G.23-I (pH 3) corresponds to $G(-B) = 1.9$. This value was obtained through chromatographic isolation (on Dowex-50) of unchanged base from an irradiated solution. Adenine is the only aminopurine of the four purines listed in Table G.23-I. The question whether the amino group is exerting a directing influence or is actually involved chemically as competing reaction locus remains to be elucidated.

Footnote and References

†J. Phys. Chem., in press (probably February 1967).
1. G. Scholes, J. F. Ward, and J. Weiss, J. Mol. Biol. 2, 379 (1960).
2. G. Hems, Radiation Res. 13, 777 (1960).
3. B. Ekert and R. Monier, Nature 188, 309 (1960).
4. R. Latarjet, B. Ekert, and P. Demerseman, Radiation Res. Suppl. 3, 247 (1963).
5. A. Kamal and W. M. Garrison, Nature 206, 1315 (1965); J. Holian and W. M. Garrison, Radiation Res. 27, 527 (1966).
6. G. Scholes, Progr. Biophys. 13, 59 (1963).
7. We use here the notation in which the carbon-carbon double bond of both the purine and pyrimidine nuclei is referred to as the 5, 6 position.
8. J. J. Conlay, Nature 197, 555 (1963).
9. B. Pullman and A. Pullman, in Comparative Effects of Radiation, Ed. by M. Burton et al. (John Wiley and Sons, New York, 1960).
10. E. Hayon, Trans. Faraday Soc. 61, 734 (1965).
11. See, for example, G. A. Howard, in Chemistry of the Carbon Compounds, Vol. IV, Ed. by E. H. Rodd (Elsevier Publishing Co., 1960).
12. B. M. Weeks and W. M. Garrison, J. Phys. Chem. 69, 4131 (1965).

Table G.23-I. Formation of carbonyl products in the γ radiolysis of purine bases in oxygenated solution.[a]

Purine	Conc (mM)	Carbonyl product	Yield (G)
Xanthine	0.3[b]	alloxan	2.0
Hypoxanthine	2	mesoxalic acid plus glyoxylic acid	1.7
Uric acid	0.3[b]	alloxan	1.2
Adenine	2	---	$< \approx 0.1$

a. Yields of the indicated carbonyl products are essentially independent of pH over the range 3 to 7.
b. Approximate solubility limit.

24. RADIATION-INDUCED OXIDATION OF CYTOSINE AND URACIL IN AQUEOUS SOLUTIONS OF Cu^{2+} †

John Holian and Warren M. Garrison

The chemical evidence is that both the hydrated electron, e^-_{aq}, and the hydroxyl radical, OH, which are formed as the principal intermediates in water radiolysis, react rapidly with the pyrimidine bases through preferential addition to the 5, 6 double bond to give the hydropyrimidyl radical, $\dot{B}H$, and the hydroxypyrimidyl radical, $\dot{B}OH$, respectively.[1-4] The yields for base destruction (molecules/100 eV) in oxygen-free solutions under γ rays are, however, consistently low, $G(-B) \leq 1$,[5-6] when compared with primary yields of the radical species derived from water, $G_{e^-_{aq}} = 2.85$, $G_{OH} = 2.9$;[7] recent work indicates that secondary reactions of $\dot{B}H$ and $\dot{B}OH$ lead to regeneration of the parent compound.[4] In oxygen-saturated solutions, e^-_{aq} is scavenged by O_2 to form O_2^- (HO_2), the regeneration reaction is quenched, and the yield for base destruction increases to $G(-B) \approx 2$ through reactions involving the peroxy radical, $B(OH)\dot{O}_2$. However, a great many organic products are formed in the removal of the intermediate, $B(OH)\dot{O}_2$, and the overall product stoichiometries are yet to be fully elucidated.[8]

We find that the use of a transition-metal ion such as Cu^{2+} and Fe^{3+} in the place of molecular oxygen as a scavenger of intermediate radicals leads to considerable simplification in the radiation chemistry of aqueous solutions of the representative bases, uracil and cytosine. The specific chemical effects of Cu^{2+} in these systems involve the preferential oxidation of the

hydroxypyrimidyl radicals to give the corresponding glycols as the principal products of radiolysis

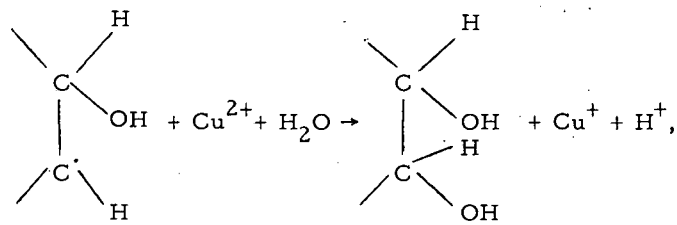

(1)

as evidenced by the data of Table G.24-I for both uracil and cytosine. Formation of the isobarbituric acid derivatives (5- hydroxypyrimidines) with $G \leq 0.5$ in each case may be attributed to a parallel branching reaction,

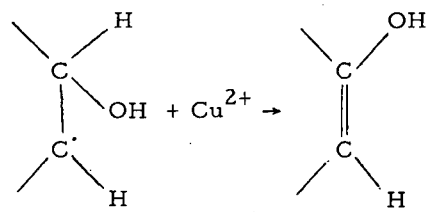

(2)

Hence, in the presence of Cu^{2+} the pyrimidine nucleus is quantitatively oxidized in accord with the stoichiometry $G(1) + G(2) \approx G_{OH} + G_{H_2O_2} = 2.9$. Reactions akin to steps 1 and 2 have been observed in other systems.[9-11]

The velocity constants for reaction of e^-_{aq} with Cu^{2+},[12] and with the pyrimidine bases,[13] are such that at the low [base]/[Cu^{2+}] ratios of Table G.24-I, capture of e^-_{aq} is predominantly by $Cu^{2+} + e^-_{aq} \rightarrow Cu^+$. However, at the higher [base]/[Cu^{2+}] values, e^-_{aq} is scavenged almost exclusively by the base. Such reaction does not lead to net chemical change in the base, since reaction of the hydropyrimidyl radical, $\dot{B}H$, with Cu^{2+} via $\dot{B}H + Cu^{2+} \rightarrow B + Cu^+ + H^+$ or $\dot{B}H + Cu^{2+} + H_2O$ $BH(OH) + Cu^+ + H^+$ followed by $BH(OH) \rightarrow B + H_2O$ leads to base regeneration.

In the experiments presented here, the glycol and isobarbituric acid derivatives were separated from the parent compounds and from Cu^{2+} by chromatography on Dowex-50 ion-exchange resin (hydrogen form). Aliquots of the irradiated solutions were placed directly on the column and, in the case of uracil, the product species were fractionally eluted with water. Product separation in the case of cytosine was effected with dilute hydrochloric acid[2] at gradually increasing concentrations over the range 0 to 2 N. The yield of 4-amino-isobarbituric acid from cytosine and of isobarbituric acid from uracil were calculated on the basis of $\epsilon_{300\ m\mu} = 5.4 \times 10^3$ (at pH<1) (Ref. 2) and $\epsilon = 6.6 \times 10^3$ (at pH < 1) (Ref. 14) respectively. Fractions containing cytosine glycol and uracil glycol were heated in 2 N HCl after the method of Ekert and Monier[2] to quantitatively convert those products to the isobarbituric acid forms for assay.

Footnote and References

†Nature 212, 394 (1966).
1. G. Scholes, J. F. Ward, and J. Weiss, J. Mol. Biol. 2, 379 (1960).
2. B. Ekert and R. Monier, Nature 188, 309 (1960).
3. B. Ekert, Nature 194, 278 (1960).
4. A. Kamal and W. M. Garrison, Nature 206, 1315 (1965).
5. R. Latarjet, B. Ekert, and P. Demerseman, Radiation Res., Suppl. 3, 247 (1963).
6. C. Ponnamperuma, R. M. Lemmon, E. L. Bennett, and M. Calvin, Science 137, 605 (1962).
7. A. O. Allen, Radiation Res. Suppl. 4, 54 (1964).
8. J. Weiss, Prog. Nucl. Acid Res. Mol Biol. 3, 103 (1964).
9. J. H. Baxendale and D. J. Smithies, J. Chem. Phys. 23, 604 (1955).
10. H. E. De La Mare, J. K. Kochi, and F. F. Rust, J. Am Chem. Soc. 85, 1437 (1963).

11. R. L. S. Willix and W. M. Garrison, J. Phys. Chem. 69, 1579 (1965).
12. S. Gordon, E. J. Hart, M. S. Matheson, J. Rabani, J. K. Thomas, J. Am. Chem. Soc. 85, 1375 (1963).
13. E. J. Hart, J. K. Thomas, and S. Gordon, Radiation Res. Suppl. 4, 74 (1964).
14. M. M. Stimson, J. Am. Chem. Soc. 71, 1470 (1949).

Table G.24-I. Product yields in the γ radiolysis of pyrimidine-Cu^{2+} solutions.

	Base (mM)	Cu^{2+}(mM)	pH	G(glycol)	G(isobarbituric)	ΣG(Products)
uracil	30	2	5	2.3	0.50	2.8
	30	1	5	2.3	0.60	2.9
	30	0.5	5	2.3	≈0.7	3.0
	10	10	3.5	2.4	0.45	2.85
cytosine	10	2	3.7	2.28	0.42	2.70
	20	1	3.1	2.25	0.45	2.70

25. THE RADIATION-INDUCED OXIDATION OF PEPTIDES IN AQUEOUS SOLUTION†

Harriette L. Atkins, Winifred Bennett-Corniea, and Warren M. Garrison

It has been proposed[1,2] that the radiation-induced oxidation of peptide forms of glycine and alanine in oxygenated solution is initiated by a preferential attack by the OH radical at the carbon-hydrogen position α to the nitrogen function. The overall reaction scheme includes the radiation-induced step[3]

$$H_2O \rightsquigarrow H_2O_2,\ H_2,\ OH,\ H,\ e^-_{aq},\ H^+ \qquad (1)$$

followed by

$$e^-_{aq}\ (H) + O_2 \longrightarrow O_2^-\ (HO_2), \qquad (2)$$

$$OH + RCONHCHR_2 \longrightarrow H_2O + RCONH\dot{C}R_2, \qquad (3)$$

$$O_2 + RCONH\dot{C}R_2 \longrightarrow RCONHC(\dot{O}_2)R_2 \qquad (4)$$

$$RCONHC(\dot{O}_2)R_2 \xrightarrow{H_2O} RCON{=}CR_2 + HO_2 \qquad (5)$$

$$RCONHC(\dot{O}_2)R_2 \xrightarrow{H_2O} RCONHC(OH)R_2 + HO_2. \qquad (6)$$

where $RCON{=}CR_2$ represents a dehydropeptide and $RCONHC(OH)R_2$ the corresponding hydrate. Such compounds readily decompose on hydrolysis,[4]

$$RCON{=}CR_2 + 2H_2O \longrightarrow RCOOH + NH_3 + R_2CO, \qquad (7)$$

$$RCONHC(OH)R_2 + H_2O \longrightarrow RCOOH + NH_3 + R_2CO. \qquad (8)$$

We have measured ammonia and carbonyl yields in the γ-ray-induced oxidation of N-acetylglycine,[2c] glycine anhydride, N-acetylalanine, and alanine anhydride in oxygenated 0.1 M solution, and we find, for each system, $G(NH_3) \approx 3$, a value consistent with recent measurements[5] of the maximal yield for the production of OH radicals in water under γ rays. However, we also find that carbonyl production in these simple peptide systems is not in accord with the quantitative requirements of the proposed oxidation scheme; the initial carbonyl yields are uniformly low, with $G(R_2CO) \leq 0.8$. There is, then, the question whether this apparent discrepancy arises from (a) an incorrect formulation of the locus of initial OH attack or from (b) unspecified complexities in the chemistry of removal of the peroxy radicals $RCONHC(O_2)R_2$.

To obtain specific information on this point, we have employed FeIII instead of O_2 as the scavenger of intermediate radicals formed in the radiolysis of N-acetylalanine and N-acetylglycine. Heavy metal ions such as FeIII and CuII oxidize organic free radicals in aqueous solution by electron transfer and by ligand transfer.[6] Such reactions in the case of the peptide radical $RCONHCR_2$ would correspond to

$$RCONH\dot{C}R_2 + FeIII \longrightarrow RCON{=}CR_2 + FeII + H^+, \qquad (9)$$

$$RCONH\dot{C}R_2 + FeIII + H_2O \longrightarrow RCONHC(OH)R_2 + FeII + H^+ \qquad (10)$$

respectively, where the organic products of Reactions 9 and 10 are identical with the products of Reactions 5 and 6.

Solutions containing the acetylamino acid (Nutritional Biochemicals, twice recrystallized) plus ferric sulfate (C. P.) were adjusted to the desired pH with sulfuric acid, evacuated, and then irradiated with ^{60}Co γ rays to a dose of not more than $\approx 5 \times 10^{18}$ eV/ml. One fraction of the solution was passed through Dowex-50 (acid form) to remove iron, then hydrolyzed, and assayed for α-keto acid and aldehyde.[7] A second fraction was assayed directly for "amids" ammonia.[8]

At the higher (FeIII)/(peptide) ratios of Fig. G.25-1, the reducing species e^-_{aq} and H are preferentially scavenged by FeIII, and the yield for peptide oxidation through OH attack is in accord with $-G(\text{peptide}) = G(NH_3) = G(RCOCOOH) \approx 3.2 \approx G_{OH} + G_{H_2O_2}$. Hydrogen peroxide formed in the radiation-induced step, 1, reacts rapidly with FeII to give an additional yield of OH radicals,[9]

$$FeII + H_2O_2 \longrightarrow FeIII + OH^- + OH \qquad (11)$$

The maximum in the yield curve shown in Fig. G.25-1 is attributed to the onset of the reaction

$$H + RCONHCHR_2 \longrightarrow RCONH\dot{C}R_2 + H_2 \qquad (12)$$

in competition with

$$H + FeIII \longrightarrow FeII + H^+ \qquad (13)$$

at the lower (FeIII)/(peptide) ratios. The $RCONH\dot{C}R_2$ radicals from both Reactions 3 and 12 are then available for oxidation by FeIII. This effect is shown more clearly in Fig. G.25-2, which gives ammonia and pyruvic acid yields as a function of acetylalanine concentration over the range 10^{-3} to 1.5 M, in the presence of 0.05 M FeIII. The limiting value for peptide oxidation at the higher acetylalanine concentrations is given by $-G(\text{peptide}) = G(NH_3) = G(R_2CO) \approx 4.0 \approx G_{OH} + G_{H_2O_2} + G_H$.

We conclude, then, that radical attack on these peptide derivatives occurs essentially quantitatively at the α-carbon position as formulated in Reactions 3 and 12.[10] The present data also establish the quantitative oxidation of $RCONH\dot{C}R_2$ radicals by FeIII via Reactions 9 and 10. In acetylalanine such oxidation appears to occur almost exclusively through ligand transfer (Reaction 10), since measurements of the optical absorption of the irradiated solutions (after removal of FeIII) reveal negligible absorption above 230 mμ when read differentially against

unirradiated control solution. Absorption by control solutions containing authentic acetyldehydroalanine (ϵ_{240} = 6050)[4] show that G values of >0.1 for Reaction 9 would be detectable.

Footnote and References

† Shortened version of J. Phys. Chem. in press (probably Feb. 1967).

1. M. E. Jayko, B. M. Weeks, and W. M. Garrison, in Proceedings of the Second International Conference on Peaceful Uses of Atomic Energy, Geneva, 1958, Vol. 29, p. 30.
2. W. M. Garrison, M. E. Jayko, and Winifred Bennett-Corniea, Radiation Res. 16, 483 (1962); W. M. Garrison and B. M. Weeks, ibid. 17, 341 (1962); W. M. Garrison, ibid., Suppl. 4, 148 (1964).
3. A. O. Allen, Radiation Res. Suppl. 4, 54 (1964); E. J. Hart, Science 146, 19 (1964).
4. J. P. Greenstein and M. Winitz, in Chemistry of the Amino Acids (John Wiley and Sons, Inc., New York, N. Y., 1961), p. 843.
5. E. Hayon, Trans. Faraday Soc. 61, 723 (1965).
6. J. H. Baxendale and D. H. Smithies, Z. physik. Chem. 7, 242 (1956); H. E. DeLaMare, J. K. Kochi, and F. F. Rust, J. Am. Chem. Soc. 85, 1437 (1963).
7. G. R. A. Johnson and G. Scholes, Analyst 79, 217 (1954); T. E. Friedmann, and G. E. Haugen, J. Biol. Chem. 147, 415 (1943).
8. E. J. Conway, Microdiffusion Analysis (Crosby Lockwood and Son, Ltd., London, 1962).
9. F. Haber and J. Weiss, Proc. Roy. Soc. (London) A147, 333 (1934).
10. We refer to radical attack at the C-H linkage α to the nitrogen function as the characteristic peptide reaction. With the more complicated amino acid residues, attack may occur in parallel or exclusively at side-chain loci. See Ref. 2, also H. A. Sokol, W. Bennett-Corniea, and W. M. Garrison, J. Am. Chem. Soc. 87, 1391 (1965).

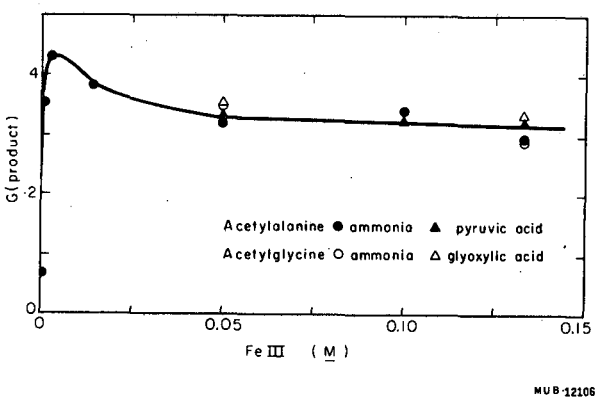

Fig. G.25-1. Effect of FeIII concentration on the yields of ammonia (●) and pyruvic acid (▲) from 0.1 M acetylalanine, and of ammonia (O) and glyoxylic acid (Δ) from 0.1 M acetylglycine, pH 3.

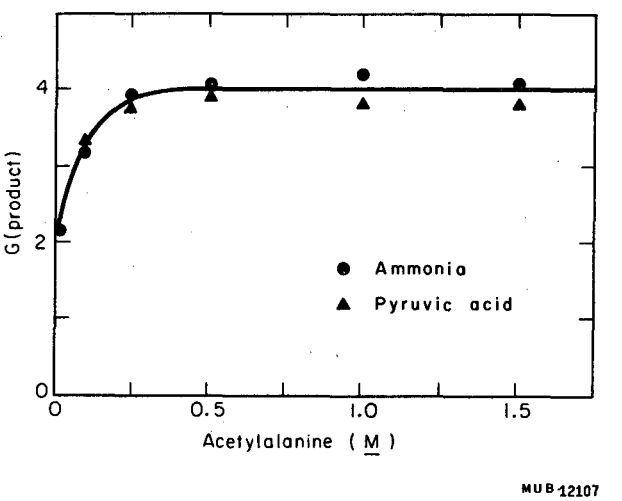

Fig. G.25-2. Effect of acetylalanine concentration on yields of ammonia (●) and of pyruvic acid (▲) from solutions containing 0.05 M FeIII, pH 3.

H. SEPARATION AND PURIFICATION PROCESSES

1. STATISTICAL THERMODYNAMICS OF PARTICULATE FLUIDIZATION†

James A. Saxton* and Theodore Vermeulen

Fluidized beds of particulate solids represent a statistical ensemble of similar or identical elements, analogous to a set of molecules in true liquid form. The upward flow of the fluidizing medium (an "ether," in the philosophical sense) brings about sufficient expansion so that the fluid-drag force ("repulsive") is always balanced closely by the gravitational force ("attractive") on the particles. The fluidized bed exhibits a relatively quiescent upper surface analogous to the free surface of a true liquid in a gravitational field. This physical analogy has been taken as a basis for using statistical thermodynamics to describe and correlate certain physical properties of water-fluidized systems of fine (50-μ to 500-μ) glass spheres.

A smoothed-potential version of the free-volume model has been used to provide an equation of state for the fluid beds. In these terms, the free volume v_f is given by $v_f = (4\pi/3)\,\gamma\, v_p\,[f(\epsilon)]^3$, with v_p the actual particle volume, γ an empirical packing factor, and

$$f(\epsilon) = (1-\epsilon)^{-1/3} - (1-\epsilon_0)^{-1/3} = 7.1 \times 10^{-4} U/d^{1.7},$$

where ϵ is the void fraction of the bed, ϵ_0 is its limiting-void fraction when contracted in a cubic lattice, U is the superficial velocity of the fluidizing liquid, and d is the sphere diameter. This result has been generalized to give

$$f(\epsilon) = 18.2\,(dU\rho/\mu)(d^3\rho \cdot g\Delta\rho/\mu^2)^{-0.9},$$

where ρ is liquid density, $\Delta\rho$ is solid density minus liquid density, g is gravitational acceleration, and μ is liquid viscosity. The first group in parentheses is the Reynolds number, and the second the Archimedes number. The experimental relation between $f(\epsilon)$ and U is shown in Fig. H. 1-1.

Viscosity of the fluidized beds was measured with a viscometer (Brookfield model LVT) equipped with a special-order rotating spindle. Qualitative agreement was found between these measurements and those made with a rising or falling sphere 0.5 inch in diameter. The viscosity data were fitted to the Collins-Raffel equation,

$$\eta = \frac{2}{5}\, d \left(\frac{m\Theta}{\pi}\right)^{1/2} \left(\frac{p_k}{\Theta} - \frac{1}{v}\right),$$

where m is the effective mass per particle, v is the total volume per particle, p_k is the kinetic pressure, and Θ is the nominal-temperature function (in energy units). This relation transforms to

$$\eta = \frac{1}{5} \cdot \sqrt{\frac{2}{3}}\; \frac{(\Delta\rho \cdot d^5 \cdot \Theta)^{1/2}}{v} \qquad \frac{(1-\epsilon_0)^{1/3}}{(1-\epsilon)^{-1/3} - (1-\epsilon_0)^{-1/3}}$$

Experimentally it was established that $\eta = 62\, d^{4.2}/v$, where the viscosity dependence of the fluidized beds upon water velocity enters entirely through the total volume v per particle. This gives rise to the following results, which are believed to be general, and to merit testing on other fluidized systems:

$$\eta v = 5.24\left(\frac{\mu^{0.2} g^{0.4}}{\rho^{0.6}}\right)(\Delta\rho)^{1.4} d^{4.2}, \quad \Theta = 2.33 \times 10^5\, \frac{\mu^2 U^2}{\rho g}.$$

The result for Θ is seen to achieve the definition of a thermodynamic "temperature" that is a function only of the properties and velocity of the fluidizing medium. From a theoretical standpoint, this is the key result of the study.

It is known that mixtures of particles of different uniform sizes will "dissolve" into a

single fluidized bed if the ratio of the particle diameters is less than about 1.4 to 1, but otherwise will divide into separate beds as shown in Fig. H. 1-2. The "solubility" of each bead size in a phase principally of another size was measured as a function of U and hence of Θ. However, a successful theoretical interpretation of the results has not yet been obtained.

The authors believe that, on the theoretical side, this study paves the way for modeling many molecular-scale liquid-phase and interfacial properties and effects with water-fluidized beds. Also, from the process standpoint, correlations of fluid-bed properties based upon the present approach should have exceptionally wide applicability and should prove useful in providing a better understanding of gas-fluidized systems.

Footnotes

†Abstracted from UCRL-17302.

*Present address: Bell Comm., Inc., Washington, D. C.

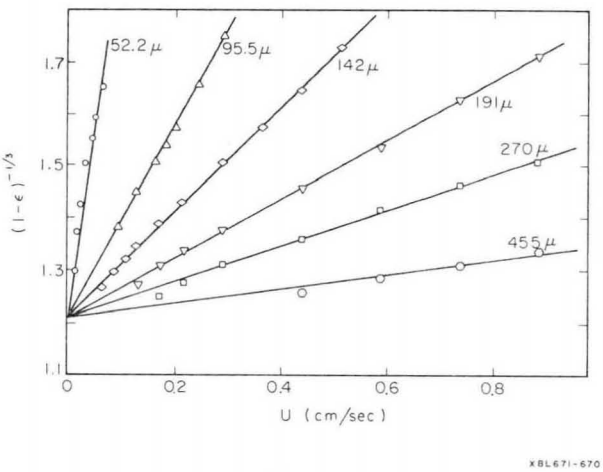

Fig. H. 1-1. Expansion-data correlation.

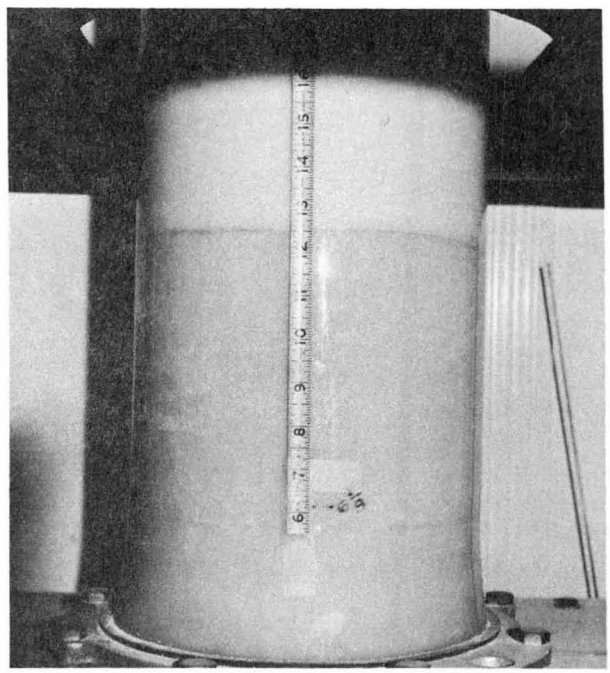

Fig. H. 1-2. Two-phase system of U = 0.055 cm/sec: upper phase, 52-μ spheres; lower phase, 270-μ spheres; ε = 0.469.

2. HEAT AND MASS TRANSFER BETWEEN FLUID PHASES†

Charles H. Byers,* Michael W. Clark, and C. Judson King

This project involves studies of interphase heat and mass transfer between flowing-gas and flowing-liquid phases. The apparatus employed is a closed horizontal rectangular channel, 3 in. wide, 1 in. high, and 18 in. long in the direction of flow. Gas and liquid streams pass through in stratified cocurrent or countercurrent flow. The channel is constructed of transparent polycarbonate, and is equipped with inlet and outlet divider plates and with thermocouple probes and hypodermic-tubing sample probes at the liquid outlet and halfway along the flow path. The height of these probes above or below the liquid surface is adjustable, so that profiles of temperature and composition normal to the gas-liquid interface can be measured. The channel assembly is shown in Fig. H. 2-1.

During 1966, studies were made of interphase mass transfer at low concentration levels, heat transfer in the absence of evaporation, and simultaneous heat and mass transfer at moderate concentration levels. Three reports were published during the year.[1-3]

The equations of transport in laminar flow were solved analytically and numerically to yield predictions of the effects on interphase mass rates resulting from

a. tangential interfacial motion,
b. the presence of confining walls at the top and bottom of the channel,
c. changes in the solubility of the solute transferring between phases.

These solutions showed that an interfacial velocity amounting to 10% or more of average gas-phase velocity produces a significant effect upon the gas-phase mass-transfer coefficient, increasing it for cocurrent flow and decreasing it for countercurrent flow. The confining walls become important if either phase reaches 50% of saturation. The principle of addition of independently measured individual phase resistances is adhered to within 2% above values of the Graetz group ($D_G x/U_m b^2$) equal to 0.4. In this ratio D_G is gas-phase diffusivity, x is the downstream distance from the point of initial phase contact, U_m is the average gas velocity, and b is the height of the gas phase. A simple approximating solution was obtained for countercurrent flow.

Figure H. 2-2 shows experimental results obtained for the evaporation of flowing ethanol into a flowing stream of carbon dioxide. The fractional saturation is shown for the outlet gas as a function of the Graetz group (L is channel length) for varying gas-flow rates with a constant liquid flow of 53.7 cm^3/sec. The solid curve represents the Graetz solution for no interfacial motion, and the other curves represent the theoretical curves obtained for cocurrent and countercurrent flow, respectively. The experimental data agree well with theoretical predictions. Similar good agreement was obtained for experimental measurements of the evaporation of stagnant ethanol, for measured concentration profiles within the gas phase, and for evaporation into oxygen and nitrogen.

Measurements were made for the evaporation of dilute diethyl ether from flowing ethanol into helium and carbon dioxide in cocurrent and countercurrent flow. The results for cocurrent flow are shown in Fig. H. 2-3. The group $\sigma\mathcal{H}$ represents $(D_G/D_L)^{\frac{1}{2}} \cdot (H/RT)$, and is indicative of the distribution of mass-transfer control between phases; D_L is liquid diffusivity; H is the Henry's law constant; R is the gas constant; and T is absolute temperature. Again the experimental data agree well with theoretical predictions.

Runs in which dilute diethyl ether was evaporated from flowing water into helium, oxygen, and carbon dioxide showed anomalously low rates of mass transfer. Subsequent investigation showed that surfactant accumulation caused the liquid surface to flow at velocities from 10 to 20% of surface velocity with no surfactant; this phenomenon accounts for the low rates of mass transfer.

Subsequent work has confirmed the applicability of the equations for transport in laminar flow to heat transfer between nitrogen and a mixture of linear C_{12}-C_{14} hydrocarbons in cocurrent flow. Modifications of the channel entry section and of the wall-insulation scheme were required to minimize extraneous heat leaks. Measurements have been made of the evaporation of n-pentane, diethyl ether, and cyclopentane from the C_{12}-C_{14} hydrocarbon liquid into nitrogen, with the liquid solute mole fraction varying from 0.001 to 0.40. Interfacial mixing cells arise at mole fractions greater than 0.02 to 0.05 and serve to accelerate liquid-phase mass transfer. Future work will be directed toward a quantitative interpretation of this effect and toward measurements of the evaporation of pure flowing liquids into flowing gases when the vapor pressure of the liquid

ranges from 1 to 95% of the total pressure. For the previous ethanol studies, the vapor pressure was always quite low compared with the total pressure.

Footnotes and References

†Condensed from UCRL-16926 and UCRL-16535.

*Present address: Department of Chemical Engineering, University of Rochester, Rochester, N. Y.

1. C. H. Byers and C. J. King, Convective Transfer Processes in Laminar Gas-Liquid Channel Flow, UCRL-16535, May 1966.
2. C. H. Byers and C. J. King, Gas-Liquid Mass Transfer with a Tangentially Moving Interface: I. Theory, A. I. Ch. E. Journal, in press.
3. C. H. Byers and C. J. King, Gas-Liquid Mass Transfer with a Tangentially Moving Interface: II. Experimental, (paper presented at A. I. Ch. E. annual meeting, Detroit, December 6, 1966), A. I. Ch. E. Journal, in press.

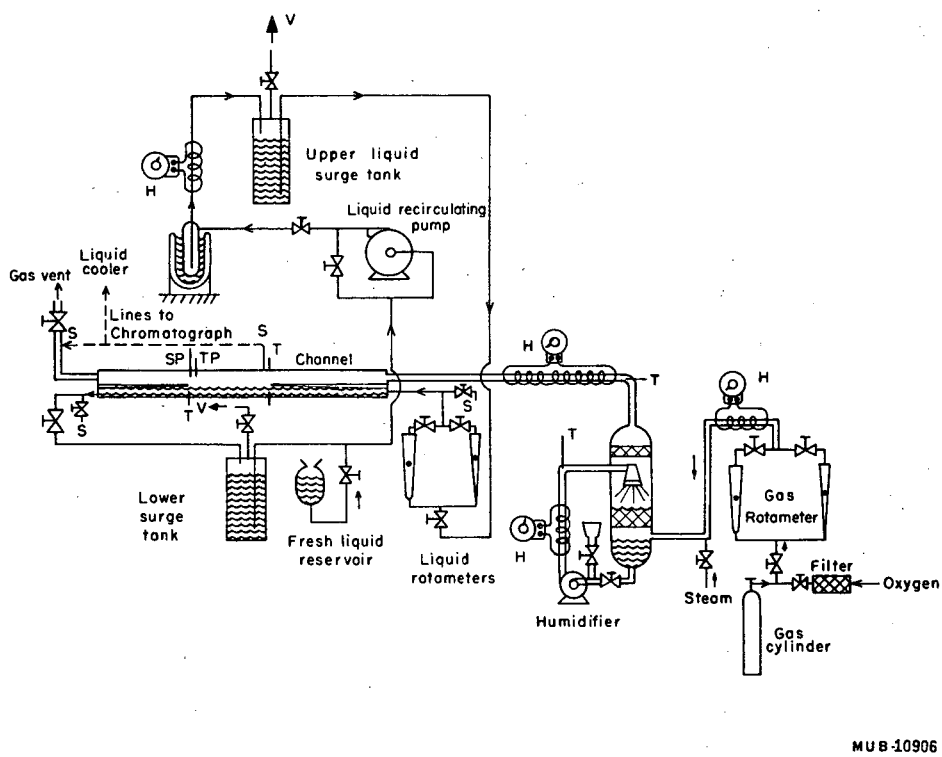

Fig. H. 2-1. Schematic diagram of the experimental apparatus. H, heater using heating tape and controlled by a Variac; S, sample point; SP, sample probe used in taking profiles; T, temperature measurement point; TP, temperature probe designed for taking profiles; V, vent on surge tanks.

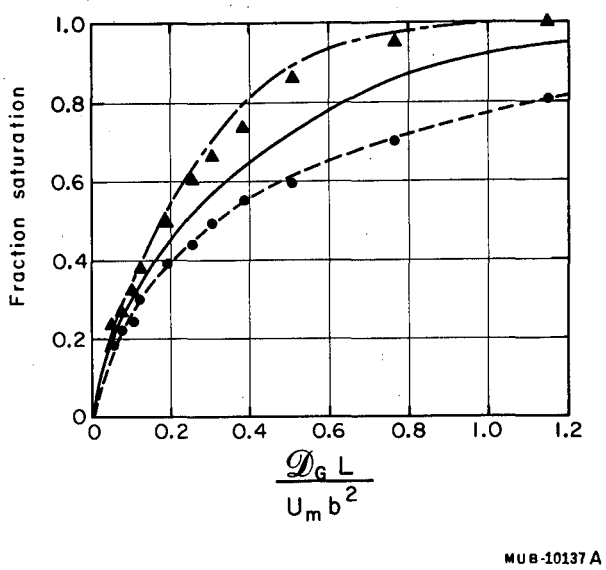

Fig. H. 2-2. A comparison of laminar single phase cocurrent and countercurrent data.
▲ Cocurrent data; — - — cocurrent theory.
— The Graetz solution. ● Countercurrent data; --- countercurrent theory.

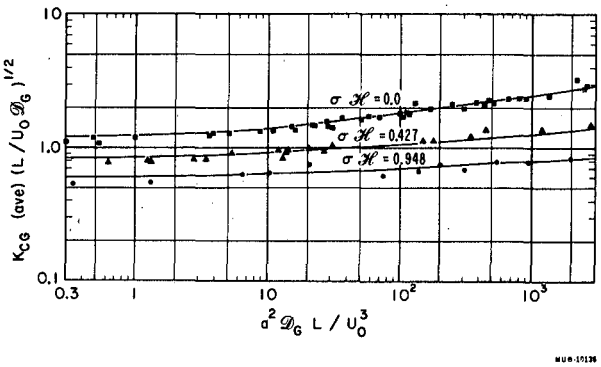

Fig. H. 2-3. Cocurrent gas-phase-controlled and interphase mass-transfer data.
■ Gas-phase-controlled data.
▲ Data for the evaporation of ether into carbon dioxide.
● Data for the evaporation of ether into helium.
— Theory for the corresponding data.

3. FLUID-PHASE MASS TRANSFER IN DIALYSIS

Richard D. Newman and C. R. Wilke

Examination of available data on dialysis-cell performance indicates that the fluid-phase mass-transfer resistances outside the membrane can be a very substantial fraction of the total resistance. The present investigation was to determine the liquid-phase mass-transfer characteristics of a dialysis cell.

A schematic diagram of the apparatus is shown in Fig. H. 3-1. Except for the stainless steel stirrers, the cell was constructed of Lucite. The dialysis membrane was glued across the front of the compartmented section so that no compartment communicated with its neighbors. In each compartment was a stirrer which operated at 600 rpm and which completely eliminated the mass-transfer resistance on that side of the membrane. The front section was a hollow area 1 cm thick in front of the membrane. The arrangement of equipment resembled as much as possible the arrangement of a typical plate and frame dialyzer. The front section of the apparatus corresponded to one frame in an industrial dialyzer. The purpose of having a number of compartments on the other side of the membrane was to permit the mass-transfer coefficients to be determined at various points in the cell. Since visual inspection during operations was desired, the material of construction was Lucite.

The membrane used in these tests was of vinyl (Nalco Chemical Company, D-30). This particular membrane was chosen because it could be glued to Lucite and could withstand repeated wetting and drying. The mass-transfer properties of Nalco D-30 are similar to those of cellophane. A detailed description of the apparatus, experimental procedure, and results are reported elsewhere.[1]

The procedure in making a run was as follows. The stirred compartments were filled with distilled water. Then NaCl solution was pumped through the front section for a predetermined period of time with the stirrers running. The flow rate was controlled by adjusting the height of the constant-head reservoir above the dialysis cell. After a predetermined period of time, the compartments were drained and samples taken. These samples were analyzed to determine the NaCl concentrations, which were used in calculating the mass-transfer coefficient outside each compartment. Feed concentrations were varied over a range from 0.1 to 2.0 molar in NaCl. All runs were made at room temperature, 23 to 25°C.

The membrane resistance to mass transfer had been determined previously in a small, well-stirred batch dialyzer, and this value was subtracted from the overall resistance to yield the liquid-phase resistance. In this way the liquid-phase resistance at various points in the dialysis cell was determined.

The initial runs were carried out with 1.0 molar NaCl and a flow rate of 280 ml/min. Because at this flow rate the NaCl concentration dropped only about 1% through the dialysis cell, bulk concentration in the front section of the dialyzer remained approximately constant. That laminar flow prevailed was borne out by the injection of dye into the front section of the apparatus. The only point where there appeared to be turbulence was at the fluid inlet port (Compartment 13). The presence of turbulence there indicated by the mass-transfer coefficient, which for this compartment was consistently higher than the coefficient for any other cell.

Results for a typical experiment are summarized in Table H. 3-I.

The results were examined in light of existing theory for mass transfer by free and forced convection. By use of the established correlation for free convection at vertical plates,[2]

$$\left[\frac{\bar{k}_L x}{D} = 0.66(ScGr)^{1/4}\right] ,$$

the average value of $\bar{k}_L$ for free convection alone is estimated to be 4.70×10^{-4} cm/sec. Correspondingly, for laminar forced convection in a rectangular channel,[3] the correlation

$$\left[\frac{\bar{k}_L d_w}{D} = 1.615 \left(\frac{Pe d_w}{x}\right)^{1/3}\right]$$

gives a value of $\bar{k}_L = 1.58 \times 10^{-4}$ (see nomenclature list at back for definitions of terms). Van der Hegge Zijnen[4] suggests that when the two mechanisms occur simultaneously, the above mass-transfer coefficients may be combined vectorially to give a resultant average coefficient. This procedure gives an average $\bar{k}_L = 4.97 \times 10^{-4}$ cm/sec which compares favorably to the experimental average of 4.87×10^{-4}.

Other experiments confirmed the importance of free convection on the mass-transfer process, and substantiated the general approach of vectorially adding the average coefficients for free and forced convections. An alternative equation derived from an integral boundary layer approach gave equally satisfactory results. Both methods account for the variation of the local mass-transfer coefficient with position in the cell. When the concentration of solute varied appreciably between the inlet and outlet of the cell, it was found by sampling that the logarithm of the concentration was linear in vertical distance.

Finally, based on the foregoing correlations and observations, a design procedure was developed for the scale-up of dialysis cells, which gives satisfactory agreement with the reported performance of one commercial scale unit.

Nomenclature

$\bar{k}_L$ = average liquid-phase mass transfer coefficient (cm/sec),

x = cell height (cm)

D = solute diffusion coefficient (cm^2/sec)

Sc = Schmidt number

Gr = Grashof number

Pc = Peclet number

d_w = hydraulic radius of flow channel (cm)

References

1. Richard D. Newman and C. R. Wilke, Fluid Phase Mass Transfer in Dialysis, UCRL-17117, Sept. 1966.
2. C. R. Wilke, C. W. Tobias, and E. Eisenberg, Chem. Eng. Progr. 49, 663 (1953).
3. J. G. Knudsen and D. L. Katz, Fluid Dynamics and Heat Transfer (McGraw-Hill, New York, 1958), p. 367.
4. B. G. Van der Hegge Zijnen, Appl. Sci. Res. Sec. A 6, 129 (1956).

Table H. 3-I. Typical experimental results.[a]

Compartment number[b]	1	2	3	4 (outlet)
k_L	3.94	3.44	4.13	3.77
Compartment number	5	6	7	8
k_L	5.09	4.63	4.85	4.40
Compartment number	9	10	11	12
k_L	6.32	5.09	4.55	4.22
Compartment number	13(inlet)	14	15	16
k_L	9.42	6.78	5.69	5.28

a. Grashof number 2.29×10^4 Schmidt number 651
Reynolds number 36.1 Feed concentration 1.0 mols/liter
Final NaCl concentration in compartments (range) 0.03 to 0.05 mols/liter
Average liquid-phase mass-transfer coefficient, k_L, 5.15×10^{-4} cm/sec
Average mass-transfer coefficient with compartment 13 omitted, 4.87×10^{-4} cm/sec.

b. The compartments are tabulated in correspondence to their geometric position in the dialysis cell (see Fig. H. 3-1).

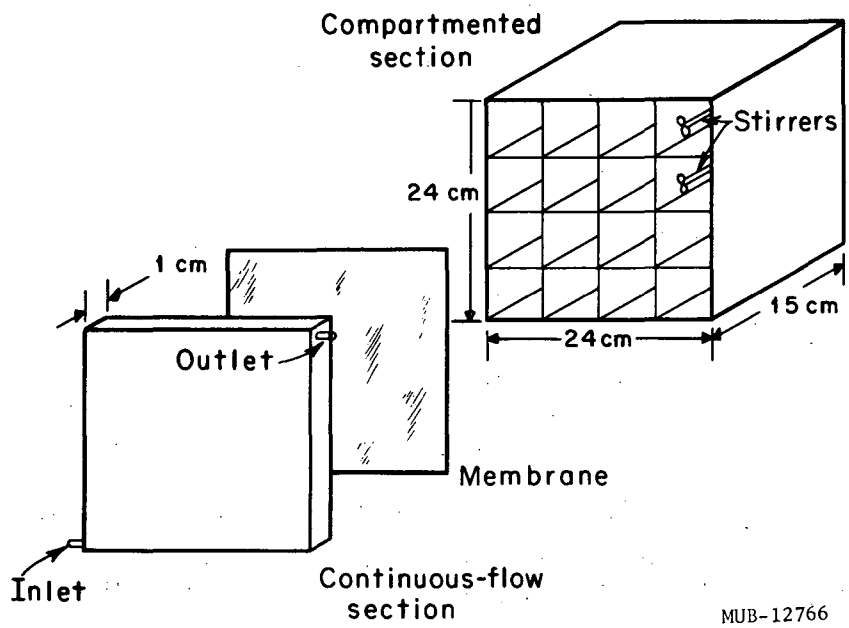

Fig. H. 3-1. Schematic diagram of experimental apparatus.

4. LIQUID DIFFUSIVITIES IN THE GLYCOL WATER SYSTEM

Charles H. Byers† and C. Judson King

As a study peripheral to those on heat and mass transfer between fluid phases, mutual diffusivities were measured for the system ethylene glycol–water over the entire range of compositions and from 25 to 70°C. A new technique was developed wherein the classical glass diaphragm cell may be used to provide differential diffusion coefficients. This was accomplished by providing only very slight differences in composition between the two sides of the cell, and monitoring the differences in concentration at the beginning and end of a run by means of a Zeiss differential interferometer. In this way a concentration difference of 1.5 wt% was determined to an accuracy of three significant figures.

Results of this study are covered in more detail elsewhere.[1] Figure H. 4-1 shows the variation of $D\eta$ with composition at 40°C, where η is viscosity. The glycol-water system obeys Raoult's law; hence the data are in agreement with theories which predict that $D\eta$ is linear in mole fraction. This system represents a unique test of such theories, since no activity-coefficient corrections are necessary and since the viscosity varies by a factor of 12 to 17 and the diffusivity varies by a factor of 3 to 5 across the range of compositions at a given temperature.

Figure H. 4-2 shows that $(D\eta/T)$ is essentially constant at all concentration levels. There T is absolute temperature.

Footnote and References

†Present address: Department of Chemical Engineering, University of Rochester, Rochester, N. Y.

1. C. H. Byers and C. J. King, Liquid Diffusivities in the Glycol-Water System, J. Phys. Chem. 70, 2499 (1966).

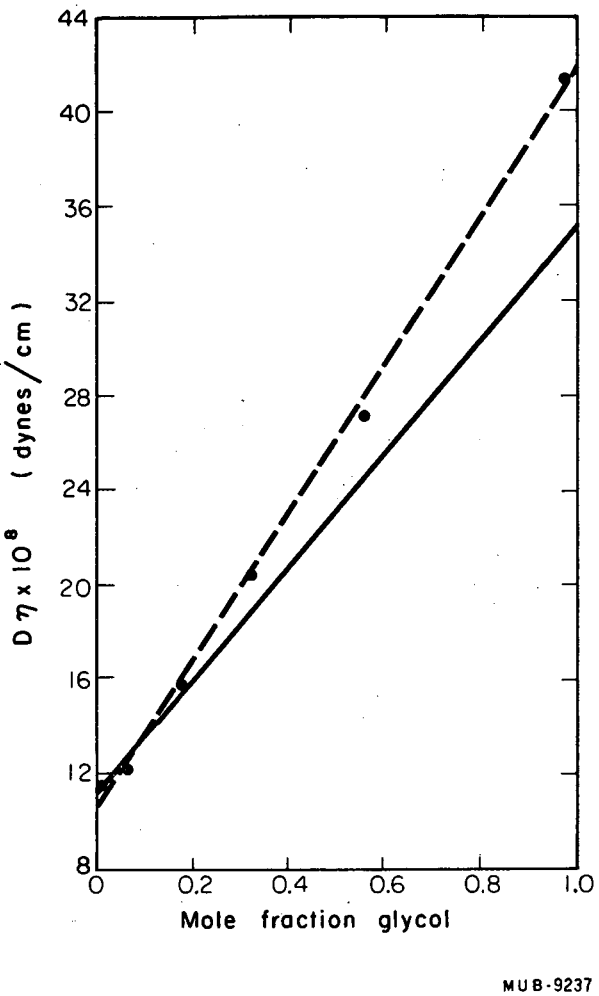

Fig. H. 4-1. Dη as a function of mole fraction ethylene glycol at 40°C. ---- best fit of data; —— theory of R. J. Bearman, J. Phys. Chem. 65, 1961 (1961).

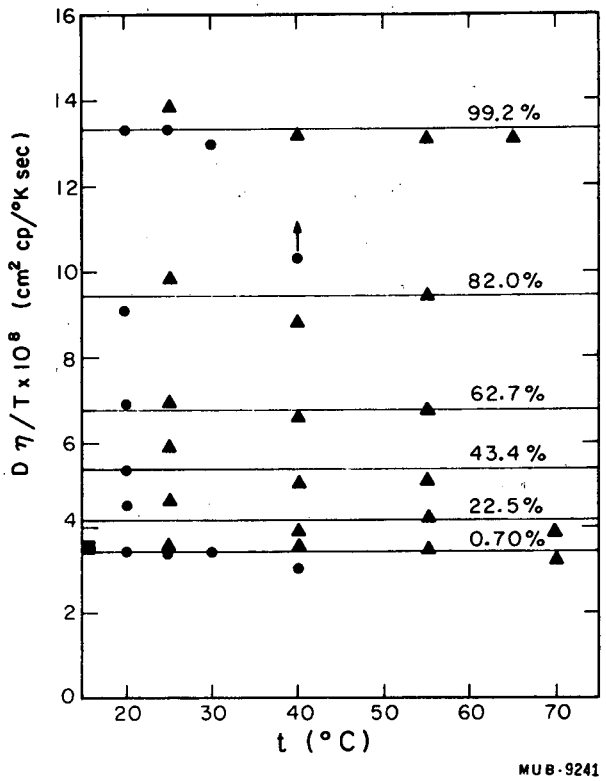

Fig. H. 4-2. Dη/T as a function of temperature. ▲ present study; ● data from F. H. Garner and P. J. M. Marchant, Trans. Inst. Chem. Engrs. 39, 397 (1961); □ data from C. Rossi, F. Bianchi, and A. Rossi, J. Chim. Phys. 55, 93 (1958). Arrow indicates 40°C data of Garner and Marchant.

5. AXIAL DISPERSION IN LIQUID FLOW THROUGH PACKED BEDS

Steven F. Miller, C. Judson King, and Theodore Vermeulen

Experimental measurements were made of the axial dispersion of step-function tracer inputs to water flowing through beds of fine glass spheres.[1] A schematic of the apparatus employed is shown in Fig. H. 5-1. The tracer was 0.01 N sodium nitrate, with conductivity probes used to monitor the dispersion. The range of relatively low Reynolds numbers (0.01 to 100) was studied, and a particular effort was made to discern any independent effect of particle size or of the ratio of bed diameter to particle diameter beyond that represented by the usual Peclet and Reynolds groups. Selected experimental results, shown in Fig. H. 5-2, compare favorably with the results of Jacques et al.[2] and Ebach and White,[3] as opposed to other values of earlier works.

These data, along with other data for the axial dispersion of heat and mass for gas and liquid flow in packed beds, were interpreted in terms of changes in the degree of mixing within bed voids. The range of Reynolds numbers covered for liquids in the present study can be analyzed

by a model of transient mass transfer between different laminar streams which enter a particular void space and then split apart.

References

1. S. F. Miller and C. J. King, Axial Dispersion in Liquid Flow Through Packed Beds, A. I. Ch. E. Journal 12, 767 (1966).
2. Gabriel Jacques, Alphonse Hennico, J. S. Moon, and Theodore Vermeulen, Segmented Laminar Flow and Other Models for Packed-Bed Longitudinal Dispersion, UCRL-10696, Part I, Nov. 1964.
3. E. A. Ebach and R. R. White, A. I. Ch. E. Journal 4, 161 (1958).

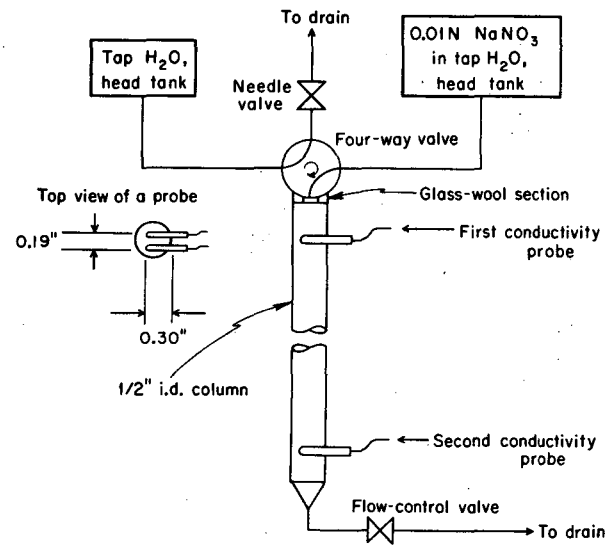

Fig. H. 5-1. Schematic of apparatus.

MU-35850

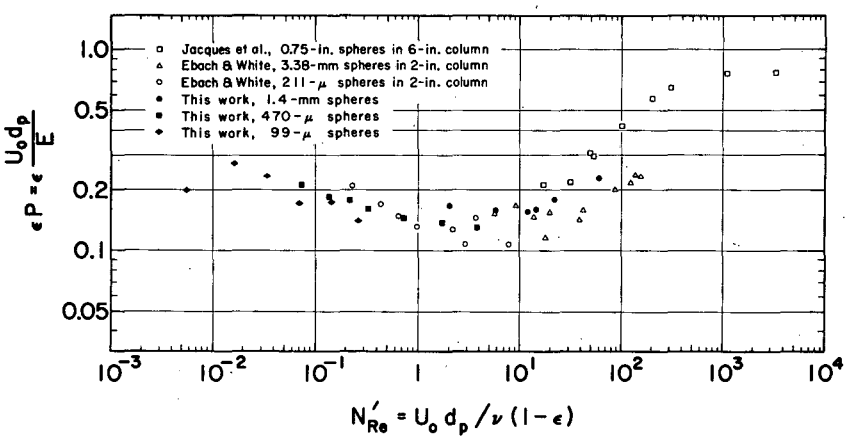

Fig. H. 5-2. Comparison of our data with those of Refs. 2 and 3.

6. FILTRATION STUDIES WITH ULTRAFINE PARTICLES

Ashok Bhagat† and C. R. Wilke

Various types of processing operations may arise in which it is desired to withdraw liquid continuously from a suspension of fine solids while retaining the solids in the system. The objective of the work reported here was to construct a device with which to do such an operation, and to determine its operating characteristics.

The flow sheet of the system is shown in Fig. H. 6-1. The system consists of a rotating filter membrane, a filter chamber, and a slurry tank. The filter membrane is supported on a cylindrical metal screen, which rotates inside a stationary filter chamber filled with a slurry of fine particles. The screen is a hollow cylinder of 6 in. diam and 3 in. height. The filter chamber is a cylinder of 8 in. diam and 13 in. height. The slurry is fed to the filter chamber and the liquid component is forced through the rotating membrane by external pressure. The filtrate fills the hollow rotor (the metal screen) and overflows through the hollow shaft into the filtrate chamber, which is a vertical cylindrical tank of 4-in. diam and 4-in. height. Particles approaching the membrane are thrown away from it by centrifugal force. By careful choice of variables, it is possible to establish conditions such that no particles will reach the membrane. Detailed description of the equipment, experimental procedure, and results are given elsewhere.[1]

Filtration experiments were conducted with two sizes of Styrene polymer latex spheres, of density 1.056 g/c^3 and diameters of 1.3, and 6 to 14 microns. Slurries fed to the apparatus contained from 0.5 to 1.0 g/liter of solids in water. Millipore micromole membranes of 150-μ thickness and with mean pore diameters of 0.45 and 3.0 μ were used for filtration of the small and large particles, respectively. During the filtration tests and in separate runs without filtration or rotation, data were taken on pressure requirements, pressure losses, power requirements, membrane and cake resistances, and limiting filtration rates for various rotational speeds and solution densities (varied by addition of NaCl). On the basis of these data, correlations were developed for prediction of pumping, power, and filtration characteristics of the apparatus.[1]

Figure H. 6-2 shows a typical result for filtration of 1.3-μ particles. If filtration is started at a given applied pressure, the filtration rate falls off as cake is formed on the membrane until a limiting filtration velocity is reached, at which drag forces carrying the particles are in dynamic equilibrium with centrifugal force and particle diffusion, and particles move outward from the membrane. If the pressure is increased, the flow will increase for a time and then settle back to the same limiting rate through a somewhat thicker cake and correspondingly greater pressure drop.

Figure H. 6-3 shows some typical data for the 6- to 14-μ slurry.

As a tentative general mechanism of the filtration behavior, it was concluded that the limiting filtration velocity is determined by a combination of the centrifugal force on the particles and eddy diffusion of particles away from the membrane. The eddy diffusion behavior was particularly important for the smallest particles, and the filtration rates for the larger particles could be predicted fairly well from a simple balance of centrifugal force against the fluid drag on the particles. Figure H. 6-4 summarizes the results of the preliminary attempt to correlate the data according to this mechanism. The limiting filtration velocity is plotted against the centrifugal force factor Z_0, which is proportional to the rpm. For the smallest particles the limiting filtration rate is on the order of tenfold greater than that which would be predicted in absence of eddy diffusion of the particles.

Additional studies are in progress in an effort to establish a more general correlation for the prediction of centrifugal filter performance; these studies are to include nonaqueous systems and a greater range of geometric and operating variables .

Footnote

†Now at Stauffer Chemical, Richmond, Calif.

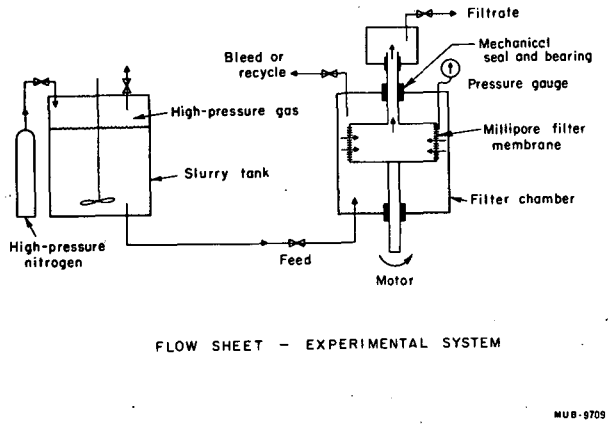

Fig. H. 6-1. Flow sheet of the experimental system.

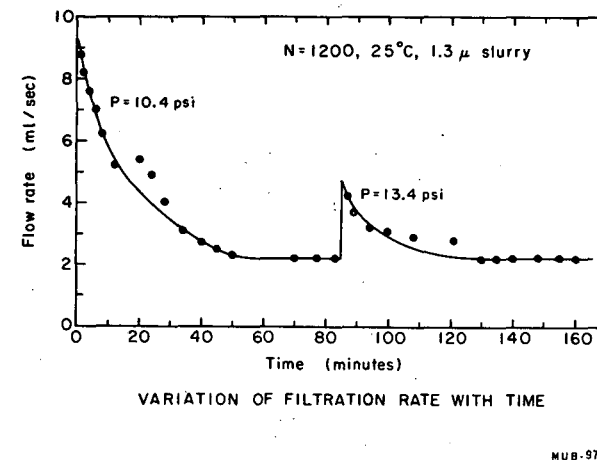

Fig. H. 6-2. Filtration rate vs time for 1.3-μ slurry at 25°C and N = 1200 rpm.

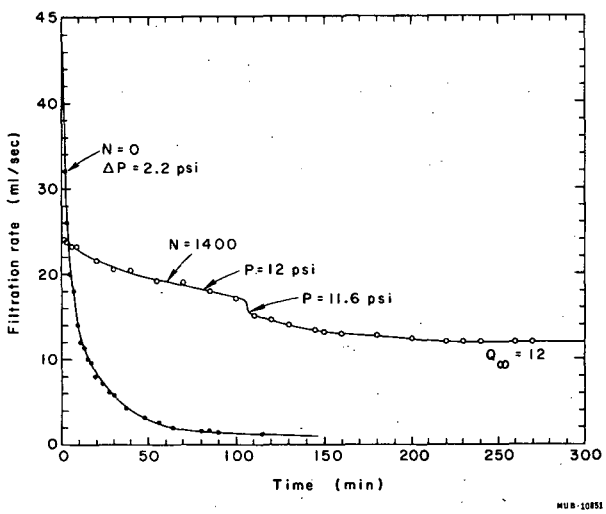

Fig. H. 6-3. Filtration rate vs time for 6- to 14-μ slurry at 25°C and 1400 rpm and no rotation. Results clearly show the effect of rotation on the filtration rate and total throughput.

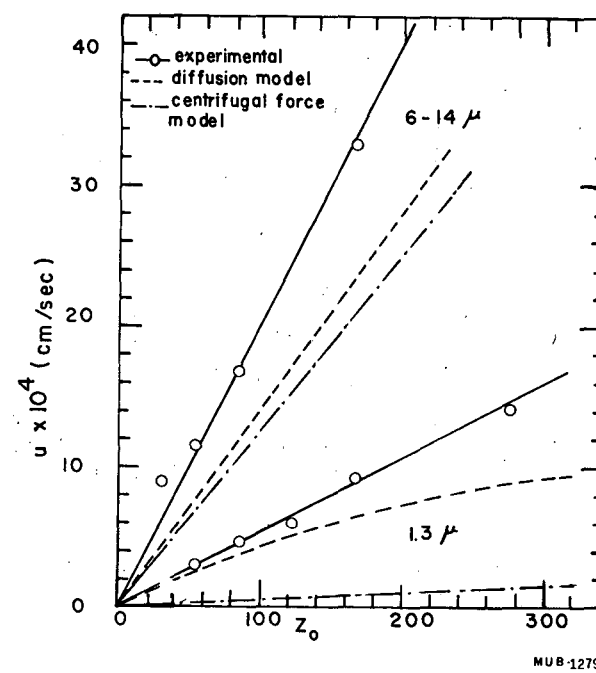

Fig. H. 6-4. Comparison of the experimental values of limiting filtration rate per area vs rpm and the values predicted by the two models.

7. THE DISPERSION OF BACTERIA

Francis G. Rust† and Charles R. Wilke

Bacteria may move randomly by their own motility. In a uniform medium that is free from convection, bacteria disperse by this motion in a manner which may be characterized by a diffusion mechanism. This behavior is of possible engineering interest in predicting the penetration of bacteria into cracks, along the interior surfaces of pipes, and through liquid media generally.

Three different experimental methods were used to measure the dispersion of bacteria. In the first, the location of individual bacteria was recorded at different times by multiple-exposure photography. The displacement of the bacteria from their original position was measured, and the diffusivity was calculated accoring to the Einstein relationship. The extent to which the motion of the bacteria had become random could also be evaluated in this experiment.

In the second method, a steep bacterial concentration gradient was established on a microscope slide and was photographed at various times for counting. From these photographs, bacterial concentration profiles were obtained. Different diffusivities were then used in a numerical solution to the diffusion equation; each diffusivity gave a different concentration profile. The calculated profiles were matched with the measured profile to determine which diffusivity gave a profile that matched the measured profile.

In the third method, a capillary tube was filled with a bacterial suspension and was immersed in stirred nutrient. After enough time had elapsed for bacteria to diffuse from the tube, the tube was removed and the number of bacteria in the tube and the number of bacteria in the solution were determined by plating on nutrient agar and counting the colonies of bacteria that grew from each viable bacterium. The diffusivities were obtained by numerically solving the partial differential equation for diffusion, sedimentation, and growth, to give concentration profiles at many different times. These concentration profiles were integrated to give the fraction of the bacteria remaining in the tube as a function of dimensionless time, Dt/l^2. The diffusivity could be determined from this function after the fraction of the bacteria remaining in the tube had been experimentally measured, provided that the time for diffusion and the length of the tube were known.

Details of the experimental systems and complete results are presented elsewhere.[1]

Scouting experiments were made on several strains of E. coli to determine how the multiplication rate, percent of bacteria that are motile, and bacterial velocity were affected by temperature, stage of growth, and composition of medium. E. coli U. C. 27 was selected for the diffusion measurements because the fraction of motile bacteria was highest in this strain.

Nutrient medium containing 5 g peptone, 3 g beef extract, 2 g glucose, to 1 liter water was used in all experiments. A medium containing peptone was used because in its absence only about half of the bacteria were motile at 20°C. This decrease in motility was observed in all defined media regardless of sugar energy source. The disadvantage of using nutrient medium was that the growth rate in its presence was so high that the diffusion experiments had to be limited to 3 hours.

A typical growth curve based on optical counts is shown (Fig. H. 7-1) for E. coli U. C. 27 at 20°C in nutrient medium. The percent of bacteria that are motile remained constant from early exponential phase to stationary phase. At the onset of stationary phase the velocity of the bacteria decreased rapidly. A growth-rate discontinuity in which the bacteria ceased to divide for a 2-hour period can be seen in the growth curve at a concentration of 5×10^7 bacteria/ml. Fowler,[2] who observed a similar discontinuity in the growth of E. coli at 37°C, has demonstrated that this failure to multiply occurs coincident with the depletion of oxygen in the medium.

Figure H. 7-2 shows data obtained by the mean displacement method. Although considerable variation is evident, the extrapolated values of D at infinite time are of the same general magnitude. This method seems the least satisfactory of those used.

Figure H. 7-3 is the chamber arrangement for microscopic measurement of concentration gradients for bacteria diffusing down a narrow channel. Figure H. 7-4 compares calculated

and observed profiles. Allowance for bacterial growth was included in the theoretical treatment.

Figure H.7-5 gives results obtained by the capillary-tube method, in which bacteria diffused out of the tube into a surrounding fluid.

On the basis of the various experiments, it was concluded that the mobility of E. coli can be described by a diffusion coefficient in the range of 2 to 3×10^{-5} cm^2/sec at 26°C in dilute aqueous medium.

Finally, general theoretical solutions to the problem of diffusion plus growth are presented. Examination of two hypothetical engineering problems indicated (a) that bacteria could diffuse through a crack into a sterile system in a few hours and (b) that bacteria would not make much headway back up a feed line against any significant flow of medium.

Footnote and References

†Present address: E. I. Dupont de Nemours & Co., Savannah River, Georgia.

1. Francis G. Rust and C. R. Wilke, The Dispersion of Bacteria, UCRL-17208, Sept. 1966.
2. Catherine B. Fowler, Relationship between Fermentation and Enzymatic Adaption, Biochim. Biophys. Acta. 7, 563 (1951).

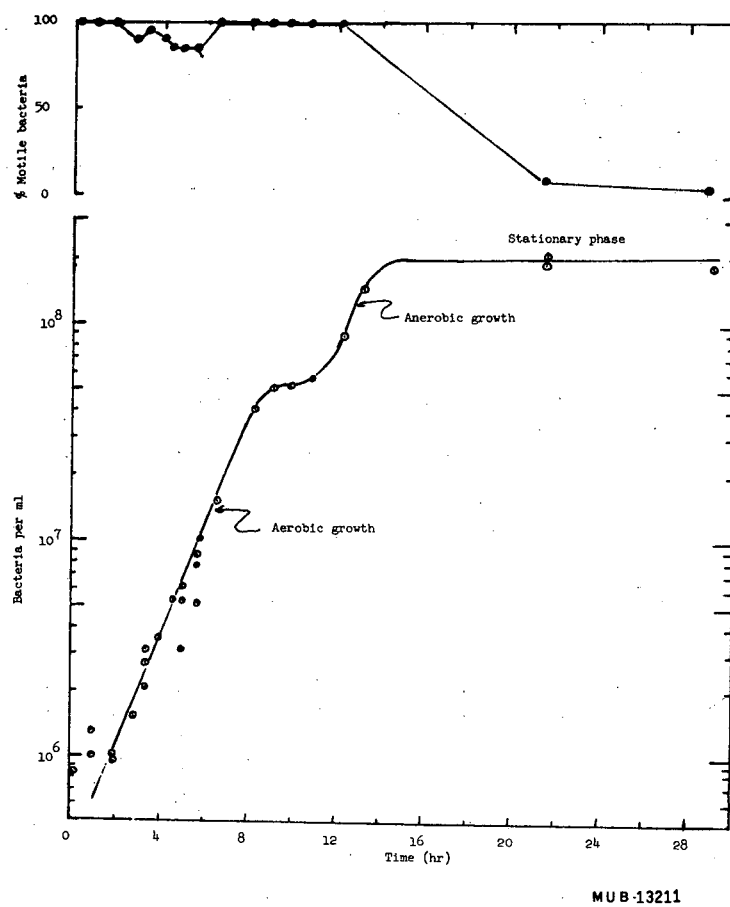

Fig. H.7-1. A typical growth curve from optical counts for E. coli 27 in nutrient medium at 20°C. Growth is aerobic until the oxygen is depleted. No further multiplication occurs until anerobic growth has started. The upper curve shows that a high percentage of the bacteria are motile until the onset of stationary phase.

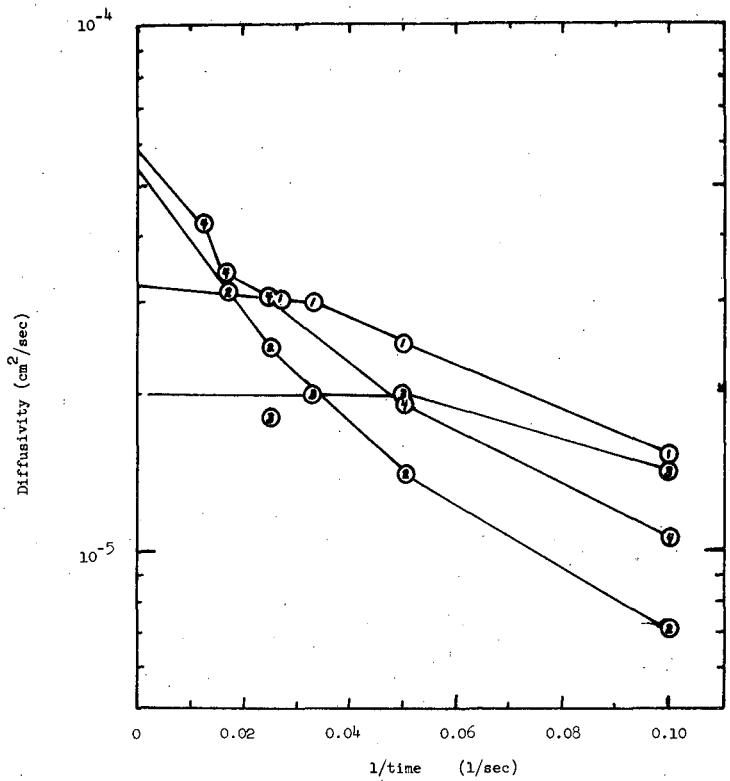

MUB 13215

Fig. H. 7-2. The log of the diffusivities from five different runs plotted against reciprocal time and extrapolated to an infinite time interval.

Run no.	$D(cm^2/sec)$ at $t = \infty$
1	3.3×10^{-5}
2	5.4×10^{-5}
3	2.0×10^{-5}
4	5.8×10^{-5}
Av	4.1×10^{-5}

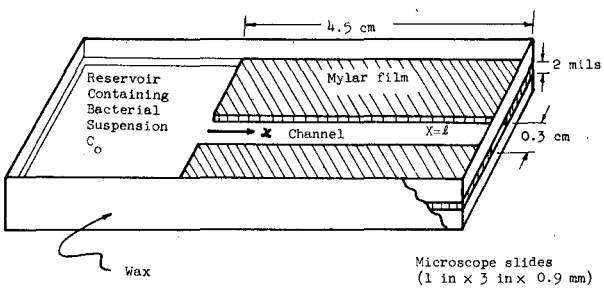

MUB 13216

Fig. H. 7-3. Chamber for the direct observation of bacterial concentration gradients with a microscope. The chamber was made by separating two microscope slides with thin sheets of "Mylar," then waxing the edges of the slides. The bacterial suspension was placed in the left-hand chamber and fresh medium was placed in the channel on the right. Diffusion occurred down the channel and could be recorded by photomicrographs.

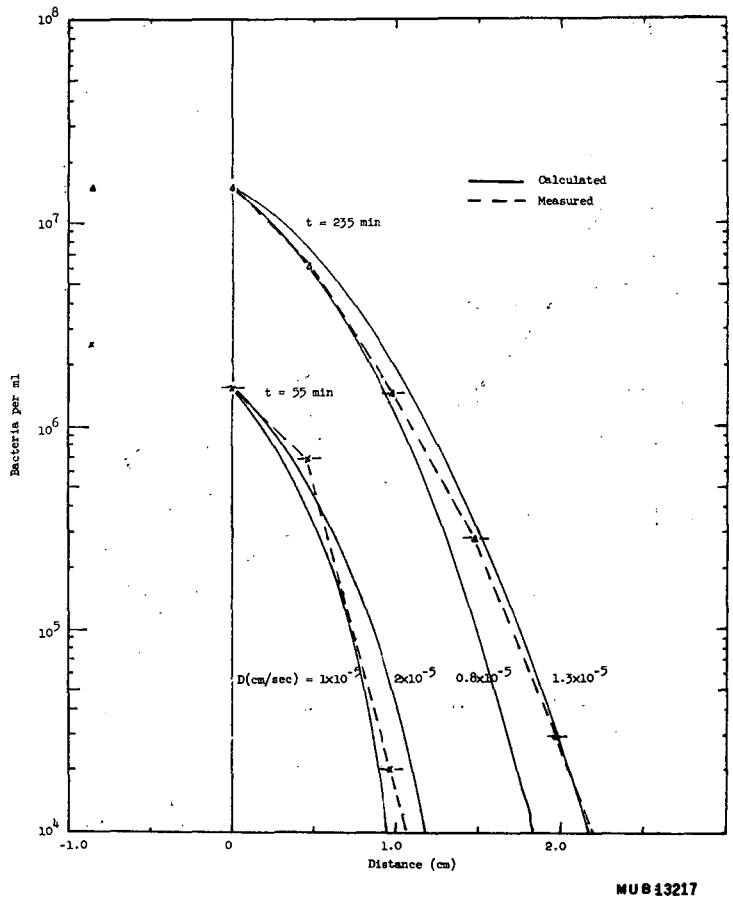

Fig. H. 7-4. Comparison of observed distributions of bacteria with calculated distributions at 55 and 235 min for a growth rate, $R = 2.3 \times 10^{-4}$/sec.

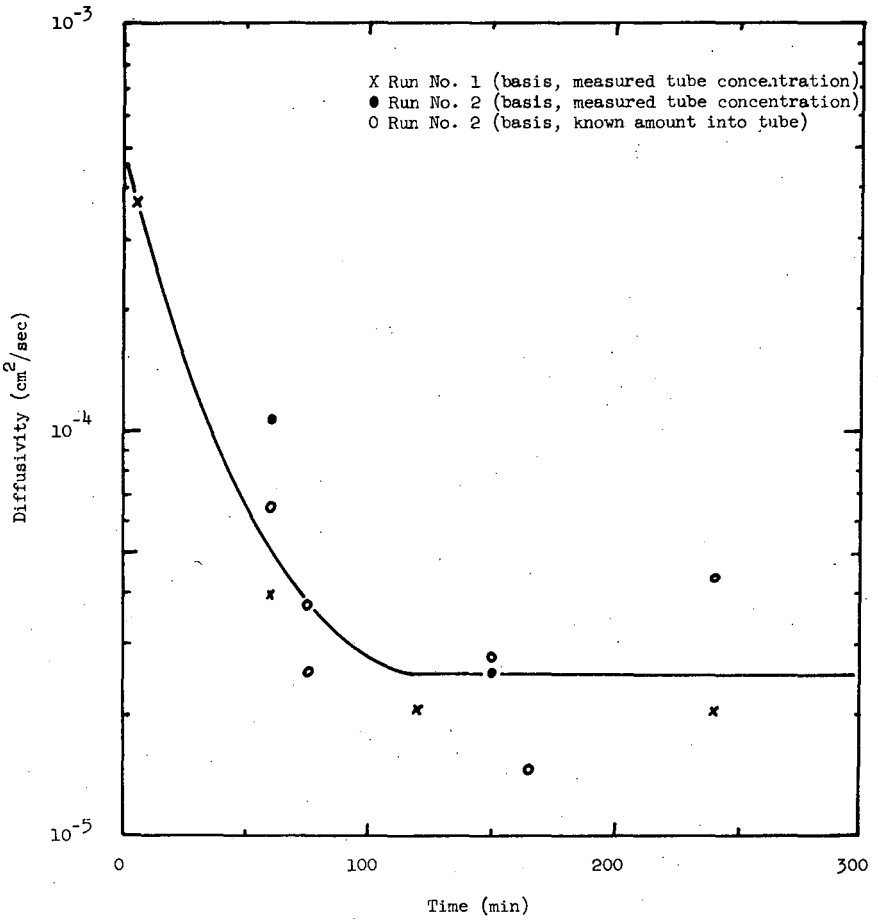

MUB 13226

Fig. H. 7-5. Diffusivities measured by the tube diffusion method for two runs are plotted against the length of time for diffusion. For very short times the measured diffusivities were high, probably because bacteria were washed out of the tube.

8. AN ECONOMIC STUDY OF SULFATE REMOVAL FROM BRINES WITH BACTERIA BASED ON A HYPOTHETICAL DESIGN

Ronald H. Charron† and Charles R. Wilke

Leban and Wilke[1] have pointed out the possibility of utilizing sulfate-reducing bacteria in brine purification, and the purpose of the study reported here is to ascertain the economic feasibility of this technique.

Data on the rate of sulfate reduction by a salt-tolerant strain of Desulfovibrio have been obtained by Leban et al.[2] These data were obtained from batch and continuous-culture experiments, with a medium containing 10% NaCl by weight and with lactic acid as carbon source. Based on this information, a process for commercial-scale removal of sulfate from a rock-salt brine containing 10% NaCl is proposed. The kinetics of sulfate reduction are assumed to follow the experimental data, although molasses is specified as carbon source in the design proposal. Details of these design and economic studies are presented elsewhere.[3]

Figure H. 8-1 is a flow sheet of the process. The essential operations are anaerobic conversion of sulfate ion to hydrogen by the bacteria, removal of H_2S from the brine by stripping, and removal of residual organic matter by a conventional activated sludge treatment.

Tables H. 8-I and H. 8-II summarize the estimated capital investment and operating costs for treatment of 85 tons of salt per day in the form of 10% aqueous solution. It is concluded that the process may compare favorably with conventional barium chloride treatment, although further experimental studies are needed to establish the performance of the bacterial process with more certainty.

Production of saturated brine by subsequent evaporation of the 10% product is also considered. It is suggested also that this method could be useful for recovering sulfur from seawater in conjunction with sulfate removal from brine in a seawater distillation plant to reduce scale formation in the evaporators. Figure H. 8-2 shows this hypothetical process.

Footnote and References

† Present address: Mobay Chemical Co., Pittsburg, Pennsylvania.

1. M. Leban and C. R. Wilke, Sulfate Reduction by Bacteria, UCRL-10966, Aug. 1963.
2. M. Leban, V. H. Edwards, and C. R. Wilke, Sulfate Reduction by Bacteria, UCRL-16420, Preliminary, Oct. 1965.
3. Ronald H. Charron and Charles R. Wilke, An Economic Study of Sulfate Removal from Brines with Bacteria Based on Hypothetical Design, UCRL-16945, August 1966.

Table H. 8-I. Estimated capital-investment statement for producing 10% sulfate-free brine by bacterial reduction.[a]

Basis: Capacity = 85 tons rock salt/day
Operating time--continuous, 360 days/year

Installed equipment	$130 200		
Piping Insulation Instrumentation Electrical installations	68 300		
Buildings and services Yard improvements	41 800		
Physical plant cost--Bacterial reduction		$240 300	
Physical plant cost--Activated sludge		104 000	
Engineering and construction	$ 69 000		
Direct plant cost--Sulfate removal		$413 300	
Direct plant cost--Sulfur recovery		36 000	
Contractor's fee	$ 16 500		
Contingency	112 000		
Fixed capital investment			$578 000

a. Probable accuracy of estimate: ±25%

Table H. 8-II. Estimated manufacturing-cost statement for producing 10% sulfate-free brine by bacterial reduction.[a]

Basis: Capacity = 85 tons rock salt/day
Operating time - continuous, 360 days/year

Raw materials	$ 70 000		
Labor Supervision Maintenance Plant supplies	59 600		
Utilities	29 300		
Direct manufacturing cost--Bacterial reduction		$158 900	
Direct manufacturing cost--Activated sludge		8 700	
Plant overhead	22 800		
Indirect manufacturing cost		22 800	
Depreciation Taxes and insurance	64 000		
Fixed manufacturing cost		74 000	
Manufacturing cost--Sulfate removal			$254 400
Manufacturing cost--Sulfur recovery			26 200
Credit for sulfur			3 200
Total manufacturing cost			277 000
Cost per pound of rock salt			0.00455

a. Probable accuracy of estimate: ±25%

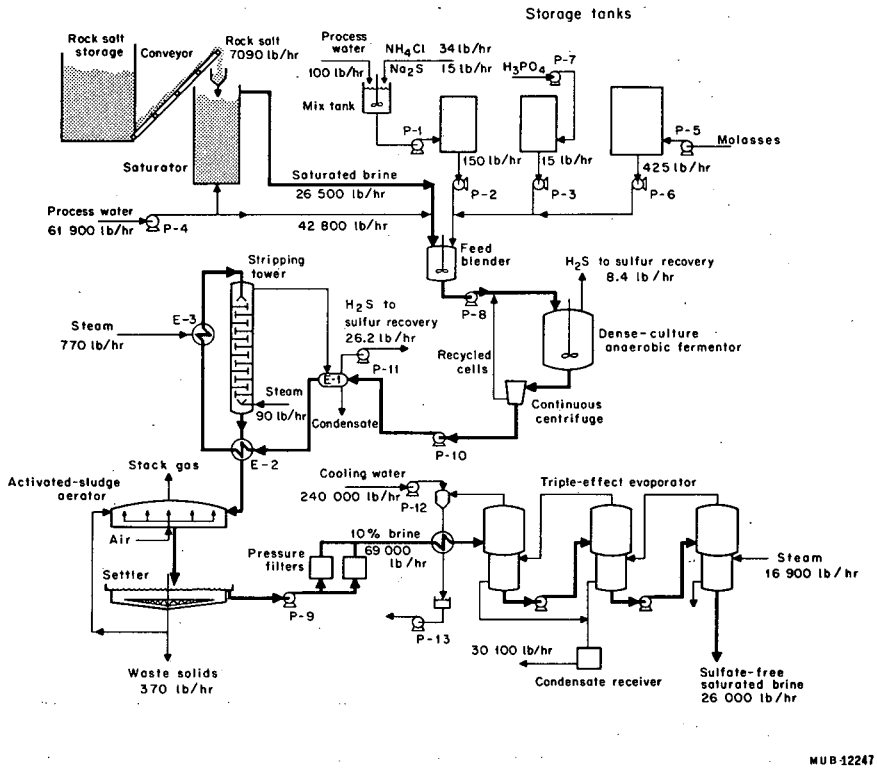

Fig. H. 8-1. Process flow diagram for removal of sulfate from 10% brine by bacterial reduction.

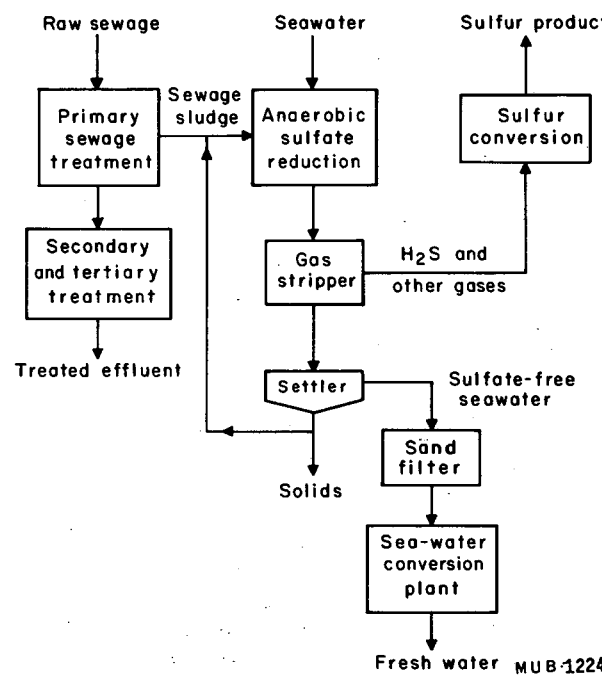

Fig. H. 8-2. Hypothetical process for recovering sulfur from seawater.

I. INSTRUMENTATION

1. CYCLOTRON BEAM DIAGNOSTICS AND INSTRUMENTATION†

D. J. Clark

Introduction

In the operation of the modern cyclotron, it is important to have adequate instrumentation in the Internal and external beam regions. This is useful both for normal tuning of the beam and for diagnosing various cyclotron problems. Both visual and electrical observation techniques are useful. The traditional visual instrument is the eyeball. More recently the telescope and then the TV camera have been used as visual tools. Electrical readouts of currents, voltages, temperatures, pressures, etc. are also extremely useful. Richardson, in a recent survey, discusses some of the techniques for investigating cyclotron beams.[1]

Internal Beam Methods

Spatial Distribution

Cyclotrons report a variety of methods for observing the spatial distribution of the internal beam. Visual observation can be made of the ionization produced by the beam near the ion source, when large currents are being accelerated. Heating of dee and dummy dee carbon liners can also be observed in this case. Quartz plates or probes painted with phosphors can be moved radially to observe the beam distribution. Radiographs of probes exposed to the beam are also used.

The most common type of probe for beam current measurement is a single insulated electrode with a connection brought to the control room. An example of this "single finger" probe as used at the 88-inch cyclotron is shown in Fig. I. 1-1.

A useful type of probe for investigating radial beam quality and centering is a radial differential probe, or "ΔR" probe.[2] A probe of this type used at the 88-inch cyclotron is shown in Fig. I. 1-2. Some runs with the ΔR probe in the 88-inch cyclotron, illustrating good and poor internal beam quality, are shown in Fig. I. 1-3.

The axial distribution of the beam can be found visually with a phosphor probe, or by electrical readout from a multifinger probe.[2] A three-finger probe used at Berkeley is shown in Fig. I. 1-4. When enough beam hits the septum, a glow can be observed with a telescope or television camera. Figure I. 1-5 shows beam illuminating the radiation-cooled tungsten septum at the 88-inch cyclotron.

Time Distribution

The measurement of the time, or phase, distribution of the internal beam is helpful in eliminating phase loss of the beam during acceleration. A direct measurement of the internal phase distribution can be found from a plot of beam current vs frequency at a fixed radius (Fig. I. 1-6(a)). The slope of this curve gives the intensity distribution vs sin ϕ (Fig. I. 1-6(b)).

Power Handling

In some of the new sector-focused cyclotrons several kW of beam power is present at full radius. Since the beam size at full radius is only several mm^2, high power densities exist. Precautions must be taken to protect probes from burnout. Most laboratories used water-cooled probes. Some also slant the surface with respect to the beam or sweep the beam across the probe.

External Beam Methods

Spatial Distribution

For observation of external beam spatial distribution, both visual and electrical methods

are used. The traditional methods are the radiograph and photographic film exposure. Telescopes or television cameras are used to view the beam on quartz plates, and various phosphors such as zinc sulfide or vacuum grease. Electrical readout is obtained from various external beam probes.

A collimating slit used in the 88-inch cyclotron is shown in Fig. I. 1-7.

The radial and vertical emittance of the external beam is an important property for beam transport and nuclear physics experiments. A convenient method of measuring the emittance is the slotted plate method described in Ref. 3. Figure I. 1-8 shows a slotted plate used for radial emittance measurements at the 88-inch cyclotron.

Time Distribution

Knowledge of the time distribution of the external beam is useful for diagnostic work and for coincidence experiments. A current-collecting probe, induction probe, or scintillator can be used directly in the external beam, or the beam can be scattered into a detector and a coincidence method can be used.

Energy Distribution

The energy of the external beam is measured by range in an absorber, by the kinematics or thresholds of certain reactions, and by the path taken by a particle in a known magnetic field of a bending or analyzing magnet. The energy distribution, or spread, is of particular interest for experiments. The energy distribution can be measured by sweeping the beam past a slit with an analyzing magnet, or by pulse-height analysis of a semiconductor detector looking at beam scattered from a thin foil. The semiconductor method is relatively cheap, fast, and accurate. Figure I. 1-9 shows a spectrum of the full external beam of the 88-inch cyclotron measured with a Li-drifted silicon detector.

Acknowledgments

The author wishes to acknowledge the information and photographs sent by many laboratories in response to the questionnaires. Also of great help were the excellent photographs by D. Pepperell, and help with other figures from Tom Chan, Roy Burton, and the cyclotron crew.

Footnote and References

† Short form of paper for International Conference on Isochronous Cyclotrons, Gatlinburg, Tennessee, May 1966.

1. J. Reginald Richardson, Sector-Focusing Cyclotrons, Prog. Nucl. Tech. Instrumentation, p. 62-75 (1965).
2. E. L. Kelley, in Proceedings of the International Conference on Sector-Focused Cyclotrons, UCLA, 1962, p. 33.
3. H. A. Grunder, F. B. Selph, and H. Atterling, in Proceedings of the International Conference on Sector-Focused Cyclotrons and Meson Factories, Geneva, 1963, p. 68

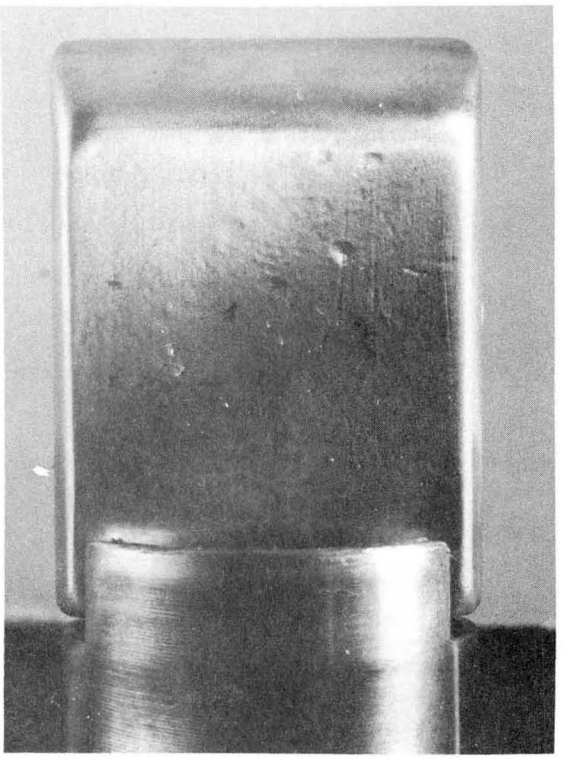

Fig. I. 1-1. Single-finger probe used to measure internal beam intensity in 88-inch cyclotron. Material is chrome-plated water-cooled copper.

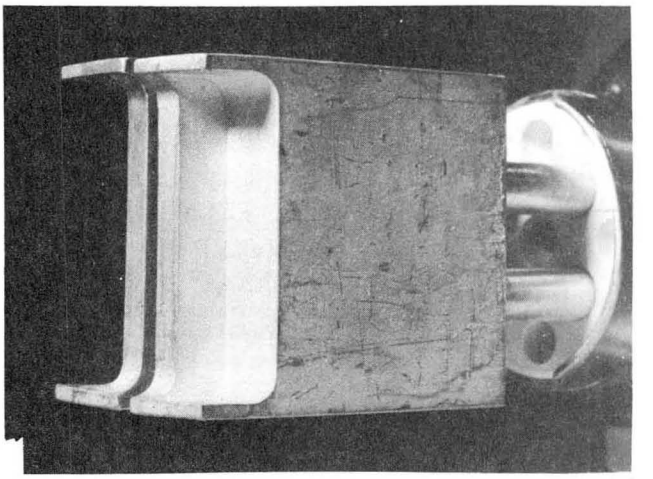

Fig. I. 1-2. "ΔR" probe used on the 88-inch cyclotron. Material is water-cooled copper.

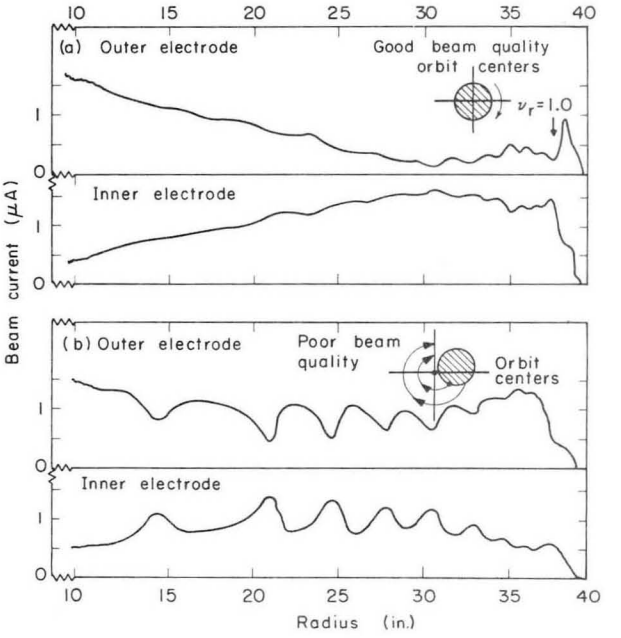

Fig. I. 1-3. Beam current vs radius on the two electrodes of a "ΔR" probe in the 88-inch cyclotron. 65-MeV α particles with 44 kV on the dee. ΔR = 0.040 in.
(a) Beam started on center, giving good quality; most of the beam is on inner electrode at large radius. (b) Beam started off center, giving poor quality; more than half of beam is on outer electrode at large radius.

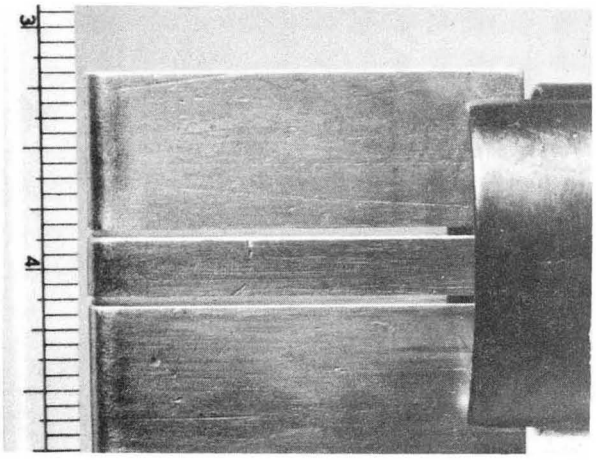

Fig. I. 1-4. Three-finger probe used at the 88-inch cyclotron. Material is water-cooled copper.

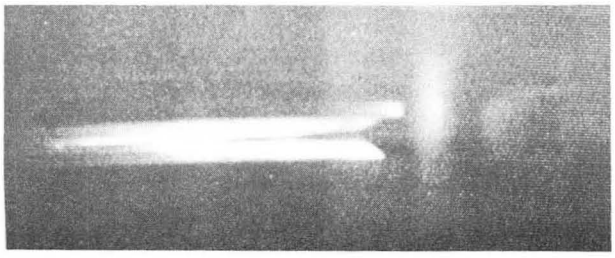

Fig. I. 1-5. Television monitor showing deflector septum illuminated by about 1.5 kW of beam in the 88-inch cyclotron.

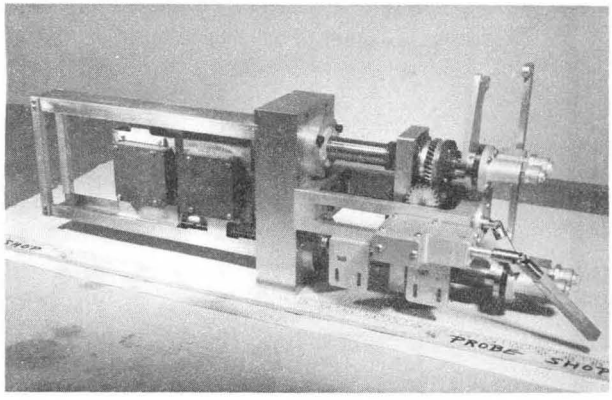

Fig. I. 1-7. Collimator used to define the external beam radially at the 88-inch cyclotron. Material is graphite on a water-cooled copper frame. Width and center position are independently adjustable.

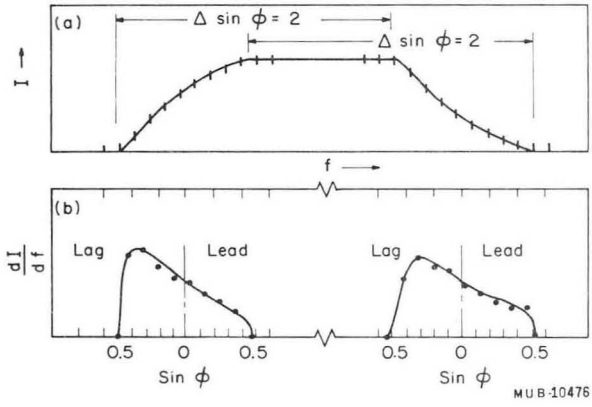

Fig. I. 1-6. (a) Internal beam current vs frequency for 65-MeV α particles at a 30-in. radius in the 88-inch cyclotron.
(b) The slope of the data above is plotted, showing the intensity distribution of beam vs sin ϕ ($\approx \Delta f$). The abscissa is calibrated by using the $\Delta \sin \phi = 2$ length from (a).

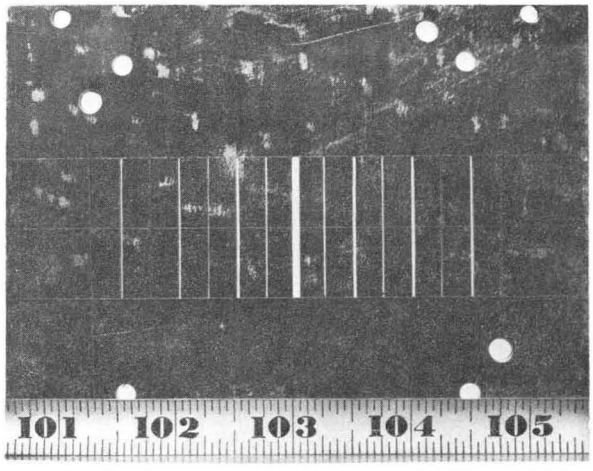

Fig. I. 1-8. Slotted plate used for radial emittance measurement at the 88-inch cyclotron. Material is 1/8-in. tantalum on a water-cooled copper frame. Slots are 0.060 in., 0.020 in., and 0.010 in. wide.

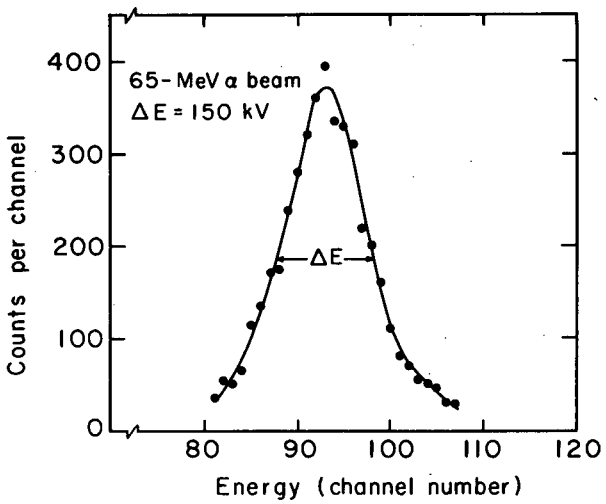

Fig. I. 1-9. Total external beam energy spectrum measured with a lithium-drifted silicon detector (supplied by the Goulding Nuclear Chemistry group) at the 88-inch cyclotron.

2. MACHINE DEVELOPMENT AT THE BERKELEY 88-INCH CYCLOTRON†

R. Burger, D. J. Clark, E. Close, and H. Kim

General Development

Operation and machine development at the 88-inch cyclotron have been described previously.[1-3] Machine settings for new particle energies are being developed on a regular basis. The beams now available include protons from 10 to 55 MeV, α particles from 15 to 130 MeV, and ^{3}He from 10 to 145 MeV. Third harmonic acceleration is used for α-particles under 24 MeV and ^{3}He under 18 MeV. Nitrogen ions have also been accelerated to 20 MeV. This mode runs well even though we do not use a dummy dee. Some high-intensity runs showed that 5 mA of protons could be accelerated to a 5-in. radius, and the estimate is that about 3 mA would have reached full energy of 25 MeV if allowed to do so. This is in reasonable agreement with the calculated space-charge limit.

Some modifications have been made to the machine and external beam line recently, as shown in Fig. I. 2-1. The three 120-deg probes are still available, and are useful for beam centering when first trying new modes of operation, such as third harmonic acceleration. The internal phase probe is no longer used. A radial probe line has been added at the "target probe" port to make "ΔR" measurements on the internal beam quality.[4] The new deflector, now in the beam-testing stage,[5] is shown in place. Two TV cameras are used to view the ion source and deflector, and prove very useful to monitor source and puller problems, and beam distribution on the deflector septum. On the external beam line a radial steering magnet, and analyzing slits forming an object for the switching magnet, have been added recently.

Before testing was begun on the new deflection system, the old system was optimized over a period of several years. The best figure for deflector transmission is 70% for 120-MeV α particles. The average transmission is about 50% over all beams. There is usually about 10% loss at the coupling resonance just before deflection. Some septum development has been done to maximize its power handling, since high beam intensities are required for many of the several hundred isotope-production runs per year. The best septum design thus far has been radiation-cooled 0.010-in. tungsten sheet with a 6-in. -long tapered slot to match the beam profile. This design provides as much external beam surrent as several water-cooled copper designs which were tried, and is cheaper, less susceptible to damage, and more easily changed. The present external beam power available is about 3 kW, e.g., 150 μA of 20-MeV protons, with about 3 kW more dropped on

the septum. Some studies are in progress on a possible water-cooled tungsten septum.

A radioactivity survey was made of the acceleration region in Nov. 1965 after a 9-day shutdown, to determine the amount of activity which had built up during about 2 years of running with large beam intensities. These measurements are shown in Fig. I. 2-2. The deflector and moving probes were removed. The general $\beta\gamma$ level is about 0.5 R/hr in the inner regions. However, most work on this area can be done remotely from a location where the activity is about 100 mR/hr or less. Some hot spots appeared on the "C probe," which shields the dee from beam, and near the septum, where some material has been evaporated or sputtered. Comparison of these measurements with some made 9 days earlier showed that the activity had decayed about 30% during this time.

Some computer calculations have been made on the problem of the gap-crossing resonance pointed out by Gordon.[6] This effect is equivalent to a first harmonic in the magnetic field, and is produced by a "beat" of the two-fold acceleration gap geometry against the threefold magnetic sector field of the 88-inch and many other cyclotrons. Figure I. 2-3 shows orbit center paths for accelerated beams with several starting phases. This resonance appears to constitute a limitation on beam quality in this cyclotron, when a wide phase width is accelerated.

External Beam Studies

Measurements have been made of the energy and time distributions of the full external beam of the cyclotron. To measure the energy, lithium-drifted silicon detectors with associated electronics were used (supplied by the Lawrence Radiation Laboratory Nuclear Chemistry Instrumentation Group, under F. S. Goulding). A gold foil was used on the beam line straight through the switching magnet, to scatter the beam 20 deg into the detector. A pulse-height analyzer was used to display the spectrum. The contribution of detector and electronics to the energy spread was less than 10%. The time distribution of the beam was measured with a semiconductor detector[7] placed directly in the beam on the same beam line.

The energy spectrum with the best cyclotron tuning is shown in Fig. I. 2-4. The full width at half maximum is 140 kV, or 0.22%, after correction for detector and electronics. The energy spectrum for average cyclotron tuning is shown in Fig. I. 2-5(a). The spread is 0.4% FWHM. This is about equal to the energy gain per turn in the cyclotron. If the cyclotron is detuned--by changing the dee voltage by several hundred volts, for example--a spectrum such as that of Fig. I. 2-5(b) can occur. The two energy peaks are believed to result from misalignment of the beam with the deflection channel, giving extraction from several precession cycles.

The beam time structure is shown in Fig. I. 2-6(a) for average cyclotron tuning, corresponding to the energy spectrum of Fig. I. 2-5(a). The pulse width is 30 deg FWHM. For a detuned beam, corresponding to the energy spectrum of Fig. I. 2-5(b), the double-peak time structure is shown in Fig. I.2-6(b). The phase width is 45 deg. Sometimes three peaks are observed for detuned beams.

Some studies have been made on the sensitivity of the beam to instability of various machine parameters. Figure I. 2-7 shows the effect of dee voltage ripple on the energy spread of the external beam, for the condition of best tuning. Ripple was injected and the cyclotron optimized for each measurement. The result shows that ripple should be kept less than 1%. Other measurements, for cases other than optimum, and on beam optics for tightly collimated beams, indicate that the dee voltage regulation should be 0.1%. The stability of the dee frequency and the main magnetic field, including trim-coil contributions, should be 0.002%.

The emittance of the external beam is about as reported previously,[2,3] 50 mm mr radially and 70 mm mr axially, including some measurement errors. The virtual sources are as reported.[3] With the small steering magnet added before the first quadrupole, all radial virtual sources can now be placed on the beam-pipe center line.

Axial Injection Progress

During the past year axial injection studies for the 88-inch cyclotron have been in progress for use with a future polarized ion source. A bench test was set up, consisting of an ion source, a 5-ft-long transport tube with electrostatic quadrupole focusing, and a probe for current measurement. Tests with this system served to try the initial components of an injection system, and helped to solve some of the problems of ion source optimization and quadrupole voltage supply leads. A test was then arranged to inject beam into the cyclotron through the upper pole. This

was a preliminary test to study the problems and efficiency of the various components of the system. The normal ion source was removed for this test and replaced afterward.

The system tested is shown in Fig. I.2-8. The ion source is a modified duo-plasmatron (provided by 90-Inch Cyclotron Group, Lawrence Radiation Laboratory, Livermore). Three electric quadrupole doublets transport the beam down to the cyclotron center. The inflector is an electric mirror beneath a grounded grid, similar to the one used by Birmingham.[8] Frames were inserted in the dee and dummy dee to give the initial particle revolutions enough energy gain to clear the inflector. The frames did not have the grid wires used at Birmingham. Injection was on center through a 1-in. hole in a temporary 8-in.-diameter iron pole plug. The injection voltage was 15 kV and the dee voltage was 60 kV, which gives a ratio of 4/1, compared with the ideal ratio of 5/1.[9] This caused the initial orbits to be off center about 0.25 in. and full power in the inner harmonic coils (15 gauss) had to be used to bring the beam back on center again. The beam intensities obtained were 400 μA at the top Faraday cup, 130 μA at the inflector, 10 to 20 μA accelerated to 4 in. radius, 1 μA extracted of 30-MeV protons. The relatively poor transmission through the acceleration region and the deflector is due to poor beam quality caused by the off-center initial orbits.

The results of this test showed the weak points of the system as presently developed. The ion source will be modified to allow injection at energies of 10 to 15 kV. Studies will be made of optics problems in the quadrupoles and inflector region. Voltage-holding problems of the inflector in the higher range of magnetic fields will be investigated.

Design Recommendations for Future 88-Inch Cyclotrons

The 88-inch cyclotron has proved to be of very sound design. It has produced external beams of the intensity and maximum energy predicted by its designers. Machine settings are repeatable after intervals of months or years. Energy is easily variable. The 8-in. pole plugs are very valuable, both for accurate positioning of the ion source and for easy conversion to an axial injection system.

In the light of several years of operational experience, there are some design modifications which one would make if the machine were built again, most of which have been or will be made on this accelerator. The vertical focusing built into the magnet is adequate for 70- to 75-MeV protons. The extraction system could extract this energy. If the rf system went up to about 18.5 MHz, the cyclotron would be capable of producing this energy. A more difficult modification is that of adding some third harmonic to the rf voltage to give a "flat top" on the rf wave. This could be done either by injecting the harmonic on the present dee, or by using a small additional dee or dees for the third harmonic. As suggested by others previously, this would combine the virtues of good beam quality with wide phase width, a significant step toward the "ideal cyclotron."

Acknowledgments

The authors wish to thank many people for help in this work: D. Elo, D. Morris, A. Hartwig, J. Meneghetti, D. Pepperell, and D. Perkins for mechanical engineering and fabrication; K. Ehlers, S. Bloom, and E. Zaharis for ion source assistance; P. Pellissier, P. Frazier, and M. Renkas for electrical engineering; F. Goulding, D. Landis, and R. Lothrop for help with detectors and electronics; A. Garren, H. Owens, and A. Kenney for computer program assistance; John Bowen and the crew for much cooperation during machine runs; H. Grunder and F. Selph for informative discussions and assistance on some machine runs; and H. Conzett, B. Harvey, and E. Goldberg for help and encouragement in this program.

Footnote and References

† Short form of paper for International Conference on Isochronous Cyclotrons, Gatlinburg, Tennessee, May 1966.

1. E. Kelley, in Proceedings of the International Conference on Sector-Focused Cyclotrons, UCLA, 1962, p. 33.
2. H. A. Grunder and F. B. Selph, in Proceedings of the International Conference on Sector-Focused Cyclotrons and Meson Factories, Geneva, 1963, p. 8; H. A. Grunder, F. B. Selph, and H. Atterling, op. cit. p. 59.
3. Hermann Grunder and Frank Selph, Operation of the 88-Inch Cyclotron, UCRL-11477, Apr. 1964.

4. D. J. Clark, Beam Diagnostics and Instrumentation, UCRL-16792, May 1966.
5. D. J. Clark, E. Close, H. A. Grunder, Hogil Kim, P. Pellissier, and B. H. Smith, Regenerative Beam Extraction for the Berkeley 88-Inch Cyclotron, UCRL-16794, May 1966.
6. M. M. Gordon, in Proceedings of the International Conference on Sector-Focused Cyclotrons, UCLA, 1962, p. 268.
7. H. E. Conzett, L. B. Robinson, and R. N. Burger, Nucl. Instr. Methods 31, 109 (1964).
8. W. B. Powell and B. L. Reece, Nucl. Instr. Methods 32, 325 (1965).
9. D. J. Clark, Rutherford Laboratory, Harwell, Cyclotron Group Design Note CDN-500-05-024, 1962.

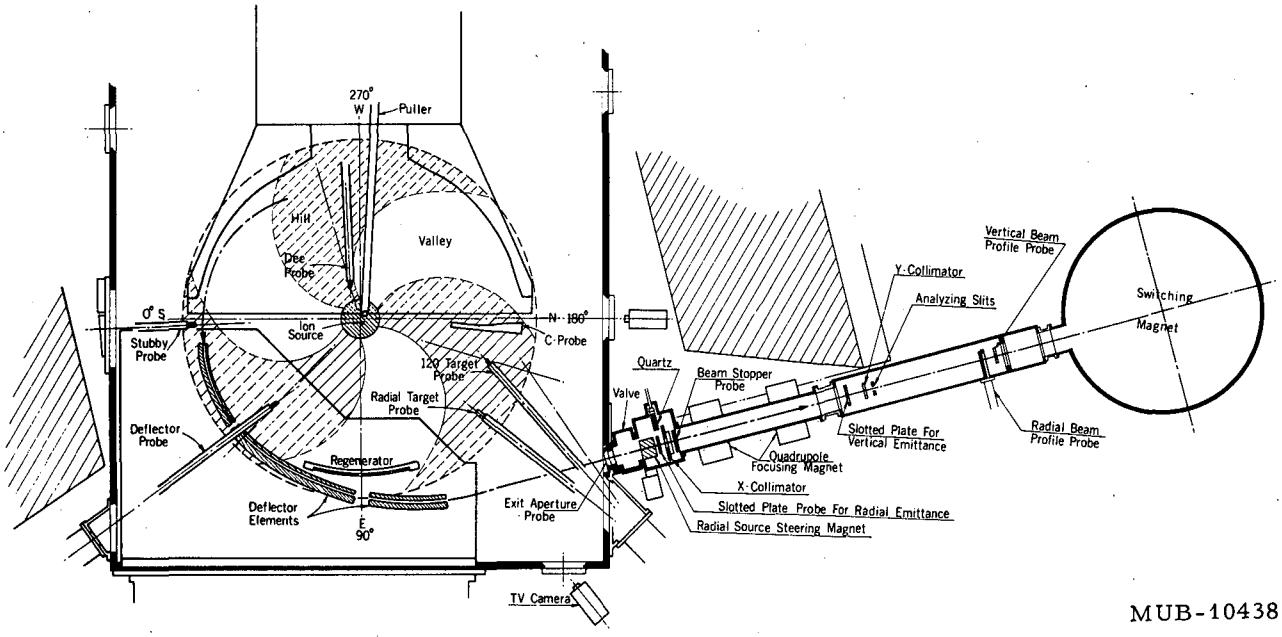

Fig. I. 2-1. Plan view of 88-inch cyclotron vacuum tank and external beam line.

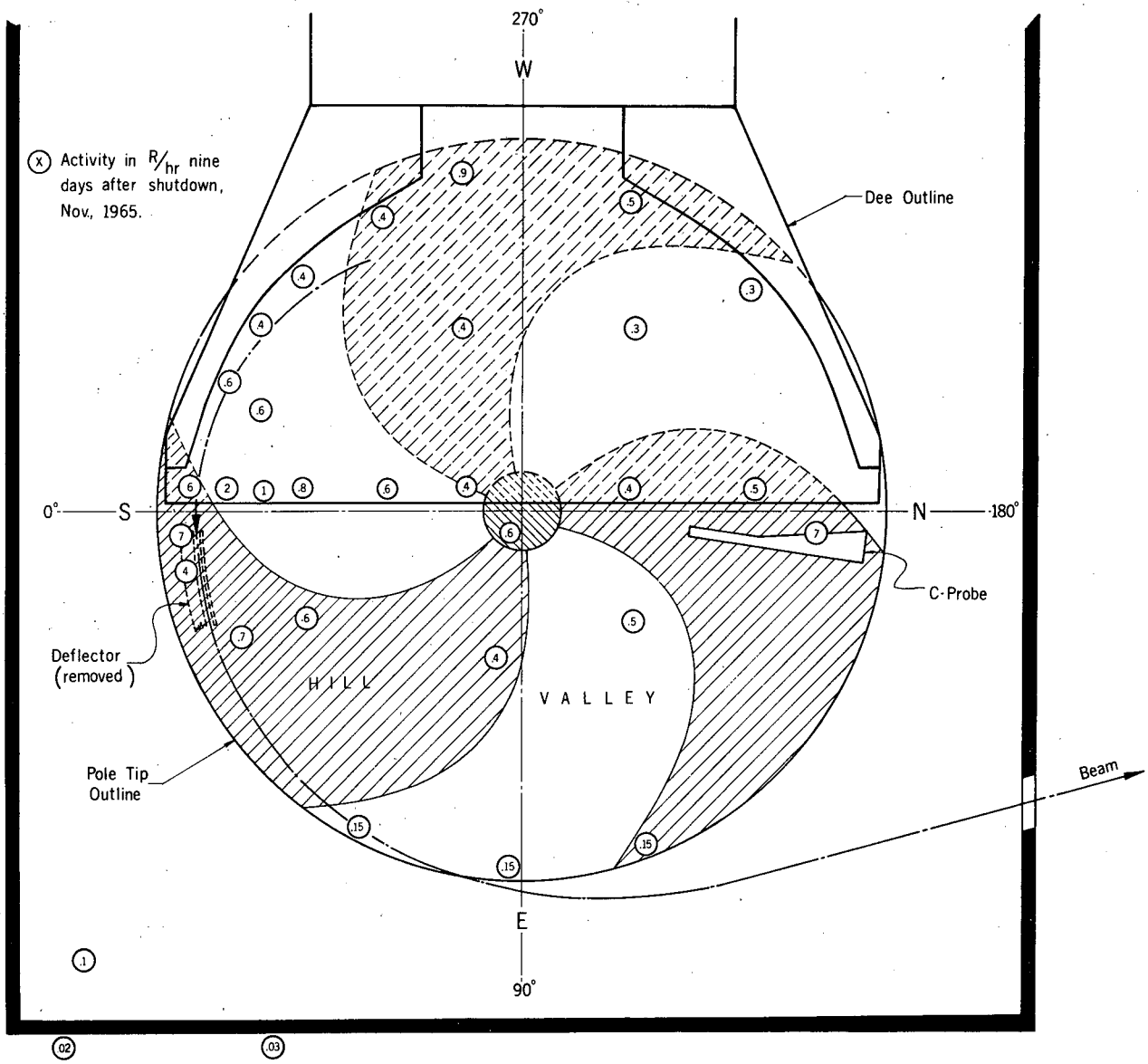

MUB-10481

Fig. I. 2-2. Radioactivity survey of 88-inch cyclotron tank 9 days after shutdown. The circled figures show the βγ activity in R/hr. The deflector and moving probes were removed from the tank.

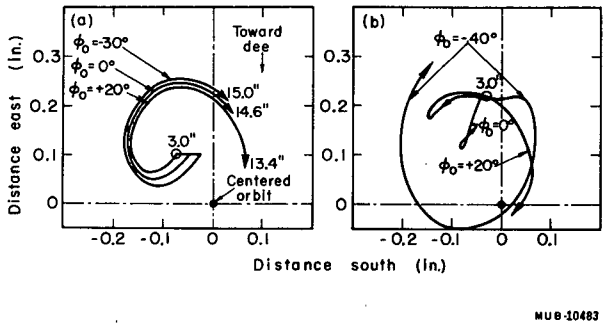

Fig. I. 2-3. Motion of orbit centers for 65-MeV α particles calculated with the general orbit code. Several starting phases are shown. A positive phase means the particle lags behind the rf. (a) Starting position adjusted to minimize center spread to about 0.2 in. (b) Starting position adjusted to bring the ϕ_0 = 0 deg particle to the precession center at 15 in. radius. Center spread is about 0.3 in.

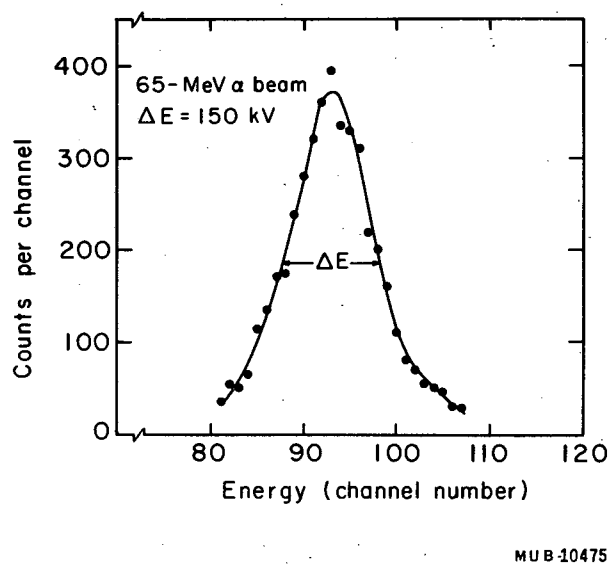

Fig. I. 2-4. Full external-beam energy spectrum with best tuning conditions. 65-MeV α-particles. 50% extraction efficiency. ΔE = 140 kV = 0.22% FWHM, after correction for electronics spread.

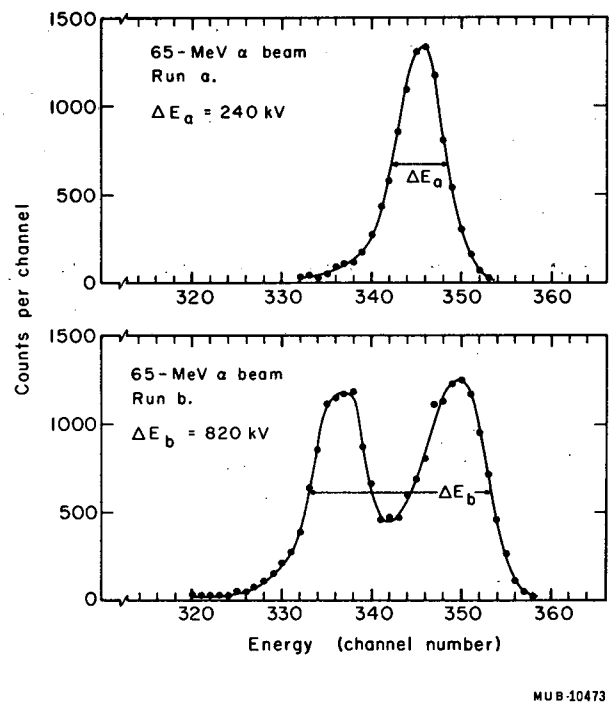

Fig. I. 2-5. (a) Typical energy spectrum for 65-MeV α particles. (b) Energy spectrum for 65-MeV α particles. Cyclotron detuned by changing dee voltage from optimum.

(a)

(b)

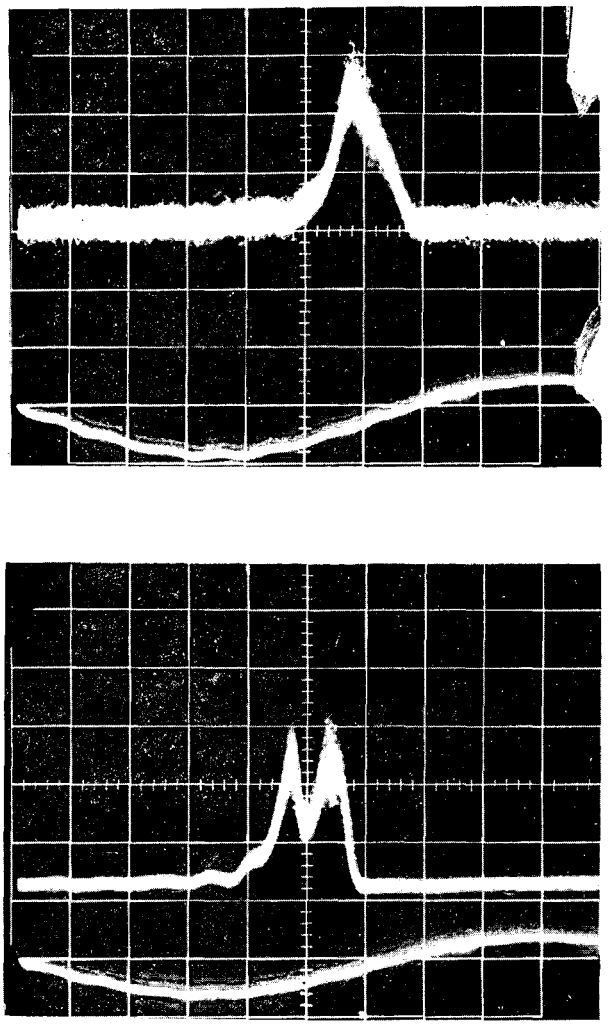

Fig. I. 2-6. (a) Typical external beam pulse on sampling oscilloscope. Beam tuning same as Fig. I. 2-5(a). Phase width = 30 deg FWHM. (b) External beam pulse with same tuning as Fig. I. 2-5(b). Phase width = 45 deg FWHM.

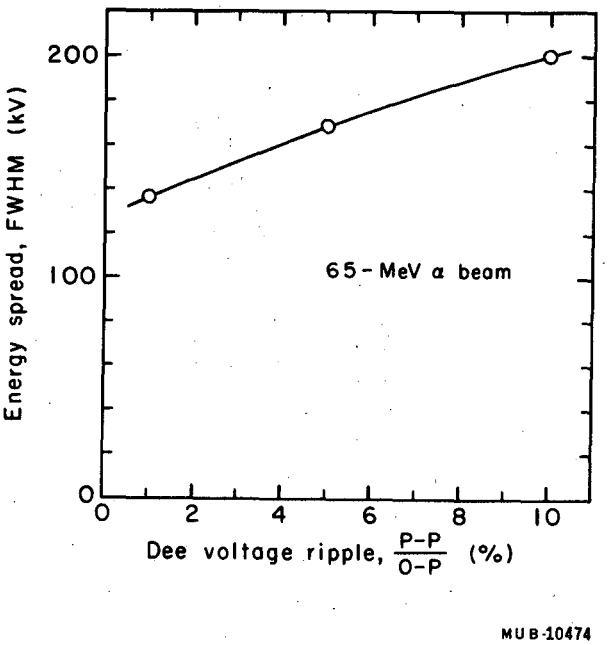

Fig. I. 2-7. Energy spread of 65-MeV α particle beam as a function of dee voltage ripple. The energy spread is full width at half maximum. The peak-to-peak ripple is divided by zero-peak dee voltage.

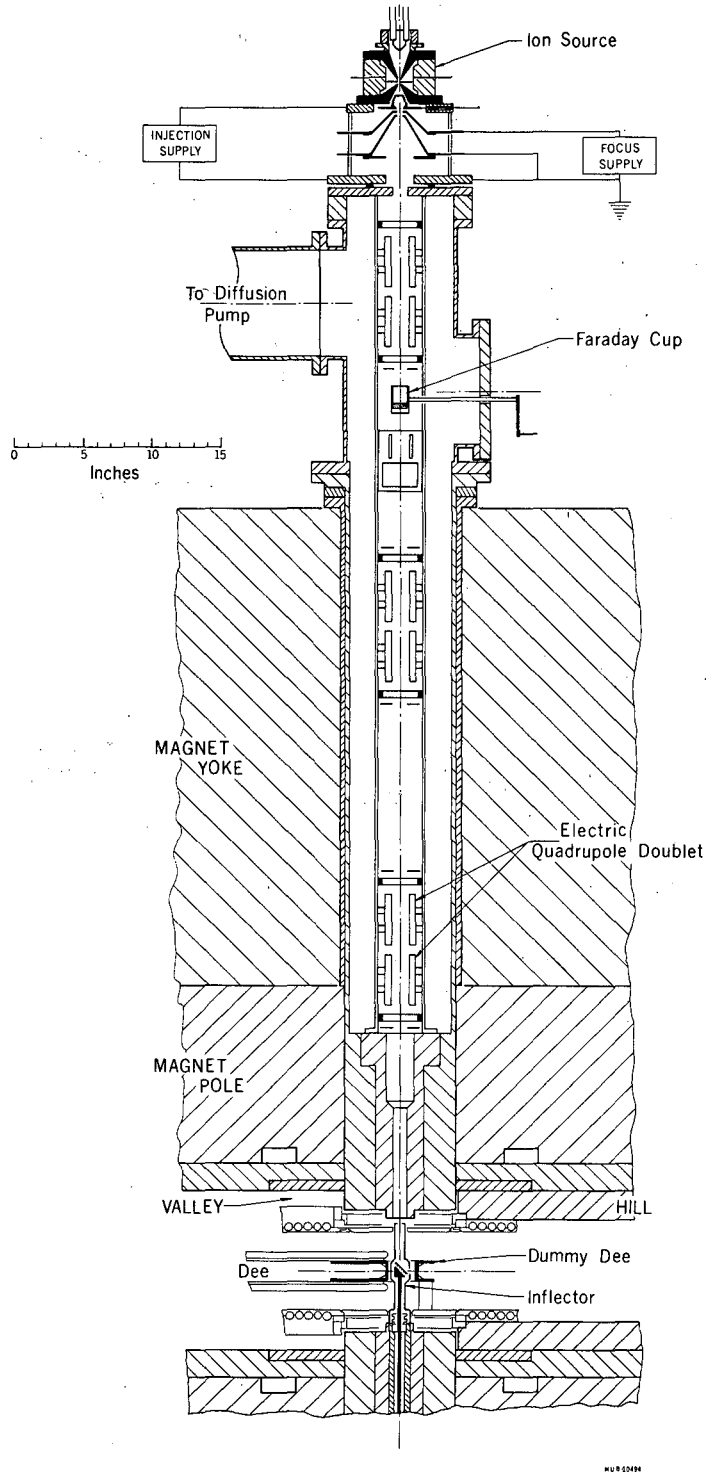

Fig. I.2-8. Axial injection system used for a preliminary test in the cyclotron. Normal axial ion source was removed for this test and replaced afterward.

3. REGENERATIVE BEAM EXTRACTION FOR THE BERKELEY 88-INCH CYCLOTRON†

D. J. Clark, E. Close, H. A. Grunder, Hogil Kim, P. Pellissier, and B. H. Smith

Introduction

For the positive-ion isochronous cyclotron, a number of beam extraction methods are proposed, namely: turn separation by energy gain and precession, nonlinear resonance, and regenerative extraction. The original beam extraction method for the Berkeley 88-inch cyclotron was investigated by Garren et al.,[1] using turn separation from energy gain and precession. The beam extraction based on this study was accomplished by Grunder et al.[2] The beam could be accelerated through $\nu_r = 1$ and $\nu_r = 2\nu_z$ resonances. About 50% extraction efficiency and 0.5% energy spread has been achieved. Later developments improved further from the above figure.[3] One may improve the system by using a beam with narrow rf phase (single-turn extraction); but it requires an accurate instrumentation and it greatly reduces the duty cycle. Extraction by the nonlinear resonance is rather difficult for the variable-energy machine.

The successful operation of the electrostatic regenerative system for the Birmingham 40-inch cyclotron[4] led to an investigation of regenerator beam extraction for the 88-inch cyclotron. This method was originally developed for synchrocyclotrons by Tuck and Teng[5] and LeCouteur.[6-8] In this method turn separation is obtained from the resonance excitation of the radial motion by the gradient harmonics. Since the turn separation does not depend, in principle, on the energy gain, a low dee voltage can be used for the cyclotron. Also the energy spread of the extracted beam can be improved.

This paper describes the investigation of regenerative beam extraction for the 88-inch cyclotron.

General Considerations and Computer Studies

The Berkeley 88-inch cyclotron is a three-sector AVF variable-energy cyclotron designed to accelerate protons up to 60 MeV, deuterons up to 65 MeV, and heavier ions up to comparable energies.[9] A plan view of the pole face and the original extraction system is shown in Fig. I.3-1. The entrance of the deflector starts at 3 deg azimuth and ends at 108 deg. The maximum deflector voltage held is given by $VE = 1.5\times10^4$ kV^2/cm.

For a given dee position and external beam line restrictions are imposed.

The cross section of the regenerator electrodes is similar to that in the Birmingham system,[4] which is shown in Fig. I.3-2. The effects of the 3/4-in. open slot is shown in Fig. I.3-3.

Analytical studies indicated the worst position of the regenerator is at about 60 deg azimuth, and the best is at about 120 deg for the 88-in cyclotron.[10] The main study is made for the regenerator at 90 deg azimuth. A regenerator 36 deg long is chosen for a reasonable maximum voltage and electrode spacing of 3 cm.

To find the best condition, corresponding to the best energy resolution, a turn separation of 0.25 in., and a reasonable vertical amplitude, we tried several radii for the regenerator position. One of the best results for 65-MeV α particles is shown in Fig. I.3-4. A quarter of the 0.5-in.-radial phase space is separated by 0.04 in. at 39.0 in. radius, at 3 deg azimuth. Individual particles have turn separation of 0.2 in. An improvement of the energy spread is clearly shown, but the wide rf phase (60 deg) of the internal beam may cause a continuous overlapping of the phase space, and the energy spread of the external beam may be 100 to 200 keV, full width half maximum. The average vertical amplitude is increased by about 30% at 39.0 in. radius. The result for 130-MeV α particles is more or less the same as for 65-MeV α, except the radius of the regenerator should be about 0.2 in. smaller. This is because the field falls off faster. The voltage of the regenerator for 130-MeV α is about 60 kV.

For the design of the electrostatic deflector channel, the CYBOUT code[11] was used, with the channel entrance at 3, 9, and 21 deg and using the initial conditions from the regenerated beam. Finally 9 deg and a flared channel shape are used: $E = (150-33\,\theta^2)$ kV/cm for 130-MeV α particles, with the entrance of the channel at 38.9 in.

For the different energy beams, the shape of the channel is different from the case of 130-MeV α particles due to the difference in the flutter and the shape of the fringe fields. Therefore, a three-section deflector is proposed to match these cases.

The positions of the virtual source for the radial and the vertical motion are approximately the same as for the original deflector, and therefore the optics of the external beam may not be changed.

Preliminary Results from Experimental Testing

To check calculations on turn separation produced by a regenerator, a model regenerator was constructed by the 88-inch cyclotron engineering group. The regenerator was 24 in. long, curved to match the 130-MeV α-particle equilibrium orbit, and had an electrode spacing of 2.5 to 3.0 cm. This was the same size as the proposed final regenerator. The model was simplified mechanically to allow a preliminary test without a deflector. The regenerator was located at 90 deg azimuth (the center of a valley) with a starting radius adjustable from 36.5 to 38.0 in. A Δr probe at 3 deg azimuth was used to obtain turn separation measurements in the cyclotron. One of the results of these measurements is given in Fig. I. 3-5. Current collected by the outer electrode of the Δr probe indicates that the necessary 0.2 in. turn separation was obtained.

The final design of the three-section electrostatic deflector with the regenerator is shown in Fig. I. 3-6. The regenerator is located at 90 deg azimuth and the radial position can be changed from 36.9 to 37.9 in. The spacing of the electrodes is 2 to 3 cm. The deflector extends from 9 to 117 deg azimuth. The septum has a 4-in. V slot. The positions of the regenerator and the deflector channel can be changed remotely from the control room. The mechanical details of the design of the system are described in a separate paper by D. Elo et al. [12] One positive high-voltage supply for the regenerator and three negative high-voltage supplies for the three-section deflector are of the Cockcroft-Walton type with silicon rectifiers and 100-kc oscillator for the primary. [13]

The primary study is made for 65-MeV α particles with and without the regenerator for comparison. For around 50 kV dee voltage the quality of the extracted beam is about the same, and the extraction efficiency is slightly lower with the regenerator. A part of the loss seems to be in the vertical direction. The deflector voltage is slightly lower with the regenerator, even though the radius of the channel is smaller in that case. For around 20 kV dee voltage, which is the lower limit of the operating voltage given by the ion source and the center region, the extraction efficiency is much higher with the regenerator. But the acceleration is more difficult due to requirements of isochronism. This low-dee-voltage run may have considerable importance for a future higher energy machine. Twenty kV dee voltage for 65-MeV α particles is about the same as 60 kV dee voltage for 100-MeV protons, as far as the number of turns is concerned. So a regenerator with a single dee at 60 kV could be used to give enough turn separation for 100-MeV protons to enter an electrostatic channel in an 88-inch cyclotron, and to ease the requirement for deflector strength. In such a design one would also want a larger-diameter machine to make deflection easier.

Conclusion

When the higher dee voltage was used, the regenerative extraction system for the 88-inch cyclotron gave about the same beam quality and extraction efficiency as the original system for normal operational dee voltage. By careful shaping of the magnetic field near the extraction radius, the system can be improved further with respect to vertical loss. The relative position of the magnetic sectors to the dee gave a tight design limit. This reduced the acceptance of the beam into the deflector channel and prevented the use of a peeler. A low-dee-voltage test indicated possible uses of the regenerator in higher energy machines with a comfortable dee voltage.

The authors wish to acknowledge the fine cooperation of the engineering group under D. Elo, A. Carneiro, and D. Morris; mechanical coordination by A. Hartwig; efficient installation by accelerator technicians under J. Menneghetti; theoretical and programming assistance from A. Garren and H. Owens; help from the operating crew under J. Bowen; and encouragement from E. Kelley, B. G. Harvey, and H. E. Conzett.

Footnote and References

† Short form of paper for International Conference on Isochronous Cyclotrons, Gatlinburg, Tennessee, May 1966.

1. A. A. Garren, D. L. Judd, L. Smith, and H. A. Willax, Nucl. Instr. Methods 18-19, 525 (1962).
2. H. A. Grunder, F. B. Selph, and H. Atterling, in Proceedings of the International Conference on Sector-Focused Cyclotrons and Meson Factories, Geneva, 1963, CERN 63-19, p. 59
3. R. Burger, D. J. Clark, E. Close, and H. Kim, Machine Development at the Berkeley 88-Inch Cyclotron (Gatlinburg Conference, 1966).
4. H. Kim, G. H. Mackenzie, W. B. Powell, and P. J. Waterton, Proceedings of the International Conference on Sector-Focused Cyclotrons and Meson Factories, Geneva, 1963, CERN 63-19, p. 73.
5. J. L. Tuck and L. C. Teng, Phys. Rev. 81, 305 (1951).
6. K. J. LeCouteur, Proc. Phys. Soc. (London) B64, 1073 (1951).
7. K. J. LeCouteur, Proc. Phys. Soc. (London) B66, 25 (1953).
8. K. J. LeCouteur and S. Lipton, Phil. Mag. 46, 1265 (1955).
9. E. L. Kelly, Nucl. Instr. Methods 18-19, 33 (1962).
10. A. A. Garren (LRL), private communication.
11. H. C. Owens, Nucl. Instr. Methods 18-19, 295 (1962).
12. D. Elo, F. Bierlein, A. Carneiro, and J. Wong. UCRL-16829, May 1966.
13. B. H. Smith, in Proceedings of the International Conference on Sector-Focused Cyclotrons and Meson Factories, Geneva, 1963, CERN 63-19, p. 301.

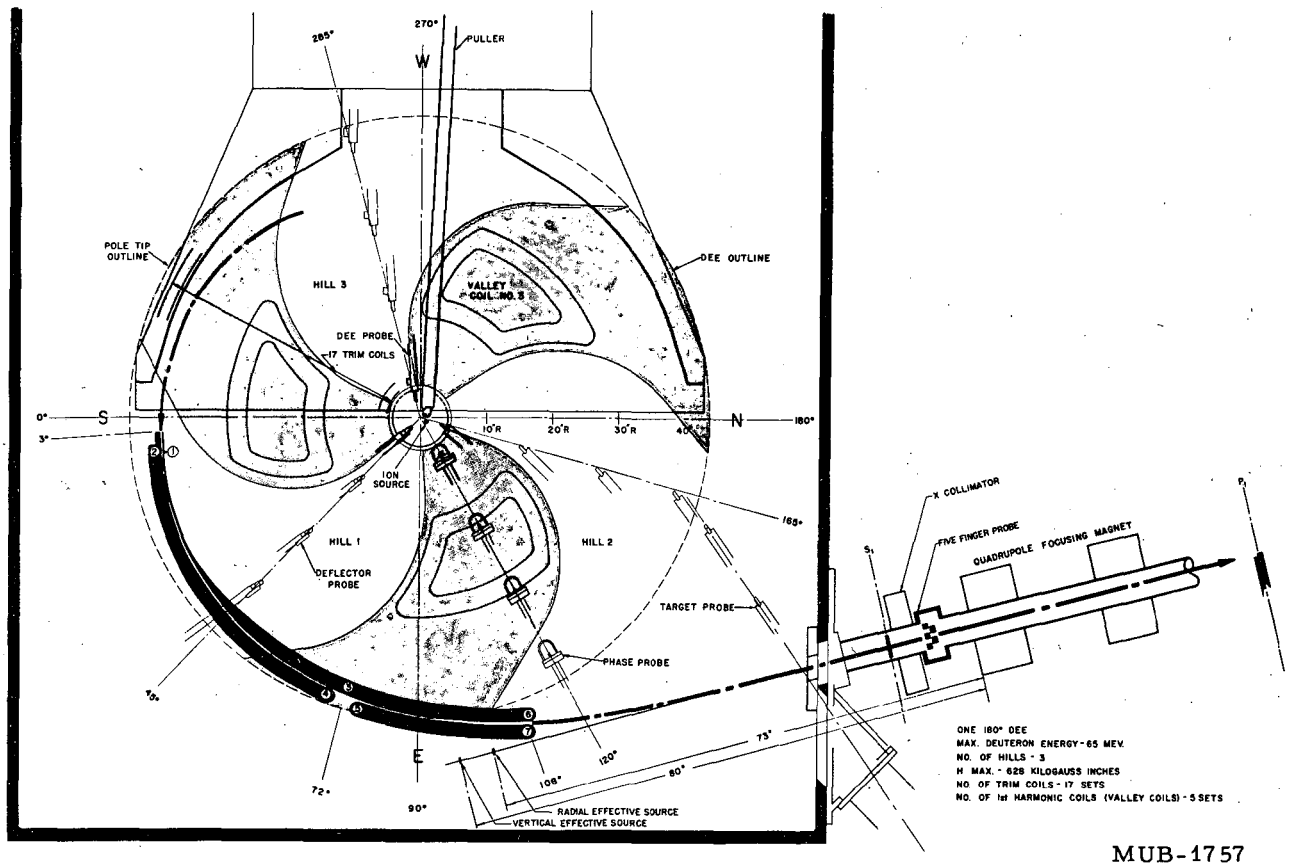

MUB-1757

Fig. I. 3-1. A plan view of the pole face and the original extraction system of the 88-inch cyclotron.

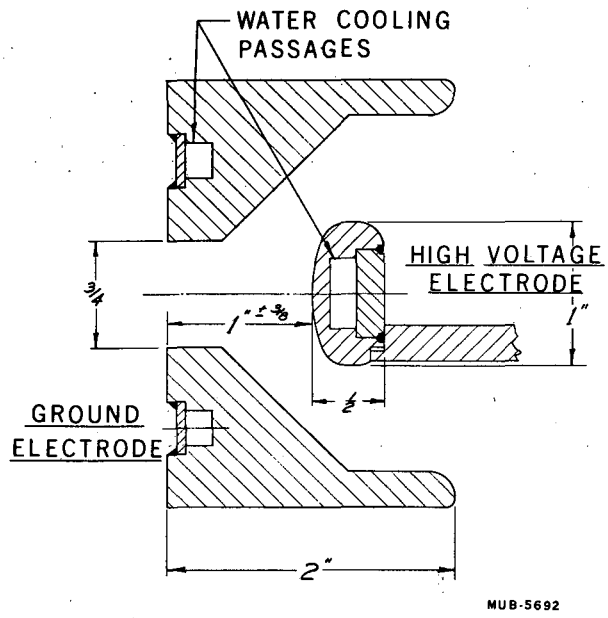

Fig. I. 3-2. A cross section of the regenerator electrodes.

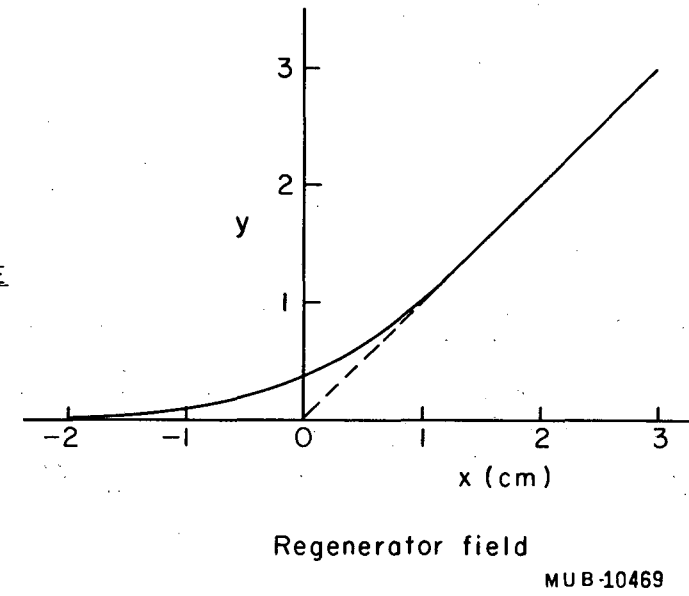

Fig. I. 3-3. Electric field of the regenerator. $E = (2\ V_0/b^2)y$; V_0 = applied voltage (kV), b = spacing of the electrode (cm), E = electric field (kV/cm).

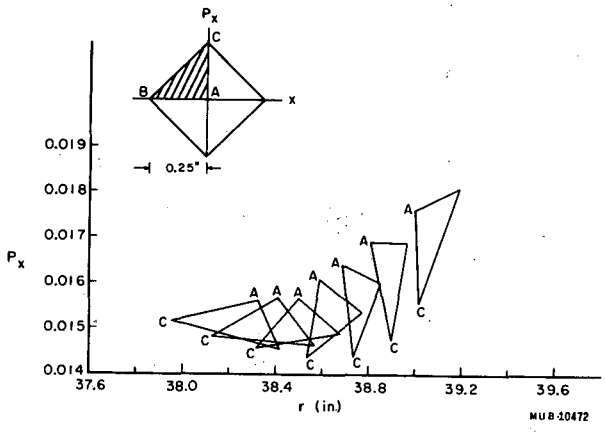

Fig. I. 3-4. A phase plot at 3 deg of 65-MeV α particle by an action of the regenerator, showing the turn separation and energy resolution improvement. Dee, 50 kV; regenerator, 32 kV; r_R = 37.3 in. at 90 deg.

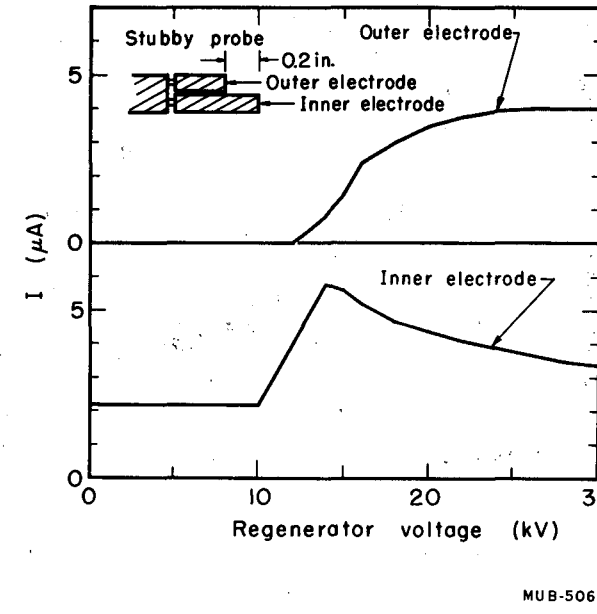

Fig. I. 3-5. A result of turns separation measurement, 45-MeV α particles.

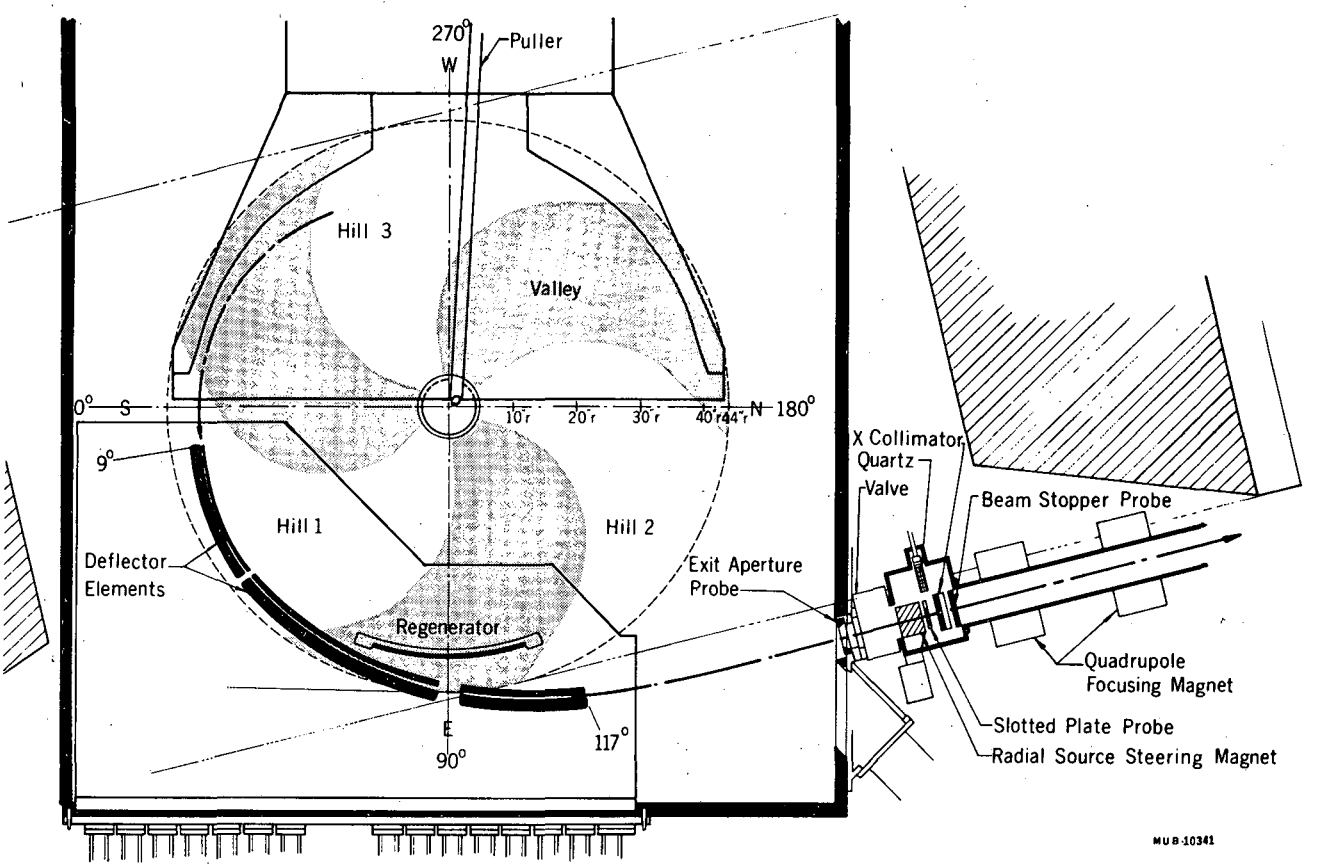

Fig. I. 3-6. A plan view of the pole face and the new extraction system, showing the position of the regenerator and a three-section deflector.

4. REGENERATIVE BEAM EXTRACTION†

Hogil Kim

Introduction

A main physical problem in beam extraction for high-energy cyclic accelerators is getting a sufficient turn separation at the extraction radius to locate a septum or a septum magnet to take the circulating beam out of the machine. One of the methods used is the regenerative beam extraction method, invented for a synchrocyclotron by Tuck and Teng[1] and developed by LeCouteur.[2-4] This method, now common in synchrocyclotrons, has been applied to the Birmingham 40-inch cyclotron.[5,6] A similar system has been tested for the Berkeley 88-inch cyclotron.[7] The feasibility of the system has been investigated for the NRDL cyclotron.[8]

Regenerative beam extraction is a type of resonance extraction method. By introducing a gradient field perturbation near the extraction radius, a resonant excitation of radial betatron oscillations is produced while the vertical motion is kept stable. The type of the resonance is mainly the 2/2 stop band.

The system is generally divided into the linear regenerative system and the nonlinear one. The linear system operates in the linear region of the main field near maximum radius and consists of the two linear gradient field perturbations which are separated by an angle < 180 deg. One gives a radially outward impulse (peeler) and the other gives a radially inward impulse (regenera-

tor). Often the regenerator alone is used, with the fast falloff of the main field providing the peeler action.

The isochronous cyclotron has higher energy gain per turn than the synchrocyclotron. Unlike the synchrocyclotron, it has modulation of the betatron motion by the sector focusing, and the effects of nonlinear forces due to sectors. All of these differences require careful consideration.

Throughout the discussions, the main emphasis is given to the linear regenerator, for we can get a much better physical insight through the linear theory.

Regenerative Extraction for the Synchrocyclotron

LeCouteur's Regenerative Theory

In the linear region of the main field, the radial and the vertical motion of the particle can be approximated as simple harmonic oscillations around the equilibrium orbit. The action of the peeler-regenerator can be written as a series of impulses, the strengths of which are proportional to the penetration into the system. The arrangements are shown in Fig. I.4-1. The operation of the system is shown in Fig. I.4-2. Here the peeler introduces an outward impulse, causing a phase delay, and the regenerator introduces an inward impulse, giving a phase advance. After one revolution, the amplitude is increased and the phase is returned to the initial phase.

One selects the parameters of the system to minimize the vertical motion. The magnetic channel is put at 60 to 80 deg from the node of the oscillation for large x and x' at extraction.

The Linear Regenerative Theory for a General Case

The amplitude of the radial oscillation of the internal beam is typically a few inches. A particle with some radial amplitude can reach the peeler-regenerator at the same radius as a centered beam of higher energy. This is shown in Fig. I.4-3.

The Nonlinear Regenerator

Since the linear regenerator is operating in the linear region of the main field, the extraction occurs several inches inside the fast-falloff region, and the energy is lower than the maximum possible. LeCouteur[3,4] investigated the possible operation of the regenerator at the end of the linear region, getting a peeler action from the falloff of the main field. To keep the vertical motion stable and the phase of the oscillation constant, one should increase the strength of the regenerator nonlinearly to match the nonlinear falloff of the main field. The maximum radius of the regenerator should be less than the radius of the $\nu_r = 2\nu_z$ resonance. For a semiquantitative discussion the linear theory may be used. An approximate evaluation of the peeler action from the falloff of the main field can be made. For design of a system, all the existing analytical methods may not be accurate enough, and numerical integration is required.

Operating Features and Improvements for the Synchrocyclotron

The linear as well as the nonlinear regenerative extraction system was first successfully operated at the Liverpool synchrocyclotron,[9] and it is now a common method in synchrocyclotrons (for example, Refs. 10-12). The extraction efficiencies are about 1 to 10%, and the energy spread of the external beam is about 0.1 to 1%. Another extraction method is used at the Tokyo synchrocyclotron. There the n = 1 resonance gives an extraction efficiency of about 50%.[13] The machine has relatively good internal beam quality to pass dangerous resonances, such as $\nu_r = 2\nu_z$. The regenerative beam extraction method is a relatively good one compared with previous systems, such as extraction by Coulomb scattering. Though the main purpose of the system was to produce good turn separation, the method also gave good beam quality. This might be a general characteristic of the resonance extraction method.

The low extraction efficiency is mainly due to poor internal beam quality, and naturally the efficiency will be improved by an improvement of the internal beam.

The Regenerator for Isochronous Cyclotrons

The main differences between the isochronous cyclotron and the synchrocyclotron are, as described in the introduction, higher energy gain per turn, modulation of the betatron oscillation,

and the nonlinear force due to sectors. None of these effects is negligible, and it requires numerical integration for a design of a system. For design guidance and for qualitative discussion, an analytical study may still be helpful.

Azimuthal Position of the Peeler-Regenerator

It has been shown that the main harmonic component for regenerative action is the second order gradient harmonics[14, 15] and the type of resonance is the 2/2 stop band. When we analyze the peeler-regenerator field by a Fourier series, there are considerable amounts of other harmonics such as the first and the third.

The betatron motion in the isochronous cyclotron has a modulation due to sectors, and these harmonics of the modulation may couple to the harmonics of the peeler-regenerator bump and create a second harmonic.[16] The second harmonic of the peeler-regenerator and the second harmonic from the coupling may be added together vectorially. When these two harmonics are in phase, the regeneration is stronger, and it is weaker when they are out of phase.

Radial Position of the Peeler-Regenerator

At the isochronous region, the value of ν_r is bigger than unity, and decreases in the fringing field. One may operate the system at the isochronous part of the field, but it requires a stronger system. The vertical motion should be investigated carefully for the stronger system. When one can shape the field near $\nu_r = 1$ for a few inches, a relatively weaker peeler-regenerator may be used. Finally, as in the nonlinear regenerator for the synchrocyclotron, one may use only the regenerator at near $\nu_r = 1$, using the falloff of the main field as a peeler. The vertical motion should be investigated carefully for this case, since the higher energy gain may introduce the $\nu_r = 2\nu_z$ resonance during regeneration.

Acceleration Effects

The accelerator effects can be neglected during regeneration for the synchrocyclotron and the system is peeling off the particles with the bigger amplitude of the radial oscillations. In the isochronous cyclotron, the higher energy gain introduces a number of effects in the regenerative system.

Duty Cycle

When we accelerate the particle by higher dee voltages, the final energies of the particles and the rf phase may have a certain relation, and the duty cycle may be small when the energy of the extracted beam is analyzed. On the other hand, when we accelerate the particles by a low dee voltage, the final energy of the particle and the rf phase may not have a simple relation, and therefore the duty cycle will be increased for an analyzed beam. For this low dee voltage the regenerative extraction might be very useful.

Present Design Features of the Regenerative System for Isochronous Cyclotrons

The regenerative systems for the Birmingham 40-inch cyclotron and the Berkeley 88-inch cyclotron are electrostatic devices. The Birmingham system has the peeler and the regenerator. It may operate at a radius $\nu_r > 1$, or at a radius $\nu_r < 1$. This system gave the maximum extraction efficiency of 70% and 0.5% energy spread at the normal operating condition. In the loss of 30%, 14% was due to vertical loss and 16% was collected at the first 4-in. septum.[17]

For the Berkeley 88-inch cyclotron the system has only the regenerator and operates at a radius where $\nu_r < 1$. The system gave about 50% extraction efficiency and about 0.3% energy spread at the best condition.[7] The reason for the loss is unknown yet.

For the NRDL cyclotron, which will accelerate protons up to 100 MeV, the system is designed for the magnetic peeler-regenerator, and the strength of the system can be changed for the different energies. The magnetic field at the peeler-regenerator is carefully shaped to give $\nu_r \approx 1$. The powerful system may give the beam out by itself, though the magnetic channel is located for an efficient beam transport.[8]

Conclusion

For the synchrocyclotron, the regenerative extraction method is the most successful

method at present, and the system might be further improved if the quality of the internal beam were improved, or if the vertical focusing were improved at the beginning of the regeneration.

For the isochronous cyclotron, the system may be very useful when the turn separation by the energy gain is small. For high dee voltages, it would be hard to obtain further gain of efficiency compared with conventional methods.

Footnote and References

† Short form of paper for International Conference on Isochronous Cyclotrons, Gatlinburg, Tennessee, May 1966.

1. J. L. Tuck and L. C. Teng, Phys. Rev. 81, 305 (1951).
2. K. J. LeCouteur, Proc. Phys. Soc. B64, 1073 (1951).
3. K. J. LeCouteur, Proc. Phys. Soc. B66, 25 (1953).
4. K. J. LeCouteur and S. Lipton, Phil. Mag. 48, 1265 (1955).
5. E. A. Finlay, Nucl. Instr. Methods 18-19, 25 (1962).
6. H. Kim, G. H. Mackenzy, W. B. Powell, and P. J. Waterton, in Proceedings of the International Conference on Sector-Focused Cyclotrons and Meson Factories, Geneva, 1963, CERN 63-19, p. 73.
7. D. J. Clark, E. Close, H. A. Grunder, H. Kim, P. Pellissier, and B. H. Smith, Regenerative Beam Extraction for the Berkeley 88-Inch Cyclotron, UCRL-16794, May 1966.
8. B. Howe, private communication.
9. A. V. Crewe and K. J. LeCouteur, Rev. Sci. Instr. 26, 725 (1955).
10. A. V. Crewe and U. E. Kruse, Rev. Sci. Instr. 27, 5 (1956).
11. J. Rosenblatt and R. J. Slobodrian, Rev. Sci. Instr. 31, 863 (1960).
12. W. F. Stubbins, Rev. Sci. Instr. 29, 722 (1958).
13. A. Suzuki et al., Institute for Nuclear Study, University of Tokyo, INSJ-23.
14. S. E. Barden, Rev. Sci. Instr. 25, 587 (1954).
15. H. Kim (Ph.D. Thesis), University of Birmingham, 1964.
16. M. M. Gordon and W. S. Hudec, Nucl. Instr. Methods 18-19, 243 (1962).
17. W. B. Powell, private communication.

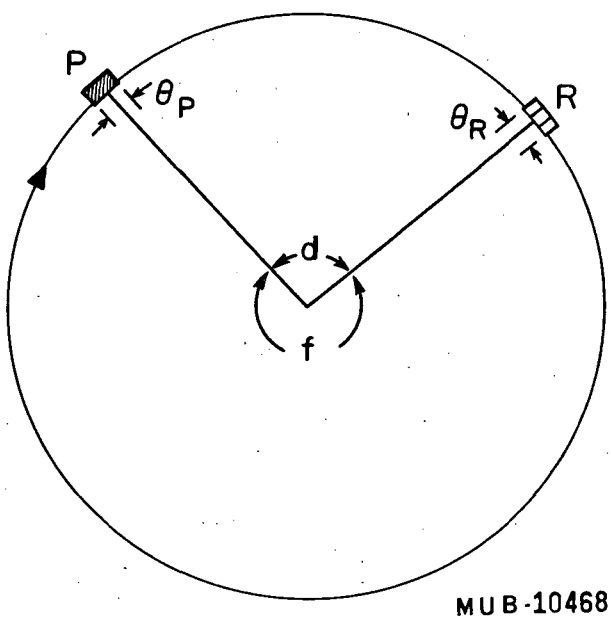

Fig. I.4-1. Position of the peeler-regenerator.

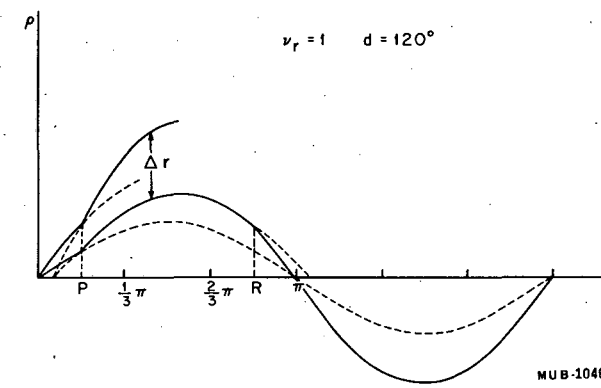

Fig. I.4-2. Action of the peeler-regenerator.

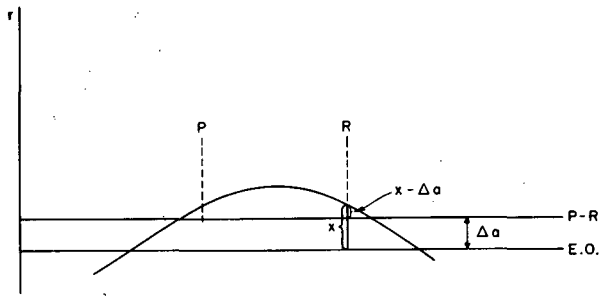

Fig. I.4-3. A general case for the equilibrium orbit less than the radius of the regenerator.

5. INFLUENCE OF CYCLOTRON BEAM PROPERTIES ON EXPERIMENTS†

H. E. Conzett

Introduction

Prior to 1960, most researchers doing nuclear physics experiments with the external beams from conventional cyclotrons accepted the 0.7 to 1% energy spread, the fixed energy, and the relatively unknown emittances and (microscopic) duty factors. These properties were taken to be characteristic of cyclotron beams.

The past five years have seen a truly amazing development of the cyclotron in terms of capability and versatility as a nuclear research instrument. It can now extend to much higher energies the very precise experiments with proton and deuteron beams that have been characteristic of the tandem Van de Graaff accelerator, whereas the ^{3}He and ^{4}He beams are, in addition, considerably more intense than those available from the rival machine. These circumstances have required us to examine in some detail the relationship between beam properties and the design of the more complicated and more precise experiments that can be done.

Beam Properties

The beam properties to be discussed are energy, energy stability, energy spread, energy variability, duty factor, and phase-space density—which, of course, encompasses both intensity and quality. I have chosen examples to illustrate the importance of these characteristics mainly from the research results from the Berkeley 88-inch cyclotron, since these have been most available to me; but similar results have been forthcoming from other sector-focused cyclotrons.

Energy

Several advantages of the higher energies are straightforward. Large amounts of highly neutron-deficient radioactive isotopes have been produced by (α,xn), where x is 5, 6, or higher. Investigations of the nucleon-nucleon, p-d, p-^{3}He, p-α, ^{3}He-α, and α-α interactions have been or will be extended to previously unexplored regions. Also, new and very interesting reactions can be studied; examples are the ^{12}C(^{3}He,^{6}He)^{9}C reaction,[1] designed to measure the mass of ^{9}C, and the ^{26}Mg(α,^{8}He)^{22}Mg reaction,[2] which was used to determine the mass of ^{8}He. The first reaction threshold is about 40 MeV, so 65-MeV ^{3}He ions were used to provide sufficient energy to the outgoing ^{6}He particles that particle identification with a (dE)/dx) -E counter telescope was simplified. The second reaction was initiated with 80-MeV α particles since the threshold energy is about 45 MeV.

Energy Stability and Energy Spread

Instability and spread in beam energy limit the final energy resolution available, for example, in an experiment which uses semiconductor detectors and does not fix precisely the incident beam energy by stringent magnetic analysis. Also, such a magnetic system would suffer beam-intensity fluctuations caused by input energy drifts. Parkinson and Tickle[3] have recently reported measured proton line widths (FWHM) of 7 keV at 21 MeV from the $^{27}Al(d,p)^{28}Al$ reaction. This beautiful example of an overall resolution of 0.033% cannot yet be matched by semiconductor detectors, but the rapid development of this truly revolutionary particle detector has provided very remarkable results at Berkeley. For example, experimental resolutions slightly better than 0.1% have been achieved with α particles up to 90 MeV[4] and with 29-MeV protons.[5] In the latter case, after correction for the 0.07% beam spread, a 0.04% contribution from a thin vacuum window, and a 0.03% electronic noise spread, the detector contribution amounted to 0.05%. Fig. I. 5-1 shows, as an example of the utility of such a detector, a spectrum of protons scattered elastically and inelastically from ^{58}Ni (Ref. 6). The triplet of levels near 4.5 MeV had not been resolved in previous work.

Energy Variability

The controlled energy variability is very likely (once one has the higher energies) the most important development of the sector-focused cyclotron. For nuclear physics research each energy setting, in steps of a few MeV, corresponds to having a separate conventional cyclotron. Many nuclear scattering and reaction processes are quite strongly energy-dependent, and only by investigating and seeing this energy dependence can theory be checked and corrected. Investigations of resonance phenomena and threshold effects, previously almost exclusively in the domain of the Van de Graaff accelerator, can now be extended to the higher energies. Figure I. 5-2 shows excitation functions at two angles in elastic α-α scattering.[7] The sharp resonance structure near 34 MeV corresponds to two states of ^{8}Be at excitations of 16.6 and 16.9 MeV. Here, data were taken at energy intervals as small as 40 keV. These data demonstrate, also, the importance of the small beam-energy spread, about 0.1%. For comparison, the data from a previous experiment[8] are shown. The beam spread of more than 2% (about 800 keV), which was due in part to the use of absorber foils for reducing the energy, washed out the sharp resonance behavior. It is worth remarking that in an experiment such as this, where there is little or no resolution requirement imposed by the need to separate lines corresponding to various states of a residual nucleus, the experimental resolution is controlled by the beam-energy spread and target thickness alone. That is, the detector records counts as a function of the energy of the intermediate or compound system, and that number is independent of the detector resolution.

Duty Factor

The effect of duty factor on experiments has been discussed at the three previous conferences on sector-focused cyclotrons, and in reading over the Proceedings, I detected something less than complete agreement on that subject. For simplicity, let us agree to discuss only the microscopic duty factor, which is imposed by the arrival of beam pulses with the rf time structure. For example, at 10 MHz, corresponding to an rf period of 100 nsec, the 88-inch cyclotron external-beam pulse length may be 10 to 15 nsec, giving a 10 to 15% duty factor.

Consider, then, at f_0 = 10 MHz an experiment to detect two outgoing particles, or a particle and a γ ray, in coincidence. Let us start with a coincidence resolving time τ of 15 nsec and a beam pulse length T of slightly longer duration. Assume that pulse pileup effects in the detectors limit the singles counting rates to something like 10^4/sec, which averages one particle detected per 10^3 beam pulses. If the real to accidental coincidences ratio $r = R/A$ is, say, something like 100, then the duty factor question is not of much concern. If, however, the cross section $d^2\sigma/d\Omega_1 d\Omega_2$ and the detector solid angles $\Delta\Omega_1$ and $\Delta\Omega_2$ are small, as they usually are, one might have a ratio r near unity. Since the accidental rate A is proportional to $(N_1 N_2 \tau)/D$, where N_1 and N_2 are the average singles rates and D is the duty factor, it can be reduced by increasing the duty factor while maintaining the same average beam intensity. Thus, a coincidence experiment with τ less than T that is limited by the real-to-accidental ratio r, and not by other factors such as pileup and beam intensity, can be improved in direct proportion to the improvement in duty factor. Unfortunately, energy analysis of the beam seems to reduce the duty factor, but it would be interesting to inquire if that correlation is absolute. On the other hand, coincidence experiments are not yet demanding the highest energy resolutions.

Phase-Space Density

Finally, the effect of beam quality on an experiment can be illustrated by a simple example. As indicated schematically in Fig. I. 5-3, both the beam width and convergence or divergence introduce a spread of scattering angles between θ_1 and θ_2. The resultant kinematical energy spread depends on the masses of the initial- and final-state particles, the initial energy, the reaction Q value, and the angle θ. In Fig. I. 5-4 the shaded area represents the horizontal effective source emittance (phase-space area) of an external beam of α particles from the Berkeley 88-inch cyclotron, a source 2 mm wide with a full divergence angle near 30 mr. (These phase-space areas are drawn as rectangles only for simplicity.) The various rectangular areas A to D are calculated to correspond to kinematical energy spreads of 0.1% introduced separately by the indicated beam width and divergence, for elastic scattering of particles of mass M_1 incident on nuclei of mass M_2. Obviously, much of the phase-space area is useless for high-resolution experiments on light nuclei with incident α particles, for example. Beam energy analysis does, of course, reduce the phase-space area, and even though we do not have a good measurement of that for the analyzed beam, the following numbers are useful. For the 65-MeV α-particle beam, some 50 μA can be provided with horizontal and vertical emittances of 50 and 70 mm mr respectively. This corresponds to 14 $\mu A/mm^2$ mster. After the beam was energy-analyzed to 0.1% and collimated to a horizontal emittance of about 5 mm mr (very nearly the area B in Fig. I. 5-4) and a vertical value of 10 mm mr, some 3.5 μA was available. This corresponds then to 70 $\mu A/mm^2$ mster, so the central phase-space density was larger by a factor of five than the average density, and that is most encouraging for those experiments that require the highest quality beams.

In summary, I think that the sector-focused cyclotron has exceeded most researchers' expectations in terms of versatility and overall performance as touched upon here.

Footnote and References

† Short form of paper for the International Conference on Isochronous Cyclotrons, Gatlinburg, Tennessee, May 1966.

1. J. Cerny, R. H. Pehl, F. S. Goulding, and D. A. Landis, Phys. Rev. Letters 13, 726 (1964).
2. J. Cerny, S. W. Cosper, G. W. Butler, R. H. Pehl, F. S. Goulding, D. A. Landis, and C. Détraz, Phys. Rev. Letters 16, 469 (1966).
3. W. C. Parkinson and R. S. Tickle, University of Michigan Report COO-921-16, May 1965.
4. B. G. Harvey (LRL), private communication.
5. R. H. Pehl, D. A. Landis, and F. S. Goulding, Detection of High-Energy Protons by Thin-Window Lithium-Drifted Germanium Counters, UCRL-16722, Feb. 1966.
6. B. G. Harvey, D. L. Hendrie, O. N. Jarvis, and J. Mahoney (LRL), private communication.
7. H. E. Conzett, P. Darriulat, H. G. Pugh, E. Shield, and R. J. Slobodrian, in Nuclear Chemistry Division Annual Report, 1965, UCRL-16580, Jan. 1966, p. 48; Bull. Am. Phys. Soc. 9, 703 (1964).
8. D. J. Bredin, W. E. Burcham, D. Evans, W. M. Gibson, J. S. C. McKee, D. J. Prowse, J. Rotblat, and J. N. Snyder, Proc. Roy. Soc. (London) A251, 143 (1959).

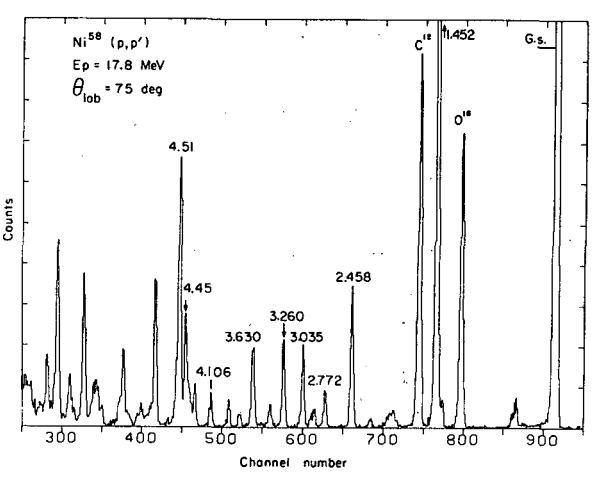

Fig. I. 5-1. Energy spectrum of protons scattered from ^{58}Ni at θ_{lab} = 75 deg with the incident proton energy E_p = 17.8 MeV.

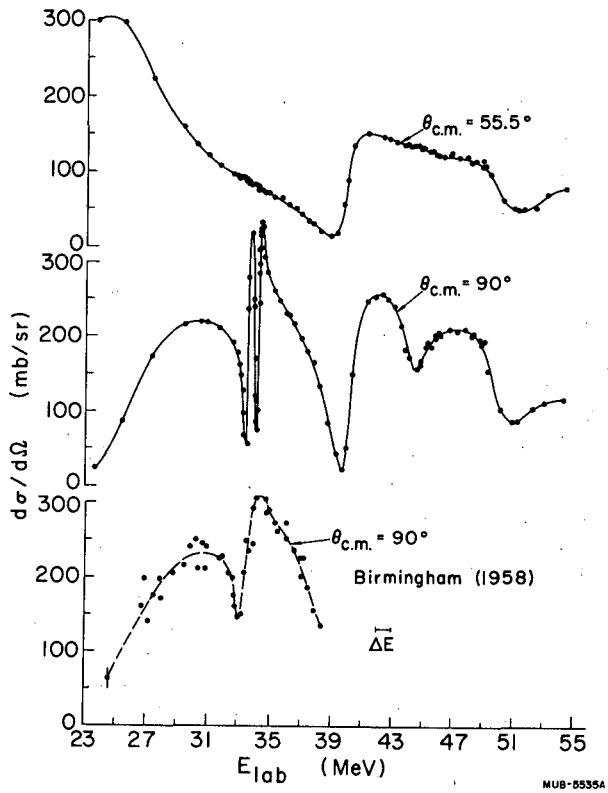

Fig. I. 5-2. Excitation curves for α-α elastic scattering at $\theta_{c.m.}$ = 55.5 and 90 deg. Data from Ref. 8 are shown below.

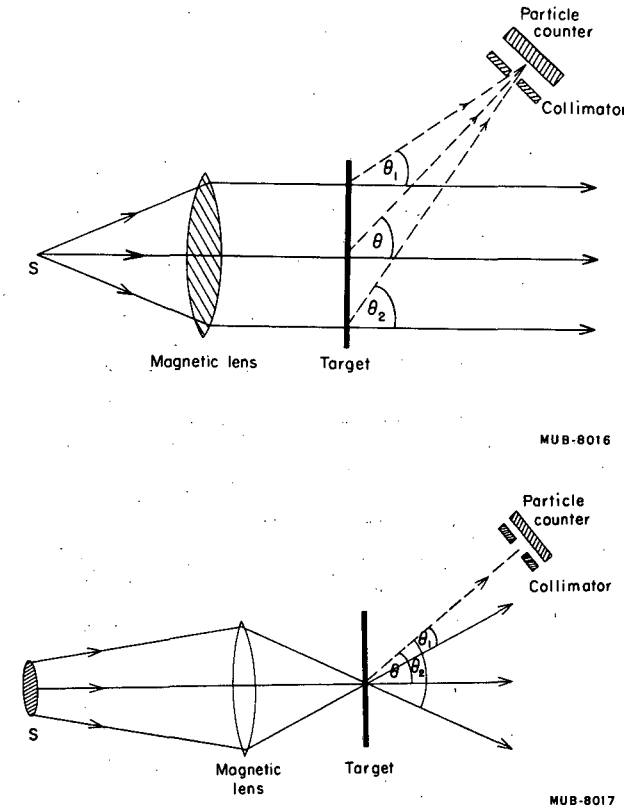

Fig. I. 5-3. Schematic diagram of typical experimental arrangement. (a) For system providing parallel beam from point source, the angle observed can vary between θ_1 and θ_2 due to the extended beam area on the target. (b) Similarly, for a small-area beam on the target from an extended source the angle observed can vary between θ_1 and θ_2 due to convergence of beam at the target position.

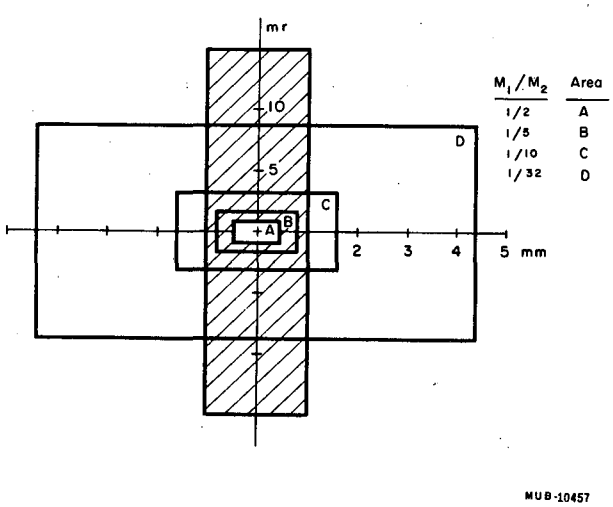

Fig. I. 5-4. The shaded area represents the external beam phase-space area (or source emittance) for an α-particle beam from the Berkeley 88-inch cyclotron. The areas A through D represent the useful areas for certain experiments, as explained in the text.

6. MECHANICAL DESIGN OF A REGENERATIVE DEFLECTOR FOR THE BERKELEY 88-INCH CYCLOTRON†

Don Elo, A. R. Carneiro, Fred Bierlein, and J. L. Wong

Introduction

Following the success of a test electrostatic regenerator unit in the Berkeley 88-inch cyclotron, a new regenerative deflection system was built. The system was comprised of a regenerator unit and an electrostatic channel.

The regenerator unit was positioned opposite the dee near extraction radius. This unit, having a positive voltage, gave the last few accelerating internal beam orbits such a bump off their normal orbit paths that their turn-to-turn separation was increased at the entrance to the deflector channel. This separation decreased the amount of beam dumped on the septum, and thus increased the efficiency of the deflector.

The regenerative deflector was installed in November 1965, and delivered beam when first tried. It is presently undergoing beam development alternately with delivery of experimental beam.

The cyclotron has a horizontal magnet gap of 5.75 in. between trim coil liners (see Fig. I. 6-1). It has one 180-deg. dee. The beam is accelerated counterclockwise. The deflector delivers beam to the external beam tubes that are normal to a radial line 104 deg from the dee exit. The deflector is mounted in an opening in the dee tank opposite the dee, and is removed on rails straight back from this opening through an opening in the accelerator vault to an area outside the shielding (not shown on the Fig.). Although the first deflector had two high-voltage electrodes and a ground plane, for the regenerative reflector we decided to use three deflector elements for more versatility. With the addition of the regenerator elements and an entrance septum jack, this meant there would have to be 15 points of adjustment instead of the previous seven. The high-voltage elements were made as small in area as practical to cut down on capacitance to ground. (Many other basic parameters are not touched upon here. [1])

Figure I. 6-2 is an overall view of the deflector as it was designed and built. The vertical faceplate formed the dee-tank vacuum barrier and supported the entire regenerative deflector assembly. The horizontal main-support plate was cantilevered out from the faceplate when the deflector assembly was rolled out of the cyclotron. On the leading edge of the main support were four small rollers which rested on the trim coil liners when the deflector was mounted in the cyclotron gap. The electrode assemblies and associated cooling water lines were all mounted on this large support plate. The high-voltage and ground pairs of electrodes broke down to three basic cross-sectional designs (Fig. I. 6-3).

The deflector's high-voltage electrodes all had similar cross sections. They were all made from 1.5-in. o. d. tubing with a nominal 1-in. flat face welded in place. The end caps were machined for cooling-water inlet and outlet, and for electrode-support pivots. The water was simply fed in one end and out the other with no reversing channels inside the electrode.

The entrance-septum electrode separated that beam which is in its last orbits inside the cyclotron from the beam which is acceptable to the deflector's electrostatic channel for external delivery. This septum is the weakest link in the 88-inch cyclotron as far as beam intensity is concerned. The first septum was made from a 2-in. -high section of tungsten 0.060 in. thick, ground to 0.010-in. thickness through a 13/16-in. -high section symmetrical to the midplane. This septum was bent logitudinally to match the curvature of the deflector channel. An inward-sloping vee slot was put in by spark erosion. The vee was made as sharp as possible to minimize the blunt face for beam deposit. This tungsten web was screwed to flanges (Inconel alloy 600) for support. The only cooling of the unit was by radiation. Future considerations for this element are copper with water cooling, tungsten webs with water-cooled flanges, and hafnium carbide webs with water-cooled flanges.

The mid and exit ground electrodes were made as thin as practical to minimize the space problem in the area of the regenerator unit (Fig. I. 6-4). They were machined from 0.5-in. -thick Inconel bar stock. An 1/8-in. -wide water channel was centered in the electrodes.

All electrodes (except those of the regenerator ground and entrance septum) were

machined longitudinally flat to the required finished cross-sectional dimensions; they were then bent to match templates. The templates were machined on a tape-controlled milling machine to match computed values[2] for extracted 130-MeV α-beam orbit. The installed electrodes matched the templates generally within 0.002 in. with a few localized departures of about 0.006 in. These templates were also used as drill jigs to make subsequent replacement electrodes to match the originals without the need of recalibrating the replacement's radial positions.

Fabrication of the support insulators for the high-voltage electrodes appeared to be a serious problem. Alumina ceramic of 97.6% purity was chosen for the insulating material because of its electrical strength, mechanical properties, and good thermal shock resistance. A corona bell housing mounted over the insulator protected the insulator from coating action inside the cyclotron and provided a spark gap away from the insulator surface.

All electrode ends were mounted on rectilinear ball carriages which in turn were mounted on the large main horizontal support plate. See Fig. I.6-5.

The positioning drive motions were transmitted from external drives to the ball carriages through a flexible rectilinear ball-bearing remote-control cable made by the Controlex Corporation of America (see Fig. I.6-6). These cables are commercially available. All materials in them are nonmagnetic stainless steel and run without lubrication. Some backlash in the electrode positioning is experienced with the use of these cables. When all precautions are taken in assembling these units in curved paths, this backlash is 0.006 in. or less, a figure we consider of marginal desirability. We might eventually have to devise a method to correct this backlash should it prove troublesome, but there are many possibilities.

The drive units provide remote electrode positioning control and readout from the control room. It was desirable to read (a) radial position of the ground electrodes, (b) gap between the ground and high-voltage electrodes and (c) septum jack elevation. It was also desirable to be able to move ground and high-voltage electrodes either independently or together and thus keep a constant gap. Figure I.6-7 schematically shows our solution to the problems. The key parameters in determining this design were gap readout and constant gap motion.

The drives for an adjustment point of the ground electrodes and the corresponding high-voltage electrode point were paired, and were driven by a common high-speed gear-reduced aircraft-type motor. Independent electrode motion was provided by use of magnetic clutches. Each quill nut was geared to a transmitter synchro and digital counter. The control-room readout panel had receiver synchros for reading radial position of ground electrode, and differential receiver synchros for reading gap, both by use of digital counters.

There was a total of seven pairs of these drive units for deflector and regenerator electrode position and one individual unit for septum jack readout (see Fig. I.6-8). Mounting these units on the dee-tank plate eliminated the necessity for mechanical uncoupling from the deflector assembly and related evils such as loss of calibration, backlash through additional linkages, and the time of removal for some maintenance problem inside the vacuum area. This approach also proved quite compatible with the interchanging of the regenerative deflector and the previous deflector.

Several things were learned in the regenerator test unit. One of these was our ability to use sleeve bearings made of molybdenum disulfide–epoxy resin in areas where a dielectrical dry lube material is desired. The 50/50 formula used has an electrical strength of 45 V/mil and a coefficient of friction of about 0.15, and is easily machined. This material is used on the electrically "floating" ground electrodes. Only time will tell its radiation characteristics, but it seems to be holding up quite well so far.

Development of water-cooled tungsten septa is at present in the trial stage. First results show a definite increase in the beam-holding capacity--enough to warrant further development.

Footnote and References

† Short form of paper for International Conference on Isochronous Cyclotrons, Gatlinburg, Tennessee, May 1966.

1. B. H. Smith and H. A. Grunder, in Proceedings of the International Conference on Sector-Focused Cyclotrons and Meson Factories, Geneva, 1963, CERN 63-19, 1963, p. 304.

2. D. J. Clark, E. Close, H. A. Grunder, Hogil Kim, P. Pellissier, and B. H. Smith, Regenerative Beam Extraction for the Berkeley 88-Inch Cyclotron, UCRL-16794, April 1966.

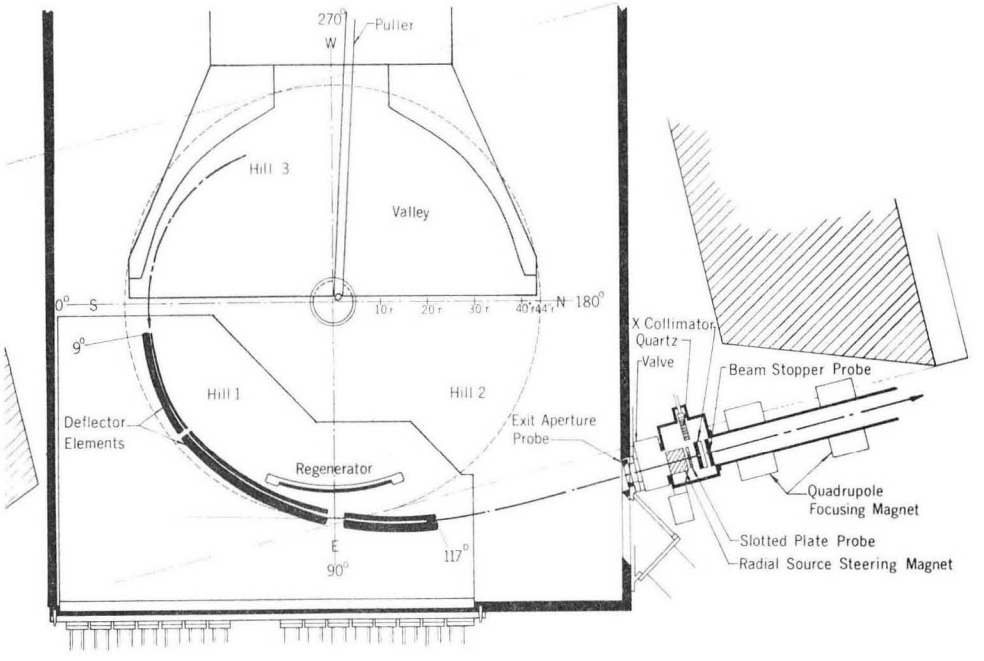

Fig. I.6-1. Plan schematic of 88-inch cyclotron and regenerative deflector.

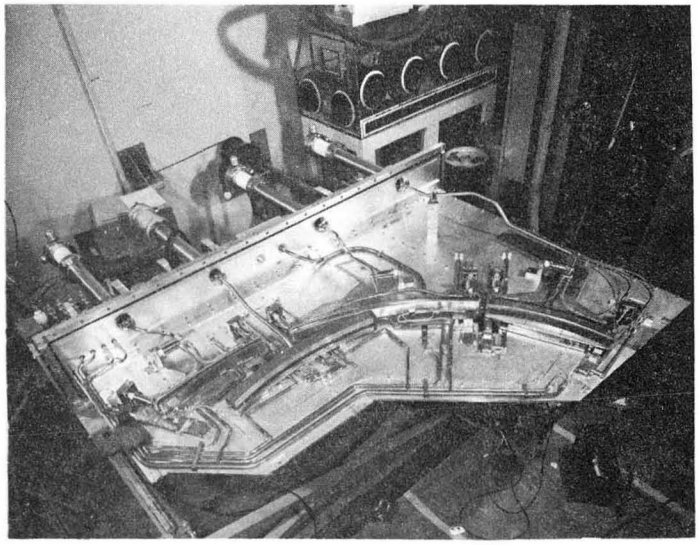

Fig. I.6-2. Regenerative deflector assembly.

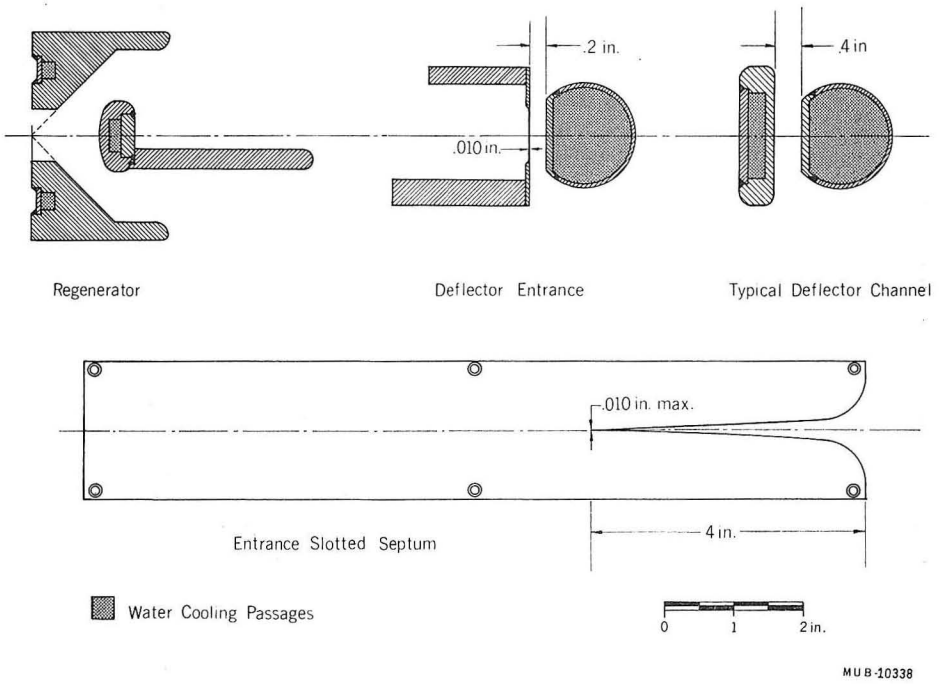

Fig. I. 6-3. Typical cross section through electrodes.

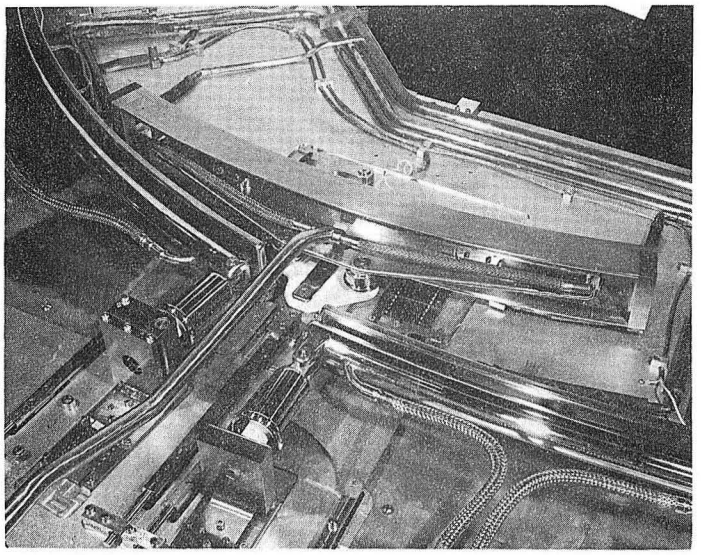

Fig. I. 6-4. Regenerator unit, rear view.

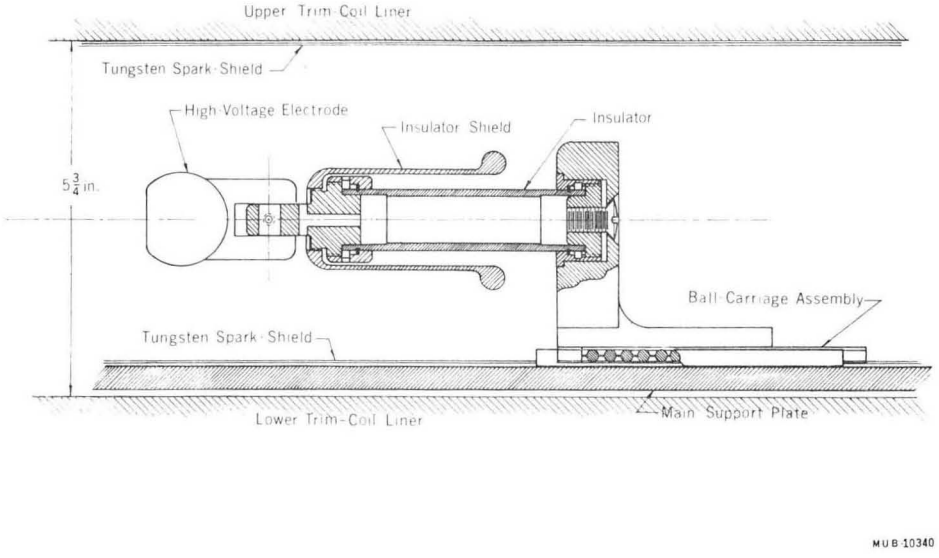

Fig. I. 6-5. Cross section of typical support for high-voltage electrode of deflector, and ball carriage assembly.

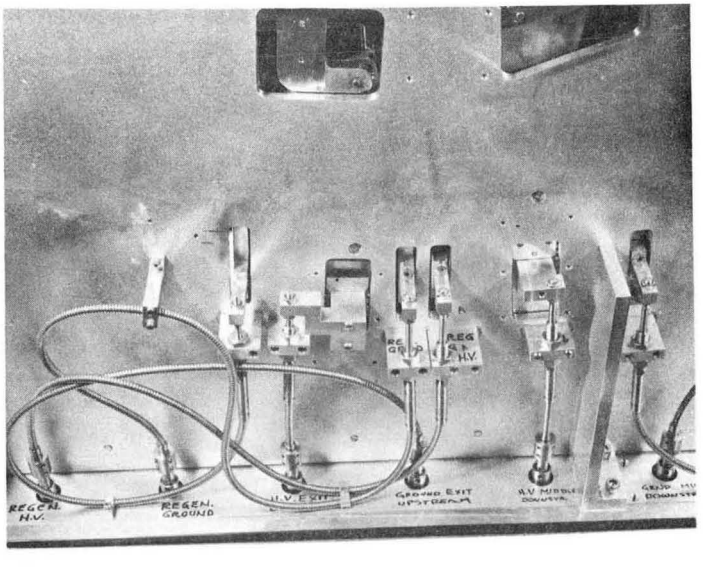

Fig. I. 6-6. Control cable installation.

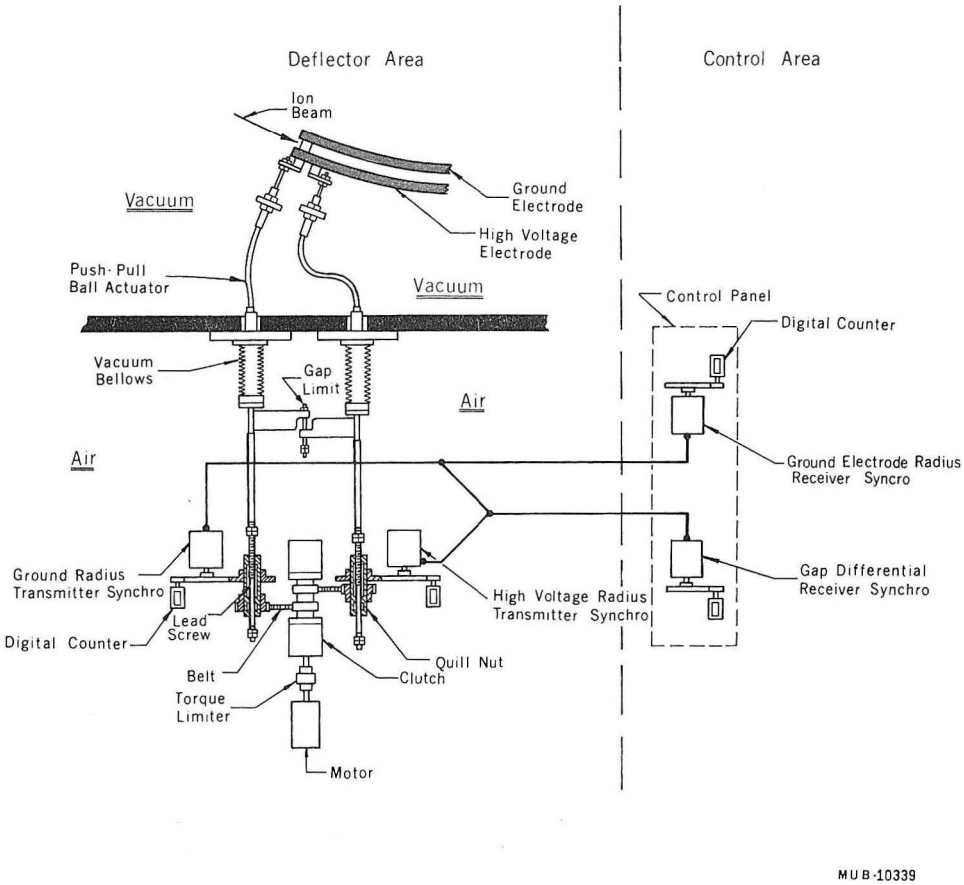

Fig. I. 6-7. Schematic of drive and readout mechanisms.

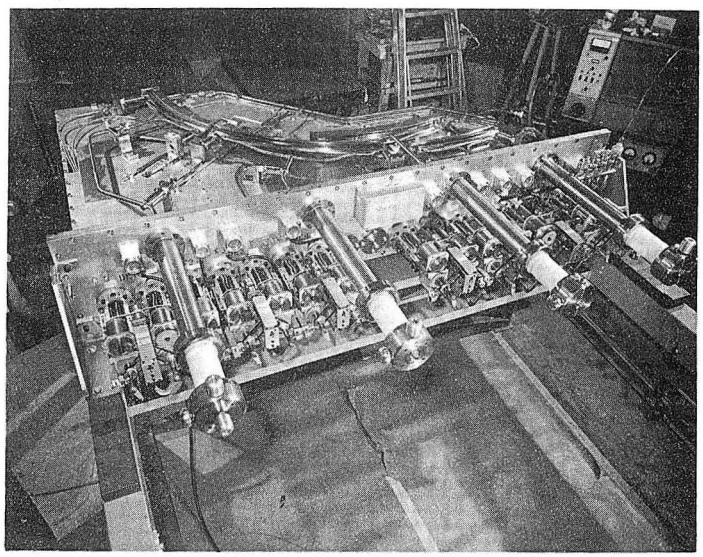

Fig. I. 6-8. Deflector drive assemblies.

7. HEAVY-ION IDENTIFICATION USING THE POWER LAW TECHNIQUE†

J. Cerny, S. W. Cosper, G. W. Butler, H. Brunnader, R. L. McGrath, and F. S. Goulding

Since some concern over[1] and some outright disbelief in[2] the ability of the power-law type of particle identifier[3] to separate heavy ions has been expressed, measurements have been made of its separation of isotopes of beryllium, boron, and carbon. The power-law type of particle identifier employs the empirical range-energy relation $R = a E^b$, where, for ions having $Z = 1$ and 2, b is 1.73 and a is approximately energy-independent but dependent on particle type. Utilizing signals from a ΔE (thickness T) and an E counter, this identifier calculates a particle output pulse proportional to $T/a = (E + \Delta E)^b - (E)^b$. In order to investigate low-yield nuclear reactions, this system has been augmented to include two ΔE counters and is denoted a triple-counter identifier.[4] In this case two identifications are made on each particle passing through the counter telescope, each using one of the ΔE signals; unless these two identifications agree with each other within preset limits, the event is rejected. This comparison therefore eliminates the majority of those relatively rare events whose energy losses in a thin detector deviate considerably from normal and which would contribute to an unwanted background in the identifier spectrum.

Very satisfactory operation of the triple-counter particle identifier for $Z = 1$, 2, and 3 particles has been achieved and has been presented elsewhere.[4] It might appear that this type of identifier would be unable to separate heavy ions, since their ranges[5] do not follow a simple power-law dependence. However, simultaneous separation of these heavy ions over fairly broad ranges of energy is possible through the adjustment of the exponent b to optimize identification in the desired part of the energy spectrum incident on the counter telescope in a given experiment.

These measurements utilized the 129-MeV α-particle beam from the 88-inch cyclotron, which impinged on a ^{12}C target in an evacuated scattering chamber. A four-counter telescope consisting of a 61μ $\Delta E2$ counter, a 32μ $\Delta E1$ counter, a 300μ E counter and a 500μ E_{reject} counter was placed at 10 deg lab. The first three detectors were fully depleted phosphorus-diffused silicon transmission counters, while the last was a lithium-drifted silicon detector. Prior to the experiment, the exponent of the power law was set to 1.65 and a minimum energy loss of 20 MeV on the E detector was demanded; calculations and pulser tests of identifier behavior based on the known heavy-ion ranges had shown these two criteria to be sufficient to separate Be, B, and C isotopes over a reasonable range of energy. No in-beam adjustments were required to produce the results presented below.

Figure I. 7-1 presents a semilog graph of the performance of the particle identifier in separating three Be isotopes, four B isotopes, and four C isotopes. No Li peaks were observed, because of the energy requirement on the E signal plus additional requirements placed on the ΔE signals, which affected only particles of $Z \leq 3$. The identified Be ions cover an energy span of ≈ 39 MeV [^9Be], which is foreshortened by the relatively thin E detector, the B ions cover ≈ 34 MeV [incident ^{10}B between 58 and 92 MeV], and the C ions, ≈ 21 MeV [incident ^{12}C from 73 to 94 MeV]. This B and C energy range was more than adequate for the experiments conducted in conjunction with these measurements; however, pulser studies showed that identical separation would occur over an energy range of at least 40 MeV for ions of both elements if the higher-energy ions were available. Essentially no ^{13}C ions are found in Fig. I. 7-1, since only one group from the $^{12}C(\alpha, {}^{13}C)^3He$ reaction could contribute under these experimental conditions. Energy spectra of most of the B and C identifier groups were taken, and confirmed their assignments; no spectrum showed an appreciable "background" from ions other than the one selected.

Figure I. 7-2 permits a comparison of these results for Be and B ions with other published data[1] on heavy-ion identification. The data of Sachs et al.[1] were taken with the equivalent of a ≈ 74μ ΔE counter and only an 11-MeV requirement on the E signal, so that a greater energy range was covered in their work. The overall performance of the two systems for this application appears comparable.

Heavy-ion identification is thus shown to be quite feasible with a power-law type of particle identifier. Although for this purpose the exponent of the power law has been treated as a (somewhat) adjustable parameter, it should be emphasized that a complete prerun pulser setup is easily accomplished, so that machine time still need not be used for parameter adjustments on this type of identifier.

Footnote and References

† Condensation from Nucl. Instr. Methods, to be published.

1. M. W. Sachs, C. Chasman, and D. A. Bromley, Nucl. Instr. Methods 41, 213 (1966).
2. D. A. Bromley, in Proceedings of the Summer Study Group on the Physics of the Emperor Tandem Van de Graaff Region, BNL-948, Vol. II, 1965, p. 713.
3. F. S. Goulding, D. A. Landis, J. Cerny, and R. H. Pehl, Nucl. Instr. Methods 31, 1 (1964).
4. F. S. Goulding, D. A. Landis, J. Cerny, and R. H. Pehl, IEEE Trans. Nucl. Sci. NS-13, 514 (1966).
5. L. C. Northcliffe, Phys. Rev. 120, 1744 (1960); and Ann. Rev. Nucl. Sci. 13, 67 (1963).

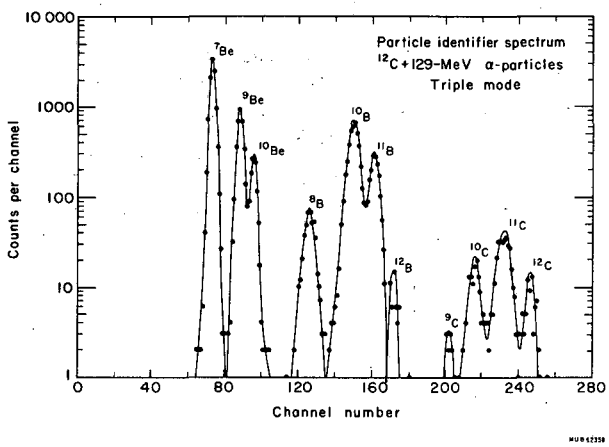

Fig. I. 7-1. A particle identifier spectrum resulting from the bombardment of ^{12}C with 129-MeV α particles (triple mode). Satisfactory agreement between two independent identification signals has been required.

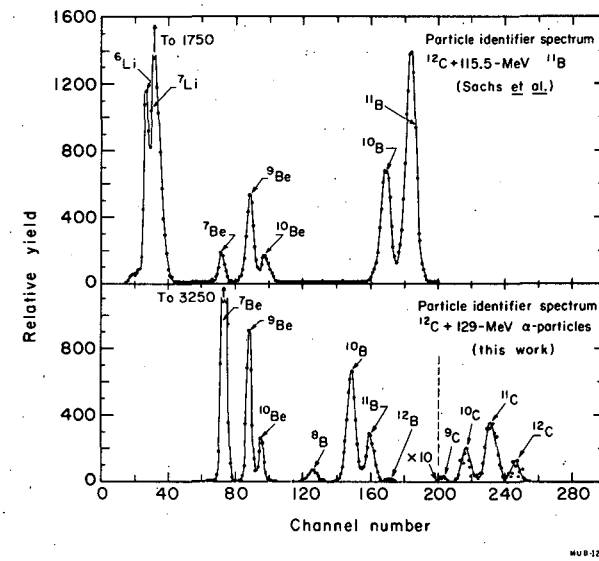

Fig. I. 7-2. A comparison of the Be and B heavy-ion identification spectrum obtained by Sachs et al (upper, ^{12}C + 115.5-MeV ^{11}B) with the data from this work (lower, 129-MeV α particles).

8. EXCITATION OF DIPOLE STATES BY INELASTIC α SCATTERING

J. M. Moss and B. G. Harvey

Inelastic α-particle scattering has, in the past few years, proven to be a useful method for studying excited nuclear states. The information obtainable includes spins, parities, and reduced-electromagnetic-transition probabilities. The theories developed for describing inelastic scattering[1,2] work well for the strongly excited "collective" states but have found no consistent success with the more weakly excited states.

Dipole transitions, in which one unit of angular momentum is transferred to the nucleus, are of the weaker noncollective type of transition. They were studied by Harvey et al.,[3] who found that one could not derive electric dipole transition probabilities from inelastic α-scattering cross sections.

Recently Blair[4] and McManus[5] have derived an approximate selection rule which forbids direct dipole transitions induced by α particles. Their reasoning is as follows: The differential cross section $d\sigma/d\Omega$ may be written $d\sigma/d\Omega = |-(\mu/2\hbar)\ T|^2$, where μ is the reduced mass,

$$T = \langle B \mid \int d\tilde{r}_\alpha \, \chi^{(-)}_{k_f} \sum_j V_{j\alpha} \, \chi^{(+)}_{k_i} \mid A \rangle.$$

A and B refer to the initial and final states of the nucleus, respectively, $\chi^{(+)}_{k_i}$ and $\chi^{(-)}_{k_f}$ refer to the incoming wave with momentum k_i and the outgoing wave with momentum k_f respectively, and $V_{j\alpha}$ is the interaction between the α particle and the jth nucleon.

Assuming that α particles may be represented by plane waves (certainly a poor assumption for strongly absorbed particles),

$$\chi^{(+)}_{k_i} \rightarrow e^{i\tilde{k}_i \cdot \tilde{r}_\alpha} \quad \text{and} \quad \chi^{(-)}_{k_f} \rightarrow e^{-i\tilde{k}_f \cdot \tilde{r}_\alpha},$$

then

$$T = \langle B \mid \int d\tilde{r}_\alpha \sum_j V_{j\alpha} \, e^{i\tilde{q} \cdot \tilde{r}_\alpha} \mid A \rangle, \quad \text{where } \tilde{q} = \tilde{k}_i - \tilde{k}_f .$$

Now let $V_{j\alpha} = U_{j\alpha} \, \delta(\tilde{r}_j - \tilde{r}_\alpha)$ (delta force interaction);

$$T = \langle B \mid \sum_j U_{j\alpha} \, e^{iq \cdot r_j} \mid A \rangle.$$

Assuming $U_{j\alpha}$ is the same for all particles and that $\tilde{q} \cdot \tilde{r} \ll 1$, one has $U_{j\alpha} \rightarrow U_\alpha$ and $e^{i\tilde{q} \cdot \tilde{r}_j} \rightarrow 1 + i\tilde{q} \cdot \tilde{r}_j$, $\tilde{q} \cdot \tilde{r}_j = qr_j \cos\theta_j = qz_j$, $T = iqU_\alpha \langle B \mid \sum_j z_j \mid A \rangle$. But $\sum_j z_j = AZ$, where Z is the z coordinate of the center of mass (A is the atomic number). Since a change in the center-of-mass coordinate is not an internal motion, the matrix element vanishes, and with the previous assumptions, dipole states should not be excited by α particles. Nevertheless dipole transitions are observed experimentally; indeed they are sometimes quite strong.

In order to investigate this disagreement between the approximate theory and experiments, we have bombarded ^{16}O and ^{20}Ne with 50- and 33-MeV α particles, respectively, and observed the excitation of the 1- states. The 0+ to 1- transition in ^{20}Ne has also been studied at 50 MeV by Harvey and Springer.[6] Angular distributions are shown in Figs. I. 8-1 through I. 8-3.

The Blair phase rule, which predicts that odd-L transitions should be in phase with the elastic angular distribution, is clearly violated at 50 MeV in ^{20}Ne. Springer[7] qualitatively explained this as being due to an octupole-quadrupole "double excitation" through the 3- state at 7.17 MeV, analogous to quadrupole-quadrupole processes observed before in ^{56}Fe[8] and many other nuclei. An additional feature of double excitation is observed in ^{16}O (50 MeV) and ^{20}Ne (33 MeV), where the envelope of oscillations falls off relatively slowly with angle. This behavior is characteristic of more complicated reaction mechanisms.

The 1- state in ^{16}O is a good candidate for octupole-quadrupole excitation, since both the B(E3; 3- to 0+) and the B(E2; 1- to 3-) are collectively enhanced transitions. In such a case one would expect the cross section for double excitation to be less by perhaps a factor of 10 than cross section to the state through which it proceeds. For excitation by inelastic scattering of 50-MeV α particles, we find the cross sections to the 3- and 1- states of ^{16}O are respectively 3.24 and 0.87 mb (integrated from 10 to 70 deg). Thus the ratio is only 3.65. This value seems rather low for double excitation, although a final conclusion can be made only after completion of coupled-channel calculations.

Before any quantitative statement can be made about the direct dipole inelastic scattering process one must determine whether the dipole selection rule retains any validity under more realistic conditions [the assumptions of plane waves and small angular momentum transfer ($\tilde{q} \cdot \tilde{r} \ll 1$) are particularly inaccurate]. To do this one must use a distorted-wave description of the process in which the center-of-mass motion has been removed. At present this is not possible. It is possible, with present theories, to determine whether a pure double excitation process could reproduce the phase and magnitude of the dipole angular distributions. This approach is presently being considered.

References

1. Taro Tamura, Rev. Mod. Phys. 37, 679 (1965).
2. N. Austern and J. S. Blair, Ann. Phys. 33, 15 (1965).
3. B. G. Harvey, J. R. Meriwether, J. Mahoney, A. Bussière de Nercy, and D. J. Horen, Phys. Rev. 146, 712 (1966).
4. J. S. Blair, private communication.
5. H. McManus, private communication.
6. A. Springer and B. G. Harvey, Phys. Rev. Letters 14, 316 (1965).
7. A. Springer, Scattering of 50.9 MeV Alpha Particles From Ne^{20} and Ca^{40} (Ph. D. Thesis), UCRL-11681, May 1965.
8. J. Saudinos, R. Beurtey, P. Catillon, R. Chaminade, M. Crut, H. Farragi, A. Papineau, and J. Thirion, Compt. rend 252, 260 (1961).

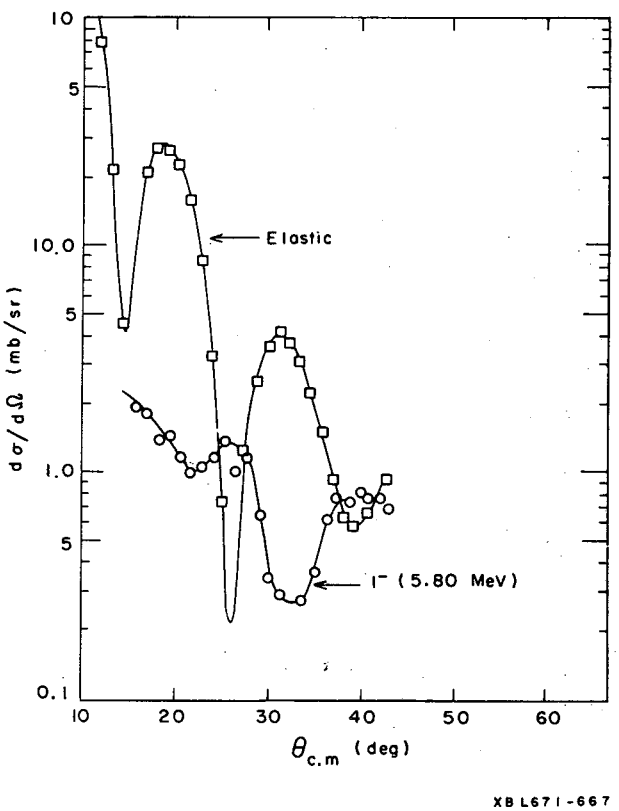

Fig. I.8-1. Angular distributions for the reaction $^{20}Ne(\alpha,\alpha')^{20}Ne^{*}$ at 50.9 MeV (from Ref. 7).

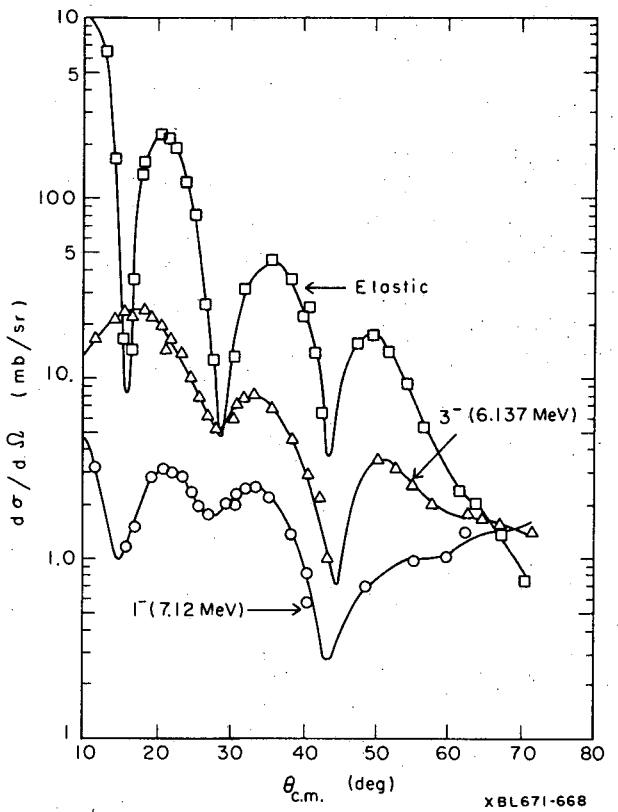

Fig. I.8-2. Angular distributions for the reaction $^{16}O(\alpha,\alpha')^{16}O^{*}$ at 50 MeV.

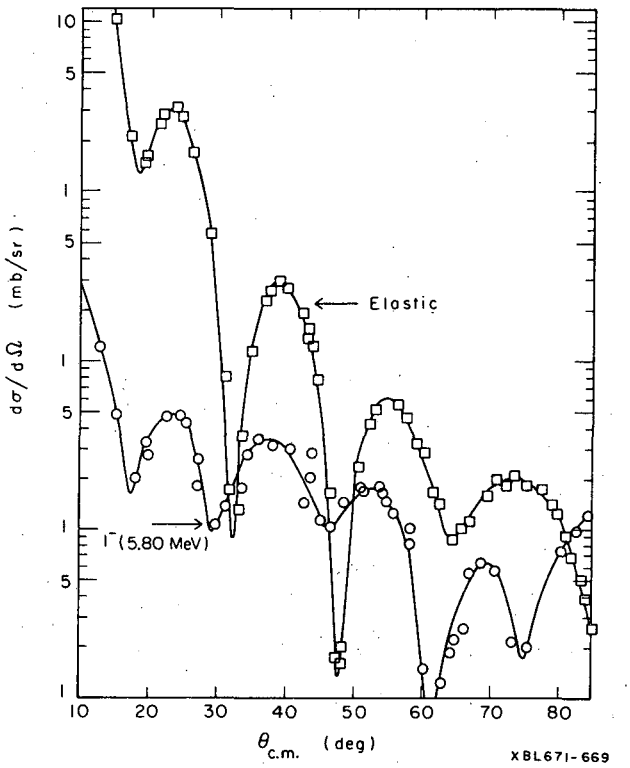

Fig. I. 8-3. Angular distributions for the reaction $^{20}Ne(\alpha,\alpha')^{20}Ne^*$ at 33 MeV.

9. AUTOMATIC CONTROL OF THE TRIM-COIL POWER SUPPLIES AT THE BERKELEY 88-INCH CYCLOTRON†

David R. Struthers

Introduction

The 88-inch cyclotron uses 17 trim coils, each with its own power supply. For each particle and energy that has been developed there is a set of 17 currents, known as the trim-coil solution, that is considered to give the optimum trimming field.

Presently these trim-coil currents, as well as many other machine parameters, are set manually by an operator and maintained constant by individual electronic regulators. An average of one particle or energy change occurs per 8-hour shift, and the resulting machine setup takes about 30 minutes. The system to be described is the first phase of a project to set most of the machine parameters within 5 min. Because there are always items such as television adjustments and fine tuning for beam, a realistic prediction of the time that will be needed for a complete energy or particle change is 15 to 20 min. The saving of 10 min per shift, at $200 per hour for cyclotron time, amounts to about $30 000 annually.

The design requirements and philosophy of our complete automatic control system are fully described elsewhere,[1] and are partially treated in this report.

System

Each of the trim-coil currents is controlled to about 0.2%, short term, by a regulator. The long-term (8 to 16 h) stability is within less than 1%. Figure I. 9-1 is a simplified block diagram of a typical trim-coil power supply and regulator. The system starts as a potentiometer, which determines the value of the reference. The potentiometer is adjusted manually when the current is to be set or changed. It is important to the operation of the cyclotron, and to further

development of beams, that this means of direct operator control not be sacrificed. The output, which is current, is converted by the feedback loop to a voltage of the same order of magnitude as the reference. The feedback loop is either a shunt or a transductor. The difference (error) between the reference and the feedback-loop output is amplified by the regulator amplifier so as to cause the output to change until the error is reduced to zero.

A simple method of automatic control of several supplies involves setting a series of input reference levels (e.g., potentiometer settings) from a known correspondence between reference setting and output. That is, the potentiometer readings from previous experiments are just reproduced automatically for a like experiment. A serious disadvantage is that, over a long period, this correspondence changes due to aging of parts, and changes again immediately upon any replacement of parts.

A better approach is to design a single, highly precise reference that supervises the existing series of references sequentially. While a particular unit of the system is being sampled, the corresponding output current is compared with the programmed output current, which is the highly precise reference, and the result of the comparison is used to reset the individual reference as necessary. The individual references maintain the power supply outputs during the rest of the cycle.

For automatic digital control, either all the existing references would have to be redesigned so as to be operated by relays or solid-state switches, or the potentiometers could be driven by stepping motors. Then the actual currents would have to be converted from their analog form to a corresponding digital representation so that they could be compared with the supervisory reference, which is either punched tape or an IBM card.

On the other hand, analog operation, which involves working directly with voltages and currents within the automatic-control system, would require either an analog supervisory reference or a digital-to-analog conversion of a punched-tape or IBM-card supervisory reference. A digital supervisory reference is advantageous in providing greater information density than an analog reference, and in being more usable in future computer studies.

A summary, then, of the most appealing automatic-control system for an operating cyclotron is:

1. Supervisory: the individual references are supervised sequentially so as to maintain required outputs;
2. Analog: all operations within the supervisory loop, as well as within the parameter-regulating systems, are analog--that is, all operands are voltage representations of the current involved;
3. Digital input: the supervisory reference is on either punched tape or IBM cards, with digital-to-analog conversion.

With the above description in mind, we can derive a suitable block diagram as shown in Fig. I.9-2. In this figure the sampling period is 0.33 sec and the sampling rate is therefore 3/sec.

Hardware

The current ratings of the 17 trim coil power supplies range from 750 to 2500 amperes; we have both silicon-controlled rectifier and magnetic-amplifier power supplies. A typical system's open-loop gain, including regulator amplifier, power supply, and transductor, is about 200 to 1000. This gives a maximum reduction in errors of about 0.1%. Due to amplifier drifts, however, the long-term, or daily, stability is about 1%.

The 17 shunt signals are fed into the input multiplexer, which consists of 17 double-pole mercury-wetted-contact relays. These relays are driven in sequence at a 3/sec rate by the multiplexer control; every other normally open contact is wired in parallel so as to provide a single two-wire output. This output is fed to the signal conditioner, which is a gain-switched, temperature-controlled differential amplifier whose gain is stable to 0.01% and whose drift is less than ±5 μV per day. The gain is switched to provide a 10-V signal for full output current of the power supply output being measured regardless of the mV-to-A rating of the shunt. The output of the signal conditioner, then, is a sequence of 17 voltages proportional to the 17 trim-coil currents, and goes to the "measurement" input of the comparator and motor drive.

The program originates on a single IBM card whose rows and columns are used to provide 40 channels (23 channels are for later use) of 24 bits each. Of these 24 bits, 13 bits are set point data and 11 are miscellaneous data. The card is read statically and therefore continuously.

These 17 program channels are fed to the input of the program multiplexer. This multiplexer consists of 17 24-pole relays, which are driven in sequence at a 3/sec rate by the multiplexer control, and whose normally open contacts are wired in parallel to provide a single 24-wire output. The output is thus a sequence of 17 24-bit binary numbers that are related to the 17 power-supply set points desired.

The set-point data are converted to voltages of 0 to 10 V in the digital-to-analog (D-to-A) converter, a Raytheon DAC-20 model. With 13 bits, the output voltage can be set to about one part in 8000. The miscellaneous data are used to program the readout system. The output of the D-to-A converter, therefore, is a sequence of 17 voltages proportional to the desired 17 set points, and goes to the "program" input of the comparator and motor drive.

In the comparator and motor drive, the "measurement" signal and the "program" signal are subtracted, and the difference (or error) is amplified to drive the motor-driven potentiometers in the trim coil power supply reference. There are actually two parallel amplifiers in this block; a low-gain amplifier is active over most of the 0.33-sec period of each measurement to provide the coarse adjustment for the motor-driven potentiometers, and a high-gain amplifier is active over a 0.03-sec period of each measurement for the fine adjustment. The outputs of the two amplifiers are added and followed by a stage of power amplification. Each amplifier input is controlled by a mercury-wetted-contact relay which keeps the input grounded until all the current-carrying relays in the following stages have switched. The mercury relays are then opened for 0.25 sec for the low-gain amplifier and 0.03 sec for the high-gain amplifier. The output of each amplifier is limited to ±10 V. Figure I. 9-3 shows the different forms of the output voltage for a given motor-potentiometer drive. The pulse lengths were derived by consideration of the maximum setup time desired, and of the curves of angular displacement of the motor-potentiometers versus both pulse length and pulse height.

The output of the comparator and motor drive is a sequence of 17 error voltages with waveforms as in Fig. I. 9-3. This output is fed to the input of the output multiplexer. This multiplexer consists of 17 four-pole relays, which are driven in sequence at a 3/sec rate by the multiplexer control. Its input is the normally open contacts wired in parallel, with the swingers providing the 17 outputs. The 17 outputs go to the 17 trim-coil power-supply reference motor-potentiometer motor leads.

A computer program has been written to convert the 17 trim-coil currents desired for a particular solution to a single punched IBM card for direct insertion into the automatic control system.

Footnote and Reference

† Short form of paper for International Conference on Isochronous Cyclotrons, Gatlinburg, Tennessee, May 1966.

1. David R. Struthers, Automatic-Control-System Design for the Berkeley 88-Inch Cyclotron, UCRL-16210, June 1965.

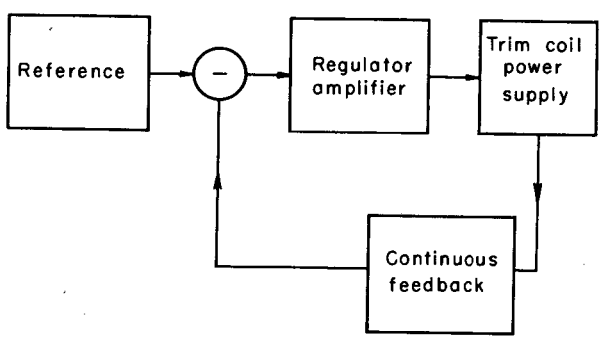

Fig. I. 9-1. Typical trim-coil power-supply regulating system.

MUB-10176

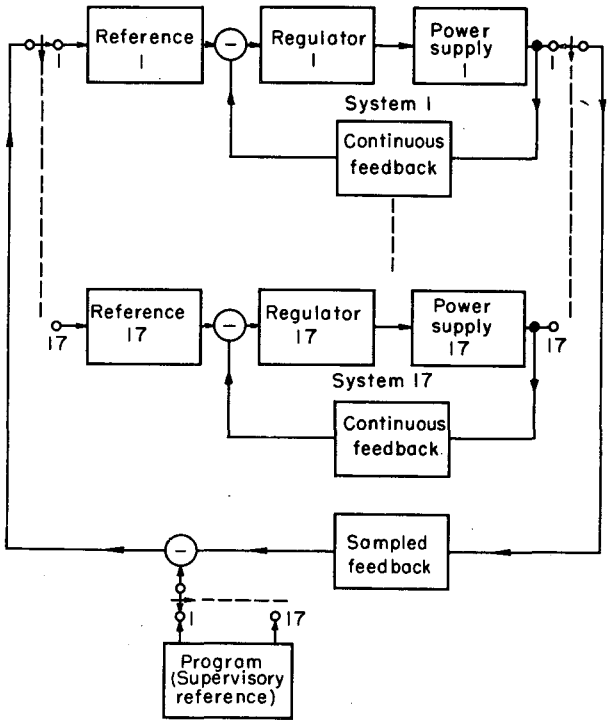

Fig. I. 9-2. Supervisory control block diagram.

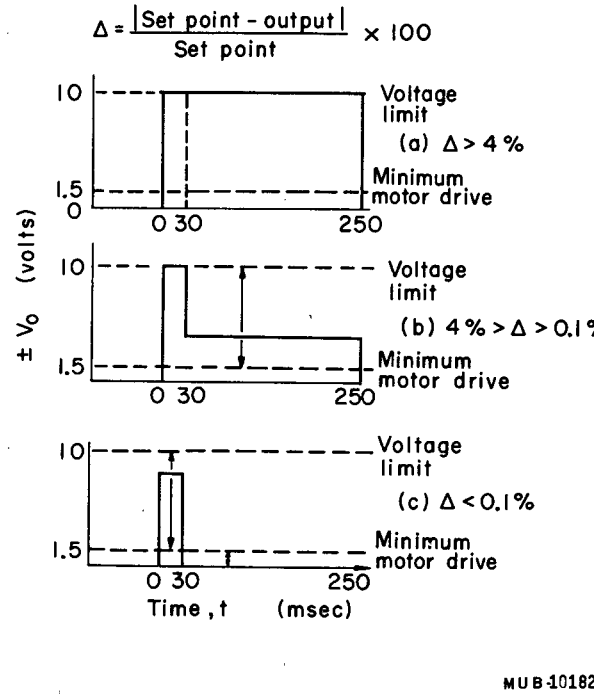

Fig. I. 9-3. Output voltage forms.

10. A NEW MICROCALORIMETER FOR THERMODYNAMIC MEASUREMENTS ON ACTINIDE ELEMENTS

Lester R. Morss and Dennis K. Fujita

Much fundamental thermodynamic data on the actinide elements have been obtained by microcalorimetry. An isothermally jacketed (semi-adiabatic) microcalorimeter, described previously,[1] has been used to obtain many heat-of-solution measurements in this Laboratory. This instrument, fabricated of tantalum, had a conventional vacuum system and used a platinum resistance thermometer. Although its temperature sensitivity was 10^{-5} °C (limiting its applicability for ± 0.1% precision to reactions yielding more than 0.2 calorie), it was subject to thermal EMF errors and substantial thermal conductivity heat leaks, and the vacuum system was a source of frequent difficulty. The impetus for design and construction of a new calorimeter was provided by the availability of reliable high-impedance thermistors and dc amplifiers, by improvements in vacuum technology, and by the desire to make measurements in hydrofluoric acid solution (for experiments with protactinium).

An attempt was made to refine heat-of-solution data for curium metal.[2] Standard metal preparative techniques were used,[3] but neither precipitation as CmF_3 or as the hydroxide (followed by fluorination with Freon-12 at 600°C) yielded satisfactorily pure and compact metal samples. In addition, the heat of bulb breaking did not appear to be reproducible.

The new calorimeter consists entirely of platinum-10% iridium, with an ion-pumped all metal vacuum system routinely capable of 5×10^{-7} mm Hg. A temperature sensitivity of 5×10^{-6} °C is attained by using precision thermistors of 100 000-ohm impedance in an efficient impedance-

matched Wheatstone bridge with solid-state dc amplification. The sensitivity, which as in the earlier calorimeter approaches the thermal noise limit, is 3×10^{-5} calorie. If other errors can be confined to this limit, precise measurements of reactions yielding only 0.05 calorie will be possible.

In order to approach this degree of precision (which corresponds to dissolving about 80 μg of an actinide metal), efforts will be made to refine metal-preparative techniques to minimize nonmetallic impurities, to use recently proposed standards such as the neutralization of tris(hydroxymethyl)aminomethane[4] to check the calorimeter's precision, and to improve the reliability of sample weighing and reaction initiation.

References

1. John L. Burnett, The Thermochemistry of Di- and Trivalent Europium (Ph. D. Thesis), UCRL-11850, Dec. 1964.
2. J. C. Wallmann, J. Fuger, H. Haug, S. A. Marei, and B. M. Bansal, The Heat of Solution of Curium Metal and the Heats of Formation of Cm^{+3} and $CmCl_3$, UCRL-16468, Oct. 1965.
3. B. B. Cunningham and J. C. Wallmann, J. Inorg. Nucl. Chem. 26, 271 (1964).
4. Stuart R. Gunn, Comparison Standards for Solution Calorimetry, J. Phys. Chem. 69, 2902 (1965).

11. A MAGNETIC STEERING DEVICE FOR ELECTRON COINCIDENCE EXPERIMENTS

R. L. Watson, H. R. Bowman, S. G. Thompson, and J. O. Rasmussen

The suitability and convenience of semiconductor detectors for simultaneous energy measurements of two or more radiations having specific time relationships has led to the increasingly important role of the coincidence method in nuclear spectroscopic investigations. Moreover, with the improved resolution now obtainable, it is now possible to extend coincidence applications to experiments designed to take advantage of the various time relationships existing between electron emission and other nuclear events. Examples of such coincidence relationships include those existing between internal conversion and subsequent x-ray emission, between β decay and subsequent γ-ray emission, between α decay and the internal conversion of subsequent nuclear transitions, between x-ray emission resulting from K capture and the internal conversion of subsequent nuclear transitions, and between γ-ray emission and the internal conversion of cascade transitions. The electron coincidence method also lends itself to many other applications, such as the study of internal conversion in coincidence with a nuclear reaction, and the investigation for which the device to be described in this paper was originally designed--the study of internal conversion in coincidence with nuclear fission.

In all the above applications, as with any coincidence measurement, a major requirement is the achievement of large total detection efficiencies (intrinsic detector efficiency times detection geometry). Furthermore, it is important that the electrons to be measured not be required to penetrate any quantity of matter (window) so great as to cause a detectable amount of dispersion or energy shift. This restriction requires that the source be located inside the same vacuum chamber as houses the electron detector, and hence gives rise to the further problem of shielding the electron detector from interfering radiations (i.e., α particles, positrons, x-rays, γ rays, fission fragments).

We have employed the fringing field of a high-gradient electromagnet along with a lithium-drifted silicon detector in a device which overcomes all the above-mentioned problems in the measurement of electron energies, and which may readily be used in conjunction with separate detectors for measuring coincident radiation energies. In this device, electrons are steered away from the source region around a 90-deg circular arc to the detector, which is shielded from other radiations emitted at the source. The magnetic field used in the steering device is one of rotational symmetry and radial dependence proportional to $1/r^n$. An electron moving in the fringing region of such a field, in general, experiences two types of drift motion--an azimuthal drift around the circumference of the magnet due to the decreasing field strength as a function of distance from the magnet center, and a vertical (Z direction) drift consisting of a spiraling motion along the magnetic lines of force.[1] Because the field lines in the fringing field region become highly convergent as they

approach the magnet pole tips, the vertical component of the electron's motion forces it to gyrate in tighter and tighter helical spirals in order to keep its magnetic moment (the ratio of the component of kinetic energy perpendicular to the field lines to the field strength, $T_\perp/H$) a constant.[2] If the field is sufficiently convergent, a point is reached where the parallel (vertical) component of the electron's kinetic energy becomes zero and the electron is reflected back in the opposite direction. This is the fundamental requirement for a magnetic mirror, and it may be shown that the condition for reflection is given by[2]

$$\sin^2 \theta_{crit} \geq H_0/H_R \,, \tag{1}$$

where θ_{crit} is the maximum angle between the initial electron trajectory and the field line at the starting point which will result in reflection, H_0 is the field strength at the starting point, and H_R is the field strength at the reflection point. Hence, for electrons emitted from a source located on the magnet symmetry plane and having vertical kinetic energy components below a critical value, the electron motion is a superposition of a trochoidal motion and a vertical oscillation through the symmetry plane.

The motion of a charged particle in such a field has been studied extensively by Malmfors.[3] Malmfors treated the problem by means of a perturbation method, and obtained, for the azimuthal angular displacement of a charged particle after one vertical oscillation through the symmetry plane, the expression

$$\Lambda = \frac{2\pi}{r_0} \frac{mc}{eH_0} \sqrt{E} \sqrt{1+E/2} \left(1 - \frac{n^2 - 8n + 4}{16} \frac{Z_R^2}{r_0^2} + \cdots\right) . \tag{2}$$

In this equation, r_0 is the radial distance from the center of the magnet to the starting point in the plane of symmetry, H_0 is the field strength at the starting point, Z_R is the oscillation amplitude (distance from the symmetry plane to point of reflection), and E is the particle energy in units of mc^2. The azimuthal angular displacement of a charged particle after one orbit in the plane of symmetry is given by

$$\Phi = \pi n \frac{\rho_0^2}{r_0^2} \left[1 + \left(\frac{3}{4} n^2 + n - 1\right) \frac{\rho_0^2}{r_0^2} + \cdots\right] , \tag{3}$$

where ρ_0 is the radius of curvature in the plane of symmetry when the oscillation amplitude is zero. Another equation of interest gives the drift time required for a particle to precess 1/4 of the distance around the magnet. It is valid in the region of relativistic velocities, and is expressed by

$$\tau = \frac{\pi r_0}{2v_{drift}} = \frac{\pi e}{2mc^2} \frac{H_0 r_0^2}{n} \cdot \frac{E+1}{E(1+E/2)} \left(1 + \frac{n(n-2)}{4} \frac{Z_R^2}{r_0^2} + \cdots\right) . \tag{4}$$

An illustration of the region of acceptance into the steering device for a point source located on the symmetry plane is shown in Fig. I. 11-1. All electrons emitted between the two cones are transmitted around the magnet. Malmfors found the transmission of the device to be given by

$$T = \frac{n}{\sqrt{2}} \frac{Z_{R\,max}}{r_0} . \tag{5}$$

It is noted that the transmission of the steering device is independent of electron energy and solely determined by the maximum oscillation amplitude of the reflection through the symmetry plane.

The magnetic field used in the steering device is produced by a 100-kVA C magnet. A plot of the magnetic field strength as a function of radial distance from the center of the magnet is shown in Fig. I. 11-2 along with a cross-section sketch of the pole face designed to create a nearly constant-n fringing field with high convergence at the pole tips. The radial position of the electron detector and source is also indicated (r_0 = 6.5 in.), and the field strength at this radius was 6 kG. The value of n in the region of the detector-source radius was found to be 3.35.

A film study of the radial distribution of ^{203}Hg conversion electrons accepted into the steering device was conducted inside a vacuum chamber placed between the pole faces. A strip of x-ray film was mounted inside the vacuum chamber radially from the center of the magnet, and an electron source--which consisted of ^{203}Hg amalgamated on the end of a thin copper wire--was mounted 90 deg around the magnet at a radial position of 16.5 cm. One of the exposed film strips showing the distribution of electrons transmitted around from the source is presented in Fig. I. 11-3, where it is seen that electrons accepted into the device are focused into a narrow band having a width approximately equal to twice the radius of curvature of the electrons in the magnetic field and a length determined by the physical dimensions of the system--in this case, the vacuum chamber width.

The transmission of the magnetic steering device can be easily calculated from Eq. 5. For our experimental design, (i.e., H_0 = 6 kG, n = 3.35, r_0 = 6.5 in., $Z_{R\ max}$ = 1 in.) the transmission is found to be 36.5%. The silicon detector employed as the spectrometer, however, has an active area with a diameter of only 0.53 in., and hence only about 25% of the electrons in the transmitted band actually hit the detector. Furthermore, an appreciable fraction of the electrons that hit the detector suffer backscattering and do not deposit their full energy. By using calibrated ^{109}Cd, ^{203}Hg, ^{207}Bi, and ^{137}Cs sources, the total efficiency for electrons transmitted around from the source and detected in the silicon detector was found to be approximately 5% of the total electrons emitted by a source. The efficiency was also found to be nearly constant as a function of energy over the energy range of 0 to 600 keV.

As an example of the quality of the measurements we are able to obtain with the magnetic steering device, a spectrum of the internal conversion electrons arising from the decay of ^{203}Hg is shown in Fig. I. 11-4, taken with a lithium-drifted silicon detector (3 mm depletion depth) in the steering device. The detector was operated at an optimum temperature of -93°C and at 318 V bias, and incorporated a field-effect transistor cooled to -135°C in the input stage of the preamplifier.[4] The measured resolution was 3.0 keV for the K line of ^{203}Hg, as shown in Fig. I. 11-5, where the L and M lines and a shoulder due to the N line may also be seen. The electron peaks display some tailing, but this is felt to be due to the thickness of the source rather than to interference from the source holder and backing.

A sketch of the basic layout used in our studies of internal conversion electrons in coincidence with nuclear fission is presented in Fig. I. 11-5.[5] As indicated, electrons starting at the symmetry plane precess in trochoidal orbits around the magnet in a 90-deg arc to the electron detector while being reflected from pole face to pole face along magnetic lines of force. (The trajectory of an electron leaving at the critical reflection angle θ_c is depicted.) The fission-fragment detectors were placed parallel to the symmetry plane, and only those electrons which were emitted near 90 deg with respect to the fragment detector axis were allowed to reach the electron detector. A large lead shield was located in a position which blocked any interfering radiation.

References

1. A. Simon, An Introduction to Thermonuclear Research (Pergamon Press, New York, 1959), p. 35.
2. J. R. Reitz and F. J. Milford, Foundations of Electromagnetic Theory (Addison-Wesley Publishing Co., Reading, Mass., 1960), p. 276.
3. K. G. Malmfors, Arkiv Fysik 13, 237 (1958).
4. E. Elad, Nucl. Instr. Methods 37, 327 (1965).
5. R. L. Watson, H. R. Bowman, S. G. Thompson, and J. O. Rasmussen, in Internal Conversion Processes, J. H. Hamilton, Ed. (Academic Press, Inc., New York, 1966), p. 423.

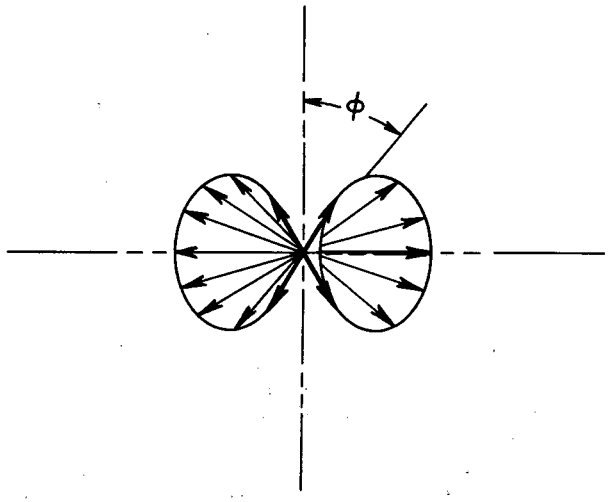

MUB-9749

Fig. I. 11-1. An illustration of the region of acceptance into the magnetic steering device for electrons emitted from a point source located on the symmetry plane. All electrons emitted between the two cones are transmitted around the magnet to the electron detector.

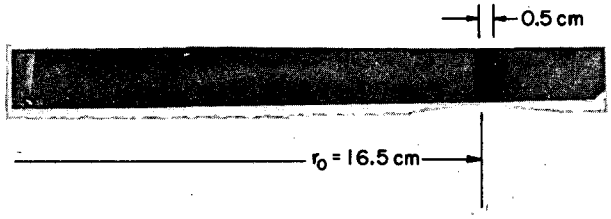

Fig. I. 11-3. A film strip which was exposed at the detector position to electrons transmitted around the magnet from the source position in the steering device.

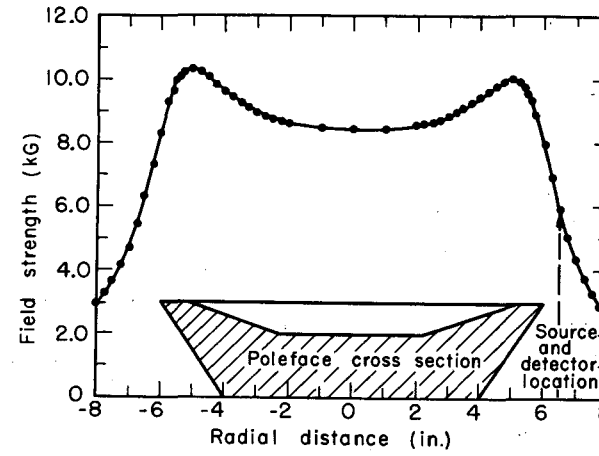

MUB-10882

Fig. I. 11-2. Magnetic field profile and sketch of pole-face cross section.

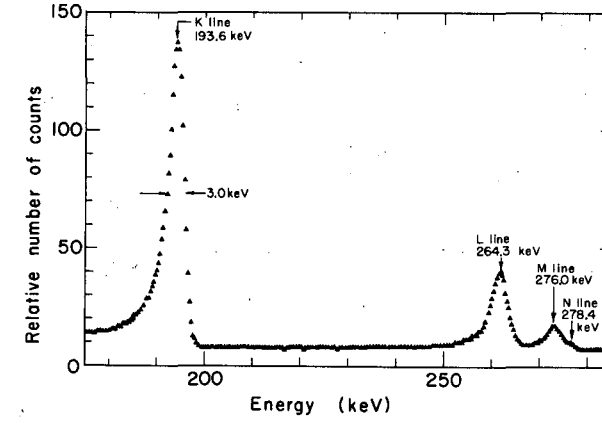

MUB-10852

Fig. I. 11-4. Spectrum of the internal conversion electrons associated with the 279.1-keV γ-ray transition in ^{203}Tl taken with a lithium-drifted silicon detector in the magnetic steering device.

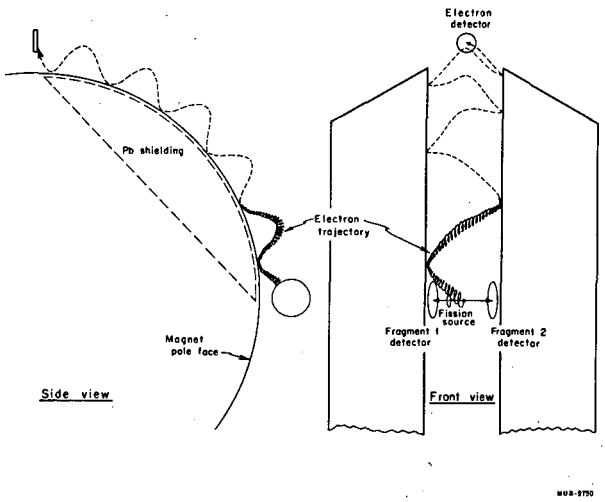

Fig. I. 11-5. A diagram depicting the magnetic steering mechanism for an electron emitted at the critical reflection angle, θ_{crit}. The electron starts at the symmetry plane and precesses in trochoidal orbits around the magnet in a 90-deg arc to the detector while being reflected from pole face to pole face along magnetic lines of force.

12. DETECTION OF HIGH ENERGY PROTONS BY THIN-WINDOW LITHIUM-DRIFTED GERMANIUM COUNTERS†

R. H. Pehl, D. A. Landis, and F. S. Goulding

Recent developments in producing thin-window Li-drifted germanium detectors[1] have enabled us to investigate their response to 29- and 40-MeV protons. The window is of negligible thickness for long-range particles. Resolutions of 28 and 44 keV (FWHM) were obtained at 29 and 40 MeV, respectively. Figure I. 12-1 shows a typical energy spectrum of 29-MeV protons scattered off Au; similar spectra were obtained when the 40-MeV proton beam was incident on Au. Pulser signals were fed in simultaneously with signals from the scattered protons. After subtraction of nondetector contributions, mainly the energy spread in the cyclotron beam, the resolutions obtained approach the theoretical limit for a Ge detector.

Footnote and Reference

† Condensed from IEEE Trans. Nucl. Sci. NS-13 3, 274 (1966).

1. F. S. Goulding and B. V. Jarrett, A Method of Making Thin-Window Germanium Detectors, UCRL-16480, Jan. 1966.

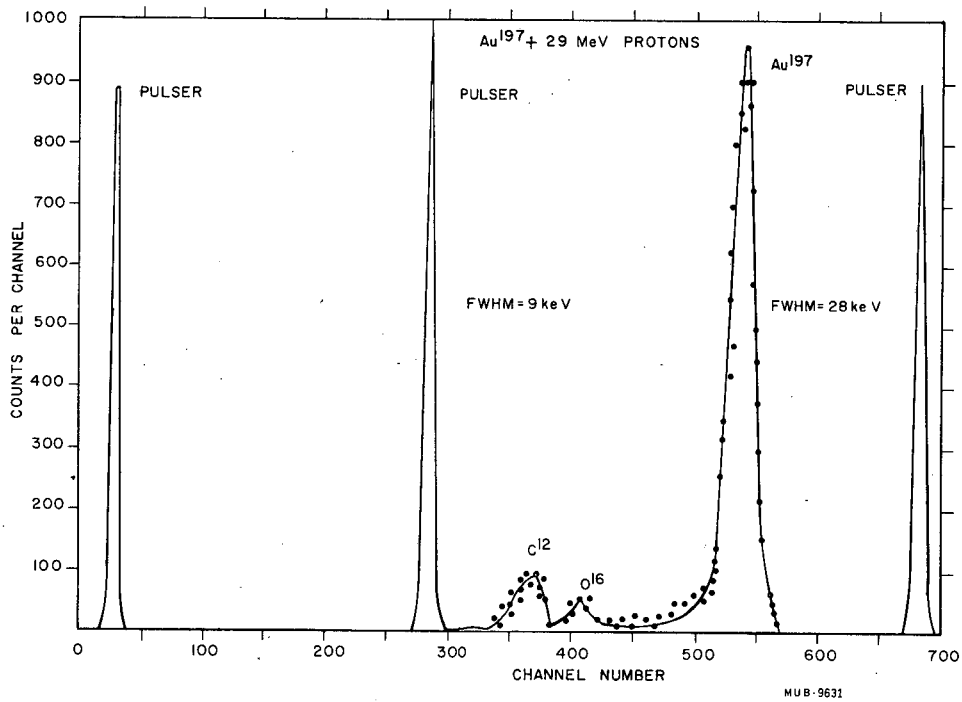

Fig. I. 12-1. Example of energy spectra recorded, showing 29-MeV protons, scattered off Au. The energy calibration is 1.46 keV per channel. Pulser signals were recorded simultaneously with signals from the scattered protons.

13. GERMANIUM RADIATION DETECTOR AND HIGH RESOLUTION SYSTEM DEVELOPMENT

R. H. Pehl, R. C. Cordi, F. S. Goulding, D. A. Landis, W. A. Maertens, D. F. Malone, and G. I. Saucedo

Progress in the development of germanium detectors continues to be largely determined by the quality of germanium crystals that can be obtained. Detectors made from several Hoboken crystals obtained early in 1966 have provided excellent results. The Fano factor has been demonstrated to be less than 0.1 for several detectors. Unfortunately, more recent crystals from this supplier are not of such high quality, although still usable. The quality of germanium from Sylvania improved at the start of 1966 in that Li ions would drift at a reasonable rate, but high-quality detectors could not be made from these crystals. Consequently no Sylvania crystals have been obtained by us since April.

During this calendar year, 42 detector systems were put into service. Included were a number of systems using a new stainless steel and aluminum holder design[1] incorporating a cooled, internal field-effect transistor as the first element of a charge-sensitive preamplifier. The temperature of the FET can be regulated over a range of about -180° to -50°C to provide the optimum temperature to obtain the best resolution for a given detector and FET. This has proven extremely valuable, since most FETs provide better resolution for reasonable-size detectors at temperatures considerably warmer than liquid nitrogen. (For very small detectors the difference in resolution as a function of FET temperature is less because of the low capacity.) One coaxial style detector with an intrinsic volume of about 35 cm^3 has been produced and successfully used. Although it has a high capacity (45 pF), resolutions of 2.5 and 3.5 keV have been obtained on photopeaks corresponding to 122 and 1173 keV, respectively. This good resolution is due in part to the ability to obtain very good FETs. The FET used has provided a zero-capacity electronic FWHM resolution of about 1 keV and a slope of about 32 eV/pF. In more optimum systems this type of FET has given zero-capacity resolution better than 600 eV with slopes less than 30 eV/pF.

Two double-drifted detector systems have also been successfully used. These detectors are made by diffusing lithium into both ends, then drifting towards the center from both directions. The drift process is stopped when only a few millimeters of p-type Ge remain. One is left with two planar detectors connected in parallel, but only a single crystal to mount.

A planar detector has been used to test a new amplifier system being developed. The virtue of the new system is that very good energy resolution can be obtained even at high counting rates. The heart of the system is a preamplifier-amplifier combination that produces a nearly gaussian-shaped single-polarity pulse, and with the use of pole-zero cancellation techniques the pulse undershoot is virtually zero. These pulses are applied to a pile-up rejection system that prevents contaminated signals from reaching the multichannel analyzer. Preliminary results indicate that better resolution can be obtained with this new system, even at counting rates about an order of magnitude higher than presently obtainable. The new system, with a 5-cm^3 planar detector (10 pF detector capacity), gave a FWHM resolution of 1.2 keV at 122 keV (^{57}Co) and 1.8 keV at 1333 keV (^{60}Co). The ^{60}Co photopeak resolution was still less than 3 keV at a counting rate (in the detector) of 50 000 counts/sec. Further work is being done to improve these results at high rates.

Reference

1. Eugene Miner, A Semiconductor Detector, UCRL-17201, Dec. 1966.

14. HIGH-VOLTAGE LITHIUM-DRIFTED SILICON DETECTORS

Robert P. Lothrop and F. S. Goulding

Introduction

Collection-time limitations of detectors having the etched mesa structure[1] of Fig. I. 14-1 make it impractical to use finished devices much more than 3 mm thick. The collection time of a 3-mm detector, at 25°C and normal voltages, is about 0.5 μsec. This collection time approaches the upper limit of practical use and increases in proportion to the square of the detector thickness. The current-vs-voltage curve of Fig. I. 14-2 is typical of that obtained with devices having this geometry. It will be seen that the leakage current rises rapidly above about 400 volts. Accompanying this increase in leakage is a large increase in noise from the detector. This places limits on the usable operating voltage. The increase in current at the higher voltages is due to the n-type channel which exists over the exposed intrinsic surface.[2] As the detector voltage is increased, the channel reaches through to the i-p junction, and surface breakdown at the i-p junction results. Thus the effects of an n-type surface inversion layer must be overcome to permit high operating voltages if very thick lithium-drifted silicon detectors are to have sufficiently short collection times.

Double-Drift Geometry

The "double-drifted" structure of Fig. I. 14-3 automatically limits the channel length and thus prevents it from reaching through to the i-p junction. The function of the thin, peripheral intrinsic region, called a "shelf," is to provide a high transverse field region which will cause depletion of the channel. Thus the effect of the n-type channel, of increasing the potential along the surface, is used to make the channel length self-limiting. Figure I. 14-4 shows surface voltage probe measurements which illustrate the self-limiting operation of the double-drift geometry. Figure I. 14-5 shows the room-temperature voltage-vs-current curve for a typical 3-mm-thick double-drifted detector. The onset of surface channel length limiting is apparent at 100 to 200 volts. Figure I. 14-6 shows the room-temperature voltage-vs-current curve for a 5-mm-thick double-drifted device.

Fabrication

The fabrication of very thick devices having the structure of Fig. I. 14-3 requires single-crystal silicon of large diameter. There are several ways, however, in which small-diameter silicon may be used. The geometry illustrated in Fig. I. 14-7, with a rectangular mesa, has been fabricated successfully in the 5- to 7-mm thickness range. The geometry illustrated in Fig. I. 14-8,

called a "top hat," seemed very promising in the thickness range beyond 5 mm. However, if the "crown" portion of the structure is more than several mm high, the surface inversion on the vertical sides so distorts the field that the device cannot be properly drifted.

The geometry of Fig. I. 14-3 is fabricated as follows: Lithium is diffused into the entire surface of a silicon wafer of the desired thickness (Fig. I. 14-9a). The diffused wafer is masked and the sides etched to yield a diode with good reverse characteristics (Fig. I. 14-9b). The etched diode is drifted to obtain an intrinsic depth of about 0.5 mm (Fig. I. 14-9c). The drifted wafer is masked and etched to obtain a mesa of the required diameter (Fig. I. 14-9d). This device is now drifted completely through (Fig. I. 14-9e). A thin gold entrance window[3] and varnish protection over a suitable treated surface complete the device (Fig. I. 14-9f).

Application

Devices 3 mm and 5 mm thick have been tested at 77°K, in low-energy spectroscopy applications. Resolution of the order of 0.75 to 1.5 keV FWHM has been obtained with bias voltages in excess of 1000 volts. An immediate advantage of these devices in this, as well as other, applications is the minimizing of trapping effects.

The use of double-drifted 5-mm-thick devices in high-energy cyclotron experiments has been reported elsewhere.[4]

References

1. F. S. Goulding and W. L. Hansen, An Automatic Lithium Drifting Apparatus for Silicon and Germanium Detectors, IEEE Trans. Nucl. Sci. NS-11, 286-290 (1964).
2. Jorge Llacer, Geometric Control of Surface Leakage Current and Noise in Lithium Drifted Silicon Radiation Detectors, Brookhaven National Laboratory, BNL-9535, 1965.
3. Robert P. Lothrop and Harry E. Smith, Lithium-Drifted Silicon Radiation Detector Production Process, UCRL-16190, June 1965.
4. R. H. Pehl, D. A. Landis, and F. S. Goulding, Detection of High Energy Protons by Thin-Window Lithium-Drifted Germanium Counters, UCRL-16722, Feb. 1966.

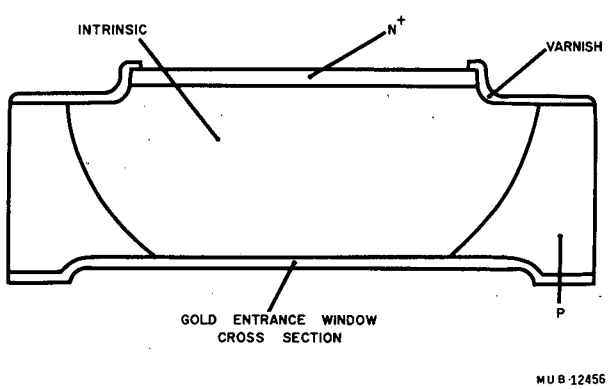

Fig. I. 14-1. Simple etched mesa geometry.

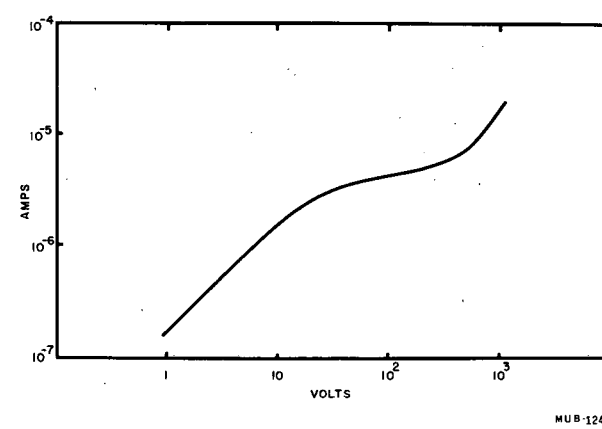

Fig. I. 14-2. V-I curve of a simple etched mesa device.

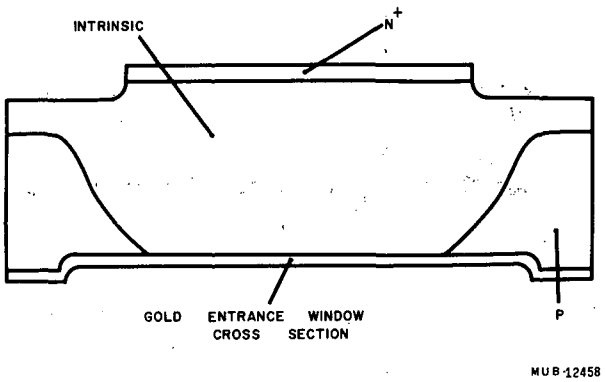

Fig. I.14-3. Double-drift geometry - I.

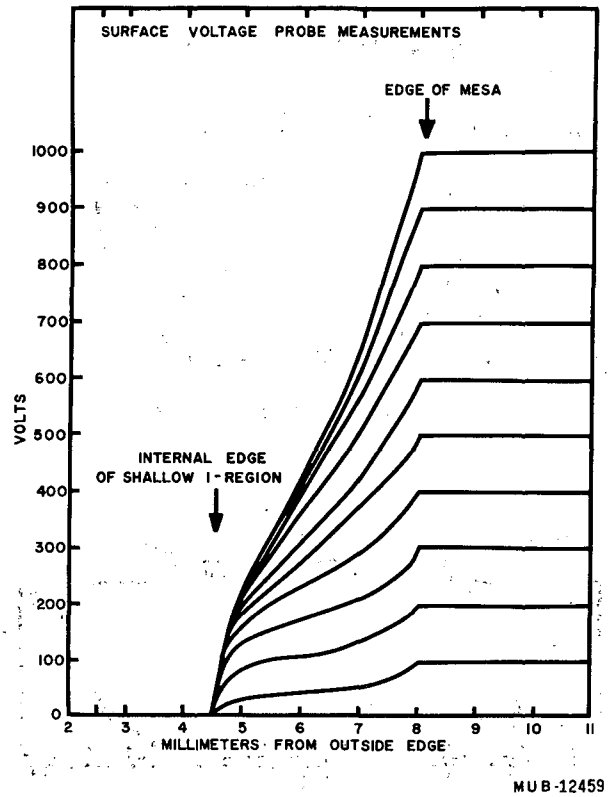

Fig. I. 14-4. Surface voltage probe curves for a double-drifted device.

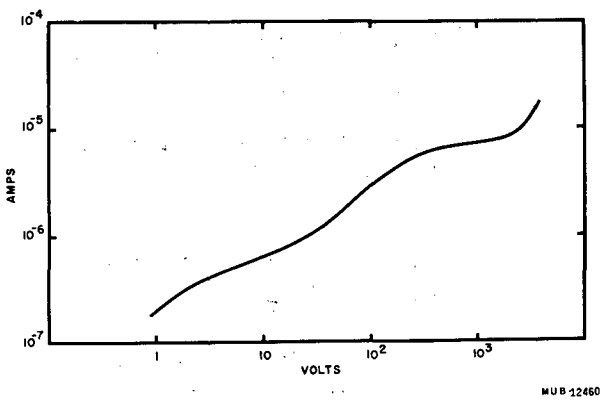

Fig. I.14-5. V-I curve of a typical 3-mm thick double-drifted device.

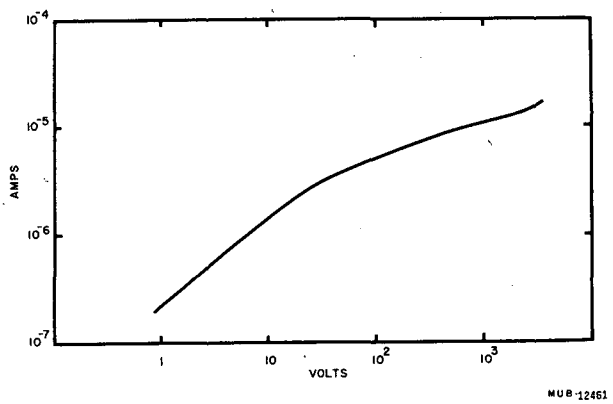

Fig. I. 14-6. V-I curve of a typical 5-mm-thick double-drifted device.

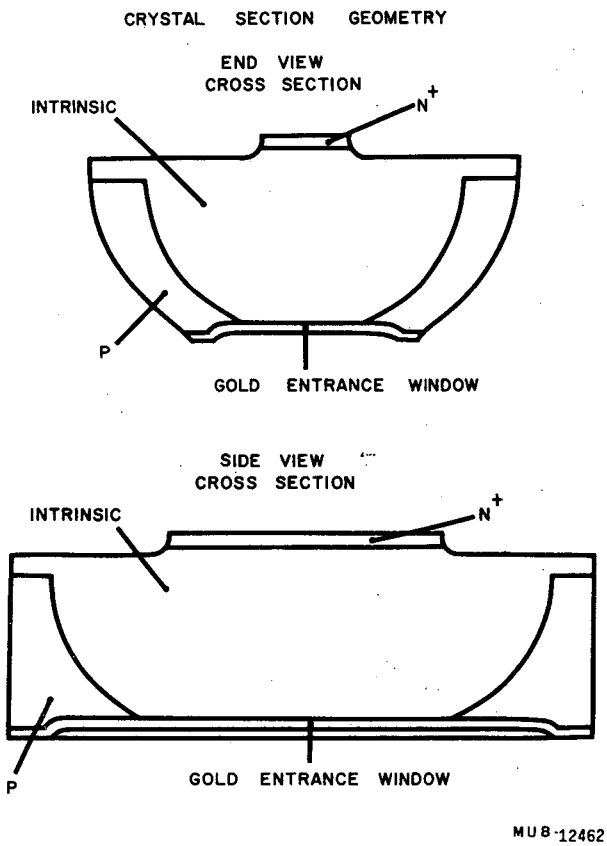

Fig. I. 14-7. Double-drift geometry - II.

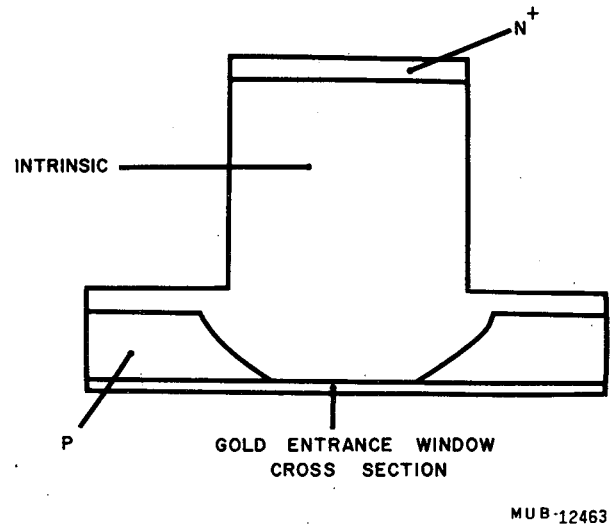

Fig. I. 14-8. Double-drift geometry - III, "the top hat."

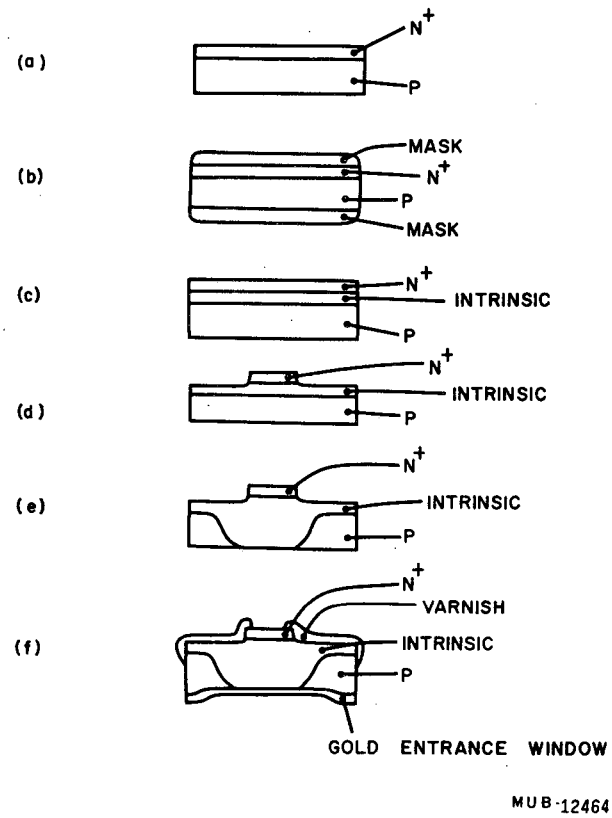

Fig. I. 14-9. Steps in double-drifted-geometry production.

15. LIQUID NITROGEN COOLED CRYOSORPTION VACUUM PUMP

R. Hintz and R. Parsons

A cryosorption vacuum pump designed to be kept cold at all times has been developed at LRL to be used both as a roughing pump (i.e., to evacuate systems from 1 atm to moderate vacuum preparatory to operation of another high-vacuum pumping system) and also as a self-contained vacuum system for use when only moderate vacuum ($\approx 10^{-5}$ to 10^{-6} torr) is sufficient. Both these functions are performed without danger of contamination of the system by pumping fluids used in mechanical pumps.

Two commercial pumps were purchased to do the evacuation job, but these pumps proved to have some undesirable features and a new design was made for subsequent use. The pump we have designed consists of a stainless steel pot of welded construction with three 0.5-in.-diam cooling coils arranged concentrically inside the pot. The pot is filled with 15 lb of Molecular Sieve.[1] The pot has a thin-wall stainless steel tube extending from its top with two thin stainless steel heat shields attached to it. The tube terminates in a 2.75-in. Varian flange.[2]

Attached to this flange is an accessory section which incorporates a thermocouple gauge,[3] a small vacuum valve[4] with a 0.5 psig relief valve,[5] and a rupture disk of LRL design with a burst pressure of 3.5-4.0 psig. Mounted on the top of the accessory section is a 1.5-in. vacuum valve[6] with 2.75-in. Varian flanges.[2] The pump is placed in a thin-wall stainless steel 50-liter Dewar[7] modified to accept a two-piece Styrofoam and aluminum cover with lifting handles. This cover is fitted with two 2.5-in.-diam liquid nitrogen fill openings.

The assembled pump has a liquid-nitrogen-holding capacity of 25 liters, and at steady state will last 4 to 5 days between fillings. So far six pumps of this style have been produced at this Laboratory, however, pumps of this design are now available commercially.[8] The testing of these pumps is not complete to date; however, as a typical example of performance we have pumped a volume of approximately 150 liters from atmospheric pressure of room air to less than 1 Micron in approximately 8 min. After approximately 1 hour to allow the molecular sieve to recool, we performed this same pumpdown again.

A base pressure of 3×10^{-6} torr has been reached after 48 hours of cooling as indicated by a Phillips vacuum gauge; however, base pressure depends to some extent on the total amount of air that has been pumped. The full pumping capacity of this pump is available only after 48 hours or more of cooling, therefore this pump is designed to be kept cold at all times. In the steady-state condition the liquid nitrogen consumption is 0.30 liter/hour, resulting in operating costs similar to mechanical vacuum pumps, but with fewer severe maintenance problems.

After pumping approximately 750 liters of air at 1 atm the pump capacity is reached and further pumping is stopped. Only with repeated pumping of large amounts of atmospheric air does regeneration become necessary. Regeneration may be effected by allowing the sieve to warm to room temperature and venting the gases evolved through the 0.5-psig relief valve to atmosphere. It is usually found desirable, if at all possible, to let systems being cryopumped up to atmospheric pressure with dry nitrogen gas instead of room air, thus reducing both the amount of helium, which is pumped only slightly, and the amount of water, which adds to the regeneration procedure. In extreme service, where quantities of water vapor, hydrocarbons, or other materials of high adsorption energy have been pumped, regeneration may require a moderate bakeout (up to 200°C) while the sieve is being flushed with dry nitrogen or is being pumped by a well trapped vacuum system. It must be noted that when these pumps are used as a holding vacuum on a tight system, regeneration should not be required for many months or even years.

These liquid-nitrogen-cooled cryosorption pumps have the following advantages. They
(a) do not contribute oil vapor or hydrocarbons to the system,
(b) do not need cooling water or interlocks,
(c) do not need electrical power, so are not affected by power failures,
(d) are vibrationless and silent,
(e) require no additional liquid nitrogen traps,
(f) have no belts to break or heaters to burn out,
(g) are not a source of electrical noise.

Cryosorption pumps have been used at this Laboratory on vacuum lock systems, such as

a conversion-coefficient spectrometer,[9] where one pump replaced a liquid-nitrogen-trapped diffusion pump and mechanical forepump on the main chamber and also replaced a carbon-dioxide-trapped mechanical pump on the vacuum lock. In several other instances a cryosorption pump has roughed the main chamber of a vacuum lock system to a low enough pressure to start an ion pump, and then taken over the job of pumping the vacuum lock. Because of the clean vacuum they produce, these pumps are used to rough ultravacuum systems, work in conjunction with ion pumps, and act as complete vacuum systems where cleanliness is of more importance than ultimate pressure.

References

1. Linde No. 5A Molecular Sieve--Molecular Sieve Products Department, Linde Division, Union Carbide Corp., 270 Park Ave., New York.
2. Varian Flange No. 954-5076--Varian Associates Vacuum Products Division, 611 Hansen Way, Palo Alto, California.
3. Hastings Thermocouple Gauge Tube No. DV-3M-"T" Calibration, Hastings-Raydist Inc., Hampton, Virginia.
4. Hoke Valve No. 4251N6Y-V, Hoke Incorporated, Cresskill, New Jersey.
5. Circle Seal Relief Valve No. 559B-1M-0.5, James Pond and Clark, Inc., Circle Seal Center, Anaheim, California.
6. California Physics Products Co. No. 1515-1.5, California Physics Products Co., Box 1015, Berkeley, California 94701.
7. Hofman Dewar No. J1, Hofman-Paul Cryogenic Division, Air Reduction Co., Inc., 225 Parkhurst St., Newark, New Jersey.
8. Varian Cryosorption Pump No. 916-0023, Varian Associates, Vacuum Products Division, 611 Hansen Way, Palo Alto, California.
9. H. T. Easterday, A. J. Haverfield, and J. M. Hollander, Nucl. Instr. Methods 32, 333 (1965).

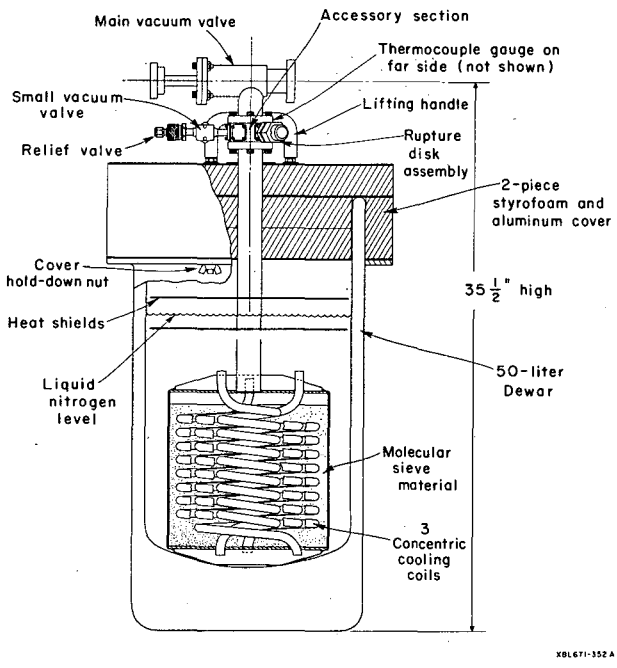

Fig. I. 15-1. Sectional drawing of liquid-nitrogen-cooled cryosorption pump.

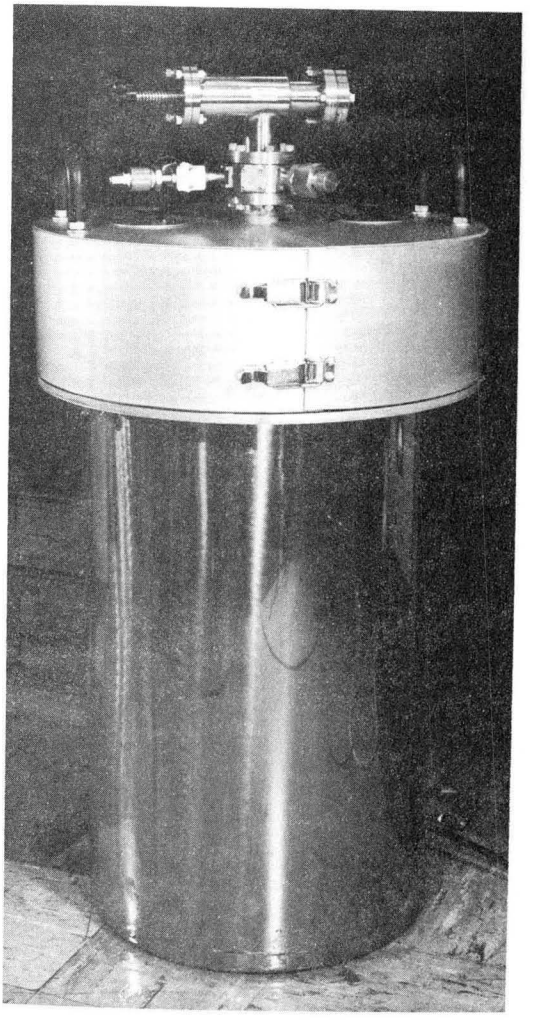

Fig. I. 15-2. Photo of cryosorption pump.

16. A SEMICONDUCTOR DETECTOR CRYOSTAT†

C. Eugene Miner

An attempt has been made to provide a standardized cryostat system which will accept many styles and sizes of nonencapsulated Ge(Li) and Si(Li) detectors, which is easy to modify, and which is consistent with experimental needs. Figure I. 16-1 is a photograph of a typical cryostat and Fig. I. 16-2 is a photograph of the same cryostat with the end cap removed to display the detector mount assembly.

The cryostat incorporates the following features:

Welded or vacuum-furnace-brazed construction. We have made an effort to control the environment of the detector by utilizing materials and techniques which we know, or have some reason to believe, are not harmful to the detector. We have adopted welding and vacuum-furnace-brazing techniques of fabrication in order to provide high-integrity joints and to eliminate possible sources of solder flux and those chemicals and solvents commonly associated with soldered fabrications.

Metal-gasketed demountable vacuum joints. Several advantages are gained in using metal-gasketed joints in the cryostat. They are clean, neither harboring materials that would contaminate the detectors nor having high-vapor-pressure materials that would contribute to the vacuum load. By limiting the vacuum load we are able to maintain the vacuum environment with a 1-liter/sec.

sputter-ion pump which adds little weight to the system, occupies little space, and is relatively inexpensive. Because the permeability of metal gaskets to helium is far lower than the sensitivity of a mass-spectrometer leak detector, these gaskets do not interfere with leak testing as dry Viton O rings and Teflon and kel-F gaskets do. Since the flange knife edges bite into the gasket material, they assure high integrity, continuous grounding, and high-frequency noise shielding throughout the cryostat assembly.

Easily replaceable ion pump. Vacuum is maintained in the cryostat at an average pressure of 3×10^{-7} torr by a 1-liter/sec sputter-ion pump. We have experienced occasional pump failure caused by prolonged operation at pressures above the 10^{-6} torr range. The pump is installed in such a way that, if a failure should occur, it could be replaced easily and quickly without breaking the main vacuum envelope.

Cooling provided by gravity-feed liquid nitrogen supply. Liquid nitrogen (LN) is supplied to the tip of the LN finger by a small, commercially available, well-insulated gravity feed reservoir, which allows the cryostat to be used conveniently on table tops and to be located very close to other equipment. A desirable characteristic of this method of cooling is that the liquid level remains constant within the cryostat and thus maintains a highly stable, fixed thermal environment.

Detector mount readily accessible and easy to change. Removal of the end cap provides complete access for installation or removal of detectors and wiring. Interchangeable detector mount assemblies permit relatively quick changeovers from one style of detector to another.

Aluminum and other low-Z materials near detector. The structural parts of the detector mount assembly, the liquid nitrogen (LN) finger, and the end cap are made of low-Z materials, usually aluminum, in order to limit nuclear scattering. Aluminum was selected for this portion of the cryostat because it is a good vacuum material, it has a low neutron-capture cross section, and it has a low scattering cross section for γ rays.

Detector mount electrically isolated. The detector mount is electrically insulated from the remainder of the cryostat by means of a sapphire rod. This allows the cryostat to accept a variety of electronic circuits, including those which require the entire detector to be above or below ground potential.

Field-effect transistor temperature adjustable. The operating temperature of the internal field-effect transistor (FET) input stage of the preamplifier can be externally adjusted between -160 and -80°C to optimize the performance of the FET.

Approximately 18 cryostats of this design are now in service at this Laboratory. Approximately 12 more are in various stages of preparation. Those now in service have performed well, are relatively trouble-free, and are convenient to use.

Footnote

† Condensed from UCRL-17201, Dec. 1966 (to be submitted to Nucl. Instr. Methods).

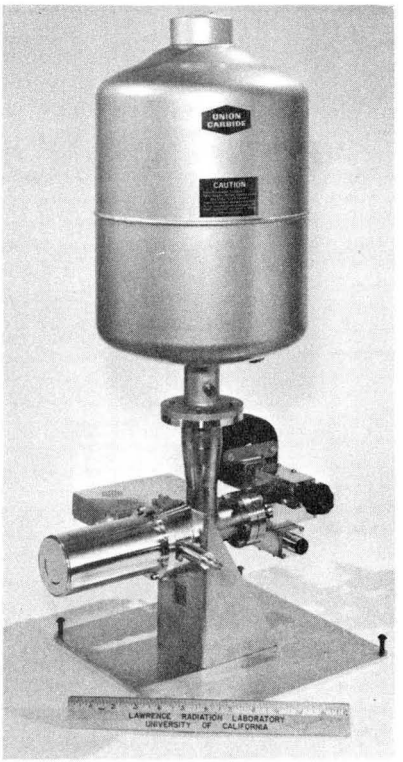

Fig. I. 16-1. Standard cryostat assembly with liquid nitrogen reservoir (top), preamplifier (left rear), and valve cluster assembly with ion pump (right rear).

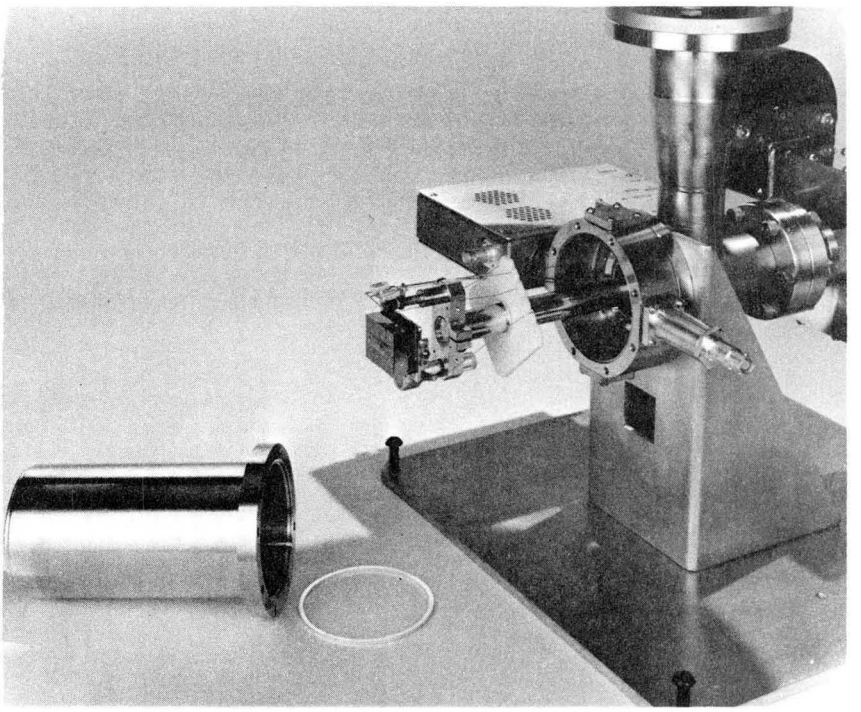

Fig. I.16-2. Standard cryostat assembly with end cap removed to display mounting arrangement for conventional Ge(Li) detector.

17. HIGH RESOLUTION β- AND γ-RAY SPECTROMETER†

Emanuel Elad and Michiyuki Nakamura

A high-resolution semiconductor β- and γ-ray spectrometer is described. The spectrometer consists of a silicon or germanium detector, low-noise field-effect transistor preamplifier,[1,2] and a linear amplifier. The line widths of x-ray spectra (5 to 25 keV) measured with a small silicon detector are 0.65 to 0.75 keV. Higher-energy x rays (50 keV) and γ rays (122 keV) measured with a low-capacitance germanium detector showed line widths of 0.65 keV and 0.8 keV FWHM respectively.

The resolution of the spectrometer is determined mainly by the input part of the system. For high resolution we require low-leakage low-capacitance detectors. We use planar lithium-drifted detectors having capacitance around 2 pF and leakage currents smaller than 5×10^{-10} A.

The input stage of the preamplifier uses cooled silicon FET (Texas Instruments' 2N3823 or Union Carbide's 2N4416). A voltage-sensitive configuration having high signal-to-noise ratio is used. The input stage is dc-coupled to the detector, eliminating the leakage current of the coupling capacitor and the thermal noise of the biasing resistors. A stage with single FET appears[3] to be the optimal solution for a high-resolution system.

Recent investigation shows that significant noise is generated by the constant boiling of the liquid nitrogen coolant. Preliminary measurements indicate a possible 20% improvement in reso-

lution. This is demonstrated by the separation of K_{β_1} and K_{β_2} lines (0.81 keV apart) of ^{241}Am spectrum shown in Fig. I. 17-1.

Footnote and References

† Short version of reports in Nucl. Instr. Methods 42, 315 (1966), and High-Resolution β- and γ-Ray Spectrometer (UCRL-17149, Sept. 1966), for the 13th Nuclear Science Symposium, IEEE, October 19-21, 1966, Boston, Massachusetts

1. E. Elad, Nucl. Instr. Methods 37, 327 (1965).
2. E. Elad and M. Nakamura, in Chemistry Division Annual Report, Jan. 1966, UCRL-16580, p. 222.
3. E. Elad and M. Nakamura, UCRL-17149, Sept. 1966).

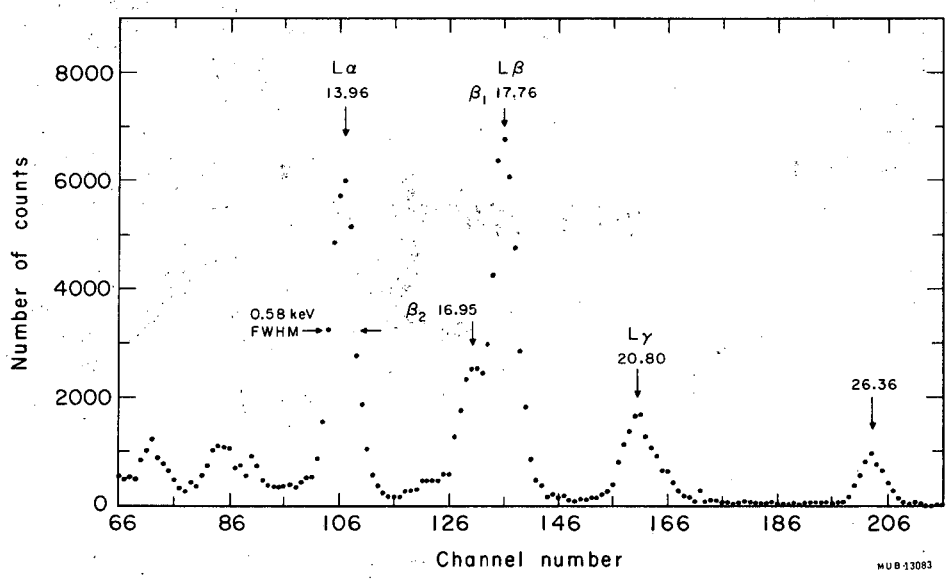

Fig. I. 17-1. x-Ray spectrum of ^{241}Am.

18. A LOW-NOISE DISTRIBUTED AMPLIFIER USING FIELD-EFFECT TRANSISTORS

Michiyuki Nakamura, Frederick E. Vogelsberg, and W. Larry Crowder

Field-effect transistors (FET's) are used extensively in low-noise preamplifiers[1] because of their excellent low-noise and moderately good gain characteristics, especially near liquid nitrogen temperatures. We felt that FET's could be used in a low-noise, wide-band amplifier employing a distributed amplifier configuration.

Since the 2N3823 FET has characteristics similar to the 6AK5 vacuum tube, we decided to make the amplifier like the Hewlett-Packard 460A wide-band distributed amplifier. To check the feasibility of such an undertaking we used Hewlett-Packard's coil forms for the gate and drain lumped lines. The input and output impedances were respectively 170 and 280 ohms. Because of the nonuniform capacitances of the FET's, we had to trim the lines to minimize the reflections caused by the varying impedance in the lines. This also caused a degradation in rise time. We used two identical halves for the amplifier with each half consisting of five FET's.

The amplifier is small and compact. Its shielding is excellent, and because only dc power is used, there is no problem with 60-cycle noise. At room temperature the amplifier had a gain of 6, a rise time of 6 nsec, and an equivalent input noise of 5.8 μV rms. At near liquid

nitrogen temperature the amplifier had a gain of 24, a rise time of 5 nsec, and an equivalent input noise of 4.6 μV rms. The output dynamic range of the amplifier is poorer than the Hewlett-Packard 460A, but the overload recovery characteristics are better. Its signal-to-noise ratio is better by a factor of 3 than the 460A.

This amplifier will be used in a mass spectrometer counting system, where low background noise and high count-rate capability are essential. With optimum design and construction of an amplifier, rise times of the order of less than 2.5 nsec are expected.

Reference

1. E. Elad, Nucl. Instr. Methods 37, 327-329 (1965).

19. AN INEXPENSIVE SPECIAL-PURPOSE COMPUTER FOR LINKING PULSE-HEIGHT ANALYZERS WITH A DIGITAL INCREMENTAL PLOTTER

Richard LaPierre and Michiyuki Nakamura

We are working on a prototype model of a fixed-wire computer that will feature the advantages of a computer–digital plotter for displaying the information stored in an analyzer. The special-purpose computer is portable and has its own digital plotter, which eliminates the inconvenience and time delay normally encountered when work is submitted to a computer center.

The prototype contains the electronics to allow it to be interfaced with either binary-coded-decimal or binary-type analyzers. The plotted output can be on linear or semilog paper. In the linear plot the counts-full-scale is selected by a front panel switch. For semilog plots the least significant decade and the number of log cycles to be plotted are selected by front panel switches. The logarithms are computed by a method reported in the literature.[1,2]

The system electronics will cost about $2500 and the plotter, a Cal-Comp model 565, costs $4500.[3] With this system the positional accuracy will be 0.01 in. for both linear and semilog plots. Semilog plots obtained from the existing hardware found in most analyzers may have an error as large as 10%.

It is intended that in the future the instrument package will also accept input data from magnetic and paper tape units.

References

1. J. N. Mitchell, Jr., Computer Multiplication and Division Using Binary Logarithms, IRE Trans. Electron. Computers, EC 11, 512-517, Aug. 1962.
2. M. Combet et al., Computation of the Base-Two Logarithm of Binary Numbers, IEEE Trans. Electronic Computers, EC 14, 863-867, Dec. 1963.
3. California Computer Products, Inc., Anaheim, California.

20. A 35-GHz SUPERHETERODYNE ELECTRON SPIN RESONANCE SPECTROMETER SYSTEM

Warren Easley and Richard LaPierre

Described in this report is a 35-GHz (Q-band) ESR spectrometer. This spectrometer is being used with a 9.5-GHz (X-band) system to study the solid-state chemical properties of the actinide elements and to investigate electron-nuclear hyperfine interactions.

A block diagram of the spectrometer system is shown in Fig. I. 20-1. The frequency of the signal oscillator is locked to the resonant frequency of the microwave cavity by applying a 60-kHz modulating signal on the oscillator's reflector voltage. the AFC loop is closed on the output of either the crystal detector or the video detector. Normally the AFC loop is initially closed on the output of the crystal detector and, once the local oscillator is locked in, the AFC loop is closed on the video detector, which gives a better signal-to-noise ratio. The balancing arm allows one to tune to either the absorption or dispersion component of the resonance signal. The 60-MHz i. f. frequency is stabilized by adding the output of the frequency discriminator in series with the reflector supply voltage to the local oscillator.

Shock-mounting the rf components and water-cooling the oscillators (as opposed to air cooling) were found to enhance the sensitivity of the system. The system detects 10^{13} ΔH spins ($S/N \approx 1$) at 300°K when 150-Hz magnetic field modulation is used.

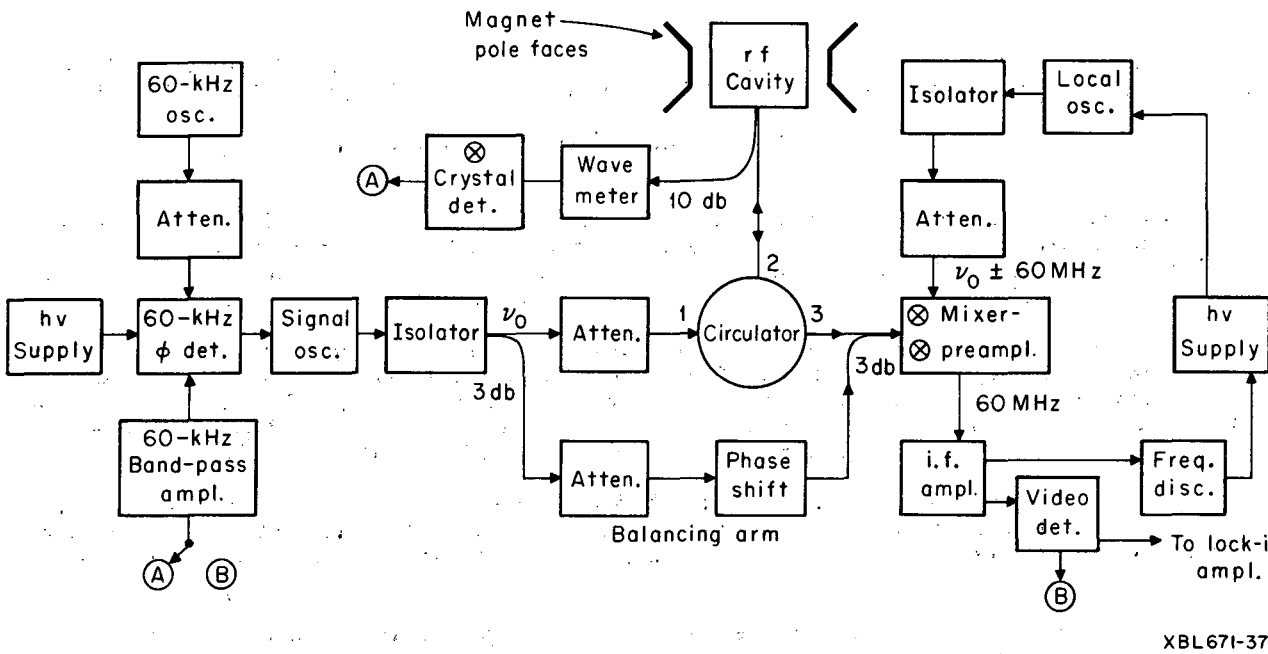

Fig. I. 20-1. Block diagram of the 35-GHz ESR system.

21. AN INVESTIGATION INTO THE CHARACTERISTICS OF A HELIUM-NEON cw LASER FOR TELEMETRY APPLICATIONS†

Richard LaPierre and Ron Zane

During the period from March 8, 1966, to March 21, 1966, a series of experiments was conducted for the purpose of studying some of the characteristics of a helium-neon gas laser for telemetry applications. It was desired to investigate alignment problems, detection systems, and hazard control measures for laser telemetry systems over moderate distances. The susceptibility of a laser beam to ambient weather conditions was of considerable interest.

The laser used was a Spectraphysics model 115 helium-neon cw gas laser. It could be operated at either 6328 or 11 523Å. The laser was initially situated on the seventh floor of University Hall. This building is at the corner of University Avenue and Oxford Street. The beam was directed along a clear line of sight to the sixth-floor west balcony of Building 50A at the Lawrence Radiation Laboratory. The line-of-sight distance was estimated to be between 3 600 and 4 000 feet (see Fig. I. 21-1).

Various detectors were used with the laser's 6328-Å beam. A Fresnel lens with a diameter of 10 in. and a focal length of 8 in. was used to gather the beam and concentrate it on the detector. A silicon solar cell, a silicon phototransistor (LS 600), and an S1 phosphor ten-stage photomultiplier all produced a signal having at least a 10-to-1 signal-to-noise ratio when the beam was modulated with a 5-kHz square wave.

The laser was mounted on a heavy-duty Hercules tripod which maintained consistent alignment throughout these tests. A receiver mounted on a homemade iron tripod, which was designed to support a telescope, rarely required readjustment.

The main disadvantage of the laser when operated at either 6328 or 11 523Å is that the beam is severely attenuated by fog. For a laser operating at 6328Å with a power output of 1 to 10 mW, care would have to be taken to insure that no one would be able to view the beam directly within approximately 1000 feet of the laser, because of potential eye injury. A laser operating in the infrared region does not present so great a safety problem because more of the beam's energy is absorbed in the aqueous humor of the eye, so that there is less dissipation in the retina.

In conclusion, the helium-neon cw gas laser presents certain advantages for telemetering applications. The main advantages are simplicity and low cost of the transmitter and the receiver. The laser provides a compact and portable communication link that may be easily installed.

Footnote

† Shortened version of UCID-2773, E.E.-1110.

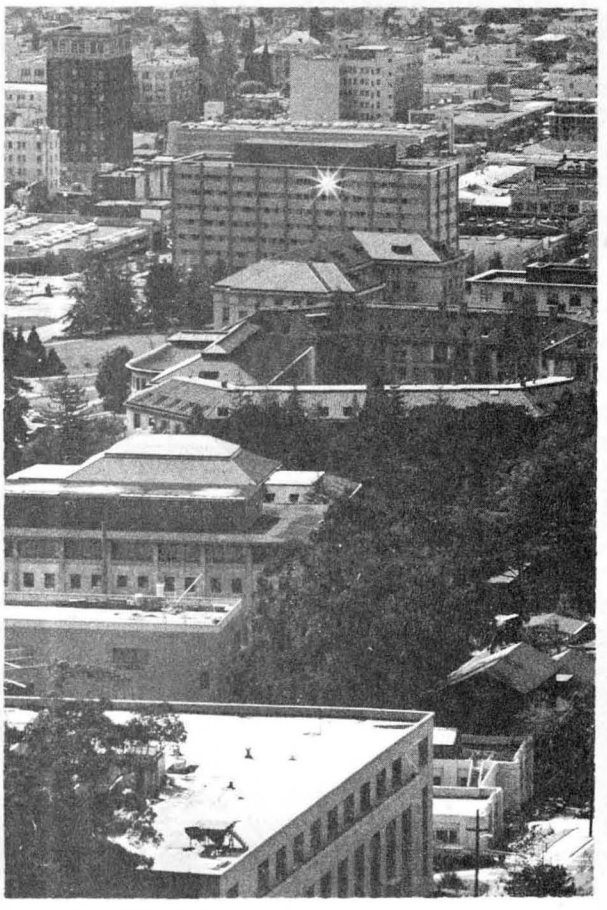

Fig. I. 21-1. The laser beam as observed from the detector.

22. PUZZLE: A PROGRAM FOR COMPUTER-AIDED DESIGN OF PRINTED-CIRCUIT LAYOUT

D. A. Wilber and Ron Zane

PUZZLE is a program developed to serve as a design aid in the production of printed-circuit layouts. The objective of the program is to reduce costs and production time of printed circuits.

In order to use PUZZLE the designer must first decide on the optimum location for components on the active area of the circuit board. Then the positions are described and an interconnection list is written, with a system of seven-digit codes used to describe all locations on a hypothetical 0.1-in. grid pattern covering the entire area. Special codes are provided for eight-pin micrologic elements and ten-pin micrologic elements which permit locating the elements on 1-in. centers and then specifying the pin number as a location. This simple procedure greatly facilitates the coding of circuits involving micrologic elements. At present, all other elements must be located by a code which identifies the exact location of each terminal associated with the device. It is expected that in the near future simplified codes will be developed for the 14-pin dual in-line package and for discrete two-terminal components which mount on 0.4-in. centers.

The program operates upon the interconnection list provided by the designer to seek paths to complete the connections. It then produces a magnetic tape which contains the information to produce an off-line drawing, on a Cal-Comp plotter, of the composite wiring diagram of the board, a component side drawing, and a wiring side drawing. The designer has the option to choose either a 1:1 scale drawing or a 2:1 scale drawing of the component and wiring sides. The xxx 1:1 drawing may be used directly to produce a printed circuit board for prototype checkout. The 2:1 drawing may be used to make high-quality artwork suitable for production runs. The composite drawing for an 11-bit scaler is shown in Fig. I. 22-1. Figures I. 22-2, I. 22-3, and I. 22-4 illustrate successive stages in the process of manufacturing a printed circuit board from the Cal-Comp drawings.

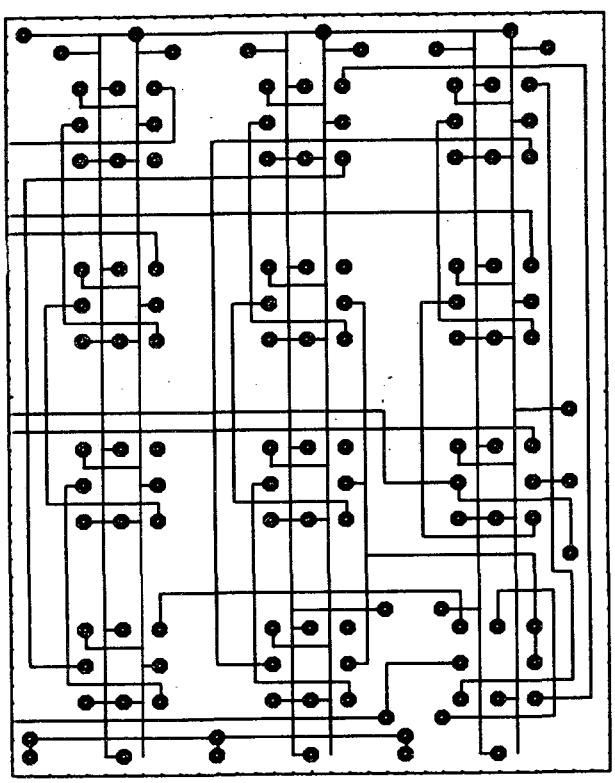

XBL671-395

Fig. I. 22-1. Composite wiring plot of 11-bit scaler.

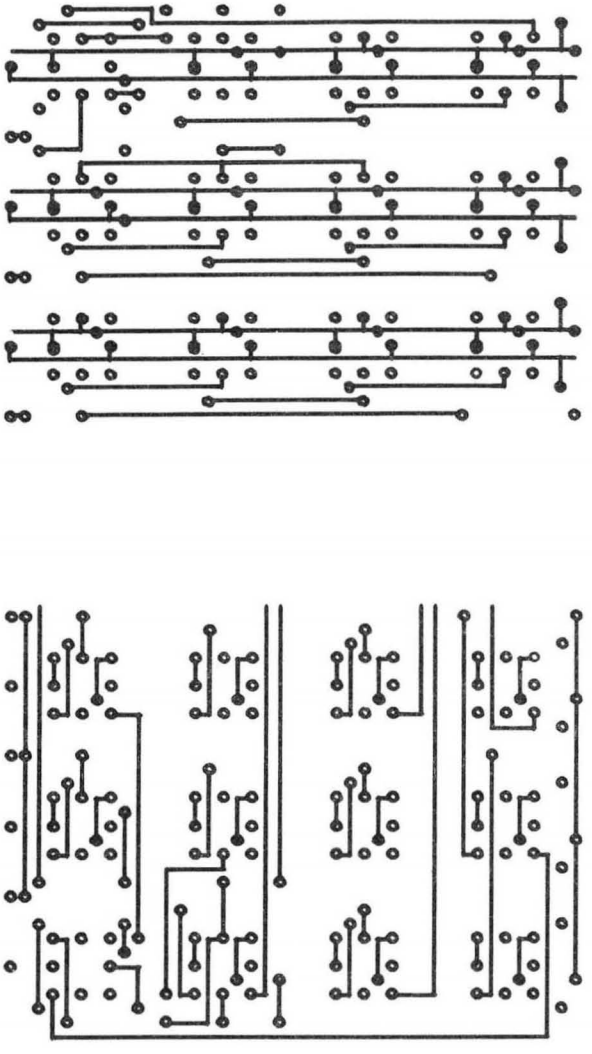

XBL671-396

Fig. I.22-2. Wiring and component plot on 11-bit scaler.

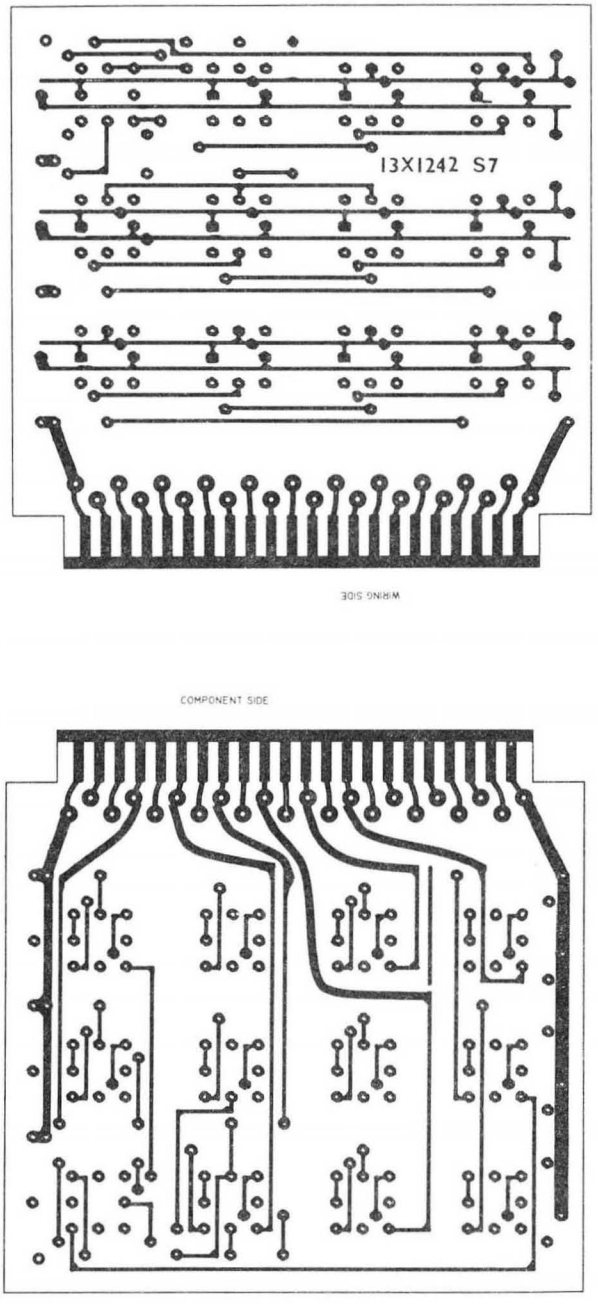

XBL671-397

Fig. I. 22-3. Plots shown in Fig. I. 22-2 after touch-up and overlay on printed circuit board outline.

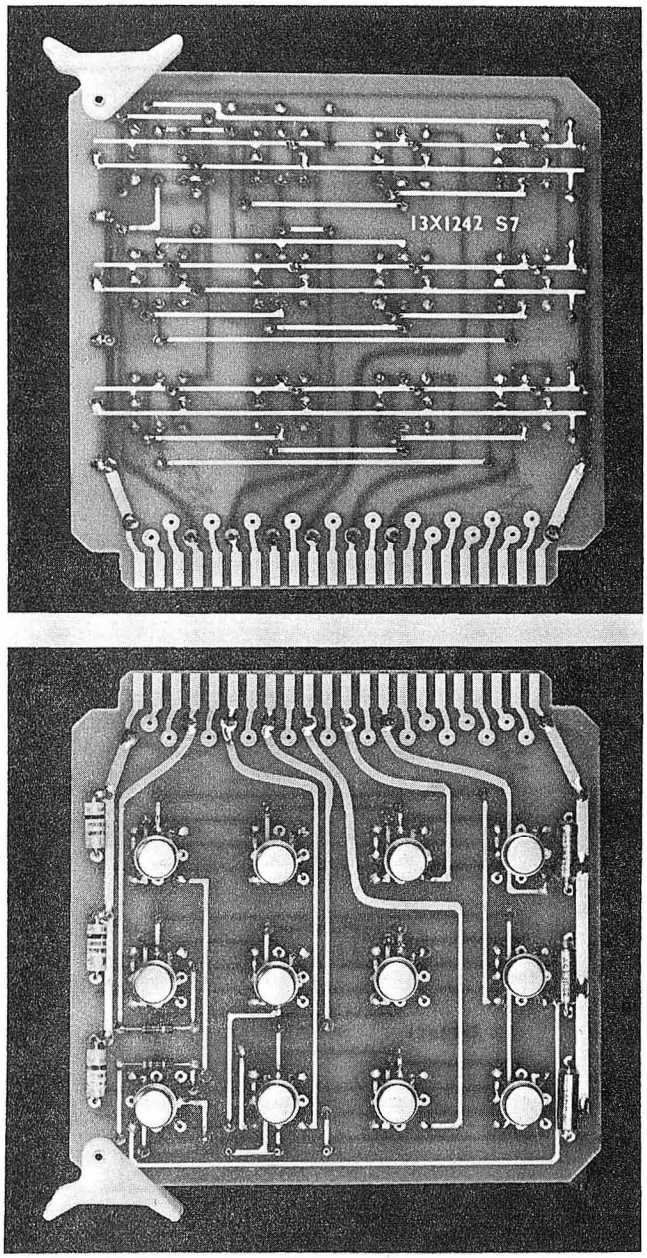

Fig. I. 22-4. Completed printed circuit as etched from retouched artwork shown in Fig. I. 22-3 and loaded with components.

23. FOUR GENERAL-PURPOSE MODULAR INSTRUMENTS

Ron Zane

These instruments have been designed to provide a variety of measurement and control functions in the Nuclear Instrumentation Bin modular concept. They have proven useful in several systems.

Triggered Ramp Generator (13X1430): provides a positive-going ramp in response to a

positive input trigger. The amplitude of the ramp may be varied from 0 to +10 V peak. The slope may be varied from a rise time of 5 msec to 1 sec (or more with external capacitors). The linearity and amplitude stability are ±0.1%.

Fairchild A007 Amplifier Module (13X1450): contains a Fairchild A007 operational amplifier. It functions as an inverting amplifier with a gain of ×1, ×2, ×5, or ×10. The maximum output voltage swing available is ±100 V.

Reference Voltage Generator and One-Shot Multivibrator (13X1470): used to aid in performing precision measurements of instantaneous values of varying voltages or voltage-dependent functions. The technique is similar to that employed with a Tektronix Type-Z plug with the additional capability of the use of the one-shot multivibrator to apply a 100-μsec pulse to the cathode of the oscilloscope, producing an intensification of the point being measured.

Programmed Coincidence Scaler (13X1310): an extremely flexible timing or pulse-counting control device. Four decades of coincidence scaler are provided with an internal time base of 1 sec/count of 1 min/count and an external count input which allows scaling at as high as 100 kHz. Count control may be under control of a front panel switch or an external signal input (0 volt=count and +2 volt=$\overline{\text{count}}$). Reset may be accomplished by allowing an automatic reset at coincidence, causing the unit to hold at coincidence until a manual reset button is pressed, or reset may be under control of an external input (+2 volt=reset). Outputs include a "coincidence" output, a "gate" output, and a single-pole double-throw mercury relay actuation at coincidence (a rear panel switch permits disabling the relay when it is not needed).

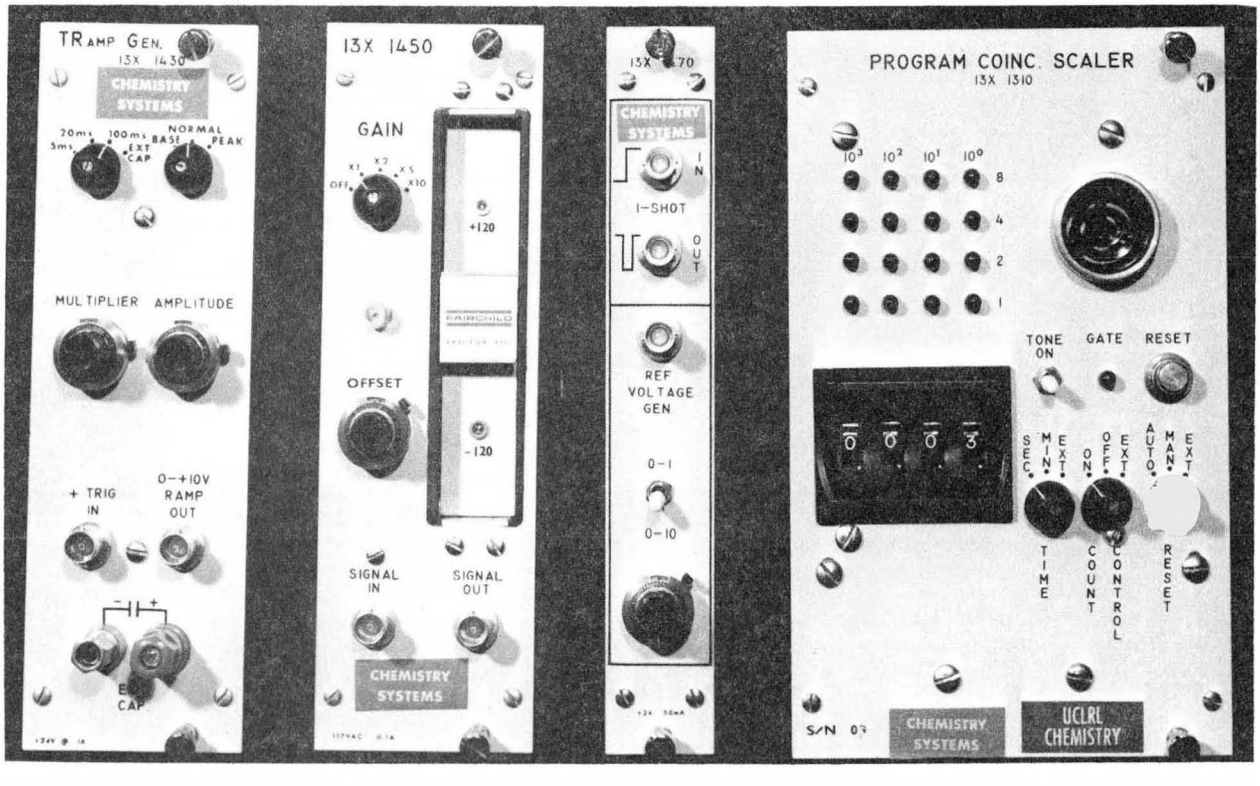

Fig. I. 23-1. From left to right: triggered ramp generator, Fairchild A007 amplifier, reference voltage generator and one-shot multivibrator, and programmed coincidence scaler.

24. MÖSSBAUER-EFFECT INSTRUMENTATION

Ron Zane

The electromechanical feedback system used in the Mössbauer-effect spectrometers has been improved through analysis of the motion and introduction of correction terms. The correction terms compensate for nonlinearities, phase lag, and amplitude errors. Compensation techniques have reduced the total "distortion" of the triangular velocity waveform to much less than 1% over more than 90% of the period. The technique is described fully in Nucl. Instr. Methods 43, 333-7 (1966): Mössbauer Effect Velocity Drive Linearized by Shape Correction, R. Zane.

The transducers used in the Mössbauer-effect spectrometers are now routinely calibrated by use of a laser version of a Michelson interferometer (Fig. I. 24-1). The results of a measurement of the motion with the interferometer are compared with a measurement of the transducer output voltage, using a voltage-to-frequency converter. The calibration data are analyzed by use of a program called METRACAL (Mössbauer Effect TRAnsducer CALibration) (Fig. I. 24-2). The laser interferometer calibration technique was first described by M. P. Klein and R. Zane in the Bio-Organic Chemistry Quarterly Report, Dec. 1964 to Feb. 1965.

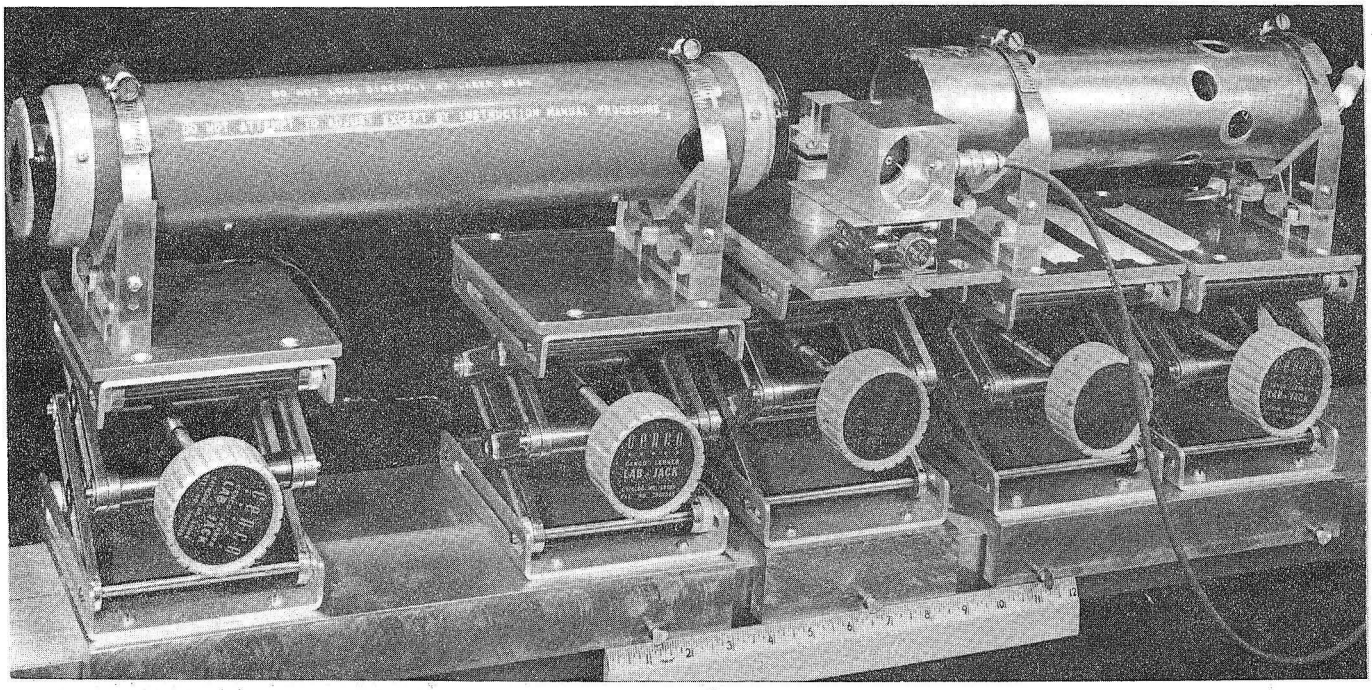

Fig. I. 24-1. Laser interferometer for calibration of Mössbauer-effect spectrometer transducers.

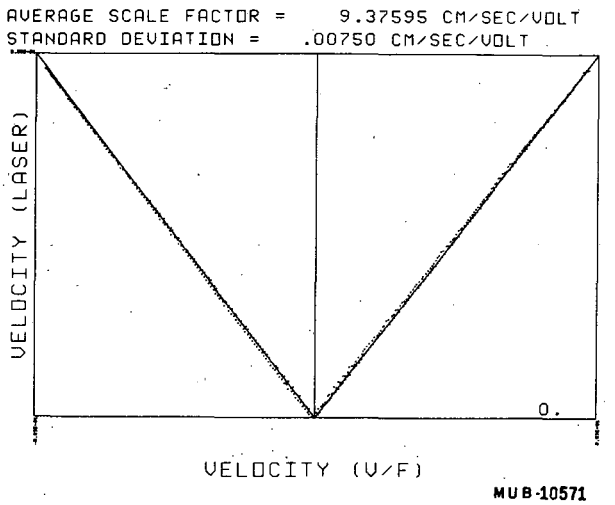

Fig. I. 24-2. Cal-Comp plot of results of a laser calibration of a Mössbauer-effect transducer. This plot is part of the output of the METRACAL calibration program.

25. THE ELECTRONIC SIZING AND COUNTING OF BACTERIA

Victor H. Edwards and Charles R. Wilke

An electronic apparatus is described that can be used to measure the size-and-concentration distribution of suspensions of particles with volumes ranging from 0.2 to 100 cubic microns. The device is based on a resistance principle discovered by Coulter.[1]

A diagram of the system is shown in Fig. I. 25-1. The particles to be analyzed are suspended in an electrolyte and the suspension is drawn through a small aperture (30 μ diam) in a tube of dielectric material by applying a vacuum to the tube. Electrodes are placed on either side of the tube and an electric potential is applied to the electrodes, causing a current to flow through the aperture. Each time a particle passes through the hole, the electrical resistance of the hole is changed by the presence of the particle. The change in resistance results in a pulse change in the aperture current, and this is magnified and shaped by the preamplifier and amplifier shown in the diagram.

The maximum fractional resistance change of the aperture during passage of a particle, $\Delta\Omega/\Omega$, and hence the response of the electronic sizing and counting system, may be determined approximately by[2]

$$\Delta\Omega/\Omega = kv, \tag{1}$$

where Ω = electrical resistance across the aperture, v = volume of particle, and k = a constant for the particular aperture, solution, and particle resistivity.

Equation 1 is a simplified form of the more general equation[2] which applies when the resistivity of the particle is much greater than that of the electrolyte and when the particle diameter is less than 10% of the aperture diameter. Equation 1 predicts that the amplitude of the fractional change of resistance of the aperture, $\Delta\Omega/\Omega$, will be directly proportional to the particle volume. In practice, the effects of the velocity and temperature profiles in the aperture, the dynamic nature of the passage of the particle, the blurring of the signal by electronic noise, and the effects of particle shape may cause some variation in the relationship between $\Delta\Omega$ and particle volume. This has the effect of broadening the apparent size distribution deduced from analysis of the pulses from a large number of particles.

The pulses are sorted and counted according to amplitude by the pulse-height analyzer, and may be displayed on a cathode-ray oscilloscope, an x-y plotter, or an electric typewriter and paper tape punch.

The system was built to measure the concentration and size distribution of bacterial cells.

The instrument is calibrated, before every experimental run, with very small plastic beads at instrument settings identical with those used in the sizing and counting of bacteria.

Counting of bacteria by this technique gave values in good agreement with values obtained with classical bacteriological techniques, including optical counting, plating, and measurement of optical density. As an example, Fig. I. 25-2 shows the agreement obtained between electronic counting and colony counting for a culture of E. coli B.

The instrument is less effective in measuring cell size distributions because of the dispersive effects mentioned earlier. Average cell volumes measured with this technique are consistently smaller than cell volumes measured optically. This can be explained by a theory of the electrical conductivity of bacterial cells proposed by Carstensen and co-workers on the basis of conductivity measurements on suspensions of bacterial cells.[3]

Further evidence supporting the model is the effect of heat killing on the "electronic size" of cells: heat killing of exponential-growth-phase cells of E. coli made them undetectable by electronic sizing, resulting in a greatly reduced count, as shown by Fig. I. 25-3. The model is also in agreement with the work of Kniseley and Throop, who showed that electronic sizing and counting[4] could be used to detect lysis of Staphylococcus aureus by the antibiotic lysostaphin.

Because of the demonstrated ability of electronic sizing and counting of bacteria to detect cell lysis, the technique should provide a powerful tool to anyone studying sterilization kinetics of cells.

References

1. W. H. Coulter, U. S. Patent 2,656,508 (1953).
2. Herbert E. Kubitschek, Nature 182 [No. 4630], 234 (1958).
3. E. L. Carstensen, H. A. Cox, Jr., W. B. Mercer, and L. A. Natale, Biophys. J. 5 [3], 289 (1965).
4. Sharon J. Knisley and Lewis J. Throop, Anal. Biochem. 13, 417 (1965).

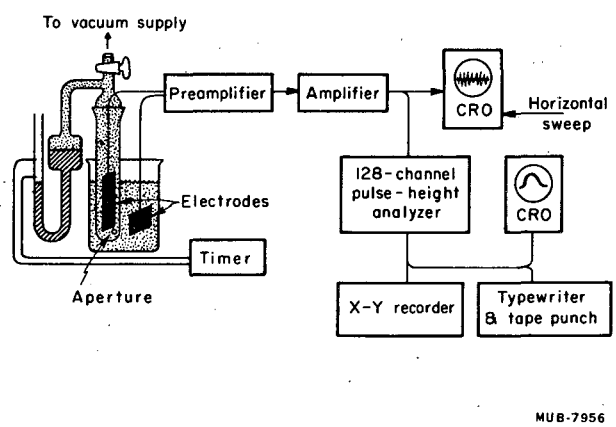

Fig. I. 25-1. Particle-counting system.

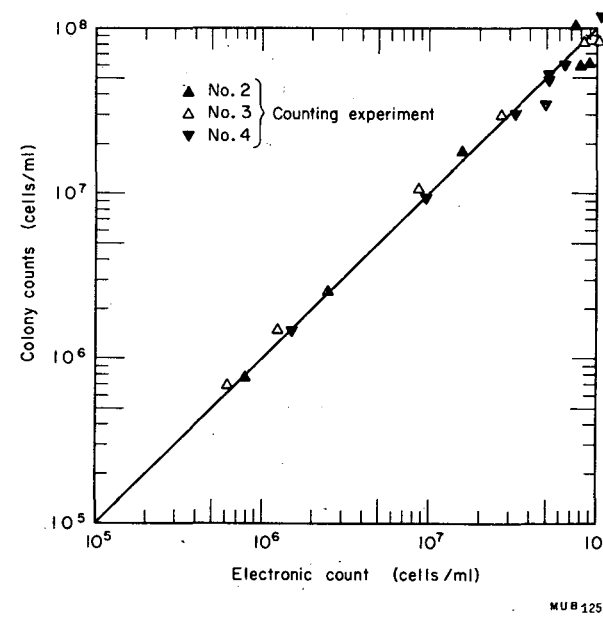

Fig. I. 25-2. Comparison of colony counts with electronic counts.

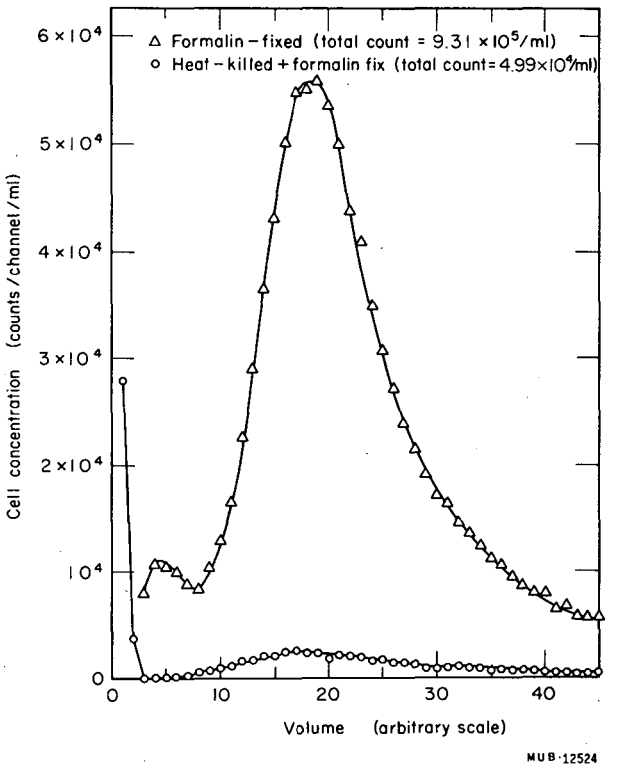

Fig. I.25-3. Effect of heat killing on electronic determination of size-and-concentration distribution.

J. THESIS ABSTRACTS

On the following pages the abstracts of theses issued in 1966 are given as they appeared in the original documents.

1. NUCLEAR SPECTROSCOPIC STUDIES OF SOME VERY HEAVY ODD-MASS NUCLIDES

Irshad Ahmad
(Ph. D. Thesis)

(From UCRL-16888)

The nuclear radiations of nuclides: ^{233}U, ^{239}Pu, ^{243}Bk, ^{244}Bk, ^{245}Bk, ^{246}Bk, ^{249}Bk, ^{249}Cf, and ^{255}Fm were investigated with high-resolution spectrometers. The α-particle spectra of all nuclides except ^{249}Bk were measured with 6-mm diameter surface-barrier detectors. ^{249}Bk α particles were analyzed with a double-focusing magnetic spectrograph. The γ singles were examined with the recently developed Ge(Li) and Si(Li) detectors coupled with very low noise "internal FET" preamplifiers. Weak α groups were observed in coincidence with γ rays, detected with a NaI(Tl) scintillation spectrometer. To improve the over-all coincidence efficiency a new coincidence apparatus was designed and built. This instrument consisted of a cooled 4.5-cm diameter semiconductor detector for α-particle detection and a 3-cm diameter by 2.7-cm long Ge(Li) detector for γ-ray analysis. The Ge(Li) detector could also be replaced with a NaI(Tl) detector. ^{249}Cf conversion electrons were measured with a cooled Si(Li) detector coupled with an internal FET preamplifier.

On the basis of the present work and previous information, energy-level diagrams of the daughter nuclei have been constructed. The levels have been grouped into rotational bands built on Nilsson single-particle states. Because of identification of several rotational members of the bands, definite Nilsson quantum number assignments have been made in most cases. The α-intensity calculations of Poggenburg were found quite helpful in making these assignments.

A strong Coriolis effect was observed in the ^{245}Am levels populated by the α groups of ^{249}Bk. Calculations were made with Nilsson wavefunctions, and these were found to agree with the experimental results. The Coriolis interaction was found important in almost all cases; the effect was very noticeable in the level spacings between the rotational members of the bands.

High-lying bands in ^{245}Cm (at 644 keV) and ^{251}Cf (at 550 keV) were observed and four rotational members of each were identified. The modes of de-excitation of these levels indicate very small or no vibrational characters in them. This suggests that the vibrational bands in this region lie at very high energies (~1 MeV) above the ground state.

2. SOME OF THE PHYSICAL PROPERTIES OF CURIUM AND PROTACTINIUM METALS AND PROTACTINIUM TETRAFLUORIDE

Brig M. Bansal
(Ph. D. Thesis)

(From UCRL-16782)

The construction and operation of a semiadiabatic microcalorimeter are discussed. The heat of solution of curium metal in 1.0 M HCl at 298.4±0.2°K has been measured and found to be -139.9±1.0 kcal/mole. This value is combined with available thermodynamic data to calculate the following standard heats of formation at 298°K: $Cm^{3+}_{(aq)}$, -140.6±1.3; $CmCl_{3(c)}$, -226.1±1.2, both in kcal/mole.

The construction and operation of a low-temperature magnetic-susceptibility apparatus are discussed in detail. The magnetic susceptibility of curium metal has been investigated from room temperature to about liquid helium temperature (6-8°K). The metal followed the Curie-Weiss law from room temperature to 145°K. Between 145 and 77°K the metal becomes ferromagnetic with a Curie temperature T_c=131±10°K. At liquid hydrogen and helium temperatures the metal again seems to show paramagnetic behavior. No evidence of antiferromagnetic behavior, however, was observed. The effective magnetic moment for the metal has been found to be 8.03±0.1 Bohr magnetons, indicating the presence of a $5f^7$ configuration in the metal.

The magnetic susceptibility of protactinium metal has been measured in the temperature range 20-298°K. The molar susceptibility is found to be $268 \pm 14 \times 10^{-6}$ cgs units at room temperature, and to be virtually independent of temperature within the experimental accuracy of ±5% over the temperature region investigated.

The molar magnetic susceptibility of PaF_4 has been calculated from the available Landé g value for octahedrally coordinated Pa(IV) ($PaCl_4$-Cs_2ZrCl_6 crystal) and the J quantum number of Pa(IV) ground state; the value so calculated is 4735×10^{-6} cgs units.

3. FILTRATION STUDIES WITH ULTRAFINE PARTICLES

Ashok Kumar Bhagat
(M. S. Thesis)

(From UCRL-16574)

A new continuous filter has been developed to filter very fine particles of about 1-6 micron size without cake formation. The slurry is filtered through a rotating filter membrane and solids are rejected as a thick slurry. A general theory has also been developed to predict the limiting filtration rate for such a filter. This theory considers the centrifugal force on the particles and their diffusion in a highly turbulent field ($6 \times 10^5 < Re_D < 11 \times 10^5$). Shear stress on the membrane and the drag coefficients were also measured and compared with the available data in the literature. Limiting filtration rates up to 33×10^{-3} ml/sec cm^2 were obtained for the systems considered. Agreement of the correlation with experimental data for 1.3 micron polystyrene latex spheres and 6-14 micron styrene divinylbenzene copolymer latex spheres is within 35%.

4. AN IMPROVED CORRELATION FOR THE HEATS OF FORMATION OF INORGANIC COMPOUNDS

Waseem Brelvi
(M. S. Thesis)

(From UCRL-16865)

An existing equation for estimating the standard heat of formation of solid inorganic compounds has been improved upon. The original equation was derived from Linus Pauling's electronegativity scale. The present form of the equation involves four characteristic parameters for each valence state of an ion present in a compound. The parameters for any ion may be correctly evaluated if experimental heats of formation of at least four of its compounds are known.

The equation has been used to correlate the known heats of formation of a large number of solid inorganic and simple metallic organic compounds. Typical compounds are metallic halides, oxides, sulfides, sulfates, silicates, tungstates, molybdates, etc. The average deviation from experimental values in correlating the heats for 611 compounds was 2.09 kcal/M. Heats of formation predicted by the correlation were estimated to be reliable to ±13 kcal/M.

Calculations based on the correlation led to a method of investigating any suspected errors in experimental data. Based on these calculations, it appears that the experimental heats of formation of Al_2S_3, $La(OH)_3$, and $FeCrO_4$ are seriously in error.

5. CONVECTIVE TRANSFER PROCESSES IN LAMINAR GAS-LIQUID CHANNEL FLOW

Charles Harry Byers
(Ph. D. Thesis)

(From UCRL-16535)

Interphase mass transfer has been studied experimentally and theoretically for cases where resistance to mass transfer is confined to the gas phase and where control is distributed between phases. A horizontal, rectangular channel of high aspect ratio has been built. The gas and liquid phases, which move in stratified laminar flow, are contacted in an 18-in.-long test section. The exit streams are analyzed in a gas-liquid chromatograph.

A numerical solution was performed of the laminar transport equation for a parabolic velocity profile with a cocurrently moving boundary. Experiments in which pure ethanol was evaporated into two gases, CO_2 and oxygen, showed agreement with this theory within the estimated experimental error of 10%. An earlier solution of a simplified theory for mass transfer to an infinite medium with an interfacial velocity and a linear slope in velocity has been modified. The appropriate experimental results agree with this theory to better than 10%. It may be concluded from this study that cocurrent motion of the interface increases mass transfer. Experiments were carried out with the same fluids in countercurrent flow. Mass transfer is hindered by a flow reversal in the gas phase. A phenomenological model developed for this case, involving the addition of a stagnant film resistance to the resistance to mass transfer of a parabolic velocity profile, correlated the data to within the experimental error of the method.

Numerical solutions were performed of two cases of interphase mass transfer. The first is for parabolic velocity profiles in both phases, and the second assumes a parabolic profile in the gas and a constant velocity in the liquid. Experiments were carried out in which ether was evaporated from dilute ethanol solutions into two gases, CO_2 and helium, in cocurrent flow. The experimental results agreed with the first interphase mass transfer solution to within 15% in all

cases. Equations for a more simplified model in which the liquid has a constant velocity and the gas velocity varies linearly with distance from the interface have been solved analytically. Results of the appropriate interphase experiments agree with this theory. Interphase countercurrent experimental results agree substantially with a model that postulates penetration for the liquid phase and with the aforementioned countercurrent model for the gas phase.

A series of cocurrent interphase experiments was made, using water as the solvent. Experimental results were lower than the predicted values by at least a factor of two. The apparent cause of the difficulty was accumulation of surfactants at the interface. Experimental mass-transfer coefficients indicate that the interfacial velocity was about 10 to 20% of the predicted velocity. This was confirmed by visual observation.

6. AN ECONOMIC STUDY OF SULFATE REMOVAL FROM BRINES WITH BACTERIA BASED ON A HYPOTHETICAL DESIGN

Ronald H. Charron
(M. S. Thesis)

(From UCRL-16945)

A practical application of the ability of a strain of Desulfovibrio to reduce sulfates to sulfide in concentrated brines is proposed. Using kinetic data from previous studies on the salt-tolerant strain, a continuous process for removal of sulfates from a 10% brine is designed, and the economics of the process are determined. A comparison is made with the economics of a conventional process which removes sulfates by precipitation with barium chloride. The results indicate that the bacterial process may be more economical for removing sulfates from brines of 10% NaCl or less, especially when large volumes are handled.

A proposal is made for adapting the bacterial reduction process to reclaiming sulfur from seawater, using a cheap carbon source such as sewage, and utilizing the sulfate-free effluent as feed for a seawater conversion plant.

7. ENVIRONMENTAL EFFECTS ON THE DECAY CONSTANT OF ^{90m_1}Nb

John A. Cooper
(Ph. D. Thesis)

(From UCRL-16910)

A new method has been developed to study changes in nuclear decay constants due to alterations in the chemical or physical environment. This method has been applied to the study of the effect of chemical state changes, the effect of a large increase in pressure, and the effect of changes into and out of the superconducting state on the decay constant of the 24-sec isomeric state in ^{90}Nb. The following results were obtained for these environmental changes:

λ(Aqueous fluoride) - λ(metal) = (-0.036 ± 0.004) λ(aqueous fluoride)
λ(100 000 atm) - λ(1 atm) = (0.006 ± 0.007) λ(100 000 atm)
λ(12°K) - λ(4.2°K, superconducting) < 0.002 λ(12°K).

These results have shown that the energy of the transition depopulating this isomeric state is very low and that an appreciable fraction of the isomeric decay takes place by ejection of valence electrons.

The γ-ray spectrum ^{90}Mo has also been investigated. Several new lines have been observed and the photon intensities have been measured. The multipolarities of many of the intense transitions have been determined and their coincidence relationships resolved with γ-γ coincidence studies. A decay scheme has been postulated from which the energy of the transition depopulating the 24-sec isomeric state has been determined from energy differences to be 2.38±0.36 keV.

8. THE ABSORPTION SPECTRUM OF Cf^{3+} AND CRYSTALLOGRAPHY OF CALIFORNIUM SESQUIOXIDE AND CALIFORNIUM TRICHLORIDE

J. L. Green
(Ph. D. Thesis)

(From UCRL-16516)

The work reported here was undertaken for the purpose of extending existing knowledge of the chemical and physical properties of element 98, californium. An essential preliminary to these studies was the development of satisfactory techniques for obtaining microgram amounts of the element in a state of satisfactory chemical purity, and for utilizing this material in spectroscopic and crystallographic investigations.

The general problems involved in small scale purification operations are discussed. The procedures used for the purification of approximately 6 μg of ^{249}Cf are described in detail, as are the analytical techniques used for purity evaluations. Adequate purity with respect to lanthanides and other actinides was demonstrated with reasonable certainty; however, it is shown that other materials are potentially present as contaminants. Arguments are presented which justify the postulation that these materials are probably Ca and/or Al.

A detailed discussion is given of the techniques which were developed for obtaining the absorption spectrum of microsamples of Cf^{3+}. Absorption spectrum data from 400 to 800 mμ are presented for Cf^{3+} absorbed in cation exchange resin beads and for solid hydrated californium trichloride. The spectrum of these materials is expected to be very similar to the spectrum of Cf^{3+} in solution. A sample of anhydrous $CfCl_3$ was prepared that apparently is a single crystal. Room temperature absorption spectra from 4000 to 9000 A were taken of this material. Tentative calculations are presented which fit these data to a theoretical energy level scheme.

Several polycrystalline samples of californium sesquioxide were prepared and studied using x-ray diffraction techniques. The structure exhibited by these samples was the monoclinic Sm_2O_3 structure having a=14.124±0.020 A, b=3.591±0.003 A, c=8.809±0.013 A, and β=100.31±0.02 deg. Similarly, preparations of $CfCl_3$ were found to exhibit the hexagonal UCl_3 structure having a=7.393±0.040 A and c=4.090±0.060 A. The ionic radius for californium computed from the trichloride data is 0.98 A. The error limits reported here are based on a statistical evaluation of the consistency of a group of determinations, accounting for nonstatistical sampling, and do not reflect the internal consistency of the data from the individual preparations.

9. I. THE MEASUREMENT OF INTERNAL CONVERSION COEFFICIENTS UTILIZING SEMICONDUCTOR DETECTORS

II. DECAY SCHEME STUDIES OF THE ODD-MASS GOLD ISOTOPES

Arthur Judd Haverfield
(Ph. D. Thesis)

(From UCRL-16969)

The application of semiconductor detectors to measurements of internal conversion coefficients has been extensively discussed, with particular emphasis being placed upon a spectrometer employing both Si(Li) and Ge(Li) detectors for the simultaneous observation of conversion electrons and γ rays. The construction, calibration and use of such a spectrometer were described. Possible improvements in this system were also discussed. It was found that this type of spectrometer is best suited for ICC measurements of transitions following electron-capture decay, but may still be useful in cases of β or positron decay.

The level schemes of the odd-mass gold isotopes of mass 199, 197, 195, and 193 were examined from the decay of the respective odd-mass platinum and mercury isotopes. The measurement of numerous internal conversion coefficients permitted the assignment of spin and parity values to many of these levels. The systematic trends of many of the nuclear phenomena associated with these isotopes were examined as a function of neutron number. The experimental data were compared to the various theoretical approaches applicable to this region of nuclei.

The internal conversion process was discussed along with the various experimental methods of ICC measurement.

The calibration of semiconductor detectors for energy and intensity measurements was discussed. Extensive tables of standards for these calibration procedures were presented.

10. THE MOLECULAR-BEAM ELECTRIC-RESONANCE SPECTRA OF LiF, NaF, AND KCl

Craig D. Hollowell
(Ph. D. Thesis)

(From UCRL-17019)

Radio-frequency spectra have been observed in the low vibrational and rotational states of $^{6}Li^{19}F$, $^{7}Li^{19}F$, $^{23}Na^{19}F$, $^{39}K^{35}Cl$, and $^{39}K^{37}Cl$ by the molecular-beam electric resonance method. Microwave $J=1 \rightarrow 0$ transitions have also been observed for $^{23}Na^{19}F$. Analysis of the spectra has made possible the determination of accurate dipole moments, rotational constants, and nuclear hyperfine interaction constants.

A polarizable ion model of the alkali halide molecules is presented. This model includes several effects, previously neglected, and successfully agrees with experimental data.

11. FISSION PROPERTIES OF SOME ELEMENTS BELOW RADIUM

Arastoo Khodai-Joopari
(Ph. D. Thesis)

(From UCRL-16489)

The fission cross sections σ_f have been measured in bombardments of ^{209}Bi, ^{208}Pb, ^{207}Pb, and ^{206}Pb with helium ions of energies 25-130 MeV and ^{209}Bi, ^{208}Pb, ^{206}Pb, and ^{197}Au with protons of energies 15-30 MeV, using (mainly) mica for the detection of fission fragments. From the comparison of the low-energy σ_f/σ_R data with three different theoretical expressions for Γ_f/Γ_n, the heights of the fission barriers, B_f, for ^{213}At, ^{212}Po, ^{210}Po, ^{209}Bi, ^{207}Bi, and ^{198}Hg have been deduced. The accuracies of the relative and the absolute values of B_f are 0.5 and 1.5 MeV, respectively. It is found that the ratio a_f/a_n is quite different (1.5 to 1.2) for these nuclei, indicating that the influence of shell effects on the level densities is still strong at moderately high excitation energies (≈16-40 MeV). A comparison of the relative values of B_f with the predictions of the conventional liquid-drop model seems to show that one obtains somewhat better agreement if a composition-dependent surface energy is used. Therefore, the values of B_f are compared with those calculated by Myers and Swiatecki (M-S) which show fairly good gross agreement. However, the saddle masses plotted relative to the smooth liquid-drop reference mass surface of M-S show a structure similar to, but much less pronounced than, that corresponding to the ground-state masses. If this structure is taken as an indication for the existence of shell effects at the saddle point, the anomaly between the experimental and theoretical values of B_f for the heavy elements and the fission-barrier systematics can be qualitatively explained. A discussion is given of the possibility that shell effects at the saddle point may affect the interpretation of the observed features of low- and medium-energy fission, along with a brief review of some of the experimental observations and theoretical viewpoints in this connection. Various aspects of the higher-energy σ_f/σ_R data are qualitatively discussed. It is shown that within the framework of the Fermi gas model, the level density parameter a_n has to increase with energy in order to account for the large discrepancy observed between the σ_f/σ_R data and the calculated values of $\Gamma_f/(\Gamma_f+\Gamma_n)$ extended to higher energies. Semiquantitative estimates of "first-chance" fission (for ^{212}Po and ^{211}Po) and of the numbers of prefission neutrons $\langle \nu_p \rangle$ are made and compared with estimates of $\langle \nu_p \rangle$ made by others in similar cases. The importance of such estimates for a correct interpretation of various distributions of fission fragments and the possibility of usefulness of these σ_f/σ_R data for a quantitative study of the behavior of level densities with energy is pointed out.

12. FLUID PHASE MASS TRANSFER IN DIALYSIS

Richard D. Newman
(M. S. Thesis)

(From UCRL-17117)

A study was made of the dialysis of sodium chloride in an apparatus built to simulate a plate and frame dialyzer. It was found that the experimental mass transfer data could be predicted in terms of the dimensionless group: Grashof number, Reynolds number, and Schmidt number. A method based on these findings was developed to predict mass transfer in industrial dialyzers. This method was found to predict quite accurately independent data which had been obtained from the literature.

13. THE X-RAY CRYSTALLOGRAPHIC STRUCTURE DETERMINATION OF VARIOUS COMPOUNDS

Roger C. Pettersen
(Ph. D. Thesis)

(From UCRL-16975)

Using techniques of x-ray crystallography, the structures of three new chemical compounds have been determined. The first, tetraamminediaquonickel (II) hexacyanoferrate (II), $[Ni(NH_3)_4(H_2O)_2]_2Fe(CN)_6$, crystallizes in space group R32 with hexagonal cell dimensions, $a_1=a_2=12.213$ A, c=17.005 A, $\alpha=\beta=90.00°$ and $\gamma=120.00°$. The iron and nickel atoms lie along the c axis or three-fold axis. The ammonia, water, and cyanide ligands are bonded to the heavy atoms in octahedral arrangements.

The second structure is the para-bromo-aniline derivative of homo-cubane carboxylic acid,

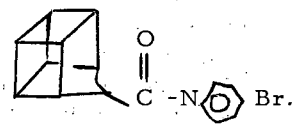

This substance crystallizes in space group $P\bar{1}$ with cell dimensions, a=10.092 A, b=12.321 A, c=11.649 A, $\alpha=100.62°$, $\beta=88.32°$, and $\gamma=114.10°$. The symmetry of the homo-cubane cage was of particular interest. Two asymmetric units were present in the unit cell, giving two independent measurements of the same molecule. The C-C bond lengths for the cages were all equal within the estimated standard deviations, the average for all of them being 1.56±0.03 A. If the bond angles are considered, one of the cages has mm^2 point symmetry and the other 2 point symmetry. Hydrogen bonding was also discovered between the carbonyl oxygen atom and the nitrogen atom of adjacent molecules.

The third structure determined is ferricinium picrate, $C_{16}H_{12}N_3O_7Fe$. It is related to the "sandwich compound" ferrocene, $Fe(C_5H_5)_2$, where the iron atom is located midway between parallel planes of five-membered carbon rings. The oxidation state of the iron in ferrocene is 2+, whereas it is 3+ in the ferricinium ion, $Fe(C_5H_5)_2^+$. Ferricinium picrate crystallizes in space group Cmcm with cell dimensions a=12.478 A, b=20.274 A, c=6.912 A, and $\alpha=\beta=\gamma=90.00°$. The results of the structure determination show the ferricinium ion to be a sandwich also, but with a slightly larger distance between the planes of the two five-membered carbon rings.

14. THE DISPERSION OF BACTERIA

Francis G. Rust
(M. S. Thesis)

(From UCRL-17208)

The dispersion of bacteria by their own motility was measured by three methods and was found to follow the behavior predicted by diffusion. The diffusivity was found to range from 2 to 3×10^{-5} cm^2/sec at 26°C in a uniform nutrient medium. Methods are presented for estimating the rate of dispersion of motile bacteria that are multiplying as they diffuse.

15. A STUDY OF THE INTERNAL CONVERSION ELECTRONS EMITTED WITHIN 3 NSEC AFTER THE SPONTANEOUS FISSION OF ^{252}Cf

Rand Lewis Watson
(Ph. D. Thesis)

(From UCRL-16798)

The spectra of internal conversion electrons of energies between 10 and 650 keV emitted in coincidence with the spontaneous fission of ^{252}Cf were measured and correlated to fragments of specific masses. A magnetic steering device was used to guide the electrons to a lithium-drifted silicon electron detector shielded against interference from fission fragments, α particles, γ rays, and x rays. This device also made possible the measurement of the electron spectra in the specific time intervals of approximately 0 to 0.9, 0.1 to 1.7, and 1.1 to 2.9 nsec after fission.

The measured spectra showed well-defined structure and were analyzed by means of a least-squares peak-fitting procedure. Many of the lines were identified as K and L conversion line pairs, thus facilitating multipolarity assignments on the basis of K-to-L ratios. Estimates of intensities and half-lives are also given for a large number of the electron lines. By correlating the electron spectra with the γ-ray measurements of Bowman, it was possible to assign many of the electron lines to specific isotopes.

Several of the analyzed electron peaks were suggested as specific examples of possible 2+ to 0+ transitions in even-even nuclides. Two transitions thought to be associated with ^{110}Ru displayed energies and multipolarities that strongly suggest a region of stable deformation near mass 110.

Binding energy calculations were carried out employing a nonrelativistic Hartree-Fock computer program developed by Roothaan. The K and L binding energies of Sr, Pd, Xe, and Sm were calculated as a function of ionic charge ranging from the neutral atom to the fully ionized ion. It was found that the K and L binding energies are both increased over the neutral atomic values by approximately 0.9 keV for the most probable ionic charges of the fission fragments, and consequently that the K x-ray energies are almost unaffected.

K. PAPERS PUBLISHED AND UCRL REPORTS ISSUED, 1966

AHMAD, I.
Nuclear spectroscopic studies of some very heavy odd-mass nuclides
UCRL-16888, September 1966
Ph. D. Thesis

AJZENBERG-SELOVE, F. (See Mangelson, N., UCRL-16688A)

AJZENBERG-SELOVE, F. (See Mangelson, N., UCRL-16849)

AJZENBERG-SELOVE, F. (See Mangelson, N., UCRL-16850)

ARMSTRONG, L., Jr., and R. Marrus
Nuclear moments of americium-244 and 16-h americium-242 and analysis of the hyperfine fields
UCRL-16494, November 1965
Phys. Rev. 144, 994 (1966)

ASARO, F. (See Lederer, C. M., UCRL-16414)

ATKINS, H. L., W. Bennett-Corniea, and W. M. Garrison
Gamma-ray induced oxidation of peptides in aqueous solution: effects of molecular oxygen and of heavy-metal ions
UCRL-16914A, June 1966
Meeting of the American Chemical Society, New York, September 11-16, 1966

ATKINS, H. L., W. Bennett-Corniea, and W. M. Garrison
The radiation-induced oxidation of peptides in aqueous solution
UCRL-17004, July 1966
J. Phys. Chem.

BABA, H. (See Kapoor, S. S., UCRL-16706)

BALL, G. C., and J. Cerny
The $^{14}N(^{3}He, t)^{14}O$ reaction and excited isospin triads in mass 14
UCRL-17038, October 1966
Phys. Rev.

BALL, G. C., and J. Cerny
A J dependence in the $(^{3}He, \alpha)$ reaction confirming new spectroscopic assignments in ^{14}N and ^{13}C
UCRL-16831, April 1966
Phys. Letters 21, 551 (1966)

BALL, G. C. (See Moss, J., UCRL-17124)

BANSAL, B. M.
Some of the physical properties of curium and protactinium metals and protactinium tetrafluoride
UCRL-16782, April 1966
Ph. D. Thesis

BAUMGARTNER, E., and H. Kim
Effects of electromagnetic fields on polarized particles
UCRL-16787

BENNETT-CORNIEA, W. (See Atkins, H. L., UCRL-16914A)

BENNETT-CORNIEA, W. (See Atkins, H. L., UCRL-17004)

BERNTHAL, F. M., and J. O. Rasmussen
Influence of Coriolis-admixed components on El transition probabilities in ^{177}Hf
UCRL-17243A, October 1966
Meeting of the American Physical Society, Stanford, California, December 28-30, 1966

BERNTHAL, F. M. (See Haverfield, A. J., UCRL-16862)

BERNTHAL, F. M. (See Haverfield, A. J., UCRL-16995)

BHAGAT, A. K., and C. R. Wilke
Filtration studies with ultrafine particles
UCRL-16574, September 1966

BOSCHITZ, E. (See Pugh, H. G., UCRL-16913)

BOWMAN, H. R. (See Hyde, E. K., UCRL-16845)

BOWMAN, H. R. (See Watson, R. L., UCRL-16563A)

BRELVI, W., and C. R. Wilke
An improved correlation for the heats of formation of inorganic compounds
UCRL-16865, May 1966

BRUNNADER, H. (See Cerny, J., UCRL-17101)

BURDE, J., R. M. Diamond, and F. S. Stephens
An 8- isomeric state in the 106-neutron nuclei: ^{180}W, ^{182}Os, and ^{184}Pt
UCRL-16163, December 1965
Nucl. Phys. 85, 481 (1966)

BURDE, J., R. M. Diamond, and F. S. Stephens
Ground-state (quasi-) rotational levels in light Os, Pt, and Hg nuclei
UCRL-17067, August 1966
Nucl. Phys.

BURDE, J., R. M. Diamond, and F. S. Stephens
In-beam spectroscopic studies of neutron-deficient nuclei of osmium, platinum, and mercury
UCRL-16734, March 1966
Izu. Akad. Nauk USSR (16th Annual National Conference on Nuclear Spectroscopy, Moscow, January 26-February 3, 1966)

BURGER, R., D. J. Clark, E. Close, and H. Kim
Machine development at the Berkeley 88-inch cyclotron
UCRL-16795, May 1966
International Conference on Isochronous Cyclotrons, Gatlinburg, Tennessee, May 2-5, 1966

BUSSIERE DE NERCY, A. (See Harvey, B. G., UCRL-16573)

BUTLER, G. W., J. Cerny, S. W. Cosper, and R. L. McGrath
Mass and excited states of ^{21}Mg
UCRL-17237A, October 1966
Meeting of the American Physical Society, Stanford, California, December 28-30, 1966

BUTLER, G. W. (See Cerny, J., UCRL-16705)

BUTLER, G. W. (See Cerny, J., UCRL-16733A)

BUTLER, G. W. (See Cerny, J., UCRL-16990)

BUTLER, G. W. (See Cerny, J., UCRL-17101)

BYERS, C. H., and C. J. King
Convective transfer processes in laminar gas-liquid channel flow
UCRL-16535, May 1966

BYERS, C. H., and C. J. King
Gas-liquid mass transfer with a tangentially moving interface: I. Theory
UCRL-16925, July 1966
A. I. Ch. E. J.

BYERS, C. H., and C. J. King
Gas-liquid mass transfer with a tangentially moving interface: II. Experimental
UCRL-16926, July 1966
A. I. Ch. E. J.

BYERS, C. H., and C. J. King
Liquid diffusivities in the glycol-water system
UCRL-16622, February 1966
J. Phys. Chem.

CERNY, J., S. W. Cosper, G. W. Butler, and R. L. McGrath
^{37}Ca and the mass 37 T=3/2 quartet
UCRL-16990, July 1966
International Conference on Nuclear Physics, Gatlinburg, Tennessee, September 12-17, 1966

CERNY, J., S. W. Cosper, G. W. Butler, H. Brunnader, R. L. McGrath, and F. S. Goulding
Heavy ion identification using the power law technique
UCRL-17101, August 1966
Nucl. Instr. and Methods

CERNY, J., S. W. Cosper, G. W. Butler, R. H. Pehl, F. S. Goulding, D. A. Landis, and C. Détraz
The mass of ^{8}He from the four-neutron transfer reaction ^{26}Mg(α, ^{8}He)^{22}Mg
UCRL-16705, February 1966
Phys. Rev. Letters 16, 469 (1966)

CERNY, J., S. W. Cosper, G. W. Butler, and R. L. McGrath
The mass 37 T=3/2 quartet
UCRL-16733A, March 1966
Meeting of the American Physical Society, Tallahassee, Florida, March 17-19, 1966

CERNY, J. (See Ball, G. C., UCRL-16831)

CERNY, J. (See Ball, G. C., UCRL-17038)

CERNY, J. (See Butler, G. W., UCRL-17237A)

CERNY, J. (See Cosper, S. W., UCRL-17127)

CERNY, J. (See Détraz, C., UCRL-16956)

CERNY, J. (See Fleming, D. G., UCRL-17241A)

CERNY, J. (See Maples, C. C., UCRL-16964)

CERNY, J. (See Maples, C. C., UCRL-17240A)

CERNY, J. (See McGrath, R. L., UCRL-17315)

CERNY, J. (See Poskanzer, A. M., UCRL-17267)

CHABRE, M. (See Pugh, H. G., UCRL-16913)

CHABRE, M. (See Springer, A., UCRL-16620)

CHARRON, R. H., and C. R. Wilke
An economic study of sulfate removal from brines with bacteria based on a hypothetical design
UCRL-16945, August 1966

CLAMPITT, R. (See Newton, A. S., UCRL-17187)

CLARK, D. J.
Beam diagnostics and instrumentation
UCRL-16792, May 1966
International Conference on Isochronous Cyclotrons, Gatlinburg, Tennessee, May 2-5, 1966

CLARK, D. J., H. Kim, K. R. MacKenzie, and J. T. Vale
Modification studies for the Berkeley 184-inch cyclotron
UCRL-16882, May 1966
International Conference on Isochronous Cyclotrons, Gatlinburg, Tennessee, May 2-5, 1966

CLARK, D. J., E. Close, H. A. Grunder, H. Kim, P. Pellissier, and B. H. Smith
Regenerative beam extraction for the Berkeley 88-inch cyclotron
UCRL-16794, April 1966
International Conference on Isochronous Cyclotrons, Gatlinburg, Tennessee, May 2-5, 1966

CLARK, D. J. (See Burger, R., UCRL-16795)

CLARK, D. J. (See McKee, J. S. C., UCRL-17239A)

CLARK, D. J. (See Slobodrian, R. J., UCRL-17233A)

CLARK, D. J. (See Tivol, W. F., UCRL-17238A)

CLARKSON, J. E., R. M. Diamond, F. S. Stephens, and I. Perlman
Collective excitations in neutron-deficient barium, xenon, and cerium isotopes
UCRL-16974, September 1966
Nucl. Phys.

CLARKSON, J. E. (See Sikkeland, T., UCRL-16773)

CLEM, R. G., and E. H. Huffman
Extraction of metal pyridine azides. Spectrophotometric determination of copper, nickel, and palladium
UCRL-16642, January 1966
Anal. Chem. 38, 926 (1966)

CLOSE, E. (See Burger, R., UCRL-16795)

CLOSE, E. (See Clark, D. J., UCRL-16794)

COLEMAN, E. (See Franco, V., UCRL-16993)

CONWAY, J. G., S. Fried, R. M. Latimer, R. McLaughlin, R. G. Gutmacher, W. T. Carnall, and P. Fields
The solution absorption spectrum of Cf^{3+}
UCRL-16971, July 1966
J. Inorg. Nucl. Chem. 28, 3064 (1966)

CONWAY, J. G. (See Gruber, J. B., J. Chem. Phys. 45, 1423 (1966))

CONWAY, J. G. (See Gruber, J. B., J. Chem. Phys. 45(2), 477 (1966))

CONZETT, H. E.
Analysis of proton-α cross section and polarization data from 20 to 60 MeV
UCRL-16767, March 1966
Meeting of the American Physical Society, New York, January 26, 1966

CONZETT, H. E., and B. G. Harvey
The Berkeley 88-inch cyclotron: progress and status, February 1966
UCRL-16726, February 1966
International Conference on Isochronous Cyclotrons, Gatlinburg, Tennessee, May 2-5, 1966

CONZETT, H. E.
Influence of cyclotron beam properties on experiments
UCRL-16727, February 1966
International Conference on Isochronous Cyclotrons, Gatlinburg, Tennessee, May 2-5, 1966

CONZETT, H. E. (See Slobodrian, R. J., UCRL-16991)

CONZETT, H. E. (See Tivol, W. F., UCRL-17238A)

COOPER, J.
Environmental effects on the decay constant of $^{90m_1}Nb$
UCRL-16910, September 1966
Ph. D. Thesis

COSPER, S. W., J. Cerny, and R. C. Gatti
Long-range particles of Z=1 to 4 emitted during the spontaneous fission of ^{252}Cf
UCRL-17127, September 1966
Phys. Rev.

COSPER, S. W. (See Butler, G. W., UCRL-17237A)

COSPER, S. W. (See Cerny, J., UCRL-16705)

COSPER, S. W. (See Cerny, J., UCRL-16733A)

COSPER, S. W. (See Cerny, J., UCRL-16990)

COSPER, S. W. (See Cerny, J., UCRL-17101)

COSPER, S. W. (See Maples, C. C., UCRL-17240A)

COSPER, S. W. (See McGrath, R. L., UCRL-17315)

COSPER, S. W. (See Poskanzer, A. M., UCRL-17267)

CUNNINGHAM, B. B. (See Green, J. L., UCRL-17079)

DÉTRAZ, C., J. Cerny, and R. H. Pehl
A study of mass 5 and 7 nuclei by (p, t) and (p, ^{3}He)
UCRL-16956, June 1966
Phys. Rev.

DÉTRAZ, C. (See Cerny, J., UCRL-16705)

DIAMOND, R. M.
Amine extraction systems
UCRL-17123, September 1966
International Conference on Solvent Extraction Chemistry, Göotenborg, Sweden, August 27-September 1, 1966

DIAMOND, R. M., and F. S. Stephens
Heavy-ion projectiles and in-beam spectroscopy
UCRL-17143, September 1966
International Symposium on Why and How Should We Investigate Nuclides Far Off the Stability Line? Lysekil, Sweden, August 21-27, 1966

DIAMOND, R. M. (See Burde, J., UCRL-16163)

DIAMOND, R. M. (See Burde, J., UCRL-16734)

DIAMOND, R. M. (See Burde, J., UCRL-17067)

DIAMOND, R. M. (See Clarkson, J. E., UCRL-16974)

DIAMOND, R. M. (See Müller, W., UCRL-16736)

DIAMOND, R. M. (See Newton, J. O., UCRL-17204)

DIAMOND, R. M. (See Newton, J. O., UCRL-17205)

EASLEY, W. (See Edelstein, N., UCRL-16608)

EASLEY, W. (See Edelstein, N., UCRL-17183)

EDELSTEIN, N., W. Easley, and R. McLaughlin
The formation and characterization of divalent americium in CaF_2 crystals
UCRL-16608, January 1966
J. Chem. Phys. 44, 3130 (1966)

EDELSTEIN, N., W. Easley, and R. McLaughlin
Optical and electron paramagnetic resonance spectroscopy of actinide ions in single crystals
UCRL-17183, October 1966
Advances in Chemistry Series

EDELSTEIN, N. (See Matthias, E., UCRL-16810A)

EDELSTEIN, N. (See Matthias, E., UCRL-16818)

EDWARDS, V. H., and C. R. Wilke
The electronic sizing and counting of bacteria
UCRL-16951A, June 1966
152nd National Meeting of the American Chemical Society, New York, September 11-16, 1966

EWAN, G. T. (See Yamazaki, T., UCRL-17260A)

FADLEY, C. S. (See Hagstrom, S. B. M., UCRL-16676A)

FLEMING, D. G., J. Cerny, and C. C. Maples
The $^{15}N(p, t)^{13}N$ and $^{15}N(p, {}^{3}He)^{13}C$ reactions
UCRL-17241A, October 1966
Meeting of the American Physical Society, Stanford, California, December 28-30, 1966

FLEMING, D. G. (See Maples, C. C., UCRL-17240A)

FORRESTER, J. D. (See Zalkin, A., UCRL-16743)

FRANCO, V., and R. Glauber
Double scattering and charge exchange effects in deuterium
UCRL-17261A, November 1966
Meeting of the American Physical Society, New York, January 30-February 2, 1967

FRANCO, V., and E. Coleman
Double scattering in high-energy elastic collisions with deuterons
UCRL-16993, July 1966
Phys. Rev. Letters 17, 827 (1966)

FRANCO, V., and R. J. Glauber
High-energy deuteron cross section: charge exchange effects
UCRL-17142, October 1966
Phys. Rev.

FRANCO, V.
High-energy deuteron-deuteron cross sections
UCRL-16694, February 1966
Phys. Letters

FRANCO, V.
High-energy proton-deuteron scattering cross sections
UCRL-16512, March 1966
Phys. Rev. Letters 16, 944 (1966)

FRANCO, V.
High-energy small-angle scattering by deuterons
UCRL-16663A, January 1966
Meeting of the American Physical Society, Washington, D. C., April 25-28, 1966

GABRIELLI, I. (See Hendrie, D. L., UCRL-16664A)

GABRIELLI, I. (See Meriwether, J. R., UCRL-16518)

GARRISON, W. M. (See Atkins, H. L., UCRL-16914A)

GARRISON, W. M. (See Atkins, H. L., UCRL-17004)

GARRISON, W. M. (See Holian, J., UCRL-16543A)

GARRISON, W. M. (See Holian, J., UCRL-16772)

GARRISON, W. M. (See Holian, J., UCRL-16915A)

GARRISON, W. M. (See Holian, J., UCRL-17029)

GARRISON, W. M. (See Holian, J., UCRL-17154)

GARRISON, W. M. (See Jayko, M. E., UCRL-16646A)

GARRISON, W. M. (See Willix, R. L. S., UCRL-16647A)

GATTI, R. C. (See Cosper, S. W., UCRL-17127)

GHIORSO, A.
New accelerators for very heavy ions - production of super-elements
UCRL-17295A, November 1966
1967 Particle Acceleration Conference, Washington, D. C., March 1-3, 1967

GHIORSO, A., R. M. Main, and B. H. Smith
The omnitron: a versatile medium energy synchrotron for the acceleration of light and heavy ions
UCRL-16839, April 1966
International Conference on Isochronous Cyclotrons, Gatlinburg, Tennessee, May 2-5, 1966

GHIORSO, A., E. L. Hubbard, R. M. Main, D. A. Spence, and F. Voelker
Partial energy beams from an ion linac
UCRL-17162, September 1966
1966 Linear Accelerator Conference, Los Alamos Scientific Laboratory, Los Alamos, October 3-7, 1966

GHIORSO, A. (See Sikkeland, T., UCRL-16773)

GLENDENNING, N. K.
Analysis of the ^{208}Pb(p, t) reaction
UCRL-17199, October 1966
Phys. Rev.

GLENDENNING, N. K.
Coupled channel calculation of inelastic scattering based on a microscopic nuclear description
UCRL-16841, April 1966
Phys. Letters 21, 549 (1966)

GLENDENNING, N. K., B. G. Harvey, D. L. Hendrie, O. N. Jarvis, and J. Mahoney
Test of a microscopic description of nickel isotopes by inelastic proton scattering
UCRL-16984, July 1966
International Conference on Nuclear Physics, Gatlinburg, Tennessee, September 12-17, 1966

GOLDSWORTHY, W.
Integrating window amplifier
UCRL-16838A, April 1966
13th Nuclear Science Symposium, Boston, Massachusetts, October 19-21, 1966

GOTH, G. W. (See Maples, C., UCRL-16964)

GOULDING, F. S. (See Cerny, J., UCRL-16705)

GOULDING, F. S. (See Cerny, J., UCRL-17101)

GOULDING, F. S. (See Pehl, R. H., UCRL-16722)

GREEN, J. L.
The absorption spectrum of Cf^{3+} and crystallography of californium sesquioxide and californium trichloride
UCRL-16516, November 1965
Ph. D. Thesis

GREEN, J. L., and B. B. Cunningham
The absorption spectrum of Cf^{3+}
UCRL-17079, August 1966
Inorg. Nucl. Chem. Letters 2, 365 (1966)

GRUBER, J. B., J. R. Henderson, M. Muramoto, K. Rajnak, and J. G. Conway
Energy levels of single-crystal erbium oxide
J. Chem. Phys. 45(2), 477 (1966)

GRUBER, J. B., W. R. Cochran, J. G. Conway, and A. T. Nicol
Optical spectra of tripositive curium-244 in lanthanum trichloride
J. Chem. Phys. 45, 1423 (1966)

HAGSTROM, S. B. M., and C. S. Fadley
High precision measurements of electron energy levels in neptunium
UCRL-16676A, January 1966
Bull. Am. Phys. Soc. 11(HI8), 389 (1966)

HAMILTON, J. H., A. V. Ramayya, B. van Nooijen, R. G. Albridge, E. F. Zganjar, S. C. Pancholi, J. M. Hollander, V. S. Shirley, and C. M. Lederer
Experimental values of internal-conversion coefficients of nuclear transitions: total and K-shell coefficients and L-subshell coefficient ratios
Nucl. Data, Section A, 1, 521 (1966)

HARRIS, J. A. (See Lamb, J. F., UCRL-16600)

HARVEY, B. G., D. L. Hendrie, O. N. Jarvis, J. Mahoney, and J. Valentin
Multiple nuclear excitation of rotational levels in ^{152}Sm and ^{154}Sm
UCRL-17303, December 1966
Phys. Letters

HARVEY, B. G., J. R. Meriwether, J. Mahoney, A. Bussiere de Nercy, and D. J. Horen
Scattering of 40.5-MeV α particles by ^{12}C, ^{13}C, ^{14}N, ^{15}N, ^{16}O, and ^{18}O
UCRL-16573, December 1965
Phys. Rev. 146, 712 (1966)

HARVEY, B. G. (See Conzett, H. E., UCRL-16726)

HARVEY, B. G. (See Glendenning, N. K., UCRL-16984)

HARVEY, B. G. (See Jarvis, O. N., UCRL-17236A)

HARVEY, B. G. (See Mangelson, N. F., UCRL-17235A)

HARVEY, B. G. (See Meriwether, J. R., UCRL-16518)

HAVERFIELD, A. J.
I. The measurement of internal conversion coefficients utilizing semiconductor detectors
II. Decay scheme studies of the odd-mass gold isotopes
UCRL-16969, November 1966
Ph. D. Thesis

HAVERFIELD, A. J., and F. M. Bernthal
New data on the decay of ^{177m}Lu
UCRL-16995, July 1966
International Conference on Nuclear Physics, Gatlinburg, Tennessee, September 12-17, 1966

HAVERFIELD, A. J., F. M. Bernthal, and J. M. Hollander
New transitions and precise energy and intensity determinations in the decay of ^{177m}Lu
UCRL-16862, May 1966
Nucl. Phys.

HENDRIE, D. L., J. Valentin, I. Gabrielli, J. Mahoney, and J. R. Meriwether
^{56}Fe(α, α') at 23.5, 33, and 50 MeV
UCRL-16664A, January 1966
Meeting of the American Physical Society, Washington, D. C., April 25-28, 1966

HENDRIE, D. L. (See Glendenning, N. K., UCRL-16984)

HENDRIE, D. L. (See Harvey, B. G., UCRL-17303)

HENDRIE, D. L. (See Jarvis, O. N., UCRL-17236A)

HENDRIE, D. L. (See Meriwether, J. R., UCRL-16518)

HENDRIE, D. L. (See Pugh, H. G., UCRL-16913)

HENDRIE, D. L. (See Springer, A., UCRL-16620)

HENDRIE, D. L. (See Yamazaki, T., UCRL-16986)

HENDRIE, D. L. (See Yamazaki, T., UCRL-16987)

HOLIAN, J., and W. M. Garrison
Effects of heavy metal ions on the radiolysis of the pyrimidine bases in oxygen-free solution
UCRL-16543A, November 1965
Radiation Res. 27, 527 (1966)

HOLIAN, J., and W. M. Garrison
Gamma-ray induced oxidation of the purine bases in oxygen-free aqueous solutions containing Fe(III)
UCRL-16915A, June 1966
Meeting of the American Chemical Society, New York, September 11-16, 1966

HOLIAN, J., and W. M. Garrison
Identification of a specific mode of oxidation in the radiolysis of the purine bases in oxygenated aqueous solution
UCRL-17154, September 1966
J. Phys. Chem.

HOLIAN, J., and W. M. Garrison
Radiation-induced oxidation of cytosine and uracil in aqueous solutions of Cu^{2+}
UCRL-16772, March 1966
Nature 212, 394 (1966)

HOLIAN, J., and W. M. Garrison
Radiolysis of the purine bases in aqueous solutions of Fe(III)
UCRL-17029, August 1966
Nature

HOLLANDER, J. M., J. O. Rasmussen, and J. H. Hamilton
Internal conversion
Phys. Today 19, 58 (1966)

HOLLANDER, J. M., and I. Perlman
The semiconductor revolution in nuclear radiation counting
UCRL-17013, July 1966
Science 154, 84 (1966)

HOLLANDER, J. M. (See Hamilton, J. H., Nucl. Data, Section A, 1, 521 (1966))

HOLLANDER, J. M. (See Haverfield, A. J., UCRL-16862)

HOLLANDER, J. M. (See Lamb, J. F., UCRL-16600)

HOLLANDER, J. M. (See Yamazaki, T., UCRL-16577)

HOLLANDER, J. M. (See Yamazaki, T., UCRL-16682A)

HOLLIDAY, R. J. (See Matthias, E., UCRL-17140)

HOLLOWELL, C. D.
The molecular-beam electric-resonance spectra of LiF, NaF, and KCl
UCRL-17019, November 1966
Ph. D. Thesis

HOPKINS, T. E.
The crystal and molecular structure of tetraphenyl arsonium tetrachloro cis-diaquo ruthenate monohydrate, $(C_6H_5)_4AsRuCl_4(H_2O)_2 \cdot H_2O$
UCRL-16639, January 1966
7th General Assembly and International Congress of the International Union of Crystallography, Moscow, July 12-19, 1966

HOPKINS, T. E. (See Zalkin, A., UCRL-16629)

HOPKINS, T. E. (See Zalkin, A., UCRL-16813)

HUBBARD, E. L. (See Ghiorso, A., UCRL-17162)

HUFFMAN, E. H. (See Clem, R. G., UCRL-16642)

HYDE, E. K., K. J. Valli, and M. J. Nurmia
Alpha spectroscopy of neutron deficient isotopes of emanation
UCRL-16963A, June 1966
Meeting of the American Physical Society, Mexico City, August 27-29, 1966

HYDE, E. K., H. R. Bowman, and D. H. Sisson
Analytical capabilities of a semiconductor x-ray emission spectrometer
UCRL-16845, May 1966
Anal. Chem.

HYDE, E. K. (See Nurmia, M. J., UCRL-17081A)

HYDE, E. K. (See Poskanzer, A. M., UCRL-17267)

HYDE, E. K. (See Valli, K. J., UCRL-16735)

JARVIS, O. N., B. G. Harvey, D. L. Hendrie, and J. Mahoney
Inelastic scattering of 17.8-MeV protons from ^{58}Ni, ^{60}Ni, and ^{120}Sn
UCRL-17236A, October 1966
Meeting of the American Physical Society, Stanford, California, December 28-30, 1966

JARVIS, O. N. (See Glendenning, N. K., UCRL-16984)

JARVIS, O. N. (See Harvey, B. G., UCRL-17303)

JAYKO, M. E., and W. M. Garrison
Radiolytic dehydrogenation of compounds containing the peptide bond
UCRL-16646A, January 1966
3rd International Congress of Radiation Research, Cortina, Italy, June 26-July 2, 1966

JENKINS, D. A., R. Kunselman, M. K. Simmons, and T. Yamazaki
$2p \rightarrow 1s$ x-ray transitions in π-mesix atoms
UCRL-16855
Phys. Rev. Letters 17, 1 (1966)

JOHNS, O., and J. O. Rasmussen
The quasiboson method and the projection of correct particle number
UCRL-17242A, October 1966
Meeting of the American Physical Society, Stanford, California, December 28-30, 1966

JUDD, B. R.
Hyperfine structures in the atomic 2p shell
UCRL-16581, January 1966
La Structure Hyperfine Magnetique des Atomes et des Molecules, Paris, June 20-24, 1966

KAPOOR, S. S., H. Baba, and S. G. Thompson
Studies of fragment angular distributions in the fission of ^{209}Bi and ^{238}U induced by α particles of energies up to 115 MeV
UCRL-16706
Phys. Rev. 149, 965 (1966)

KHODAI-JOOPARI, A.
Fission properties of some elements below radium
UCRL-16489, July 1966
Ph. D. Thesis

KERN, J., G. Struble, and R. K. Sheline
Study of the levels in ^{140}La by (d, p) stripping reaction
UCRL-16598, December 1965
Phys. Rev.

KIM, H.
Regenerative beam extraction
UCRL-16793, April 1966
International Conference on Isochronous Cyclotrons, Gatlinburg, Tennessee, May 2-5, 1966

KIM, H. (See Baumgartner, E., UCRL-16787)

KIM, H. (See Burger, R., UCRL-16795)

KIM, H. (See Clark, D. J., UCRL-16794)

KIM, H. (See Clark, D. J., UCRL-16882)

KING, C. J. (See Byers, C. H., UCRL-16535)

KING, C. J. (See Byers, C. H., UCRL-16622)

KING, C. J. (See Byers, C. H., UCRL-16925)

KING, C. J. (See Byers, C. H., UCRL-16926)

KLEIN, M. P. (See Matthias, E., UCRL-16810A)

KLEIN, M. P. (See Matthias, E., UCRL-16818)

KLEIN, M. P. (See Wickman, H. H., UCRL-16669)

KUMAR, K.
Collective potential energy, quantum mechanical fluctuations and tunneling effects in even nuclei I
UCRL-16768, March 1966

LAMB, J. F., S. G. Prussin, J. A. Harris, and J. M. Hollander
Application of lithium-drifted germanium γ-ray detectors to neutron activation analysis: nondestructive analysis of a sulfide ore
UCRL-16600, January 1966
Anal. Chem. 38, 813 (1966)

LANDIS, D. A. (See Cerny, J., UCRL-16705)

LANDIS, D. A. (See Pehl, R. H., UCRL-16722)

LATIMER, R. M. (See Conway, J. G., UCRL-16971)

LEBECK, D. F. (See Sikkeland, T., UCRL-16773)

LEDERER, C. M., J. K. Poggenburg, F. Asaro, J. O. Rasmussen, and I. Perlman
The α decay of ^{241}Am (energy levels of ^{237}Np: I. The α decay of ^{241}Am)
UCRL-16414, September 1965
Nucl. Phys. 84, 481 (1966)

LEDERER, C. M. (See Hamilton, J. H., Nucl. Data, Section A, 1, 521 (1966))

LU, C. C. (See Mangelson, N., UCRL-16688A)

LU, C. C. (See Mangelson, N., UCRL-16849)

LU, C. C. (See Mangelson, N., UCRL-16850)

MACKENZIE, K. R. (See Clark, D. J., UCRL-16882)

MAHONEY, J. (See Glendenning, N. K., UCRL-16984)

MAHONEY, J. (See Harvey, B. G., UCRL-16573)

MAHONEY, J. (See Harvey, B. G., UCRL-17303)

MAHONEY, J. (See Hendrie, D. L., UCRL-16664A)

MAHONEY, J. (See Jarvis, O. N., UCRL-17236A)

MAHONEY, J. (See Meriwether, J. R., UCRL-16518)

MAIN, R. M. (See Ghiorso, A., UCRL-16839)

MAIN, R. M. (See Ghiorso, A., UCRL-17162)

MANGELSON, N. F., and B. G. Harvey
Analysis of the reaction ^{12}C(^{3}He, p)^{14}N at E(^{3}He)=20 MeV
UCRL-17235A, October 1966
Meeting of the American Physical Society, Stanford, California, December 28-30, 1966

MANGELSON, N., F. Ajzenberg-Selove, M. Reed, and C. C. Lu
Excited states in ^{6}Be and ^{10}C
UCRL-16849, May 1966
Nucl. Phys.

MANGELSON, N., M. Reed, C. C. Lu, and F. Ajzenberg-Selove
The masses and excited states of ^{24}Al and ^{28}P
UCRL-16850, May 1966
Phys. Letters 21, 661 (1966)

MANGELSON, N., F. Ajzenberg-Selove, M. Reed, and C. C. Lu
Tritons from the ^{3}He bombardment of ^{6}Li, ^{10}B, ^{24}Mg, and ^{28}Si
UCRL-16688A, February 1966
Bull. Am. Phys. Soc. 11(EA8), 350 (1966)

MAPLES, C. C., G. Goth, and J. Cerny
Nuclear reactions q-values
UCRL-16964

MAPLES, C. C., J. Cerny, D. G. Fleming, and S. W. Cosper
Observation of T=3/2 states in ^{11}B and ^{11}C via (p, ^{3}He) and (p, t) reactions on ^{13}C
UCRL-17240A, October 1966
Meeting of the American Physical Society, Stanford, California, December 28-30, 1966

MAPLES, C. C. (See Fleming, D. G., UCRL-17241A)

MARRUS, R., and D. McColm
Atomic beam method for the study of isotope shifts
UCRL-16415, October 1965
Phys. Rev. Letters 15, 813 (1965)

MARRUS, R. (See Armstrong, L., Jr., UCRL-16494)

MATTHIAS, E., D. A. Shirley, M. P. Klein, and N. Edelstein
Detection of nuclear magnetic resonance in a 235 nsec nuclear state by perturbed angular correlations
UCRL-16818, April 1966
Phys. Rev. Letters 16, 974 (1966)

MATTHIAS, E., and D. A. Shirley
Digital analysis of perturbed angular correlations
UCRL-16779, April 1966
Nucl. Instr. Methods 45, 309 (1966)

MATTHIAS, E., and R. J. Holliday
Nuclear magnetic resonance in polarized nuclei
UCRL-17140, September 1966
Phys. Rev. Letters 17, 897 (1966)

MATTHIAS, E., D. A. Shirley, M. P. Klein, and N. Edelstein
Nuclear magnetic resonance in a 235-nsec excited state
UCRL-16810A, April 1966
Meeting of the American Physical Society, Washington, D. C., April 25-28, 1966

MATTHIAS, E., and D. A. Shirley
Precise determination of hyperfine frequencies by digital analysis of perturbed angular correlations
UCRL-16683A, February 1966
Bull. Am. Phys. Soc. 11(EB13), 353 (1966)

MATTHIAS, E. (See Newton, J. O., UCRL-17204)

MCCARTHY, I. E. (See Pugh, H. G., UCRL-16913)

MCCOLM, D. (See Marrus, R., UCRL-16415)

MCGRATH, R. L., S. W. Cosper, and J. Cerny
Isospin-forbidden decay of the ^{24}Mg, 15.43-MeV, O+, T=2 state
UCRL-17315, December 1966
Phys. Rev. Letters

MCGRATH, R. L. (See Butler, G. W., UCRL-17237A)

MCGRATH, R. L. (See Cerny, J., UCRL-16733A)

MCGRATH, R. L. (See Cerny, J., UCRL-16990)

MCGRATH, R. L. (See Cerny, J., UCRL-17101)

MCKEE, J. S. C., D J. Clark, R. J. Slobodrian, and W. F. Tivol
Polarization of proton elasticity scattered from deuterium at 10.5 MeV
UCRL-17239A, October 1966
Meeting of the American Physical Society, Stanford, California, December 28-30, 1966

MCKEE J. S. C. (See Slobodrian, R. J., UCRL-17233A)

MCKEE, J. S. C (See Tivol, W. F., UCRL-17238A)

MCLAUGHLIN, R. (See Conway, J. G., UCRL-16971)

MCLAUGHLIN, R. (See Edelstein, N., UCRL-16608)

MCLAUGHLIN, R. (See Edelstein, N., UCRL-17183)

MELDNER, H.
Predictions of new magic regions and masses for super heavy nuclei from calculations with realistic shell model single particle hamiltonians
UCRL-16843, April 1966
International Symposium on Why and How Should We Investigate Nuclides Far Off the Stability Line? Lysekil, Sweden, August 21-26, 1966

MERIWETHER, J. R., I. Gabrielli, D. L. Hendrie, J. Mahoney, and B. G. Harvey
The scattering of α particles by ^{52}Cr, ^{53}Cr, and ^{51}V
UCRL-16518, December 1965
Phys. Rev. 146, 804 (1966)

MERIWETHER, J. R. (See Harvey, B. G., UCRL-16573)

MERIWETHER, J. R. (See Hendrie, D. L., UCRL-16664A)

MILLERON, N.
Some recent developments in vacuum technique for accelerators
UCRL-17296A, November 1966
1967 Particle Acceleration Conference, Washington, D. C., March 1-3, 1967

MILLERON, N.
Tests of pumps, mass filters, He detectors and fail safe vacuum components for the omnitron accelerator
UCRL-16947A, June 1966
American Vacuum Society Symposium, San Francisco, October 26-28, 1966

MOSS, J., and G. C. Ball
Energy resolution in cyclotron experiments
UCRL-17124, September 1966

MÜLLER, W., and R. M. Diamond
The extraction of hydrohalic acids by trilaurylamine
UCRL-16736, February 1966
J. Phys. Chem. 70, 3469 (1966)

NEWMAN, R., and C. R. Wilke
Fluid phase mass transfer in dialysis
UCRL-17117, September 1966
M.S. Thesis

NEWTON, A. S.
Metastable ion peak shapes in Dempster-type mass spectrometers
UCRL-16483 Rev, January 1966
J. Chem. Phys. 44, 4015 (1966)

NEWTON, A. S., and A. F. Sciamanna
Metastable peaks in the mass spectra of N_2O and NO_2
UCRL-16567 Rev, February 1966
J. Chem. Phys. 44, 4327 (1966)

NEWTON, A. S., A. F. Sciamanna, and R. Clampitt
Surface-induced transitions in highly excited noble gas ions and quasimetastable peaks in the mass spectra of the noble gases
UCRL-17187, October 1966
J. Chem. Phys.

NEWTON, J. O., F. S. Stephens, R. M. Diamond, K. Kotajima, and E. Matthias
Angular distributions of γ rays produced in reactions with heavy ions
UCRL-17204, October 1966
Nucl. Phys.

NEWTON, J. O., F. S. Stephens, and R. M. Diamond
The rotational states of ^{184}Os, ^{186}Os, and ^{188}Os
UCRL-17205, October 1966
Nucl. Phys.

NIX, J. R.
The normal modes of oscillation of a uniformly charged drop about its saddle-point shape
UCRL-16786, April 1966
Ann. Phys.

NOVAKOV, T.
M1-E2 mixing from L subshell conversion ratios
"Internal Conversion Processes," ed. by Joseph H. Hamilton (Academic Press Inc., New York, 1966) p. 497

NURMIA, M. J., K. J. Valli, and E. K. Hyde
Alpha spectroscopy of neutron deficient isotopes of emanation
UCRL-17081A, August 1966
Meeting of the American Physical Society, Mexico City, August 29-31, 1966

NURMIA, M. J. (See Hyde, E. K., UCRL-16963A)

NURMIA, M. J. (See Valli, K. J. UCRL-16735)

PEHL, R. H., D. A. Landis, and F. S. Goulding
Detection of high energy protons by thin-window lithium-drifted germanium counters
UCRL-16722, February 1966
IEEE Trans. Nucl. Sci. 13, 274 (1966)

PEHL, R. H. (See Cerny, J., UCRL-16705)

PEHL, R. H. (See Détraz, C., UCRL-16956)

PELLISSIER, P. (See Clark, D. J., UCRL-16794)

PERLMAN, I. (See Clarkson, J. E., UCRL-16974)

PERLMAN, I. (See Hollander, J. M., UCRL-17013)

PERLMAN, I. (See Lederer, C. M., UCRL-16414)

PETTERSEN, R. C.
The x-ray crystallographic structure determination of various compounds
UCRL-16975, July 1966
Ph. D. Thesis

POGGENBURG, J. K. (See Lederer, C. M., UCRL-16414)

POSKANZER, A. M., S. W. Cosper, E. K. Hyde, and J. Cerny
New isotopes: ^{11}Li, ^{14}B, and ^{15}B
UCRL-17267, November 1966
Phys. Rev. Letters

PRUSSIN, S. G. (See Lamb, J. F., UCRL-16600)

PRUSSIN, S. G. (See Yamazaki, T., UCRL-17260A)

PUGH, H. G., D. L. Hendrie, M. Chabre, E. Boschitz, and I. E. McCarthy
The ^{12}C(p, 2p)^{11}B reaction at 50 MeV
UCRL-16913, August 1966
Phys. Rev.

PUGH, H. G. (See Springer, A., UCRL-16620)

RASMUSSEN, J. O.
Conference summary
"Internal conversion processes," ed. by Joseph H. Hamilton (Academic Press, Inc., New York, 1966) p. 574

RASMUSSEN, J. O., and T. T. Sugihara
Gamma-ray yields from nuclear reactions and level densities of deformed nuclei
UCRL-16916, June 1966
Phys. Rev. 151, 992 (1966)

RASMUSSEN, J. O., and C. W. Ma
The moment-of-inertia of the high spin rotational states of deformed nuclei
UCRL-17234A, October 1966
Meeting of the American Physical Society, Stanford, California, December 28-30, 1966

RASMUSSEN, J. O. (See Bernthal, F. M., UCRL-17243A)

RASMUSSEN, J. O. (See Hollander, J. M., Phys. Today 19, 58 (1966))

RASMUSSEN, J. O. (See Johns, O., UCRL-17242A)

RASMUSSEN, J. O. (See Lederer, C. M., UCRL-16414)

RASMUSSEN, J. O. (See Rauscher, E., UCRL-16351)

RASMUSSEN, J. O. (See Watson, R. L., UCRL-16563A)

RAUSCHER, E., J. O. Rasmussen, and K. Harada
Coupled channel α-decay rate theory applied to ^{212m}Po
UCRL-16351, October 1966
Nucl. Phys.

REED, M. (See Mangelson, N., UCRL-16688A)

REED, M. (See Mangelson, N., UCRL-16849)

REED, M. (See Mangelson, N., UCRL-16850)

REYNOLDS, F. L.
Fabrication of single crystal tungsten ribbon filaments
UCRL-16903, June 1966
Rev. Sci. Instr.

ROOK, J. R.
Absolute cross sections for triton and ^{3}He induced reactions
UCRL-17119, September 1966
Nucl. Phys.

RUST, F. G., and C. R. Wilke
The dispersion of bacteria
UCRL-17208, October 1966
M. S. Thesis

SAKAI, M. (See Yamazaki, T., UCRL-16636)

SCIAMANNA, A. F. (See Newton, A. S., UCRL-16567 Rev)

SCIAMANNA, A. F. (See Newton, A. S., UCRL-17187)

SHELINE, R. K. (See Kern, J., UCRL-16598)

SHIELD, E. (See Slobodrian, R. J., UCRL-16991)

SHIRLEY, D. A.
Hyperfine fields at solutes in Fe, Co, and Ni
UCRL-16836A, April 1966
10th International Conference on Low Temperature Physics, Moscow, August 31-September 6, 1966

SHIRLEY, D. A.
Mössbauer spectroscopy in the heavy elements
UCRL-16621, January 1966
Chapter IX of "Chemical application of the Mössbauer effect"

SHIRLEY, D. A.
Thermal equilibrium nuclear orientation
UCRL-16764, March 1966
Ann. Rev. Nucl. Sci. 16, 89 (1966)

SHIRLEY, D. A. (See Matthias, E., UCRL-16683A)

SHIRLEY, D. A. (See Matthias, E., UCRL-16779)

SHIRLEY, D. A. (See Matthias, E., UCRL-16810A)

SHIRLEY, D. A. (See Matthias, E., UCRL-16818)

SHIRLEY, D. A. (See Wickman, H. H., UCRL-16669)

SHIRLEY, D. A. (See Wickman, H. H., J. Appl. Phys. 37, 1246 (1966))

SHIRLEY, V. S. (See Hamilton, J. H., Nucl. Data, Section A, 1, 521 (1966))

SIIVOLA, A.
Alpha active iridium isotopes
UCRL-17298, November 1966
Nucl. Phys.

SIKKELAND, T., J. E. Clarkson, D. F. Lebeck, and A. Ghiorso
On the production of nuclides in the region of Z=126 and N=184
UCRL-16773, April 1966
J. Inorg. and Nucl. Chem. Letters

SIKKELAND, T.
On the synthesis of super heavy nuclei
UCRL-16819A, April 1966
International Symposium on Why and How Should We Investigate Nuclides Far Off the Stability Line? Lysekil, Sweden, August 21-27, 1966

SISSON, D. H. (See Hyde, E. K., UCRL-16845)

SLOBODRIAN, R. J.
Extended electromagnetic structure effects on low-energy proton-proton scattering
UCRL-16322 Rev, January 1966
Phys. Rev. 145, 766 (1966)

SLOBODRIAN, R. J.
The $^1S_0$ p-p scattering parameters obtained from a reanalysis of experimental data
UCRL-16690, February 1966
Nucl. Phys. 85, 33 (1966)

SLOBODRIAN, R. J., H. E. Conzett, E. Shield, and W. F. Tivol
Proton-proton scattering between 4.2 and 10 MeV and the $^1S_0$ shape dependent scattering parameters
UCRL-16991, July 1966
International Conference on Nuclear Physics, Gatlinburg, Tennessee, September 12-17, 1966

SLOBODRIAN, R. J., D. J. Clark, J. S. C. McKee, W. F. Tivol, and T. A. Tombrello
The 2p final-state interaction in the $^3He(^3He, \alpha)2p$ reaction
UCRL-17233A, October 1966
Meeting of the American Physical Society, Stanford, California, December 28-30, 1966

SLOBODRIAN, R. J. (See McKee, J. S. C., UCRL-17239A)

SLOBODRIAN, R. J. (See Tivol, W. F., UCRL-17238A)

SLOBODRIAN, R. J. (See Tombrello, T. A., UCRL-17232A)

SMITH, B. H. (See Clark, D. J., UCRL-16794)

SMITH, B. H. (See Ghiorso, A., UCRL-16839)

SPENCE, D. A. (See Ghiorso, A., UCRL-17162)

SPRINGER, A., M. Chabre, D. L. Hendrie, and H. G. Pugh
Comparison of the elastic scattering of ^3He and ^4He by ^{40}Ca
UCRL-16620, January 1966
Phys. Letters

STEPHENS, F. S. (See Burde, J., UCRL-16163)

STEPHENS, F. S. (See Burde, J., UCRL-16734)

STEPHENS, F. S. (See Burde, J., UCRL-17067)

STEPHENS, F. S. (See Clarkson, J. E., UCRL-16974)

STEPHENS, F. S. (See Diamond, R. M., UCRL-17143)

STEPHENS, F. S. (See Newton, J. O., UCRL-17204)

STEPHENS, F. S. (See Newton, J. O., UCRL-17205)

STRUBLE, G. L.
A quasiparticle model for ^{140}La
UCRL-16692, February 1966
Phys. Rev.

STRUBLE, G. L. (See Kern, J., UCRL-16598)

TEMPLETON, D. H. (See Zalkin, A., UCRL-16629)

TEMPLETON, D. H. (See Zalkin, A., UCRL-16743)

TEMPLETON, D. H. (See Zalkin, A., UCRL-16813)

THOMPSON, S. G. (See Kapoor, S. S., UCRL-16706)

THOMPSON, S. G. (See Watson, R. L., UCRL-16563A)

TIVOL, W. F., D. J. Clark, H. E. Conzett, J. S. C. McKee, and R. J. Slobodrian
Proton-^{3}He polarization in the range from 10 to 20 MeV
UCRL-17238A, October 1966
Meeting of the American Physical Society, Stanford, California, December 28-30, 1966

TIVOL, W. F. (See McKee, J. S. C., UCRL-17239A)

TIVOL, W. F. (See Slobodrian, R. J., UCRL-16991)

TIVOL, W. F. (See Slobodrian, R. J., UCRL-17233A)

TOMBRELLO, T. A., and R. J. Slobodrian
The ^{3}He(^{3}He, t)3p reaction at 44 MeV
UCRL-17232A, October 1966)
Meeting of the American Physical Society, Stanford, California, December 28-30, 1966

TREYTL, W., and K. J. Valli
Alpha decay of neutron deficient astatine isotopes
UCRL-17194, October 1966
Nucl. Phys.

VALE, J. T. (See Clark, D. J., UCRL-16882)

VALENTIN, J. (See Harvey, B. G., UCRL-17303)

VALENTIN, J. (See Hendrie, D. L., UCRL-16664A)

VALLI, K. J., M. J. Nurmia, and E. K. Hyde
Alpha decay properties of neutron deficient isotopes of emanation
UCRL-16735 Rev, December 1966
Phys. Rev.

VALLI, K. J. (See Hyde, E. K., UCRL-16963A)

VALLI, K. J. (See Nurmia, M. J., UCRL-17081A)

VALLI, K. J. (See Treytl, W., UCRL-17194)

VERMEULEN, T., J. S. Moon, A. Hennico, and T. Miyauchi
Axial dispersion in extraction column performance
UCRL-17160, September 1966
Chem. Eng. Progr. 62, 95 (1966)

VOELKER, F. (See Ghiorso, A., UCRL-17162)

WASAN, D. T., and C. R. Wilke
Role of concentration level of the nondiffusing species in turbulent gas-phase mass transfer at ordinary mass transfer rates
UCRL-16221, January 1965
A. I. Ch. E. J.

WATSON, R. L.
A study of the internal conversion electrons emitted within three nanoseconds after the spontaneous fission of ^{252}Cf
UCRL-16798, July 1966
Ph. D. Thesis

WATSON, R. L., H. R. Bowman, S. G. Thompson, and J. O. Rasmussen
Gamma ray and internal conversion electron studies of primary ^{252}Cf fission fragments
UCRL-16563A, December 1965
Meeting of the American Chemical Society, Pittsburgh, March 28-31, 1966

WICKMAN, H. H., I. Nowick, J. H. Wernick, D. A. Shirley, and R. B. Frankel
Hyperfine fields and isomer shifts in magnetically ordered europium compounds
J. Appl. Phys. 37, 1246 (1966)

WICKMAN, H. H., M. P. Klein, and D. A. Shirley
Paramagnetic hyperfine structure and relaxation effects in Mössbauer spectra: ^{57}Fe in ferrichrome A
UCRL-16669, April 1966
Phys. Rev.

WILKE, C. R. (See Bhagat, A. K., UCRL-16574)

WILKE, C. R. (See Brelvi, W., UCRL-16865)

WILKE, C. R. (See Charron, R. H., UCRL-16945)

WILKE, C. R. (See Edwards, V. H., UCRL-16951A)

WILKE, C. R. (See Newman, R., UCRL-17117)

WILKE, C. R. (See Rust, F. G., UCRL-17208)

WILKE, C. R. (See Wasan, D. T., UCRL-16221)

WILLIX, R. L. S., and W. M. Garrison
Reductive deamination reactions in irradiated solution: factors influencing the reactivities of amino acids, peptides, and related compounds
UCRL-16647A, January 1966
3rd International Congress of Radiation Research, Cortina, Italy, June 26-July 2, 1966

YAMAZAKI, T., and D. L. Hendrie
Angular distributions of γ rays emitted in $^{197}Au(p, 2n)^{196}Hg$ and $^{197}Au(p, 4n)^{194}Hg$ reactions
UCRL-16987, July 1966
International Conference on Nuclear Physics, Gatlinburg, Tennessee, September 12-17, 1966

YAMAZAKI, T.
Clebsch-Gordan coefficients for nuclear transition probabilities for even deformed nuclei
UCRL-16784, March 1966
Nucl. Data, Section A, 1, 453 (1966)

YAMAZAKI, T., and J. M. Hollander
Energy levels of ^{237}Np: II. High resolution study of transitions in the decay of ^{237}U
UCRL-16577, January 1966
Nucl. Phys. 84, 505 (1966)

YAMAZAKI, T., and D. L. Hendrie
Gamma-vibrational bands in ^{182}Os and ^{184}Os
UCRL-16986, July 1966
International Conference on Nuclear Physics, Gatlinburg, Tennessee, September 12-17, 1966

YAMAZAKI, T., G. T. Ewan, and S. G. Prussin
Isomeric states in the 5~200 nsec range populated by nuclear reactions
UCRL-17260A, November 1966
Meeting of the American Physical Society, New York, January 30-February 2, 1967

YAMAZAKI, T., J. Sato, Y. Yokoyama, S. Baba, H. Ikegami, and M. Sakai
Levels of ^{188}Os populated by ^{188}Re and ^{188}Ir
UCRL-16996, July 1966
International Conference on Nuclear Physics, Gatlinburg, Tennessee, September 12-17, 1966

YAMAZAKI, T., and J. M. Hollander
Levels of ^{237}Np populated by ^{237}U
UCRL-16682A, February 1966
Bull. Am. Phys. Soc. 11(EB5), 352 (1966)

YAMAZAKI, T., M. Sakai, and O. Mikoshiba
Nature of the K=2 states in even deformed nuclei
UCRL-16636, April 1966
Phys. Letters

YAMAZAKI, T.
Tables of coefficients for angular distribution of γ rays from aligned nuclei
UCRL-17086, August 1966
Nucl. Data

YAMAZAKI, T. (See Jenkins, D. A., UCRL-16855)

ZALKIN, A., T. E. Hopkins, and D. H. Templeton
The crystal structure of $(B_9C_2H_{11})Re(CO)_3Cs$
UCRL-16629, January 1966
Inorg. Chem. 5, 1189 (1966)

ZALKIN, A., T. E. Hopkins, and D. H. Templeton
The crystal structure of chlorothiodiazyl chloride, $S_3N_2Cl_2$
UCRL-16813, April 1966
Inorg. Chem. 5, 1767 (1966)

ZALKIN, A., J. D. Forrester, and D. H. Templeton
Ferrichrome-A tetrahydrate. Determination of crystal and molecular structure
UCRL-16743, February 1966
J. Am. Chem. Soc. 88, 1810 (1966)

2. CONTRIBUTIONS TO THIS REPORT

ADAMSON, M. G.
G. 16, 17

AHMAD, I.
J. 1

AJZENBERG-SELOVE, F.
B. 8, 9

ALI, D.
G. 15

ARMSTRONG, L., Jr.
G. 15

ASARO, F.
A. 2

ATKINS, H. L.
G. 25

BABA, H.
D. 6

BABA, S.
A. 23

BALL, G. C.
B. 12, 13

BANSAL, B. M.
J. 2

BARCLAY, J. A.
E. 7

BAUMGARTNER, E.
B. 5

BAYBARZ, R. D.
G. 7

BENNETT-CORNIEA, W.
G. 22, 25

BERNTHAL, F. M.
A. 3

BHAGAT, A. K.
H. 6
J. 3

BIERLEIN, F.
I. 6

BOWMAN, H. R.
A. 15
I. 11

BRELVI, W.
G. 6
J. 4

BRITT, H. C.
D. 7

BROMLEY, L. A.
G. 6

BRUNNADER, H.
I. 7

BURDE, J.
A. 16

BURGER, R.
I. 2

BURNETT, D. S.
D. 7

BUTLER, G. W.
B. 11
I. 7

BYERS, C. H.
H. 2, 4
J. 5

CARNALL, W. T.
G. 7, 8

CARNEIRO, A. R.
I. 6

CERNY, J.
A. 11
B. 10, 11, 12, 13, 14
D. 3
I. 7

CHARRON, R. H.
H. 8
J. 6

CLAMPITT, R.
F. 1, 2, 3

CLARK, D. J.
B. 1, 2, 3
I. 1, 2, 3

CLARK, M. W.
H. 2

CLARKSON, J. E.
A. 17

CLEM, R. G.
G. 3

CLOSE, E.
I. 2, 3

COCHRAN, W. R.
G. 10

COHEN, D.
G. 7

COLEMAN, E.
C. 5

CONWAY, J. G.
E. 8
G. 7, 8, 9, 10

CONZETT, H. E.
B. 1, 4, 5
I. 5

COOPER, J.
J. 7

CORDI, R. C.
I. 13

COSPER, S. W.
A. 11
B. 11
D. 3
I. 7

CROWDER, W. L.
I. 18

CUNNINGHAM, B. B.
G. 1

DÉTRAZ, C.
B. 10, 11

DIAMOND, R. M.
A. 16, 17, 18, 19

EASLEY, W. C.
E. 7
G. 11
I. 20

EDELSTEIN, N.
E. 5, 6
G. 11, 12

EDWARDS, V. H.
I. 25

ELAD, E.
I. 17

ELO, D.
I. 6

EWAN, G. T.
A. 24, 25

FADLEY, C. S.
G. 2

FIELDS, P.
G. 8

FRANCO, V.
C. 2, 3, 4, 5

FRIED, S.
G. 8

FUJITA, D. K.
I. 10

GARRISON, W. M.
G. 22, 23, 24, 25

GATTI, R. C.
D. 3, 4, 5

GHIORSO, A.
A. 12, 13, 14

GILAT, J.
A. 5

GILBERT, A.
C. 11

GLAUBER, R. J.
C. 4

GLENDENNING, N. K.
C. 6, 7, 8

GOTH, G. W.
B. 14

GOULDING, F. S.
B. 11
I. 7, 12, 13, 14

GREEN, J. L.
J. 8

GRUBER, J. B.
G. 10

GRUNDER, H. A.
I. 3

GUTMACHER, R. G.
G. 7, 8

HADEISHI, T.
G. 15

HAGSTROM, S. B. M.
G. 2

HARVEY, B. G.
B. 6, 7, 15, 16, 17, 18
C. 7
I. 8

HAUSMANN, E. D.
G. 21

HAVERFIELD, A. J.
A. 3
J. 9

HEBERT, A. J.
G. 14

HENDRIE, D. L.
A. 20, 22
B. 15, 16, 17, 18
C. 7

HINTZ, R.
I. 15

HOLIAN, J.
G. 23, 24

HOLLANDER, J. M.
A. 1, 3
G. 2

HOLLIDAY, R. J.
E. 1

HOLLOWELL, C. D.
G. 14
J. 10

HOPKINS, T. E.
G. 16, 17, 18, 19, 20

HUFFMAN, E. H.
G. 3

HUIZENGA, J. R.
D. 5

HULET, E. K.
E. 8
G. 7

HYDE, E. K.
A. 6, 7, 8, 9, 11

IKEGAMI, H.
A. 23

JARED, R. C.
A. 15

JARVIS, O. N.
B. 17, 18
C. 7

JAYKO, M. E.
G. 22

KAPOOR, S. S.
D. 6

KEENAN, T. K.
G. 7

KHODAI-JOOPARI, A.
J. 11

KIM, H.
I. 2, 3, 4

KING, C. J.
G. 21
H. 2, 4, 5

KLEIN, M. P.
E. 6
G. 2

KORNER, H. J.
E. 5

LAMB, J. F.
G. 4, 5

LANDIS, D. A.
B. 11
I. 12, 13

LAPIERRE, R.
I. 19, 20, 21

LATIMER, R. M.
G. 8

LEDERER, C. M.
A. 1, 2

LEE, D. M.
G. 4, 5

LOTHROP, R. P.
I. 14

LOUGHEED, R.
E. 8
G. 7

LOVAS, F. J.
G. 14

LU, C. C.
B. 6, 8, 9

MAERTENS, W. A.
I. 13

MAHONEY, J.
B. 15, 17, 18
C. 7

MALONE, D. F.
I. 13

MALY, J.
A. 13
C. 9

MANGELSON, N. F.
B. 7, 8, 9

MAPLES, C.
B. 14

MARKOWITZ, S. S.
G. 4, 5

MARRUS, R.
G. 13

MATTHIAS, E.
A. 4, 19
E. 1, 2, 3, 4, 5, 6

MCCOLM, D.
G. 13

MCGRATH, R. L.
I. 7

MCKEE, J. S. C.
B. 1, 2, 3

MCLAUGHLIN, R.
G. 8, 11, 12

MELDNER, H.
C. 10

MERIWETHER, J. R.
B. 15

MILLER, S. F.
H. 5

MINER, C. E.
I. 16

MORETTO, L. G.
D. 4, 5

MORSS, L. R.
I. 10

MOSS, J. M.
I. 8

NAKAMURA, M.
I. 17, 18, 19

NEWMAN, R. D.
H. 3
J. 12

NEWTON, A. S.
F. 1, 2, 3

NEWTON, J. O.
A. 18, 19

NICOL, A. T.
G. 10

NIX, J. R.
C. 9
D. 1, 2

NURMIA, M. J.
A. 9, 13, 14

OLSEN, B. A.
E. 2

PARSONS, R.
I. 15

PEHL, R. H.
B. 10, 11
I. 12, 13

PELLISSIER, P.
I. 3

PERLMAN, I.
A. 1, 2, 17

PETERSON, J. R.
G. 1

PETTERSEN, R. C.
J. 13

PLASIL, F.
D. 7

POGGENBURG, J. K.
A. 2

POSKANZER, A. M.
A. 11

PRUSSIN, S. G.
A. 25

RAJNAK, K.
G. 9

RASMUSSEN, J. O.
A. 2
D. 5, 8, 9
I. 11

REED, M. F.
B. 8, 9, 16

ROSENBLUM, S. S.
E. 3

RUST, F. G.
H. 7
J. 14

SAKAI, M.
A. 23

SATO, J.
A. 23

SAUCEDO, G. I.
I. 13

SAXTON, J. A.
H. 1

SCIAMANNA, A. F.
F. 2, 3

SHIELD, E.
B. 1, 4, 5

SHIRLEY, D. A.
E. 3, 4, 5, 6, 7
G. 2

SIKKELAND, T.
A. 12, 13, 14

SLOBODRIAN, R. J.
B. 1, 2, 3, 4, 5
C. 1

SMITH, B. H.
I. 3

SOKOL, H. A.
G. 22

STEPHENS, F. S.
A. 16, 17, 18, 19

STREET, K., Jr.
G. 14

STRUTHERS, D. R.
I. 9

TAKEKOSHI, E.
D. 10

TEMPLETON, D. H.
G. 16, 17, 18, 19, 20

THOMPSON, S. G.
A. 15
D. 4, 5, 6, 7, 9, 10
I. 11

TIVOL, W. F.
B. 1, 2, 3, 4, 18

TOMBRELLO, T. A.
B. 3

TREYTL, W. J.
A. 4, 5, 6, 7, 8, 10

VALENTIN, J.
B. 17

VALLI, K.
A. 6, 7, 8, 9, 10

VERMEULEN, T.
H. 1, 5

VOGELSBERG, F. E.
I. 18

WATSON, R. L.
A. 15
D. 8
I. 11
J. 15

WEEKS, B. M.
G. 22

WHITE, R.
G. 12

WILBER, D. A.
I. 22

WILHELMY, J. B.
A. 15
D. 9

WILKE, C. R.
H. 3, 6, 7, 8
I. 25

WONG, J. L.
I. 6

WORDEN, E. F.
E. 8

YAMAZAKI, T.
A. 20, 21, 22, 23, 24, 25

YELLIN, J.
G. 13

YOKOHAMA, Y.
A. 23

ZALKIN, A.
G. 16, 17, 18, 19, 20

ZANE, R.
I. 21, 22, 23, 24

This report was prepared as an account of Government sponsored work. Neither the United States, nor the Commission, nor any person acting on behalf of the Commission:

A. Makes any warranty or representation, expressed or implied, with respect to the accuracy, completeness, or usefulness of the information contained in this report, or that the use of any information, apparatus, method, or process disclosed in this report may not infringe privately owned rights; or

B. Assumes any liabilities with respect to the use of, or for damages resulting from the use of any information, apparatus, method, or process disclosed in this report.

As used in the above, "person acting on behalf of the Commission" includes any employee or contractor of the Commission, or employee of such contractor, to the extent that such employee or contractor of the Commission, or employee of such contractor prepares, disseminates, or provides access to, any information pursuant to his employment or contract with the Commission, or his employment with such contractor.